Factorization and Resummation
for Precision Physics at the LHC

Dissertation

zur Erlangung des Doktorgrades
an der Fakultät für Mathematik,
Informatik und Naturwissenschaften

Fachbereich Physik

der Universität Hamburg

vorgelegt von

JOHANNES MICHEL

Hamburg

2020

For Ruth, whose time to explore this world has only just begun.

Abstract

The LHC precision program aims to more thoroughly test the Standard Model of particle physics than ever before. Precise theory predictions for realistic experimental observables are a key ingredient in this program. Experimental observables that are sensitive to radiation in the soft and/or collinear limit of Quantum Chromodynamics often admit a factorization into simpler pieces that encode the dynamics at different scales. Factorization in turn enables the use of the renormalization group to predict, at fixed order, or resum, to all orders in perturbation theory, contributions from large logarithms that can dominate the cross section.

In this thesis we derive new factorization results for hadronic collisions using the language of Soft-Collinear Effective Theory. These results extend and improve existing resummation methods, in particular towards a more detailed description of the final state. We extend the standard jet p_T (jet veto) resummation into a systematic framework that accounts for a finite jet rapidity cut up to which jets are reconstructed, as required by the finite detector acceptance in experiments. We also consider the case of a step in the veto parameter at some value of rapidity, which is of experimental relevance to avoid the increased contamination from unsuppressed pile-up beyond the reach of the tracking detectors. We next consider the production cross section for a Z boson differential in the Z boson transverse momentum p_T^Z and the 0-jettiness event shape $\mathcal{T}_0$. We perform, for the first time, the simultaneous analytic resummation of all large logarithms in both p_T^Z and $\mathcal{T}_0$ at NNLL+NLO, and present the first analytic predictions for a Sudakov peak in two independent resolution variables in pp collisions. We present and prove a generalization of the classic soft threshold factorization theorem that holds in the limit where only one proton is probed at a large momentum fraction by the hard process and collinear radiation into the final state is kinematically still allowed. This is a much weaker limit than the standard soft limit of taking both momentum fractions to one. At the partonic level, the new factorization theorem captures all singular terms in the partonic cross section, including in particular off-diagonal partonic channels. As a first illustrative example of its many applications, we use it to derive a nontrivial set of terms in the N^{3}LO Drell-Yan rapidity spectrum. Using consistency relations with known soft matrix elements that in part arise from our new factorization theorem, we derive the leading eikonal terms at third order in perturbation theory for the q_T and $\mathcal{T}_0$ beam functions. Finally, we show how to perform the resummation of so-called fiducial power corrections in p_T^Z or p_T^W that arise from experimental measurements on the decay products of a Z or W boson. We find an improved agreement with precision ATLAS and CMS measurements of the p_T^Z and ϕ^* spectrum when including the resummation of these power corrections in cutting-edge N^{3}LL+NNLO predictions. Using the same approach, we present the first analytically resummed result for the lepton p_T^ℓ spectrum in W decays at N^{3}LL+NNLO.

Zusammenfassung

Präzisionsmessungen am LHC zielen darauf ab, das Standardmodell der Teilchenphysik in unerreichtem Detail zu testen. Eine Voraussetzung dafür sind präzise theoretische Vorhersagen für realistische experimentelle Messgrößen. Messgrößen, die sensitiv auf Abstrahlung im langwelligen oder kollinearen Grenzfall der Quantenchromodynamik sind, können häufig in einzelne Terme faktorisiert werden, die die Dynamik an unterschiedlichen Energieskalen beschreiben. Faktorisierung wiederum ermöglicht die Verwendung der Renormierungsgruppe, um dominante logarithmische Terme im Wirkungsquerschnitt entweder zu fester Ordnung in der Störungstheorie vorherzusagen oder zu allen Ordnungen zu resummieren.

In dieser Arbeit werden neue Faktorisierungsformeln für Hadronenkollisionen im Formalismus der *Soft-Collinear Effective Theory* hergeleitet. Diese Ergebnisse erweitern und verbessern die vorhandenen Resummationsmethoden insbesondere hin zu einer detaillierteren Beschreibungen des Endzustands der Kollision. Zunächst wird die übliche Resummation für den Transversalimpuls des energetischsten Jets, d.h. eines kollimierten Teilchenbündels, systematisch erweitert um den Effekt einer maximalen Jet-Rapidität, wie sie die geometrische Akzeptanz des Detektors erfordert. Dabei wird auch die Möglichkeit einer gelockerten Impulsschwelle berücksichtigt, die zur Vermeidung von Kontamination durch mehrere simultane Kollisionsereignisse in denjenigen Bereichen nützlich ist, in denen der Spurdetektor hierfür nicht mehr greift. Daraufhin wird der differentielle Wirkungsquerschnitt für die Produktion eines Z-Bosons als Funktion seines Transversalimpulses p_T^Z und der *0-Jettiness* Variable $\mathcal{T}_0$ berechnet, die hadronische Aktivität misst. Dies stellt die erste analytische, gleichzeitige Resummation aller dominanten Logarithmen von p_T^Z und $\mathcal{T}_0$ dar, in diesem Fall auf NNLL+NLO, und die erste analytische Vorhersage für ein Sudakov-Spektrum in zwei Variablen, die unabhängig voneinander Abstrahlungen in Proton-Proton-Kollisionen charakterisieren. Weiterhin wird die Verallgemeinerung eines klassischen Faktorisierungstheorems gezeigt, das Hadronenkollisionen knapp oberhalb der Energieschwelle für einen gegebenen Endzustand beschreibt. In der verallgemeinerten Fassung wird nur aus einem der zwei Protonen (statt im klassischen Fall aus beiden) ein großer Impuls- und Energieanteil in den Endzustand absorbiert, so dass kollineare Abstrahlung weiter möglich ist. Das neue Theorem beschreibt alle singulären Terme im partonischen Wirkungsquerschnitt und insbesondere den Beitrag nebendiagonaler Kanäle, also z.B. den Effekt kollinearer Paarerzeugung. Um die vielfältigen Anwendungen des Theorems zu veranschaulichen, wird eine Reihe nichttrivialer Terme im Rapiditätsspektrum des Drell-Yan-Prozesses auf N³LO hergeleitet. Darauf aufbauend werden Relationen zu bekannten Matrixelementen im niederenergetischen Grenzfall ausgenutzt, um die führenden Terme in der eikonalen Näherung kollinearer Proton-Matrixelemente auf N³LO herzuleiten. Zuletzt wird die Resummation von Korrekturen der Ordnung p_T^Z oder p_T^W hergeleitet, die durch eine Vermessung der Zerfallsprodukte des Z- or W-Bosons entstehen. Die Resummation dieser Terme verbessert die Übereinstimmung von Vorhersagen auf N³LL+NNLO mit präzisen Messungen der p_T^Z- und ϕ^*-Spektren in den ATLAS- und CMS-Experimenten. Analog wird das Transversalimpulsspektrum von Leptonen in W-Zerfällen zum ersten Mal auf N³LL+NNLO errechnet.

List of publications

Journal articles:

[1] M. A. Ebert, J. K. L. Michel and F. J. Tackmann, *Resummation Improved Rapidity Spectrum for Gluon Fusion Higgs Production*, JHEP **05** (2017) 088 [1702.00794].

[2] J. K. Michel, P. Pietrulewicz and F. J. Tackmann, *Jet Veto Resummation with Jet Rapidity Cuts*, JHEP **04** (2019) 142 [1810.12911].

[3] G. Lustermans, J. K. Michel, F. J. Tackmann and W. J. Waalewijn, *Joint two-dimensional resummation in q_T and 0-jettiness at NNLL*, JHEP **03** (2019) 124 [1901.03331].

Preprints:

[4] G. Lustermans, J. K. Michel and F. J. Tackmann, *Generalized Threshold Factorization with Full Collinear Dynamics*, 1908.00985.

[5] G. Billis, M. A. Ebert, J. K. Michel and F. J. Tackmann, *A Toolbox for q_T and 0-Jettiness Subtractions at N^3LO*, 1909.00811.

[6] M. A. Ebert, J. K. Michel, I. W. Stewart and F. J. Tackmann, *Drell-Yan q_T Resummation of Fiducial Power Corrections at N^3LL*, 2006.11382.

Contributions to conference proceedings:

[7] S. Amoroso et al., *Les Houches 2019: Physics at TeV Colliders: Standard Model Working Group Report*, in *11th Les Houches Workshop on Physics at TeV Colliders: PhysTeV Les Houches*, 3, 2020, 2003.01700.

In preparation:

[8] M. A. Ebert, J. K. L. Michel, F. J. Tackmann et al., *SCETlib: A C++ Package for Numerical Calculations in QCD and Soft-Collinear Effective Theory*, public version in development, webpage: `http://scetlib.desy.de`.

This thesis is based on the publications refs. [2–6], reflecting the author's contributions. The thesis also contains results from ongoing work in ref. [8].

Acknowledgements

Contents

List of figures

8 Conclusion and outlook   291

A Notation and conventions   299

B Hard scattering processes   305

C Anomalous dimensions   311

D Renormalization group evolution   315

E Fixed-order ingredients   319

F Analytic NLO rapidity spectra   325

G Additional numerical results   329

List of tables

List of acronyms

Pages with relevant material are listed after the entry where applicable.

Chapter 1

Introduction

The search for the fundamental building blocks of Nature has been driving scientific insight for centuries. Entire fields of science have branched off as the quest has moved on from electrons and atomic nuclei, held together by the electromagnetic interaction responsible for all of chemistry, to the protons and neutrons inside the nucleus described by nuclear physics. A milestone in this quest was reached in 2012 with the discovery of the Higgs boson at the Large Hadron Collider (LHC) [9, 10]. The Higgs boson was the last, long-expected piece in the Standard Model of particle physics [11–14], the theory of all known particles and (almost all) their interactions.

In the Standard Model (SM), the coupling to a field (the Higgs field) that permeates the visible universe is responsible for the masses of the fundamental particles that propagate through it. The technical implementation of this idea in terms of a spontaneously broken symmetry is called the Brout-Englert-Higgs (BEH) mechanism [15–18]. Importantly, the rate to produce a Higgs boson at the LHC, i.e., to trigger a quantum excitation of the Higgs field, precisely depends on the coupling of the Higgs field to the other particles that interact with it, which by the BEH mechanism is tied to their mass.[1] These relations between production rates and particle masses are so far found to be consistent with experimental results [19–22]. It is quite thrilling that the Higgs boson, a cornerstone of the SM, was only experimentally confirmed more than 40 years after it was proposed. A non-discovery of the Higgs boson at the LHC could well have brought down the whole edifice of the SM; instead, it withstood the test in a triumph of human ingenuity and international cooperation.

Yet we have good evidence that the SM cannot be the fundamental theory of Nature. For one, the observation of neutrino oscillations [23, 24] implies that neutrinos, contrary to the SM expectation, must have distinct, nonzero masses. More fundamentally, it is unclear how to unify the SM with General Relativity, the theory of gravity, in a consistent theoretical framework at energies near the so-called Planck scale $M_{\mathrm{Pl}} \approx 10^{19}\,\mathrm{GeV}$ where effective gravitational interactions between SM particles become an $\mathcal{O}(1)$ effect. (It is also unclear how to empirically *test* such a unification; for comparison, the Higgs boson was discovered in proton-proton collisions at center-of-mass energies $E_{\mathrm{cm}} = 7\,\mathrm{TeV} = 7000\,\mathrm{GeV}$ and its mass is now measured to be $m_H = 125.18 \pm 0.16\,\mathrm{GeV}$ [25].) Lastly, there are unexplained deviations in astronomical observations from galactic to cosmological scales when compared to the predictions of General Relativity, if only the particle content of

---

[1]That humanity can cause such an excitation in the lab, even just for a brief time, may fill those so inclined with a sense of immense wonder.

the SM is assumed. These deviations point to new degrees of freedom known as Dark Matter. *If* the Dark Matter is of particle nature, and *if* it does not just have gravitational interactions, it may leave an imprint in low-energy detection experiments or be produced at the LHC. In any case it is unaccounted for in our current description of Nature.

These phenomena motivate the, admittedly rather open, search for phenomena *beyond* the Standard Model (BSM). This search is made challenging by the fact, very much a mixed blessing, that the Standard Model in isolation and without the effects of gravity is in principle valid at any energy scale. More specifically, its interactions are *self-similar* at every energy scale, with the coupling strengths at different scales related to each other by a calculable pattern known as *renormalization*. Thus there is no indication from the theory itself at what energies we should look for new phenomena. Likewise, searches for new resonances, i.e., the excitation of new degrees of freedom, at the energies directly accessible at the LHC have so far returned empty-handed [26–29].

Precision measurements at the LHC

In this situation, a strategy that maximizes the machine potential of the LHC is that of *precision measurements*, i.e., to hunt for small, indirect effects of high-energy physics. As a rule of thumb, the relative effect of new physics at a high energy scale Λ on an observable $\mathcal{O}$ measured on final states produced at the LHC, i.e., around the electroweak scale $\sim m_H$, scales as

$$\frac{\Delta\mathcal{O}}{\mathcal{O}} \sim \frac{m_H}{\Lambda}. \tag{1.1}$$

Thus to constrain new physics up to energies of $\sim 10\,\mathrm{TeV}$, we should measure $\mathcal{O}$ down to a percent; permille-level measurements may even constrain new physics up to energies of $\sim 100\,\mathrm{TeV}$, well beyond the direct energy reach of the LHC.

This undertaking is made possible on the experimental side by a huge effort in continuously upgrading and calibrating the LHC detectors to push down systematic uncertainties and faithfully reconstruct particles from the (sometimes subtle) traces they leave in the detector. Time itself also favors a precision program as relative statistic uncertainties roughly decrease as $1/\sqrt{N}$ as the data sample size N grows. E.g., the Higgs discovery was made at an integrated luminosity $\mathcal{L}_{\mathrm{int}} \propto N$ of $\mathcal{L}_{\mathrm{int}} \approx 10\,\mathrm{fb}^{-1}$, while the most recent measurements can already rely on $\approx 140\,\mathrm{fb}^{-1}$. Projections for the end of the high-luminosity LHC era put the achievable integrated luminosity at $3000\,\mathrm{fb}^{-1}$, after further upgrades to the machine to maximize the rate of collisions that are scheduled to be completed in 2027 [30].

A key role in precision measurements is played by first-principle theory predictions, i.e., calculations of observable quantities using the Lagrangian of the Standard Model as an input. In the most obvious case, they enter in a final interpretation step where predictions are compared to the experimental outcome to search for deviations. Often, theory input is also required during intermediate steps, e.g. when parameters first need to be determined from one data set to later predict another. In any of these cases it is mandatory that theory predictions are pushed at least to the same level of precision as the data so as not to limit
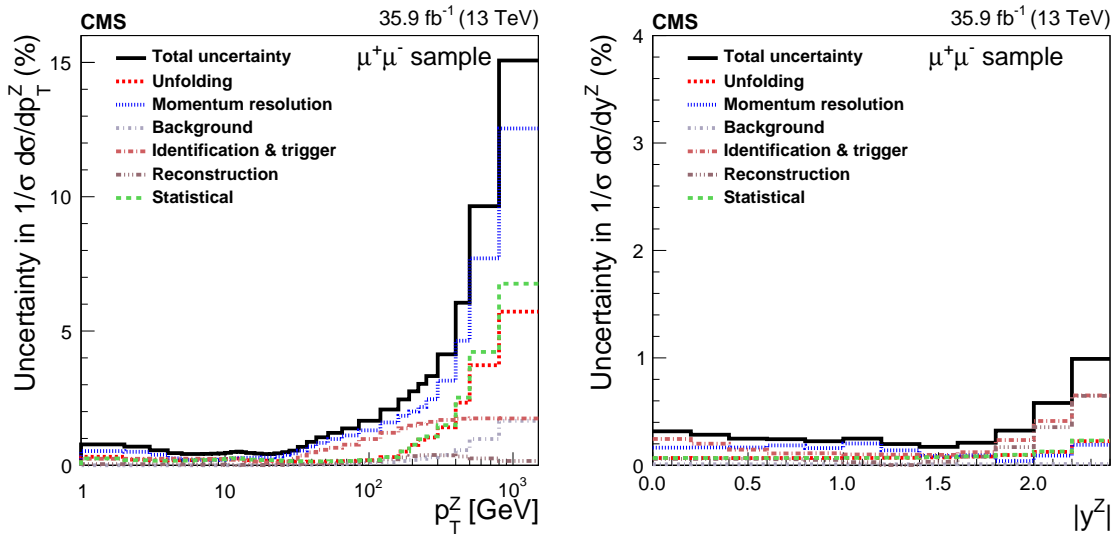
Figure 1.1: Breakdown of relative statistical and systematic uncertainties in the normalized transverse momentum spectrum (p_T^Z, left) and the rapidity spectrum (y_Z, right) of Z bosons decaying in the $\mu^+\mu^-$ channel as measured by the CMS collaboration at the LHC [31]. The actual data, rather than just their uncertainty, can be found in figure 7.14 for the p_T^Z spectrum, where we also compare to our predictions. A new tool to improve predictions for the y^Z spectrum is presented in chapter 5.

Both panels from ref. [31].

the experimental sensitivity. In particular, all approximations involved in the prediction must be well controlled and systematically improvable.

The challenge posed to theory is illustrated in figure 1.1: It shows the uncertainty budget of the normalized transverse momentum spectrum (p_T^Z, left) and the rapidity spectrum (y^Z, right) of Z bosons decaying in the $\mu^+\mu^-$ channel as measured by the CMS collaboration at the LHC [31]. The measurement reaches sub-percent precision in wide ranges of the spectra; a similar level of experimental precision for Z boson spectra has been reached in refs. [32–35].

Understanding spectra like these at the same level of precision from the theory side is crucial for several important physics goals of the LHC program. For the y^Z spectrum that encodes the distribution of Z bosons along the beam direction, this is immediately clear because it gives access to the longitudinal momentum fractions carried by the quarks and gluons, collectively called partons, that make up the proton. This is a piece of information that enters virtually any prediction for other LHC processes. To appreciate the importance of the p_T^Z spectrum, which we will deal with repeatedly in this thesis, let us take a step back and recall that in the SM the masses of all fundamental particles have a common origin in the BEH mechanism. In particular, a precise test of the SM can be constructed by considering the *ratio* of the Z boson mass to that of the W boson, its electrically charged counterpart. In the SM, this ratio is related, by the BEH mechanism, to the well-measured couplings of the Z and W to leptons. To constrain BSM physics using this ratio, we should measure the Z and W boson masses m_Z and m_W as precisely as possible.

3

This is challenging for the W because the W decays into a lepton (ℓ) and a neutrino (ν). The neutrino escapes the detector, so we cannot directly reconstruct the invariant mass $Q^2 = (p_\ell + p_\nu)^2$ of the pair to determine the position of the W resonance. Instead, one way to determine m_W at the LHC is to consider the transverse momentum p_T^ℓ of the detected lepton. If the W itself is produced with exactly zero transverse momentum $p_T^W = 0$, the maximum transverse momentum that the detected lepton can carry is $p_T^\ell \leq Q/2$. Combining contributions from Q slightly above and below the resonance, the p_T^ℓ spectrum develops a characteristic sharp peak at $p_T^\ell \approx m_W/2$, known as a Jacobian peak, from whose position m_W can be measured. Of course, in reality the W boson is never actually produced exactly at $p_T^W = 0$ because any additional bit of radiation from the colliding particles will recoil the W (and thus the ℓ) a bit in the transverse plane, smearing out the Jacobian peak. However, because the neutrino is lost, p_T^W cannot be measured to the precision required to account for the smearing, either. As a result, the systematic uncertainty due to the modelling of the p_T^W distribution is the largest uncertainty contribution in the recent ATLAS determination of m_W [36],

$$m_W = 80370 \pm 7_{\text{stat.}} \pm 11_{\text{exp. syst.}} \pm 14_{\text{modelling syst.}} \,\text{MeV} = 80370 \pm 19 \,\text{MeV} \qquad (1.2)$$

To maximize the new-physics reach of this permille-level measurement, we must address this uncertainty component.

This is the point where the p_T^Z spectrum above enters: The W and Z are so similar that if a prediction is successfully validated against the Z transverse momentum spectrum, it can be used to *predict* the p_T^W spectrum and therefore the precise amount of smearing in the Jacobian peak. More generally, a thorough theory calculation must also quantify the *dissimilarities* between the Z and W. If these are understood, we may also predict ratios of the two transverse momentum spectra, exploiting that correlated uncertainty components cancel, or fit the prediction to the Z spectrum first to determine universal parameters.[2]

For another example, we can consider the p_T^H spectrum of the Higgs boson itself. At small $p_T^H \ll m_H$, this spectrum is sensitive to the couplings of the Higgs boson to light quarks. These particles are too light, i.e., their couplings to the Higgs field are too small, to leave any imprint in total Higgs boson production rates, but the shape of their contributions to the spectrum is sufficiently characteristic that one can hope to disentangle them and measure the couplings, or at least constrain them to some multiple of their expected SM value [37]. This requires precise theory inputs not just for the light-quark signals, but in particular for the overwhelming background where the Higgs is produced through a quantum excitation of the much heavier top quark.

---

[2]We stress that for this later reason, precision analyses of this kind also serve another purpose that will be fruitful even in the short term: Much like chemistry, which has not suddenly been *solved* by the discovery of its microscopic origins in the electromagnetic interaction, there are unexplained phenomena *within* the Standard Model unrelated to the quest for more fundamental physics. These notably include the behavior of the strong force at low energies, where the fundamental quarks and gluons of the Standard Model form nonperturbative bound states like the proton. Precisely how this happens is still being explored, but determinations of the three-dimensional proton structure, as also required as ingredients for the p_T^W spectrum, will help shed light on this issue.

Theory predictions for the LHC

Producing first-principle theory predictions is, in general, hard. By the rules of quantum mechanics, we must include an in principle infinite set of degenerate final states that contribute to the observable in question. For example, for the p_T^Z spectrum we encountered earlier, there is no way of knowing against *how many* additional particles the Z boson recoiled to acquire the measured p_T^Z. To be able to compute anything in the first place, we use *perturbation theory*, relying on the fact that the probability for an additional particle to be emitted is suppressed by a factor of the coupling strength between particles. Even for Quantum Chromodynamics (QCD), the theory of the strong interactions, the coupling strength $\alpha_s \sim 0.1$ at typical LHC energies justifies such an expansion. For a given cross section σ, i.e., the total probability for a given process to occur, it takes the form

$$\sigma = \sigma^{(0)} + \alpha_s \, \sigma^{(1)} + \alpha_s^2 \, \sigma^{(2)} + \dots . \tag{1.3}$$

The first term is referred to as the leading-order (LO) cross section, the second-term as the next-to-leading-order (NLO) correction, and so forth. The series can be truncated when the precision requirement is met. At any given order, we still need to integrate over the possible momenta of intermediate particles, e.g., there are many ways for two particles with momenta $\vec{p}_T^{1,2}$ in the transverse plane to give a total recoil of $p_T^Z = |\vec{p}_T^1 + \vec{p}_T^2|$ to a Z boson, but at least only a finite *number* of particles need to be considered at every order in perturbation theory.

As we have seen, first-principle theory predictions enter precision measurements at the LHC in various ways. Depending on the use case, they typically come in one of the following three forms:

(A) Analytic predictions. Here the experimental measurement is sufficiently simple and well-defined that the integral over the momenta of intermediate particles at a given order can be evaluated analytically.

(B) Fully-differential predictions. In this case any measurement may be specified by the user, but only in terms of the momenta of the (few) particles present at a given order in perturbation theory. The remaining integrals are then performed numerically.

(C) Event-level predictions that provide the user with a fully realistic list of particles and their momenta (an event record), as would be obtained from a real-life collision. The measurement is implemented by generating and binning a large sample of events.

Clearly, the versatility of the prediction and its ability to describe the real-life experiment increase from (A) to (C). On the other hand, the complexity of the calculation at a given order increases as well, both in terms of organizing and understanding the calculation and in terms of the numerical cost to evaluate it on computers.

Soft and collinear limits

A challenge common to the computation of radiative corrections in all three approaches is that in QCD, the probability for an additional emission *diverges* in the limit where the

emitted particle either becomes soft, i.e., carries little energy compared to the emitter, or collinear, i.e., is emitted at a small angle.

To make this more precise, let us denote by z the energy fraction carried by the emitted particle, such that the emitter retains a fraction $1 - z$, and let θ be the angle between the two. Then the differential emission probability in the limit where both $z \to 0$ and $\theta \to 0$ behaves as

$$\mathrm{d}z \, \mathrm{d}\theta \, P(z, \theta) \sim \alpha_s \frac{\mathrm{d}z}{z} \frac{\mathrm{d}\theta}{\theta} \,. \tag{1.4}$$

Let us deliberately ignore the obvious issue that the integral over this probability distribution does not exist, and instead pretend that we already know the total NLO correction $\sigma^{(1)}$ for the process of interest. (In the real calculation, the total NLO cross section is rendered finite by the presence of *virtual* particles in the sum over degenerate states that are not radiated into the final state, but exhibit the same soft and collinear divergences with opposite sign in the integral over their momenta.) We now attempt a type (A) calculation of the NLO cross section $\sigma^{(1)}(z_{\mathrm{cut}}, \theta_{\mathrm{cut}})$ for an experimental selection that rejects events where the emission has $z > z_{\mathrm{cut}}$ and $\theta > \theta_{\mathrm{cut}}$. This is not unreasonable since detectors have finite resolution in energy and angles, so we can think of this as rejecting any emission that the detector can see.

We can easily evaluate this cross section in the limit of a tight selection, $z_{\mathrm{cut}}, \theta_{\mathrm{cut}} \ll 1$, by subtracting from the full NLO result the contributions from emissions *above* the cuts,

$$\alpha_s \big[\sigma^{(1)}(z_{\mathrm{cut}}, \theta_{\mathrm{cut}}) - \sigma^{(1)} \big] = - \int_{z_{\mathrm{cut}}}^{1} \mathrm{d}z \int_{\theta_{\mathrm{cut}}}^{\pi} \mathrm{d}\theta \, P(z, \theta) \tag{1.5}$$

$$= -\alpha_s \big[\ln z_{\mathrm{cut}} \ln \theta_{\mathrm{cut}} + \mathcal{O}(\ln z_{\mathrm{cut}}, \ln \theta_{\mathrm{cut}}) + \mathcal{O}(z_{\mathrm{cut}}, \theta_{\mathrm{cut}}) \big] \,.$$

We see that the divergent emission probability manifests itself in the cross section as a double logarithmic dependence on the cuts, and a logarithmic divergence as either z_{cut} or $\theta_{\mathrm{cut}} \to 0$. The integral runs over regions where the approximation in eq. (1.4) is not valid, but these corrections only lead to single logarithms or power corrections in the cuts. (For the same reason, the precise upper integration boundary in θ is irrelevant.)

In many applications, the cuts on energy and angle are set simultaneously by one overall experimental constraint τ_{cut}. For example, measuring the transverse momentum $p_T \leq p_T^{\mathrm{cut}}$ of the emission (also indirectly through recoil) roughly translates to a measurement on the product $z\theta \leq \tau_{\mathrm{cut}} = p_T^{\mathrm{cut}}/Q$, where Q is the energy carried by a primary emitting parton inside the proton that later annihilates into an observed final state like the Z boson. For a single constraint, the analytic cross section to all orders takes the analytic form

$$\sigma(\tau_{\mathrm{cut}}) = \sigma^{(0)} \sum_{n=0}^{\infty} \sum_{m=0}^{2n} C_{n,m} \, \alpha_s^n \ln^m \tau_{\mathrm{cut}} + \mathcal{O}(\tau_{\mathrm{cut}}) \,. \tag{1.6}$$

Of course, we could have guessed that on general grounds, the leading term in a power expansion of the functions $\sigma^{(n)}(\tau_{\mathrm{cut}})$ can only contain logarithms of τ_{cut} with some coefficients $C_{n,m}$. Still, the fact that at most two new powers of $\ln \tau_{\mathrm{cut}}$ appear at every order in

perturbation theory contains physical information, namely, that the most divergent contribution from an additional emission arises from the limit where it becomes simultaneously soft and collinear.

Resummation

The result in eq. (1.6) is problematic because for $\tau_{\text{cut}} \ll 1$, the double logarithms of τ_{cut} become large and overcome the suppression by α_s, so the perturbative series *diverges* and cannot be truncated. To arrive at any meaningful prediction, we must find a way to reorganize, or *resum*, the perturbative series. To do so, we retain to first approximation only the most singular *leading logarithmic* (LL) terms $m = 2n$. Using the fact that eq. (1.4) holds recursively for every subsequent emission, one can show that the coefficients satisfy $C_{n,2n} = (-C)^n/n!$ with $C > 0$ a constant that depends on the charge of the primary emitter. (A pedagogical derivation can be found in ref. [38].) These are the coefficients of an exponential series, so we find

$$\sigma(\tau_{\text{cut}}) = \sigma^{(0)} \exp\left[-C\,\alpha_s \ln^2 \tau_{\text{cut}} \right] + (\text{terms with } m < 2n) + \mathcal{O}(\tau_{\text{cut}}) \,. \qquad (1.7)$$

This result is known as the Sudakov form factor [39], and is perfectly convergent for $\tau_{\text{cut}} \to 0$, where it tends to 0. It is the basis of the most elementary type (C) predictions: These so-called *parton showers* [40] recursively add emissions in a Markov process using eq. (1.7) as the probability for no emission to occur above a given cut. It is important to realize that eq. (1.7), despite being an all-order result in α_s, is only the first term in a systematic expansion to higher logarithmic order, and on its own is essentially as precise (or imprecise) as a leading-order calculation in the cases where fixed-order perturbation theory converges.

To increase the precision of this result, we should include the next-to-leading logarithmic (NLL) terms $m = 2n-1$, the next-to-next-to-leading logarithmic (NNLL) terms $m = 2n-2$, and so forth. Many methods exist to extend the analytic resummation to subleading logarithmic orders. They all rely on the principle of *factorization*, i.e., a systematic separation of the dynamics at the low energy scale $\tau_{\text{cut}}Q$, where soft and collinear radiation is emitted, from the hard production process that occurs at the scale $Q \gg \tau_{\text{cut}}Q$. Specifically, we will make use of *effective field theory* in this thesis to make the separation of scales manifest at the level of the cross section.

The drawback of all these methods is that they only apply to type (A) predictions in the presence of, typically, a single experimental constraint. A common theme of this thesis is the extension of these analytic resummation methods to more differential observables. In this way, realistic experimental observables that could previously only be computed using parton showers can now systematically be computed to higher logarithmic orders for the first time, extending the range of observables that can benefit from precise analytically resummed type (A) predictions. In other cases, a component of the calculation that would otherwise have to be calculated in an expensive type (B) calculation can now be evaluated in much shorter time using our results.

Of course, the benefits of the more versatile type (B) and (C) calculations still stand, and we stress that our results will also enable improving their formal accuracy in the future: For one, they can serve as very nontrivial benchmarks for efforts that strive to improve the formal accuracy of parton showers. More importantly, our results will also *enable* the systematic improvement of type (B) and (C) predictions because the infrared (soft and collinear) structure of QCD is an input to these calculations. For example, type (B) fixed-order predictions require a systematic way of isolating singularities from the limit where as in eq. (1.4), n and $n+1$ emission configurations become degenerate. These procedures, known as (fixed-order) subtractions, become particularly challenging starting at NNLO, where a variety of approaches exists [41–56]. Type (C) predictions in addition require some infrared cutoff below which the quarks and gluons of perturbative QCD form nonperturbative bound states. The resummation of logarithms of this cutoff *is* perturbative, and can be improved using tools from analytic resummation. We will return to these points in our outlook in chapter 8, where we highlight how both applications will benefit from our results.

Survey of research presented in this thesis

We turn to a brief survey of the main research results presented in this thesis, corresponding to chapters 3–7. A condensed outline of the entire manuscript is given afterwards.

Jet veto resummation with jet rapidity cuts. Collimated bunches of particles called *jets* play an important role in many LHC analyses. Binning events by the number of jets is a widely-used tool to distinguish different hard-interaction processes. Typically, jets are categorized by whether they pass a certain cut $p_T < p_T^{\rm cut}$ on their total transverse momentum. Jet-binned cross sections are a prime example of an observable that involves large Sudakov logarithms of $p_T^{\rm cut}$ and requires all-order resummation to obtain an optimal prediction. The resummation for the 0-jet, or jet-vetoed, production cross section of color-singlet (i.e., neutral under QCD) final states like the Higgs or the Z boson has been achieved to high perturbative accuracy [57–71].

Experimental jet selections require a cut on the (pseudo)rapidity of reconstructed jets, $|\eta_{\rm jet}| \leq \eta_{\rm cut}$, due to the finite acceptance of the detector. We extend the standard jet p_T (jet veto) resummation, which implicitly works in the limit $\eta_{\rm cut} \to \infty$, by incorporating a finite jet rapidity cut. We also consider the case of a step in the required $p_T^{\rm cut}$ at an intermediate value of $|\eta| \simeq 2.5$. This is of experimental relevance to avoid the increased contamination from unsuppressed pile-up beyond the reach of the tracking detectors, i.e., of radiation from unrelated scattering processes between other protons in the LHC beams. We identify all relevant parametric regimes, discuss their factorization and resummation as well as the relations between them, and show that the phenomenologically relevant regimes are free of large so-called nonglobal logarithms. The $\eta_{\rm cut}$ dependence of all resummation ingredients is computed to the same order to which they are currently known for $\eta_{\rm cut} \to \infty$. Our results pave the way for carrying out the jet veto resummation including a sharp cut

or a step at η_{cut} to the same order as is currently available in the $\eta_{\text{cut}} \to \infty$ limit. The numerical impact of the jet rapidity cut is illustrated for several benchmark LHC processes at NLL'+NLO. We find that a rapidity cut at high $\eta_{\text{cut}} = 4.5$ is safe to use and has little effect on the cross section. A sharp cut at $\eta_{\text{cut}} = 2.5$ can in some cases lead to a substantial increase in the perturbative uncertainties, which can be mitigated by instead using a step in the veto.

Joint two-dimensional resummation in q_T and 0-jettiness at NNLL. We next consider a simultaneous measurement of the Z-boson transverse momentum $q_T \equiv p_T^Z$ and the 0-jettiness event shape $\mathcal{T}_0$ that quantifies the amount of additional radiation in an event. Since both observables resolve the initial-state radiation, the double-differential cross section in q_T and $\mathcal{T}_0$ contains Sudakov double logarithms of both q_T/Q and $\mathcal{T}_0/Q$. We simultaneously resum the logarithms in q_T and $\mathcal{T}_0$ to next-to-next-to-leading logarithmic order (NNLL) matched to next-to-leading fixed order (NLO). Our results provide the first genuinely two-dimensional analytic Sudakov resummation for initial-state radiation. Integrating the resummed double-differential spectrum over either $\mathcal{T}_0$ or q_T recovers the corresponding single-differential resummation for the remaining variable. We discuss in detail the required effective field theory setups and their combination using two-dimensional resummation profile scales. We also introduce a new method to perform the q_T resummation where the underlying resummation is carried out in impact-parameter space, but is consistently turned off depending on the momentum-space target value for q_T. Our methods apply at any order and for any color-singlet production process, such that our results can be systematically extended when the relevant perturbative ingredients become available.

Generalized threshold factorization with full collinear dynamics. Soft threshold factorization has been widely used to study hadronic collisions. It is derived in the limit where the momentum fractions $x_{a,b}$ carried by the partons that annihilate into the observed final state approach $x_{a,b} \to 1$. Intuitively, the energy available from the initial state is just above the production threshold for the observed final state, so any remaining radiation must be soft. We present and prove a generalized threshold factorization theorem for color-singlet processes, which holds in the weaker limit of only $x_a \to 1$ for generic x_b (or vice versa). The physical intuition for this limit is that the color-singlet final state is produced at generic energies, but large absolute rapidity, such that all additional radiation is forced to become collinear to the opposite proton beam. The factorization theorem is found to be much more powerful than the classic soft one, capturing the full singular structure of the partonic cross section including off-diagonal partonic channels and its full collinear structure. We show this explicitly for the Drell-Yan rapidity spectrum and use it to predict a nontrivial set of its N³LO corrections.

N³LO beam functions in the eikonal limit. Beam functions are universal collinear matrix elements that describe the multi-dimensional momentum distribution of partons

extracted from the proton and enter, for example, in the factorization and resummation for q_T or $\mathcal{T}_0$. Using consistency relations with known soft matrix elements, we derive the leading contributions to the beam functions at $\mathcal{O}(\alpha_s^3)$ in the so-called eikonal limit where the primary parton carries almost all the energy. These results constitute an important cross check on the complete calculations of the beam functions to third order in perturbation theory, which in turn enable fully-differential calculations at N^{3}LO and resummed predictions at N^{4}LL.

Resumming fiducial power corrections at N^{3}LL. We consider the production and decay of a vector boson $pp \to V^* X \to LX$ at small $q_T \ll Q$, where $q_T = p_T^V$ is the total transverse momentum of $V = Z, W, \gamma$. (Here X denotes any additional radiation into the final state.) Experimental measurements require fiducial acceptance cuts on the decay products L of V, which in general introduce enhanced, linear power corrections in q_T/Q. We show that they can be unambiguously predicted from factorization, and resummed to the same order as the leading-power contribution. For the fiducial q_T spectrum, they constitute the complete linear power corrections. We thus obtain predictions for the fiducial q_T spectrum to N^{3}LL and next-to-leading-power in q_T/Q. Matching to full NNLO (α_s^2), we find that the linear power corrections are indeed the dominant ones and once they are included by factorization, the remaining fixed-order corrections become almost negligible below $q_T \lesssim 40\,\mathrm{GeV}$. We also discuss the implications for more complicated observables, and provide predictions for the fiducial ϕ^* spectrum at N^{3}LL+NNLO. We find excellent agreement with ATLAS and CMS measurements of q_T and ϕ^*. We also consider the transverse momentum (p_T^ℓ) spectrum of the lepton from a W decay, as relevant for determinations of the W mass at the LHC. We show that it develops leptonic power corrections in $q_T/(Q - 2p_T^\ell)$, which diverge near the Jacobian peak $p_T^\ell \sim Q/2$ and must be kept to all powers to obtain a meaningful result there. Doing so, we obtain for the first time an analytically resummed result for the p_T^ℓ spectrum around the Jacobian peak at N^{3}LL+NNLO. Our method is based on performing a complete tensor decomposition for the hadronic and leptonic tensors that encode the production and decay of the V, as well as the correlations between them that arise from angular momentum conservation. We show that in practice this is equivalent to often-used recoil prescriptions, for which our results now provide rigorous, formal justification. Our tensor decomposition yields nine Lorentz-scalar hadronic structure functions, which for $Z/\gamma^* \to \ell\ell$ or $W \to \ell\nu$ directly map onto the angular coefficients commonly considered in experimental analyses, but it continues to hold for arbitrary leptonic final states. In particular, for suitably defined Born-projected leptons it still yields a LO-like angular decomposition even when including electromagnetic final-state radiation, which makes this lepton definition theoretically preferred.

Outline

This thesis is structured as follows. In chapter 2 we review the basic principles of Quantum Chromodynamics, introduce the effective field theory description of its soft and collinear limits, and show how the latter generically give rise to factorization. We also review the single-differential factorization for several important observables at the LHC that continue to play a role in our later results.

In chapter 3 we present our analysis of jet veto cross sections with a jet rapidity cut, highlighting how the single-differential resummation can be seamlessly extended to account for it. In chapter 4, we produce the first predictions at NNLL+NLO for the double-differential spectrum in the two independent resolution variables q_T and $\mathcal{T}_0$, yielding the first systematically improvable prediction for a Sudakov peak in two dimensions. In chapter 5 we present the generalized threshold factorization theorem that accounts for the full collinear dynamics of initial-state radiation. In chapter 6 we derive the leading eikonal terms at third order in perturbation theory for the q_T and $\mathcal{T}_0$ beam functions. In chapter 7 we demonstrate how to perform the resummation of fiducial power corrections that arise from experimental measurements on the decay products of a Z or W boson. We provide predictions at $N^3LL+NNLO$, including the resummation of fiducial power corrections, and find excellent agreement with ATLAS and CMS measurements of q_T and the related ϕ^* observable. We also present the first analytically resummed result for the p_T^ℓ spectrum near the Jacobian peak at $N^3LL+NNLO$.

We conclude and discuss future applications of our results in chapter 8. Notation and relevant conventions used in this thesis are summarized in appendix A. Details on the hard scattering processes considered in this thesis are given in appendix B, where the generalization to other color-singlet processes is also discussed. In appendix C we collect the required anomalous dimensions that govern the resummation of large logarithms through the renormalization group evolution. Explicit expressions for the latter are collected in appendix D. Expressions for beam and soft functions to the perturbative order required are collected in appendix E. In appendix F we give compact analytic expressions for the NLO Z and Higgs partonic rapidity spectra in a convenient parametrization. Additional numerical results, including further comparisons to data, are given in appendix G.

Chapter 2

Factorization and resummation

This chapter sets the scene for the research described in this thesis, introducing its greater context and the tools and methods used to perform it. In section 2.1, we review the basic principles of Quantum Chromodynamics as the theory of the strong interactions. We introduce some key processes at hadron colliders, focusing on the most precisely measured cases where a color-singlet probe like the Z boson or photon couples to the strong dynamics. In section 2.2, we introduce the effective field theory paradigm and review the soft-collinear effective theory that describes low-energy or small-angle emissions in QCD. Setting up concepts and notation used throughout this thesis, we show how the soft-collinear effective theory generically gives rise to *factorization*. In section 2.3, we discuss how the factorized form of cross sections enables the *resummation* of large logarithms to all orders in perturbation theory using the renormalization group. In section 2.4, we introduce several important experimental observables at hadron colliders and review the concrete form that factorization takes in each case.

2.1 Quantum Chromodynamics at hadron colliders

2.1.1 Basic principles of QCD

The quantum field theory of the strong interactions is known as Quantum Chromodynamics (QCD) [72–77]. Its fundamental degrees of freedom are spin-1/2 fermions called *quarks* that carry an internal quantum number called color, and vector bosons called *gluons* that mediate the interaction between them and themselves carry color. Quarks are described by a Dirac spinor field $q^i(x)$ that transforms in the fundamental representation of the special unitary group $\mathrm{SU}(N_c)$, with $N_c = 3$ the number of colors,

$$q^i(x) \xrightarrow{U} \sum_{j=1}^{N_c} U^{ij} q^j(x), \qquad U \in \mathrm{SU}(N_c). \tag{2.1}$$

In the following we will suppress the indices i, j for the fundamental representation and write $q(x) \mapsto Uq(x)$ for short. In this notation the antiquark field transforms as $\bar{q}(x) \mapsto \bar{q}(x) U^\dagger$, with $U^\dagger U = \mathbf{1}_F$. Gluons are represented by a vector field $A_\mu(x)$ that transforms in the adjoint representation of $\mathrm{SU}(N_c)$,

$$A_\mu(x) \equiv A_\mu^a(x) T^a \xrightarrow{U} A_\mu^a(x) U T^a U^\dagger = U A_\mu U^\dagger, \tag{2.2}$$

13

where the matrices T^a are the generators of $\mathrm{SU}(N_c)$ in the fundamental representation, and we implicitly sum over adjoint indices a. Since $\mathrm{SU}(N_c)$ is nonabelian, its Lie algebra has nonvanishing structure constants f^{abc},

$$[T^a, T^b] = \mathrm{i} f^{abc} T^c \, . \tag{2.3}$$

We conventionally normalize the generators as

$$\mathrm{Tr}\big[T^a T^b\big] = T_F \delta^{ab} = \frac{1}{2} \delta^{ab} \, . \tag{2.4}$$

The quadratic Casimir operators C_F and C_A of the fundamental and adjoint representation are given in terms of the T^a and f^{abc} by

$$T^a T^a = C_F \, \mathbf{1}_F \, , \qquad f^{acd} f^{bcd} = C_A \, \delta^{ab} \, , \tag{2.5}$$

and for $\mathrm{SU}(N_c)$ with $N_c = 3$ we have

$$C_F = \frac{N_c^2 - 1}{2N_c} = \frac{4}{3} \, , \qquad C_A = N_c = 3 \, . \tag{2.6}$$

We can ask to what extent invariance under global color rotations U, which implies conservation of the total color charge. already determines the form of the QCD Lagrangian. The operators that can appear in it should be polynomials of fields and derivatives of total mass dimension four, since there is no explicit mass scale in the theory. In addition, the operators must be Lorentz scalars to preserve Lorentz invariance. This leaves the $\mathrm{SU}(N_c)$-invariant combinations

$$\mathcal{L}_{\mathrm{QCD}} \supset \bar{q}\, \mathrm{i} \slashed{\partial} q \, , \quad \bar{q} \slashed{A} q \, , \quad \mathrm{Tr}\Big[\partial^n A^{4-n}\Big] \, , \tag{2.7}$$

where the last term represents any Lorentz-scalar contraction of derivatives and gluon fields, traced over fundamental indices. All of these operators so far can appear with arbitrary coefficients; while we may eliminate two of them by choosing a normalization for the quark and gluon fields, the resulting Lagrangian is clearly underdetermined, in particular in the gluon sector.

Instead, all the dynamics of QCD (and its predictive power) follow from promoting eqs. (2.1) and (2.2) to a *local gauge symmetry* under transformations $U(x) \in \mathrm{SU}(N_c)$ that depend on the spacetime point,

$$q(x) \xmapsto{\;U(x)\;} U(x)\, q(x) \, , \qquad A_\mu(x) \xmapsto{\;U(x)\;} U(x) A_\mu(x) U^\dagger(x) + U(x)\Big[\frac{\mathrm{i}}{g}\partial_\mu U^\dagger(x)\Big] \, , \tag{2.8}$$

where g in the last term is the *gauge coupling parameter*. Assuming this transformation behavior of $A_\mu(x)$ allows us to write down a derivative operator with homogeneous behavior under gauge transformations, the *covariant derivative*, given in the fundamental representation by

$$D_\mu \equiv \partial_\mu - \mathrm{i} g A_\mu(x) \, . \tag{2.9}$$

It satisfies

$$D_\mu \xmapsto{U(x)} U(x) D_\mu U^\dagger(x) \,, \tag{2.10}$$

where the derivative operator acts on all terms to its right, i.e., on the product of the gauge transformation $U^\dagger(x)$ and the (implicit) test function. Note that eq. (2.9) is the only combination in which derivatives and the gauge field may appear in the Lagrangian as otherwise, gauge transformations would induce an uncanceled term $\propto U[\partial U^\dagger] = -[\partial U] U^\dagger$. This uniquely fixes all terms in the Lagrangian involving the quark field to

$$\mathcal{L}_{\mathrm{QCD}} \supset \bar{q}\, \mathrm{i} \slashed{D} q \,. \tag{2.11}$$

Furthermore, the only polynomial derivative operators $F(D_\mu)$ built out of D_μ that may appear in the remaining terms in the Lagrangian are those that satisfy

$$F(D_\mu)\, f(x) = \big[F(D_\mu)\big] f(x) \,, \tag{2.12}$$

for any test function $f(x)$, i.e., they are proportional to the identity because all derivatives are saturated within the square brackets by the gauge field itself. To identify these operators, we can rewrite all derivatives of the gauge field as commutators acting on test functions,

$$\big[\partial_\mu A_\nu(x)\big] f(x) = \partial_\mu \big[A_\nu(x) f(x)\big] - A_\nu(x)\, \partial_\mu f(x) = \big[\partial_\mu, A_\nu(x)\big] f(x) \,. \tag{2.13}$$

It follows by gauge invariance that all $F(D_\mu)$ that satisfy eq. (2.12) depend on D_μ only through the *gluon field strength tensor*

$$G_{\mu\nu} = \frac{\mathrm{i}}{g} \big[D_\mu, D_\nu\big] \,, \tag{2.14}$$

which may be written out in terms of $\mathrm{SU}(N_c)$ generators and structure constants as

$$G_{\mu\nu} = G_{\mu\nu}^a T^a \,, \qquad G_{\mu\nu}^a = \partial_\mu A_\nu^a - \partial_\nu A_\mu^a + g f^{abc} A_\mu^b A_\nu^c \,. \tag{2.15}$$

At mass dimension four, we therefore find exactly three Lorentz-scalar operators that are invariant under local gauge transformations,

$$\mathcal{L}_{\mathrm{QCD}} = \bar{q}\, \mathrm{i} \slashed{D} q - \frac{1}{4} G_{\mu\nu}^a G^{a,\mu\nu} + \theta_{\mathrm{QCD}}\, \frac{g^2}{32\pi^2}\, \epsilon_{\mu\nu\rho\sigma} G^{a,\rho\sigma} G^{a,\mu\nu} \,. \tag{2.16}$$

The first and second term are the QCD quark and the Yang-Mills Lagrangian [78], respectively. Their normalization is fixed by canonically normalizing the quark and gluon kinetic terms that they contain. They depend on g through the covariant derivative as their single parameter. Compared to eq. (2.7), the relative coefficient of the two possible terms in the quark Lagrangian and the (many) coefficients in the gluon Lagragian have been fixed by the gauge symmetry to powers of g. The interaction vertices that arise from the first two terms are illustrated in figure 2.1.

The coefficient of the third term introduces an additional free parameter θ_{QCD} into the theory, with a conventional factor pulled out. Since this term is proportional to

$$g(T^a)_{ji} \qquad\qquad g f^{abc} \qquad\qquad g^2 f^{abe} f^{cde} + \textbf{perm.}$$
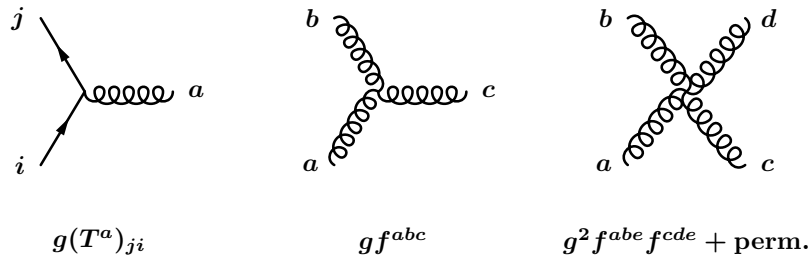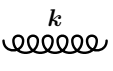
Figure 2.1: Interaction vertices of QCD, their color structure, and scaling with the gauge coupling. The Lorentz and spin structure of the vertices is suppressed. In general gauges, an additional ghost interaction vertex needs to be added.

a total derivative, it never contributes in perturbative calculations (as relevant for this thesis), where the field is assumed to vanish asymptotically. It can, however, contribute for nonperturbative bound states where the field does not vanish on the boundary. In this case its phenomenological significance is that it explicitly breaks the CP (charge conjugation and parity) symmetry that is otherwise preserved by eq. (2.16). Searches for a permanent electric dipole moment of the neutron and of mercury atoms [79, 80] set strong limits on $|\theta_{\text{QCD}}| \lesssim 10^{-10}$ compatible with zero, and there has been much speculation (and some elegant proposals [81]) why this should be so. In the following we set $\theta_{\text{QCD}} = 0$.

Two further modifications of the (classical) QCD Lagrangian in eq. (2.16) are in order. The first modification is practical and concerns the fact that in a quantum path integral over the gluon field A_μ, many configurations only differ by pure gauge transformations which leave the action unchanged. This overcounting of physical degrees of freedom cancels between the numerator and denominator in the normalized partition function when computing gauge-invariant quantities, but for perturbative calculations, a definite answer is also required for gauge-dependent quantities like the gluon propagator. This is achieved by inserting a gauge constraint $\delta\big[G(A_\mu)\big]$, with suitable Jacobian, into the functional integral over A_μ, where G is some functional of the field strength. In the Faddeev-Popov method [82], the gauge constraint is elegantly represented as a functional integral over complex, Grassman-valued anticommuting fields $c^a(x)$ called ghosts that, like gluons, transform in the adjoint representation. This allows the gauge constraint to be written as a simple modification of the action, leading to additional Feynman rules that remedy the overcounting of degrees of freedom in the sum over diagrams at any given order in perturbation theory. The precise form of the ghost action depends on $G(A_\mu)$. In axial gauge, where one picks some reference vector n^μ and imposes $G(A_\mu) = n \cdot A = 0$, the ghosts in fact do not propagate and also decouple from the gluon field, at the cost of explicitly breaking Lorentz invariance by n^μ (which typically is already present in the problem). On the other hand, in covariant gauges where $G(A_\mu)$ is a function of $\partial^\mu A_\mu$, the ghost Lagrangian and the gauge-fixing term implementing $G(A_\mu)$ are given by

$$\mathcal{L}_{\text{ghost}} = \bar{c}^a (\mathrm{i}\partial^\mu)(\mathrm{i}D_\mu^{ab})c^b\,, \qquad \mathcal{L}_{\text{fix}} = \frac{1}{2\xi}(\mathrm{i}\partial^\mu A_\mu^a)(\mathrm{i}\partial^\nu A_\nu^a)\,, \qquad (2.17)$$

where the covariant derivative in the adjoint representation is $D_\mu^{ab} = \delta^{ab}\partial_\mu + gf^{abc}A_\mu^c$, and ξ parametrizes the precise choice of gauge. In this gauge, the gluon propagator is given by

$$\mu, a \;\; \text{\scriptsize$k$} \;\; \nu, b \;\; = \frac{-\mathrm{i}\delta^{ab}}{k^2 + \mathrm{i}0}\left[g_{\mu\nu} - (1-\xi)\frac{k_\mu k_\nu}{k^2}\right]. \tag{2.18}$$

In this thesis we will use Feynman gauge ($\xi = 1$) throughout such that the second term vanishes. Note that even the gauge-fixed Lagrangian containing eq. (2.17) exhibits a residual symmetry under so-called BRST transformations [83, 84]. These are key in the all-order proof of the Slavnov-Taylor identities [85, 86] relating the basic Green's functions of QCD that generalize the propagators and the elementary vertices in figure 2.1. Since the divergences of arbitrary higher n-point functions can be represented in terms of these building blocks, one can then prove using the Slavnov-Taylor identities that all ultraviolet (UV) divergences from loop integrals may indeed be absorbed into g, i.e., that the QCD Lagrangian in eq. (2.16) is renormalizable [74].

The second modification is that in Nature, quarks are found to carry an additional quantum number called flavor that is conserved by the strong interactions. Flavor can take the values u (up), d (down), c (charm), s (strange), b (bottom, or beauty), and t (top, or more rarely, truth). Quarks of different flavor f are distinguished by their masses m_f. The masses enter the QCD Lagrangian as the dimensionful coefficients of (six copies of) the SU(3)-invariant operator $\bar{q}_f q_f$,

$$\mathcal{L}_{\text{QCD}} = \sum_f \bar{q}_f(\mathrm{i}\slashed{D} - m_f)q_f - \frac{1}{4}G_{\mu\nu}^a G^{a,\mu\nu} + \mathcal{L}_{\text{fix}} + \mathcal{L}_{\text{ghost}}. \tag{2.19}$$

Quarks of flavor u, c, t are further distinguished from d, s, b by their electromagnetic and weak charges, as discussed in the next sections. The quark masses exhibit a strong hierarchy, with the top quark at $m_t \approx 170\,\text{GeV}$ by far the most massive, $m_b \approx 5\,\text{GeV}$ and $m_c \approx 1\,\text{GeV}$ next in line, and the remaining quarks at $m_s \approx 100\,\text{MeV}$, $m_d \approx 5\,\text{MeV}$, and $m_u \approx 2\,\text{MeV}$, respectively [25]. Why this hierarchy should be there, or why the quarks and leptons should come in three generations only distinguished by their masses in the first place, is unclear.

At typical production energies of $m_W, m_Z, m_H \approx 100\,\text{GeV}$ at the LHC, the light quark masses can usually be set to zero to good approximation, while the top quark is too heavy to be excited as a quantum fluctuation and does not contribute to the dynamics. For this reason, QCD with $n_f = 5$ massless flavors is the appropriate theory to describe most phenomena considered in this thesis, with the gauge coupling g as its only parameter. As hinted at earlier, all UV divergences from quantum corrections can be absorbed by *renormalizing* the coupling. The most common renormalization scheme, also employed in this thesis, is the modified minimal subtraction ($\overline{\text{MS}}$) scheme. In this scheme the renormalized strong coupling constant $\alpha_s(\mu)$ is related to the bare gauge coupling g as

$$\frac{g^2}{4\pi} = \mu^{2\epsilon}\alpha_s(\mu)\,Z_{\alpha_s}(\epsilon, \mu), \tag{2.20}$$

where UV divergences are regulated by *dimensional regularization*, i.e., by performing the calculation in $d = 4 - 2\epsilon$ spacetime dimensions [87], μ is the *renormalization scale* or the

subtraction point with unit mass dimension, and

$$Z_{\alpha_s}(\epsilon, \mu) = \frac{e^{\epsilon \gamma_E}}{(4\pi)^\epsilon} \left[1 + \frac{\alpha_s(\mu)}{4\pi} \left(-\frac{\beta_0}{\epsilon} \right) + \mathcal{O}(\alpha_s^2) \right] \tag{2.21}$$

is the $\overline{\text{MS}}$ renormalization factor for the coupling. (The prefactor involving the Euler-Mascheroni constant γ_E is conventional.) By virtue of the Slavnov-Taylor identities, the renormalization factor may be obtained by computing the UV divergences in some convenient set of elementary Green's functions; impressively, it is by now known to five loops [88, 89]. Note that the bare coupling on the left-hand side of eq. (2.20) has mass dimension $[g] = +\epsilon$ to give the interaction Lagrangian the correct mass dimension when analytically continuing to d dimensions.[1] This in turn requires a dimensionful factor $\mu^{2\epsilon}$ on the right-hand side to ensure that $\alpha_s(\mu)$ is dimensionless. Renormalizability of QCD is the powerful statement that in any given perturbative series in $\alpha_s(\mu)$, reexpanding the counterterm Z_{α_s} against the lower order terms will precisely cancel the UV poles at the next order, with a universal coefficient

$$\beta_0 = \frac{11}{3} C_A - \frac{4}{3} T_F n_f \,. \tag{2.22}$$

Since the bare coupling is independent of the renormalization scale that we arbitrarily introduced, $\mu \, dg/d\mu = 0$, we find, by taking derivatives of both sides of eq. (2.20),

$$\mu \frac{d\alpha_s}{d\mu} = -2\epsilon \alpha_s(\mu) - \mu \frac{d}{d\mu} \ln Z_{\alpha_s}(\epsilon, \mu) \,. \tag{2.23}$$

Solving this order by order in α_s and taking $\epsilon \to 0$ in the end, we find the finite result

$$\mu \frac{d\alpha_s(\mu)}{d\mu} = \beta[\alpha_s(\mu)] = -2\alpha_s(\mu) \left[\beta_0 \frac{\alpha_s(\mu)}{4\pi} + \mathcal{O}(\alpha_s^2) \right] \,. \tag{2.24}$$

This expression is known as the *β function* [90, 91] of QCD. It governs the dependence of $\alpha_s(Q)$ on the physical scale $Q \sim \mu$ probed by a given measurement.[2] Crucially, $\beta_0 > 0$ for $N_c = 3$ and $n_f < 17$, and therefore $\alpha_s(Q)$ *decreases* as the energy scale Q increases, as can be seen by truncating eq. (2.24) to the leading term and solving it in closed form,

$$\alpha_s(\mu) = \frac{\alpha_s(\mu_0)}{1 + \alpha_s(\mu_0) \frac{\beta_0}{2\pi} \ln \frac{\mu}{\mu_0}} \,. \tag{2.25}$$

---

[1] This can most easily be seen by noting that $[\mathcal{L}] = d$ since the action has $0 = [d^d x] + [\mathcal{L}]$, and comparing $d = [\partial^2 A^2] = 2 + 2[A] = [g^2 A^4] = 2[g] + 4[A]$ for the gluon kinetic term and the four-gluon interaction.

[2] To see the connection between the (in principle arbitrary) renormalization scale μ and the physical energy scale Q, note that by dimensional analysis, the coefficients of the perturbative series for a given observable can only depend on Q/μ. In addition, the physical observable must be independent of the scale μ, which implies that the coefficient of α_s^n contains terms up to $\ln^n Q/\mu$ that are precisely canceled, order by order, by the β function. To arrive at any sensible prediction, we are forced to choose $\mu \sim Q$ as otherwise *large logarithms* of Q/μ would spoil the perturbative convergence. This will be a recurring theme in the following chapters.
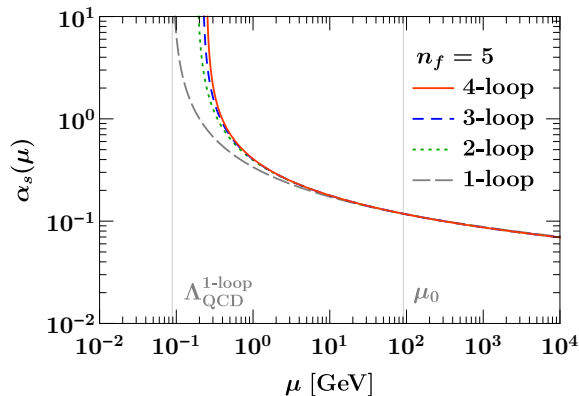
Figure 2.2: The strong coupling constant $\alpha_s(\mu)$ of QCD, evolved using the β function for $n_f = 5$ active flavors at different loop orders. The vertical lines indicate the input scale $\mu_0 = m_Z$ and the 1-loop result for the QCD scale Λ_{QCD} where the coupling diverges.

Here $\alpha_s(\mu_0)$ is a boundary condition for the *running coupling* which must be extracted at an input scale μ_0 from experiment. The current world average, with $\mu_0 = m_Z$ the mass of the Z boson, is $\alpha_s(m_Z) = 0.1181(11)$ [25]. The same behavior of decreasing coupling with increasing energy persists at higher orders in the β function, as shown in figure 2.2. This special property of QCD, which arises from the nonabelian coupling $\sim C_A$ of gluons to themselves, is known as *asymptotic freedom* [76, 77]. It implies that at sufficiently high scales, perturbation theory with quark and gluon degrees of freedom will give meaningful results. On the other hand, at low scales $\alpha_s(Q)$ diverges towards the *Landau pole* $Q \to \Lambda_{\mathrm{QCD}}$, where at one loop

$$\Lambda_{\mathrm{QCD}}^{\text{1-loop}} = \mu_0 \exp\left[-\frac{2\pi}{\beta_0\, \alpha_s(\mu_0)}\right] \approx 100\,\mathrm{MeV}\,. \tag{2.26}$$

This can serve as an indication that at energy scales $\lesssim 1\,\mathrm{GeV}$, we should expect the formation of quark bound states by the exchange of many gluons, as indeed observed in Nature in the form of mesons (quark-antiquark) and baryons (three-quark bound states), collectively called hadrons. Importantly, all observed hadrons are color singlets, and no free quarks or gluons are observed, a phenomenon known as *(color) confinement.* Lattice QCD, i.e., the numerical study of eq. (2.19) using a discretized Euclidean spacetime lattice [92–94], provides evidence that QCD indeed correctly describes the hadron spectrum. In addition, the quantum numbers of the quarks, as well as the approximate symmetries implied by the relations between their masses, are compatible with the observed properties and interactions of hadrons. Finally, the observed distributions of *jets* in detectors, i.e., of collimated sprays of hadronic radiation, are compatible with the assumption that they are initiated by primary partons scattered by QCD dynamics [95]. However, despite this overwhelming empirical evidence, no precise analytic argument is known *how* eq. (2.19) leads to confinement.

The challenge one faces when describing the collision of hadrons in perturbative QCD is that (at least) the initial state involves hadronic bound states with intrinsically non-perturbative dynamics. In the remainder of this section we review some key quark and
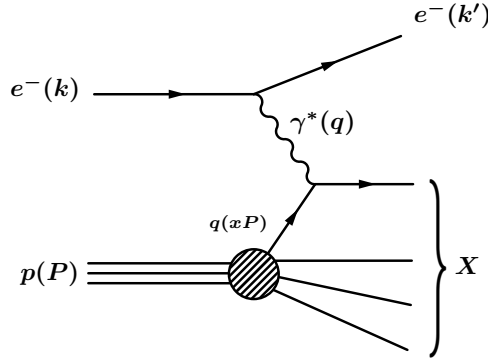
Figure 2.3: Kinematics of deep-inelastic scattering and the leading contribution in QCD.

gluon-initiated processes at electron-proton and hadron colliders, introduce the techniques needed to deal with hadrons in the initial state, and discuss the historical significance of these processes in establishing QCD as the theory of strong interactions and their current significance for precision phenomenology at the LHC.

2.1.2 Deep-inelastic scattering

Deep-inelastic scattering (DIS) refers to a lepton scattering off a hadron target in the regime where the energy transfer is large compared to the binding energy of the hadron, allowing one to resolve the hadron's constituents and, in the process, break it up. The prototypical example is an electron scattering off an unpolarized proton target,

$$e^-(k)\, p(P) \rightarrow e^-(k')\, X(p_X)\,, \tag{2.27}$$

where the unresolved hadronic final state X is the remnant of the proton. For simplicity, we restrict to the electromagnetic interaction between the electron and the charged proton constituents. To leading order in the electromagnetic coupling α_{em}, the interaction is mediated by a single off-shell photon γ^* carrying momentum

$$q = k - k'\,, \qquad Q^2 \equiv -q^2 > 0\,. \tag{2.28}$$

The process is illustrated in figure 2.3. By our assumptions, we will neglect the proton (and electron) mass as small compared to the momentum transfer, $m_p, m_e \ll Q$. The matrix element for the process factorizes as

$$\mathcal{M}(e^-p \rightarrow e^-X) = \mathcal{M}^\mu_{e \rightarrow e\gamma}\, \langle X | J_{\gamma\mu} | p \rangle\,, \tag{2.29}$$

where $\mathcal{M}^\mu_{e \rightarrow e\gamma}$ is the amplitude for the emission and propagation of γ^*, and

$$J^\mu_\gamma = |e| \sum_f Q_f\, \bar{q}_f \gamma^\mu q_f\,, \tag{2.30}$$

is the contribution of the quark and antiquark fields to the electromagnetic current. The sum runs over all active quark flavors $f = \{u, d, s, c, b, t\}$, and the electromagnetic charges of the quarks in units of the elementary charge $|e|$ are $Q_{u,c,t} = 2/3$ and $Q_{d,s,b} = -1/3$. The polarizations of the hadronic current and of the intermediate photon are encoded in the Lorentz indices of J_γ^μ and $\mathcal{M}_{e \to e\gamma}^\mu$.

The DIS cross section in the center-of-mass frame of the collision, differential in the momentum of the scattered lepton k', is given by the square of eq. (2.29) integrated over the phase space of hadronic radiation,

$$\mathrm{d}\sigma = \frac{1}{2E_{\mathrm{cm}}^2} \frac{\mathrm{d}^4 k'}{(2\pi)^3} \, \delta_+(k'^2) \sum_X \hspace{-1.2em}\int |\mathcal{M}(e^- p \to e^- X)|^2 \, (2\pi)^4 \delta^4(P + k - k' - p_X) \,, \qquad (2.31)$$

where $E_{\mathrm{cm}}^2 = (P + k)^2 = 2P \cdot k$ and we write the on-shell constraint as $\delta_+(p^2 - m^2) \equiv \theta(p^0) \, \delta(p^2 - m^2)$ for a particle with momentum p, energy p^0, and mass m. We have also introduced the abbreviation

$$\sum_X \hspace{-1.2em}\int \; \equiv \sum_X \int \mathrm{d}^4 p_X \prod_{i \in X} \int \frac{\mathrm{d}^4 p_i}{(2\pi)^3} \, \delta_+(p_i^2 - m_i^2) \, \delta^4 \Big(\sum_{i \in X} p_i - p_X \Big) \qquad (2.32)$$

for the sum over all possible hadronic final states X with total momentum p_X, integrated over their respective phase space. This definition is chosen such that by the optical theorem,

$$\sum_X \hspace{-1.2em}\int \; |X\rangle\langle X| = \mathbf{1} \qquad (2.33)$$

is a complete set of states on the Hilbert space of hadronic radiation. Note that we keep the sum (average) over final-state (initial-state) polarizations implicit in all squared matrix elements. Inserting the factorized matrix element into eq. (2.29) yields

$$\mathrm{d}\sigma = \frac{1}{2E_{\mathrm{cm}}^2} \frac{\mathrm{d}^4 k'}{(2\pi)^3} \, \delta_+(k'^2) \, L^{\mu\nu}(k, k') \, W_{\mu\nu}(k - k', P) \,, \qquad (2.34)$$

where the leptonic tensor $L^{\mu\nu} \equiv \mathcal{M}_{e \to e\gamma}^{*\mu} \mathcal{M}_{e \to e\gamma}^\nu$ is defined as the square of the leptonic matrix element, and evaluates to

$$L^{\mu\nu}(k, k') = \frac{2e^2}{q^4} (k^\mu k'^\nu + k^\nu k'^\mu - g^{\mu\nu} k \cdot k') \,. \qquad (2.35)$$

The hadronic tensor $W^{\mu\nu}$ is defined as

$$W^{\mu\nu}(q, P) = \sum_X \hspace{-1.2em}\int \; \langle p|J_\gamma^{\dagger\mu}|X\rangle\langle X|J_\gamma^\nu|p\rangle \, (2\pi)^4 \delta^4(P + q - p_X) \,, \qquad (2.36)$$

and encodes the hadronic dynamics of the collision. In addition to the proton momentum P, it only depends on the momentum q injected into the hadronic system.

It is conventional to parametrize the kinematics of DIS in terms of two dimensionless Lorentz-invariant quantities, namely the Bjorken variable x and the elasticity y defined as

$$x \equiv \frac{-q^2}{2P \cdot q}, \qquad y \equiv \frac{P \cdot q}{P \cdot k}. \tag{2.37}$$

The integral over the azimuthal angle of k' is trivial because we consider an azimuthally symmetric unpolarized scattering; changing variables to x and y, we arrive at

$$\frac{\mathrm{d}\sigma}{\mathrm{d}x\,\mathrm{d}y} = \frac{y}{32\pi^2} L^{\mu\nu}(k,k')\, W_{\mu\nu}(k-k',P), \tag{2.38}$$

where on the right-hand side, k' (and therefore q and p_X) is fully specified in terms of x and y. In particular,

$$Q^2 = xy\, E_{\mathrm{cm}}^2, \qquad p_X^2 = \frac{1-x}{x}\, Q^2. \tag{2.39}$$

To make progress, we decompose the hadronic tensor $W^{\mu\nu}(q,P)$ in a covariant way in terms of its arguments. First note that conservation of the vector current in QCD, $\partial_\mu J_\gamma^\mu = 0$, implies

$$q_\mu W^{\mu\nu} = q_\nu W^{\mu\nu} = 0. \tag{2.40}$$

In addition, it is clear from the definition in eq. (2.36) that the hadronic tensor is hermitian, $W^{\mu\nu} = W^{*\nu\mu}$. Finally, since the electromagnetic interaction preserves parity, the hadronic tensor must satisfy $\bar{W}^{\mu\nu}(\bar{q},\bar{P}) = W^{\mu\nu}(q,P)$, where $\bar{x}^\mu = (x^0, -\vec{x})$. This restricts the tensor structures that can appear to[3]

$$W^{\mu\nu}(q,P) = \alpha_{\mathrm{em}}(4\pi)^2 \Big(-g^{\mu\nu} + \frac{q^\mu q^\nu}{q^2}\Big) F_1(x,Q^2)$$
$$+ \frac{\alpha_{\mathrm{em}}(4\pi)^2}{P \cdot q}\Big(P^\mu - \frac{P \cdot q}{q^2}q^\mu\Big)\Big(P^\nu - \frac{P \cdot q}{q^2}q^\nu\Big) F_2(x,Q^2). \tag{2.41}$$

The DIS structure functions F_i are scalar functions of q and P and by Lorentz invariance can only depend on their invariants, i.e., on q^2 and $q \cdot P$, or equivalently on Q^2 and Bjorken x as indicated. Inserting eq. (2.41) into eq. (2.38) and contracting, we find

$$\frac{\mathrm{d}\sigma}{\mathrm{d}x\,\mathrm{d}y} = \frac{2\pi\alpha_{\mathrm{em}}^2 E_{\mathrm{cm}}^2}{q^4}\big[2xy^2 F_1(x,Q^2) + 2(1-y)F_2(x,Q^2)\big]. \tag{2.42}$$

So far, we have not actually made use of QCD in our description of DIS, other than anticipating that the electromagnetic current in eq. (2.30) would be sourced by quark fields. The key point where the properties of QCD enter is that since we take the hard scale Q to be large compared to the onset of the nonperturbative regime at scales $\Lambda_{\mathrm{QCD}} \ll Q$, the

---

[3]Note that we have absorbed a factor $\propto \alpha_{\mathrm{em}}$ into $W^{\mu\nu}$ in order to be consistent with the following sections, but compensate for it in this definition of the F_i to recover their standard normalization, see e.g. ref. [96].

DIS structure functions can be *factorized*, using an operator product expansion (OPE) or, more generally, the methods of effective field theory:

$$F_1(x, Q^2) = \frac{1}{2} \sum_k \int \frac{\mathrm{d}z}{z} \, C_{1,k}(z, Q^2, \mu) \, f_k\Big(\frac{x}{z}, \mu\Big) \Big[1 + \mathcal{O}\Big(\frac{\Lambda_{\mathrm{QCD}}}{Q}\Big)\Big],$$

$$F_2(x, Q^2) = x \sum_k \int \frac{\mathrm{d}z}{z} \, C_{2,k}(z, Q^2, \mu) \, f_k\Big(\frac{x}{z}, \mu\Big) \Big[1 + \mathcal{O}\Big(\frac{\Lambda_{\mathrm{QCD}}}{Q}\Big)\Big]. \qquad (2.43)$$

Here the parton distribution functions (PDFs) $f_k(\xi, \mu)$ encode the density of partons of type k at a given momentum fraction ξ inside the proton. Formally, the PDFs are given by nonperturbative proton matrix elements of effective local quark and gluon operators that arise in the OPE of the two electromagnetic currents in the hadronic tensor.

These effective operators are independent of the ultraviolet (UV) dynamics at the perturbative scale Q, which are absorbed into the matching coefficients $C_{i,k}$. Beyond tree level, this separation gives rise to additional UV divergences in matrix elements of the PDF operators, and hence the *renormalization* of the PDFs (and the matching coefficients) at the renormalization scale μ. This is discussed in section 2.3.1 in more detail. Physically, the matching coefficients encode the effect of perturbative initial-state radiation, which may lead to both energy loss (encoded in the momentum fraction $z \leq 1$) and a change of parton type (encoded in the sum over k). E.g., a gluon $k = g$ extracted from the proton may split into a $q\bar{q}$ pair, one of which then couples to the photon. At tree level, none of these things can happen, and the partonic coefficient functions evaluate to

$$C_{1,k}(z, Q^2) = \sum_q Q_q^2 \big(\delta_{kq} + \delta_{k\bar{q}}\big) \delta(1 - z) + \mathcal{O}(\alpha_s),$$

$$C_{2,k}(z, Q^2) = C_{1,k}(z, Q^2) + \mathcal{O}(\alpha_s), \qquad (2.44)$$

as can be seen by direct evaluation of eq. (2.36) with quark external states [97]. To strict leading order we may also neglect the renormalization of the PDFs, leading to

$$F_{1,\mathrm{LO}}(x) = \frac{1}{2x} F_{2,\mathrm{LO}}(x) = \frac{1}{2} \sum_q Q_q^2 \big[f_q(x) + f_{\bar{q}}(x)\big]. \qquad (2.45)$$

This is the prediction of the *parton model* for the DIS structure functions [98]. In this model, the cross section is given by the incoherent sum of partonic scattering cross sections weighted with the probability density to find a parton of momentum fraction x in the proton. A key feature of this result is that the structure functions exhibit Bjorken scaling, i.e., they only depend on the Bjorken ratio x, but no longer on the momentum transfer Q. Since we have pulled out the overall $\sim Q^{-4}$ dependence of the Møller cross section, this is indicative of pointlike proton constituents, as composite objects would set an additional characteristic length scale a that can be probed by the scattering if $Q \sim 1/a$.

Another important feature is that the tree-level results for $F_{1,2}$ satisfy the Callan-Gross relation $2xF_1 = F_2$ [99]. (In other words, the fact that the $C_{i,k}$ in our normalization in eq. (2.43) were exactly equal at tree level.) This is a direct consequence of the assumption
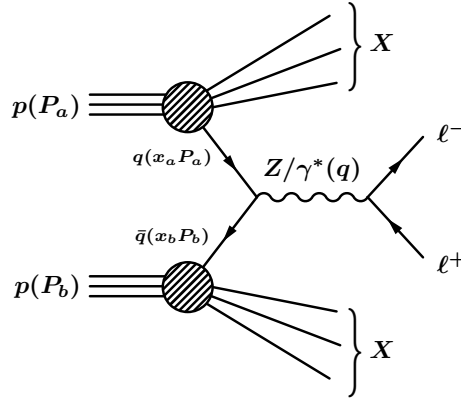
Figure 2.4: Kinematics of Drell-Yan production and the leading contribution in QCD.

that spin-1/2 partons source the electromagnetic current: By repeating the calculation in ref. [97] for hypothetical massless *scalar* partons ϕ with electromagnetic charge Q_ϕ, one instead finds

$$F_{1,\text{LO}}(x) = 0 \,, \qquad F_{2,\text{LO}}(x) = x\, Q_\phi^2 \big[f_\phi(x) + f_{\bar\phi}(x) \big] \,. \tag{2.46}$$

The experimental observation of Bjorken scaling and the Callan-Gross relation [100, 101] therefore amounted to the discovery of quarks as the constituents of the proton and were key in establishing QCD as the theory of strong interactions. In hindsight, it is pleasing that the intuitive parton model is indeed recovered by the all-order factorization theorem in eq. (2.43) at tree level, and that its success is explained by asymptotic freedom.

2.1.3 Drell-Yan production

We now turn to the production and decay of an electroweak vector boson in unpolarized proton-proton collisions at the LHC. The most important case is the Drell-Yan process, where the vector boson immediately decays into a lepton pair [102],

$$pp \to Z/\gamma^* X \to \ell^+ \ell^- X \,, \qquad pp \to W^+ X \to \ell^+ \nu X \,, \qquad pp \to W^- X \to \ell^- \bar\nu X \,, \quad (2.47)$$

referred to as neutral-current Drell-Yan production for the Z and γ^*, and charged-current Drell-Yan production for the $W^\pm$. As before, X denotes a generic hadronic final state. The process is illustrated in figure 2.4

As discussed in the introduction, the Drell-Yan process is a precision benchmark at the LHC due to the experimentally clean final state and the copious statistics, in particular if the Z or W is produced near its resonance. It also is a prototype for any process where a colorless leptonic final state L couples to the hadronic dynamics through a single (possibly off-shell) electroweak vector boson. Important examples include the generalization of eq. (2.47) to arbitrary QED final-state radiation (FSR), and the Higgsstrahlung process $V^* \to VH$, and we will generically write

$$p(P_a)\, p(P_a) \to V(q)\, X(p_X) \to L(q)\, X(p_X). \tag{2.48}$$

At leading order in the electroweak interaction, the matrix element factorizes as for DIS,

$$\mathcal{M}(pp \to V + X \to L + X) = \mathcal{M}^\mu_{V \to L} \langle X | J_{V\,\mu} | pp \rangle \,, \tag{2.49}$$

where $\mathcal{M}^\mu_{V \to L}$ is the amplitude for V to propagate and decay into the leptonic final state L, and J^μ_V is the electroweak $q\bar{q}$ current that couples to V, including electroweak charges and couplings. The current for $V = \gamma$ is the same as in eq. (2.30). The current for $V = Z$ reads [103]

$$J^\mu_Z = -|e| \sum_f \bar{q}_f \gamma^\mu \big(v_f - a_f \gamma_5 \big) q_f \,, \tag{2.50}$$

where the sum again runs over quark flavors $f = \{u, d, s, c, b, t\}$. The vector and axial couplings of flavor f to the Z boson are

$$v_f = \frac{T^f_3 - 2Q_f \sin^2 \theta_w}{\sin(2\theta_w)} \,, \qquad a_f = \frac{T^f_3}{\sin(2\theta_w)} \,, \tag{2.51}$$

where $T^{u,d}_3 = \pm 1/2$ is the weak isospin, and θ_w is the weak mixing angle. For $V = W^\pm$, the currents are given by

$$J^\mu_{W^+} = -\frac{|e|}{\sqrt{2}\sin\theta_w} \sum_{f,f'} V_{ff'}\, \bar{q}_f \gamma^\mu \frac{1 - \gamma_5}{2} q_{f'} \,, \qquad J^\mu_{W^-} = \big(J^\mu_{W^+} \big)^\dagger \,, \tag{2.52}$$

where the sum runs over $f = \{u, c, t\}$ and $f' = \{d, s, b\}$, and $V_{ff'}$ is the corresponding CKM matrix element.

The differential cross section for $pp \to VX \to LX$ in the lab frame, which we take to be the hadronic center-of-mass frame, is given by the square of eq. (2.49), integrated over phase space, and factorizes as

$$\frac{\mathrm{d}\sigma}{\mathrm{d}^4q\,\mathrm{d}\mathcal{O}_L\,\mathrm{d}\mathcal{O}_X} = \frac{1}{2E^2_{\mathrm{cm}}} \sum_{V,V'} L_{VV'\,\mu\nu}(q, \mathcal{O}_L)\, W^{\mu\nu}_{VV'}(q, P_a, P_b, \mathcal{O}_X)$$

$$\equiv \frac{1}{2E^2_{\mathrm{cm}}} L_{\mu\nu}(q, \mathcal{O}_L)\, W^{\mu\nu}(q, P_a, P_b, \mathcal{O}_X) \,. \tag{2.53}$$

Here, q is the total momentum of the leptonic final state L (i.e., the momentum carried by V or V'). Parametrizing it in terms of the total leptonic invariant mass $Q^2 = q^2 > 0$ and the rapidity Y and transverse momentum $\vec{q}_T$ of L, we have

$$q^\mu = (m_T \cosh Y, \vec{q}_T, m_T \sinh Y)\,, \quad m_T = \sqrt{Q^2 + q^2_T}\,, \qquad \mathrm{d}^4q = \frac{1}{2}\mathrm{d}Q^2\,\mathrm{d}Y\,\mathrm{d}^2\vec{q}_T\,, \tag{2.54}$$

where m_T is also known as the transverse mass. Importantly, in addition to q, the cross section depends on the observable measured on the leptonic final state L, which we generically denote by $\mathcal{O}_L$. For example, we could measure the transverse momentum of one of the leptons or apply fiducial acceptance cuts. Unlike the case of inclusive DIS, we also allow for a generic observable $\mathcal{O}_X$ to be measured on the hadronic final state; this could e.g. be

the transverse momentum of the leading jet. The sum over V, V' in eq. (2.53) runs over all intermediate vector bosons that contribute to the observed final state. In particular, it encodes the interference of $V = \gamma$ with $V' = Z$ for neutral-current Drell-Yan. In the following, we suppress the dependence on V, V', as in the second line of eq. (2.53), unless it is of some relevance.

The hadronic tensor $W_{VV'}^{\mu\nu}$ describes the QCD dynamics of the proton-proton collision. It is integrated over all hadronic radiation X, subject to the measurement $\mathcal{O}_X$, but independent of the measurement performed on L,

$$
\begin{aligned}
&W_{VV'}^{\mu\nu}(q, P_a, P_b, \mathcal{O}_X) \\
&\equiv \sum_X \hspace{-1.2em} \int \; \langle pp|J_V^{\dagger\mu}|X\rangle\langle X|J_{V'}^\nu|pp\rangle \, \delta^4(P_a + P_b - q - p_X) \, \delta[\mathcal{O}_X - \hat{\mathcal{O}}_X(X)] \,,
\end{aligned} \tag{2.55}
$$

where the matrix elements of J_V^μ are implicitly averaged over proton spins. In addition to q, it depends on the incoming proton momenta $P_{a,b}$. In the lab frame (and neglecting proton masses),

$$
P_a^\mu = \frac{E_{\mathrm{cm}}}{2}(1, 0, 0, 1)\,, \qquad P_b^\mu = \frac{E_{\mathrm{cm}}}{2}(1, 0, 0, -1)\,, \tag{2.56}
$$

where $E_{\mathrm{cm}}^2 \equiv (P_a + P_b)^2$ is the hadronic center-of-mass energy.

The leptonic tensor $L_{VV'}^{\mu\nu}$ describes the propagation and decay of the intermediate vector boson,

$$
\begin{aligned}
L_{VV'}^{\mu\nu}(q, \mathcal{O}_L) &\equiv \int \mathrm{d}\Phi_L(q) \, L_{VV'}^{\mu\nu}(\Phi_L) \, \delta[\mathcal{O}_L - \hat{\mathcal{O}}_L(q, \Phi_L)] \,, \\
L_{VV'}^{\mu\nu}(\Phi_L) &\equiv \mathcal{M}_{V\to L}^{*\mu}(\Phi_L)\mathcal{M}_{V'\to L}^{\nu}(\Phi_L) \,.
\end{aligned} \tag{2.57}
$$

In addition to q and the polarization of V encoded in the Lorentz indices, it depends on the measurement $\mathcal{O}_L$ acting on the leptonic phase space point Φ_L. Here the leptonic phase-space measure with total momentum q is defined as

$$
\mathrm{d}\Phi_L(q) = \left[\prod_{i\in L} \frac{\mathrm{d}^4 p_i}{(2\pi)^3} \, \theta(p_i^0)\delta(p_i^2 - m_i^2)\right] (2\pi)^4 \delta^4\Big(q - \sum_{i\in L} p_i\Big)\,. \tag{2.58}
$$

For the most part of this thesis, we will consider the cross section fully inclusive over the decay products, i.e., integrated over $\mathcal{O}_L$, such that $L^{\mu\nu}$ only depends on the total vector boson momentum q. In addition, we mostly focus on the standard Drell-Yan process in eq. (2.47) with vanishing lepton masses $m_\ell = m_\nu = 0$. In this case the leptonic current is conserved, $q_\mu L^{\mu\nu} = q_\nu L^{\mu\nu}$, and the leptonic tensor in eq. (2.57) by covariance must take the form

$$
L^{\mu\nu}(q) = \int \mathrm{d}\Phi_L(q) \, L^{\mu\nu}(\Phi_L) = \Big(\frac{q^\mu q^\nu}{q^2} - g^{\mu\nu}\Big) L(q^2)\,. \tag{2.59}
$$

Inserting eq. (2.59) into eq. (2.53) yields

$$
\frac{\mathrm{d}\sigma}{\mathrm{d}^4 q \, \mathrm{d}\mathcal{O}_X} = \frac{1}{2E_{\mathrm{cm}}^2} \, L(q^2) \, W_{\mathrm{incl}}(q, P_a, P_b, \mathcal{O}_X)\,, \tag{2.60}
$$

where all QCD dynamics are encoded in a single Lorentz-scalar inclusive hadronic structure function

$$W_{\text{incl}}(q, P_a, P_b, \mathcal{O}_X) \equiv \left(\frac{q^\mu q^\nu}{q^2} - g^{\mu\nu} \right) W_{\mu\nu}(q, P_a, P_b, \mathcal{O}_X) \,. \qquad (2.61)$$

Explicit expressions for the scalar coefficients $L(q^2)$ for the case of Drell-Yan are given in appendix B.2. Since the leptonic dynamics at this point only amount to an overall prefactor, we will often directly quote results for the cross section on the left-hand side of eq. (2.60); the underlying hadronic structure function can then easily be recovered, e.g. to apply our results to an (inclusive) measurement of another Drell-Yan-like process. In chapter 7, we will carefully do the analogue of the covariant DIS decomposition in eq. (2.41) to allow for fully generic leptonic observables, and explore its implications for the structure of power corrections at small $q_T \ll Q$. A dedicated discussion of non-conserved contributions to the leptonic and hadronic tensor is also given there.

To introduce the analogue of the DIS factorization in eq. (2.43), let us consider a yet more inclusive observable and measure only the invariant mass Q^2 and rapidity Y of the leptonic final state. We define the momentum fractions

$$x_a = \frac{Q}{E_{\text{cm}}} e^{+Y} \,, \quad x_b = \frac{Q}{E_{\text{cm}}} e^{-Y} \,, \qquad (2.62)$$

which are in one-to-one correspondence to Q and Y, and generalize the Bjorken fraction x for Drell-Yan production. The cross section differential in $x_{a,b}$ relates to eq. (2.60) as

$$\frac{\mathrm{d}\sigma}{\mathrm{d}x_a \, \mathrm{d}x_b} = \frac{1}{4} L(Q^2) \int \mathrm{d}^2 \vec{q}_T \, W_{\text{incl}}(q, P_a, P_b) \,, \qquad (2.63)$$

where $W_{\text{incl}}(q, P_a, P_b)$ is the inclusive hadronic structure function integrated over any $\mathcal{O}_X$. For $\Lambda_{\text{QCD}} \ll Q$, the double-differential cross section satisfies the *collinear factorization theorem* [104–106]

$$\frac{\mathrm{d}\sigma}{\mathrm{d}x_a \, \mathrm{d}x_b} = \sum_{i,j} \int \frac{\mathrm{d}z_a}{z_a} \frac{\mathrm{d}z_b}{z_b} \, \hat{\sigma}_{ij}(z_a, z_b, Q, \mu) \, f_i\left(\frac{x_a}{z_a}, \mu\right) f_j\left(\frac{x_b}{z_b}, \mu\right) \left[1 + \mathcal{O}\left(\frac{\Lambda_{\text{QCD}}}{Q}\right) \right], \quad (2.64)$$

where $\hat{\sigma}_{ij}(z_a, z_b, Q, \mu)$ denotes the perturbatively calculable partonic cross section for the scattering of partons i and j into the observed final state, allowing for energy loss through perturbative initial-state radiation encoded in the momentum fractions $z_{a,b} \leq 1$. Importantly, the $f_i(x, \mu)$ are the same PDFs as in DIS in eq. (2.43), so they may e.g. be extracted from DIS data like the precise data taken at the HERA $e^- p$ collider at DESY, and then be used to produce predictions for the LHC [107, 108]. More commonly, a global fit to all available data including pp data sets is performed [109–112]. In either case, higher-order contributions to the partonic cross section in eq. (2.64) are crucial for a precise prediction (or extraction), and for the inclusive rapidity spectrum have been known analytically to NNLO for quite some time [113, 114].

Generalizations of eq. (2.64) also hold for the more differential cross section in eq. (2.60), with the partonic cross section now in addition differential in $\vec{q}_T$ and $\mathcal{O}_X$ [104–106],

$$\frac{\mathrm{d}\sigma}{\mathrm{d}x_a \, \mathrm{d}x_b \, \mathrm{d}^2\vec{q}_T \, \mathrm{d}\mathcal{O}_X} = \sum_{i,j} \int \frac{\mathrm{d}z_a}{z_a} \frac{\mathrm{d}z_b}{z_b} \, \hat{\sigma}_{ij}(z_a, z_b, Q, \vec{q}_T, \mathcal{O}_X, \mu) \, f_i\Big(\frac{x_a}{z_a}, \mu\Big) f_j\Big(\frac{x_b}{z_b}, \mu\Big)$$

$$\times \Big[1 + \mathcal{O}\Big(\frac{\Lambda_{\mathrm{QCD}}}{\Lambda_X}\Big)\Big] , \tag{2.65}$$

In this case the leading power corrections are of the form $\Lambda_{\mathrm{QCD}}/\Lambda_X$, where Λ_X is the lowest energy or transverse momentum scale probed by the measurement on the hadronic state. This scale may be set directly through $\mathcal{O}_X$, or indirectly by probing small q_T. The fully-differential Drell-Yan cross section, including the dependence on the decay products, is known at NNLO [115–119], also combined with parton showers [120–122]. NLO electroweak corrections have also been calculated [123–133], as well as the mixed NNLO QCD+QED and QCD+electroweak corrections in the limit where production and decay are factorized as in eq. (2.53) [134–140].

Eq. (2.64) again has a parton-model interpretation when evaluating the partonic cross section at tree level,[4]

$$\hat{\sigma}_{ij}(z_a, z_b, Q, \mu) = \frac{4\pi\alpha_{\mathrm{em}}^2}{3N_c Q^2} \sum_q Q_q^2 \big[\delta_{iq}\delta_{j\bar{q}} + \delta_{i\bar{q}}\delta_{jq}\big] \, \delta(1 - z_a)\delta(1 - z_b) + \mathcal{O}(\alpha_s) , \tag{2.66}$$

forcing a quark and an antiquark of the same flavor that are extracted from the proton to directly annihilate into the vector boson, with no radiative energy loss:

$$\frac{\mathrm{d}\sigma_{\mathrm{LO}}}{\mathrm{d}x_a \, \mathrm{d}x_b} = \frac{4\pi\alpha_{\mathrm{em}}^2}{3N_c Q^2} \sum_q Q_q^2 \big[f_q(x_a)f_{\bar{q}}(x_b) + f_{\bar{q}}(x_a)f_q(x_b)\big] . \tag{2.67}$$

As before, the parton-model interpretation of the PDF as a probability density applies: In this case there are two independent probability densities for finding a quark at a momentum fraction x_a and an antiquark at a momentum fraction x_b (or vice-versa), so the cross section is given by their product times the $q\bar{q}$ annihilation cross section. The analogous statement to Bjorken scaling in this case is that the QCD dynamics are fully determined in terms of the two momentum fractions $x_{a,b}$, but no longer depend on Q^2 after pulling out the overall Q^2 dependence of the propagator.

We note that if the rapidity Y is fully integrated over, Drell-Yan production can be characterized in terms of a single momentum fraction like DIS,

$$\tau = x_a x_b = \frac{Q^2}{E_{\mathrm{cm}}^2} , \tag{2.68}$$

---

[4]Here we restrict to photon exchange $V = V' = \gamma^*$ for simplicity. Complete NLO expressions for $\hat{\sigma}_{ij}$ can be found in appendix F.

and the collinear factorization theorem eq. (2.64) projects onto

$$\frac{\mathrm{d}\sigma}{\mathrm{d}\tau} = E_{\mathrm{cm}}^2 \frac{\mathrm{d}\sigma}{\mathrm{d}Q^2} = \int \mathrm{d}x_a \, \mathrm{d}x_b \, \frac{\mathrm{d}\sigma}{\mathrm{d}x_a \, \mathrm{d}x_b} \, \delta(\tau - x_a x_b)$$

$$= \sum_{i,j} \int \frac{\mathrm{d}z}{z} \, \hat{\sigma}_{ij}(z, Q, \mu) \, \mathit{ff}_{ij}\Big(\frac{\tau}{z}, \mu\Big) \,. \tag{2.69}$$

On the second line we have defined the partonic luminosity function

$$\mathit{ff}_{ij}(\xi, \mu) \equiv \int \mathrm{d}Y \, f_i\big(\xi e^{+Y}, \mu\big) \, f_j\big(\xi e^{-Y}, \mu\big) \,, \tag{2.70}$$

and the projected partonic cross section

$$\hat{\sigma}_{ij}(z, Q, \mu) \equiv \int \mathrm{d}z_a \, \mathrm{d}z_b \, \hat{\sigma}_{ij}(z_a, z_b, Q, \mu) \, \delta(z - z_a z_b) \,, \tag{2.71}$$

which likewise is a function of only a single partonic momentum fraction. This partonic cross section has a much simpler structure than the partonic rapidity spectrum, and has recently been calculated to N^{3}LO for photon exchange [141] and charged-current Drell-Yan [142]. (Earlier results at NNLO were given in refs. [143–145].) These calculations provide intriguing evidence that perturbative corrections to Drell-Yan production beyond two loops, previously assumed to be well-convergent, are in fact quite sizable. The use of these N^{3}LO results for PDF phenomenology, however, is limited because they only provide access to the aggregate partonic luminosity in eq. (2.70), whereas double-differential measurements in Q and Y provide access to the full dependence of both PDFs on x_a and x_b. (Realistically, even more fine-grained calculations differential in the decay products are needed as detectors have limited fiducial acceptance.)

2.1.4 Higgs production

Measuring and interpreting the properties of the Higgs boson discovered in 2012 is a key part of the LHC physics program. In the Standard Model, the Higgs boson couples to quarks through the scalar current

$$J_H = \sum_f y_f \, \bar{q}_f q_f \,, \qquad y_f \propto \frac{m_f}{v} \,, \tag{2.72}$$

after electroweak symmetry breaking. The fermion mass term and eq. (2.72) arise from the same interaction term for the Higgs doublet and the fermion fields in the unbroken phase of the Standard Model, so the Yukawa couplings y_f are proportional to the ratio of the quark mass m_f and the Higgs vacuum expectation value v.

The production mechanisms for the Higgs boson at the LHC can be classified by whether the Higgs directly couples to the quark Yukawa current in eq. (2.72), figure 2.5, or whether the interaction is mediated by weak vector bosons, figure 2.6. All of these processes pose unique challenges when attempting to describe them in QCD. For example, the gluon-fusion process in figure 2.5, left, is purely loop induced, only starts at $\mathcal{O}(\alpha_s^2)$ and involves the two
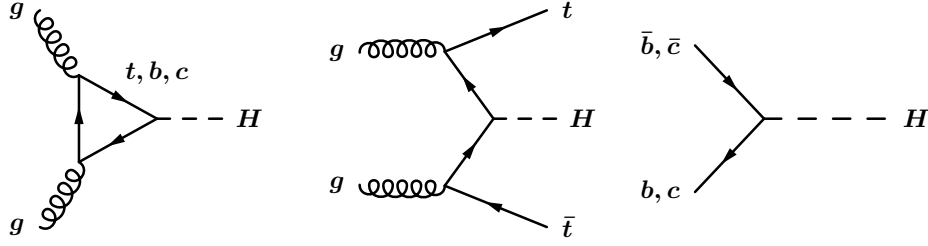
Figure 2.5: Higgs boson production modes at the LHC that arise directly from the quark Yukawa interaction in eq. (2.72). From left to right: gluon fusion $gg \to H$, associated $t\bar{t}H$ production, and bottom and charm quark annihilation $b\bar{b}, c\bar{c} \to H$. The proton-proton initial state is as in figure 2.4 and omitted for clarity.
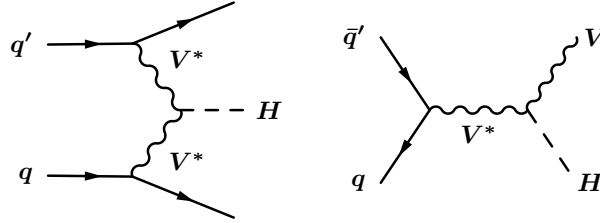
Figure 2.6: Higgs boson production modes at the LHC that are mediated by weak vector bosons $V = W^+, Z$. Left: vector boson fusion (VBF). Right: Higgsstrahlung (VH production).

Production mode	$\sigma(13\,\text{TeV})$	Order	Ref.
$gg \to H$	$48.61\,\text{pb}$	$\text{N}^3\text{LO}_{\text{rEFT}} + \text{NLO}_{\text{exact } m_q} + \text{LO}_{\text{EW}}$	[146]
$t\bar{t}H$	$0.51\,\text{pb}$	$\text{NLO} + \text{NLO}_{\text{EW}}$	[146]
$b\bar{b} \to H$	$0.49\,\text{pb}$	NNLO	[147]
VBF	$3.77\,\text{pb}$	$\text{NNLO}_{\text{DIS}} + \text{NLO}_{\text{EW}}$	[146]
WH	$1.36\,\text{pb}$	$\text{NNLO} + \text{NLO}_{\text{EW}}$	[146]
ZH	$0.88\,\text{pb}$	$\text{NNLO} + \text{NLO}_{\text{EW}}$	[146]

Table 2.1: Theory predictions for the inclusive Higgs production cross section in different production modes at the $E_{\text{cm}} = 13\,\text{TeV}$ LHC for $m_H = 125.09\,\text{GeV}$, and the corresponding order in fixed-order perturbation theory in the strong (N^nLO) and electroweak ($\text{N}^n\text{LO}_{\text{EW}}$) couplings. The subscript rEFT refers to taking the limit of $m_t \to \infty$ in all higher-order QCD corrections, see eqs. (2.73) and (2.74). The subscript DIS denotes the structure function approach described in the text. References to the original calculations can be found in refs. [146, 147].

distinct scales of m_H and the quark mass. Nevertheless, much of the technology developed to describe DIS and Drell-Yan production can be applied to Higgs production, as well. This is most obvious for the VH and $b\bar{b}, c\bar{c} \to H$ processes, which at most differ from the Drell-Yan case in the spin structure of the quark vertex. In the *structure function approach* to VBF, the two subprocesses that produce the intermediate vector bosons are treated as independent, allowing one to relate the partonic cross section to the product of DIS hard scattering coefficients in eq. (2.43). Most importantly, the factorization of the process into a hard scattering cross section and the nonperturbative PDF as in eq. (2.65) underlies all theory predictions for Higgs production at the LHC.

Up-to-date predictions for the inclusive production cross sections from refs. [146, 147] are compiled in table 2.1, together with the status of the calculation. Notable progress in QCD fixed-order predictions beyond the status summarized in refs. [146, 147] includes the calculation of the inclusive $b\bar{b} \to H$ cross section to N^3LO [148], the calculation of the inclusive VBF cross section to N^3LO_{DIS} [149], and a (re)assessment and elegant calculation of the dominant corrections to the structure function approach to VBF [150].

The gluon fusion ($gg \to H$) production mode by far dominates the total production cross section, and by virtue of the large statistics allows for the most detailed measurement of differential Higgs cross sections. The gluon fusion cross section in turn receives its dominant contribution from diagrams with a top quark mediating the interaction between gluons and the Higgs. The calculation of the production rate is greatly simplified by working to leading power in the limit $m_H \ll 2m_t$, where $2m_t$ is the energy required to produce an additional on-shell top quark pair at rest. This approximation is well justified for quantities like the total cross section or the Higgs transverse momentum spectrum for $p_{T,H} \lesssim m_H$ that probe no kinematic scales of $\mathcal{O}(m_t)$, and the corrections to it are quadratic in $m_H/(2m_t)$. The approximation breaks down e.g. at large $p_{T,H} \gg m_H$, where the Higgs can recoil against an additional hard emission that resolves the top loop. In the limit $m_H \ll 2m_t$, the top loop can be approximated by an effective gluon current coupling to the Higgs boson directly [151–154],

$$J_H^{\text{EFT}} = \frac{\alpha_s C_t}{12\pi v} G_{\mu\nu}^a G^{a,\mu\nu} \,. \tag{2.73}$$

The prefactor of α_s and the matching coefficient $C_t = 1 + \mathcal{O}(\alpha_s)$ are determined by power expanding the full amplitude (figure 2.7) and matching it onto a matrix element of the effective current. The explicit suppression of the current by $1/m_t$ combines with the Yukawa coupling into a prefactor proportional to $1/v$, which gives the corresponding term $\mathcal{L} \supset -H J_H^{\text{EFT}}$ in the Lagrangian the correct mass dimension. This effective coupling can also serve as a prototype for the production of a hypothetical new heavy scalar at the LHC that couples to gluons indirectly through new strongly interacting physics at another, much higher scale. In chapter 3 we will provide predictions for the signal strength in such a scenario under realistic jet selection criteria. In practical applications, the approximation for Higgs production can be improved by rescaling the effective current by the full m_t
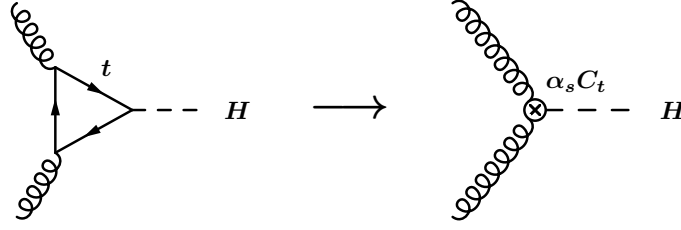
Figure 2.7: The top-triangle diagram (left) giving the dominant contribution to gluon-fusion Higgs production in the Standard Model, and the effective interaction vertex it matches onto (right). Virtual corrections that resolve the top loop are captured by the matching coefficient $C_t = 1 + \mathcal{O}(\alpha_s)$.

Figure adapted from ref. [155].

dependent leading-order amplitude $F_0(\rho)$,

$$J_H^{\mathrm{rEFT}} = F_0\left(\frac{m_H^2}{4m_t^2}\right) J_H^{\mathrm{EFT}}, \qquad F_0(\rho) = \frac{3}{2\rho} - \frac{3}{2\rho}\left|1 - \frac{1}{\rho}\right|\arcsin^2(\sqrt{\rho}) \quad \text{for } \rho < 1. \quad (2.74)$$

This *rescaled EFT* (rEFT) method pushes corrections to the EFT limit down to $\mathcal{O}(\alpha_s/m_t)$.

For completeness and later reference, we give the general form of the Higgs production cross section for generic measurements $\mathcal{O}_L$ and $\mathcal{O}_X$ on the decay products L of the Higgs boson and the hadronic final state X. The most important decay channels for precision determinations of Higgs differential spectra are $H \to L = \gamma\gamma$, with the decay mediated by top and $W^\pm$ loops, and the "golden channel" $H \to ZZ^* \to 4\ell$; see refs. [156–161] for recent results. In analogy to eq. (2.53) for Drell-Yan, the cross section takes the form

$$\frac{\mathrm{d}\sigma}{\mathrm{d}^4 q\,\mathrm{d}\mathcal{O}_L\,\mathrm{d}\mathcal{O}_X} = \frac{1}{2E_{\mathrm{cm}}^2} L(q, \mathcal{O}_L)\, W(q, P_a, P_b, \mathcal{O}_X). \quad (2.75)$$

Here the hadronic and leptonic "tensors" W and L are in fact, like the Higgs and the currents it couples to, Lorentz scalars, and the polarization of the decay products in L is fully uncorrelated with the production mechanism. The hadronic and leptonic tensors read, with $J_H = \{J_H, J_H^{\mathrm{EFT}}, J_H^{\mathrm{rEFT}}\}$ any of the currents introduced above,

$$W(q, P_a, P_b, \mathcal{O}_X) = \sum_X \langle pp|J_H^\dagger|X\rangle\langle X|J_H|pp\rangle\, \delta^4(P_a + P_b - q - p_X)\, \delta[\mathcal{O}_X - \hat{\mathcal{O}}_X(X)],$$

$$L(q, \mathcal{O}) = \int \mathrm{d}\Phi_L(q)\, |\mathcal{M}_{H\to L}(\Phi_L)|^2\, \delta[\mathcal{O} - \hat{\mathcal{O}}(q, \Phi_L)], \quad (2.76)$$

where $\mathcal{M}_{H\to L}$ is the matrix element for the propagation and decay of H into L,

$$\mathcal{M}_{H\to L}(\Phi_L) = \frac{1}{q^2 - m_H^2 + \mathrm{i}\Gamma_H m_H}\, \mathcal{M}_{\mathrm{decay}}(\Phi_L). \quad (2.77)$$

The decay matrix element $\mathcal{M}_{\mathrm{decay}}$ is related to the differential Higgs decay rate in the Higgs rest frame by

$$\frac{\mathrm{d}\Gamma_{H\to L}}{\mathrm{d}\Phi_L} = \frac{1}{2m_H}|\mathcal{M}_{\mathrm{decay}}(\Phi_L)|^2. \quad (2.78)$$

An important property of the Higgs boson is that its total width Γ_H is narrow, $\Gamma_H \ll m_H$: The predicted width in the SM is $\Gamma_H \approx 4\,\mathrm{MeV}$ [25], while the most stringent experimental constraint is $\Gamma_H < 13\,\mathrm{MeV}$ at a 95% confidence level [162]. In the limit $\Gamma_H \ll m_H$, the *narrow width approximation* of the squared propagator by a δ function applies,

$$
|\mathcal{M}_{H\to L}(\Phi_L)|^2 = \left|\frac{1}{q^2 - m_H^2 + \mathrm{i}\Gamma_H m_H}\right|^2 2m_H \frac{\mathrm{d}\Gamma_{H\to L}}{\mathrm{d}\Phi_L}
$$
$$
\to 2\pi\delta(q^2 - m_H^2)\frac{1}{\Gamma_H}\frac{\mathrm{d}\Gamma_{H\to L}}{\mathrm{d}\Phi_L}\,. \tag{2.79}
$$

Inserting this result into the expression for the cross section, we find

$$
\frac{\mathrm{d}\sigma}{\mathrm{d}Y\,\mathrm{d}\vec{q}_T\,\mathrm{d}\mathcal{O}_L\,\mathrm{d}\mathcal{O}_X} = \frac{\pi}{2E_{\mathrm{cm}}^2}W(q, P_a, P_b, \mathcal{O}_X)
$$
$$
\times \frac{1}{\Gamma_H}\int \mathrm{d}\Phi_L(q)\frac{\mathrm{d}\Gamma_{H\to L}}{\mathrm{d}\Phi_L}\,\delta[\mathcal{O}_L - \hat{\mathcal{O}}_L(q, \Phi_L)]\,, \tag{2.80}
$$

where $q^2 = m_H$ is fixed on the right-hand side. Importantly, the observed on-shell signal cross section is only sensitive to the *normalized* differential decay rate, making it challenging to directly observe (rather than put limits on) the total Higgs decay width at the LHC.

If the measurement $\mathcal{O}_L$ is inclusive over the distribution of the decay products, the leptonic tensor simplifies further,

$$
L(q^2) = 2\pi\delta(q^2 - m_H^2)\frac{1}{\Gamma_H}\int \mathrm{d}\Phi_L \frac{\mathrm{d}\Gamma_{H\to L}}{\mathrm{d}\Phi_L(q)}
$$
$$
= 2\pi\delta(q^2 - m_H^2)\frac{\Gamma_{H\to L}}{\Gamma_H} \equiv 2\pi\delta(q^2 - m_H^2)\,\mathrm{Br}_{H\to L}\,. \tag{2.81}
$$

On the last line we defined the branching fraction $\mathrm{Br}_{H\to L}$ for the decay channel L. With this, the cross section reads

$$
\frac{\mathrm{d}\sigma}{\mathrm{d}Y\,\mathrm{d}\vec{q}_T\,\mathrm{d}\mathcal{O}_X} = \frac{\pi}{2E_{\mathrm{cm}}^2}W(q, P_a, P_b, \mathcal{O}_X)\,\mathrm{Br}_{H\to L} \tag{2.82}
$$

In both eqs. (2.80) and (2.81), accounting for the Higgs decay amounts to a simple multiplicative factor, so in this thesis we will simply quote results for the production cross section of an on-shell Higgs boson, which is given by $\pi W/(2E_{\mathrm{cm}}^2)$ and captures all the initial-state QCD dynamics.

2.2 Factorization from Soft-Collinear Effective Theory

2.2.1 Effective field theory

Effective field theory (EFT) is a tool to make the separation of energy scales $p \ll Q$ manifest at the level of the cross section (or the decay width, the spectrum of states, or any other physical observable) in a systematic power expansion in p/Q. The general strategy is the following:

1. Identify the low-energy degrees of freedom at the scale p. In quantum field theory, these are the propagating fields with virtualities or masses $\lesssim p^2$.

2. Write down all possible terms (operators) $O_i \subset \mathcal{L}_{\text{eff}}$ in their Lagrangian that are consistent with the symmetries of the theory, keeping terms to the desired order in the power counting in p/Q.

3. In a third, optional step known as *matching*, calculate the coefficients C_i in $\mathcal{L}_{\text{eff}} = \sum_i C_i O_i$ by comparing a set of Green's functions in the full and the effective theory.

4. Compute the observable using the low-energy Lagrangian.

EFTs whose full theories are known and admit a matching calculation as in step 3 are known as *top-down* EFTs. In *bottom-up* EFTs, the coefficients instead need to be determined from experiment and can then be used to derive predictions.

The EFT paradigm underlies much of physics. A simple, familiar example of a top-down EFT is the multipole expansion in classical electrodynamics: The dynamics of a rigid body with charge distribution $\rho(\vec{x})$ localized at short distances $|\vec{x}| \sim 1/Q$ can be described in terms of a few multipole moments if the electromagnetic field only varies slowly and over longer distances $|\vec{x}| \sim 1/p$. Retaining higher terms in the multipole expansion precisely corresponds to working to higher power in p/Q, and the calculable multipole moments are the matching coefficients C_i. More generally, and in somewhat ahistorical hindsight, turning bottom-up into top-down EFTs is the way in which humanity has learned about Nature: As our ability to probe higher energy scales and shorter distances increases, the number of parameters (matching coefficients) we had to simply accept has decreased, and they instead have been explained by more fundamental theories. An example is the magnetic dipole moment of the electron as probed by a field varying over long distances $|\vec{x}| \sim 1/p$. Its value is predicted in QED [163], the more fundamental theory at the scale $2m_e \sim Q$ where quantum excitations of the electron field are probed, and the prediction and experimental measurements have by now reached astonishing precision and agreement.

In the context of contemporary particle physics, an important bottom-up EFT is the Standard Model itself, where we do not know what lies at energy scales Λ beyond the weak scale. We can hope, however, to find experimental deviations pointing to nonzero coefficients C_i at the first subleading orders in $1/\Lambda$ that would offer a hint to possible UV completions. Another example are effective theories for low-energy hadron interactions like chiral perturbation theory. Here the matching coefficients are challenging to compute because the full theory (QCD) is nonperturbative at the relevant scales, but truncating the power expansion ensures these theories remain predictive.

As for top-down effective field theories in collider phenomenology, we have already encountered one explicit example in section 2.1.4, where quantum fluctuations of the top quark at the scale $2m_t$ were integrated out, resulting in an effective operator coupling gluons to the Higgs boson. In this section we review the soft-collinear effective theory (SCET) [164–169], following the EFT recipe above. The review in part follows ref. [170], with some segments adapted from ref. [155]. SCET is different from the heavy top quark
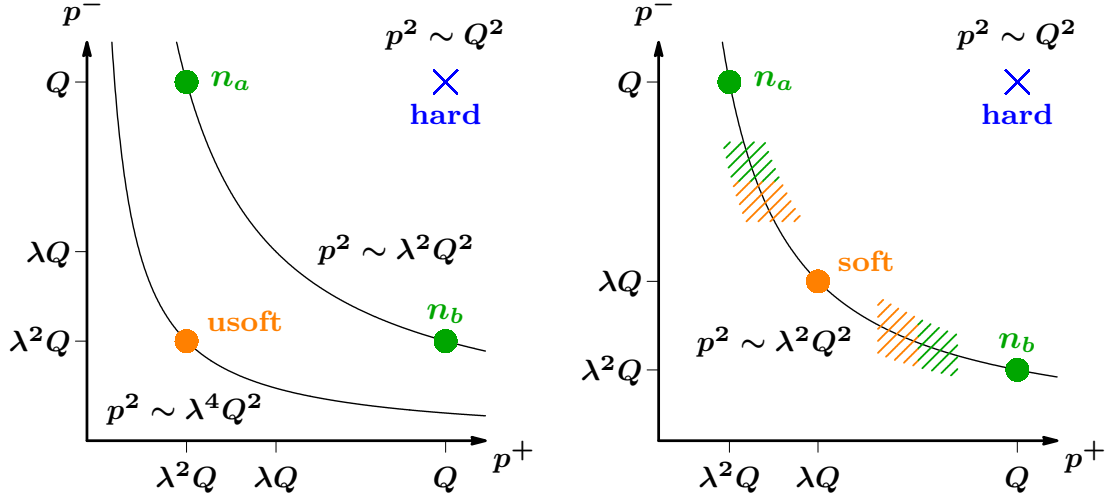
Figure 2.8: Mode setup in SCET$_\text{I}$ (left) and SCET$_\text{II}$ (right) in the (p^+, p^-) plane. In SCET$_\text{I}$, collinear (green) and ultrasoft modes (orange) contribute to the measurement and have parametrically distinct virtuality and perpendicular momentum $p^2 \sim p_\perp^2 \sim p^+ p^-$. In SCET$_\text{II}$, collinear and soft modes with the same virtuality $p \sim \lambda^2 Q^2$ contribute to the measurement. In the hatched regions soft and collinear modes overlap, giving rise to rapidity divergences. In either case, hard modes (blue) are integrated out and captured by the matching. Glauber modes are off shell and are not shown.

Both panels from ref. [155].

limit as it does not involve integrating out an entire particle. Instead, the low-energy degrees of freedom are those modes of the quark and gluon fields that are near the mass shell, and only the off-shell modes of the fields are integrated out and absorbed into matching coefficients. SCET has rich applications and can be used, for example, to formulate the factorization theorems in eqs. (2.43) and (2.64) [171]. In this thesis, we will be mostly be interested in its applications to problems with Sudakov double logarithms, as described in the introduction. We use the label momentum formalism of [164–167] to perform the power expansions yielding the leading-power SCET Lagrangian and, later in this thesis, power expand and factorize measurement operators. One may also carry out the power expansion directly in position space [168, 169], see also ref. [172] for a review.

2.2.2 Degrees of freedom

SCET is an effective field theory of QCD that describes the interactions of collinear and soft particles in the presence of a hard interaction. Soft particles are low-energy, long-wavelength fluctuations of the fields. Collinear particles are energetic, but are collimated with a lightlike direction n_i^μ. This could be the direction of motion of an incoming hadron, or an outgoing hadron or jet. For every n_i^μ we pick a second lightlike reference vector $\bar{n}_i^\mu$ with $n_i^2 = \bar{n}_i^2 = 0$ and $n_i \cdot \bar{n}_i = 2$. A common choice is

$$n_i^\mu = (1, \vec{n}_i), \qquad \bar{n}_i^\mu = (1, -\vec{n}_i), \tag{2.83}$$

with $\vec{n}_i$ a unit three-vector. In terms of $n_i, \bar{n}_i$, any four-momentum p can be decomposed in *light-cone coordinates* as

$$p^\mu = \bar{n}\cdot p\, \frac{n_i^\mu}{2} + n\cdot p\, \frac{\bar{n}_i^\mu}{2} + p_\perp^\mu \equiv (n_i\cdot p, \bar{n}_i\cdot p, \vec{p}_\perp) \equiv (p^+, p^-, \vec{p}_\perp)\,. \tag{2.84}$$

We can also decompose the metric and define an antisymmetric tensor in the $\perp$ plane as

$$g^{\mu\nu} = \frac{n^\mu \bar{n}^\nu}{2} + \frac{\bar{n}^\mu n^\nu}{2} + g_\perp^{\mu\nu}\,, \qquad \epsilon_\perp^{\mu\nu} = \frac{1}{2}\epsilon^{\mu\nu}{}_{\rho\sigma}\, n^\rho \bar{n}^\sigma\,. \tag{2.85}$$

It follows in particular that $p^2 = p^+ p^- + p_\perp^2 = p^+ p^- - \vec{p}_\perp^2$. Collinear particles close to n_i^μ have $p^- \gg |\vec{p}_\perp| \gg p^+$. We formalize this by introducing a power counting parameter λ,

$$n_i\text{-collinear:}\quad p^\mu \sim Q(\lambda^2, 1, \lambda)\,, \qquad \lambda \ll 1\,, \tag{2.86}$$

where $Q \sim \bar{n}_i$ is the energy available from (or absorbed by) the hard interaction process. The precise definition of λ depends on the experimental observable, and we will see various examples in this thesis. The collinear modes of the QCD quantum fields that satisfy eq. (2.86) are one of the degrees of freedom of SCET.

In general, there are distinct n_i-collinear modes for every strongly interacting collinear sector in the problem. Color-singlet production in proton-proton collisions involves two sectors n_a and n_b, one for each incoming proton. Unless noted otherwise, we pick

$$n_a^\mu = (1, +\hat{z})_{\text{lep}}\,, \qquad n_b^\mu = (1, -\hat{z})_{\text{lep}} \tag{2.87}$$

in the *leptonic* frame, i.e., the frame where the color-singlet final state has vanishing rapidity and longitudinal momentum. The z-axis of the leptonic frame and the spatial components of the $n_{a,b}$ are aligned with the beam axis. The leptonic frame is reached from the lab frame through a longitudinal boost by the rapidity Y,

$$n_a^\mu = e^{-Y}(1, +\hat{z})_{\text{lab}}\,, \qquad n_b^\mu = e^{+Y}(1, -\hat{z})_{\text{lab}} \tag{2.88}$$

so the leptonic final state can still have nonzero transverse momentum. For the proton momenta we have in this convention, neglecting proton masses,

$$P_a^\mu = e^{-Y} E_{\text{cm}}\, \frac{n_a^\mu}{2} = P_a^-\, \frac{n_a^\mu}{2}\,, \qquad P_b^\mu = e^{+Y} E_{\text{cm}}\, \frac{n_b^\mu}{2} = P_b^-\, \frac{n_b^\mu}{2}\,. \tag{2.89}$$

Since $n_a \cdot n_b = 2$, we can pick

$$\bar{n}_a^\mu = n_b^\mu\,, \qquad \bar{n}_b^\mu = n_a^\mu\,. \tag{2.90}$$

This choice is convenient because it allows all light-cone components to be written with respect to a single $n \equiv n_a$,

$$n_a\text{-collinear:}\quad p^\mu \sim Q(\lambda^2, 1, \lambda)\,, \qquad n_b\text{-collinear:}\quad p^\mu \sim Q(1, \lambda^2, \lambda)\,. \tag{2.91}$$

In addition, the $\perp$ space for this choice coincides with the transverse plane in the detector. In these coordinates, the color-singlet momentum q^μ is given by

$$q^\mu = (q^+, q^-, \vec{q}_\perp) = \left(\sqrt{Q^2 + q_T^2}, \sqrt{Q^2 + q_T^2}, \vec{q}_T\right). \tag{2.92}$$

Our list of degrees of freedom is not yet complete. We wish to integrate out physics at scales $p^2 \sim \lambda Q^2, Q^2$, but retain as dynamical degrees of freedom all modes that, like the collinear modes, have $p^2 \lesssim \lambda^2 Q^2$. This includes isotropic *soft* modes with low energy,

$$\text{soft:} \quad p^\mu \sim Q(\lambda, \lambda, \lambda). \tag{2.93}$$

Since one of their $p^\pm$ components is parametrically larger than the respective entry for $n_{a,b}$-collinear modes, interactions between soft and collinear particles take the collinear particle off its mass shell. These interactions are therefore incorporated during the matching, see section 2.2.7. Soft modes can, however, always interact with other modes indirectly through *Glauber* modes

$$\text{Glauber:} \quad p^\mu \sim Q(\lambda^2, \lambda^2, \lambda). \tag{2.94}$$

These modes are parametrically off shell and therefore cannot be radiated into the final state. Virtual Glauber exchanges, on the other hand, keep collinear (and soft) particles on shell and therefore in principle couple all collinear sectors to each other. At the lowest energies, there are ultrasoft (or usoft) modes,

$$\text{ultrasoft:} \quad p^\mu \sim Q(\lambda^2, \lambda^2, \lambda^2). \tag{2.95}$$

Like the soft modes, ultrasoft radiation is isotropic, but unlike soft modes it keeps the emitting (or absorbing) collinear particles parametrically on shell. These interactions are therefore part of the collinear dynamics, as we will see below.

In summary, the prototypical modes describing color-singlet production in SCET are

$$\begin{aligned}
n_a\text{-collinear:} &\quad p^\mu \sim Q(\lambda^2, 1, \lambda), &\quad \text{soft:} &\quad p^\mu \sim Q(\lambda, \lambda, \lambda), \\
n_b\text{-collinear:} &\quad p^\mu \sim Q(1, \lambda^2, \lambda), &\quad \text{Glauber:} &\quad p^\mu \sim Q(\lambda^2, \lambda^2, \lambda), \\
\text{ultrasoft:} &\quad p^\mu \sim Q(\lambda^2, \lambda^2, \lambda^2).
\end{aligned} \tag{2.96}$$

Very often, a given observable (up to Glauber exchanges) can be described by collinear modes and either usoft or soft modes alone, depending on the type of radiation that the experimental measurement permits or is sensitive to. These scenarios are referred to as SCET$_\text{I}$, when only usoft modes contribute, and as SCET$_\text{II}$ in the soft case. The relevant mode setups are summarized in figure 2.8.

In general, the SCET Lagrangian is given by the sum of hard scattering operators $\mathcal{L}_\text{hard}$, which for color-singlet production arise from the coupling to the external color-singlet field, and a dynamical Lagrangian $\mathcal{L}_\text{dyn}$ encoding the low-energy interactions. Both contributions to the Lagrangian can be systematically expanded in λ,

$$\mathcal{L}_\text{SCET} = \mathcal{L}_\text{hard} + \mathcal{L}_\text{dyn} = \sum_{i=0}^{\infty} \mathcal{L}_\text{hard}^{(i)} + \mathcal{L}_G^{(0)} + \sum_{i=0}^{\infty} \mathcal{L}_\text{dyn}^{(i)}, \tag{2.97}$$

where (i) denotes power suppression of $\mathcal{O}(\lambda^i)$. The leading-power Glauber Lagrangian $\mathcal{L}_G^{(0)}$, conventionally pulled out of $\mathcal{L}_{\text{dyn}}^{(0)}$, describes leading-power interactions between soft and all collinear modes through Glauber potentials [173]. The remaining leading-power dynamical Lagrangian only involves interactions that are local at the scale λQ, and is given by

$$\mathcal{L}_{\text{dyn}}^{(0)} = \sum_{n_i} \mathcal{L}_{n_i}^{(0)} + \mathcal{L}_{us}^{(0)} + \mathcal{L}_s^{(0)} \,, \tag{2.98}$$

where $\mathcal{L}_{n_i}^{(0)}$ describes the leading-power interactions of particles in a collinear sector n_i with each other and with ultrasoft gluons, and $\mathcal{L}_{us}^{(0)}$ and $\mathcal{L}_s^{(0)}$ describe the interactions of soft and ultrasoft particles among themselves.

In the following we focus on the interactions $\mathcal{L}_{n_i}^{(0)}$ of usoft particles and particles in a single n_i-collinear sector and write $n \equiv n_i$ for short. Collinear quarks are described by a spinor field $\xi_n(x)$. (We suppress flavor indices for now.) The collinear quark field satisfies

$$\not{n}\, \xi_n(x) = 0 \,, \tag{2.99}$$

i.e., it has two nonzero components corresponding to the two physical helicities of an on-shell massless quark with respect to its direction of motion. Collinear gluons, ultrasoft gluons, and ultrasoft quarks are described by vector fields $A_n^\mu(x)$, $A_{us}^\mu(x)$, and a four-component Dirac spinor field $q_{us}(x)$, respectively. The derivatives and components of these fields have definite power counting in a sense that we will make precise now.

2.2.3 Symmetries of SCET

Ultrasoft and collinear gauge invariance. Like for the QCD Lagrangian, $\text{SU}(N_c)$ gauge invariance is the guiding principle in writing down the SCET Lagrangian. However, not all gauge transformations map propagating degrees of freedom onto each other. Consider, for example, a gauge transformation

$$\mathrm{i}\partial^\mu U(x) \sim Q(1,1,1)\, U(x) \,. \tag{2.100}$$

By eq. (2.8), this injects a large momentum into the quark and gauge fields, taking soft or collinear modes off shell. Instead, we must restrict to collinear and ultrasoft gauge transformations whose scaling respects the power counting of the theory,

$$\mathrm{i}\partial^\mu \hat{U}_n(x) \sim Q(\lambda^2, 1, \lambda)\, \hat{U}_n(x) \,, \qquad \mathrm{i}\partial^\mu U_{us}(x) \sim Q(\lambda^2, \lambda^2, \lambda^2)\, U_{us}(x) \,. \tag{2.101}$$

These two independent sets of transformations define the residual gauge symmetry of SCET. To avoid double-counting a global color rotation, we fix $\hat{U}_n(n \cdot x \to \infty) \to \mathbf{1}_F$.

The action of $U_{us}(x)$ on the soft fields is the same as that of $U(x)$ on full QCD fields because the scaling of all momenta and spacetime directions is homogeneous,

$$q_{us}(x) \xmapsto{\;U_{us}(x)\;} U_{us}(x)\, q_{us}(x) \,,$$

$$A_{us}^\mu(x) \xmapsto{\;U_{us}(x)\;} U_{us}(x) A_{us}^\mu(x) U_{us}^\dagger(x) + U_{us}(x)\Big[\frac{\mathrm{i}}{g}\partial^\mu U_{us}^\dagger(x)\Big] \,. \tag{2.102}$$
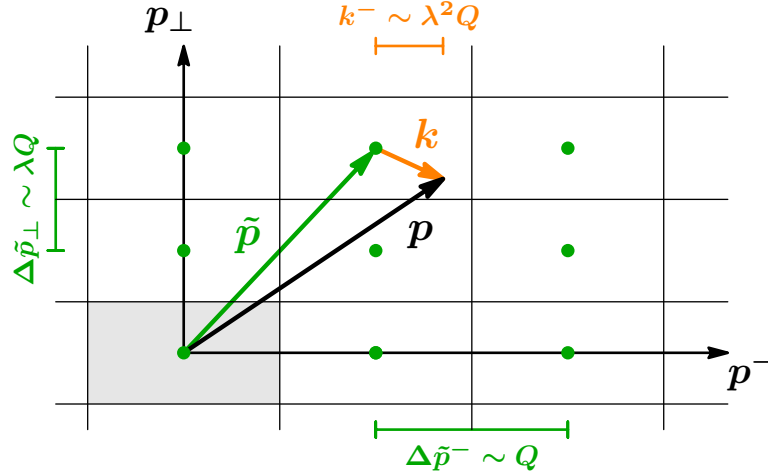
Figure 2.9: Decomposition of a momentum p into label ($\tilde{p}$) and residual momentum (k). The label momentum $\tilde{p}$ takes discrete values on a grid with spacing $\sim Q$ in the p^- and $\sim \lambda Q$ in the $p_\perp$ direction. Only one component of the $p_\perp$ momentum is shown. The $p^+ = k^+$ component is likewise not shown. The gray-shaded area at the bottom left is the zero bin $\tilde{p} = (0, 0, 0)$ where collinear and ultrasoft modes overlap.

<div align="center">Figure adapted from ref. [155].</div>

For collinear fields, $U_{us}(x)$ amounts to a slowly varying local rotation of the color space, i.e., a *background gauge transformation*,

$$\xi_n(x) \xmapsto{U_{us}(x)} U_{us}(x)\,\xi_n(x)\,,$$
$$A_n^\mu(x) \xmapsto{U_{us}(x)} U_{us}(x)A_n^\mu(x)U_{us}^\dagger(x)\,. \tag{2.103}$$

To write down the action of $\hat{U}_n(x)$ on the fields, we need some additional notation. Take the Fourier transform of a given $\hat{U}_n(x)$,

$$\tilde{U}(p) = \int \mathrm{d}^4x\, e^{\mathrm{i}p\cdot x}\hat{U}_n(x)\,. \tag{2.104}$$

By our assumptions we know that $\tilde{U}(p)$ only has support in the region where $p^\mu \sim Q(\lambda^2, 1, \lambda)$. Now decompose the momentum p as

$$p^\mu = \tilde{p}^\mu + k^\mu = \bar{n}\cdot\tilde{p}\,\frac{n^\mu}{2} + \tilde{p}_\perp^\mu + k^\mu\,, \tag{2.105}$$

where $\tilde{p}_\perp^\mu \sim Q(0, 1, \lambda)$ is a large *label momentum* whose first component exactly vanishes, $\tilde{p}^+ = 0$, and $k^\mu \sim Q(\lambda^2, \lambda^2, \lambda^2)$ is a small *residual momentum*. This decomposition is redundant to the extent that we can shuffle $\mathcal{O}(\lambda^2)$ momenta in and out of $\tilde{p}^-, \tilde{p}_\perp$. More formally, $\tilde{p}^\mu + k^\mu$ lies in a quotient set $\mathbb{R}^3 \times \mathbb{R}^4/\mathcal{I}$ with $\mathcal{I}$ a set of equivalence relations that specify the redundancy to our working order in λ. One way of choosing $\mathcal{I}$ to make eq. (2.105) unique is to make $\tilde{p}$ a *discrete* label with grid spacings $\Delta\tilde{p}^- \sim 1$ and $\Delta\tilde{p}_\perp \sim \lambda$,

taking the continuum limit in the end. As illustrated in figure 2.9, any collinear momentum p then falls into a bin with a grid point $\tilde{p}$ at its center, and the distance from $\tilde{p}$ defines k.

With this decomposition, we can define

$$U_{n,\tilde{p}}(x) \equiv \int \frac{\mathrm{d}^4 k}{(2\pi)^4} \, e^{-\mathrm{i} k \cdot x} \, \tilde{U}_n(\tilde{p} + k) \,, \tag{2.106}$$

where the dependence on the residual momentum is transformed back to position space, and write the collinear gauge transformation as

$$\hat{U}_n(x) = \int \frac{\mathrm{d}^4 p}{(2\pi)^4} \, e^{-\mathrm{i} p \cdot x} \, \tilde{U}_n(p) = \sum_{\tilde{p}} \int \frac{\mathrm{d}^4 k}{(2\pi)^4} e^{-\mathrm{i}(\tilde{p}+k)\cdot x} \, \tilde{U}_n(\tilde{p} + k)$$

$$= \sum_{\tilde{p}} e^{-\mathrm{i}\tilde{p}\cdot x} \, U_{n,\tilde{p}}(x) \,. \tag{2.107}$$

The x dependence of the $U_{n,\tilde{p}}(x)$ is purely residual since we have pulled out the large label component, i.e.,

$$\mathrm{i}\partial^\mu U_{n,\tilde{p}}(x) \sim Q(\lambda^2, \lambda^2, \lambda^2) \, U_{n,\tilde{p}}(x) \,. \tag{2.108}$$

The requirement that $\hat{U}_n(n \cdot x \to \infty) \to \mathbf{1}_F$ now becomes $U_{n,\tilde{p}=0}(x) = \mathbf{1}_F$ for the slowest-oscillating mode $\tilde{p} = 0$. This mode is called the *zero bin* and is indicated by gray shading in figure 2.9. Note that if we did not impose this constraint, the zero bin would precisely double-count an ultrasoft gauge transformation.

The collinear quark and gluon field are decomposed in an analogous way,

$$\xi_n(x) \equiv \sum_{\tilde{p}\neq 0} \xi_{n,\tilde{p}}(x) \,, \qquad A_n^\mu(x) \equiv \sum_{\tilde{p}\neq 0} A_{n,\tilde{p}}^\mu(x) \,. \tag{2.109}$$

The sum explicitly excludes the zero-bin to remove the overlap with the ultrasoft fields that also carry a total momentum $p^\mu = k^\mu \sim Q(\lambda^2, \lambda^2, \lambda^2)$.[5] Fields $\xi_{n,\tilde{p}}$ and $\xi_{n,\tilde{q}}$ (or $A_{n,\tilde{p}}^\mu$ and $A_{n,\tilde{q}}^\mu$) with different label momenta $\tilde{q} \neq \tilde{p}$ are orthogonal. Our convention is such that $\xi_{n,\tilde{p}}$ for $\bar{n} \cdot \tilde{p} > 0$ annihilates a quark and for $\bar{n} \cdot \tilde{p} < 0$ creates an antiquark, and vice versa for $\bar{\xi}_{n,\tilde{p}}$. The field $A_{n,\tilde{p}}$ annihilates (creates) a gluon for $\bar{n} \cdot \tilde{p} > 0$ ($\bar{n} \cdot \tilde{p} < 0$).

The combination that enters in a mode decomposition of the full quark field, and therefore transforms like the full quark field under collinear gauge transformations, is

$$e^{-\mathrm{i}\tilde{p}\cdot x} \, \xi_{n,\tilde{p}}(x) \xmapsto{\hat{U}_n(x)} e^{-\mathrm{i}\tilde{p}\cdot x} \, \hat{U}_n(x) \, \xi_{n,\tilde{p}}(x) \,. \tag{2.110}$$

Written out explicitly, we have

$$e^{-\mathrm{i}\tilde{p}\cdot x} \, \xi_{n,\tilde{p}}(x) \xmapsto{\hat{U}_n(x)} \sum_{\tilde{q}} e^{-\mathrm{i}(\tilde{p}+\tilde{q})\cdot x} U_{n,\tilde{q}}(x) \, \xi_{n,\tilde{p}}(x) \,, \tag{2.111}$$

---

[5]In practice this means that loop integrals over collinear momenta are also restricted to $\int \mathrm{d}^4 p = \sum_{\tilde{p}\neq 0} \int \mathrm{d}^4 k$. In dimensional regularization, it is convenient to take the continuum limit of this integral in d dimensions before evaluating the integral. This is achieved by subtracting the integrand reexpanded in the limit where all collinear momenta are purely residual [174]. Most commonly, and for all examples in this thesis, this *zero-bin subtraction* only produces a scaleless integral $\int \mathrm{d}k \, k^{-1+\epsilon}$ which vanishes in dimensional regularization.

which is a mode of total label momentum $\tilde{p} + \tilde{q}$. We can interpret this as label momentum conservation between the gauge transformation and the field. This is expected because the gauge transformation is a product in position space, and therefore should be a convolution in momentum space. We can make this more compact by introducing the *label momentum operator* $\mathcal{P}^\mu$,

$$\mathcal{P}^\mu \, X_{n,\tilde{p}}(x) \equiv \tilde{p}^\mu \, X_{n,\tilde{p}}(x) \,, \qquad X_{n,\tilde{p}} = \{U_{n,\tilde{p}}, \xi_{n,\tilde{p}}, A^\mu_{n,\tilde{p}}\} \,. \tag{2.112}$$

Like a derivative operator, it acts on products as

$$\mathcal{P}^\mu \, X_{n,\tilde{p}}(x) \, Y_{n,\tilde{q}}(x) = (\tilde{p}^\mu + \tilde{q}^\mu) X_{n,\tilde{p}}(x) \, Y_{n,\tilde{q}}(x) \,. \tag{2.113}$$

It is common to abbreviate the large component as $\overline{\mathcal{P}} \equiv \bar{n} \cdot \mathcal{P}$. When different collinear sectors are present, we will indicate by a subscript that $\mathcal{P}_{n_i}$ belongs to the sector n_i, with $\overline{\mathcal{P}}_{n_i} \equiv \bar{n}_i \cdot \mathcal{P}_{n_i}$. The label momentum operator allows us to pull phases out of sums,[6]

$$\hat{U}_n(x) = \sum_{\tilde{p}} e^{-i\tilde{p}\cdot x} \, U_{n,\tilde{p}}(x) = e^{-i\mathcal{P}\cdot x} \sum_{\tilde{p}} U_{n,\tilde{p}}(x) \equiv e^{-i\mathcal{P}\cdot x} \, U_n(x) \,. \tag{2.114}$$

With this, we can compactly write the transformation of $\xi_n(x)$ as

$$e^{-i\mathcal{P}\cdot x} \, \xi_n(x) \xmapsto{\;U_n(x)\;} e^{-i\mathcal{P}\cdot x} U_n(x) \, \xi_n(x) \,, \tag{2.115}$$

where label momentum conservation is encoded in the overall, rapidly oscillating phases.

We are now ready to write down the action of collinear gauge transformations on all fields in the theory. Soft fields do not transform because as we have seen, $U_n(x)$ would inject a large momentum into them, making them collinear instead,

$$q_{us}(x) \xmapsto{\;U_n(x)\;} q_{us}(x) \,, \qquad A^\mu_{us}(x) \xmapsto{\;U_n(x)\;} A^\mu_{us}(x) \,. \tag{2.116}$$

The collinear fields transform as

$$e^{-i\mathcal{P}\cdot x} \xi_n(x) \xmapsto{\;U_n(x)\;} e^{-i\mathcal{P}\cdot x} U_n(x) \, \xi_n(x) \ ,$$
$$e^{-i\mathcal{P}\cdot x} A^\mu_n(x) \xmapsto{\;U_n(x)\;} e^{-i\mathcal{P}\cdot x} U_n A^\mu_n(x) U^\dagger_n(x)$$
$$+ e^{-i\mathcal{P}\cdot x} U_n(x) \frac{1}{g} \Big[\Big(\mathcal{P}^\mu + i n \cdot D^\mu_{us} \frac{\bar{n}^\mu}{2} \Big) U^\dagger_n(x) \Big] \,. \tag{2.117}$$

In particular, $U_n(x)$ transformations inject large momentum $\mathcal{P}^\mu$ into the collinear gauge field as expected. The presence of the usoft covariant derivative $D^\mu_{us} = \partial^\mu - ig A^\mu_{us}(x)$ on the third line (instead of a regular derivative) ensures that the collinear transformation rule is itself covariant with respect to usoft background gauge transformations. Both the label and the usoft covariant derivative operator only act within the square brackets.

---

[6]Note that the roles of $\hat{U}_n(x)$ and the shorthand $U_n(x)$ that we have defined on the last equality are usually interchanged in the literature, see e.g. ref. [170]. There, $U_n(x)$ denotes the original collinear gauge transformation and a matrix notation in label momentum space is adopted to define $\hat{U}_n(x)$. We prefer to use a single notation in terms of $\mathcal{P}$ to indicate label momentum conservation.

Reparametrization invariance. The second principle that fixed the form of the QCD Lagrangian was Lorentz invariance. In SCET, Lorentz invariance is broken by the explicit reference vectors n and $\bar{n}$. The choice of n and $\bar{n}$, however, is arbitrary to the extent that it continues to satisfy $n \cdot \bar{n} = 2$ and leaves the scaling of the modes in eq. (2.96) unchanged. This freedom is manifest as a symmetry of the effective theory known as reparametrization invariance (RPI) [175, 176]. There are three types of RPI transformations on n and $\bar{n}$,

RPI-I	**RPI-II**	**RPI-III**
$n_i^\mu \mapsto n_i^\mu + \Delta_\perp^\mu, \quad \Delta_\perp \sim \lambda$	$n_i^\mu \mapsto n_i^\mu$	$n_i^\mu \mapsto e^{+\alpha} n_i^\mu, \quad \alpha \sim \lambda^0$
$\bar{n}_i^\mu \mapsto \bar{n}_i^\mu$	$\bar{n}_i^\mu \mapsto \bar{n}_i^\mu + \epsilon_\perp^\mu, \quad \epsilon_\perp \sim \lambda^0$	$\bar{n}_i^\mu \mapsto e^{-\alpha} n_i^\mu$

$$\text{(2.118)}$$

RPI-I and RPI-II transformations rotate the reference vectors into the transverse plane by an infinitesimal amount $\Delta_\perp^\mu$ or $\epsilon_\perp^\mu$, with $n_i \cdot \Delta_\perp = \bar{n}_i \cdot \Delta_\perp = 0$ and $n_i \cdot \epsilon_\perp = \bar{n}_i \cdot \epsilon_\perp = 0$. The power-counting constraint on the RPI-I parameter $\Delta_\perp^\mu \sim \lambda$ is more stringent than for $\epsilon_\perp^\mu$ because it mixes the large component of collinear momenta into the smaller ones. Type III is a finite transformation on the normalization of the reference vectors. Invariants under RPI-III are particularly easy to identify because for given four-vectors A^μ, B^μ, they can only involve ratios or products of the form

$$\frac{n \cdot A}{n \cdot B} = \frac{A^+}{B^+}, \qquad \frac{\bar{n} \cdot A}{\bar{n} \cdot B} = \frac{A^-}{B^-}, \qquad (n \cdot A)(\bar{n} \cdot B) = A^+ B^-, \qquad A_\perp \cdot B_\perp. \qquad \text{(2.119)}$$

2.2.4 Leading-power SCET Lagrangian

We can now write down the leading-power SCET Lagrangian $\mathcal{L}_{n\xi}^{(0)}$ for the collinear quark field. The complete Dirac basis of bilinears in ξ_n (which satisfies $\not{n}\xi_n = 0$), is given by $\not{\bar{n}}$, $\not{\bar{n}}\gamma_5$, and $\not{\bar{n}}\gamma_\perp^\mu$ [171], so all operators have the form $\bar{\xi}_n \cdots \not{\bar{n}}\xi_n$, with $\cdots$ a set of derivative operators. Collinear and usoft gauge invariance imply that derivatives and gauge fields can only enter the collinear quark Lagrangian in the covariant combinations

$$
\begin{aligned}
\mathrm{i}\bar{n} \cdot D_n &\equiv \overline{\mathcal{P}} + g A_n^\mu & &\sim \lambda^0, \\
\mathrm{i} D_{n\perp}^\mu &\equiv \mathcal{P}_\perp^\mu + g A_{n\perp}^\mu & &\sim \lambda, \\
\mathrm{i} n \cdot D &\equiv \mathrm{i} n \cdot \partial + g n \cdot A_{us} + g n \cdot A_n & &\sim \lambda^2.
\end{aligned}
\qquad \text{(2.120)}
$$

In general, to higher orders in the power counting, $\mathcal{P}^\mu + \partial^\mu$ (and associated gauge fields) must appear together because of the freedom in the split between label and residual momenta. Here we have already expanded away $\partial_\perp^\mu, \bar{n} \cdot \partial \sim \lambda^2$ as subleading to obtain covariant derivative operators with definite power counting.

The collinear integration measure in the action scales as $\mathrm{d}^4 x \sim (p^+ p^- p_\perp^2)^{-1} \sim \lambda^{-4}$, so the leading-power Lagrangian must scale as $\mathcal{L}_{n\xi}^{(0)} \sim \lambda^4$ in order for repeated insertions of the interaction Lagrangian to have uniform power counting. Let us take the approach that we do not know the power counting of the field $\xi_n \sim \lambda^k$ beforehand, but instead deduce k from the first nontrivial Lagrangian consistent with gauge invariance and RPI that we find

in the power counting. At $\mathcal{O}(\lambda^{2k})$, we can only write down a single operator involving the large component $\mathrm{i}\bar{n}\cdot D_n$, suppressing the overall label-momentum conserving phase $e^{-\mathrm{i}\mathcal{P}\cdot x}$,

$$\bar{\xi}_n(\mathrm{i}\bar{n}\cdot D_n)\slashed{\bar{n}}\,\xi_n\,. \tag{2.121}$$

which breaks RPI-III and therefore is ruled out. At $\mathcal{O}(\lambda^{2k+1})$, the only candidate derivative is $D_\perp^\mu$, which must be contracted with another vector to form a scalar. The only available vector bilinear is $\slashed{\bar{n}}\gamma_\perp^\mu$, resulting in

$$\bar{\xi}_n\slashed{\bar{n}}\,\mathrm{i}\slashed{D}_\perp\,\xi_n\,, \tag{2.122}$$

which again breaks RPI-III. Thus the first nontrivial operators in the power counting arise at $\mathcal{O}(\lambda^{2k+2})$, where we have for example

$$\bar{\xi}_n\,\mathrm{i}n\cdot D\frac{\slashed{\bar{n}}}{2}\xi_n\,, \qquad \bar{\xi}_n\mathrm{i}\slashed{D}_{n\perp}\frac{1}{\mathrm{i}\bar{n}\cdot D_n}\mathrm{i}\slashed{D}_{n\perp}\frac{\slashed{\bar{n}}}{2}\xi_n\,, \qquad \bar{\xi}_n\mathrm{i}D_{n\perp}^\mu\frac{1}{\mathrm{i}\bar{n}\cdot D_n}\mathrm{i}D_{n\perp\mu}\frac{\slashed{\bar{n}}}{2}\xi_n\,. \tag{2.123}$$

We can use this to fix $4 = 2k + 2$, so the collinear field scales as $\xi_n \sim \lambda$. One can show [175] that the unique result for $\mathcal{L}_{n\xi}^{(0)}$ compatible with RPI is

$$\mathcal{L}_{n\xi}^{(0)} = e^{-\mathrm{i}\mathcal{P}\cdot x}\bar{\xi}_n\left(\mathrm{i}n\cdot D + \mathrm{i}\slashed{D}_{n\perp}\frac{1}{\mathrm{i}\bar{n}\cdot D_n}\mathrm{i}\slashed{D}_{n\perp}\right)\frac{\slashed{\bar{n}}}{2}\xi_n\,. \tag{2.124}$$

implying that its form is not affected by loop corrections. The complete calculation is too lengthy to repeat here; it crucially relies on RPI-II to rule out the third term in eq. (2.123). It also relies on RPI-II to rule out operators with arbitrary insertions of $(\mathrm{i}\bar{n}\cdot D)\cdots(\mathrm{i}\bar{n}\cdot D)^{-1}$ sandwiching other derivatives, which are compatible with the power counting and have the correct mass dimension. An interesting remark is that the relative coefficient of the two terms in eq. (2.124) is fixed already by RPI-I, which ties together the $n\cdot D$ and $D_{n\perp}^\mu$ derivatives. The normalization of the collinear quark Lagrangian can be derived by a tree-level matching from the full QCD Lagrangian by explicitly integrating out the two subleading components of the quark field. (In fact, this is how eq. (2.124) is most commonly derived.)

For physical intuition, note that in eq. (2.124) usoft gluons couple to collinear quarks only through their $n\cdot A_{us}$ component and do not exchange label momentum with them, so the amplitude for the emission of soft gluons only depends on the direction n^μ of the mother particle and its color charge. This is known as an *eikonal* coupling; the corresponding Feynman rules are given in figure 2.10. An important consequence is that matrix elements of color-singlet operators computed in the soft limit exhibit *Casimir scaling* at the lowest few orders in perturbation theory, i.e., the results for scattering particles in the adjoint or fundamental representation only differ by an overall factor C_F versus C_A. (Starting at four loops, higher group invariants start to enter, but still only depend on the representation.) Unlike soft emissions, large momentum can be exchanged between collinear fields, allowing for collinear splittings along the light-cone direction.

$$\mathbf{i}g(T^a)_{ji}\, n^\mu\, \frac{\slashed{\bar{n}}}{2} \qquad\qquad gf^{abc}\, n^\mu\, \bar{n}\!\cdot\! p\, g^{\rho\sigma}$$
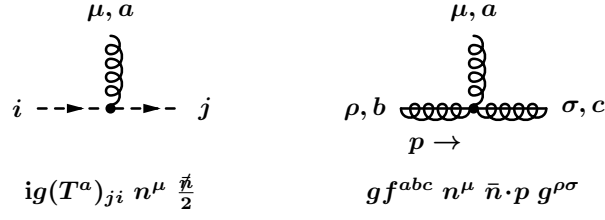
Figure 2.10: SCET Feynman rules for the eikonal interaction between a soft gluon (spring) and a collinear quark (dashed fermion line, left) or a collinear gluon (strikethrough spring, right) in Feynman gauge. The amplitude only depends on the direction n^μ (up to an overall factor for gluons) and the color charge of the emitting particle.

The leading-power collinear gluon Lagrangian is fixed by power counting and gauge invariance [167],

$$
\begin{aligned}
\mathcal{L}_{ng}^{(0)} = {}& e^{-\mathrm{i}\mathcal{P}\cdot x}\frac{1}{2g^2}\,\mathrm{Tr}\big\{[\mathrm{i}\mathcal{D}^\mu,\mathrm{i}\mathcal{D}^\nu][\mathrm{i}\mathcal{D}_\mu,\mathrm{i}\mathcal{D}_\nu]\big\} \\
&+ 2e^{-\mathrm{i}\mathcal{P}\cdot x}\,\mathrm{Tr}\big\{\bar{c}_n[\mathrm{i}\mathcal{D}_{us}^\mu,[\mathrm{i}\mathcal{D}^\mu,c_n]]\big\} + e^{-\mathrm{i}\mathcal{P}\cdot x}\frac{1}{\xi_n}\,\mathrm{Tr}\big\{[\mathrm{i}\mathcal{D}_{us}^\mu, A_{n\mu}][\mathrm{i}\mathcal{D}_{us}^\nu, A_{n\nu}]\big\}\,, \quad (2.125)
\end{aligned}
$$

where the field-strength tensor is given in terms of the leading components of the covariant derivative in eq. (2.120) as

$$
\mathcal{D}^\mu \equiv \bar{n}\!\cdot\! D_n \frac{n^\mu}{2} + D_{n\perp}^\mu + n\!\cdot\! D\frac{\bar{n}^\mu}{2}\,. \tag{2.126}
$$

The last term contains the coupling to usoft gluons, which is again eikonal and leads to the second Feynman rule in figure 2.10. While the individual terms in $\mathcal{D}^\mu$ differ in their power counting, their nonzero contractions in the Lagrangian have homogeneous power counting. The gauge fixing terms on the second line of eq. (2.125) are covariant with respect to the usoft background field to ensure they only fix the collinear gauge,

$$
\mathcal{D}_{us}^\mu \equiv \overline{\mathcal{P}}\frac{n^\mu}{2} + \mathcal{P}_\perp^\mu + n\!\cdot\! D_{us}\frac{\bar{n}^\mu}{2} = \mathcal{D}^\mu - gA_n^\mu\,. \tag{2.127}
$$

Note that also the collinear ghost fields c_n carry label momentum. The gauge parameter ξ_n may be chosen independently of the choice made for full QCD because as we will see shortly, the matching is performed at the level of gauge invariant quantities.

With this we have gathered all ingredients in the leading-power dynamical SCET Lagrangian in eq. (2.98), where the total collinear Lagrangian for a sector n is

$$
\mathcal{L}_n^{(0)} = \mathcal{L}_{n\xi}^{(0)} + \mathcal{L}_{ng}^{(0)}\,. \tag{2.128}
$$

The soft and ultrasoft Lagrangians in eq. (2.98) are simply copies of the QCD Lagrangian in eq. (2.19) due to the isotropy of the modes, and again contain independent gauge fixing terms with gauge parameters ξ_{us} and ξ_s.

2.2.5 Hard matching and operator building blocks

We now turn to the hard scattering Lagrangian $\mathcal{L}_{\text{hard}}$ in eq. (2.97). We are most often interested in the case where an external color-singlet field mediates an interaction between two distinct collinear sectors n_1, n_2 by injecting (or absorbing) a large momentum $q^\mu \sim Q(1, 1, 1)$. For definiteness, let us focus on the case of an electroweak vector field V_μ which couples to a QCD current J_V^μ as $\mathcal{L} \supset -V_\mu J_V^\mu$. The hard scattering Lagrangian is obtained order by order in the power counting by matching the full-theory current onto EFT currents $J_V^{(i)\mu}$ with an explicit power suppression of $\mathcal{O}(\lambda^i)$ relative to the leading term,

$$J_V^\mu \mapsto \sum_{i \geq 0} J_V^{(i)\mu}, \qquad \mathcal{L}_{\text{hard}}^{(i)} = -V_\mu J_V^{(i)\mu}. \tag{2.129}$$

The $J_V^{(i)\mu}$ are given by a sum over $\mathcal{O}(\lambda^i)$ operators $O_A^{(i)}$ built out of EFT fields with matching coefficient $C_A^{(i)\mu}$,

$$J_{V\,n_1 n_2}^{(i)\mu}(x) = \sum_A \Big[\prod_{i=1}^{\ell_A} \int \mathrm{d}\omega_i \Big] \sum_{\{m_A\}} C_{A,\{m_A\}}^{(i)\mu}(n_1, n_2; \omega_1, \cdots, \omega_{\ell_A})$$
$$\times O_{A,\{m_A\}}^{(i)}(n_1, n_2; \omega_1, \cdots, \omega_{\ell_A}; x). \tag{2.130}$$

The matching coefficients $C_A^{(i)\mu}$ are determined by comparing suitable matrix elements of the full theory and EFT currents. The most general EFT current involves a sum over all possible collinear directions n_1, n_2,

$$J_V^{(i)\mu}(x) = \sum_{n_1, n_2} J_{V\,n_1 n_2}^{(i)\mu}(x). \tag{2.131}$$

We will typically calculate matrix elements of these operators between n_a and n_b-collinear proton states, and therefore by label momentum conservation will only need the cases $n_1 = n_a, n_2 = n_b$ and vice versa. The sum over directions is relevant in the case of final-state collinear sectors, e.g. for $e^+ e^- \rightarrow$ hadrons or for the jet clustering calculation in section 3.4.4, where it becomes part of the phase space integral.

Apart from the collinear directions $n_{1,2}$, the matching coefficients (and operators) depend on the large-label momentum components ω_i carried by the ℓ_A different collinear fields in the operator, and are summed over a set of flavor, spin, and color indices $\{m_A\}$. The matching coefficients carry the overall vector index μ. In practice, the sum over $\{m_A\}$ is greatly simplified, and made tractable at subleading power in the first place, by using operators of definite helicity [177, 178]. Using this approach, the hard-scattering operators for color-singlet production to $\mathcal{O}(\lambda^2)$ have been constructed in refs. [179–181].

The individual operators in eq. (2.130) must respect the symmetries of SCET described in section 2.2.3, in particular usoft gauge invariance and collinear gauge invariance within each sector. To make the latter property manifest at the level of the operators, it is convenient to define gauge-invariant operator building blocks in terms of the fields in each sector n. There must be at least one excess quark field ξ_n in the building block because the external

current annihilates quarks from different sectors, so trivial combinations $\bar{\xi}_n \cdots \xi_n$ do not qualify. Therefore the task is to find a combination of gauge fields $A_n^\mu(x)$ that precisely counteracts the transformation behavior of ξ_n under collinear gauge transformations in eq. (2.117). The unique object that fits the bill is the *collinear Wilson line*,

$$W_n(x) = \mathrm{P}\left\{ \exp\left[\mathrm{i}g \int_{-\infty}^0 \mathrm{d}s \, \bar{n} \cdot A_n(x + \bar{n}s) \right] \right\} = \sum_{\mathrm{perm.}} \exp\left[\frac{-g}{\overline{\mathcal{P}}} \, \bar{n} \cdot A_n(x) \right], \qquad (2.132)$$

where P denotes path ordering of the color generators in the exponential along the path parametrized by s. On the second equality we have Fourier-transformed the fields to momentum space, performed the integral over $s_1 < s_2 < \cdots$ for each term in the Dyson series in terms of the label momentum, and Fourier-transformed the residual component back to position space. In this case we sum over all permutations of the color generators.

To see that the collinear Wilson line indeed transforms as

$$e^{-\mathrm{i}\mathcal{P}\cdot x} W_n(x) \xmapsto{\ U_n(x)\ } e^{-\mathrm{i}\mathcal{P}\cdot x} U_n(x) \, W_n(x) \qquad (2.133)$$

as desired, note that it satisfies the linear equation

$$\left[\overline{\mathcal{P}} + g\bar{n} \cdot A_n(x) \right] W_n(x) = 0 \,. \qquad (2.134)$$

With the boundary condition $W_n(x \to -\infty) \to \mathbf{1}_F$ this uniquely determines $W_n(x)$. On the other hand, we can see that $U_n(x) \, W_n(x)$, satisfies the same equation with the transformed gauge field [167]: Suppressing overall phases $e^{-\mathrm{i}\mathcal{P}\cdot x}$, we have

$$\begin{aligned}
&\left\{ \overline{\mathcal{P}} + gU_n\bar{n} \cdot A_nU_n^\dagger + U_n\big[\overline{\mathcal{P}}U_n^\dagger\big] \right\} U_nW_n \\
&= U_n\left\{ U_n^\dagger\overline{\mathcal{P}} + g\bar{n} \cdot A_nU_n^\dagger + \big[\overline{\mathcal{P}}U_n^\dagger\big] \right\} U_nW_n \\
&= U_n\left\{ \overline{\mathcal{P}}U_n^\dagger + g\bar{n} \cdot A_nU_n^\dagger \right\} U_nW_n \\
&= U_n\left\{ \overline{\mathcal{P}} + g\bar{n} \cdot A_n \right\} W_n = 0 \,,
\end{aligned} \qquad (2.135)$$

where on the first equality we inserted $\mathbf{1}_F = U_nU_n^\dagger$ and pulled out the overall U_n, on the second equality we used the product rule $\overline{\mathcal{P}}U_n^\dagger = U_n^\dagger\overline{\mathcal{P}} + \big[\overline{\mathcal{P}}U_n^\dagger\big]$, and on the third equality we canceled off $U_n^\dagger U_n = \mathbf{1}_F$ on the right to recover the defining eq. (2.134). Therefore U_nW_n is the image of W_n under the gauge transformation, and the combination

$$e^{-\mathrm{i}\mathcal{P}\cdot x}\chi_n(x) = e^{-\mathrm{i}\mathcal{P}\cdot x} \, W_n^\dagger(x) \, \xi_n(x) \,, \qquad (2.136)$$

is invariant under n-collinear gauge transformations. In many applications it is convenient to pick out a definite, *continuous* large label momentum component ω from χ_n,

$$\chi_{n,\omega}(x) = \left[\delta(\omega - \overline{\mathcal{P}}) \, W_n^\dagger(x) \, \xi_n(x) \right] \,. \qquad (2.137)$$

This notation is to be understood as follows,

$$\sum_{\tilde{\omega}} e^{-i\tilde{\omega}x^+/2} \chi_{n,\tilde{\omega}}(x^+, x^-, \vec{x}_\perp) = \sum_{\tilde{\omega}} \int \mathrm{d}k^- \, e^{-i(\tilde{\omega}+k^-)x^+/2} \chi_{n,\tilde{\omega}}(x^-, \vec{x}_\perp)$$

$$\equiv \int \mathrm{d}k^- \, e^{-i\omega x^+/2} \chi_{n,\omega}(x^-, \vec{x}_\perp) \,, \tag{2.138}$$

i.e., the label momentum $\omega = \tilde{\omega} + k^-$ is made continuous by absorbing the residual momentum k^- carried by the field, and the resulting field $\chi_{n,\omega}(x)$ is exactly flat in the x^+ spacetime direction. Note that we already used continuous label momenta when writing down eq. (2.130). Sometimes we will also need the field $\chi_{n,p}$ with a definite continuous label momentum p in all three label directions,

$$\chi_{n,p}(x) = \left[\delta(\omega - \overline{\mathcal{P}}) \, \delta^2(\vec{p}_\perp - \vec{\mathcal{P}}_\perp) W_n^\dagger(x) \, \xi_n(x) \right], \qquad p^\mu = \omega \frac{n^\mu}{2} + p_\perp^\mu \,, \tag{2.139}$$

which is independent of both x^+ and $\vec{x}_\perp$, $\chi_{n,p}(x) = \chi_{n,p}(x^-)$. Using W_n, we can also write down a collinearly gauge-invariant gluon building block $\mathcal{B}_{n,\omega\perp}^\mu$, and analogously for $\mathcal{B}_{n,p\perp}^\mu$,[7]

$$\mathcal{B}_{n,\omega\perp}^\mu(x) = \frac{1}{g} \left[\delta(\omega + \overline{\mathcal{P}}) \, W_n^\dagger(x) \, iD_{n\perp}^\mu \, W_n(x) \right]. \tag{2.140}$$

The operator building blocks $\chi_{n,\omega}$ and $\mathcal{B}_{n,\omega\perp}^\mu$ power count as

$$\chi_{n,\omega} \sim \lambda \,, \qquad \mathcal{B}_{n,\omega\perp}^\mu \sim \lambda \tag{2.141}$$

To see this, recall that $\xi_n(x), D_{n\perp}^\mu \sim \lambda$, and $\overline{\mathcal{P}}, \bar{n}\cdot A_n \sim \lambda^0$, so the $\overline{\mathcal{P}}$ operator δ function and the collinear Wilson line both scale as λ^0. Importantly, these operators are not invariant under usoft gauge transformations under which the Wilson line transforms as a local product of collinear gauge fields, i.e.,

$$W_n(x) \xmapsto{U_{us}(x)} U_{us}(x) \, W_n(x) \, U_{us}^\dagger(x) \,. \tag{2.142}$$

Their usoft transformation behavior must be compensated by the opposite collinear sector, and we can write down exactly two leading-power hard operators with the right mass dimension that are overall singlets under usoft (and all collinear) gauge transformations. Restoring flavor labels q, q' for quark fields, the two operators are

$$O_{q\bar{q}'}^{(0)\alpha\beta}(n_1, n_2; \omega_1, \omega_2; x) = \bar{\chi}_{q\,n_1,-\omega_1}^\alpha(x) \, \chi_{q'\,n_2,\omega_2}^\beta(x) \,,$$

$$O_{gg}^{(0)\mu\nu}(n_1, n_2; \omega_1, \omega_2; x) = \sqrt{\omega_1\omega_2} \, \mathcal{B}_{n_1,-\omega_1\perp}^{\mu,a}(x) \, \mathcal{B}_{n_2,-\omega_2\perp}^{\nu,a}(x) \,, \tag{2.143}$$

where the quark fields carry Dirac indices α, β, and fundamental color indices are implicit. Both operators involve exactly one building block from each collinear sector, with the label momentum signs chosen to annihilate incoming particles for $\omega_i > 0$ and preserve fermion number [57]. Note that the flavor indices on $O_{q\bar{q}'}^{(0)\alpha\beta}$ refer to the quantum numbers of the

---

[7] Note the sign flip in the δ function, where $\omega > 0$ ($\omega < 0$) now creates (annihilates) a gluon.

operator (not the external states it overlaps with), so it annihilates an n_1-collinear antiquark $\bar{q}$ and an n_2-collinear quark q'. The complete set of operator building blocks in SCET$_{\mathrm{I}}$ in addition includes $\mathcal{P}_\perp^\mu \sim \lambda$, the usoft quark field $q_{us} \sim \lambda^3$, and the usoft covariant derivative $D_{us}^\mu \sim \lambda^2$ [180], but all of them lead to an additional power suppression. In terms of these operators, the hard matching in eq. (2.130) at leading power reduces to

$$
J_{V\,n_1 n_2}^{(0)\mu}(x) = \int \mathrm{d}\omega_1 \, \mathrm{d}\omega_2 \, e^{-\mathrm{i}(\omega_1 n_1 \cdot x + \omega_2 n_2 \cdot x)/2}
$$
$$
\times \left[\sum_{q,q'} C_{V\,q\bar{q}'}^{(0)\mu\,\alpha\beta}(n_1, n_2; \omega_1, \omega_2)\, O_{q\bar{q}'}^{(0)\alpha\beta}(n_1, n_2; \omega_1, \omega_2; x) \right.
$$
$$
\left. + C_{V\,gg\,\rho\sigma}^{(0)\mu}(n_1, n_2; \omega_1, \omega_2)\, O_{gg}^{(0)\rho\sigma}(n_1, n_2; \omega_1, \omega_2; x) \right].
\tag{2.144}
$$

A few comments on eq. (2.144) are in order. First, the factorization of the physics at the scales Q and λQ is manifest in eq. (2.144). Specifically, matrix elements of the individual collinear fields at the low scale will only depend on one of the two label momenta at a time, but the only possible high-scale quantities $\omega_1^2 \sim \omega_2^2 \sim Q^2$ formed out of them are not RPI invariant, so the physical scale of the collinear dynamics can at most be λQ. (In other words, label momenta are not dynamic anymore in the EFT.) On the other hand, the matching coefficients depend on both label momenta and in particular on their product $\omega_1 \omega_2 \sim Q^2$. They are determined by comparing two-point functions of the full QCD current, also known as form factors, to two-point functions of the effective operators, and thus encode virtual corrections at the scale $\mu \sim Q$.

Second, we stress that this leading-power matching relation holds true to all orders in the strong coupling. Specifically, the collinear Wilson lines encode the emission of an arbitrary number of collinear gluons $\sim [g\bar{n} \cdot A_n(x)]^n$ which all contribute at the same (leading) order in the power counting. In a sense, collinear gauge invariance allows us to fix the relative coefficients in an infinite series of operators that arise from integrating out n-collinear gluon attachments to other sectors at different orders in g, and condense them all into two simple objects.

As a third, technical comment, note that the flavor indices q, q' carried by the SCET operators are in general distinct from the flavors that couple to the vector boson. This is because starting at two loops in the full theory calculation that determines the matching coefficients, the vector boson may couple to a closed (heavy) quark loop instead. In the same way, the gluon operator can contribute to vector boson production: Since the vector boson may be off shell, the relevant full-theory diagrams are not subject to the Landau-Yang theorem [182, 183] and do not vanish in general. Details on this, the spin structure, and the perturbative expansion of the matching coefficients can be found in chapter 7 and appendix B.

2.2.6 Ultrasoft-collinear factorization

The dynamical Lagrangian in eq. (2.98) currently has the form

$$\mathcal{L}_{\text{dyn}}^{(0)} = \sum_{n_i} \mathcal{L}_{n_i}^{(0)}(\xi_{n_i}, A_{n_i}^\mu, c_{n_i}, n_i \cdot A_{us}) + \mathcal{L}_{us}^{(0)}(q_{us}, A_{us}^\mu) + \mathcal{L}_{us}^{(0)}(q_s, A_s^\mu). \tag{2.145}$$

At this point, the usoft gauge field still interacts with all collinear sectors through its respective $n_i \cdot A_{us}$ component and couples together all sectors. Similarly, we saw that the hard operator building blocks introduced in the previous section still transform in a nontrivial way under usoft gauge transformations.

The key ingredients that allow us to fully factorize collinear and usoft dynamics are ultrasoft Wilson lines $Y_{n_i}(x)$ along the n_i directions,

$$Y_{n_i}(x) = \mathrm{P}\left\{ \exp\left[\mathrm{i}g \int_{-\infty}^0 \mathrm{d}s\, n_i \cdot A_{us}(x + n_i s) \right] \right\}. \tag{2.146}$$

This expression is valid for an initial-state collinear sector n_i; for a final-state sector, the integral runs over $s \in [0, +\infty)$.[8] Ultrasoft Wilson lines satisfy the defining equation

$$\mathrm{i}n_i \cdot D_{us} Y_{n_i} = 0, \tag{2.147}$$

which together with $Y_{n_i}^\dagger Y_{n_i} = \mathbf{1}_F$ implies the operator relation

$$Y_{n_i}^\dagger \mathrm{i}n_i D_{us} Y_{n_i} = \mathrm{i}n_i \cdot \partial. \tag{2.148}$$

This relation motivates the Bauer-Pirjol-Stewart (BPS) field redefinition [167],

$$\xi_{n_i} = Y_{n_i} \xi_{n_i}^{\text{BPS}}, \qquad A_{n_i}^\mu = Y_{n_i} A_{n_i}^{\text{BPS}\,\mu} Y_{n_i}^\dagger, \qquad c_{n_i} = Y_{n_i} c_{n_i}^{\text{BPS}} Y_{n_i}^\dagger. \tag{2.149}$$

Note that in these expressions, Y_{n_i} commutes with the label momentum operator. The redefinition of the collinear gauge field implies

$$W_{n_i} = Y_{n_i} W_{n_i}^{\text{BPS}} Y_{n_i}^\dagger \tag{2.150}$$

for the n_i-collinear Wilson lines. After replacing all fields in the collinear Lagrangian by their BPS-redefined counterparts, all occurrences of $n_i \cdot D_{us}$ are sandwiched by usoft Wilson lines and can be converted to simple partial derivatives, eliminating the coupling to the usoft gauge field:

$$\mathcal{L}_{n_i}^{(0)}(\xi_{n_i}, A_{n_i}^\mu, c_{n_i}, n_i \cdot A_{us}) = \mathcal{L}_{n_i}^{(0)}(\xi_{n_i}^{\text{BPS}}, A_{n_i}^{\text{BPS}\,\mu}, c_{n_i}^{\text{BPS}}, 0). \tag{2.151}$$

---

[8]Consequently, the momentum-space Feynman rules for the two cases differ by i0 prescriptions whose signs can be derived by requiring that the Fourier transform is finite. Alternatively, the signs can be fixed by explicitly considering the full-theory diagrams that reduce to the Wilson line Feynman rule in the eikonal limit. Explicit Feynman rules for (ultra)soft and collinear-soft Wilson lines are given in ref. [155].

The physical effect of the usoft interactions is of course still present and moved to the hard operators instead, which at leading power only involved collinear fields before the field redefinition. The BPS-transformed collinear building blocks read

$$\chi_{n_i,\omega} = Y_{n_i} \chi_{n_i,\omega}^{\mathrm{BPS}}, \qquad \mathcal{B}_{n_i,\omega\perp}^\mu = Y_{n_i} \mathcal{B}_{n_i,\omega\perp}^{\mathrm{BPS}\,\mu} Y_{n_i}^\dagger. \tag{2.152}$$

It is convenient to write the second relation in terms of a Wilson line $\mathcal{Y}_{n_i}^{ab}$ in the adjoint representation,

$$T^a \mathcal{Y}_{n_i}^{ab} \equiv Y_{n_i} T^b Y_{n_i}^\dagger, \qquad \mathcal{B}_{n_i,\omega\perp}^{\mu\,a} = \mathcal{Y}_{n_i}^{ab} \mathcal{B}_{n_i,\omega\perp}^{\mathrm{BPS}\,\mu\,b}. \tag{2.153}$$

After the BPS field redefinition, the leading-power hard operators read, with all color indices explicit,

$$O_{q\bar{q}'}^{(0)\alpha\beta}(n_1, n_2; \omega_1, \omega_2; x) = \bar{\chi}_{q\,n_1,-\omega_1}^{\mathrm{BPS}\,\alpha j}(x)\, \mathrm{T}\big[Y_{n_1}^\dagger(x)\, Y_{n_2}(x)\big]^{jk} \chi_{q'\,n_2,\omega_2}^{\mathrm{BPS}\,\beta k}(x),$$

$$O_{gg}^{(0)\mu\nu}(n_1, n_2; \omega_1, \omega_2; x) = \sqrt{\omega_a \omega_b}\, \mathcal{B}_{n_1,-\omega_a\perp}^{\mathrm{BPS}\,\mu,a}(x)\, \mathrm{T}\big[\mathcal{Y}_{n_1}^\dagger(x)\, \mathcal{Y}_{n_2}(x)\big]^{ab} \mathcal{B}_{n_2,-\omega_b\perp}^{\mathrm{BPS}\,\nu,b}(x). \tag{2.154}$$

The time ordering T ensures the proper ordering of ultrasoft gluon fields, with the ordering of color generators still governed by the (anti)path ordering in the Wilson lines [57]. In eq. (2.154), the factorization of modes is manifest at the level of the operators. Matrix elements of eq. (2.154) may be evaluated for each sector individually, using the corresponding leading-power Lagrangian. In the following we will always work with BPS-redefined fields and suppress the superscript BPS.

2.2.7 SCET$_{\mathrm{II}}$ and rapidity divergences

SCET$_{\mathrm{II}}$ is characterized by the sensitivity of the experimental measurement to soft radiation $p^\mu \sim Q(\lambda, \lambda, \lambda)$. Interactions between soft and collinear modes lead to off-shell fluctuations with $p^\mu \sim Q(\lambda, 1, \lambda)$ and $p^2 \sim \lambda Q^2$ and are therefore not part of the dynamics of the effective theory. Instead, these interactions give rise to soft Wilson lines during the matching,

$$S_{n_i}(x) = \mathrm{P}\bigg\{\exp\Big[ig\int_{-\infty}^0 \mathrm{d}s\, n_i \cdot A_s(x + n_i s)\Big]\bigg\},$$

$$= \sum_{\mathrm{perm.}} \exp\bigg\{\frac{-g}{n_i \cdot \mathcal{P}}\, n_i \cdot A_s(x)\bigg\}, \qquad T^a \mathcal{S}_{n_i}^{ab} = S_{n_i} T^b S_{n_i}^\dagger, \tag{2.155}$$

which carry label momentum $n_i \cdot \mathcal{P} \sim \lambda$ and $\mathcal{P}_\perp \sim \lambda$. On the second line we used this to write down a compact expression for the Fourier transform of the Dyson exponential, where all $\bar{n}_i \cdot x$ dependence is purely residual and only the $x_\perp \sim \lambda^{-1}$ dependence is still conjugate to a label momentum. A proof that only the $n_i \cdot A_s$ component of the soft gauge field appears at leading power was given in ref. [167], using the auxiliary Lagrangian method to explicitly integrate out off-shell fluctuations with $p^2 \sim \lambda Q^2$. The hard scattering operators in SCET$_{\mathrm{II}}$ are the same as in eq. (2.154), but with ultrasoft Wilson lines $Y_{n_i}(x), \mathcal{Y}_{n_i}(x)$ replaced by soft ones, $S_{n_i}(x), \mathcal{S}_{n_i}(x)$, as dictated by invariance under soft gauge transformations.

One can directly construct SCET_{II} and reproduce these operators by first matching onto a SCET_{I} theory with a power counting parameter $\lambda' \sim \sqrt{\lambda}$, whose ultrasoft modes can be identified with the soft modes in the final theory, and performing the BPS field redefinition. In the second step, the collinear modes $(\lambda'^2, 1, \lambda')$ of the SCET_{I} theory are matched onto the final collinear modes $(\lambda^2, 1, \lambda)$. Since the BPS redefined Lagrangians are identical, the matching coefficient from the second step (also known as "lowering the virtuality" of collinear modes) is trivial [184].

An important feature of many SCET_{II}-like measurements is that individual soft and collinear matrix elements are not well-defined in dimensional regularization alone due to the presence of *rapidity divergences* [185–191]. Consider, for example, a common *soft function*, i.e., a vacuum expectation value of Wilson lines, with a measurement that picks out the total soft transverse momentum $\vec{k}_s$ in a configuration with two collinear sectors $n = n_a$, $\bar{n} = n_b$,[9]

$$S(\vec{k}_s) = \frac{1}{N_c} \langle 0 | \, \text{Tr} \big\{ \bar{\text{T}} \big[S_{\bar{n}}^\dagger S_n \big] \, \delta^{d-2}(\vec{k}_s - \vec{\mathcal{P}}_\perp) \, \text{T} \big[S_n^\dagger S_{\bar{n}} \big] \big\} | 0 \rangle \,. \tag{2.156}$$

Up to $\mathcal{O}(\alpha_s^2)$, we would find the following bare result in plain dimensional regularization,

$$S(\vec{k}_s) \stackrel{?}{=} \delta^{d-2}(\vec{k}_s) + \frac{\alpha_s}{4\pi} C_F \frac{e^{\epsilon \gamma_E}}{\Gamma(1-\epsilon)} \int_0^\infty \frac{\mathrm{d}k^-}{k^-} \int_0^\infty \frac{\mathrm{d}k^+}{k^+} \frac{1}{\pi} \delta(\vec{k}_s^2 - k^+ k^-) \Big(\frac{k^+ k^-}{\mu^2} \Big)^{-\epsilon}$$

$$= \delta^{d-2}(\vec{k}_s) + \frac{\alpha_s}{4\pi} C_F \frac{e^{\epsilon \gamma_E}}{\Gamma(1-\epsilon)} \frac{\theta(\vec{k}_s^2)}{\pi \vec{k}_s^2} \Big(\frac{\vec{k}_s^2}{\mu^2} \Big)^{-\epsilon} \int_{-\infty}^\infty \mathrm{d}y_k \,. \tag{2.157}$$

On the second line we changed variables to $\kappa = k^+ k^-$ and the rapidity $y_k = \frac{1}{2} \ln(k^-/k^+)$ of the soft emission, where $\mathrm{d}k^- \mathrm{d}k^+ = \mathrm{d}\kappa \, \mathrm{d}y_k$, and performed the integral over κ. Clearly, the unconstrained integral over the rapidity diverges. The physical reason is that for $y_k \to \pm\infty$, the soft emission enters the momentum regions with collinear scaling, as indicated by the hatching in figure 2.8. (Note that this is specific to SCET_{II}, as in SCET_{I} ultrasoft and collinear emissions have distinct virtualities.) There are similar unregulated integrals in the calculation of the collinear matrix elements where the collinear momentum has small absolute rapidity and becomes soft.

A complete separation of the soft and collinear contributions requires breaking the boost invariance of the soft and collinear matrix elements by an appropriate *rapidity regulator*. (Dimensional regularization preserves boost invariance and therefore, as we saw, is insufficient.) A large variety of regulators exists in the literature [185–193]. In explicit perturbative calculations in this thesis, and in particular for results related to jet veto resummation, see section 2.4.5 and chapter 3, we will use the η regulator of refs. [190, 191].

---

[9]Here all soft Wilson lines are evaluated at a common spacetime position x which we can take to be $x = 0$ by translational invariance. In the following we continue to suppress the spacetime argument in translationally invariant matrix elements when it is the same for all fields. Also note that we have decided to measure $\vec{k}_s$ in d dimensions for simplicity in this illustrative example, which amounts to a scheme choice in dimensional regularization. A more common choice is to measure transverse momentum in exactly two dimensions such that the soft function has integer mass dimension and include an unconstrained momentum component in -2ϵ dimensions to correct for this.

It is implemented by inserting an additional term (in square brackets) into the collinear and soft Wilson lines in eqs. (2.132) and (2.155),

$$W_n(x) = \sum_{\text{perm.}} \exp\left\{ \frac{-g}{\overline{\mathcal{P}}} \left[w^2 \frac{|\bar{n} \cdot \mathcal{P}_g|^{-\eta}}{\nu^{-\eta}} \right] \bar{n} \cdot A_n(x) \right\},$$

$$S_n(x) = \sum_{\text{perm.}} \exp\left\{ \frac{-g}{n \cdot \mathcal{P}} \left[w \frac{|2\mathcal{P}_g^3|^{-\eta/2}}{\nu^{-\eta/2}} \right] n \cdot A_s(x) \right\}. \tag{2.158}$$

Here $\mathcal{P}_g$ denotes the group momentum injected into a connected web (c-web), i.e., a maximally nonabelian subdiagram. At one loop, this is simply the momentum of the emission, so for the soft matrix element above we have $|k^3/\nu|^\eta = |\sqrt{\kappa}\sinh y_k|^\eta$ for the z-component of the momentum, which regulates the y_k integral for $\eta \neq 0$.

Expanding matrix elements of the modified Wilson lines yields poles in η that are minimally subtracted in $\overline{\text{MS}}$, just like standard poles $1/\epsilon^n$ in dimensional regularization. The different powers of η in the collinear and soft Wilson line are fixed by requiring that poles cancel in the cross section. The additional mass scale ν is required to make the bare Wilson lines dimensionless. The book-keeping parameter w renders the bare matrix element independent of ν by

$$\nu \frac{\mathrm{d}w}{\mathrm{d}\nu} = -\frac{\eta}{2} w, \tag{2.159}$$

in analogy to the renormalized coupling in $d = 4 - 2\epsilon$ dimensions in eq. (2.23). It is set to $w = 1$ when the limit $\eta \to 0$ is taken in the renormalized result. The final renormalized result depends on the new scale ν in addition to the $\overline{\text{MS}}$ scale μ, and the *rapidity renormalization group* equations with respect to ν can be derived from the ν-independence of the bare result.

For results related to q_T (or TMD) factorization, see section 2.4.3, we will use the exponential regulator of ref. [192], for which results are known to high perturbative orders. In this case one exploits that the soft and collinear matrix elements become finite in dimensional regularization if an additional light-cone momentum component is measured, or equivalently, if the fields are separated by some $x^\pm$ along the light cone. The regulated matrix elements are then defined by taking, in a particular way, the limit $x^\pm \to \infty$ and associating $1/x^\pm$ with the rapidity scale ν. The results obtained in this way have the same functional form as renormalized results in the η regulator scheme, and the perturbative results up to two loops have even been found to be identical. In chapter 6 we will exploit the renormalization condition in the exponential regulator scheme to extract, in a simple way, the eikonal limit of the collinear proton matrix elements relevant for q_T factorization.

2.2.8 SCET$_+$

SCET$_+$ is an effective theory designed to describe multi-differential measurements that set several physical scales at once [194, 195]. In particular, these scenarios generically involve an additional power counting parameter λ', and extend SCET by additional collinear-soft

modes,

$$\text{collinear-soft:} \quad p^\mu \sim Q(\lambda^2/\lambda', \lambda', \lambda) \,. \tag{2.160}$$

The dominant direction of these modes depends on the hierarchy between λ' and λ. For $\lambda \ll \lambda'$, the above modes are boosted into the $n \equiv n_a$ direction compared to soft modes, but still have parametrically smaller energy $\sim \lambda' Q$ than genuine n-collinear modes. In this case the additional modes are also referred to as n-collinear-soft. Depending on the problem at hand, a second set of $\bar{n}$-collinear-soft modes in the opposite $\bar{n} \equiv n_b$ direction may be present. The collinear-soft modes have a SCET$_I$-like relation to other modes with the same parametric p^- scaling, e.g. $\bar{n}$-collinear modes with $p^\mu \sim (1, \lambda', \sqrt{\lambda'})$, and are separated from them in virtuality by $\lambda^2 \ll \lambda'$. Factorizing their interactions by the analogue of the BPS field redefinition gives rise to a n-collinear-soft Wilson line along the $\bar{n}$-collinear quark trajectory,

$$V_n(x) = \mathrm{P}\left\{ \exp\left[ig \int_{-\infty}^{0} ds\, \bar{n} \cdot A_{cs}(x + \bar{n}s) \right] \right\} \,. \tag{2.161}$$

Note that the subscript in this case refers to the type of gluon and not the direction of the Wilson line. After this redefinition, the leading-power dynamics of collinear-soft modes are described by a copy $\mathcal{L}_{cs}^{(0)}$ of the QCD Lagrangian. On the other hand, the collinear-soft modes have a SCET$_{II}$-like relation to other modes on the same invariant-mass hyperbola $p^2 \sim \lambda^2 Q^2$. These could e.g. be n-collinear modes with $p^\mu \sim (\lambda, 1, \lambda)$. Interactions of these n-collinear modes with n-collinear-soft gluons take the former off shell and are therefore captured by another distinct collinear-soft Wilson line during the matching,

$$X_n(x) = \mathrm{P}\left\{ \exp\left[ig \int_{-\infty}^{0} ds\, n \cdot A_{cs}(x + ns) \right] \right\} \,. \tag{2.162}$$

The precise number and type of Wilson lines in the leading-power SCET$_+$ current depends again on the physics scenario, but can in any case be inferred from gauge invariance in each respective sector, and we will see a concrete example in chapter 5. To regulate rapidity divergences in collinear-soft matrix elements, we introduce the η regulator into the label-momentum space Wilson lines in the form

$$V_n = \sum_{\text{perm.}} \exp\left\{ \frac{-g}{\bar{n} \cdot \mathcal{P}} \left[w \frac{|\bar{n} \cdot \mathcal{P}_g|^{-\eta/2}}{\nu^{-\eta/2}} \right] \bar{n} \cdot A_{cs} \right\},$$

$$X_n = \sum_{\text{perm.}} \exp\left\{ \frac{-g}{n \cdot \mathcal{P}} \left[w \frac{|\bar{n} \cdot \mathcal{P}_g|^{-\eta/2}}{\nu^{-\eta/2}} \right] n \cdot A_{cs} \right\}. \tag{2.163}$$

Note that like for the collinear Wilson line in eq. (2.158), we have expanded the regulator to leading order in the power counting and only kept the dominant component $\bar{n} \cdot \mathcal{P}_g$ of the collinear-soft group momentum. On the other hand, the exponent $-\eta/2$ is like for the soft Wilson line in eq. (2.158) and follows again from demanding that poles cancel in the cross section.

2.3 Resummation from renormalization-group evolution

2.3.1 DGLAP evolution and Bjorken scaling violation

In eq. (2.43) we introduced the separation of the DIS structure functions into perturbative matching coefficients and nonperturbative PDFs as the prototypical example of factorization. In SCET, the PDFs are proton matrix elements of effective operators built out of collinear quark fields with $p^\mu \sim (\Lambda_{\mathrm{QCD}}^2/Q, Q, \Lambda_{\mathrm{QCD}})$ along the proton momentum, and the matching coefficients $C_{i,k}$ arise when matching QCD onto these operators at the scale Q. As a consequence of this separation, additional UV divergences arise when evaluating matrix elements of the effective operators beyond tree level. One way to understand the origin of these additional divergences is to think of the EFT as having an explicit cutoff on momenta $p^2 \geq \Lambda^2 \sim Q^2$. Lifting the cutoff $\Lambda \to \infty$ to recover the result in plain dimensional regularization leads to additional UV poles in ϵ, which at finite Λ would manifest themselves as logarithms of Λ. Minimally subtracting these poles results in an additional dependence of the PDFs on the renormalization scale μ described by the Dokshitzer-Gribov-Lipatov-Altarelli-Parisi (DGLAP) equation [196–198],

$$\mu\frac{\mathrm{d}}{\mathrm{d}\mu}f_i(x,\mu) = \sum_j \int_x^1 \frac{\mathrm{d}z}{z}\, 2P_{ij}[\alpha_s(\mu), z]\, f_j\Big(\frac{x}{z}, \mu\Big),$$

$$P_{ij}(\alpha_s, z) = \sum_{n=0}^{\infty} P_{ij}^{(n)}(z)\left(\frac{\alpha_s}{4\pi}\right)^{n+1}, \tag{2.164}$$

where the sum runs over all parton types in the proton, including gluons, $j = g$. By contrast, the matrix elements of the conserved vector current J_γ^μ in the full hadronic tensor are UV-finite. Therefore the same UV divergences (with opposite sign) arise in the matching coefficient $C_{i,k}$ when computed as the difference of full and effective theory matrix elements, and the dependence on μ exactly cancels between the renormalized quantities,

$$\mu\frac{\mathrm{d}}{\mathrm{d}\mu}C_{i,k}(z, Q^2, \mu) = -\sum_j \int_z^1 \frac{\mathrm{d}z'}{z'}\, C_{i,j}\Big(\frac{z}{z'}, Q^2, \mu\Big) 2P_{jk}[\alpha_s(\mu), z']. \tag{2.165}$$

The *splitting functions* $P_{kj}^{(n)}(z)$ that drive the renormalization of the PDFs are known exactly to three loops [199, 200], with partial results at four loops available [201].

Eq. (2.164) has important physical consequences that correct the naive parton model result in eq. (2.45). These corrections come into play when attempting to compare the DIS structure functions at two different values of $Q_0 \ll Q$. Assume that we have measured the structure functions at Q_0, and now would like to extract the PDFs. To do so, note that the coefficient functions $C_{i,k}(z, Q^2, \mu^2)$ can only depend on Q^2/μ^2 for dimensional reasons, and by eq. (2.165) only depend on $\ln(Q^2/\mu^2)$. Specifically, the coefficient functions contain terms up to $\alpha_s^n \ln^n(Q^2/\mu^2)$ at each $\mathcal{O}(\alpha_s^n)$ in perturbation theory. We can eliminate these logarithms by setting $\mu = Q_0$ to extract the parton distribution functions $f_k(x, Q_0)$ at Q_0, but then consistency requires us to also pick $\mu = Q_0$ in the prediction we make for the

structure functions at Q. In that prediction, however, the logarithms $\ln(Q_0^2/Q^2) \gg 1$ will invalidate the perturbative expansion of $C_{i,k}(z, Q^2, Q_0^2)$ as soon as they become comparable to $1/\alpha_s$. If, on the other hand, we pick $\mu = Q$, we already face these *large logarithms* during the extraction step.

This issue is resolved by renormalization group (RG) evolution of the PDFs, restoring the predictivity of the DIS factorization. Specifically, from the PDFs we extracted at $\mu = Q_0$, we can obtain the PDF at $\mu = Q$ by *solving the differential equation* in eq. (2.164) with the input PDF at μ_0 as a boundary condition, a procedure also known as *running*. (Since eq. (2.164) is an integro-differential equation, this is most commonly done numerically for the PDFs.) Including at least the first nonvanishing $\mathcal{O}(\alpha_s)$ term in eq. (2.164) in the differential equation to capture the leading logarithms, this leads to the characteristic prediction of Bjorken scaling violation, i.e., a weak logarithmic dependence of the full structure functions on Q even when using the tree-level coefficient functions. Note that the renormalization of the PDFs involves an integral over the momentum fraction z and a sum over parton types. The physical interpretation is that as a function of the energy scale probed, the distribution of proton momentum is reshuffled between different parton types. Bjorken scaling violation is well confirmed experimentally e.g. by the precise data from HERA [202], which covers much wider ranges of Q than were accessible in the early days of DIS measurements, and allows for an indirect determination of the gluon PDF which mixes into the quark PDFs through eq. (2.164). Eq. (2.164) also is at the heart of all modern PDF fits, which successfully describe DIS and hadron-collider data over wide ranges of energies.

2.3.2 Resumming Sudakov double logarithms

In this thesis, we are mostly concerned with physics scenarios that involve several parametrically separated perturbative scales in one single measurement. This is unlike the case of inclusive DIS structure functions measured at different scales in different experiments. As an example, consider a color-singlet production cross section $\sigma_0(p_T^{\mathrm{cut}})$ at the LHC with a cut on the transverse momentum $p_T < p_T^{\mathrm{cut}}$ of identified jets in the final states, also known as a jet veto. In the limit $p_T^{\mathrm{cut}} \ll Q$, this 0-jet cross section schematically factorizes as

$$\sigma_0(p_T^{\mathrm{cut}}) = H(Q, \mu) \, F(p_T^{\mathrm{cut}}, \mu) \Big[1 + \mathcal{O}\Big(\frac{p_T^{\mathrm{cut}}}{Q} \Big) \Big]. \tag{2.166}$$

A factorized structure like this one generically comes about from factorizing the matrix element in SCET based on eq. (2.144), where the hard function $H(Q)$ is the square of the matching coefficient. The function $F(p_T^{\mathrm{cut}})$ describing the low-energy dynamics is given by the squared matrix element of the effective operator. (In reality, the factorization of the 0-jet cross section is more complicated, and is described in section 2.4.5.) We stress that factorization can be achieved by means other than effective field theory as well, e.g. by a diagrammatic analysis that identifies the leading singular behavior of intermediate propagators, but the following steps based on the renormalization of the factorized ingredients apply in either case.
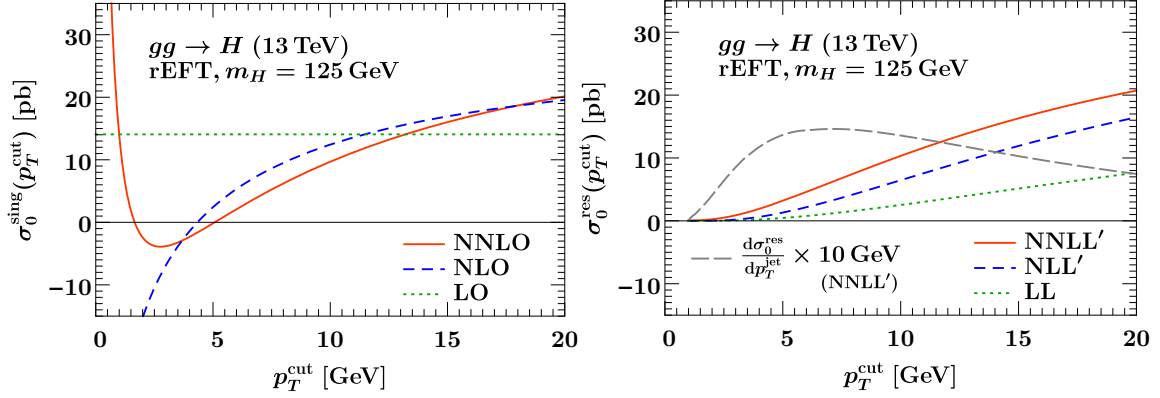
Figure 2.11: The singular 0-jet cross section for gluon-fusion Higgs production at fixed order in α_s (left) and in resummed perturbation theory (right). The gray dashed line indicates the p_T^{jet} spectrum of the leading jet at NNLL′, i.e., the derivative of the solid red line. We use the input parameters from ref. [67] for illustration. For the details of the resummation setup, see sections 2.4.5 and 3.5.

Large logarithms of p_T^{cut}/Q are fully captured by eq. (2.166) since they are not suppressed by powers of p_T^{cut}/Q, and are split up between the two single-scale pieces as

$$\ln \frac{p_T^{\text{cut}}}{Q} = \underbrace{\ln \frac{\mu}{Q}}_{H} + \underbrace{\ln \frac{p_T^{\text{cut}}}{\mu}}_{F} . \qquad (2.167)$$

At fixed order, these logarithms lead to a divergence of the cross section towards small values of p_T^{cut}, and a complete breakdown of the perturbative series, as illustrated (using the real factorization formula) for gluon-fusion Higgs production in the left panel of figure 2.11. For this reason, the leading-power contribution to $\sigma_0(p_T^{\text{cut}})$ in eq. (2.166) is also known as the *singular* cross section $\sigma_0^{\text{sing}}(p_T^{\text{cut}})$. For the spectrum differential in the transverse momentum p_T^{jet} of the leading jet, which is related to $\sigma_0(p_T^{\text{cut}})$ by a derivative, we would have a $\delta(p_T^{\text{jet}})$ at tree level that at higher orders is dressed with divergent terms $[\ln^n(p_T^{\text{jet}}/Q)/p_T^{\text{jet}}]_+$ of alternating sign.

The key tool to arrive at a sensible prediction are the renormalization group properties of the factorized ingredients. The μ dependence of the renormalized ingredients in eq. (2.166) is governed by *renormalization group equations* that schematically read

$$\mu \frac{\mathrm{d}}{\mathrm{d}\mu} H(Q, \mu) = \gamma_H(\mu)\, H(Q, \mu)\,, \qquad \mu \frac{\mathrm{d}}{\mathrm{d}\mu} F(p_T^{\text{cut}}, \mu) = \gamma_F(\mu)\, F(p_T^{\text{cut}}, \mu)\,, \qquad (2.168)$$

where γ_H (γ_F) is the *anomalous dimension* of H (F). The all-order resummation of large logarithms is achieved by evaluating the two functions at their *canonical scales*,

$$\mu_H = Q\,, \qquad \mu_F = p_T^{\text{cut}}\,, \qquad (2.169)$$

and, as for the PDFs, solving the renormalization group equations to evolve them to a common scale μ,

$$\sigma_0^{\text{res}}(p_T^{\text{cut}}) = H(Q, \mu_H)\, U_H(\mu_H, \mu)\, F(Q, \mu_F)\, U_F(\mu_F, \mu)\,. \qquad (2.170)$$

Here the renormalization group evolution factors $U_X(\mu_X, \mu)$ for $X = H, F$ are given by

$$U_X(\mu_X, \mu) = \exp\left[\int_{\mu_X}^{\mu} \frac{\mathrm{d}\mu'}{\mu'} \gamma_X(\mu') \right]. \tag{2.171}$$

They satisfy a group property by construction

$$U_X(\mu_1, \mu_2) \, U_X(\mu_2, \mu_3) = U_X(\mu_1, \mu_3). \tag{2.172}$$

Importantly, like the DIS coefficient functions at their intrinsic scale, the boundary conditions $H(Q, \mu_H)$ and $F(p_T^{\mathrm{cut}}, \mu_F)$ in eq. (2.170) are free of large logarithms, and can be evaluated in fixed-order perturbation theory. On the other hand, the large logarithms of $\mu_F/\mu_Q \sim p_T^{\mathrm{cut}}/Q$ are exponentiated, or "resummed", to all orders by the evolution factors. This is the generalization of the leading-logarithmic Sudakov form factor in eq. (1.7) to higher orders in resummed perturbation theory. The outcome of this procedure is shown in the right panel of figure 2.11: The resummation induces a physical *Sudakov suppression* as the veto is made tighter towards $p_T^{\mathrm{cut}} \to 0$, ensuring that the probability to emit no radiation above p_T^{cut} tends to zero in this limit. (In other words, *some* emission is guaranteed to happen with unit probability in massless gauge theory.) At the same time, the convergence of the series towards higher orders in resummed perturbation theory is restored. At the level of the p_T^{jet} spectrum, indicated by a gray dashed line in figure 2.11, the resummation leads to a characteristic peak at, in this case, $p_T^{\mathrm{jet}} \sim 7\,\mathrm{GeV}$. The p_T^{jet} spectrum drops off again towards higher values of p_T^{jet} as the resummed 0-jet cross section begins to saturate. This *Sudakov peak* is a key prediction of resummed perturbation theory when applied to massless gauge theories. Its position and width are sensitive to the color charge of the partons initiating the hard scattering. In chapter 4 we will obtain the first analytically resummed result for a Sudakov peak in the two-dimensional emission plane of two independent resolution variables in pp collisions.

We will often appeal to (or check) RG consistency, i.e., the statement that, in this simple scenario, the anomalous dimensions must cancel as

$$\mu \frac{\mathrm{d}}{\mathrm{d}\mu} \sigma_0(p_T^{\mathrm{cut}}) = 0 \qquad \Rightarrow \qquad \gamma_H(\mu) = -\gamma_F(\mu), \tag{2.173}$$

because the physical cross section is independent of μ. An equivalent statement is that the poles whose renormalization produces $\gamma_{H,F}(\mu)$ cancel between the bare ingredients. In particular, the evolution factors are the inverse of each other,

$$U_H(\mu_1, \mu_2) = U_H^{-1}(\mu_2, \mu_1) = U_F(\mu_2, \mu_1) = U_F^{-1}(\mu_1, \mu_2), \tag{2.174}$$

and the resummed cross section in eq. (2.170) is in fact *exactly* independent of the common scale μ, not just upon reexpansion in α_s.

In reality, the anomalous dimension of the hard function is more complicated than in the above toy example, and itself contains a logarithm of Q/μ,

$$\gamma_H^i(Q, \mu) = 4\Gamma_{\mathrm{cusp}}^i[\alpha_s(\mu)] \ln \frac{Q}{\mu} + \gamma_H^i[\alpha_s(\mu)]. \tag{2.175}$$

Order	$\Gamma_{\rm cusp}$	γ_X	β	X	nonsingular
LL	1-loop	-	1-loop	LO	-
NLL	2-loop	1-loop	2-loop	LO	-
NNLL	3-loop	2-loop	3-loop	NLO	-
N^3LL	4-loop	3-loop	4-loop	NNLO	-
$NLL'+NLO$	2-loop	1-loop	2-loop	NLO	NLO
$NNLL+NLO$	3-loop	2-loop	3-loop	NLO	NLO
$NNLL'+NNLO$	3-loop	2-loop	3-loop	NNLO	NNLO
$N^3LL+NNLO$	4-loop	3-loop	4-loop	NNLO	NNLO

Table 2.2: Required perturbative ingredients at various orders in resummed perturbation theory. Here Γ is the cusp anomalous dimension, X stands for any of the ingredients in the factorized singular cross section with noncusp anomalous dimension γ_X, and β is the β function of QCD. At N^nLL, the fixed-order boundary conditions for X must be included to $N^{n-1}LO$ to ensure the formal cancellation of scale dependence between boundary condition and evolution factor. If we include the fixed-order expansion of X to fixed N^nLO in addition, we indicate this by N^nLL'. The inclusion of nonsingular corrections by matching to the fixed-order cross section at N^mLO is indicated by $+N^mLO$. Here N^mLO always refers to the order relative to the underlying color-singlet process at Born level, sometimes made explicit by a superscript N^mLO_0.

The coefficient $\Gamma^i_{\rm cusp}(\alpha_s)$ of the explicit logarithm is the universal cusp anomalous dimension, which only depends on the color representation of the annihilating parton i, but otherwise is common to all soft and collinear matrix elements containing lightlike Wilson line configurations. The noncusp anomalous dimension $\gamma^i_H(\alpha_s)$ is specific to the hard function.[10] Both are a pure perturbative series in α_s and only depend on μ through α_s. Due to the explicit logarithm in the cusp term, the RGE $U_H(Q, \mu_H, \mu)$ of the hard function resums Sudakov double logarithms $\alpha_s^n \ln^m(\mu/Q)$ with $m \le 2n$, and similarly for many soft and collinear matrix elements we will introduce later on. In resummed perturbation theory, the standard order counting in powers of α_s (LO, NLO, etc.) needs to be generalized to account for different possible truncation orders in the anomalous dimensions and the fixed-order boundary conditions. For physics problems with Sudakov double logarithms, the required perturbative ingredients at different orders in resummed perturbation theory are summarized in table 2.2. For example, to resum all terms at leading-logarithmic (LL) order, we only require the leading coefficient of the cusp anomalous dimension, since it is enhanced by an explicit logarithm compared to the leading noncusp term, and the leading β function coefficient to ensure that the scale dependence in $\Gamma^i_{\rm cusp}[\alpha_s(\mu')]$ under the integral in the evolution factor is properly captured. (This can most easily be seen when explicitly changing variables from μ to $\alpha_s(\mu)$ using the β function, in which case β_0 has a manifest LL

---

[10]We always distinguish $\gamma^i_H(Q, \mu)$ and $\gamma_H(\alpha_s)$ by their arguments.

effect, see appendix D.) At next-to-leading-logarithmic (NLL) order, we require the first noncusp term in addition, and Γ_{cusp} and β to two loops. At NNLL, the $\mathcal{O}(\alpha_s)$ corrections to the fixed-order boundary terms are required, which are down by another logarithm compared to the leading noncusp term. We note in closing that slightly different ways of counting logarithmic orders exist [203, 204]. In this thesis we take the approach that the perturbative order to which the boundary coefficients and anomalous dimensions in the RGE are evaluated *defines* the overall logarithmic order, exploiting the fact that they individually are convergent series.

2.3.3 Fixed-order matching and profile scales

Leading-power factorization theorems, like the toy example in eq. (2.166), only hold up to power corrections in the ratio of physical scales, in this case p_T^{cut}/Q. When p_T^{cut} becomes large, it becomes necessary to include those power corrections in the prediction. This can most straightforwardly be done at fixed order by *matching* the resummed prediction to the full fixed-order calculation in QCD,

$$\sigma_0(p_T^{\text{cut}}) = \sigma_0^{\text{res}}(p_T^{\text{cut}}) + \left[\sigma_0^{\text{FO}}(p_T^{\text{cut}}) - \sigma_0^{\text{sing}}(p_T^{\text{cut}})\right] \equiv \sigma_0^{\text{res}}(p_T^{\text{cut}}) + \sigma_0^{\text{nons}}(p_T^{\text{cut}}). \qquad (2.176)$$

The overlap between the two contributions needs to be subtracted to avoid double counting. As indicated, the overlap is given by the fixed-order reexpansion of the resummed cross section, i.e., the singular cross section with all ingredients evaluated at the scale $\mu_{\text{FO}} \sim Q$ of the fixed-order calculation. The matching, in this form known as additive matching, preserves the formal accuracy of the individual contributions: Upon fixed-order reexpansion, the resummed and singular cross sections cancel, so the result has the same formal fixed-order accuracy as σ_0^{FO}. On the other hand, the term in square brackets, known as the *nonsingular* cross section σ_0^{nons}, is of $\mathcal{O}(p_T^{\text{cut}}/Q)$ because the factorized cross section in the singular limit agrees with σ_0^{FO}. Thus in the limit $p_T^{\text{cut}} \ll Q$ the formal logarithmic accuracy is that of the resummed cross section. We denote the outcome of matching the N^{n}LL to the fixed N^{m}LO cross section by N^{n}LL+N^{m}LO.

Note that for differential spectra like the p_T^{jet} spectrum, the first contribution at finite $p_T^{\text{jet}} > 0$ arises at $\mathcal{O}(\alpha_s)$, so we should specify what we mean by the leading order in this case. For spectra, we will take LO to mean the $\delta(p_T^{\text{jet}})$ term at strict tree level in the underlying color-singlet process, i.e., without any QCD emissions. In this way, the NLO spectrum, which includes the NLO virtual corrections $\propto \delta(p_T^{\text{jet}})$, consistently integrates to the NLO total cross section for the underlying color-singlet production process. When we wish to be very explicit, we indicate this by a subscript 0 for the (inclusive) number of hard QCD emissions into the final state, e.g., the LO$_0$ spectrum is $\propto \delta(p_T^{\text{jet}})$, whereas the LO$_1$ spectrum is the leading contribution to the process where the color-singlet is produced in association with at least one hard jet with $p_T^{\text{jet}} > 0$.

We note that eq. (2.176) is not the most general, or most sophisticated, approach to incorporating the power corrections. In particular, as the precision requirements increase, the impact of unresummed logarithms $x \ln^n x$ at *subleading* order in $x = p_T^{\text{cut}}/Q$ may be-

come noticeable. Their resummation is challenging in general. While SCET makes the analysis of power corrections at least conceptionally straightforward by consistently working to subleading power everywhere in the EFT construction (including the hard scattering Lagrangian, dynamical Lagrangian insertions, and the factorization of the measurement operator), the all-order resummation of even just the leading logarithms at next-to-leading power has only been achieved for very select observables [205–208] because the all-order factorization structure is still largely unclear. In chapter 7, we will see that in the experimentally relevant case of the color-singlet transverse momentum spectrum with fiducial acceptance cuts, these complications can be bypassed, by showing that the leading (linear) power corrections uniquely arise from the cuts and multiply leading-power SCET dynamics.

As $p_T^{\mathrm{cut}} \to Q$, the formula in eq. (2.176) requires additional modification because in this region, the resummation is no longer justified and we should recover the fixed-order result exactly. In particular, the σ_0^{sing} term in square brackets continues to grow like some power of a logarithm (with uncontrolled sign) as p_T^{cut} passes Q, whereas the fixed-order result, like the physical jet veto cross section in this limit, saturates towards the total production cross section. (The resummed cross section stays roughly constant if all scales are canonical.) To ensure these rather delicate cancellations between the resummed and singular cross section towards the fixed-order result, which in practice are already active around $p_T^{\mathrm{cut}} \sim 0.75Q$, the resummation must be turned off towards $p_T^{\mathrm{cut}} \to Q$. This is most easily achieved by recalling that in our toy example, the resummation is controlled by the scale μ_F chosen in the low-energy matrix element. (The hard scale $\mu_H \sim Q$ can always be chosen as $\mu_H = \mu_{\mathrm{FO}}$.) In short, the requirements on μ_F are

$$\mu_F \sim p_T^{\mathrm{cut}} \quad \text{for} \quad p_T^{\mathrm{cut}} \ll Q \quad \text{and} \quad \mu_F \to \mu_H \quad \text{for} \quad p_T^{\mathrm{cut}} \to Q\,. \qquad (2.177)$$

A construction that achieves this, suitably generalized to the many low-energy scales in real factorization theorems, are so-called *profile scales* that make $\mu_F(p_T^{\mathrm{cut}})$ an explicit, continuous function of p_T^{cut} [203, 209]. Importantly, these setups can easily be extended to account for individual *scale variations* in the factorized ingredients over some central choices $\mu_F = p_T^{\mathrm{cut}}$ and $\mu_H = Q$, conventionally by a factor of 2. These variations amount to including uncanceled higher-order β function or PDF evolution terms in the fixed-order boundary conditions that very roughly estimate the typical size of perturbative corrections in the individual perturbative series for F and H. Using a profile scale setup, it is then easy to turn off these independent variations as $p_T^{\mathrm{cut}} \to Q$ and the singular and nonsingular cross sections combine into the total cross section with a single, correlated variation of $\mu_{\mathrm{FO}} \sim Q$.

As a final comment, note that if a complete, continuous description of the spectrum or the veto cross section for all values of p_T^{jet} (p_T^{cut}) is desired, rather than just of the singular limit, and eq. (2.176) is used for this purpose, only some combinations of resummed and fixed orders are practically viable because the two orders essentially need to go in lockstep to simultaneously satisfy the requirements on nonsingular power suppression as $p_T^{\mathrm{cut}} \to 0$ and singular-nonsingular cancellation as $p_T^{\mathrm{cut}} \to Q$. The viable combinations relevant for this thesis are summarized in the bottom half of table 2.2.
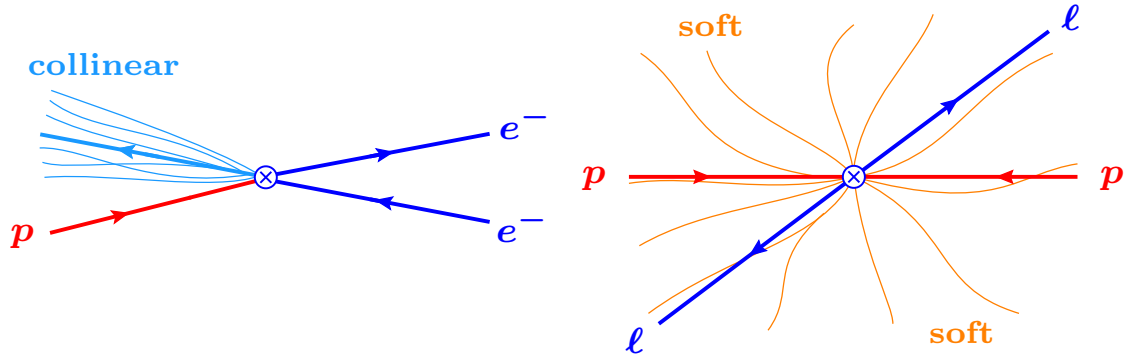
Figure 2.12: Left: Illustration of deep-inelastic scattering at large Bjorken $x \to 1$ in the Breit frame, where the hadronic system originating from the proton (red) backscatters against the electron (dark blue). We include a small vertical offset for clarity. As x approaches the kinematic endpoint, the hadronic final state (light blue) becomes a collimated jet. Right: Illustration of Drell-Yan production near the hadronic production threshold $Q \to E_{\rm cm}$. In this limit, almost all the energy from the initial-state protons (red) is converted into the observed Drell-Yan pair (blue), and the remaining hadronic radiation is constrained to be soft (orange).

<div style="text-align:center">Right panel adapted from ref. [155].</div>

2.4 Review of factorization for key observables

2.4.1 Deep inelastic scattering at large Bjorken x

The most basic factorization theorems capturing Sudakov double logarithms do not involve an explicit measurement on the hadronic final state. Instead, the hadronic final state is indirectly constrained by measuring the leptonic dynamics near a kinematic endpoint. For DIS, this endpoint is the limit of large Bjorken fraction $x \to 1$. We can see from eq. (2.39) that this limit in particular implies $p_X^2 \sim (1-x)Q^2 \to 0$ for the invariant mass of the hadronic final state, i.e., the hadronic final state turns into a single collimated jet initiated by a primary parton close to its mass shell. This physical picture is particularly clear in the Breit frame, where the longitudinal momentum of the electron is reversed during the scattering, $k'^3 = -k^3 = Q/2$, knocking the hadronic system backwards.[11] DIS near endpoint in the Breit frame is illustrated in the left panel of figure 2.12.

Aligning a lightlike reference vector n^μ with the initial-state proton, and $\bar{n}^\mu$ with the hadronic final state, the relevant low-energy degrees of freedom are

$$\bar{n}\text{-collinear:} \quad p^\mu \sim (Q, Q\lambda^2, Q\lambda)\,, \qquad \lambda \sim \sqrt{1-x}\,,$$

$$n\text{-collinear-soft:} \quad p^\mu \sim \left(\tfrac{\Lambda_{\rm QCD}^2}{Q\lambda^2}, Q\lambda^2, \Lambda_{\rm QCD}\right),$$

---

[11]It is of course possible to boost to a frame where the hadronic final state is approximately at rest and could instead be characterized as soft. Note, however, that in this frame the other components of the hadronic system are now highly boosted for $x \to 1$, so the interpretation of X as collinear *relative* to the incoming proton and in particular the proton remnant is unchanged.

$$n\text{-collinear:} \quad p^\mu \sim \left(\frac{\Lambda_{\text{QCD}}^2}{Q}, Q, \Lambda_{\text{QCD}}\right). \tag{2.178}$$

The $\bar{n}$-collinear modes describe the hadronic final state. The n-collinear modes describe the components of the proton that initiate the hard scattering, and the collinear-soft modes describe the remnant of the proton as $x \to 1$. The collinear-soft modes are often simply called soft modes, counting $\Lambda_{\text{QCD}} \sim Q\lambda^2$ without loss of generality.

The corresponding factorization theorem for the DIS structure functions reads [210–216]

$$F_1(x,Q) = \frac{1}{2x} F_2(x) = \sum_{i,j} \frac{1}{2} H_{ij}^{\text{DIS}}(Q^2, \mu) \int ds\, f_i^{\text{thr}}\left[x_-\left(1 + \frac{s}{Q^2}\right), \mu\right] J_j(s, \mu). \tag{2.179}$$

It holds up to power corrections in $1 - x$. The DIS hard function $H_{ij}^{\text{DIS}}(Q^2, \mu)$ is given by the square of (the IR-finite part of) the quark form factor at spacelike momentum transfer. In SCET it is formally defined as the square of the hard matching coefficient, see appendix B. The hard function is summed over the parton types i, j participating in the scattering, e.g. $H_{ij} = \delta_{ij}\, Q_i^2 \big[1 + \mathcal{O}(\alpha_s)\big]$ for the flavor-conserving electromagnetic current. Note that additional hard gluon emissions that could carry away angular momentum are power suppressed in the $x \to 1$ limit, so the Callan-Gross relation becomes an all-order relation in this limit.

The bare quark jet function is defined as a vacuum matrix element of $\bar{n}$-collinear fields,

$$J_q(s) = \frac{(2\pi)^3}{N_c}\Big\langle 0 \Big| \text{tr}\Big\{\frac{\slashed{n}}{2}\chi_{q\bar{n}}\big[\delta(\omega + \overline{\mathcal{P}}_{\bar{n}})\, \delta^2(\vec{\mathcal{P}}_\perp)\, \delta(s - \omega\, \bar{n}\cdot\hat{p})\, \bar{\chi}_{q\bar{n}}\big]\Big\}\Big| 0\Big\rangle. \tag{2.180}$$

The collinear field in square brackets has continuous label momentum in both the $\bar{n}$ and perpendicular direction in the sense of eq. (2.139). The residual momentum operator is $\hat{p}^\mu = i\partial^\mu$, tr denotes a trace over spin, and we take $\bar{\chi}_{q\bar{n}}$ to be a column vector in color space in this definition for notational simplicity. The jet function describes the formation of a final-state jet from a primary parton with virtuality s. The antiquark jet function $J_{\bar{q}}(s)$ is obtained by the replacement

$$\text{tr}\Big\{\frac{\slashed{n}}{2}\chi_{q\bar{n}}(x)\cdots\bar{\chi}_{q\bar{n}}(y)\Big\} \leftrightarrow \bar{\chi}_{q\bar{n}}(x)\cdots\frac{\slashed{n}}{2}\chi_{q\bar{n}}(y), \tag{2.181}$$

where the ellipses denote the measurement δ functions acting on the field to their right. Quark and antiquark collinear matrix elements like beam and jet functions are quite generally related to each other by this replacement, and for brevity we will only give definitions for the quark case in the following. The renormalized jet function satisfies the RGE

$$\mu\frac{d}{d\mu}J_j(s, \mu) = \int ds'\, \gamma_J^j(s', \mu)\, J_j(s - s', \mu),$$
$$\gamma_J^j(s, \mu) = -2\Gamma_{\text{cusp}}^j[\alpha_s(\mu)]\, \mathcal{L}_0(s, \mu^2) + \gamma_J^j[\alpha_s(\mu)]\, \delta(s). \tag{2.182}$$

Note that it is renormalized by a convolution in its argument s, but the renormalization (unlike the DGLAP equation) is diagonal in flavor.

The threshold PDF f_i^{thr} describes the extraction of a parton from the proton as $x \to 1$ and in that limit coincides with the standard PDF. We defer its formal definition in terms of n-collinear and collinear-soft fields to section 5.3.6, where we will also argue that eq. (2.179) is indeed the correct convolution structure of the factorization theorem. Physically, the convolution structure encodes that by momentum conservation, the quark initiating the final-state jet may only be off shell by an amount dictated by the momentum available from the proton in addition to Q.

The key utility of the factorization theorem in eq. (2.179) is that it predicts the all-order structure of the leading singular terms in the perturbative DIS coefficient functions. For simplicity, we consider the coefficient functions at $\mu = Q$. (Other choices are straightforward to recover using the RGE.) Comparing eq. (2.179) to eq. (2.43) in the limit $x \to 1$, one has

$$C_{i,k}(z, Q, \mu = Q) = \sum_j \hat{H}_{kj}^{\text{DIS}} \hat{J}_j(z) \big[1 + \mathcal{O}(1 - z) \big], \qquad (2.183)$$

where we abbreviated, suppressing the residual dependence on Q through $\alpha_s(Q)$,

$$\hat{H}_{ij}^{\text{DIS}} = H_{ij}^{\text{DIS}}(Q^2, \mu = Q), \qquad \hat{J}_j(z) = Q^2 J_j\big[Q^2(1 - z), \mu = Q\big]. \qquad (2.184)$$

The jet function $J_j(s, \mu^2)$ depends on s through terms like $\delta(s)$ and plus distributions $\mathcal{L}_n(s, \mu^2)$ at each order in perturbation theory, so the rescaled jet function $\hat{J}_j(z)$ together with the hard function predicts all singular terms $\delta(1 - z)$ and $\mathcal{L}_n(1 - z)$ in the coefficient function. The relation eq. (2.183) was recently used to extract the three-loop quark and gluon jet functions from the known DIS coefficient functions [217], confirming a previous direct three-loop calculation of the quark jet function [218].

The resummation of the leading singular terms is most commonly performed in Mellin space, with $N \gg 1$ the Mellin conjugate variable to $z \to 1$. This diagonalizes the jet function RGE, so the resummation can be achieved by multiplicative RG evolution between the canonical Mellin-space jet scale $\mu_J \sim Q/\sqrt{N}$ and the hard scale Q [210, 211]. The resummation can also be performed directly at the level of eq. (2.179) by making a judicious, fixed choice of the jet scale motivated by the large x power-law behavior of the PDF [213].

2.4.2 Soft threshold factorization

In pp collisions at the LHC, the most obvious kinematic endpoint is the absolute production threshold $Q \to E_{\text{cm}}$ for a final state with invariant mass Q. In this limit, where $\tau = x_a x_b = Q^2/E_{\text{cm}}^2 \to 1$ and thus both $x_{a,b} = (Qe^{\pm Y})/E_{\text{cm}} \to 1$ in the notation of section 2.1.3, the hadronic final state becomes (ultra)soft,[12]

$$\text{soft:} \quad p^\mu \sim (\lambda^2 Q, \lambda^2 Q, \lambda^2 Q), \qquad \lambda \sim \sqrt{1 - x_{a,b}}. \qquad (2.185)$$

For color-singlet production, the additional low-energy degrees of freedom are separate pairs of $n_{a,b}$-collinear and $n_{a,b}$-collinear-soft modes that respectively describe the active

---

[12]Here we take $1 - x_a \sim 1 - x_b$ without loss of generality, because eq. (2.186) is valid for any hierarchy between them as long as both are small, see section 5.3.5.

constituents and the remnants of the two protons in analogy to the endpoint DIS case. Drell-Yan production for $Q \to E_{\mathrm{cm}}$ is illustrated in figure 2.12, right. In the soft threshold limit, the following factorization theorem holds for the color-singlet production cross section differential in Q and Y (x_a and x_b), up to power corrections in $1-x_a$ and $1-x_b$ [210, 211, 219–222],

$$\frac{\mathrm{d}\sigma}{\mathrm{d}x_a \mathrm{d}x_b} = \sum_{i,j} H_{ij}(Q^2, \mu) \int \mathrm{d}k^- \, \mathrm{d}k^+ S_i(k^-, k^+, \mu) \tag{2.186}$$

$$\times f_i^{\mathrm{thr}}\Big[x_a\Big(1 + \frac{k^-}{Qe^{+Y}}\Big), \mu\Big] f_j^{\mathrm{thr}}\Big[x_b\Big(1 + \frac{k^+}{Qe^{-Y}}\Big), \mu\Big].$$

The hard function H_{ij} is related to the DIS hard function H_{ij}^{DIS} by crossing. It is given by the square of the short-distance matrix element for the hard process $ij \to L$ that produces the leptonic final state, and in particular contains the process-dependent hard virtual corrections, e.g. the square of the timelike quark form factor in Drell-Yan production. On the other hand, it is independent of the precise low-energy observable, and thus is common to all factorization results for color-singlet production in pp collisions that we review in this section or derive in this thesis.[13] The hard function is summed over the partons i, j that participate in the hard process.

The soft function S_i encodes soft-gluon emissions from the colliding hard partons. The bare soft function for quark annihilation is defined as

$$S_q(k^-, k^+) = \frac{1}{N_c}\big\langle 0\big| \mathrm{Tr}\big\{\bar{\mathrm{T}}\big[Y_{n_b}^\dagger Y_{n_a}\big] \delta(k^- - \hat{p}^-) \, \delta(k^+ - \hat{p}^+) \, \mathrm{T}\big[Y_{n_a}^\dagger Y_{n_b}\big]\big\}\big|0\big\rangle. \tag{2.187}$$

The gluon case is obtained by taking all Wilson lines to be in the adjoint representation and adjusting the normalization factor to $1/(N_c^2 - 1)$. This replacement is again generally valid for all the color-singlet soft functions we introduce in the following. Compact expressions for the threshold soft function to three loops are given in section 6.2.2.

The threshold soft function S_i only depends on the SU(3) representation of the parton i, but not on the precise flavor, so we could have equally well written S_j instead of S_i. In particular, soft radiation cannot change the initial parton type (the index i is fixed under the sum), so only the hard Born process contributes in the soft limit, e.g. $q\bar{q} \to Z$ or $gg \to H$, where the quarks or gluons are directly extracted from the proton. Any off-diagonal partonic channels like $qg \to Lq$ vanish for $\tau \to 1$.

Similar to DIS near endpoint, the key application of eq. (2.186) is to predict and resum the singular structure of the perturbative partonic cross section. At partonic level, eq. (2.186) implies that for $z = z_a z_b \to 1$,

$$\hat{\sigma}_{ij}(z_a, z_b, Q, \mu = Q) = \hat{H}_{ij}\, \hat{S}_i(z_a, z_b)\big[1 + \mathcal{O}(1 - z_a) + \mathcal{O}(1 - z_b)\big], \tag{2.188}$$

---

[13]We leave the leptonic tensor, proportional to the squared decay matrix element, and an occasional Jacobian implicit in the hard function for readability. Explicit expressions for each case are compiled in appendix B.

up to power corrections in $1 - z_{a,b}$, where we have rescaled the soft function as

$$\hat{S}_i(z_a, z_b) \equiv Q^2 \, S_i \big[Q e^Y (1 - z_a), Q e^{-Y} (1 - z_b), \mu = Q \big] . \qquad (2.189)$$

Eq. (2.188) has been in ubiquitous use in cutting-edge LHC phenomenology. It predicts all terms that are leading in the simultaneous limit $z = z_a z_b \to 1$, of the form

$$\hat{\sigma}_{ij}(z_a, z_b, Q, \mu) \supset \delta(1 - z_a) \, \delta(1 - z_b) , \qquad \mathcal{L}_n(1 - z_a) \, \delta(1 - z_b) ,$$
$$\delta(1 - z_a) \, \mathcal{L}_n(1 - z_b) , \quad \mathcal{L}_n(1 - z_a) \, \mathcal{L}_m(1 - z_b) , \qquad (2.190)$$

and enables their all-order resummation, typically performed using Mellin-space techniques. Terms of this kind are enhanced even away from the hadronic threshold limit (at $\tau \ll 1$) due to the steep fall-off of the PDFs towards larger momentum fractions. For a selection of resummation techniques and phenomenological results for color-singlet production, see refs. [210, 211, 219–240]. (Generalizations also exist and are in widespread use for processes with final-state color like $t\bar{t}$ production.) Another key application is in approximating fixed-order cross sections by expanding in $1 - z$, e.g. at N^3LO [219, 229, 241–250].

The catch to the soft threshold limit is that it receives relative power corrections in both $1 - z_a$ and $1 - z_b$. In particular, there is a tower of terms $\mathcal{L}_n(1 - z_a) \, r_n(z_b)$ that are singular in z_a, but multiplied by regular functions of z_b that are also enhanced in the convolution against the PDFs. Notably, all singular contributions from off-diagonal partonic channels are of this kind. This much reduces the usefulness of soft threshold factorization in quark-induced processes, where contributions from the gq initial state at NLO are typically of comparable size to the $q\bar{q}$ channel. (Most of the successes of the soft threshold limit are in fact in gluon-induced processes like Higgs or $t\bar{t}$ production, where the relative size of the quark contributions at NLO is smaller.) In chapter 5 we rectify this situation by deriving, for the first time, the all-order factorization theorem valid in the limit where only one of the momentum fractions approaches unity. As a byproduct, we resolve a long-running debate in the literature on the relation between the factorization theorem in eq. (2.186) and the analogous (but simpler) factorization theorem for the cross section differential only in Q^2.

2.4.3 Factorization at small transverse momentum

Another important kinematic limit at the LHC that is dominated by soft and collinear dynamics is the color-singlet transverse momentum distribution $d\sigma/d\vec{q}_T$ at small $q_T \equiv |\vec{q}_T| \ll Q$. As discussed in the introduction, experimental measurements of Drell-Yan production in this kinematic range have by now reached sub-percent precision. The relevant modes describing QCD initial-state radiation are characterized by their transverse momentum being of $\mathcal{O}(q_T)$,

$$n_a\text{-collinear:} \quad p^\mu \sim \left(Q, \tfrac{q_T^2}{Q}, q_T \right) ,$$
$$n_b\text{-collinear:} \quad p^\mu \sim \left(\tfrac{q_T^2}{Q}, Q, q_T \right) ,$$
$$\text{soft:} \quad p^\mu \sim \left(q_T, q_T, q_T \right) , \qquad (2.191)$$
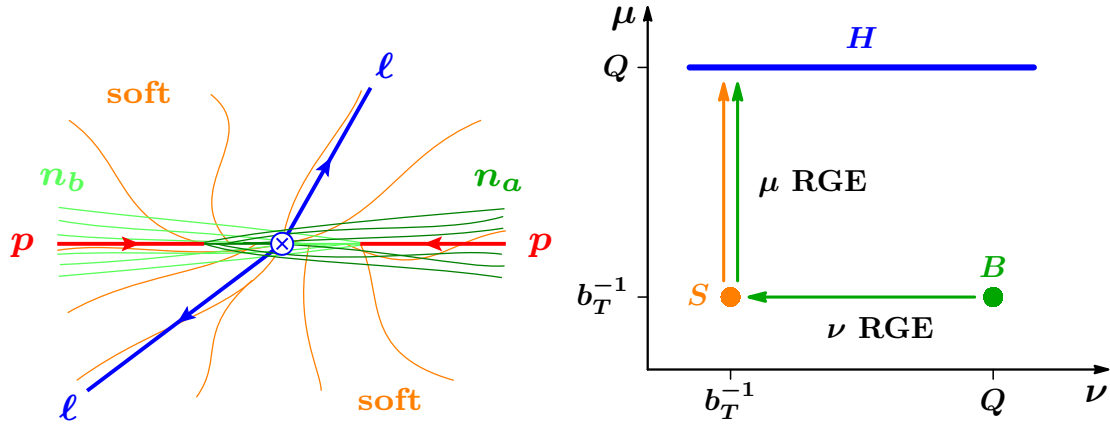
Figure 2.13: Left: Illustration of Drell-Yan production at small transverse momentum. The Drell-Yan pair (blue) picks up a small amount of recoil from soft (orange) and collinear radiation (green) along the directions of the incoming protons (red). Right: A possible renormalization group evolution path in the (μ, ν) plane that resums all large logarithms in the transverse momentum spectrum.

<div align="center">Left panel adapted from ref. [57].</div>

such that the leptonic final state can pick up a small amount of recoil from them. This is a prototypical SCET$_{\mathrm{II}}$ setup. The physical picture of Drell-Yan production at small q_T is illustrated in the left panel of figure 2.13. The factorization of the $\vec{q}_T$ distribution in the limit $q_T \equiv |\vec{q}_T| \ll Q$ in terms of these modes was first established by Collins, Soper, and Sterman (CSS) [185, 251–253], and was later elaborated on in refs. [254–257]. Within the framework of SCET, the factorization for q_T was shown in refs. [188, 189, 191, 192]. The factorization theorem for the transverse momentum distribution, sometimes also referred to as transverse momentum dependent (TMD) factorization, reads

$$\frac{\mathrm{d}\sigma}{\mathrm{d}Q^2\,\mathrm{d}Y\,\mathrm{d}^2\vec{q}_T} = \sum_{i,j} H_{ij}(Q^2, \mu)\, [B_i B_j S_i](Q^2, x_a, x_b, \vec{q}_T, \mu) \left[1 + \mathcal{O}\Big(\frac{q_T^2}{Q^2}, \frac{\Lambda_{\mathrm{QCD}}^2}{Q^2}\Big)\right]. \quad (2.192)$$

As written, the factorization theorem receives power corrections in q_T/Q and Λ_{QCD}/Q, but remains valid in the nonperturbative regime $q_T \sim \Lambda_{\mathrm{QCD}}$. In chapter 7 we will point out that reconstructing the decay products in general induces *linear* power corrections in q_T/Q and demonstrate how to perform their all-order resummation. The hard function H_{ij} is the same as in eq. (2.186) and encodes the hard production process $ij \to L$ at the scale $\mu \sim Q$. The second factor in eq. (2.192) encodes the physics at the low scale $\mu \sim q_T$, and can be written in several equivalent forms,

$$[B_i B_j S_i](Q^2, x_a, x_b, \vec{q}_T, \mu)$$
$$\equiv \int \mathrm{d}^2\vec{k}_a\, \mathrm{d}^2\vec{k}_b\, \mathrm{d}^2\vec{k}_s\, \delta^2(\vec{q}_T - \vec{k}_a - \vec{k}_b - \vec{k}_s)$$
$$\times B_i(x_a, \vec{k}_a, \mu, \nu/\omega_a)\, B_j(x_b, \vec{k}_b, \mu, \nu/\omega_b)\, S_i(\vec{k}_s, \mu, \nu) \quad (2.193a)$$

$$\equiv \int \frac{\mathrm{d}^2 \vec{b}_T}{(2\pi)^2} \, e^{\mathrm{i}\vec{b}_T \cdot \vec{q}_T} \, \tilde{B}_i(x_a, \vec{b}_T, \mu, \nu/\omega_a) \, \tilde{B}_j(x_b, \vec{b}_T, \mu, \nu/\omega_b) \, \tilde{S}_i(b_T, \mu, \nu) \tag{2.193b}$$

$$\equiv \int \frac{\mathrm{d}^2 \vec{b}_T}{(2\pi)^2} \, e^{\mathrm{i}\vec{b}_T \cdot \vec{q}_T} \, \tilde{f}_i(x_a, \vec{b}_T, \mu, \zeta_a) \, \tilde{f}_j(x_b, \vec{b}_T, \mu, \zeta_b) \,. \tag{2.193c}$$

We first focus on eq. (2.193a). The *beam function* $B_i(x, \vec{k}_T, \mu, \nu/\omega)$ describes the extraction of an unpolarized parton i with longitudinal momentum fraction x and transverse momentum $\vec{k}_T$ from an unpolarized proton with momentum $P_n^\mu = P_n^- n^\mu/2$. In SCET, the bare quark and gluon beam functions are defined as proton matrix elements of collinear fields,

$$B_q\Big(\frac{\omega}{P_n^-}, \vec{k}_T\Big) = \theta(\omega)\langle p_n | \bar{\chi}_{qn} \big[\delta(\omega - \overline{\mathcal{P}}) \, \delta^2(\vec{k}_T - \vec{\mathcal{P}}_\perp) \, \frac{\slashed{n}}{2} \chi_{qn} \big] | p_n \rangle \,,$$

$$B_g^{\mu\nu}\Big(\frac{\omega}{P_n^-}, \vec{k}_T\Big) = \theta(\omega_n)\omega\langle p_n | \mathcal{B}_{n\perp}^\mu \big[\delta(\omega - \overline{\mathcal{P}}) \, \delta^2(\vec{k}_T - \vec{\mathcal{P}}_\perp) \, \mathcal{B}_{n\perp}^\nu \big] | p_n \rangle \tag{2.194}$$

As usual, the average over proton spin is implicit and fields without arguments are evaluated at equal spacetime position. Here and in all following n-collinear proton matrix elements, we take the proton to carry momentum $P_n^\mu = P_n^- n^\mu/2$. Note that in eqs. (2.192) and (2.193) we suppressed the Lorentz tensor structure of the gluon beam function. There is in general a nontrivial polarized contribution $\propto (k_T^\mu k_T^\nu/k_T^2 - g_\perp^{\mu\nu}/2)$ to the gluon beam function due to the vectorial nature of the measurement [258]. The transverse momentum-dependent beam functions in eq. (2.194) also appear in the q_T factorization for $Z + j$ and $\gamma + j$ production [259, 260], in a recently derived factorization theorem for the closely related (but theoretically much cleaner) observable of the azimuthal angle between the orientation and total transverse momentum of the $V + j$ system [261], and in the factorization for the transverse energy-energy correlator (TEEC) in the back-to-back limit [262].

The soft function $S_i(\vec{k}_T, \mu, \nu)$ encodes soft radiation with total transverse momentum $\vec{k}_T$, and we already encountered the definition of the bare soft function for $i = q$ in eq. (2.156). Unlike the beam function, the soft function is specific to color-singlet production.

The δ function $\delta^2(\vec{q}_T - \cdots)$ in eq. (2.193a) encodes momentum conservation in the transverse plane. Eq. (2.193b) shows the same expression in Fourier space, where $\tilde{B}_i$ and $\tilde{S}_i$ are the Fourier transforms of B_i and S_i in the transverse plane and $\vec{b}_T$ is the Fourier conjugate of $\vec{q}_T$. The overall momentum conservation in this case is encoded in the beam and soft functions being evaluated at equal $\vec{b}_T$. Yet another equivalent way of writing this is shown in eq. (2.193c), where the transverse momentum dependent beam and soft functions have been combined into transverse momentum dependent PDFs (TMDPDFs),

$$\tilde{f}_i(x, \vec{b}_T, \mu, \zeta) = \tilde{B}_i\big(x, \vec{b}_T, \mu, \nu/\sqrt{\zeta}\big) \sqrt{\tilde{S}_i(b_T, \mu, \nu)} \,. \tag{2.195}$$

In the gluon case this relation includes polarization indices that we suppress. The arguments ζ and ν of the renormalized functions are discussed below. Note that the larger universality of the beam function is lost in the TMDPDF, which in the form above is specific to color-singlet production due to the presence of the soft function.[14] Of course, this may be a

[14]Explicit constraints on soft radiation into the hadronic final state also upset the universality of the TMDPDF, whereas the beam function in such a scenario is still the same, see section 4.2.3.

desired feature when fitting TMDPDFs in the nonperturbative domain $q_T \sim \Lambda_{\text{QCD}}$ to data: If the data set contains only color-singlet spectra, the nonperturbative soft and beam functions are degenerate in the fit and it is expedient to combine them into a single model function.

The soft function and the quark beam function in eqs. (2.156) and (2.194) are azimuthally symmetric, so their Fourier transforms $\tilde{S}_i(b_T)$ and $\tilde{B}_q(x, b_T)$ only depend on the magnitude $b_T \equiv |\vec{b}_T|$. Similarly, the gluon beam function can be decomposed in terms of two orthogonal tensor structures $g_\perp^{\mu\nu}/2$ and $k_T^\mu k_T^\nu/k_T^2 - g_\perp^{\mu\nu}/2$ whose coefficients in Fourier space only depend on b_T. After these steps, we can simplify eq. (2.193b) further by performing the integral over the azimuth of $\vec{b}_T$,[15]

$$
\begin{aligned}
&[B_i B_j S_i](Q^2, x_a, x_b, \vec{q}_T, \mu) \\
&= \frac{1}{2\pi} \int_0^\infty \mathrm{d}b_T \, b_T \, J_0(b_T q_T) \tilde{B}_i(x_a, b_T, \mu, \nu/\omega_a) \, \tilde{B}_j(x_b, b_T, \mu, \nu/\omega_b) \, \tilde{S}_i(b_T, \mu, \nu) \,, \quad (2.196)
\end{aligned}
$$

where $J_0(|x|) = \frac{1}{2\pi} \int_0^{2\pi} \mathrm{d}\varphi \, \exp(\mathrm{i}x \cos\varphi)$ is the zeroth-order Bessel function of the first kind. We will continue to use this form in the following, where it is understood from the argument b_T that the gluon beam function has been decomposed, effectively absorbing the tensor structure as two distinct terms for unpolarized and polarized gluons into the sum over flavors in eq. (2.192).

Renormalization. As discussed in section 2.2.7, the q_T factorization is affected by rapidity divergences that must be regulated by a dedicated rapidity regulator. This gives rise to an additional rapidity scale denoted by ν in eq. (2.193). For all results related to q_T factorization in this thesis we use the exponential regulator of ref. [192], where up to two loops the renormalized results are the same as for the η regulator of refs. [190, 191]. Note that eq. (2.194) as defined in SCET includes a zero-bin subtraction in integrals over collinear momenta, which is scaleless for the exponential and η regulator, but for some choices of rapidity regulator does not vanish.

The renormalized beam and soft functions in Fourier space obey the coupled RGEs

$$
\mu \frac{\mathrm{d}}{\mathrm{d}\mu} \ln \tilde{B}_i(x, b_T, \mu, \nu/\omega) = \tilde{\gamma}_B^i(\mu, \nu/\omega) \,, \qquad \mu \frac{\mathrm{d}}{\mathrm{d}\mu} \ln \tilde{S}_i(b_T, \mu, \nu) = \tilde{\gamma}_S^i(\mu, \nu) \,,
$$

$$
\nu \frac{\mathrm{d}}{\mathrm{d}\nu} \ln \tilde{B}_i(x, b_T, \mu, \nu/\omega) = -\frac{1}{2} \tilde{\gamma}_\nu^i(b_T, \mu) \,, \qquad \nu \frac{\mathrm{d}}{\mathrm{d}\nu} \ln \tilde{S}_i(b_T, \mu, \nu) = \tilde{\gamma}_\nu^i(b_T, \mu) \,. \quad (2.197)
$$

Importantly, their renormalization group evolution does not just follow a line in μ, but follows a path in the (μ, ν) plane, as illustrated in the right panel of figure 2.13. Note that the beam function renormalization, unlike the DGLAP evolution of the PDF, holds the flavor and the momentum fraction x fixed. The renormalization also does not mix unpolarized and polarized contributions in the gluon beam function.

---

[15]We stress that for the gluon case, this relies on the hard function being a Lorentz scalar (like for the Higgs), so no cross terms of polarized and unpolarized gluon beam functions appear. In other cases, like the gluon-induced contribution to diphoton production, there is in general a nontrivial azimuthal dependence relative to the diphoton orientation.

The μ anomalous dimensions on the first line have the all-order form

$$\tilde{\gamma}_B^i(\mu, \nu/\omega) = 2\Gamma_{\text{cusp}}^i[\alpha_s(\mu)] \ln \frac{\nu}{\omega} + \tilde{\gamma}_B^i[\alpha_s(\mu)] \,,$$

$$\tilde{\gamma}_S^i(\mu, \nu) = 4\Gamma_{\text{cusp}}^i[\alpha_s(\mu)] \ln \frac{\mu}{\nu} + \tilde{\gamma}_S^i[\alpha_s(\mu)] \,. \tag{2.198}$$

We will use a tilde to indicate that these belong to the soft and beam functions in the q_T factorization theorem, even though the μ anomalous dimensions themselves are independent of the space and of q_T or b_T. The split of the noncusp μ anomalous dimension into $\tilde{\gamma}_B^i$ and $\tilde{\gamma}_S^i$ depends on the rapidity regularization scheme, but their sum combines to cancel the hard noncusp anomalous dimension independent of the scheme.

The ν anomalous dimension $\tilde{\gamma}_\nu^i$ has a richer structure. The cross section and the hard function are ν independent, so $\tilde{\gamma}_\nu^i$ must appear with a relative factor of $-1/2$ in the ν RGE of the beam function for the two beam functions to cancel the ν dependence of the soft function.[16] This also implies that like the soft function, $\tilde{\gamma}_\nu^i$ only depends on the group representation, but not the specific flavor of i. Since the soft and beam functions are evaluated at the same b_T, RG consistency does not forbid (and in fact requires) an explicit physical dependence of $\tilde{\gamma}_\nu^i$ on b_T. In particular, $\tilde{\gamma}_\nu^i$ is itself renormalized at the scale $\mu \sim 1/b_T$ and satisfies the additive RGE

$$\mu \frac{\mathrm{d}}{\mathrm{d}\mu} \tilde{\gamma}_\nu^i(b_T, \mu) = -4\Gamma_{\text{cusp}}^i[\alpha_s(\mu)] = \nu \frac{\mathrm{d}}{\mathrm{d}\nu} \tilde{\gamma}_S^i(\mu, \nu) \,. \tag{2.199}$$

The second equality follows from *path independence* in the (μ, ν) plane, which is locally equivalent to the integrability condition

$$\left[\frac{\mathrm{d}}{\mathrm{d}\mu}, \frac{\mathrm{d}}{\mathrm{d}\nu} \right] = 0 \tag{2.200}$$

for the RG flow generators acting on $\tilde{B}_i$ and $\tilde{S}_i$. Path independence generalizes the group property in eq. (2.172) to two dimensions. In momentum space, the b_T dependence of $\tilde{\gamma}_\nu^i$ translates into a distribution-valued $\gamma_\nu^i(\vec{k}_T)$ and the beam and soft functions are renormalized by a convolution over the full transverse plane [263].

Before discussing the detailed structure of $\tilde{\gamma}_\nu^i$, it is worthwhile to point out the physical consequences of the rapidity renormalization. As discussed in section 2.2.7, the rapidity regulator must (softly) break boost invariance to disentangle the soft and collinear sectors. For the beam function this means that it acquires an explicit logarithmic dependence on the large light-cone component $\omega_{a,b}$ of the extracted parton's momentum,[17]

$$\omega_a = x_a P_a^- \,, \qquad \omega_b = x_b P_b^- \tag{2.201}$$

---

[16]We caution the reader that associating $\tilde{\gamma}_\nu^i$ with the ν anomalous dimension of $\tilde{S}_i$ is a common, but by no means universal convention in the literature.

[17]The explicit values of $\omega_{a,b}$ and $\zeta_{a,b}$ depend on the choice of light-cone variables. For our default choice of light-cone variables in terms of $n_{a,b}^\mu = (1, \pm \hat{z})_{\text{lep}}$ in the leptonic frame, $\omega_{a,b} = Q$, whereas for $n_{a,b}^\mu$ chosen in the lab frame we would have $\omega_{a,b} = Qe^{\pm Y}$. Note, however, that the product of the two beam functions or TMDPDFs only depends on the product $\omega_a \omega_b = Q^2$ and $\zeta_a \zeta_b = Q^4$, which is the same in either case.

Similarly, when combining the beam and soft function into a TMDPDF as in eq. (2.195), the ν dependence cancels between them, but leaves behind an explicit dependence on the Collins-Soper scale $\zeta_{a,b} = \omega_{a,b}^2$. This should be contrasted with PDFs that only depend on the dimensionless momentum fraction $x_{a,b}$. In the context of TMDPDFs, the rapidity anomalous dimension is also known as the Collins-Soper kernel [185, 251], which governs the ζ dependence of TMD distributions.

Structure of the rapidity anomalous dimension. If the ν evolution is performed at scales $\mu \gg \mu_0$ much higher than the intrinsic scale $\mu_0 \sim 1/b_T$ of $\tilde\gamma_\nu^i$, the rapidity anomalous dimension itself requires resummation. Solving eq. (2.199) between μ_0 and μ, we have

$$\tilde\gamma_\nu^i(b_T, \mu) = -4\eta_\Gamma^i(\mu_0, \mu) + \tilde\gamma_{\nu,\mathrm{FO}}^i(b_T, \mu_0) + \tilde\gamma_{\nu,\mathrm{np}}^i(b_T) \,, \tag{2.202}$$

where all logarithms of μ/μ_0 are resummed inside

$$\eta_\Gamma^i(\mu_0, \mu) = \int_{\mu_0}^{\mu} \frac{\mathrm{d}\mu'}{\mu'} \Gamma_{\mathrm{cusp}}^i[\alpha_s(\mu')] \,. \tag{2.203}$$

For $\mu_0 \sim 1/b_T \gg \Lambda_{\mathrm{QCD}}$ the boundary condition $\tilde\gamma_{\nu,\mathrm{FO}}^i(b_T, \mu_0)$ can safely be evaluated in fixed-order perturbation theory,

$$\tilde\gamma_{\nu,\mathrm{FO}}^i(b_T, \mu_0) = \sum_{n=0}^{\infty} \tilde\gamma_\nu^{i\,(n)}(b_T/\mu_0) \left[\frac{\alpha_s(\mu_0)}{4\pi}\right]^{n+1} \tag{2.204}$$

The logarithmic dependence of $\tilde\gamma_\nu^{i\,(n)}$ on b_T/μ_0 is predicted by a recursive solution of eq. (2.199), accounting for the β function. Up to three loops, one has

$$\begin{aligned}
\tilde\gamma_\nu^{i\,(0)}(b_T/\mu) &= -L_b\, 2\Gamma_0^i + \tilde\gamma_{\nu\,0}^i \,, \\
\tilde\gamma_\nu^{i\,(1)}(b_T/\mu) &= -L_b^2\, \Gamma_0^i \beta_0 + L_b\big(\beta_0 \tilde\gamma_{\nu\,0}^i - 2\Gamma_1^i\big) + \tilde\gamma_{\nu\,1}^i \,, \\
\tilde\gamma_\nu^{i\,(2)}(b_T/\mu) &= -L_b^3 \frac{2}{3}\Gamma_0^i \beta_0^2 + L_b^2\big(\beta_0^2 \tilde\gamma_{\nu\,0}^i - 2\Gamma_1^i \beta_0 - \Gamma_0^i \beta_1\big) \\
&\quad + L_b\big(2\beta_0 \tilde\gamma_{\nu\,1}^i + \beta_1 \tilde\gamma_{\nu\,0}^i - 2\Gamma_2^i\big) + \tilde\gamma_{\nu\,2}^i \,.
\end{aligned} \tag{2.205}$$

The boundary coefficients $\tilde\gamma_{\nu\,n}^i$ are known to three loops [264–266], see eq. (C.14). In eq. (2.205) we used the shorthand

$$L_b = L_b\Big(\frac{b_T}{\mu}\Big) = \ln\frac{b_T^2 \mu^2}{b_0^2} \,, \qquad b_0 = 2e^{-\gamma_E} \approx 1.12292 \,. \tag{2.206}$$

Powers of L_b naturally appear in perturbative calculations of b_T-space ingredients as the Fourier transform of $\vec{q}_T$-dependent plus distributions $\mathcal{L}_n(\vec{q}_T, \mu)$. It is therefore common to include a conventional factor of $b_0 = \mathcal{O}(1)$ in b_T-space boundary scales to fully eliminate the L_b. For example, the canonical choice of μ_0 that eliminates all (large) logarithms in the fixed-order boundary condition $\tilde\gamma_\nu^{\mathrm{FO}}(b_T, \mu_0)$ is

$$\mu_0 \sim b_0/b_T \,. \tag{2.207}$$

As b_T increases towards long distances $1/\Lambda_{\rm QCD}$, the boundary condition for the rapidity anomalous dimension becomes sensitive to nonperturbative physics. One possibility to smoothly extend the perturbative result into this region is to choose μ_0 as a function of b_T such that it freezes out at a perturbative scale at large b_T, avoiding the Landau pole at $\mu_0 \sim 1/\Lambda_{\rm QCD}$ in the fixed-order boundary condition. This is the strategy we will pursue in chapter 4, and our explicit choice of $\mu_0(b_T)$ is given there. The mismatch to the full result can then in principle be captured by a nonperturbative model $\tilde{\gamma}^i_{\nu,\rm np}(b_T) = \mathcal{O}(b_T\Lambda_{\rm QCD})$, which can be extracted from experimental measurements at small q_T, see refs. [267, 268] for recent fits. Recently it was shown that $\tilde{\gamma}^i_{\nu,\rm np}$ may also be determined from lattice calculations [269–273], and that estimates of the first subleading power in $b_T\Lambda_{\rm QCD}$ can be related to the gluon condensate [274]. For the purposes of chapter 4, where nonperturbative effects are not the main focus, we will set $\tilde{\gamma}^i_{\nu,\rm np} = 0$ for simplicity. An alternative, even simpler strategy to extend the perturbative description is to freeze out the entire running coupling at a perturbative value, which is the approach we will use in chapter 7.

Canonical scales and resummation. The factorization in eq. (2.192) separates the physics at the invariant-mass and rapidity scales

$$\mu_H \sim Q\,, \qquad \mu_B \sim q_T\,, \qquad \mu_S \sim q_T\,, \qquad \mu_0 \sim q_T\,,$$
$$\nu_B \sim Q\,, \qquad \nu_S \sim q_T\,. \tag{2.208}$$

It has been known for a long time [275] that directly resumming the logarithms of q_T/Q in momentum space based on eq. (2.193a) is challenging due to the vectorial nature of $\vec{q}_T$, though by now approaches for doing so exist [263, 276]. For phenomenological results in this thesis we bypass this issue, as is commonly done, by carrying out the resummation in conjugate (b_T) space using eq. (2.193b) [185, 251, 252, 277]. In this formulation, the canonical scales in b_T-space are given by

$$\mu_H \sim Q\,, \qquad \mu_B \sim b_0/b_T\,, \qquad \mu_S \sim b_0/b_T\,, \qquad \mu_0 \sim b_0/b_T\,,$$
$$\nu_B \sim Q\,, \qquad \nu_S \sim b_0/b_T\,, \tag{2.209}$$

where $b_0 = \mathcal{O}(1)$ as discussed is conventional. (In practice this choice is always covered by scale variations that form part of the uncertainty estimate.) By evaluating the functions in the factorization theorem at their canonical scales and evolving them to a common scale in both μ and ν, all logarithms of $\mu_B/\mu_H \sim \mu_S/\mu_H \sim \nu_S/\nu_B \sim (b_0/b_T)/Q$ are resummed. A possible RG evolution path that connects these scales is shown in the right panel of figure 2.13. Explicit expressions for the RG evolution factors are given in appendix D. In ref. [263] it was shown that the canonical resummation in b_T space is in fact equivalent to the exact solution of the RGE in momentum space, except for the fact that one effectively uses a shifted set of finite terms in the boundary conditions (similar to the difference between renormalization schemes). We exploit this and require that for $q_T \ll Q$, eq. (2.209) is exactly satisfied, such that the resummed q_T spectrum in this region is obtained from the inverse Fourier transform of the canonical b_T-space result. A set of profile scales that implements these requirements is given in chapter 4.

Perturbative content of beam and soft functions. The operator definitions of the beam and soft functions (or TMDPDFs) are true to all orders and allow for a rigorous field-theoretic treatment of the $\vec{q}_T$ spectrum in the nonperturbative regime $q_T \sim b_0/b_T \sim \Lambda_{\mathrm{QCD}}$. For $b_0/b_T \gg \Lambda_{\mathrm{QCD}}$, the soft and beam functions exhibit additional perturbative structure. The soft function in this regime becomes purely perturbative since it is defined by a vacuum matrix element and involves no hadronic external state. It is known to $\mathcal{O}(\alpha_s^2)$ for several regulators [264, 278–280] and has been calculated to $\mathcal{O}(\alpha_s^3)$ using the exponential regulator [265].

For the beam functions, the separation of scales $\Lambda_{\mathrm{QCD}} \ll b_0/b_T$ in the perturbative regime justifies an OPE of the defining beam function operator in Fourier space, with fields separated by $\vec{b}_T$, in terms of local operators. This is very similar to the OPE that gives rise to the factorization theorem for inclusive DIS in eq. (2.43), where $\mu \sim b_0/b_T$ takes the role of the hard scale $\mu \sim Q$, and the proton matrix elements of the leading term in the expansion are in fact exactly the leading-twist PDFs. For the quark q_T beam function in Fourier space, the matching relation in our notation reads [252, 281]

$$\tilde{B}_q(x, b_T, \mu, \nu/\omega) = \sum_j \int_x^1 \frac{\mathrm{d}z}{z} \, \tilde{\mathcal{I}}_{qj}(z, b_T, \mu, \nu/\omega) \, f_j\!\left(\frac{x}{z}, \mu\right) \left[1 + \mathcal{O}(\Lambda_{\mathrm{QCD}}^2 b_T^2)\right]. \qquad (2.210)$$

where the $\tilde{\mathcal{I}}_{qj}$ are perturbatively calculable matching coefficients. In the gluon case there are two distinct matching coefficients $\tilde{\mathcal{I}}_{gj}$ and $\tilde{\mathcal{J}}_{gj}$ for the unpolarized and polarized contribution, respectively. The physical interpretation of eq. (2.210) is that the only required nonperturbative input is the longitudinal momentum distribution described by the PDF, whereas the collinear dynamics that shape the transverse momentum spectrum (and reshuffle flavor and longitudinal momentum in the process) are perturbative. All matching coefficients $\mathcal{I}_{ij} = \delta_{ij}\,\delta(1-z) + \mathcal{O}(\alpha_s)$ are as of recently known to $\mathcal{O}(\alpha_s^3)$ [265, 278, 279, 282–288]. In chapter 6, the all-order structure of the matching coefficients in the $z \to 1$ limit is derived and the leading terms in this limit are predicted at $\mathcal{O}(\alpha_s^3)$, which were still unknown at the time of their original publication in ref. [5] and have later been used as cross checks on the full calculation in refs. [287, 288]. The matching coefficient $\mathcal{J}_{gj}$ starts at $\mathcal{O}(\alpha_s)$ and is known to $\mathcal{O}(\alpha_s^2)$ [286, 289].

2.4.4 0-jettiness factorization

The observables discussed in the previous sections constrain hadronic radiation only indirectly by measuring properties of the color-singlet final state. The simplest kind of hadronic observables, at least from the point of view of factorization, are *event shapes* that measure an aggregate property of all hadronic radiation in the event. Here we focus on the N-jettiness event shape, $\mathcal{T}_N$, and specifically the case of color-singlet production in hadronic collisions with $N = 0$ jets in the final state, where it coincides with beam thrust [57, 59]. 0-jettiness can be defined in terms of generic distance measures $Q_{a,b}$ as [290, 291]

$$\mathcal{T}_0 = \sum_{i \in X} \min\!\left\{\frac{2q_a \cdot k_i}{Q_a}, \frac{2q_b \cdot k_i}{Q_b}\right\}, \qquad (2.211)$$

where the sum runs over the momenta k_i of all particles in the hadronic final state. The reference vectors $q_{a,b} = Q\,(1, \pm\hat{z})_{\text{lab}}$ are aligned with the beam axis in the lab frame. The distance measures $Q_{a,b}$ determine different definitions of 0-jettiness. Two possible choices, corresponding to the original definitions in refs. [57, 59], are

$$\text{leptonic:} \qquad Q_a = Q_b = Q\,, \qquad \mathcal{T}_0^{\text{lep}} = \sum_i \min\left\{ n_a \cdot k_i\,,\ n_b \cdot k_i \right\}$$

$$\text{hadronic:} \qquad Q_{a,b} = Q\,e^{\pm Y}\,, \qquad \mathcal{T}_0^{\text{cm}} = \sum_i \min\left\{ e^{-Y} n_a \cdot k_i\,,\ e^{+Y} n_b \cdot k_i \right\}\,, \qquad (2.212)$$

and we remind the reader that our default convention is $n_{a,b} = (1, \pm\hat{z})_{\text{lep}}$ in the leptonic frame, leading to the additional factors of $e^{\pm Y}$ on the second line. For explicit numerical results in this thesis we will use the leptonic definition. For conceptional purposes the precise choice of the Q_i is not important, so we will simply use the symbol $\mathcal{T}_0$.

The factorization formula for N-jettiness has been derived using SCET in refs. [57, 290, 291]. The relevant degrees of freedom for $N = 0$ are

$$n_a\text{-collinear:} \quad p^\mu \sim \left(\mathcal{T}_0, Q, \sqrt{Q\mathcal{T}_0} \right)\,,$$

$$n_b\text{-collinear:} \quad p^\mu \sim \left(Q, \mathcal{T}_0, \sqrt{Q\mathcal{T}_0} \right)\,,$$

$$\text{ultrasoft:} \quad p^\mu \sim \left(\mathcal{T}_0, \mathcal{T}_0, \mathcal{T}_0 \right)\,. \qquad (2.213)$$

The scalar products and the minimum in eq. (2.211) constrain the smaller light-cone component for each emission. For this reason only ultrasoft radiation is allowed at central rapidities (making this a SCET$_\text{I}$ problem), while collinear radiation at larger absolute rapidities can have parametrically larger transverse momentum as long as the smaller light-cone component stays of $\mathcal{O}(\mathcal{T}_0)$.

The factorization formula derived from eq. (2.213) reads [57]

$$\frac{\mathrm{d}\sigma}{\mathrm{d}Q^2\mathrm{d}Y\mathrm{d}\mathcal{T}_0} = \sum_{i,j} H_{ij}(Q^2, \mu) \int \mathrm{d}t_a\,\mathrm{d}t_b\, B_i(t_a, x_a, \mu)\, B_j(t_b, x_b, \mu)\, S_i\!\left(\mathcal{T}_0 - \frac{t_a}{Q_a} - \frac{t_b}{Q_b}, \mu \right)$$

$$\times \left[1 + \mathcal{O}\!\left(\frac{\mathcal{T}_0}{Q} \right) \right]\,. \qquad (2.214)$$

For $N > 0$ the minimum in eq. (2.211) in addition includes the projections of the k_i onto the jet directions, which can themselves be chosen to minimize the overall $\mathcal{T}_N$. In this case, the factorization formula includes an additional inclusive jet function as defined in eq. (2.180) for every final-state jet, and the hard and soft functions become matrices in color space that depend on the angles $n_i \cdot n_j$ between the different collinear sectors.

The beam function in eq. (2.214) is the inclusive virtuality-dependent (SCET$_\text{I}$) beam function. It is universal to many event shape factorization formulas involving hadrons in the initial state, including in particular event shapes measured in deep-inelastic scattering [292]. In chapter 5 we will show that it also appears in a generalized threshold factorization

theorem for inclusive color-singlet production in hadronic collisions. The bare quark and gluon beam functions are defined as

$$B_q\Big(t, \frac{\omega}{P_n^-}\Big) = \theta(\omega)\langle p_n|\bar{\chi}_{qn}\big[\delta(\omega - \overline{\mathcal{P}})\,\delta(t + \omega\hat{p}^+)\,\frac{\slashed{\bar{n}}}{2}\chi_{qn}\big]|p_n\rangle\,,$$

$$B_g\Big(t, \frac{\omega}{P_n^-}\Big) = \theta(\omega)\omega\langle p_n|\mathcal{B}_{n\perp}^\mu\big[\delta(\omega - \overline{\mathcal{P}})\,\delta(t + \omega\hat{p}^+)\,\mathcal{B}_{n\perp\mu}\big]|p_n\rangle\,, \qquad (2.215)$$

where $\hat{p}^\mu = \mathrm{i}\partial^\mu$ is the residual momentum operator. Since it acts on a collinear field that annihilates a parton from the proton, it picks up a negative value and thus the *transverse virtuality* $t > 0$ of that parton is positive. Note that unlike the q_T gluon beam function, the virtuality-dependent gluon beam function is intrinsically unpolarized because the measurement is scalar, and the Lorentz indices of the gluon fields are contracted within its definition. The beam function is renormalized as [57, 293]

$$\mu\frac{\mathrm{d}}{\mathrm{d}\mu}B_i(t, x, \mu) = \int \mathrm{d}t'\,\gamma_B^i(t - t', \mu)\,B_i(t', x, \mu)\,,$$

$$\gamma_B^i(t, \mu) = -2\Gamma_{\mathrm{cusp}}^i[\alpha_s(\mu)]\,\mathcal{L}_0(t, \mu^2) + \gamma_B^i[\alpha_s(\mu)]\,\delta(t)\,. \qquad (2.216)$$

The noncusp anomalous dimension $\gamma_B^i(\alpha_s)$ is equal to the jet noncusp anomalous dimension $\gamma_J^i(\alpha_s)$ in eq. (2.182) to all orders in perturbation theory [293]. Similar to the q_T beam function, the virtuality dependent beam functions can be matched onto PDFs for $\Lambda_{\mathrm{QCD}} \ll t$ [57, 293],

$$B_i(t, x, \mu) = \sum_j \int \frac{\mathrm{d}z}{z}\,\mathcal{I}_{ij}(t, z, \mu)\,f_j\Big(\frac{x}{z}, \mu\Big)\,. \qquad (2.217)$$

The matching coefficients $\mathcal{I}_{ij}$ have recently become available to $\mathcal{O}(\alpha_s^3)$ [59, 293–297] The results of chapter 5 imply a powerful consistency relation with the threshold soft function in eq. (2.187). In chapter 6 we demonstrate how the leading $z \to 1$ terms at $\mathcal{O}(\alpha_s^3)$ were extracted based on this relation in ref. [5], providing key cross checks on the later ref. [298] and the full calculation in ref. [299].

The soft function $S_i(k, \mu)$ in eq. (2.214) is the hemisphere soft function for incoming Wilson lines. It is defined by measuring $k = \sum_i \min\{k_i^+, k_i^-\}$ on all emissions k_i in the soft final state. The RGE of the soft function reads [57, 293]

$$\mu\frac{\mathrm{d}}{\mathrm{d}\mu}S_i(k, \mu) = \int \mathrm{d}k'\gamma_S^i(k - k', \mu)\,S_i(k', \mu)\,,$$

$$\gamma_S^i(k, \mu) = 4\Gamma_{\mathrm{cusp}}^i[\alpha_s(\mu)]\,\mathcal{L}_0(k, \mu) + \gamma_S^i[\alpha_s(\mu)]\,\delta(k)\,. \qquad (2.218)$$

It is closely related to the hemisphere soft function for $e^+e^- \to$ jets, which is known to NNLO [300–304]. They have the same anomalous dimensions to all orders [57, 293], and are equal to NNLO [57, 305]. It is an open question whether they remain equivalent at higher fixed orders.

The factorization in eq. (2.214) receives power corrections suppressed by $\mathcal{T}_0/Q$, as indicated. It also does not account for effects from Glauber gluon exchange. For active-parton scattering these are expected to enter at $\mathcal{O}(\alpha_s^4)$ (N⁴LL′) [306, 307] and can in principle be included using the framework of ref. [173]. For proton initial states the factorization formula in addition does not account for spectator forward scattering effects.

The factorization in eq. (4.2) separates the physics at the canonical scales

$$\mu_H \sim Q\,, \qquad \mu_B \sim \sqrt{Q\mathcal{T}_0}\,, \qquad \mu_S \sim \mathcal{T}_0\,. \qquad (2.219)$$

Note that the individual ingredients are well-separated in virtuality, so no evolution in rapidity is required. By evaluating the ingredients at their natural scale and evolving them to a common scale, all logarithms of $\mathcal{T}_0/Q \sim \mu_S/\mu_H \sim (\mu_B/\mu_H)^2 \sim (\mu_S/\mu_B)^2$ in the $\mathcal{T}_0$ spectrum are resummed. Explicit expressions for the RG evolution factors are given in appendix D.

2.4.5 Jet veto resummation

Experimentally it is very common to characterize the hadronic final state X not just in terms of a single number (an event shape), but in terms of the observed *jets* and their four-momenta. To make the abstract definition of jets as "collimated sprays of hadronic radiation" operational, a *jet algorithm* is required that maps X onto a set of identified jets by clustering together particles that are close to each other. The characteristic size of the identified jets is controlled by a jet radius parameter R that enters the jet definition in a way specific to the algorithm. At the LHC, the most common jet algorithms belong to the k_T class of algorithms [308–312] that cluster particles recursively. To preserve invariance under longitudinal boosts, the distance measure is defined in terms of the separation in azimuthal angle and rapidity, rather than the solid angle about the collision point. In addition, different k_T-type algorithms differ in how the distance measure is weighted with the individual particle transverse momenta. For our purposes here and in chapter 3, the details of the algorithm are not relevant at our working order, and we only require that R parametrically controls the angular separation of particles within the same jet.

An important jet-based observable at the LHC are exclusive 0-jet cross sections where no jet with transverse momentum $p_T > p_T^{\mathrm{cut}}$ above a certain cut is observed. Measurements that involve a *jet veto* like this, or more generally, measurements that bin events by the number of observed jets above some p_T^{cut}, play an important role e.g. in Higgs and diboson measurements or in searches for physics beyond the Standard Model where they are used to suppress background processes and differentiate between contributions to the signal.

Experimental analyses typically choose veto parameters $p_T^{\mathrm{cut}} = 25 - 30\,\mathrm{GeV}$ (with jet radii $R = 0.4 - 0.5$), These relatively tight choices of the veto, $p_T^{\mathrm{cut}} \ll Q$, are motivated by an even split of the total cross section between the bins with 0 and ≥ 1 jet, exploiting the Sudakov suppression in this limit. The modes describing initial-state radiation that passes

the jet veto in the limit $p_T^{\text{cut}} \ll Q$ are

$$
\begin{aligned}
\text{soft:} \quad & p^\mu \sim \left(p_T^{\text{cut}}, p_T^{\text{cut}}, p_T^{\text{cut}} \right), \\
n_a\text{-collinear:} \quad & p^\mu \sim \left(\frac{(p_T^{\text{cut}})^2}{Q}, Q, p_T^{\text{cut}} \right), \\
n_b\text{-collinear:} \quad & p^\mu \sim \left(Q, \frac{(p_T^{\text{cut}})^2}{Q}, p_T^{\text{cut}} \right).
\end{aligned}
\tag{2.220}
$$

Since both collinear and soft radiation with characteristic transverse momentum $p_T \lesssim p_T^{\text{cut}}$ is allowed, this is a SCET_{II} scenario. The 0-jet cross section differential in the Born kinematics Q, Y factorizes as [61, 62, 67],

$$
\begin{aligned}
\frac{\mathrm{d}\sigma_0(p_T^{\text{cut}}, R)}{\mathrm{d}Q^2\,\mathrm{d}Y} = \sum_{i,j} & H_{ij}(Q^2, \mu)\, B_i(p_T^{\text{cut}}, R, \omega_a, \mu, \nu)\, B_j(p_T^{\text{cut}}, R, \omega_b, \mu, \nu) \\
& \times S_i(p_T^{\text{cut}}, R, \mu, \nu) \left[1 + \mathcal{O}\!\left(\frac{p_T^{\text{cut}}}{Q}, R^2 \right) \right].
\end{aligned}
\tag{2.221}
$$

The structure of eq. (2.221) is very similar to the q_T-dependent factorization in eq. (2.193), with the hard function being the same and the beam and soft functions being rapidity regulated.[18] The important difference is that the beam and soft functions enter in a product rather than a convolution. This reflects the nature of the measurement, which requires that after clustering emissions into jets in each separate factorized sector, the hardest jet *in each sector* must pass the veto. The rate for this to happen is proportional to the product of individual rates in each sector.[19]

By contrast, the convolution in the q_T-dependent factorization theorem encodes the fact that we indirectly measure the total vectorial transverse momentum of all initial-state radiation combined. The formal definitions of the beam and soft functions are analogous to the q_T case with the measurement replaced, but writing out the factorized measurement in a formula takes exactly as long as saying it in words, so we defer it to the actual perturbative calculations of jet veto beam and soft functions in section 3.4.1.

The beam functions are given by a standard matching onto inclusive PDFs,

$$
B_i(p_T^{\text{cut}}, R, \omega, \mu, \nu) = \sum_j \int_x^1 \frac{\mathrm{d}z}{z}\, \mathcal{I}_{ij}(p_T^{\text{cut}}, R, \omega, z, \mu, \nu)\, f_j\!\left(\frac{\omega}{z E_{\text{cm}}}, \mu \right) \left[1 + \mathcal{O}\!\left(\frac{\Lambda_{\text{QCD}}}{p_T^{\text{cut}}} \right) \right].
\tag{2.222}
$$

---

[18]We note that the ordering of beam function arguments is entirely conventional and that we have made no effort to make it consistent between observables. As in eq. (2.193), the relevant large label momenta at which the beam functions are evaluated are $\omega_{a,b} = Q$ for our standard choice of $n_{a,b}$ in the leptonic frame, but the product of two beam functions in any case only depends on the invariant $\omega_a \omega_b = Q^2$. Also note that we use the same symbols for B_i, S_i and their anomalous dimensions as in the 0-jettiness factorization in eq. (2.214), but the meaning will always be clear from the context.

[19]As discussed in refs. [62, 67], one formally needs to count $R \ll 1$ to avoid soft-collinear mixing terms of $\mathcal{O}(R^2)$, as indicated in eq. (2.221). A detailed discussion of possible approaches to include them at $\mathcal{O}(\alpha_s^2)$ can be found in ref. [313].

Unlike the case of q_T, the power corrections to this relation can essentially always be neglected for relevant values of p_T^{cut}. In analogy to eq. (2.197), the renormalized soft and beam functions obey the following set of coupled multiplicative renormalization group equations,

$$\mu \frac{\mathrm{d}}{\mathrm{d}\mu} \ln B_i(p_T^{\text{cut}}, R, \omega, \mu, \nu) = \gamma_B^i(\omega, \mu, \nu), \qquad \mu \frac{\mathrm{d}}{\mathrm{d}\mu} \ln S_i(p_T^{\text{cut}}, R, \mu, \nu) = \gamma_S^i(\mu, \nu),$$
$$\nu \frac{\mathrm{d}}{\mathrm{d}\nu} \ln B_i(p_T^{\text{cut}}, R, \omega, \mu, \nu) = -\frac{1}{2}\gamma_\nu^i(p_T^{\text{cut}}, R, \mu), \quad \nu \frac{\mathrm{d}}{\mathrm{d}\nu} \ln S_i(p_T^{\text{cut}}, R, \mu, \nu) = \gamma_\nu^i(p_T^{\text{cut}}, R, \mu).$$

$$(2.223)$$

The μ anomalous dimensions have the all-order form,

$$\gamma_B^i(\omega, \mu, \nu) = 2\Gamma_{\text{cusp}}^i[\alpha_s(\mu)] \ln \frac{\nu}{\omega} + \gamma_B^i[\alpha_s(\mu)],$$
$$\gamma_S^i(\mu, \nu) = 4\Gamma_{\text{cusp}}^i[\alpha_s(\mu)] \ln \frac{\mu}{\nu} + \gamma_S^i[\alpha_s(\mu)] \tag{2.224}$$

while the resummed ν anomalous dimension is given by

$$\gamma_\nu^i(p_T^{\text{cut}}, R, \mu) = -4\eta_\Gamma^i(p_T^{\text{cut}}, \mu) + \gamma_\nu^i[\alpha_s(p_T^{\text{cut}}), R]. \tag{2.225}$$

Compared to eq. (2.202), we have picked a fixed value of the boundary scale $\mu_0 = p_T^{\text{cut}}$ and dropped the nonperturbative contribution since $\Lambda_{\text{QCD}} \ll p_T^{\text{cut}}$. By consistency, the ν anomalous dimension can depend on all physical quantities that both the soft and beam function depend on, and in this case the finite term $\gamma_\nu^i(\alpha_s, R)$ indeed depends on the jet radius R.

As usual, all large logarithms of the ratio p_T^{cut}/Q in eq. (2.221) are resummed by evaluating the hard, beam, and soft functions at their canonical virtuality and rapidity scales,

$$\mu_H \sim Q, \quad \mu_B \sim \mu_S \sim p_T^{\text{cut}}, \quad \nu_B \sim Q, \quad \nu_S \sim p_T^{\text{cut}}, \tag{2.226}$$

and evolving them to common scales μ, ν using RG evolution. The power corrections in eq. (2.221) can be included at fixed order in α_s by matching the resummed result to the corresponding fixed-order result in full QCD, and a profile scale setup that streamlines this process was given in ref. [67]. In the next chapter, we will return to eq. (2.221) and show how to extend it to the experimentally relevant case where jets are only reconstructed (and vetoed) in a finite rapidity range in the detector.

Chapter 3

Jet veto resummation with jet rapidity cuts

Experimental jet selections at the LHC require a cut on the (pseudo)rapidity of reconstructed jets, $|\eta_{\mathrm{jet}}| \leq \eta_{\mathrm{cut}}$. In this chapter, we extend the standard jet p_T (jet veto) resummation, which implicitly works in the limit $\eta_{\mathrm{cut}} \to \infty$, by incorporating a finite jet rapidity cut. We also consider the case of a step in the required p_T^{cut} at an intermediate value of $|\eta| \simeq 2.5$, which is of experimental relevance to avoid the increased pile-up contamination beyond the reach of the tracking detectors.

This chapter is based on ref. [2], reflecting the author's contribution. Compared to the version published in ref. [2], the amount of detail in sections 3.4.1 and 3.4.5 has been expanded for this thesis, and a new all-order result and its derivation have been added in section 3.4.4, generalizing a two-loop result in ref. [2].

3.1 Motivation

Measurements that involve a veto on additional jets, or more generally that divide events into exclusive jet bins, play an important role at the LHC, e.g. in Higgs and diboson measurements or in searches for physics beyond the Standard Model. The jet binning differentiates between hard processes that differ in the number of hard signal jets, and hence allows one to separate signal and background processes. The separation into 0-jet and $\geq$ 1-jet bins also provides a model-independent way to discriminate between $q\bar{q}$ and gg initiated processes [314].

A veto on jets with transverse momentum $p_T > p_T^{\mathrm{cut}}$ gives rise to double logarithms $\ln^2(p_T^{\mathrm{cut}}/Q)$ at each order in α_s, where Q is the characteristic momentum transfer of the hard interaction. These logarithms dominate the perturbative series when $p_T^{\mathrm{cut}} \ll Q$, and represent an important source of theory uncertainty [59, 315]. As reviewed in section 2.4.5, they can be systematically resummed to improve the perturbative predictions and assess the associated uncertainties, which has been well-developed in Drell-Yan and Higgs production [57–71], and has also been applied to several other color-singlet processes [314, 316–323].

Experiments can only reconstruct jets up to some maximal pseudorapidity $|\eta| \leq \eta_{\mathrm{cut}}$ due to the range of the detector, e.g. for ATLAS and CMS $\eta_{\mathrm{cut}} \sim 4.5$. In principle, the utility of the jet binning to discriminate between different hard processes increases for a tighter jet
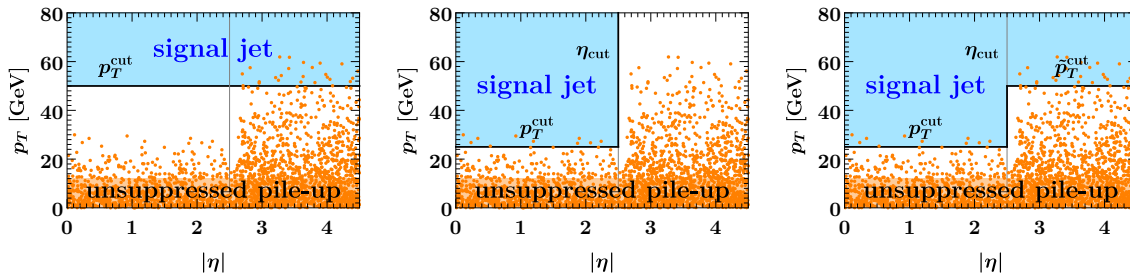
Figure 3.1: Cartoon of possible strategies to avoid contamination from unsuppressed pile up in jet-binned analyses. The pile-up suppression is much better in the pseudorapidity range $|\eta| \lesssim 2.5$, where it can use information from the tracking detectors. To avoid the higher pile-up contamination in the forward region, one can raise the jet threshold (left panel), only consider central jets (middle panel), or combine both approaches by using a step-like jet selection (right panel).

veto (smaller p_T^{cut}). However, jets with small transverse momenta are difficult to reconstruct experimentally, especially for pseudorapidity $|\eta| \gtrsim 2.5$ beyond the reach of the tracking detectors, which are important to suppress the large contamination from pile up (e.g. in the jet vertex tagging algorithm used by ATLAS [324]). This is illustrated in figure 3.1. As the LHC luminosity increases and pile-up conditions become harsher, the contamination from unsuppressed pile-up jets grows worse and must be avoided. One option is to increase the overall p_T^{cut}. For example, in the context of Higgs measurements, the increased pile up in Run 2 has forced raising the jet threshold from 25 GeV to 30 GeV. This however weakens the jet veto and thus reduces its utility. Alternatively, to avoid raising the jet threshold, one can consider jets only in a restricted pseudorapidity range of $|\eta| \lesssim 2.5$. However, this looses the discrimination power from forward jets, which are a distinguishing feature of some processes (most notably weak-boson fusion topologies in Higgs and diboson production, cf. figure 2.6). The best possible option combines both approaches and performs a step-like jet selection, with a lower p_T^{cut} threshold for central jets and a somewhat higher $\tilde{p}_T^{\text{cut}}$ threshold for forward jets. For example, recent ATLAS Higgs measurements [325] reconstruct jets using $p_T^{\text{cut}} = 25$ GeV for $|\eta| < 2.4$ and $\tilde{p}_T^{\text{cut}} = 30$ GeV for $|\eta| > 2.4$ (and no jets beyond rapidity $|y| = 4.4$).

A discontinuous step in the jet threshold can also pose challenges on its own, as it makes the experimental measurements more complex. Theoretically, we will see that it can complicate the resummation of logarithms in some extreme cases. An alternative to a step is to use jet vetoes that smoothly depend on the jet rapidity [70, 313], providing a tighter veto at central rapidities and a looser one at forward rapidities.[1]

The usual jet p_T resummations [60–63, 66, 67] do not account for any jet rapidity dependence, i.e., the resummation is performed for $\eta_{\text{cut}} \to \infty$. Using parton-shower Monte Carlos, one finds that a jet rapidity cut at $\eta_{\text{cut}} = 4.5$ has a very small numerical effect, while $\eta_{\text{cut}} = 2.5$ has a sizable effect on the jet p_T spectrum in Higgs production (see e.g.

---

[1]These rapidity-dependent vetoes can also be supplemented with an additional sharp jet rapidity cut, see appendix B of ref. [2].

refs. [59, 60]), so it is important to properly include it in the resummation. This was already pointed out in ref. [62], where it was also speculated that a jet rapidity cut might change the resummation structure.

Our analysis in this chapter fully addresses these questions by systematically incorporating the jet rapidity cut into the jet p_T resummation, including in particular the case of a step-like veto. For this purpose, we extend the formalism of refs. [62, 67] reviewed in section 2.4.5. To be concrete, our discussion focuses on color-singlet production, including the important cases of Higgs and Drell-Yan production. Our results for how to incorporate the η_{cut} dependence also carry over to processes with additional signal jets in the final state to the same extent to which the usual jet p_T resummation for color-singlet production carries over to such cases [64, 65].

We identify all relevant parametric regimes in the veto parameters p_T^{cut}, η_{cut}, $\tilde{p}_T^{\mathrm{cut}}$, and discuss the factorization and resummation structure for each regime. We also study the relations between the different regimes and perform numerical studies to check their respective ranges of validity. An important conclusion of our analysis is that all regions of parameter space that are of phenomenological interest can be described by parametric regimes that are free of large so-called nonglobal logarithms, i.e., logarithms of parametrically distinct constraints in different regions of phase space that cannot (straightforwardly) be predicted by solving an RGE.

We analytically compute the η_{cut} dependence of all ingredients at $\mathcal{O}(\alpha_s)$ as well as of the dominant $\mathcal{O}(\alpha_s^2)$ corrections (those enhanced by jet veto or jet clustering logarithms), which matches the order to which they are currently known in the $\eta_{\mathrm{cut}} \to \infty$ limit. Our results allow for carrying out the jet veto resummation including jet rapidity cuts to the same order as is currently available without such cuts, which for color-singlet production is NNLL′+NNLO. (Reaching this level also requires the still unknown nonlogarithmic $\mathcal{O}(\alpha_s^2)$, which can be extracted numerically from the full NNLO calculation, as was done for $\eta_{\mathrm{cut}} \to \infty$ in ref. [67]. Carrying out such an analysis is beyond the scope of this thesis.)

The effect of a rapidity cut for transverse momentum vetoes has also been considered independently in refs. [326, 327] for dijet production, and more recently for the transverse energy event shape in Drell-Yan in ref. [328]. We compare their results to our results for the case of a sharp cut at η_{cut} and no measurement beyond in section 3.2.5.

This chapter is organized as follows: In section 3.2, we discuss the parametric regimes and corresponding effective field theory (EFT) setups for a sharp cut on reconstructed jets at η_{cut} and no measurement beyond, as in the middle panel of figure 3.1. We give the perturbative ingredients at $\mathcal{O}(\alpha_s)$ and the leading small-R clustering terms at $\mathcal{O}(\alpha_s^2)$ for all partonic channels. We numerically validate the EFT setup by comparing to the relevant singular limits of full QCD, and also compare the regimes to each other and identify their respective ranges of validity. In section 3.3, we generalize the results of section 3.2 to a step in the jet veto at η_{cut}, as in the right panel of figure 3.1. In section 3.4 we describe the perturbative calculation of the relevant ingredients and elucidate the all-order structure of clustering logarithms in the jet veto beam function both with and without a jet rapidity cut. In section 3.5, we illustrate the numerical impact of the rapidity cut at NLL′+NLO

for Drell-Yan at $Q = m_Z$ and $Q = 1\,\text{TeV}$ and for $gg \to H$ at $m_H = 125\,\text{GeV}$ and $gg \to X$ at $m_X = 1\,\text{TeV}$ for different values of η_{cut}. We summarize our results in section 3.6.

3.2 Factorization with no constraint beyond η_{cut} ($\tilde{p}_T^{\text{cut}} = \infty$)

3.2.1 Overview of parametric regimes

We consider exclusive 0-jet cross sections, where the veto is applied by identifying jets in the hadronic final state X using a jet algorithm with radius parameter R and cutting on the transverse momentum p_T^{jet} of the leading jet within $|\eta_{\text{jet}}| < \eta_{\text{cut}}$,

$$\max_{k \in \text{jets}(X,R):\, |\eta_k| < \eta_{\text{cut}}} |\vec{p}_{T,k}| < p_T^{\text{cut}} . \tag{3.1}$$

The resulting constraints on the rapidities and transverse momenta of initial-state radiation (ISR) are displayed as black lines in figure 3.2. We can identify two distinct power-counting parameters that govern the typical angular size of energetic collinear ISR with energy $E \sim Q$, where Q is the momentum transferred in the hard interaction: First, the p_T of the emissions is constrained by $p_T < p_T^{\text{cut}}$ for $|\eta| < \eta_{\text{cut}}$, corresponding to a maximum opening angle

$$\frac{p_T}{E} \lesssim \frac{p_T^{\text{cut}}}{Q} . \tag{3.2}$$

Second, the p_T of an energetic emission at rapidity η is parametrically $p_T \sim Qe^{-|\eta|}$. The rapidity cut removes the first constraint for $|\eta| > \eta_{\text{cut}}$. Hence, if η_{cut} is central enough, emissions beyond η_{cut} can reach a characteristic $p_T \lesssim Qe^{-|\eta_{\text{cut}}|}$, corresponding to a maximum opening angle

$$\frac{p_T}{E} \lesssim e^{-\eta_{\text{cut}}} . \tag{3.3}$$

There are three parametric regimes for p_T^{cut}/Q and $e^{-\eta_{\text{cut}}}$, which are illustrated in figure 3.2 for $\eta_{\text{cut}} = 2.5$. The thick black lines show the veto for different values of p_T^{cut}/Q. The thick gray curve shows the relation $p_T/Q = e^{-|\eta|}$, while the thin gray lines show the values of η_{cut} and $p_T/Q = e^{-\eta_{\text{cut}}}$.

The first parametric regime is $p_T^{\text{cut}}/Q \gg e^{-\eta_{\text{cut}}}$. As we will demonstrate in section 3.2.2, in this regime effects due to the rapidity cut are power suppressed by $Qe^{-\eta_{\text{cut}}}/p_T^{\text{cut}}$. Hence, they can be treated as a fixed-order power correction to the standard jet veto resummation, which implicitly works in the limit $\eta_{\text{cut}} = \infty$. For Higgs measurements with $p_T^{\text{cut}} = 25\,\text{GeV}$, $\eta_{\text{cut}} = 4.5$, $Q \equiv m_H = 125\,\text{GeV}$, this parametric assumption is well justified, as $m_H e^{-\eta_{\text{cut}}}/p_T^{\text{cut}} \sim 5\%$.

For heavier final states and/or more central rapidity cuts the relevant parametric regime is $p_T^{\text{cut}}/Q \sim e^{-\eta_{\text{cut}}}$. This is the case for example for $Q = 1\,\text{TeV}$ and $\eta_{\text{cut}} = 4.5$ or $Q = 125\,\text{GeV}$ and $\eta_{\text{cut}} = 2.5$ at $p_T^{\text{cut}} = 25\,\text{GeV}$. In section 3.2.3, we show that in this regime the rapidity cut effects must be treated as a leading-power correction, and that they can be seamlessly incorporated into the existing jet veto resummation without rapidity cut. We will see that
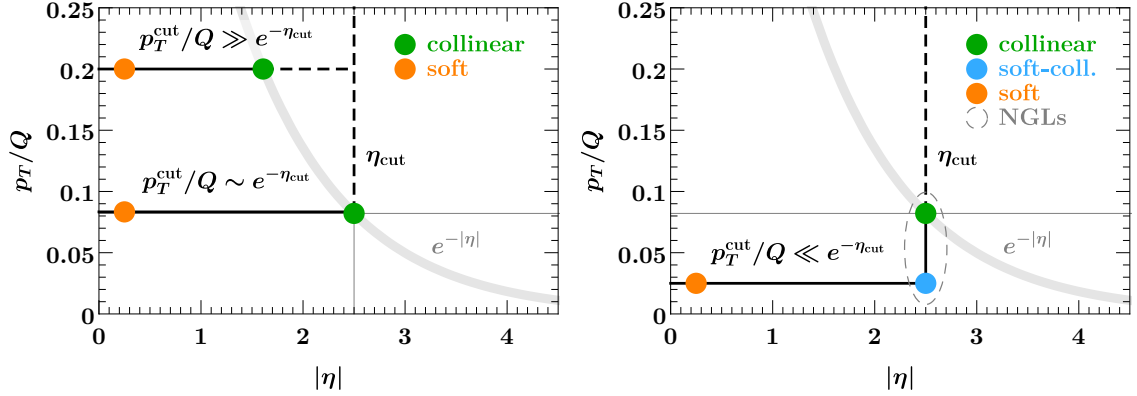
Figure 3.2: Illustration of the parametric regimes for a jet veto with a jet rapidity cut. Emissions above the black solid lines are vetoed as $p_T > p_T^{\text{cut}}$ up to $|\eta| < \eta_{\text{cut}} = 2.5$. The thick gray line corresponds to $p_T/Q = e^{-|\eta|}$, and emissions above and to the right of it are power suppressed. The colored circles indicate the relevant modes in the effective theory for a given hierarchy between p_T^{cut}/Q and $e^{-\eta_{\text{cut}}}$. For $p_T^{\text{cut}} = 25\,\text{GeV}$, the given examples for p_T^{cut}/Q correspond to $Q = 125\,\text{GeV}$ (left panel, upper case), $Q = 300\,\text{GeV}$ (left panel, lower case), $Q = 1\,\text{TeV}$ (right panel).

they affect only the boundary terms in the resummed cross section, but not the anomalous dimensions and evolution factors. Hence, they start contributing at NLL$'$ or NNLL.

Finally in section 3.2.4, we discuss the parametric regime $p_T^{\text{cut}}/Q \ll e^{-\eta_{\text{cut}}}$. This case is conceptually interesting, since logarithms of the ratio of scales $Qe^{-\eta_{\text{cut}}}$ and p_T^{cut} appear, changing the logarithmic structure already at leading-logarithmic (LL) order. In addition, formally large nonglobal logarithms of the same ratio appear. This regime is of very limited phenomenological relevance for typical jet-binned analyses at the LHC. For example, for $\eta_{\text{cut}} = 2.3$ corresponding to $e^{-\eta_{\text{cut}}} = 0.1$, it would require an extremely tight jet veto $p_T^{\text{cut}} \ll 0.1\,Q$, which is unrealistic as it would leave almost no signal in the 0-jet cross section. For the purpose of explicitly probing this regime experimentally, one could lower $\eta_{\text{cut}} \simeq 1.0 - 1.5$, such that the jet veto only acts on radiation in the very central region.

3.2.2 Regime 1: $p_T^{\text{cut}}/Q \gg e^{-\eta_{\text{cut}}}$ (standard jet veto resummation)

As usual, the scaling of the modes in the EFT follows from the nontrivial constraints imposed on emissions by the measurement. Soft emissions at central rapidities are always restricted by the jet veto. Collinear emissions with energy $\sim Q$ and rapidity η have a transverse momentum $\sim Qe^{-|\eta|}$ and are constrained by the measurement if $Qe^{-|\eta|} \sim p_T^{\text{cut}}$, which determines their scaling. Since $Qe^{-\eta_{\text{cut}}} \ll p_T^{\text{cut}}$, these collinear modes are parametrically not forward enough to be sensitive to the rapidity cut, such that the description of their dynamics is simply governed by the power counting in p_T^{cut}/Q. The relevant EFT modes in this regime are thus the same as for a jet veto without any rapidity cut,

$$\text{soft:} \quad p^\mu \sim \left(p_T^{\text{cut}}, p_T^{\text{cut}}, p_T^{\text{cut}}\right),$$

$$n_a\text{-collinear:} \quad p^\mu \sim \left(\frac{(p_T^{\text{cut}})^2}{Q}, Q, p_T^{\text{cut}}\right),$$

$$n_b\text{-collinear:} \quad p^\mu \sim \left(Q, \frac{(p_T^{\text{cut}})^2}{Q}, p_T^{\text{cut}}\right). \tag{3.4}$$

Here and below, we give the scaling of momenta in terms of light-cone components defined as (with $n \equiv n_a$, $\bar{n} \equiv n_b$),

$$p^\mu = \bar{n}{\cdot}p\, \frac{n^\mu}{2} + n{\cdot}p\, \frac{\bar{n}^\mu}{2} + p_\perp^\mu \equiv (n{\cdot}p, \bar{n}{\cdot}p, \vec{p}_\perp) \equiv (p^+, p^-, \vec{p}_\perp). \tag{3.5}$$

In addition, there are the usual inclusive collinear modes that describe the initial protons at the scale Λ_{QCD}, and which are not specific to our discussion here.

In principle, we can consider collinear emissions that are forward enough to resolve rapidities $|\eta| \sim \eta_{\text{cut}}$,

$$n_a\text{-collinear } (\eta_{\text{cut}}): \quad p^\mu \sim \left(Qe^{-2\eta_{\text{cut}}}, Q, Qe^{-\eta_{\text{cut}}}\right),$$
$$n_b\text{-collinear } (\eta_{\text{cut}}): \quad p^\mu \sim \left(Q, Qe^{-2\eta_{\text{cut}}}, Qe^{-\eta_{\text{cut}}}\right). \tag{3.6}$$

However, since $Qe^{-\eta_{\text{cut}}} \ll p_T^{\text{cut}}$, these emissions have too little transverse momentum to be affected by the jet veto, and are therefore unconstrained and integrated over without requiring additional modes in the EFT. To explicitly see that the η_{cut} dependence is power suppressed, note that the full jet veto measurement for the collinear modes contains a θ function

$$\theta(\eta_{\text{cut}} - |\eta|) = \theta(1 - e^{|\eta| - \eta_{\text{cut}}}) = 1 + \mathcal{O}(Qe^{-\eta_{\text{cut}}}/p_T^{\text{cut}}), \tag{3.7}$$

which thus only induces power corrections in $Qe^{-\eta_{\text{cut}}}/p_T^{\text{cut}}$.

Therefore, at leading order in the power expansion, we recover the factorization for the 0-jet cross section with $\eta_{\text{cut}} = \infty$ in eq. (2.221),

$$\frac{\mathrm{d}\sigma_0(p_T^{\text{cut}}, \eta_{\text{cut}}, R)}{\mathrm{d}Q^2\,\mathrm{d}Y} = \sum_{i,j} H_{ij}(Q^2, \mu)\, B_i(p_T^{\text{cut}}, R, \omega_a, \mu, \nu)\, B_j(p_T^{\text{cut}}, R, \omega_b, \mu, \nu)$$
$$\times S_i(p_T^{\text{cut}}, R, \mu, \nu) \left[1 + \mathcal{O}\left(\frac{p_T^{\text{cut}}}{Q}, \frac{Qe^{-\eta_{\text{cut}}}}{p_T^{\text{cut}}}, R^2\right)\right]. \tag{3.8}$$

The important difference is the presence of the additional power corrections in $Qe^{-\eta_{\text{cut}}}/p_T^{\text{cut}}$. This provides formal justification for using the standard result for $\eta_{\text{cut}} \to \infty$ in the presence of a cut at sufficiently large η_{cut}, and gives precise meaning to what is sufficient, namely $Qe^{-\eta_{\text{cut}}}/p_T^{\text{cut}} \ll 1$ should be negligible at the desired accuracy. The $\mathcal{O}(Qe^{-\eta_{\text{cut}}}/p_T^{\text{cut}})$ corrections stop being suppressed for large Q, small p_T^{cut}, or central η_{cut}. In the next section, we show that they can be incorporated into the beam functions in eq. (3.8).

3.2.3 Regime 2: $p_T^{\text{cut}}/Q \sim e^{-\eta_{\text{cut}}}$ (η_{cut} dependent beam functions)

In this regime, the scaling of soft and collinear modes is unchanged from the previous case. However, the characteristic rapidity of the collinear modes now coincides parametrically

with η_{cut}, i.e.,

$$\text{soft:} \quad p^\mu \sim \left(p_T^{\text{cut}}, p_T^{\text{cut}}, p_T^{\text{cut}} \right),$$

$$n_a\text{-collinear:} \quad p^\mu \sim \left(\frac{(p_T^{\text{cut}})^2}{Q}, Q, p_T^{\text{cut}} \right) \sim \left(Q e^{-2\eta_{\text{cut}}}, Q, Q e^{-\eta_{\text{cut}}} \right),$$

$$n_b\text{-collinear:} \quad p^\mu \sim \left(Q, \frac{(p_T^{\text{cut}})^2}{Q}, p_T^{\text{cut}} \right) \sim \left(Q, Q e^{-2\eta_{\text{cut}}}, Q e^{-\eta_{\text{cut}}} \right). \tag{3.9}$$

Thus, collinear emissions resolve the rapidity cut, and are constrained by the jet veto for $|\eta| < \eta_{\text{cut}}$, while for $|\eta| > \eta_{\text{cut}}$ they are unconstrained. As a result, the cross section factorizes at leading power as

$$
\begin{aligned}
&\frac{\mathrm{d}\sigma_0(p_T^{\text{cut}}, \eta_{\text{cut}}, R)}{\mathrm{d}Q^2\,\mathrm{d}Y} \\
&= \sum_{i,j} H_{ij}(Q^2, \mu)\, B_i(p_T^{\text{cut}}, \eta_{\text{cut}}, R, \omega_a, \mu, \nu)\, B_j(p_T^{\text{cut}}, \eta_{\text{cut}}, R, \omega_b, \mu, \nu) \\
&\quad \times S_i(p_T^{\text{cut}}, \mu, \nu) \left[1 + \mathcal{O}\left(\frac{p_T^{\text{cut}}}{Q}, e^{-\eta_{\text{cut}}}, R^2 \right) \right].
\end{aligned} \tag{3.10}
$$

The beam functions now explicitly depend on both p_T^{cut} and η_{cut}, while the hard and soft functions are unchanged, with the characteristic scales still given by eq. (2.226). Eq. (3.10) encodes the key new insight of this chapter, namely, that the leading dependence on the rapidity cut can be incorporated directly into the resummation by making the low-energy matrix elements more differential. The following sections elaborate on this idea by treating other possible hierarchies of p_T^{cut} and $Q e^{-\eta_{\text{cut}}}$, and generalizing the idea to a step in the jet veto.

The RG consistency of the cross section fixes the anomalous dimensions of the beam function in terms of those for the soft and hard functions. Thus, the η_{cut} dependence cannot change the renormalization of the beam function, i.e.,

$$\mu \frac{\mathrm{d}}{\mathrm{d}\mu} \ln B_i(p_T^{\text{cut}}, \eta_{\text{cut}}, R, \omega, x, \mu, \nu) = \gamma_B^i(\omega, \mu, \nu),$$

$$\nu \frac{\mathrm{d}}{\mathrm{d}\nu} \ln B_i(p_T^{\text{cut}}, \eta_{\text{cut}}, R, \omega, x, \mu, \nu) = -\frac{1}{2} \gamma_\nu^i(p_T^{\text{cut}}, R, \mu), \tag{3.11}$$

where the anomalous dimensions are the same as the ones in the $\eta_{\text{cut}} \to \infty$ limit given in eqs. (2.224) and (2.225), Hence, the η_{cut} effects do not affect the RG evolution itself, but only change the beam function boundary conditions, and therefore first appear at NLL$'$. The RG evolution between $\mu_B \sim p_T^{\text{cut}} \sim Q e^{-\eta_{\text{cut}}}$ and $\mu_H \sim Q$ now resums all large logarithms of $\mu_B/\mu_H \sim p_T^{\text{cut}}/Q \sim e^{-\eta_{\text{cut}}}$, while the beam function boundary condition now explicitly depends on the ratio $Q e^{-\eta_{\text{cut}}}/p_T^{\text{cut}} \sim \mathcal{O}(1)$, which in contrast to regime 1 is not power suppressed anymore. Power corrections that depend on η_{cut} are now pushed down to $e^{-\eta_{\text{cut}}} \sim p_T^{\text{cut}}/Q$ which sets the characteristic opening angle of collinear modes in the EFT.

In analogy to eq. (2.222) the beam functions can be factorized into collinear matching coefficients, which now also depend on η_{cut}, and the PDFs. We write the matching coefficients as the sum of the usual η_{cut}-independent matching coefficients plus a correction term

that encodes the $\eta_{\rm cut}$ dependence,

$$\mathcal{I}_{ij}(p_T^{\rm cut}, \eta_{\rm cut}, R, \omega, z, \mu, \nu) = \mathcal{I}_{ij}(p_T^{\rm cut}, R, \omega, z, \mu, \nu) + \Delta\mathcal{I}_{ij}(p_T^{\rm cut}, \eta_{\rm cut}, R, \omega, z, \mu, \nu). \quad (3.12)$$

The $\eta_{\rm cut}$-independent $\mathcal{I}_{ij}$ are given in appendix E.4, and in the following we focus on the correction terms $\Delta\mathcal{I}_{ij}$.

Consistency between the cross sections in eqs. (3.8) and (3.10) implies that $\Delta\mathcal{I}_{ij}$ vanishes as $\eta_{\rm cut} \to \infty$. Specifically, defining

$$\zeta_{\rm cut} \equiv \omega e^{-\eta_{\rm cut}}/p_T^{\rm cut}, \quad (3.13)$$

the $\Delta\mathcal{I}_{ij}$ scale like

$$\Delta\mathcal{I}_{ij}\big(p_T^{\rm cut}, \eta_{\rm cut}, R, \omega, z, \mu, \nu\big) \sim \mathcal{O}(\zeta_{\rm cut}) \qquad \text{for } \zeta_{\rm cut} \to 0, \quad (3.14)$$

which is simply the statement from the previous subsection that the $\eta_{\rm cut}$ effects are power suppressed in $\zeta_{\rm cut}$ for $\zeta_{\rm cut} \ll 1$.

In fact, $\Delta\mathcal{I}_{ij}$ vanishes altogether for $z > \zeta_{\rm cut}/(1 + \zeta_{\rm cut})$, which can be seen from purely kinematic considerations as follows: For the n-collinear sector the term $\Delta\mathcal{I}_{ij}$ accounts for the case where at least one jet with $p_T^{\rm jet} \geq p_T^{\rm cut}$ and $\eta_{\rm jet} \geq \eta_{\rm cut}$ is reconstructed (and no jet with $\eta_{\rm jet} < \eta_{\rm cut}$). For $R \ll 1$ all radiation in this jet has $\eta \geq \eta_{\rm cut}$, as well. Thus, contributions to $\Delta\mathcal{I}_{ij}$ can only appear if

$$p_T^{\rm cut} \leq |\vec{p}_T^{\rm jet}| \leq \sum_{k \in \rm jets} |\vec{p}_{T,k}| = \sum_{k \in \rm jets} p_k^- e^{-\eta_k}, \quad (3.15)$$

where the second equality follows from the jets being massless for $R \ll 1$. Rewriting this in terms of momentum fractions $p_k^- = z_k P_n^- = z_k\, \omega/z$ yields, with $\sum_k z_k + z = 1$ and P_n^- the momentum of the initial state proton,

$$p_T^{\rm cut} \leq \sum_{k \in \rm jets} \frac{z_k}{z}\, \omega e^{-\eta_k} \leq \frac{1-z}{z}\, \omega e^{-\eta_{\rm cut}}. \quad (3.16)$$

The second inequality follows from all reconstructed n-collinear jets having $\eta_k > \eta_{\rm cut}$. This implies that eq. (3.14) is trivially satisfied since the domain of integration in z scales as $x \leq z \lesssim \zeta_{\rm cut}$. Hence $\Delta\mathcal{I}_{ij}$ is parametrically important for $\zeta_{\rm cut} \sim z \sim 1$, but vanishes in the threshold limit $z \to 1$. This leads to an additional numerical suppression due to the falloff of the PDFs towards larger partonic momentum fractions.

The RGE of $\Delta\mathcal{I}_{ij}$ follows from the beam-function RGE eq. (3.11) and the analogue of the matching onto the PDFs in eq. (2.222). It is given by (with the remaining arguments of $\Delta\mathcal{I}_{ij}$ understood)

$$\mu\frac{\rm d}{{\rm d}\mu}\Delta\mathcal{I}_{ij}(z, \mu, \nu) = \gamma_B^i(\omega, \mu, \nu)\, \Delta\mathcal{I}_{ij}(z, \mu, \nu) - \sum_k \int \frac{{\rm d}z'}{z'}\, \Delta\mathcal{I}_{ik}\Big(\frac{z}{z'}, \mu, \nu\Big)\, 2P_{kj}[\alpha_s(\mu), z'],$$

$$\nu\frac{\rm d}{{\rm d}\nu}\Delta\mathcal{I}_{ij}(z, \mu, \nu) = -\frac{1}{2}\gamma_\nu^i(p_T^{\rm cut}, R, \mu)\, \Delta\mathcal{I}_{ij}(z, \mu, \nu). \quad (3.17)$$

where $2P_{ij}(\alpha_s, z)$ are the DGLAP kernels that renormalize the PDF, see eq. (2.164). Note that the RGE in eq. (3.17) does not mix $\Delta\mathcal{I}_{ij}$ with $\mathcal{I}_{ij}$ and therefore does not change the $\zeta_{\rm cut}$ scaling in eq. (3.14). Solving eq. (3.17) order by order in perturbation theory, we find the following structure through two loops:

$$\Delta\mathcal{I}_{ij}(z) = \frac{\alpha_s(\mu)}{4\pi}\,\Delta\mathcal{I}_{ij}^{(1)}(z) + \frac{\alpha_s^2(\mu)}{(4\pi)^2}\,\Delta\mathcal{I}_{ij}^{(2)}(z) + \mathcal{O}(\alpha_s^3)\,, \tag{3.18}$$

$$\Delta\mathcal{I}_{ij}^{(1)}(z) = \Delta I_{ij}^{(1)}\Big(\frac{\omega e^{-\eta_{\rm cut}}}{p_T^{\rm cut}}, z\Big)\,,$$

$$\Delta\mathcal{I}_{ij}^{(2)}(z) = \ln\frac{\mu}{p_T^{\rm cut}}\Big[2\Gamma_0^i\ln\frac{\nu}{\omega} + 2\beta_0 + \gamma_{B\,0}^i\Big]\,\Delta I_{ij}^{(1)}\Big(\frac{\omega e^{-\eta_{\rm cut}}}{p_T^{\rm cut}}, z\Big)$$

$$-\,2\ln\frac{\mu}{p_T^{\rm cut}}\sum_k\int\frac{\mathrm{d}z'}{z'}\,\Delta I_{ik}^{(1)}\Big(\frac{\omega e^{-\eta_{\rm cut}}}{p_T^{\rm cut}}, \frac{z}{z'}\Big)P_{kj}^{(0)}(z') + \Delta I_{ij}^{(2)}\Big(\frac{\omega e^{-\eta_{\rm cut}}}{p_T^{\rm cut}}, R, z\Big)\,,$$

where $\Delta I_{ij}^{(n)}$ is the boundary condition of the RGE at $\mu = p_T^{\rm cut}$, $\nu = \omega$, and the required anomalous dimension coefficients are collected in appendix C. By dimensional analysis and boost invariance, $\Delta I_{ij}^{(n)}$ can only depend on $\zeta_{\rm cut} = \omega e^{-\eta_{\rm cut}}/p_T^{\rm cut}$ in addition to R and z.

In section 3.4.1 we determine the one-loop contribution $\Delta I_{ij}^{(1)}$, which has the simple form

$$\Delta I_{ij}^{(1)}\big(\zeta_{\rm cut}, z\big) = \theta\Big(\frac{\zeta_{\rm cut}}{1 + \zeta_{\rm cut}} - z\Big)\,2P_{ij}^{(0)}(z)\,\ln\frac{\zeta_{\rm cut}(1 - z)}{z}\,, \tag{3.19}$$

with the one-loop splitting functions $P_{ij}^{(0)}(z)$ as given in eq. (C.6). The correction vanishes at the kinematic threshold encoded in the overall θ-function, which also cuts off the singular distributions in $P_{ij}^{(0)}(z)$ at $z = 1$.[2]

While the computation of the full two-loop contribution $\Delta I_{ij}^{(2)}$ is beyond the scope of this thesis, we analytically compute its leading contribution in the small-R limit, which contains a clustering logarithm of R. We write the full two-loop result as

$$\Delta I_{ij}^{(2)}(\zeta_{\rm cut}, R, z) = \ln R\,\Delta I_{ij}^{(2,\ln R)}(\zeta_{\rm cut}, z) + \Delta I_{ij}^{(2,c)}(\zeta_{\rm cut}, z) + \mathcal{O}(R^2)\,. \tag{3.20}$$

In the limit $R \ll 1$, we can exploit that for the emission of two close-by collinear partons with relative rapidity $\Delta\eta \sim R$, the collinear matrix element factorizes into two sequential collinear splittings at the scale $\mu \sim p_T^{\rm cut}$ and $\mu \sim p_T^{\rm cut}R$, respectively. In section 3.4.4, we formalize this procedure using effective field theory methods to separate the two scales. The result is a formula that predicts the leading logarithms $\alpha_s^{n+1}\ln^n R$ in the beam function matching coefficient to all orders in perturbation theory, including the exact dependence on the jet rapidity cut, as a convolution of the $\mathcal{O}(\alpha_s)$ amplitude for a primary collinear emission and the so-called leading jet function $J_{m\,\rm lead}(z_J)$ [329]. The latter describes the probability to observe the hardest subjet in a sample of subjets initiated by a primary

---

[2]Additional details on the Mellin convolutions of $\Delta I_{ik}^{(1)} \otimes_z P_{kj}^{(0)}$ appearing in the coefficient of $\ln(\mu/p_T^{\rm cut})$ in $\Delta\mathcal{I}_{ij}^{(2)}(z)$ are given in appendix A.6 of ref. [2].

parton m at some given momentum fraction z_J. For $\Delta I_{ij}^{(2)}$, we find at $n = 1$

$$\Delta I_{ij}^{(2,\ln R)}(\zeta_{\text{cut}}, z) = \theta\Big(\frac{\zeta_{\text{cut}}}{1+\zeta_{\text{cut}}} - z\Big) 2 P_{ij}^{(0)}(z)\Big[\theta\Big(z - \frac{\zeta_{\text{cut}}}{2+\zeta_{\text{cut}}}\Big) c_{ij}^{R,\text{cut}}\Big(\frac{z}{\zeta_{\text{cut}}(1-z)}\Big) - c_{ij}^{R}\Big],$$

$$(3.21)$$

where the coefficient functions $c_{ij}^{R,\text{cut}}$ are given by

$$c_{gg}^{R,\text{cut}}(x) = c_{qq}^{R,\text{cut}}(x) = -2\int_{1/2}^{x}\frac{\mathrm{d}z'}{z'}\int_{1/2}^{z'}\mathrm{d}z_J\Big[P_{gg}^{(0)}(z_J) + 2n_f P_{qg}^{(0)}(z_J)\Big],$$

$$c_{gq}^{R,\text{cut}}(x) = c_{qg}^{R,\text{cut}}(x) = -2\int_{1/2}^{x}\frac{\mathrm{d}z'}{z'}\int_{1/2}^{z'}\mathrm{d}z_J\Big[P_{qq}^{(0)}(z_J) + P_{gq}^{(0)}(z_J)\Big],$$

$$(3.22)$$

depending on whether the primary emission we split is a gluon (first line) or a quark (second line). Their explicit expressions read

$$c_{gg}^{R,\text{cut}}(x) = c_{qq}^{R,\text{cut}}(x) = 2C_A\Big[\frac{5}{8} + \frac{\pi^2}{3} - 3x + \frac{9}{2}x^2 - 2x^3 - 2\ln^2 x - 4\,\mathrm{Li}_2(x)\Big]$$
$$+ 2\beta_0\Big[-\frac{29}{24} - \ln 2 + 3x - \frac{3}{2}x^2 + \frac{2}{3}x^3 - \ln x\Big],$$

$$c_{gq}^{R,\text{cut}}(x) = c_{qg}^{R,\text{cut}}(x) = 2C_F\Big[-3 + \frac{\pi^2}{3} - 3\ln 2 + 6x - 3\ln x - 2\ln^2 x - 4\,\mathrm{Li}_2(x)\Big]. \quad (3.23)$$

The coefficients c_{ij}^{R} in eq. (3.21) are the (in principle known) coefficients of $\ln R$ in the η_{cut}-independent two-loop beam function [67, 317], which we also verified.[3] They satisfy

$$c_{ij}^{R} = \lim_{x\to 1} c_{ij}^{R,\text{cut}}(x), \quad (3.24)$$

and are given by

$$c_{gg}^{R} = c_{qq}^{R} = \frac{1}{4}\Big[\Big(1 - \frac{8\pi^2}{3}\Big)C_A + \Big(\frac{23}{3} - 8\ln 2\Big)\beta_0\Big],$$

$$c_{qg}^{R} = c_{gq}^{R} = 2C_F\Big(3 - \frac{\pi^2}{3} - 3\ln 2\Big). \quad (3.25)$$

Our general setup for computing the small-R clustering contributions, described in more detail in section 3.4.4, implies that the coefficient of the $\ln R$ terms of the two-loop rapidity anomalous dimension in eq. (C.16) must be equal to $c_{gg}^{R} = c_{qq}^{R}$, in agreement with the corresponding result given in refs. [62, 67]. In addition, it also applies to the leading $\ln^2 R$ and $\ln R$ terms in the beam functions for rapidity dependent jet vetoes in ref. [313], with which we agree as well.

The R-independent term $\Delta I_{ik}^{(2,c)}(\zeta_{\text{cut}}, z)$ and the $\mathcal{O}(R^2)$ terms in eq. (3.20) are currently unknown. Their contribution to the cross section can in principle be obtained numerically from the singular limit of the full-theory calculation at $\mathcal{O}(\alpha_s^2)$, as was done for the corresponding η_{cut}-independent pieces in ref. [67].
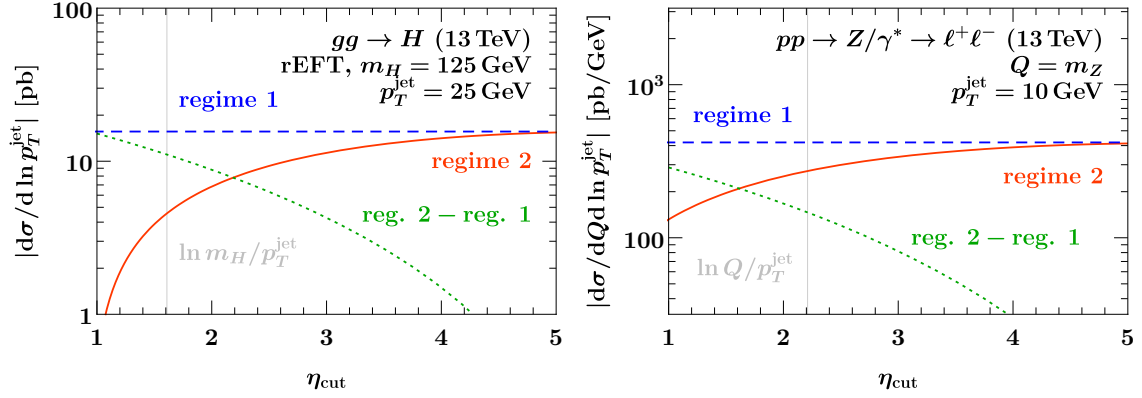
Figure 3.3: Comparison of the singular contributions to the fixed $\mathcal{O}(\alpha_s)$ (LO$_1$) p_T^{jet} spectrum for $gg \to H$ (left) and Drell-Yan (right). The orange solid lines show the singular contributions in regime 2 with η_{cut} dependent beam functions. The dashed blue lines show the singular contributions in regime 1 in the limit $\eta_{\mathrm{cut}} = \infty$, $p_T^{\mathrm{cut}} \gg Q e^{-\eta_{\mathrm{cut}}}$. Their difference, shown by the dotted green lines, correctly scales as a power in $Q e^{-\eta_{\mathrm{cut}}}/p_T^{\mathrm{jet}}$. The vertical lines indicate the point $p_T^{\mathrm{jet}} = Q e^{-\eta_{\mathrm{cut}}}$.
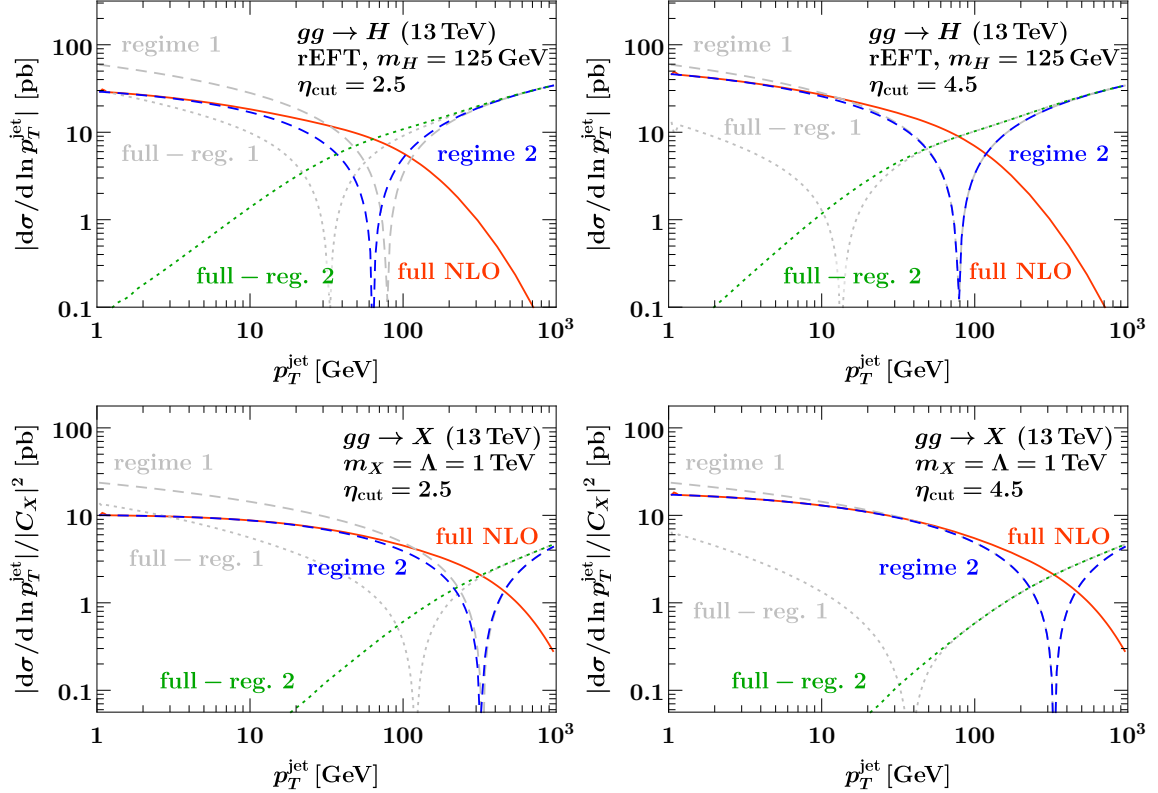
Figure 3.4: Comparison of singular and nonsingular contributions to the fixed $\mathcal{O}(\alpha_s)$ (LO$_1$) p_T^{jet} spectrum with rapidity cut $|\eta_{\mathrm{jet}}| < \eta_{\mathrm{cut}}$ for $gg \to H$ (top row) and $gg \to X$ (bottom row), $\eta_{\mathrm{cut}} = 2.5$ (left) and $\eta_{\mathrm{cut}} = 4.5$ (right). The orange solid lines show the full results, the dashed blue lines the regime 2 results with η_{cut} dependent beam functions, and the dotted green lines their difference. The dashed and dotted gray lines show the corresponding regime 1 results, which do not describe the singular behavior of the full cross section for finite η_{cut}.

89
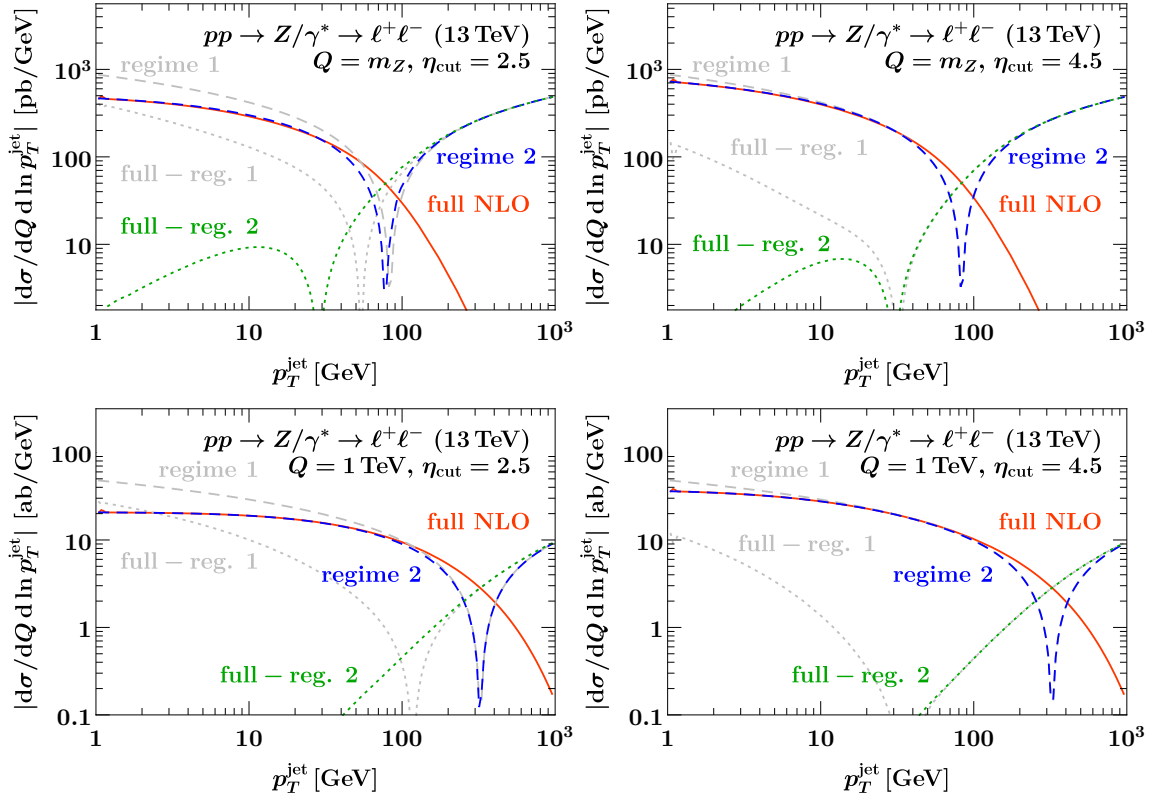
Figure 3.5: Comparison of singular and nonsingular contributions to the fixed $\mathcal{O}(\alpha_s)$ (LO$_1$) p_T^{jet} spectrum with rapidity cut $|\eta_{\text{jet}}| < \eta_{\text{cut}}$ for Drell-Yan at $Q = m_Z$ (top row) and $Q = 1\,\text{TeV}$ (bottom row), $\eta_{\text{cut}} = 2.5$ (left) and $\eta_{\text{cut}} = 4.5$ (right). The meaning of the curves are as in figure 3.4.

Numerical validation. To validate our results numerically and highlight the differences in the singular behavior for regimes 1 and 2, we consider the fixed $\mathcal{O}(\alpha_s)$ p_T^{jet} spectrum, $d\sigma/dp_T^{\text{jet}}$, where p_T^{jet} is the transverse momentum of the leading jet within $|\eta_{\text{jet}}| < \eta_{\text{cut}}$. Its relation to the jet veto cross section with a jet rapidity cut is simply

$$\sigma_0(p_T^{\text{cut}}, \eta_{\text{cut}}, R) = \int_0^{p_T^{\text{cut}}} dp_T^{\text{jet}} \, \frac{d\sigma(\eta_{\text{cut}}, R)}{dp_T^{\text{jet}}} \,. \tag{3.26}$$

At leading power in p_T^{jet}/Q, we obtain it by taking the derivative with respect to p_T^{cut} of either eq. (3.10), retaining the exact dependence on η_{cut} in the beam functions (regime 2), or of eq. (3.8), incurring power corrections in $Qe^{-\eta_{\text{cut}}}/p_T^{\text{jet}}$ (regime 1). The numerical results for all singular spectra are obtained with the help of `SCETlib` [8]. The $\mathcal{O}(\alpha_s)$ spectra in full QCD are obtained from `MCFM 8.0` [330–332].

As representative gluon-induced processes, we consider gluon-fusion Higgs production $gg \to H$ at $m_H = 125\,\text{GeV}$ in the infinite top-mass limit, rescaled with the exact LO

---

[3]The coefficient of the c_{gq}^R contribution in eq. (39) of ref. [67] has a typo, missing an overall factor of 2. We also find that the C_A term of the coefficient c_{qq}^R in eq. (9) of ref. [317] misses a factor of 1/2 compared to ref. [67] and our result.

top-mass dependence for $m_t = 172.5\,\text{GeV}$ (rEFT), see eq. (2.74). In addition, we consider gluon fusion to a hypothetical heavy color-singlet scalar X, $gg \to X$, mediated by a contact operator

$$\mathcal{L}_{\text{eff}} = -\frac{C_X}{\Lambda}\,\alpha_s\,G^a_{\mu\nu}G^{a,\mu\nu}X\,. \tag{3.27}$$

We always choose $m_X = 1\,\text{TeV}$, $\Lambda = 1\,\text{TeV}$, and divide the cross section by $|C_X|^2$. To the order we are working, this is equivalent to setting $C_X \equiv 1$, since C_X only starts to run at $\mathcal{O}(\alpha_s^2)$.[4] For quark-induced processes we consider Drell-Yan $pp \to Z/\gamma^* \to \ell^+\ell^-$ at the Z pole ($Q = m_Z$) and at $Q = 1\,\text{TeV}$, where $Q = m_{\ell\ell}$ is the invariant mass of the lepton pair. Here we set all scales to $\mu_{\text{FO}} = m_H$, m_X, or Q, respectively. We use `PDF4LHC_nnlo_100` [109, 110, 337–340] NNLO PDFs with $\alpha_s(m_Z) = 0.118$ and $n_f = 5$ active flavors throughout.

In figure 3.3, we compare the regime 2 and regime 1 leading-power (singular) results for $d\sigma/dp_T^{\text{jet}}$ at fixed p_T^{jet} as a function of η_{cut} for $gg \to H$ and Drell-Yan. The regime 1 result (dashed blue) does not depend on η_{cut}, while the regime 2 result (solid orange) decreases as η_{cut} becomes more central. The difference between the two (dotted green) has the expected behavior, vanishing as $Qe^{-\eta_{\text{cut}}}/p_T^{\text{jet}}$ for $\eta_{\text{cut}} \to \infty$. We observe that regime 1 is applicable beyond $\eta_{\text{cut}} \gtrsim 4$, where the difference to regime 2 is suppressed by an order of magnitude.

Another check is provided by comparing the regime 1 and regime 2 singular results to the full QCD result, which is shown in figures 3.4 and 3.5 for gluon-fusion and Drell-Yan. For $\eta_{\text{cut}} = 2.5$ (left panels), it is clear that regime 1 (dashed gray) fails to describe the singular limit of full QCD, with their difference (dotted gray) diverging for $p_T^{\text{jet}} \to 0$ like an inverse power of p_T^{jet} as expected. While the singular mismatch becomes less pronounced for $\eta_{\text{cut}} = 4.5$ (right panels), the uncanceled singular contributions are still clearly visible in the difference. On the other hand, regime 2 (dashed blue) correctly reproduces the singular limit $p_T^{\text{jet}} \to 0$, with the difference (dotted green) vanishing like a power of p_T^{jet} as it must. This provides a strong check of the intricate p_T^{cut} dependence encoded in our $\mathcal{O}(\alpha_s)$ results for $\Delta\mathcal{I}_{ij}$. (The power corrections in $e^{-\eta_{\text{cut}}}$, which are present in regime 2, drop out when taking the derivative of the fixed-order cumulant with respect to p_T^{cut}.)

Note that at $m_X = 1\,\text{TeV}$ or $Q = 1\,\text{TeV}$, the fixed-order spectrum is completely dominated by the rapidity-cut dependent singular result up to $p_T^{\text{jet}} \lesssim 100\,\text{GeV}$. Hence, the resummation should provide a significant improvement over the fixed-order result for typical $p_T^{\text{cut}} \sim 50\,\text{GeV}$, which we will indeed find in section 3.5.

3.2.4 Regime 3: $p_T^{\text{cut}}/Q \ll e^{-\eta_{\text{cut}}}$ (collinear NGLs)

The hierarchy $p_T^{\text{cut}} \ll Qe^{-\eta_{\text{cut}}}$ (with $e^{-\eta_{\text{cut}}} \ll 1$) exhibits different features than the regimes discussed before. The typical transverse momentum for emissions with $|\eta| > \eta_{\text{cut}}$ is parametrically $Qe^{-|\eta|}$, indicated by the horizontal gray line in figure 3.2, which is now much

---

[4]In `MCFM 8.0` we mock up this process using a standard-model Higgs with $m_H = 1\,\text{TeV}$ and manually account for the nonzero one-loop contribution from integrating out the top quark in the SM, which differs from our choice of $C_X = 1 + \mathcal{O}(\alpha_s^2)$ for the effective coupling of X to gluons. We also checked the results against the native $gg \to X$ support of `SusHi 1.6.1` [333–336].

larger than for the strongly constrained emissions at $|\eta| < \eta_{\rm cut}$. While the soft modes at central rapidities are not affected, there are now two types of collinear modes at forward rapidities with $|\eta| \sim \eta_{\rm cut}$,

$$n_a\text{-collinear:} \quad p^\mu \sim Q\Big(e^{-2\eta_{\rm cut}}, 1, e^{-\eta_{\rm cut}}\Big) ,$$

$$n_a\text{-soft-collinear:} \quad p^\mu \sim \Big(p_T^{\rm cut} e^{-\eta_{\rm cut}}, p_T^{\rm cut} e^{\eta_{\rm cut}}, p_T^{\rm cut}\Big) = p_T^{\rm cut} e^{\eta_{\rm cut}} \Big(e^{-2\eta_{\rm cut}}, 1, e^{-\eta_{\rm cut}}\Big) , \quad (3.28)$$

and analogously for the n_b-collinear sector. The collinear and soft-collinear modes have the same angular resolution and only differ in their energy.[5] This makes their all-order factorization challenging and leads to the appearance of nonglobal logarithms $\ln(Qe^{-\eta_{\rm cut}}/p_T^{\rm cut})$ starting at $\mathcal{O}(\alpha_s^2)$. Their factorization and resummation requires the marginalization over all possible configurations of energetic collinear emissions, involving soft-collinear matrix elements with a separate Wilson line along each individual energetic collinear emission, see e.g. refs. [341–344].

Since this regime has no immediate phenomenological relevance, we will not carry out this complete procedure but restrict ourselves to the configuration with soft-collinear Wilson lines along n and $\bar{n}$, i.e, along the two main collinear emitters. This is sufficient for the LL resummation, for isolating the nonglobal effects, and for discussing the relation to the other regimes. Our discussion here is in close analogy to the regime 3 in the factorization of the exclusive jet mass spectrum with small jet radius R in ref. [345], where the rapidity cut $e^{-\eta_{\rm cut}}$ here takes the role of R there.[6]

The factorized cross section takes the form

$$\frac{\mathrm{d}\sigma_0(p_T^{\rm cut}, \eta_{\rm cut}, R)}{\mathrm{d}Q^2\,\mathrm{d}Y} = \sum_{i,j} H_{ij}(Q^2, \mu)\,\mathcal{B}_i(p_T^{\rm cut}, \eta_{\rm cut}, R, \omega_a, \mu, \nu)\,\mathcal{B}_j(p_T^{\rm cut}, \eta_{\rm cut}, R, \omega_b, \mu, \nu)$$

$$\times\, S_i(p_T^{\rm cut}, R, \mu, \nu)\left[1 + \mathcal{O}\Big(\frac{p_T^{\rm cut}}{Qe^{-\eta_{\rm cut}}}, e^{-\eta_{\rm cut}}, R^2\Big)\right] . \quad (3.29)$$

The initial-state collinear functions $\mathcal{B}_i$ encode the contributions of both soft-collinear and energetic collinear modes. They are related to the $\eta_{\rm cut}$ dependent beam functions B_i in eq. (3.10) by an expansion in the limit $p_T^{\rm cut}/(\omega e^{-\eta_{\rm cut}}) \ll 1$,

$$B_i(p_T^{\rm cut}, \eta_{\rm cut}, R, \omega, \mu, \nu) = \mathcal{B}_i(p_T^{\rm cut}, \eta_{\rm cut}, R, \omega, \mu, \nu)\left[1 + \mathcal{O}\Big(\frac{p_T^{\rm cut}}{\omega e^{-\eta_{\rm cut}}}\Big)\right] . \quad (3.30)$$

Without further factorization, $\mathcal{B}_i$ contains large unresummed Sudakov double logarithms

---

[5] While we refer to the additional modes as soft-collinear in this chapter for this reason, the corresponding Wilson line configurations at the lowest nontrivial order are the same as for the generic collinear-soft modes of SCET$_+$ for color-singlet production described in section 2.2.8.

[6] The main difference is that here, emissions for $|\eta| < \eta_{\rm cut}$ are constrained by their p_T relative to the same collinear (beam) direction. In the jet mass case, emissions outside the jet are not constrained by their p_T relative to the same collinear (jet) direction (but also relative to the beam direction).

$\alpha_s^n \ln^{2n}(p_T^{\text{cut}}/\omega e^{-\eta_{\text{cut}}})$. To resum the leading double logarithms, we can decompose $\mathcal{B}_i$ as

$$\mathcal{B}_i(p_T^{\text{cut}}, \eta_{\text{cut}}, R, \omega, \mu, \nu) = B_i^{(\text{cut})}(\eta_{\text{cut}}, \omega, \mu) \, \mathcal{S}_i^{(\text{cut})}(p_T^{\text{cut}}, \eta_{\text{cut}}, R, \mu, \nu)$$

$$\times \left[1 + \mathcal{B}_i^{(\text{NG})}\Big(\frac{p_T^{\text{cut}}}{\omega e^{-\eta_{\text{cut}}}}, \omega, R \Big) \right]. \tag{3.31}$$

The function $B_i^{(\text{cut})}$ mainly describes contributions from the energetic collinear modes. It was dubbed "unmeasured" beam function in refs. [326, 327], in analogy to the unmeasured jet function [346]. At one loop its matching coefficients account for an energetic collinear emission with $|\eta| > \eta_{\text{cut}}$. They are calculated in section 3.4.1 and read

$$\mathcal{I}_{gg}^{(\text{cut})}(\eta_{\text{cut}}, \omega, z, \mu) = \delta(1-z) + \frac{\alpha_s(\mu)\, C_A}{4\pi} \left[\delta(1-z)\left(4\ln^2 \frac{\omega e^{-\eta_{\text{cut}}}}{\mu} - \frac{\pi^2}{6} \right) \right.$$

$$\left. + 4P_{gg}(z) \ln \frac{\omega e^{-\eta_{\text{cut}}}}{\mu\, z} + 8\mathcal{L}_1(1-z) + 8\left(\frac{1}{z} - 2 + z - z^2 \right)\ln(1-z) \right]$$

$$+ \mathcal{O}(\alpha_s^2)\,,$$

$$\mathcal{I}_{gq}^{(\text{cut})}(\eta_{\text{cut}}, \omega, z, \mu) = \frac{\alpha_s(\mu)\, C_F}{4\pi} \left[4P_{gq}(z) \ln \frac{\omega e^{-\eta_{\text{cut}}}(1-z)}{\mu\, z} + 2z \right] + \mathcal{O}(\alpha_s^2)\,,$$

$$\mathcal{I}_{qqV}^{(\text{cut})}(\eta_{\text{cut}}, \omega, z, \mu) = \delta(1-z) + \frac{\alpha_s(\mu)\, C_F}{4\pi} \left[\delta(1-z)\left(4\ln^2 \frac{\omega e^{-\eta_{\text{cut}}}}{\mu} - 6\ln \frac{\omega e^{-\eta_{\text{cut}}}}{\mu} - \frac{\pi^2}{6} \right) \right.$$

$$\left. + 4P_{qq}(z) \ln \frac{\omega e^{-\eta_{\text{cut}}}}{\mu\, z} + 8\mathcal{L}_1(1-z) - 4(1+z)\ln(1-z) + 2(1-z) \right]$$

$$+ \mathcal{O}(\alpha_s^2)\,,$$

$$\mathcal{I}_{qg}^{(\text{cut})}(\eta_{\text{cut}}, \omega, z, \mu) = \frac{\alpha_s(\mu)\, T_F}{4\pi} \left[4P_{qg}(z) \ln \frac{\omega e^{-\eta_{\text{cut}}}(1-z)}{\mu\, z} + 4z(1-z) \right] + \mathcal{O}(\alpha_s^2)\,, \tag{3.32}$$

where the $P_{ij}(z)$ are the color-stripped LO splitting functions given in eq. (C.7), and we have decomposed the flavor structure as in eq. (A.29). As argued in ref. [326] the results are directly related to the matching coefficients for fragmenting jet functions in ref. [347].

In eq. (3.31), the $\mathcal{S}_i^{(\text{cut})}$ mainly describes contributions from soft-collinear modes. At one loop it accounts for a soft-collinear emission that couples eikonally to the incoming collinear parton i. The emission is constrained to $p_T < p_T^{\text{cut}}$ for $|\eta| < \eta_{\text{cut}}$ by the jet veto, and is unconstrained for $|\eta| > \eta_{\text{cut}}$. Using the η regulator [190, 191] it is given by (see section 3.4.2)

$$\mathcal{S}_i^{(\text{cut})}(p_T^{\text{cut}}, \eta_{\text{cut}}, R, \mu, \nu) = 1 + \frac{\alpha_s(\mu)}{4\pi} \mathcal{S}_i^{(\text{cut},1)} + \frac{\alpha_s^2(\mu)}{(4\pi)^2} \mathcal{S}^{(\text{cut},2)} + \mathcal{O}(\alpha_s^3)\,,$$

$$\mathcal{S}_i^{(\text{cut},1)}(p_T^{\text{cut}}, \eta_{\text{cut}}, R, \mu, \nu) = C_i \left(4\ln^2 \frac{p_T^{\text{cut}}}{\mu} - 8\ln \frac{p_T^{\text{cut}}}{\mu} \ln \frac{\nu e^{-\eta_{\text{cut}}}}{\mu} + \frac{\pi^2}{6} \right), \tag{3.33}$$

where $C_i = C_F$ for an incoming quark or antiquark and C_A for an incoming gluon. We checked explicitly that the above results obey the consistency constraint in eq. (3.30). For this purpose, one has to note that eq. (3.19) becomes distribution valued in $(1-z)$ when taking the limit $\zeta_{\text{cut}} \gg 1$, see section 3.4.5.

At two loops $\mathcal{S}_i^{(\text{cut})}$ contains a $\ln R$ enhanced term. Focusing on the constant terms not predicted by the RG evolution, we have

$$\mathcal{S}_i^{(\text{cut},2)}(p_T^{\text{cut}}, \eta_{\text{cut}}, R, \mu = p_T^{\text{cut}}, \nu = \mu e^{\eta_{\text{cut}}}) = \ln R \, \mathcal{S}_i^{(\text{cut},2,\ln R)} + \mathcal{S}_i^{(\text{cut},2,c)} + \mathcal{O}(R^2) \,, \quad (3.34)$$

with $\mathcal{S}_i^{(\text{cut},2,c)}$ an unknown two-loop constant. The coefficient of $\ln R$ is obtained by taking the limit $\zeta_{\text{cut}} \to \infty$ of the $\ln R$ coefficient in the η_{cut} dependent beam function [see eqs. (3.21) and (E.14)], where it becomes proportional to $\delta(1 - z)$. This leads to a beautifully simple relation, derived in detail in section 3.4.5,

$$\mathcal{S}_i^{(\text{cut},2,\ln R)} = 8 C_i \int_{1/2}^{1} \frac{\mathrm{d}x}{x} c_{ii}^{R,\text{cut}}(x) \,. \qquad (3.35)$$

Inserting eq. (3.22), this is a three-fold iterated integral of one-loop QCD splitting functions over the range $[1/2, 1]$ that evaluates to

$$\mathcal{S}_i^{(\text{cut},2,\ln R)} = C_i \left\{ C_A \left[\frac{1622}{27} - \frac{548}{9} \ln 2 - \frac{88}{3} \ln^2 2 - 8\zeta_3 \right] \right.$$
$$\left. + n_f T_F \left[-\frac{652}{27} + \frac{232}{9} \ln 2 + \frac{32}{3} \ln^2 2 \right] \right\} \,. \qquad (3.36)$$

The anomalous dimensions of $B_i^{(\text{cut})}$ and $\mathcal{S}_i^{(\text{cut})}$ have the general structure

$$\gamma_{\mathcal{S}^{\text{cut}}}^i(\eta_{\text{cut}}, \mu, \nu) = 2\Gamma_{\text{cusp}}^i[\alpha_s(\mu)] \ln \frac{\nu e^{-\eta_{\text{cut}}}}{\mu} + \gamma_{\mathcal{S}^{\text{cut}}}^i[\alpha_s(\mu)] \,,$$

$$\gamma_{\nu,\mathcal{S}^{\text{cut}}}^i(p_T^{\text{cut}}, R, \mu) = 2\eta_\Gamma^i(p_T^{\text{cut}}, \mu) + \gamma_{\nu,\mathcal{S}^{\text{cut}}}^i[\alpha_s(p_T^{\text{cut}}), R] \,,$$

$$\gamma_{B^{\text{cut}}}^i(\omega e^{-\eta_{\text{cut}}}, \mu) = 2\Gamma_{\text{cusp}}^i[\alpha_s(\mu)] \ln \frac{\mu}{\omega e^{-\eta_{\text{cut}}}} + \gamma_{B^{\text{cut}}}^i[\alpha_s(\mu)] \,, \qquad (3.37)$$

where the coefficients of the cusp anomalous dimension follow from our explicit one-loop calculation. Consistency with eq. (3.11) implies

$$\gamma_{\mathcal{S}^{\text{cut}}}^i(\alpha_s) + \gamma_{B^{\text{cut}}}^i(\alpha_s) = \gamma_B^i(\alpha_s) \,,$$

$$\gamma_{\nu,\mathcal{S}^{\text{cut}}}^i(\alpha_s, R) = \gamma_{\nu,B}^i(\alpha_s, R) = -\frac{1}{2}\gamma_\nu^i(\alpha_s, R) \,. \qquad (3.38)$$

All of the above noncusp anomalous dimensions vanish at one loop. The canonical scales for $B_i^{(\text{cut})}$ and $\mathcal{S}_i^{(\text{cut})}$ are

$$\mu_B^{(\text{cut})} \sim Q e^{-\eta_{\text{cut}}} \,, \quad \mu_{\mathcal{S}}^{(\text{cut})} \sim p_T^{\text{cut}} \,, \quad \nu_{\mathcal{S}}^{(\text{cut})} \sim p_T^{\text{cut}} e^{\eta_{\text{cut}}} \,. \qquad (3.39)$$

With these choices and the anomalous dimensions in eq. (3.37) one may resum logarithms of $e^{\eta_{\text{cut}}}$, p_T^{cut}/Q to any logarithmic order, and at LL also logarithms of $p_T^{\text{cut}}/Q e^{-\eta_{\text{cut}}}$.

Starting at $\mathcal{O}(\alpha_s^2)$, the $\mathcal{B}_i^{(\text{NG})}$ term in eq. (3.31) contains nonglobal logarithms of the form $\alpha_s^n \ln^n(p_T^{\text{cut}}/Q e^{-\eta_{\text{cut}}})$. A boost by η_{cut} translates the measurement into two hemispheres with one loose ($\eta > \eta_{\text{cut}}$) and one tight constraint ($\eta < \eta_{\text{cut}}$) on emissions. The nonglobal structure in such a scenario is well understood [304]. Depending on the desired accuracy,
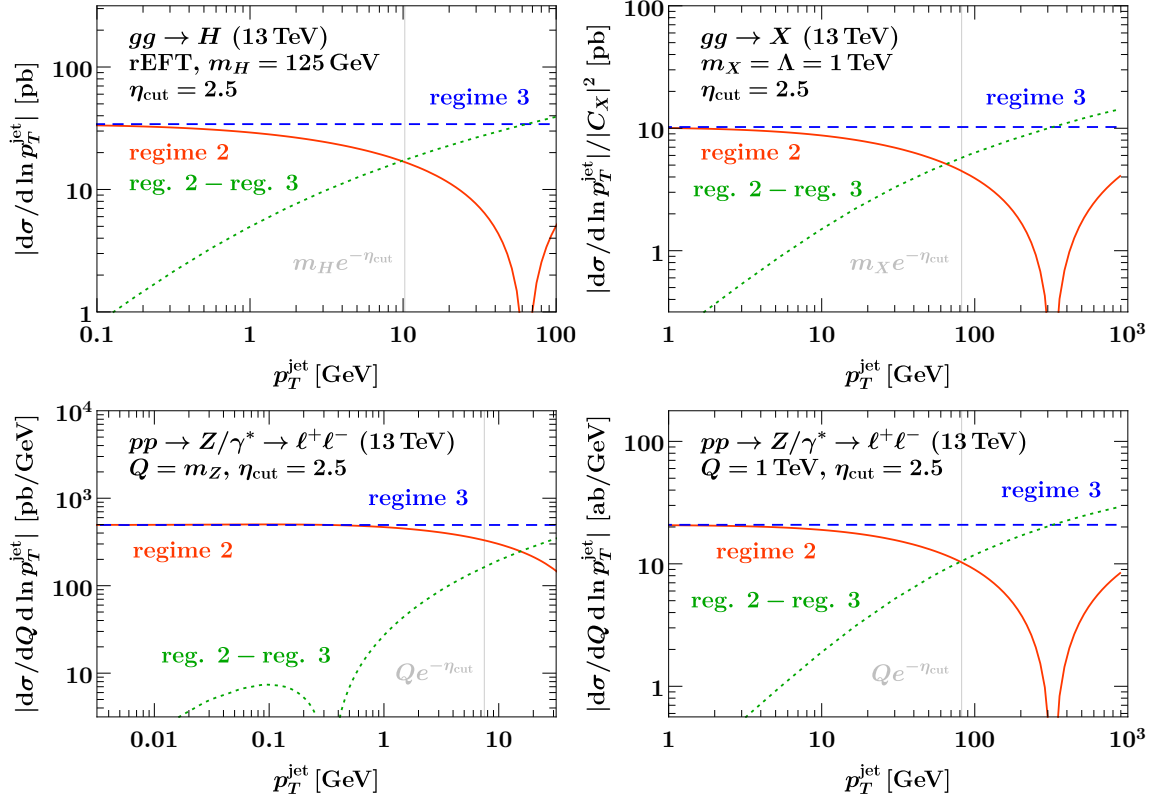
Figure 3.6: Comparison of the singular contributions to the fixed $\mathcal{O}(\alpha_s)$ p_T^{jet} spectrum for $gg \to H$ (top left), $gg \to X$ (top right), and Drell-Yan at $Q = m_Z$ (bottom left) and $Q = 1\,\mathrm{TeV}$ (bottom right). The solid orange lines show the full regime 2 singular spectrum, the blue dashed lines the further factorized regime 3 result. Their difference shown by the dotted green lines vanishes as a power in $p_T^{\mathrm{jet}}/Qe^{-\eta_{\mathrm{cut}}}$ for small p_T^{jet}. The vertical lines indicate where the relation $p_T^{\mathrm{jet}} = Qe^{-\eta_{\mathrm{cut}}}$ is satisfied.

the NGLs may be included at fixed order via $\mathcal{B}_i^{(\mathrm{NG})}$ as indicated in eq. (3.31), or (partially) summed using more steps in a dressed parton expansion [343].

Note that beyond one loop there is some freedom in the choice of measurement that defines the $B_i^{(\mathrm{cut})}$ and $\mathcal{S}_i^{(\mathrm{cut})}$. In particular, different measurements that reduce to eqs. (3.32) and (3.33) for a single emission could give rise to different results for the two-loop noncusp anomalous dimensions and finite terms because the difference can be absorbed into $\mathcal{B}_i^{(\mathrm{NG})}$. We stress that the result eq. (3.36) for the $\ln R$ coefficient in the two-loop soft-collinear function is, however, still unique. This is because a $\ln R$ contribution to $\mathcal{B}^{(\mathrm{NG})}$ requires a collinear parton in the unconstrained region to emit a soft-collinear gluon into the constrained region, which then undergoes a further collinear splitting. This is only possible starting at $\mathcal{O}(\alpha_s^3)$.

Numerical validation. To illustrate the numerical relevance of regime 3, we again consider the fixed $\mathcal{O}(\alpha_s)$ p_T^{jet} spectrum. In regime 2, it is given to leading power in p_T^{jet}/Q

by the derivative of eq. (3.10), while in regime 3, it is given to leading power in $p_T^{\mathrm{jet}}/(Qe^{-\eta_{\mathrm{cut}}})$ by the derivative of eq. (3.29).

In figure 3.6 we compare the two results for $\eta_{\mathrm{cut}} = 2.5$. In regime 3, the 0-jet cross section at $\mathcal{O}(\alpha_s)$ contains only single logarithms of p_T^{cut}, because the double logarithms cancel between the soft and soft-collinear functions. For this reason, the dashed-blue regime 3 spectrum with respect to $\ln p_T^{\mathrm{jet}}$ is just a constant. The exact regime 2 result (solid orange) becomes well approximated by the further factorized regime 3 expression for $p_T^{\mathrm{jet}} \to 0$, with their difference (dotted green) behaving like a power in p_T^{jet}. This provides a strong check of the regime 3 ingredients, more precisely, of the p_T^{cut} dependence encoded in the soft-collinear function. (Since the beam function in regime 3 is independent of p_T^{cut}, it drops out when computing the fixed-order spectrum.)

We also observe that for $gg \to H$ and Drell-Yan at $Q = m_Z$, the regime 3 limit is applicable only at very small $p_T^{\mathrm{jet}} \lesssim 1\,\mathrm{GeV}$ and already at $p_T^{\mathrm{jet}} \sim 10 - 20\,\mathrm{GeV}$ the power corrections with respect to regime 2 are of the same size as the full regime 2 result. This means that one would have to turn off the additional regime 3 resummation above this region. For $gg \to X$ with $m_X = 1\,\mathrm{TeV}$ and Drell-Yan at $Q = 1\,\mathrm{TeV}$, the canonical regime 3 resummation region, i.e., the region where the regime 3 singular corrections clearly dominate, extends up to $p_T^{\mathrm{jet}} \lesssim 10\,\mathrm{GeV}$, while regime 2 power corrections become $\mathcal{O}(1)$ around $p_T^{\mathrm{jet}} \sim 60\,\mathrm{GeV}$.

Hence, we find that the additional resummation of logarithms of $p_T^{\mathrm{jet}}/(Qe^{-\eta_{\mathrm{cut}}})$ in regime 3 is not relevant for jet veto analyses at the LHC, where the lowest jet cuts are $p_T^{\mathrm{cut}} \sim 25\,\mathrm{GeV}$, for $\eta_{\mathrm{cut}} = 2.5$ and final states in the $Q \sim 100\,\mathrm{GeV}$ range. This also holds for final states at very high invariant mass, e.g. in new physics searches, since in this case one would typically also apply higher jet thresholds to retain enough signal in the 0-jet bin. Realistically, one would not go below $p_T^{\mathrm{cut}} \sim 0.1Q$, which means one never enters the limit where the regime 3 resummation is necessary. This of course does not exclude the possibility that measurements designed to probe simultaneously very high Q and very low p_T^{jet} could benefit from the regime 3 resummation. To explicitly explore this regime experimentally, the best option is to restrict the jet veto to the very central region with $\eta_{\mathrm{cut}} \sim 1 - 1.5$.

3.2.5 Comparison to the literature

Jet vetoes in a restricted rapidity range were already encountered in ref. [326] for the case of dijet production. Without spelling it out explicitly, ref. [326] used a factorization for the regime 3 hierarchy $p_T^{\mathrm{cut}} \ll Qe^{-\eta_{\mathrm{cut}}} \ll Q$, but did not distinguish between the soft and soft-collinear modes necessary in this regime. As a result, parametrically large rapidity logarithms $\ln e^{\eta_{\mathrm{cut}}}$ were not captured, which are relevant starting at NLL. The numerical results in ref. [326] were obtained for $Q \sim 1\,\mathrm{TeV}$, $\eta_{\mathrm{cut}} = 5$, and $p_T^{\mathrm{cut}} = 20\,\mathrm{GeV}$, which rather corresponds to the opposite regime 1, $p_T^{\mathrm{cut}} \gg Qe^{-\eta_{\mathrm{cut}}}$. The difference between regimes 1 and 3 already matters at LL.

In ref. [327], the soft and soft-collinear modes in regime 3 are distinguished and the presence of nonglobal logarithms in this regime is recognized. Their factorization for dijet

production is carried out at a level analogous to ours in the previous subsection. That is, at NLL and beyond it only captures logarithms of "global" origin, but does not capture nonglobal logarithms that are parametrically of the same size. Our results for the one-loop quark matching coefficients in eq. (3.32) and the one-loop soft-collinear function in eq. (3.33) agree with ref. [327] [see their eqs. (3.27), (B.3), and (B.5)]. Our results for the gluon channels and the two-loop clustering corrections are new.

Ref. [327] does not consider regime 2 as a separate parametric regime. Instead, it attempts to extend the validity of the regime 3 factorization into regime 2. This is done by effectively adding the regime 2 nonsingular corrections appearing in eq. (3.30) to the unmeasured beam functions. Since some of the regime 3 modes become redundant in regime 2, this also requires them to account for a nontrivial soft-collinear zero bin. At fixed order, the sum of all their contributions must reproduce our result for the regime 2 beam function; in section 3.4.3 we check that this is indeed the case for the quark matrix elements given in ref. [327]. As we have seen in figure 3.6, outside the canonical regime 3, there are large cancellations between the terms that are singular in the regime 3 limit and the remaining regime 2 nonsingular contributions. This means that the distinction between these contributions becomes arbitrary in regime 2 and that they must not be treated differently, as otherwise one risks inducing large miscancellations. (This is completely analogous to the situation when matching to full QCD, in which case the p_T^{cut} resummation must be turned off when entering the fixed-order region at large p_T^{cut} to properly recover the full-QCD result.) In particular, in regime 2 all contributions that belong to the full η_{cut}-dependent regime 2 beam function must be evaluated at a common scale $\mu \simeq p_T^{\text{cut}}$ and evolved together according to eq. (3.11). This is not the case in ref. [327], where individual contributions to the regime 2 beam function are evaluated at different scales throughout (μ_B^{cut} and μ_S^{cut} in our notation).

Recently, the setup of ref. [327] was applied in ref. [328] to the case of transverse energy E_T in a restricted rapidity range in Drell-Yan. In ref. [328], profile scales are used to combine regimes 3 and 1, requiring that asymptotically $\mu_B^{(\text{cut})} = \mu_S^{(\text{cut})}$ in the regime 1 limit $E_T \gg Qe^{-\eta_{\text{cut}}}$. While this can alleviate the issue raised above, formally this relation must be satisfied already in regime 2 for $E_T \sim Qe^{-\eta_{\text{cut}}}$.

As we have seen in section 3.2.3, there is no need to distinguish collinear and soft-collinear modes in regime 2. Since for jet veto analyses regimes 1 and 2 are the phenomenologically relevant ones, doing so unnecessarily complicates the description. Recovering the NNLL′ structure in regime 2 [see eq. (3.18)] based on regime 3 would be quite challenging due to the intricate nonglobal structure in regime 3. Our dedicated treatment of regime 2 makes the absence of nonglobal logarithms manifest, avoiding the associated complications, and automatically ensures the correct treatment of the regime 2 nonsingular terms. Furthermore, it shows how regime 2 generalizes the well-understood regime 1, and as we will see in the next section allows for the generalization to a step in the jet veto.

Concerning regime 1, ref. [328] also gave an argument that regime 1 holds up to power corrections in $Qe^{-\eta_{\text{cut}}}/E_T$, which was more intricate due to directly comparing regime 1 to regime 3. The power suppression of η_{cut} effects at sufficiently large η_{cut} was also pointed

out briefly in a somewhat different context in ref. [348].

3.3 Generalization to a step in the jet veto at η_{cut}

3.3.1 Overview of parametric regimes

We now generalize our results to the experimentally relevant scenario of the step-like jet veto illustrated in the right panel of figure 3.1. Here, jets with $p_T^{\mathrm{jet}} > p_T^{\mathrm{cut}}$ are vetoed if $|\eta_{\mathrm{jet}}| < \eta_{\mathrm{cut}}$, while for $|\eta_{\mathrm{jet}}| > \eta_{\mathrm{cut}}$ the veto is loosened to $p_T^{\mathrm{jet}} > \tilde{p}_T^{\mathrm{cut}} > p_T^{\mathrm{cut}}$. The 0-jet cross section is thus defined by the following measurement:

$$\max_{k\in\mathrm{jets}:\,|\eta_k|<\eta_{\mathrm{cut}}} |\vec{p}_{T,k}| < p_T^{\mathrm{cut}} \qquad \text{and} \qquad \max_{k\in\mathrm{jets}:\,|\eta_k|>\eta_{\mathrm{cut}}} |\vec{p}_{T,k}| < \tilde{p}_T^{\mathrm{cut}} \,. \tag{3.40}$$

There are now three relevant power-counting parameters p_T^{cut}/Q, $\tilde{p}_T^{\mathrm{cut}}/Q$, and $e^{-\eta_{\mathrm{cut}}}$ with four distinct parametric regimes (assuming $p_T^{\mathrm{cut}} \leq \tilde{p}_T^{\mathrm{cut}}$), illustrated in figure 3.7:

- $p_T^{\mathrm{cut}}/Q \sim \tilde{p}_T^{\mathrm{cut}}/Q \sim e^{-\eta_{\mathrm{cut}}}$ (collinear step, top left),

- $p_T^{\mathrm{cut}}/Q \ll \tilde{p}_T^{\mathrm{cut}}/Q \sim e^{-\eta_{\mathrm{cut}}}$ (collinear NGLs, top right),

- $p_T^{\mathrm{cut}}/Q \sim \tilde{p}_T^{\mathrm{cut}}/Q \ll e^{-\eta_{\mathrm{cut}}}$ (soft-collinear step, bottom left),

- $p_T^{\mathrm{cut}}/Q \ll \tilde{p}_T^{\mathrm{cut}}/Q \ll e^{-\eta_{\mathrm{cut}}}$ (soft-collinear NGLs, bottom right).

We discuss each of them in turn in the following subsections. For $p_T^{\mathrm{cut}}/Q \sim e^{-\eta_{\mathrm{cut}}}$ (top left) the only relevant case is $\tilde{p}_T^{\mathrm{cut}} \sim p_T^{\mathrm{cut}}$, leading to a modified measurement on the collinear modes, a collinear step, compared to the case without a step ($\tilde{p}_T^{\mathrm{cut}} = p_T^{\mathrm{cut}}$).

For $p_T^{\mathrm{cut}}/Q \ll e^{-\eta_{\mathrm{cut}}}$, we have to distinguish three cases depending on $\tilde{p}_T^{\mathrm{cut}}$. Keeping $\tilde{p}_T^{\mathrm{cut}} \sim e^{-\eta_{\mathrm{cut}}}$ implies the hierarchy $p_T^{\mathrm{cut}}/Q \ll \tilde{p}_T^{\mathrm{cut}}/Q \sim e^{-\eta_{\mathrm{cut}}}$ (top right). Here, the mode setup is the same as for regime 3 without step (corresponding to $\tilde{p}_T^{\mathrm{cut}} = \infty$). As in that case, the large difference in the constraints on collinear radiation above and below η_{cut} gives rise to collinear NGLs.

For $\tilde{p}_T^{\mathrm{cut}}/Q \ll e^{-\eta_{\mathrm{cut}}}$, we can then have either $p_T^{\mathrm{cut}}/Q \sim \tilde{p}_T^{\mathrm{cut}}/Q \ll e^{-\eta_{\mathrm{cut}}}$ (bottom left) or $p_T^{\mathrm{cut}}/Q \ll \tilde{p}_T^{\mathrm{cut}}/Q \ll e^{-\eta_{\mathrm{cut}}}$ (bottom right). For the former, the standard jet veto factorization is recovered except that there are additional soft-collinear modes that resolve the shallow step at η_{cut}. For the latter, the steep step $p_T^{\mathrm{cut}} \ll \tilde{p}_T^{\mathrm{cut}}$ at η_{cut} gives rise to two distinct sets of soft-collinear modes with parametrically large soft-collinear NGLs between them.

3.3.2 $p_T^{\mathrm{cut}}/Q \sim \tilde{p}_T^{\mathrm{cut}}/Q \sim e^{-\eta_{\mathrm{cut}}}$ (collinear step)

We first note that the hierarchy $p_T^{\mathrm{cut}}/Q \sim e^{-\eta_{\mathrm{cut}}} \ll \tilde{p}_T^{\mathrm{cut}}/Q$ is effectively equivalent to the case without any jet veto beyond η_{cut} (regime 2 in section 3.2.3). Since collinear emissions with $|\eta| > \eta_{\mathrm{cut}}$ cannot resolve the loose veto at $\tilde{p}_T^{\mathrm{cut}}$, its effect is suppressed by $1/\tilde{p}_T^{\mathrm{cut}}$ and vanishes for $\tilde{p}_T^{\mathrm{cut}} \to \infty$.
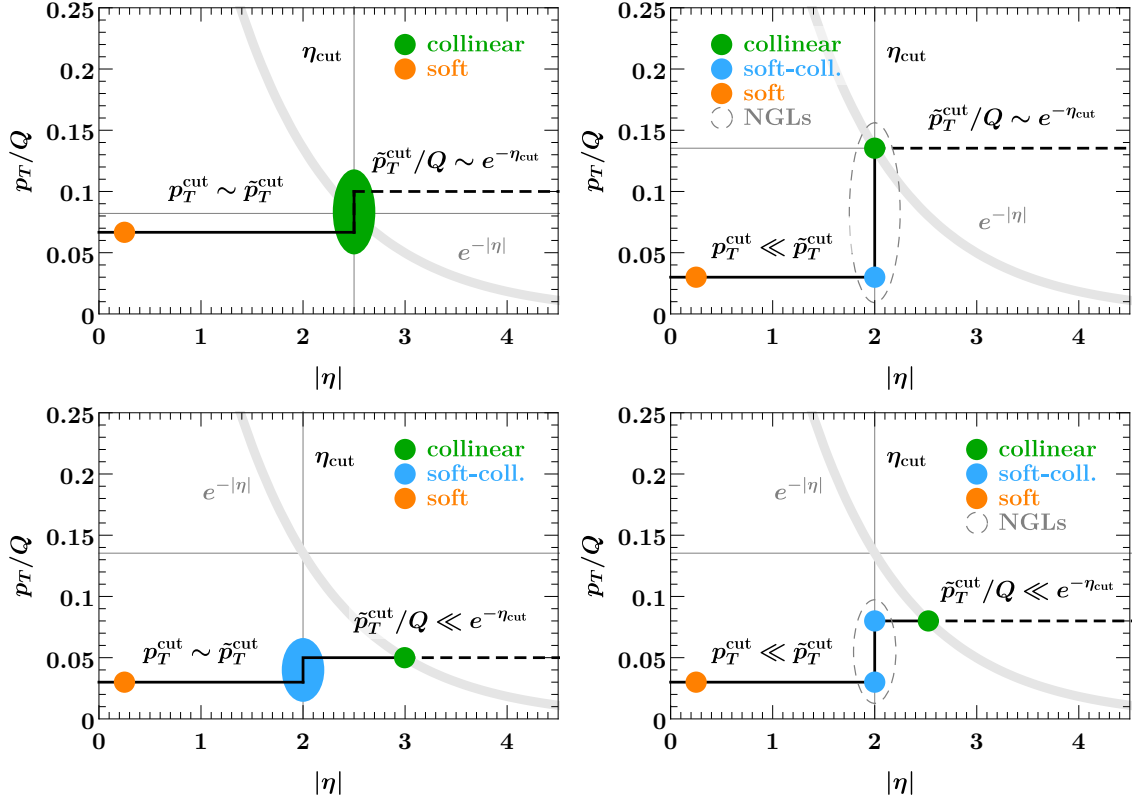
Figure 3.7: Illustration of the parametric regimes for a jet veto with a step. Emissions above the black lines are vetoed, and the thick gray line corresponds to $p_T/Q = e^{-|\eta|}$. The colored circles indicate the relevant modes in the effective theory. The regimes in the top row are characterized by $\tilde{p}_T^{\text{cut}} \sim e^{-\eta_{\text{cut}}}$, while those in the bottom row have $\tilde{p}_T^{\text{cut}} \ll e^{-\eta_{\text{cut}}}$. The regimes on the left have $p_T^{\text{cut}} \sim \tilde{p}_T^{\text{cut}}$, while those on the right have $p_T^{\text{cut}} \ll \tilde{p}_T^{\text{cut}}$ and involve parametrically large non-global logarithms.

The first nontrivial hierarchy is $p_T^{\text{cut}}/Q \sim \tilde{p}_T^{\text{cut}}/Q \sim e^{-\eta_{\text{cut}}}$, illustrated in the top left panel of figure 3.7. In this regime, the required modes are the same as in regime 2 in section 3.2.3. The collinear radiation resolves the step at η_{cut} while soft emissions are insensitive to it, leading to a generalization of eq. (3.10),

$$
\begin{aligned}
\frac{\mathrm{d}\sigma_0(p_T^{\text{cut}}, \tilde{p}_T^{\text{cut}}, \eta_{\text{cut}}, R)}{\mathrm{d}Q^2 \, \mathrm{d}Y} = \sum_{i,j} & H_{ij}(Q^2, \mu) \\
& \times B_i(p_T^{\text{cut}}, \tilde{p}_T^{\text{cut}}, \eta_{\text{cut}}, R, \omega_a, \mu, \nu) \, B_j(p_T^{\text{cut}}, \tilde{p}_T^{\text{cut}}, \eta_{\text{cut}}, R, \omega_b, \mu, \nu) \\
& \times S_i(p_T^{\text{cut}}, R, \mu, \nu) \left[1 + \mathcal{O}\left(\frac{p_T^{\text{cut}}}{Q}, \frac{\tilde{p}_T^{\text{cut}}}{Q}, e^{-\eta_{\text{cut}}}, R^2 \right) \right],
\end{aligned}
\tag{3.41}
$$

with the beam functions now additionally dependent on $\tilde{p}_T^{\text{cut}}$. In analogy to eq. (3.12) we write the modified beam function matching coefficients as

$$
\mathcal{I}_{ij}(p_T^{\text{cut}}, \tilde{p}_T^{\text{cut}}, \eta_{\text{cut}}, R, \omega, z, \mu, \nu) = \mathcal{I}_{ij}(p_T^{\text{cut}}, R, \omega, z, \mu, \nu) + \Delta\mathcal{I}_{ij}(p_T^{\text{cut}}, \tilde{p}_T^{\text{cut}}, \eta_{\text{cut}}, R, \omega, z, \mu, \nu).
\tag{3.42}
$$

The first term on the right-hand side is again the matching coefficient for a single veto at p_T^{cut} without any rapidity dependence. The second term is the correction due to the step in the jet veto at $|\eta| = \eta_{\mathrm{cut}}$, which vanishes for $p_T^{\mathrm{cut}} = \tilde{p}_T^{\mathrm{cut}}$. The correction is again renormalized according to eq. (3.17), which as before follows from RG consistency. In particular, its two-loop structure predicted by the RGE is the same as in eq. (3.18), where the finite terms now depend on two dimensionless ratios,

$$\zeta_{\mathrm{cut}} = \frac{\omega e^{-\eta_{\mathrm{cut}}}}{p_T^{\mathrm{cut}}}\,, \qquad \tilde{\zeta}_{\mathrm{cut}} = \frac{\omega e^{-\eta_{\mathrm{cut}}}}{\tilde{p}_T^{\mathrm{cut}}}\,. \tag{3.43}$$

The one-loop and $\ln R$ enhanced two-loop finite terms in $\Delta\mathcal{I}_{ij}$ can be written in terms of the results in eqs. (3.19) and (3.21) as

$$\Delta I_{ij}^{(1)}(\zeta_{\mathrm{cut}}, \tilde{\zeta}_{\mathrm{cut}}, z) = \Delta I_{ij}^{(1)}(\zeta_{\mathrm{cut}}, z) - \Delta I_{ij}^{(1)}(\tilde{\zeta}_{\mathrm{cut}}, z)\,,$$
$$\Delta I_{ij}^{(2)}(\zeta_{\mathrm{cut}}, \tilde{\zeta}_{\mathrm{cut}}, R, z) = \ln R \left[\Delta I_{ij}^{(2,\ln R)}(\zeta_{\mathrm{cut}}, z) - \Delta I_{ij}^{(2,\ln R)}(\tilde{\zeta}_{\mathrm{cut}}, z) \right]\,,$$
$$+ \Delta I_{ij}^{(2,c)}(\zeta_{\mathrm{cut}}, \tilde{\zeta}_{\mathrm{cut}}, z) + \mathcal{O}(R^2)\,, \tag{3.44}$$

since for a single (primary) n_a-collinear emission at (η, p_T) the measurement function for the step correction can be rewritten as

$$\theta(\eta - \eta_{\mathrm{cut}})\big[\theta(\tilde{p}_T^{\mathrm{cut}} - p_T) - \theta(p_T^{\mathrm{cut}} - p_T)\big]$$
$$= \theta(\eta - \eta_{\mathrm{cut}})\,\theta(p_T - p_T^{\mathrm{cut}}) - \theta(\eta - \eta_{\mathrm{cut}})\,\theta(p_T - \tilde{p}_T^{\mathrm{cut}})\,. \tag{3.45}$$

Due to the presence of correlated emissions with rapidities smaller and larger than η_{cut} at two loops, this decomposition no longer applies for the full two-loop finite term $\Delta I_{ij}^{(2,c)}$, which therefore needs to be determined separately.

This regime is free of large nonglobal logarithms and is of direct phenomenological interest. The parametric assumptions are satisfied e.g. for high-mass searches, $Q \gtrsim 300\,\mathrm{GeV}$, a realistic rapidity cut $\eta_{\mathrm{cut}} = 2.5$, and veto parameters $p_T^{\mathrm{cut}} = 25\,\mathrm{GeV}$, $\tilde{p}_T^{\mathrm{cut}} = 50\,\mathrm{GeV}$, which clearly warrant resummation of logarithms of $p_T^{\mathrm{cut}}/Q \sim \tilde{p}_T^{\mathrm{cut}}/Q \sim e^{-\eta_{\mathrm{cut}}}$. Evolving the beam function from $\mu_B \sim p_T^{\mathrm{cut}} \sim \tilde{p}_T^{\mathrm{cut}} \sim Q e^{-\eta_{\mathrm{cut}}}$ to $\mu_H \sim Q$ achieves this resummation for all of the above large ratios in the cross section, while the full (logarithmic and nonlogarithmic) dependence on all of the $\mathcal{O}(1)$ ratios $p_T^{\mathrm{cut}}/\tilde{p}_T^{\mathrm{cut}}$, $Q e^{-\eta_{\mathrm{cut}}}/p_T^{\mathrm{cut}}$, and $Q e^{-\eta_{\mathrm{cut}}}/\tilde{p}_T^{\mathrm{cut}}$ is included at fixed order via the beam function boundary condition.

Numerical validation. We now check that the factorized 0-jet cross section in eq. (3.41) reproduces the singular limit of full QCD. For this purpose, we construct an observable that simultaneously forces $p_T^{\mathrm{cut}} \to 0$ and $\tilde{p}_T^{\mathrm{cut}} \to 0$ as it approaches its singular limit. Following the rapidity-dependent jet vetoes in ref. [70], we define

$$\mathcal{T}_{\mathrm{step}} = \max_{k \in \mathrm{jets}} |\vec{p}_{T,k}| f_{\mathrm{step}}(\eta_k)\,, \qquad f_{\mathrm{step}}(\eta) = \begin{cases} \frac{1}{\rho}, & |\eta| > \eta_{\mathrm{cut}}\,, \\ 1, & |\eta| < \eta_{\mathrm{cut}}\,, \end{cases} \tag{3.46}$$

Figure 3.8: Comparison of singular and nonsingular contributions to the fixed $\mathcal{O}(\alpha_s)$ (LO_1) $\mathcal{T}_{\text{step}}$ spectrum with a step at $\eta_{\text{cut}} = 2.5$ and $\rho = \tilde{p}_T^{\text{cut}}/p_T^{\text{cut}} = 2$ for $gg \to H$ (left) and Drell-Yan at $Q = m_Z$ (right). The orange solid lines show the full results, the dashed blue lines the singular result that accounts for the jet veto step at η_{cut} in the beam function, and the dotted green lines their difference. The dashed and dotted gray lines show the corresponding results without taking into account the step in the jet veto, which do not describe the singular behavior of the full cross section.

i.e., we can express the step veto by ordering the jets with respect to their weighted transverse momenta, where for $|\eta| > \eta_{\text{cut}}$ the corresponding step weight function $f_{\text{step}}(\eta)$ is given by the ratio of veto parameters,

$$\rho \equiv \frac{\tilde{p}_T^{\text{cut}}}{p_T^{\text{cut}}} > 1 \,. \tag{3.47}$$

The differential spectrum in $\mathcal{T}_{\text{step}}$ is then related to the jet-vetoed cross section with a step by the relation

$$\sigma_0(p_T^{\text{cut}}, \rho\, p_T^{\text{cut}}, \eta_{\text{cut}}, R) = \int_0^{p_T^{\text{cut}}} \mathrm{d}\mathcal{T}_{\text{step}} \, \frac{\mathrm{d}\sigma(\rho, \eta_{\text{cut}}, R)}{\mathrm{d}\mathcal{T}_{\text{step}}} \,. \tag{3.48}$$

In figure 3.8 we compare $\mathrm{d}\sigma(\rho, \eta_{\text{cut}})/\mathrm{d}\mathcal{T}_{\text{step}}$ at fixed $\mathcal{O}(\alpha_s)$ in full QCD to the singular spectrum predicted by eq. (3.41) as well as the standard factorization eq. (3.8) without a step for $gg \to H$ (left panel) and Drell-Yan at the Z pole (right panel). The singular result using the full $\tilde{p}_T^{\text{cut}}$ and η_{cut} dependent beam functions (dashed blue) correctly reproduces the singular behavior of full QCD (solid orange) in the limit $\mathcal{T}_{\text{step}} \to 0$, with the difference to the full QCD spectrum (dotted green) vanishing like a power in $\mathcal{T}_{\text{step}}$ as it should. On the other hand, the standard factorization without step (dashed gray) does not reproduce the correct singular behavior of full QCD, with the difference (dotted gray) diverging for $\mathcal{T}_{\text{step}} \to 0$. Note that the mismatch here is reduced compared to the $\tilde{p}_T^{\text{cut}} = \infty$ case shown in figures 3.4 and 3.5, owing to the larger phase space available to unconstrained radiation at $|\eta| > \eta_{\text{cut}}$ for $\tilde{p}_T^{\text{cut}} = \infty$.

3.3.3 $p_T^{\text{cut}}/Q \ll \tilde{p}_T^{\text{cut}}/Q \sim e^{-\eta_{\text{cut}}}$ (collinear NGLs)

This regime is a direct extension of regime 3 without a step in section 3.2.4. For $e^{-\eta_{\text{cut}}} \ll \tilde{p}_T^{\text{cut}}/Q$, the effect of $\tilde{p}_T^{\text{cut}}$ is again suppressed by $1/\tilde{p}_T^{\text{cut}}$ and vanishes for $\tilde{p}_T^{\text{cut}} \to \infty$, yielding the same result as in section 3.2.4. The nontrivial new hierarchy is $p_T^{\text{cut}}/Q \ll \tilde{p}_T^{\text{cut}}/Q \sim e^{-\eta_{\text{cut}}}$, shown in the top right panel of figure 3.7. In this regime, the mode setup is as in section 3.2.4. However, the collinear modes are now additionally constrained for $|\eta| > \eta_{\text{cut}}$ by the jet veto at $\tilde{p}_T^{\text{cut}}$, making them sensitive to both $\tilde{p}_T^{\text{cut}}$ and the kinematic scale $Q e^{-\eta_{\text{cut}}}$. This leads to a modification of the overall initial-state collinear functions in eqs. (3.29) and (3.30) by

$$\mathcal{B}_i(p_T^{\text{cut}}, \tilde{p}_T^{\text{cut}}, \eta_{\text{cut}}, R, \omega, \mu, \nu) = B_i^{(\text{cut})}(\tilde{p}_T^{\text{cut}}, \eta_{\text{cut}}, R, \omega, \mu) \, \mathcal{S}_i^{(\text{cut})}(p_T^{\text{cut}}, \eta_{\text{cut}}, R, \mu, \nu)$$
$$\times \left[1 + \mathcal{B}_i^{(\text{NG})}\left(\frac{p_T^{\text{cut}}}{\omega e^{-\eta_{\text{cut}}}}, \frac{p_T^{\text{cut}}}{\tilde{p}_T^{\text{cut}}}, \omega, R \right) \right]. \tag{3.49}$$

Here $\mathcal{S}_i^{(\text{cut})}$ is the same soft-collinear function as in eq. (3.31). By RG consistency the functions $B_i^{(\text{cut})}$ have the same renormalization as those in eq. (3.31), i.e., the additional dependence on $\tilde{p}_T^{\text{cut}}$ does not change their renormalization. The associated matching coefficients at one loop are given by subtracting the correction term $\Delta I_{ij}^{(1)}$ in eq. (3.19), which accounts for an n-collinear emission with $\eta > \eta_{\text{cut}}$ and $p_T > \tilde{p}_T^{\text{cut}}$, from the coefficient $\mathcal{I}_{ij}^{(\text{cut})}$ in eq. (3.32), which accounts for an n-collinear emission with $\eta > \eta_{\text{cut}}$ without constraints from a jet veto, such that

$$\mathcal{I}_{ij}^{(\text{cut})}(\tilde{p}_T^{\text{cut}}, \eta_{\text{cut}}, R, \omega, z, \mu) = \mathcal{I}_{ij}^{(\text{cut})}(\eta_{\text{cut}}, \omega, z, \mu) - \frac{\alpha_s(\mu)}{4\pi} \Delta I_{ij}^{(1)}\left(\frac{\omega e^{-\eta_{\text{cut}}}}{\tilde{p}_T^{\text{cut}}}, z, R \right) + \mathcal{O}(\alpha_s^2). \tag{3.50}$$

The $\mathcal{B}_i^{(\text{NG})}$ term in eq. (3.49) contains nonglobal logarithms of $p_T^{\text{cut}}/\tilde{p}_T^{\text{cut}} \sim p_T^{\text{cut}}/Q e^{-\eta_{\text{cut}}}$.

3.3.4 $p_T^{\text{cut}}/Q \sim \tilde{p}_T^{\text{cut}}/Q \ll e^{-\eta_{\text{cut}}}$ (soft-collinear step)

In this regime (bottom left panel of figure 3.7), the mode setup in section 3.2.2 is extended by soft-collinear modes that resolve the step in the jet veto at η_{cut},

$$n_a\text{-soft-collinear:} \quad p^\mu \sim p_T^{\text{cut}}(e^{-\eta_{\text{cut}}}, e^{\eta_{\text{cut}}}, 1) \sim \tilde{p}_T^{\text{cut}}(e^{-\eta_{\text{cut}}}, e^{\eta_{\text{cut}}}, 1),$$
$$n_b\text{-soft-collinear:} \quad p^\mu \sim p_T^{\text{cut}}(e^{\eta_{\text{cut}}}, e^{-\eta_{\text{cut}}}, 1) \sim \tilde{p}_T^{\text{cut}}(e^{\eta_{\text{cut}}}, e^{-\eta_{\text{cut}}}, 1). \tag{3.51}$$

At the same time, the collinear modes only see the jet veto at $\tilde{p}_T^{\text{cut}}$, while the soft modes only see the veto at p_T^{cut}. This yields the factorized cross section

$$\frac{d\sigma_0(p_T^{\text{cut}}, \tilde{p}_T^{\text{cut}}, \eta_{\text{cut}}, R)}{dQ^2 \, dY} = \sum_{i,j} H_{ij}(\Phi, \mu) \, B_i(\tilde{p}_T^{\text{cut}}, R, \omega, \mu, \nu) \, B_j(\tilde{p}_T^{\text{cut}}, R, \omega, \mu, \nu) \, S_i(p_T^{\text{cut}}, \mu, \nu)$$
$$\times \mathcal{S}_i(p_T^{\text{cut}}, \tilde{p}_T^{\text{cut}}, \eta_{\text{cut}}, R, \mu, \nu) \, \mathcal{S}_j(p_T^{\text{cut}}, \tilde{p}_T^{\text{cut}}, \eta_{\text{cut}}, R, \mu, \nu)$$
$$\times \left[1 + \mathcal{O}\left(\frac{p_T^{\text{cut}}}{Q}, \frac{\tilde{p}_T^{\text{cut}}}{Q}, \frac{p_T^{\text{cut}}}{Q e^{-\eta_{\text{cut}}}}, \frac{\tilde{p}_T^{\text{cut}}}{Q e^{-\eta_{\text{cut}}}}, R^2 \right) \right]. \tag{3.52}$$

The soft-collinear function $\mathcal{S}_i$ encodes the actual step at $\eta_{\rm cut}$ and is defined by the measurement eq. (3.40). For $\tilde{p}_T^{\rm cut} = p_T^{\rm cut}$ there is no step in the jet veto and $\mathcal{S}_i$ has to vanish. The RG consistency of the cross section implies that its μ anomalous dimension vanishes in general, while its resummed ν anomalous dimension is given by

$$\gamma_{\nu,\mathcal{S}}^i(p_T^{\rm cut}, \tilde{p}_T^{\rm cut}, R) = 2\eta_\Gamma^i(p_T^{\rm cut}, \tilde{p}_T^{\rm cut}) + \frac{1}{2}\Big\{ \gamma_\nu^i[\alpha_s(\tilde{p}_T^{\rm cut}), R] - \gamma_\nu^i[\alpha_s(p_T^{\rm cut}), R] \Big\}. \qquad (3.53)$$

It does not depend on μ at all, as required by exact path independence in the (μ, ν) plane. Note that the beam functions in eq. (3.52) depend on $\tilde{p}_T^{\rm cut}$ (rather than $p_T^{\rm cut}$) because collinear radiation is too forward to be constrained by the tighter central veto. This is reflected in the somewhat curious rapidity anomalous dimension of $\mathcal{S}_i$ in eq. (3.53), which accounts for the mismatch between the logarithms of $p_T^{\rm cut}$ and $\tilde{p}_T^{\rm cut}$ generated by the soft and beam rapidity evolution, respectively.

Solving eq. (3.53) order by order in α_s we find the following very simple structure of the soft-collinear function through two loops:

$$\mathcal{S}_i(p_T^{\rm cut}, \tilde{p}_T^{\rm cut}, \eta_{\rm cut}, R, \mu, \nu) = 1 + \frac{\alpha_s(\mu)}{4\pi}\Big[2\Gamma_0^i \ln\rho\, L_{\mathcal{S}}^\nu + \mathcal{S}_{i,1}(\rho) \Big] \qquad (3.54)$$

$$+ \frac{\alpha_s^2(\mu)}{(4\pi)^2}\Big\{ 2(\Gamma_0^i)^2 \ln^2\rho\, (L_{\mathcal{S}}^\nu)^2 + 2\ln\rho\, L_{\mathcal{S}}^\nu \big[2L_{\mathcal{S}}^\mu \beta_0 \Gamma_0^i + \Gamma_0^i \mathcal{S}_{i,1}(\rho) + \Gamma_1^i \big]$$

$$+ 2\beta_0 L_{\mathcal{S}}^\mu \mathcal{S}_{i,1}(\rho) + \mathcal{S}_{i,2}(\rho, R) \Big\} + \mathcal{O}(\alpha_s^3),$$

where

$$\rho \equiv \frac{\tilde{p}_T^{\rm cut}}{p_T^{\rm cut}}, \qquad L_{\mathcal{S}}^\nu \equiv \ln\frac{\nu}{\sqrt{p_T^{\rm cut}\tilde{p}_T^{\rm cut}}e^{\eta_{\rm cut}}}, \qquad L_{\mathcal{S}}^\mu \equiv \ln\frac{\mu}{\sqrt{p_T^{\rm cut}\tilde{p}_T^{\rm cut}}}. \qquad (3.55)$$

It is straightforward to check that the one-loop finite term vanishes (see section 3.4.2),

$$\mathcal{S}_{i,1} = 0. \qquad (3.56)$$

The two-loop finite term is a generic function of the dimensionless ratio ρ and the jet radius parameter R, which must satisfy $\mathcal{S}_{i,2}(\rho = 1, R) = 0$. As usual, we can decompose it according to its R dependence as

$$\mathcal{S}_{i,2}(\rho, R) = -8C_i c_{ii}^R \ln\rho \ln R + \mathcal{S}_{i,2}^{(c)}(\rho) + \mathcal{O}(R^2), \qquad (3.57)$$

where c_{ii}^R is given by eq. (3.25) and $C_i = C_F\,(C_A)$ for $i = q\,(g)$. The coefficient of $\ln R$ at this order is completely determined by the R dependence of the noncusp rapidity anomalous dimensions in eq. (3.53). The full two-loop finite term $\mathcal{S}_{i,2}(\rho, R)$ could readily be obtained numerically using the methods of refs. [349, 350], which would enable the full NNLL′ resummation.

This regime is again free of nonglobal logarithms and hence can easily be applied to phenomenological studies. It can be used to supplement the EFT setup from section 3.3.2, which enables the resummation of logarithms of the ratio $p_T^{\rm cut}/Q \sim \tilde{p}_T^{\rm cut}/Q$, with an additional resummation of logarithms of the ratio $p_T^{\rm cut}/Qe^{-\eta_{\rm cut}} \sim \tilde{p}_T^{\rm cut}/Qe^{-\eta_{\rm cut}}$ by choosing the

canonical scales

$$\mu_B \sim \tilde{p}_T^{\mathrm{cut}}, \quad \mu_{\mathcal{S}} \sim \sqrt{p_T^{\mathrm{cut}}\tilde{p}_T^{\mathrm{cut}}}, \qquad \mu_S \sim p_T^{\mathrm{cut}},$$

$$\nu_B \sim Q, \qquad \nu_{\mathcal{S}} \sim \sqrt{p_T^{\mathrm{cut}}\tilde{p}_T^{\mathrm{cut}}}\, e^{\eta_{\mathrm{cut}}}, \quad \nu_S \sim p_T^{\mathrm{cut}}. \tag{3.58}$$

Here, the rapidity evolution between $\nu_{\mathcal{S}}$ and ν_S is responsible for resumming the large logarithms of $e^{-\eta_{\mathrm{cut}}} \sim \nu_S/\nu_{\mathcal{S}}$.

Numerical Validation. To validate our setup in this regime, we exploit that eq. (3.52) provides a refactorization of the collinear step in eq. (3.41), where

$$\mathcal{I}_{ij}(p_T^{\mathrm{cut}}, \tilde{p}_T^{\mathrm{cut}}, \eta_{\mathrm{cut}}, R, \omega, z, \mu, \nu) = \mathcal{S}_i(p_T^{\mathrm{cut}}, \tilde{p}_T^{\mathrm{cut}}, \eta_{\mathrm{cut}}, R, \mu, \nu)\, \mathcal{I}_{ij}(p_T^{\mathrm{cut}}, R, \omega, z, \mu, \nu)$$

$$\times \left[1 + \mathcal{O}\Big(\frac{p_T^{\mathrm{cut}}}{\omega e^{-\eta_{\mathrm{cut}}}}, \frac{\tilde{p}_T^{\mathrm{cut}}}{\omega e^{-\eta_{\mathrm{cut}}}}, R^2\Big)\right]. \tag{3.59}$$

In particular, eq. (3.52) must reproduce eq. (3.41) up to power corrections in $p_T^{\mathrm{cut}}/Q e^{-\eta_{\mathrm{cut}}}$ and $\tilde{p}_T^{\mathrm{cut}}/Q e^{-\eta_{\mathrm{cut}}}$. We can test this numerically using the $\mathcal{T}_{\mathrm{step}}$ observable defined in section 3.3.2, which simultaneously probes both classes of power corrections. In figure 3.9, we show the fixed $\mathcal{O}(\alpha_s)$ $\mathcal{T}_{\mathrm{step}}$ spectra for the collinear step (solid orange) and soft-collinear step (dashed blue). In all cases their difference (dotted green) vanishes like a power in $\mathcal{T}_{\mathrm{step}}$.

The additional resummation using the soft-collinear step may be applicable up to values of $p_T^{\mathrm{cut}} = 20\,\mathrm{GeV}$ ($p_T^{\mathrm{cut}} = 80\,\mathrm{GeV}$) for $Q \sim 100\,\mathrm{GeV}$ ($Q = 1\,\mathrm{TeV}$), for the choice of $\rho = 2, \eta_{\mathrm{cut}} = 2.5$ displayed in figure 3.9. This can be read off from the relative size of leading-power (soft-collinear step) and subleading power (difference) contributions, which leave some room where resummation in the leading-power cross section can improve the prediction. We find a slightly larger potential resummation region than for the analogous refactorization in the $\tilde{p}_T^{\mathrm{cut}} = \infty$ case, where an earlier onset of the power corrections was observed in figure 3.6.

3.3.5 $p_T^{\mathrm{cut}}/Q \ll \tilde{p}_T^{\mathrm{cut}}/Q \ll e^{-\eta_{\mathrm{cut}}}$ (soft-collinear NGLs)

For this hierarchy (bottom right panel of figure 3.7), two types of soft-collinear modes arise,

$$n_a\text{-soft-collinear } (p_T^{\mathrm{cut}}): \quad p^\mu \sim p_T^{\mathrm{cut}}(e^{-\eta_{\mathrm{cut}}}, e^{\eta_{\mathrm{cut}}}, 1),$$

$$n_a\text{-soft-collinear } (\tilde{p}_T^{\mathrm{cut}}): \quad p^\mu \sim \tilde{p}_T^{\mathrm{cut}}(e^{-\eta_{\mathrm{cut}}}, e^{\eta_{\mathrm{cut}}}, 1), \tag{3.60}$$

and analogously for the n_b-soft-collinear sectors, which are both parametrically distinct from the energetic collinear modes. Compared to the regime $p_T^{\mathrm{cut}} \sim \tilde{p}_T^{\mathrm{cut}} \ll Q e^{-\eta_{\mathrm{cut}}}$ there are now parametrically large logarithms $\ln(p_T^{\mathrm{cut}}/\tilde{p}_T^{\mathrm{cut}})$ in the soft-collinear function $\mathcal{S}_i$ in eq. (3.52). The cross section can be written as in eq. (3.52), where the soft-collinear function is refactorized as

$$\mathcal{S}_i(p_T^{\mathrm{cut}}, \tilde{p}_T^{\mathrm{cut}}, \eta_{\mathrm{cut}}, R, \mu, \nu) = \mathcal{S}_i^{(\mathrm{cut})}(p_T^{\mathrm{cut}}, \eta_{\mathrm{cut}}, R, \mu, \nu)\left[\mathcal{S}_i^{(\mathrm{cut})}(\tilde{p}_T^{\mathrm{cut}}, \eta_{\mathrm{cut}}, R, \mu, \nu)\right]^{-1}$$

$$\times \left[1 + \mathcal{S}_i^{(\mathrm{NG})}\Big(\frac{p_T^{\mathrm{cut}}}{\tilde{p}_T^{\mathrm{cut}}}, R\Big)\right] \times \left[1 + \mathcal{O}\Big(\frac{p_T^{\mathrm{cut}}}{\tilde{p}_T^{\mathrm{cut}}}\Big)\right], \tag{3.61}$$
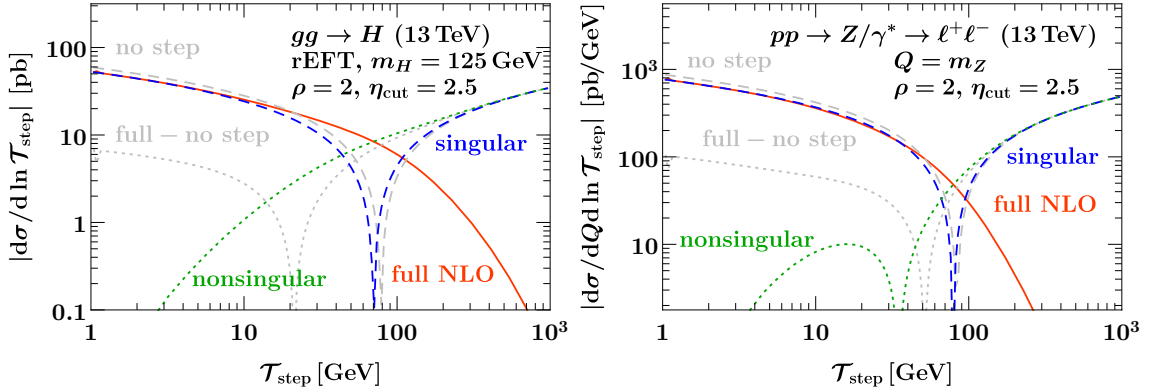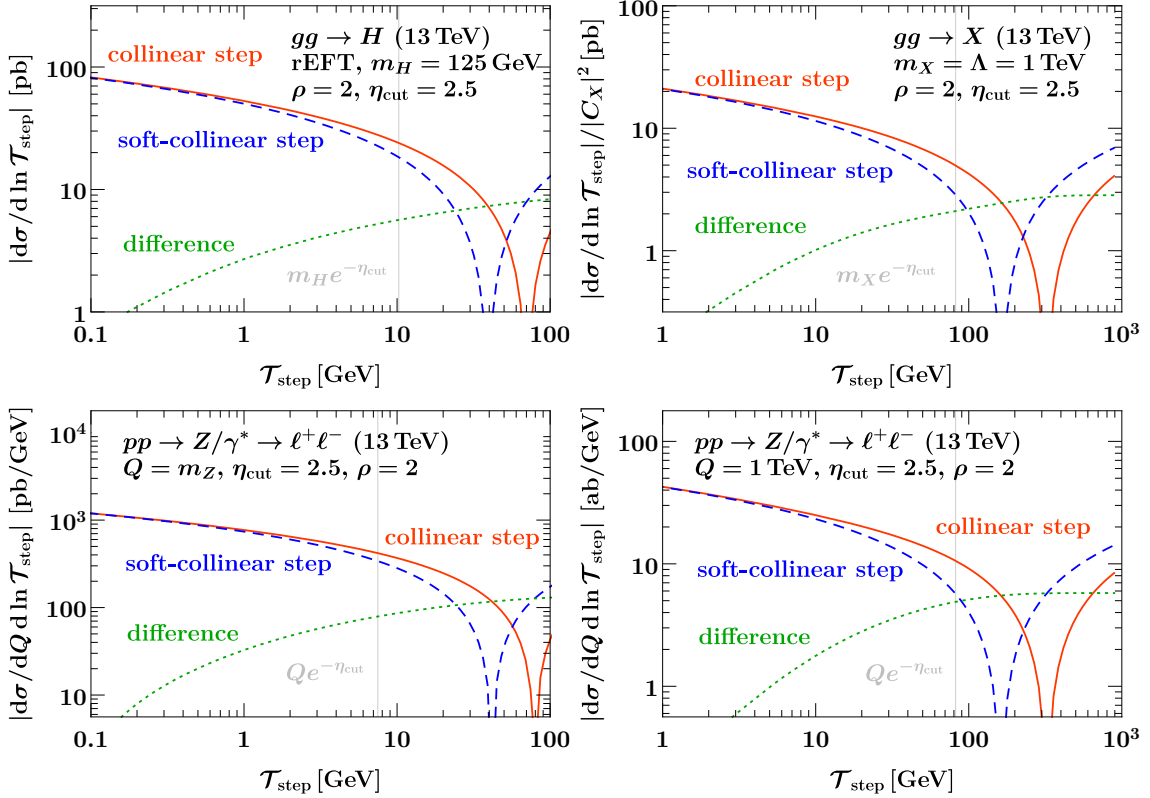
Figure 3.9: Comparison of the singular contributions to the fixed $\mathcal{O}(\alpha_s)$ (LO$_1$) $\mathcal{T}_{\text{step}}$ spectrum for $\eta_{\text{cut}} = 2.5$ and $\rho = 2$ for $gg \to H$ (top left), $gg \to X$ (top right), and Drell-Yan at $Q = m_Z$ (bottom left) and $Q = 1\,\text{TeV}$ (bottom right). The solid orange lines show the singular spectrum for the collinear-step regime and the blue dashed lines the further factorized result in the soft-collinear-step regime. Their difference, shown by the dotted green lines vanishes as a power of $\mathcal{T}_{\text{step}}$. The vertical lines indicate where the parametric relation $\mathcal{T}_{\text{step}}/Q = e^{-\eta_{\text{cut}}}$ is satisfied.

with $\mathcal{S}_i^{(\text{cut})}$ the same soft-collinear function as in eqs. (3.31) and (3.49). Both the power corrections and the nonglobal piece $\mathcal{S}_i^{(\text{NG})}$ are absent at one loop and at $\mathcal{O}(\alpha_s^2 \ln R)$. Equivalently this regime can be interpreted as a refactorization of eq. (3.49), where compared to the hierarchy for $p_T^{\text{cut}} \ll \tilde{p}_T^{\text{cut}} \sim Q e^{-\eta_{\text{cut}}}$ there are large (rapidity) logarithms $\ln(\tilde{p}_T^{\text{cut}} e^{\eta_{\text{cut}}}/Q)$ in the beam function $B_i^{(\text{cut})}$. Evolving the two soft-collinear functions to separate renormalization scales $\mu_{\mathcal{S},1} = p_T^{\text{cut}}$, $\nu_{\mathcal{S},1} = p_T^{\text{cut}} e^{\eta_{\text{cut}}}$ and $\mu_{\mathcal{S},2} = \tilde{p}_T^{\text{cut}}$, $\nu_{\mathcal{S},2} = \tilde{p}_T^{\text{cut}} e^{\eta_{\text{cut}}}$ resums Sudakov logarithms of $p_T^{\text{cut}}/\tilde{p}_T^{\text{cut}}$, but does not account for the nonglobal logarithms of the same ratio in $\mathcal{S}_i^{(\text{NG})}$.

3.4 Calculation of perturbative ingredients

In this section we provide details on the calculation of all new perturbative ingredients introduced above. In section 3.4.1 we document the computation of the one-loop beam function matching coefficients with a jet rapidity cut in eqs. (3.19) and (3.32), also setting

the scene for calculating beam functions in general. In section 3.4.2 we compute the soft-collinear functions in eqs. (3.33) and (3.54). In section 3.4.3 we compare to the one-loop results of ref. [327]. In section 3.4.4 we derive an all-order formula for the leading clustering logarithms in jet veto beam functions and use it to compute the very nontrivial clustering coefficients in the two-loop beam function with a jet rapidity cut in eq. (3.21). In section 3.4.5 we provide analytic details on how to check (or use) the consistency relation between regimes 2 and 3 in eq. (3.30).

3.4.1 Rapidity cut dependent beam functions at one loop

In this section we give the detailed computation of the one-loop beam function matching coefficients in eqs. (3.19) and (3.32). Some intermediate results are also needed as ingredients for the all-order calculation of clustering logarithms in section 3.4.4.

General strategy. Beam functions are in general defined by the measurements or cuts they impose on collinear initial-state radiation. They may also indirectly constrain the collinear final state by measuring properties of the annihilating collinear parton. For a general measurement $\hat{\mathcal{M}}_B$ acting on a collinear final state $|X\rangle$ as

$$\hat{\mathcal{M}}_B(m)|X\rangle = \mathcal{M}_B(m; X)|X\rangle \,, \tag{3.62}$$

the corresponding bare beam functions are defined as forward proton matrix elements of the beam function operators

$$B_i\Big(m, \frac{\omega}{P_n^-}\Big) = \big\langle p_n\big(P_n^- \tfrac{n^\mu}{2}\big)\big|\theta(\omega)\mathcal{O}_i(m,\omega)\big|p_n\big(P_n^- \tfrac{n^\mu}{2}\big)\big\rangle \,,$$

$$\mathcal{O}_q(m,\omega) = \bar{\chi}_{qn}\,\hat{\mathcal{M}}_B(m)\big[\delta(\omega - \overline{\mathcal{P}})\tfrac{\not{\bar{n}}}{2}\chi_{qn}\big] \,,$$

$$\mathcal{O}_g(m,\omega) = \omega\mathcal{B}_{n\perp}^\mu\,\hat{\mathcal{M}}_B(m)\big[\delta(\omega - \overline{\mathcal{P}})\,\mathcal{B}_{n\perp\mu}\big] \,. \tag{3.63}$$

The beam function and the operators on the left-hand side of eq. (3.63) also depend on the parameters m of $\mathcal{M}_B$, e.g. $m = \{p_T^{\text{cut}}, \eta_{\text{cut}}, R\}$. Here we assume that, as in the case of the jet veto at hand, $\mathcal{M}_B(m, X)$ only depends on the magnitude of transverse momenta, so all three operators are scalars under rotations in the transverse plane and the collinear gluon fields are contracted with each other.

If the lowest scale Λ_X probed by the measurement on collinear radiation is perturbative, $\Lambda_{\text{QCD}} \ll \Lambda_X$, the beam function operators can be expanded in an operator product expansion. The leading term for $\omega > 0$ is given by the leading-twist PDF operators $\mathcal{Q}_i$. In SCET the bare PDF operators have the same form as the $\mathcal{O}_i$ in eq. (3.63), but are fully inclusive over radiation up to the overall label momentum constraint,

$$f_i\Big(\frac{\omega}{P_n^-}\Big) = \big\langle p_n\big(P_n^- \tfrac{n^\mu}{2}\big)\big|\theta(\omega)\mathcal{Q}_i(\omega)\big|p_n\big(P_n^- \tfrac{n^\mu}{2}\big)\big\rangle \,,$$

$$\mathcal{Q}_q(\omega) = \bar{\chi}_{qn}\big[\delta(\omega - \overline{\mathcal{P}})\tfrac{\not{\bar{n}}}{2}\chi_{qn}\big] \,,$$

$$\mathcal{Q}_g(\omega) = \omega\mathcal{B}_{n\perp}^\mu\big[\delta(\omega - \overline{\mathcal{P}})\,\mathcal{B}_{n\perp\mu}\big] \,. \tag{3.64}$$

This definition is equivalent to the standard definition in terms of full-QCD quark and gluon fields connected by Wilson line segments along the light cone [293]. The bare perturbative beam function matching coefficients $\mathcal{I}_{ij}(m, z)$ are computed as the difference of partonic matrix elements of the bare $\mathcal{O}_i(m, \omega)$ and $\mathcal{Q}_j(\omega')$ [293],

$$
\langle j_n(p)|\theta(\omega)\mathcal{O}_i(m, \omega)|j_n(p)\rangle
$$
$$
= \sum_k \int \frac{\mathrm{d}\omega'}{\omega'} \, \mathcal{I}_{ik}\left(m, \frac{\omega}{\omega'}\right) \langle j_n(p)|\theta(\omega')\mathcal{Q}_k(\omega')|j_n(p)\rangle \, . \tag{3.65}
$$

We match the forward matrix element averaged over the spin and color indices of j_n without loss of generality because the operators are scalar color singlets. To simplify the calculation, we pick a state with $\vec{p}_\perp = 0$. As a consequence of the explicit scale separation, only the matching coefficients can depend on the details m of the measurement. Taking *proton* matrix elements of the renormalized operators then leads to beam function matching relations such as eqs. (2.210), (2.217), and (2.222). Eq. (3.65) can be leveraged as a check on the EFT construction by computing the PDF and beam function matrix elements with an explicit IR regulator, for example by retaining $p^2 = p^- p^+ \neq 0$, and verifying that the matching coefficient is indeed independent of the regulator [293].

In practical calculations, eq. (3.65) is greatly simplified by using dimensional regularization for both UV and IR divergences, i.e., setting $p^+ = 0$. In this case, radiative corrections to the PDF matrix elements are proportional to scaleless integrals, so to all orders,

$$
p^2 = 0 : \quad \langle j_n(p)|\theta(\omega)\mathcal{Q}_i(\omega)|j_n(p)\rangle = p^- \delta_{ij}\delta(\omega - p^-) \, . \tag{3.66}
$$

We will follow this approach in our calculation.[7] We evaluate the partonic beam function matrix elements by inserting a complete set of states, e.g. for the quark beam function,

$$
\langle j_n(p)|\theta(\omega)\mathcal{O}_q(m, \omega)|j_n(p)\rangle
$$
$$
= \theta(\omega) \sum_X \!\!\!\!\! \int \langle j_n(p)|\bar{\chi}_{q\,n}\,\hat{\mathcal{M}}_B(m)|X\rangle\langle X|\big[\delta(\omega - \overline{\mathcal{P}})\frac{\slashed{\bar{n}}}{2}\chi_{q\,n}\big]|j_n(p)\rangle
$$
$$
= \theta(\omega) \sum_X \!\!\!\!\! \int \delta(p_X^- - \omega - p^-)\langle j_n(p)|\bar{\chi}_{q\,n}\,\hat{\mathcal{M}}_B(m)|X\rangle\langle X|\frac{\slashed{\bar{n}}}{2}\chi_{q\,n}|j_n(p)\rangle \, , \tag{3.67}
$$

and evaluate the two matrix elements in time-ordered perturbation theory using standard Feynman rules. This amounts to taking the discontinuity of the full forward scattering

---

[7]In this case, it is *assumed* that the IR poles in the beam function matrix elements are captured by the scaleless PDF diagrams, so that all remaining poles in the matching coefficient have a UV origin and either contribute to the overall renormalization of the beam function operator at the scale of the measurement, or cancel the renormalization of the PDF operators.
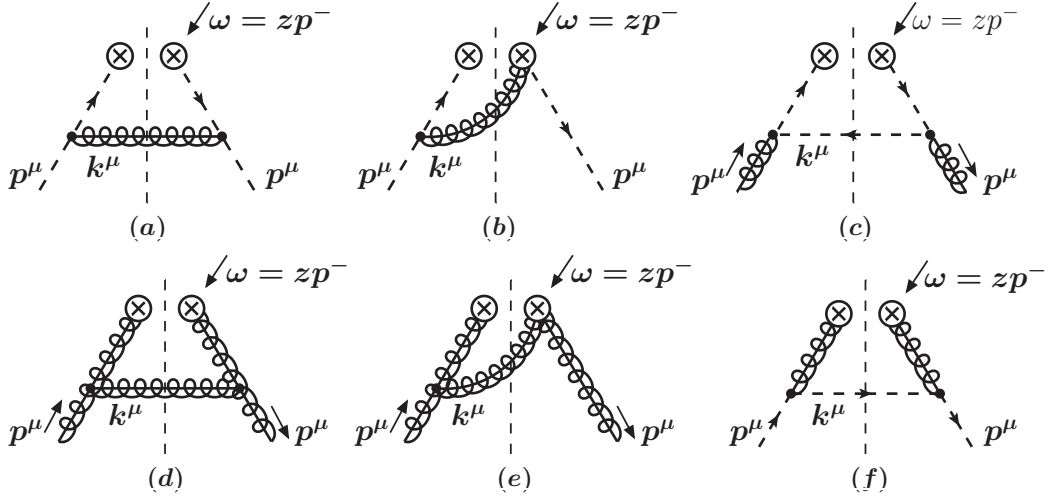
Figure 3.10: Nonvanishing diagrams for the computation of the one-loop beam function in pure dimensional regularization and Feynman gauge. Mirror diagrams of (b) and (e) are implicit. The measurement acts on particles crossing the on-shell cut indicated by the vertical dashed line.

diagram directly at the level of the integrand by cutting propagators,[8]

$$\frac{1}{k^2 + i0} \mapsto -2\pi i\, \delta_+(k^2)\,. \tag{3.68}$$

On the second equality in eq. (3.67) we used label momentum conservation to evaluate $\overline{\mathcal{P}}$ (that acts on the field) in terms of p_X^-. We further use the η regulator as described in section 2.2.7 to regulate rapidity divergences. This ensures that virtual diagrams with $|X\rangle = |0\rangle$ and zero-bin subtractions are also scaleless. We work in Feynman gauge.

One-loop amplitudes. The relevant real-radiation diagrams for a generic beam function at one loop are displayed in figure 3.10. They arise from the interference of collinear Lagrangian insertions, (a), (c), (d), and (f), or the contraction of a Lagrangian insertion with a Wilson line in the operator, (b) and (e). In Feynman gauge the Wilson line diagrams cannot interfere with themselves due to $n^2 = 0$. The cut real-emission diagrams take the generic form

$$\langle j_n | \theta(\omega) \mathcal{O}_i(m, \omega) | j_n \rangle^{(1)}$$
$$= \theta(z) \int \frac{\mathrm{d}^d k}{(2\pi)^{d-1}}\, \delta_+(k^2)\, \delta(p^- - k^- - \omega)\, g^2 \mathcal{A}_{ij}^{(1)}(p, k)\, \mathcal{M}_B(m; k^\mu)\,, \tag{3.69}$$

where $\mathcal{M}_B(m; k^\mu)$ is the action of $\hat{\mathcal{M}}_B(m)$ on an on-shell one-particle state with momentum k^μ. We will also refer to $\mathcal{M}_B(m; k^\mu)$ as the single-emission measurement. Using the

---

[8]In the one-loop calculation of the inclusive (virtuality-dependent) beam function in ref. [293], the discontinuity is instead taken at the level of the full forward matrix element of the *time-ordered* beam function operator because there, the two fields in the operator in general have timelike separation for nonzero virtualities. Since we consider transverse momenta (spacelike separation) and the collinear fields are local in the p^- direction due to the multipole expansion, this is not necessary in our case.

Feynman rules [351] derived from the collinear Lagrangian in eq. (2.124) and the Wilson line in eq. (2.132), the spin-averaged squared amplitudes $\mathcal{A}_{ij}^{(1)}$ for the quark case are

$$\mathcal{A}_{qq}^{(1)} = \mathcal{A}^{(a)} + \mathcal{A}^{(b)} , \qquad \mathcal{A}_{qg}^{(1)} = \mathcal{A}^{(c)} ,$$

$$\mathcal{A}^{(a)} = -C_F \frac{p^-(d-2)k_\perp^2}{[(p-k)^2 + \mathrm{i}0]^2} ,$$

$$\mathcal{A}^{(b)} = -C_F \frac{4p^-(p^- - k^-)}{[-k^-][(p-k)^2 + \mathrm{i}0]} w^2 \left| \frac{k^-}{\nu} \right|^{-\eta} ,$$

$$\mathcal{A}^{(c)} = -2T_F \left[\frac{(p^-)^2}{k^-} - \frac{4(p^- - k^-)}{d-2} \right] \frac{k_\perp^2}{[(p-k)^2 + \mathrm{i}0]^2} . \tag{3.70}$$

A sign in diagram (c) is due to the closed fermion loop. Note that $\mathcal{A}^{(b)}$ also contains the contribution from the mirror diagram of (b). The results for antiquarks are equal by charge conjugation. Label momentum conservation fixes

$$k^- = \frac{p^- - \omega}{p^-} = \frac{1-z}{z} \omega . \tag{3.71}$$

We find it convenient to continue to use k^-, where it is understood as the above fixed function of ω and z. Both the amplitude and, by our assumptions, the measurement only depend on $\vec{k}_\perp^2$, so we can use the on-shell constraint to eliminate $\vec{k}_\perp$,

$$\int \frac{\mathrm{d}^{2-2\epsilon}\vec{k}_\perp}{(2\pi)^{2-2\epsilon}} \, \delta_+(k^2) = \frac{1}{4\pi} \frac{\Omega_{2-2\epsilon}}{(2\pi)^{1-\epsilon}} \int_0^\infty \mathrm{d}|\vec{k}_\perp|^2 \, |\vec{k}_\perp|^{-2\epsilon} \, \theta(k^+ + k^-) \, \delta(k^+ k^- - |\vec{k}_\perp|^2)$$

$$= \frac{1}{4\pi} \frac{(4\pi)^\epsilon}{\Gamma(1-\epsilon)} (k^+ k^-)^{-\epsilon} \, \theta(k^+) \, \theta(k^-) . \tag{3.72}$$

This leaves a single k^+ integral that depends on the measurement,

$$\theta(\omega) \langle j_n | \theta(\omega) \mathcal{O}_i | j_n \rangle^{(1)}$$

$$= \theta(z) \theta(1-z) \frac{\alpha_s}{4\pi} \frac{e^{\epsilon\gamma_E}}{\Gamma(1-\epsilon)} A_{ij}(z, \omega/\nu) \left(\frac{k^-}{\mu} \right)^{-\epsilon} \int_0^\infty \frac{\mathrm{d}k^+}{k^+} \left(\frac{k^+}{\mu} \right)^{-\epsilon} \mathcal{M}_B(m; k^\mu) , \tag{3.73}$$

where we have inserted the $\overline{\text{MS}}$ coupling in eq. (2.20) and defined dimensionless squared amplitudes $A_{ij}^{(1)}(z, \omega/\nu) \equiv k^+ \mathcal{A}_{ij}^{(1)}$,

$$A_{qqV}^{(1)} = A^{(a)} + A^{(b)} , \qquad A_{qg}^{(1)} = A^{(c)} ,$$

$$A^{(a)} = C_F (d-2)(1-z) ,$$

$$A^{(b)} = C_F 4w^2 \left(\frac{z}{1-z} \right)^{1+\eta} \left(\frac{\omega}{\nu} \right)^{-\eta} ,$$

$$A^{(c)} = T_F 2 \left[\frac{1}{1-z} - \frac{4z}{d-2} \right] (1-z) . \tag{3.74}$$

These expressions for $\eta \to 0$ agree with the ones given in ref. [293].[9] The corresponding expressions for the gluon diagrams are found to be, cf. app. A of ref. [59],

$$A_{gg}^{(1)} = A^{(\mathrm{d})} + A^{(\mathrm{e})}, \qquad A_{gq}^{(1)} = A^{(\mathrm{f})},$$

$$A^{(\mathrm{d})} = C_A \, 4 \Big[\frac{1-z}{z} + z(1-z) + \frac{z}{2} \Big],$$

$$A^{(\mathrm{e})} = C_A \, 2(1+z) w^2 \Big(\frac{z}{1-z} \Big)^{1+\eta} \Big(\frac{\omega}{\nu} \Big)^{-\eta},$$

$$A^{(\mathrm{f})} = C_F \, 2 \Big[\frac{1 + (1-z)^2}{z} - \epsilon z \Big]. \tag{3.75}$$

Results for the beam function with a jet rapidity cut. To evaluate the beam function in eq. (3.10) at one loop, note that a single on-shell n-collinear emission with momentum k^μ constitutes a jet of its own with transverse momentum and rapidity

$$k_T = \sqrt{k^+ k^-}, \qquad \eta = \frac{1}{2} \ln \frac{k^-}{k^+}. \tag{3.76}$$

The single-emission measurement is independent of R and reads

$$\mathcal{M}_B(p_T^{\mathrm{cut}}, \eta_{\mathrm{cut}}; k^\mu) = \theta\Big(e^{2\eta_{\mathrm{cut}}} - \frac{k^-}{k^+} \Big) \theta(p_T^{\mathrm{cut}} - k_T) + \theta\Big(\frac{k^-}{k^+} - e^{2\eta_{\mathrm{cut}}} \Big)$$

$$\equiv \mathcal{M}_B^{(\eta < \eta_{\mathrm{cut}})}(p_T^{\mathrm{cut}}, \eta_{\mathrm{cut}}; k^\mu) + \mathcal{M}_B^{(\eta > \eta_{\mathrm{cut}})}(\eta_{\mathrm{cut}}; k^\mu). \tag{3.77}$$

Here we will separately display the result for each diagram with $\mathcal{O}_i^{(\eta < \eta_{\mathrm{cut}})} \propto \hat{\mathcal{M}}_B^{(\eta < \eta_{\mathrm{cut}})}$ and $\mathcal{O}_i^{(\eta > \eta_{\mathrm{cut}})} \propto \hat{\mathcal{M}}_B^{(\eta > \eta_{\mathrm{cut}})}$ inserted, respectively. This also allows one to read off the one-loop result for the $B_i^{(\mathrm{cut})}$ beam function in eq. (3.32), for which the measurement on a single emission is just $\mathcal{M}_B^{(\eta > \eta_{\mathrm{cut}})}$. On the other hand, for a direct computation of the finite correction due to the rapidity cut in eq. (3.19) it is more convenient to decompose the measurement function as

$$\mathcal{M}_B(p_T^{\mathrm{cut}}, \eta_{\mathrm{cut}}; k^\mu) = \theta(p_T^{\mathrm{cut}} - |\vec{k}_T|) + \theta(|\vec{k}_T| - p_T^{\mathrm{cut}}) \, \theta\Big(\frac{k^-}{k^+} - e^{2\eta_{\mathrm{cut}}} \Big)$$

$$= \mathcal{M}_B(p_T^{\mathrm{cut}}; k^\mu) + \Delta \mathcal{M}_B(p_T^{\mathrm{cut}}, \eta_{\mathrm{cut}}; k^\mu). \tag{3.78}$$

Inserting the first term into matrix elements yields the known results for the matching coefficients without any rapidity cut, while the second term yields the correction.

The relevant diagrams for the computation of the matching coefficient $\mathcal{I}_{qqV}$ are (a) and

---

[9]Note that there is a potential typo in eq. (C.7) of ref. [293], which differs in the z dependence at $\mathcal{O}(\epsilon)$ from our $A^{(\mathrm{c})}$.

(b). For diagram (a) we find, performing the k^+ integrals and expanding in ϵ,

$$\langle q_n | \theta(\omega)\, \mathcal{O}_q^{(\eta<\eta_{\text{cut}})}(p_T^{\text{cut}}, \eta_{\text{cut}}, \omega) | q_n \rangle^{(a)}$$
$$= \frac{\alpha_s C_F}{\pi} \theta\!\left(z - \frac{\omega e^{-\eta_{\text{cut}}}}{p_T^{\text{cut}} + \omega e^{-\eta_{\text{cut}}}}\right) \theta(1-z)\,(1-z) \ln \frac{p_T^{\text{cut}}\, z}{\omega e^{-\eta_{\text{cut}}}(1-z)} + \mathcal{O}(\epsilon),$$
$$\langle q_n | \theta(\omega)\, \mathcal{O}_q^{(\eta>\eta_{\text{cut}})}(\eta_{\text{cut}}, \omega) | q_n \rangle^{(a)}$$
$$= \frac{\alpha_s C_F}{\pi} \theta(z)\,\theta(1-z)\,(1-z)\left[-\frac{1}{2\epsilon} + \ln \frac{\omega e^{-\eta_{\text{cut}}}(1-z)}{\mu\, z} + \frac{1}{2} + \mathcal{O}(\epsilon)\right]. \tag{3.79}$$

Diagram (b) together with its mirror diagram gives, after expanding in η and ϵ,[10]

$$\langle q_n | \theta(\omega)\, \mathcal{O}_q^{(\eta<\eta_{\text{cut}})}(p_T^{\text{cut}}, \eta_{\text{cut}}, \omega) | q_n \rangle^{(b)} \tag{3.80}$$
$$= \frac{\alpha_s C_F}{\pi} \theta\!\left(z - \frac{\omega e^{-\eta_{\text{cut}}}}{p_T^{\text{cut}} + \omega e^{-\eta_{\text{cut}}}}\right) \theta(1-z)\Bigg\{\delta(1-z)\left[\frac{1}{\eta}\left(\frac{1}{\epsilon} - 2\ln\frac{p_T^{\text{cut}}}{\mu} + \mathcal{O}(\epsilon)\right) - \frac{1}{2\epsilon^2}\right.$$
$$\left. + \frac{1}{\epsilon}\ln\frac{\nu e^{-\eta_{\text{cut}}}}{\mu} - \ln^2\frac{\omega e^{-\eta_{\text{cut}}}}{\mu} + 2\ln\frac{p_T^{\text{cut}}}{\mu}\ln\frac{\omega}{\nu} + \frac{\pi^2}{24}\right] + 2\mathcal{L}_0(1-z)\ln\frac{p_T^{\text{cut}}\, z}{\omega e^{-\eta_{\text{cut}}}}$$
$$- 2\mathcal{L}_1(1-z) - 2\ln\frac{p_T^{\text{cut}}\, z}{\omega e^{-\eta_{\text{cut}}}(1-z)} + \mathcal{O}(\eta, \epsilon)\Bigg\},$$
$$\langle q_n | \theta(\omega)\, \mathcal{O}_q^{(\eta>\eta_{\text{cut}})}(\eta_{\text{cut}}, \omega) | q_n \rangle^{(b)}$$
$$= \frac{\alpha_s C_F}{\pi} \theta(z)\,\theta(1-z)\Bigg\{\delta(1-z)\left[\frac{1}{2\epsilon^2} - \frac{1}{\epsilon}\ln\frac{\omega e^{-\eta_{\text{cut}}}}{\mu} + \ln^2\frac{\omega e^{-\eta_{\text{cut}}}}{\mu} - \frac{\pi^2}{24}\right]$$
$$+ \mathcal{L}_0(1-z)\left[-\frac{1}{\epsilon} + 2\ln\frac{\omega e^{-\eta_{\text{cut}}}}{\mu\, z}\right] + 2\mathcal{L}_1(1-z) + \frac{1}{\epsilon} - 2\ln\frac{\omega e^{-\eta_{\text{cut}}}(1-z)}{\mu\, z} + \mathcal{O}(\epsilon)\Bigg\}.$$

The matching coefficient $\mathcal{I}_{qg}$ is computed from diagram (c) giving

$$\langle g_n | \theta(\omega)\, \mathcal{O}_q^{(\eta<\eta_{\text{cut}})}(p_T^{\text{cut}}, \eta_{\text{cut}}, \omega) | g_n \rangle^{(c)} \tag{3.81}$$
$$= \frac{\alpha_s T_F}{\pi} \theta\!\left(z - \frac{\omega e^{-\eta_{\text{cut}}}}{p_T^{\text{cut}} + \omega e^{-\eta_{\text{cut}}}}\right) \theta(1-z)\,(1-2z+2z^2) \ln \frac{p_T^{\text{cut}}\, z}{\omega e^{-\eta_{\text{cut}}}(1-z)} + \mathcal{O}(\epsilon),$$
$$\langle g_n | \theta(\omega)\, \mathcal{O}_q^{(\eta>\eta_{\text{cut}})}(\eta_{\text{cut}}, \omega) | g_n \rangle^{(c)}$$
$$= \frac{\alpha_s T_F}{\pi} \theta(z)\,\theta(1-z)\Bigg\{(1-2z+2z^2)\left[-\frac{1}{2\epsilon} + \ln\frac{\omega e^{-\eta_{\text{cut}}}(1-z)}{\mu\, z}\right] + z(1-z) + \mathcal{O}(\epsilon)\Bigg\}.$$

The relevant diagrams for the computation of the matching coefficient $\mathcal{I}_{gg}$ are (d) and (e), which yield

$$\langle g_n | \theta(\omega)\, \mathcal{O}_g^{(\eta<\eta_{\text{cut}})}(p_T^{\text{cut}}, \eta_{\text{cut}}, \omega) | g_n \rangle^{(d)}$$
$$= \frac{\alpha_s C_A}{\pi} \theta\!\left(z - \frac{\omega e^{-\eta_{\text{cut}}}}{p_T^{\text{cut}} + \omega e^{-\eta_{\text{cut}}}}\right) \theta(1-z)\,\frac{2 - 2z + 3z^2 - 2z^3}{z} \ln \frac{p_T^{\text{cut}}\, z}{\omega e^{-\eta_{\text{cut}}}(1-z)} + \mathcal{O}(\epsilon),$$
$$\langle g_n | \theta(\omega)\, \mathcal{O}_g^{(\eta>\eta_{\text{cut}})}(\eta_{\text{cut}}, \omega) | g_n \rangle^{(d)}$$
$$= \frac{\alpha_s C_A}{\pi} \theta(z)\,\theta(1-z)\,\frac{2 - 2z + 3z^2 - 2z^3}{z}\left[-\frac{1}{2\epsilon} + \ln\frac{\omega e^{-\eta_{\text{cut}}}(1-z)}{\mu\, z} + \mathcal{O}(\epsilon)\right], \tag{3.82}$$

---

[10]For the renormalization one needs to account for the full d dimensional coefficient of the $1/\eta$ divergence, which we do not display here for simplicity.

and, including the symmetric contribution of (e),

$$\langle g_n | \theta(\omega) \, \mathcal{O}_g^{(\eta<\eta_{\rm cut})}(p_T^{\rm cut}, \eta_{\rm cut}, \omega) | g_n \rangle^{(e)}$$

$$= \frac{\alpha_s C_A}{\pi} \, \theta\Big(z - \frac{\omega e^{-\eta_{\rm cut}}}{p_T^{\rm cut} + \omega e^{-\eta_{\rm cut}}}\Big) \theta(1-z) \bigg\{ \delta(1-z) \bigg[\frac{1}{\eta}\Big(\frac{1}{\epsilon} - 2\ln\frac{p_T^{\rm cut}}{\mu} + \mathcal{O}(\epsilon) \Big) - \frac{1}{2\epsilon^2}$$

$$+ \frac{1}{\epsilon}\ln\frac{\nu e^{-\eta_{\rm cut}}}{\mu} - \ln^2\frac{\omega e^{-\eta_{\rm cut}}}{\mu} + 2\ln\frac{p_T^{\rm cut}}{\mu}\ln\frac{\omega}{\nu} + \frac{\pi^2}{24} \bigg] + 2\mathcal{L}_0(1-z)\ln\frac{p_T^{\rm cut} z}{\omega e^{-\eta_{\rm cut}}}$$

$$- 2\mathcal{L}_1(1-z) - (2+z)\ln\frac{p_T^{\rm cut} z}{\omega e^{-\eta_{\rm cut}}(1-z)} + \mathcal{O}(\eta, \epsilon) \bigg\},$$

$$\langle g_n | \theta(\omega) \, \mathcal{O}_g^{(\eta>\eta_{\rm cut})}(\eta_{\rm cut}, \omega) | g_n \rangle^{(e)}$$

$$= \frac{\alpha_s C_A}{\pi} \, \theta(z) \, \theta(1-z) \bigg\{ \delta(1-z) \bigg[\frac{1}{2\epsilon^2} - \frac{1}{\epsilon}\ln\frac{\omega e^{-\eta_{\rm cut}}}{\mu} + \ln^2\frac{\omega e^{-\eta_{\rm cut}}}{\mu} - \frac{\pi^2}{24} \bigg]$$

$$+ \mathcal{L}_0(1-z)\bigg[-\frac{1}{\epsilon} + 2\ln\frac{\omega e^{-\eta_{\rm cut}}}{\mu z} \bigg] + 2\mathcal{L}_1(1-z) + (2+z)\bigg[\frac{1}{2\epsilon} - \ln\frac{\omega e^{-\eta_{\rm cut}}(1-z)}{\mu z} \bigg]$$

$$+ \mathcal{O}(\epsilon) \bigg\}. \tag{3.83}$$

The matching coefficient $\mathcal{I}_{gq}$ is computed from diagram (f), giving

$$\langle q_n | \theta(\omega) \, \mathcal{O}_g^{(\eta<\eta_{\rm cut})}(p_T^{\rm cut}, \eta_{\rm cut}, \omega) | q_n \rangle^{(f)}$$

$$= \frac{\alpha_s C_F}{\pi} \, \theta\Big(z - \frac{\omega e^{-\eta_{\rm cut}}}{p_T^{\rm cut} + \omega e^{-\eta_{\rm cut}}}\Big) \theta(1-z) \frac{2 - 2z + z^2}{z}\ln\frac{p_T^{\rm cut} z}{\omega e^{-\eta_{\rm cut}}(1-z)} + \mathcal{O}(\epsilon),$$

$$\langle q_n | \theta(\omega) \, \mathcal{O}_g^{(\eta>\eta_{\rm cut})}(\eta_{\rm cut}, \omega) | q_n \rangle^{(f)}$$

$$= \frac{\alpha_s C_F}{\pi} \, \theta(z) \, \theta(1-z) \bigg\{ \frac{2 - 2z + z^2}{z}\bigg[-\frac{1}{2\epsilon} + \ln\frac{\omega e^{-\eta_{\rm cut}}(1-z)}{\mu z} \bigg] + \frac{z}{2} + \mathcal{O}(\epsilon) \bigg\}. \tag{3.84}$$

Combining eqs. (3.65) and (3.66), we can directly read off the bare matching coefficients. Minimally subtracting the poles, the renormalized beam function matching coefficients are given by the $\mathcal{O}(\epsilon^0 \eta^0)$ terms in these expressions. From the results for $\mathcal{M}_B^{(\eta>\eta_{\rm cut})}$ we get $\mathcal{I}_{ij}^{({\rm cut},1)}$ in eq. (3.32), while adding $\mathcal{M}_B^{(\eta<\eta_{\rm cut})}$ gives the sum of eq. (3.19) and the second line of eq. (E.11). Using our setup, we also recalculated the known beam functions for smoothly rapidity-dependent jet vetoes [62, 70, 313] as a check, and in addition calculated the corrections for a finite $\eta_{\rm cut}$ in an otherwise smoothly rapidity-dependent veto, see appendix B of ref. [2].

3.4.2 Soft-collinear functions at one loop

We next describe the explicit one-loop calculation of the soft-collinear functions in eq. (3.33) and its relation to the soft-collinear function resolving the step in the jet veto in eq. (3.52). We again use pure dimensional regularization and the η regulator, so virtual diagrams and soft zero-bin subtractions are scaleless. Note that we expand the η regulator to leading power using the soft-collinear scaling, cf. eq. (2.163). This choice leads to a scaleless soft

zero bin. In Feynman gauge the bare one-loop real contribution to the n-soft-collinear function $\mathcal{S}_i^{(\text{cut})}$ in eq. (3.31) is given by[11]

$$
\mathcal{S}_i^{(\text{cut})}(p_T^{\text{cut}}, \eta_{\text{cut}}) = 1 + 4g^2 C_i \int \frac{\mathrm{d}^d k}{(2\pi)^{d-1}} \left| \frac{\nu}{k^-} \right|^\eta \frac{\delta_+(k^2)}{k^- k^+} \mathcal{M}_{\mathcal{S}}^{(\text{cut})}(p_T^{\text{cut}}, \eta_{\text{cut}}; k^\mu) + \mathcal{O}(\alpha_s^2),
$$

(3.85)

where $C_i = C_F$ (C_A) for $i = q$ (g) and the single-emission measurement reads

$$
\mathcal{M}_{\mathcal{S}}^{(\text{cut})}(p_T^{\text{cut}}, \eta_{\text{cut}}; k^\mu) = \theta(p_T^{\text{cut}} - |\vec{k}_T|) \theta\left(e^{2\eta_{\text{cut}}} - \frac{k^-}{k^+}\right) + \theta\left(\frac{k^-}{k^+} - e^{2\eta_{\text{cut}}}\right).
$$

(3.86)

The second term yields a scaleless contribution, while the first term corresponds to a boosted hemisphere and leads to the result

$$
\mathcal{S}_i^{(\text{cut})}(p_T^{\text{cut}}, \eta_{\text{cut}}) = 1 + \frac{\alpha_s C_i}{\pi} \left\{ \frac{1}{\eta} \left[\frac{1}{\epsilon} - 2 \ln \frac{p_T^{\text{cut}}}{\mu} + \mathcal{O}(\epsilon) \right] - \frac{1}{2\epsilon^2} + \frac{1}{\epsilon} \ln \frac{\nu e^{-\eta_{\text{cut}}}}{\mu} + \ln^2 \frac{p_T^{\text{cut}}}{\mu} \right.
$$
$$
\left. - 2 \ln \frac{p_T^{\text{cut}}}{\mu} \ln \frac{\nu e^{-\eta_{\text{cut}}}}{\mu} + \frac{\pi^2}{24} + \mathcal{O}(\eta, \epsilon) \right\} + \mathcal{O}(\alpha_s^2).
$$

(3.87)

Absorbing the divergent terms (including contributions of the form ϵ^n/η, which are not shown) into counterterms yields the renormalized one-loop result in eq. (3.33).

The bare one-loop contribution to the soft-collinear function in eq. (3.52) resolving the step in the jet veto is again given by eq. (3.85), but this time the single-emission measurement reads

$$
\mathcal{M}_{\mathcal{S}}^{(\text{step})}(p_T^{\text{cut}}, \tilde{p}_T^{\text{cut}}, \eta_{\text{cut}}; k^\mu) = \theta(p_T^{\text{cut}} - |\vec{k}_T|) \theta\left(e^{2\eta_{\text{cut}}} - \frac{k^-}{k^+}\right) + \theta(\tilde{p}_T^{\text{cut}} - |\vec{k}_T|) \theta\left(\frac{k^-}{k^+} - e^{2\eta_{\text{cut}}}\right).
$$

(3.88)

Successively dropping terms that yield scaleless integrals we can replace ($\mapsto$)

$$
\mathcal{M}_{\mathcal{S}}^{(\text{step})}(p_T^{\text{cut}}, \tilde{p}_T^{\text{cut}}, \eta_{\text{cut}}; k^\mu) \mapsto \theta\left(\frac{k^-}{k^+} - e^{2\eta_{\text{cut}}}\right) \left[\theta(\tilde{p}_T^{\text{cut}} - |\vec{k}_T|) - \theta(p_T^{\text{cut}} - |\vec{k}_T|) \right]
$$
$$
\mapsto \theta\left(e^{2\eta_{\text{cut}}} - \frac{k^-}{k^+}\right) \left[\theta(p_T^{\text{cut}} - |\vec{k}_T|) - \theta(\tilde{p}_T^{\text{cut}} - |\vec{k}_T|) \right]
$$
$$
= \mathcal{M}_{\mathcal{S}}^{(\text{cut})}(p_T^{\text{cut}}, \eta_{\text{cut}}; k^\mu) - \mathcal{M}_{\mathcal{S}}^{(\text{cut})}(\tilde{p}_T^{\text{cut}}, \eta_{\text{cut}}; k^\mu),
$$

(3.89)

so at one loop we find a simple relation between bare results,

$$
\mathcal{S}_i^{(1)}(p_T^{\text{cut}}, \tilde{p}_T^{\text{cut}}, \eta_{\text{cut}}) = \mathcal{S}_i^{(\text{cut},1)}(p_T^{\text{cut}}, \eta_{\text{cut}}) - \mathcal{S}_i^{(\text{cut},1)}(\tilde{p}_T^{\text{cut}}, \eta_{\text{cut}}).
$$

(3.90)

Remapping the measurement on the primary emission as in eq. (3.89), which is justified in the small-R limit (see the detailed beam function clustering calculation below), yields the analogous relation for the small-R clustering contributions.

---

[11]Note that in ref. [2], g denotes the dimensionless renormalized gauge coupling.

3.4.3 Comparison to quark beam function results in the literature

In ref. [327] the regime $p_T^{\text{cut}} \sim Qe^{-\eta_{\text{cut}}}$ was accounted for by adding a finite contribution $\Delta B_{i/j}^{(1)}$ from so-called out-of-jet radiation to the unmeasured beam function in eq. (3.31) as

$$\mathcal{I}_{ij}^{(\text{cut},1)}(\eta_{\text{cut}}, \omega, z, \mu) \mapsto \mathcal{I}_{ij}^{(\text{cut},1)}(\eta_{\text{cut}}, \omega, z, \mu) + \Delta B_{i/j}^{(1)}(p_T^{\text{cut}}, z, \omega, e^{-\eta_{\text{cut}}}). \tag{3.91}$$

One-loop consistency with our eq. (3.10) reads, at the level of bare ingredients,

$$\begin{aligned}
&\mathcal{I}_{ij}^{(1)}(p_T^{\text{cut}}, \eta_{\text{cut}}, \omega, z) \\
&= \mathcal{I}_{ij}^{(\text{cut},1)}(\eta_{\text{cut}}, \omega, z) + \Delta B_{i/j}^{(1)}(p_T^{\text{cut}}, z, \omega, e^{-\eta_{\text{cut}}}) + \delta_{ij}\delta(1-z)\,\mathcal{S}_i^{(\text{cut},1)}(p_T^{\text{cut}}, \eta_{\text{cut}}),
\end{aligned} \tag{3.92}$$

where $\mathcal{S}_i^{(\text{cut},1)}$ is the bare soft-collinear function at one loop, see eq. (3.87). By eq. (3.77) we have, in terms of bare collinear matrix elements up to scaleless PDF diagrams,

$$\mathcal{I}_{qq}^{(1)}(p_T^{\text{cut}}, \eta_{\text{cut}}, \omega, z) = \mathcal{I}_{qq}^{(\text{cut},1)}(\eta_{\text{cut}}, \omega, z) + \langle q_n | \theta(\omega)\, \mathcal{O}_q^{(\eta < \eta_{\text{cut}})}(p_T^{\text{cut}}, \eta_{\text{cut}}, \omega) | q_n \rangle, \tag{3.93}$$

and similarly for $\mathcal{I}_{qg}$. With this, eq. (3.92) simplifies to

$$\begin{aligned}
\langle q_n | \theta(\omega)\, \mathcal{O}_q^{(\eta < \eta_{\text{cut}})}(p_T^{\text{cut}}, \eta_{\text{cut}}, \omega) | q_n \rangle &= \Delta B_{q/q}^{(1)}(p_T^{\text{cut}}, z, \omega, e^{-\eta_{\text{cut}}}) + \delta(1-z)\,\mathcal{S}_q^{(\text{cut},1)}(p_T^{\text{cut}}, \eta_{\text{cut}}), \\
\langle g_n | \theta(\omega)\, \mathcal{O}_q^{(\eta < \eta_{\text{cut}})}(p_T^{\text{cut}}, \eta_{\text{cut}}, \omega) | g_n \rangle &= \Delta B_{q/g}^{(1)}(p_T^{\text{cut}}, z, \omega, e^{-\eta_{\text{cut}}}).
\end{aligned} \tag{3.94}$$

Both relations are readily checked after summing over all contributing diagrams.

3.4.4 Leading jet clustering logarithms in beam functions to all orders

We next turn to the computation of the clustering logarithms $\propto \alpha_s^2 \ln R$ in the two-loop η_{cut}-dependent beam function in eq. (3.21). We will address the question more generally and derive an all-order result for the leading clustering logarithms $\propto \alpha_s^{n+1} \ln^n R$ in jet veto beam functions.

To set the scene, note that the dependence on R in the two-loop matching coefficient $\mathcal{I}_{ij}^{(2)}$ can only come from diagrams where two partons (with momenta k_1 and k_2) cross the on-shell cut. This is because a single real emission dressed with a virtual correction is always clustered with itself independently of R, while in the double virtual case nothing happens. In particular, the logarithmic divergence $\propto \ln R$ at $R \ll 1$ corresponds to a region of phase space where an intermediate parton with momentum ℓ that splits into k_1 and k_2 can almost go on shell. This region contains the limit of either k_1 or k_2 becoming soft and the limit of the two becoming collinear to each other. The soft limit is independent of R because even if the soft parton is clustered into a separate soft jet, the other jet is harder and determines whether the event passes the veto. Thus the logarithm of R must arise from the limit where k_1 and k_2 are collinear to each other with $\ell^2 = 2k_1 \cdot k_2 \sim R p_T^{\text{cut}} \ll p_T^{\text{cut}}$.

This limit, for a primary parton emitted approximately along a lightlike direction n_J^μ, can be described by SCET with a single n_J-collinear sector at the scale $R p_T^{\text{cut}} \ll p_T^{\text{cut}}$,

$$n_J\text{-collinear:} \quad p^\mu = (p \cdot n_J, p \cdot \bar{n}_J, \vec{p}_\perp) \sim p_T^{\text{cut}}(R^2, 1, R). \tag{3.95}$$
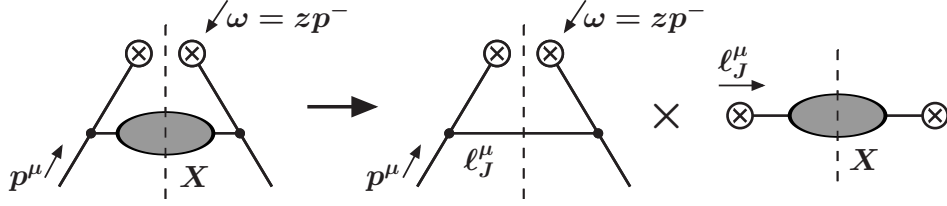
Figure 3.11: Matching of the full partonic beam function matrix element (left) onto an effective operator describing the formation of small-R jets from a single primary parton. The matrix element factorizes into a hard matching coefficient (left) at the scale of the jet veto, $\mu \sim p_T^{\text{cut}}$, and the effective operator matrix element at the scale $\mu \sim R\, p_T^{\text{cut}}$ (right). In the leading-order matching, we take $|X\rangle$ to be a single on-shell parton.

Here we picked $\bar{n}_J = (1, -\vec{n}_J)$ and we work in the frame where the n-collinear final state has zero rapidity. In this subsection we reserve $\vec{p}_\perp$ for the momentum perpendicular to the $n_J, \bar{n}_J$ of the primary emission and use $\vec{p}_T$ for the momentum perpendicular to the overall $n, \bar{n}$, i.e., for the momentum transverse to the beam axis. Explicit light-cone components $p^\pm$ still refer to $n, \bar{n}$, while light-cone components with respect to $n_J, \bar{n}_J$ are written out as above.

Hard matching. To set up the "hard" matching of the n-collinear beam function operator at the scale p_T^{cut} onto an effective n_J-collinear operator at the scale $R p_T^{\text{cut}}$, we find it convenient to open up the relevant matrix elements of the beam function operator and define, for a fixed n-collinear initial state $|j_n(p)\rangle$ averaged over color and spin,

$$\mathcal{O}_{qj}(p, \omega) = \theta(\omega)\, \text{tr}\left\{ \left[\delta(\omega - \overline{\mathcal{P}}_n)\, \frac{\slashed{\bar{n}}}{2} \chi_n \right] |j_n(p)\rangle\langle j_n(p)| \bar{\chi}_n \right\},$$

$$\mathcal{O}_{gj}(p, \omega) = \theta(\omega)\, \omega \left[\delta(\omega - \overline{\mathcal{P}}_n)\, \mathcal{B}_{n,\omega\perp}^\mu \right] |j_n(p)\rangle\langle j_n(p)| \mathcal{B}_{n,\perp\mu}. \tag{3.96}$$

Forward matrix elements of $\mathcal{O}_i$, which determine the bare beam function matching coefficients by eqs. (3.65) and (3.66), are recovered by tracing $\mathcal{O}_{ij}$ over hadronic radiation under the measurement constraint,

$$\langle j_n(p)|\theta(\omega)\mathcal{O}_i(p_T^{\text{cut}}, \eta_{\text{cut}}, R, \omega)|j_n(p)\rangle = \sum_X \!\!\!\!\!\!\! \int \langle X|\mathcal{O}_{ij}(p, \omega)\, \hat{\mathcal{M}}_B(p_T^{\text{cut}}, \eta_{\text{cut}}, R)|X\rangle. \tag{3.97}$$

So far these are considerations in the full theory at the scale p_T^{cut}. Suppressing a sum over flavors and the antiquark contribution, the hard matching for $\mathcal{O}_{ij}$ takes the form

$$\mathcal{O}_{ij}(p, \omega) = \int \frac{\mathrm{d}^d \ell_J}{(2\pi)^{d-1}}\, \delta_+(\ell_J^2) \left[H_{j\to i^*q}^{\alpha\beta}(p, \omega, \ell_J)\, O_q^{\beta\alpha}(\ell_J) + H_{j\to i^*g}^{\mu\nu}(p, \omega, \ell_J)\, O_{g\,\mu\nu}(\ell_J) \right]$$

$$+ \text{ higher multiplicities } (N \geq 2) + \mathcal{O}(R). \tag{3.98}$$

The terms on the first line have the standard form for matching onto a single collinear sector in SCET [171]. The two gauge-invariant operators at leading power are defined in

terms of the same building blocks as the ones for two collinear sectors in eq. (2.154),

$$O_q^{\beta\alpha}(\omega_J n_J) = \frac{2(2\pi)^{d-1}}{N_c} \bar{\chi}_{n_J}^\alpha |0\rangle\langle 0| \left[\delta(\omega_J - \overline{\mathcal{P}}_{n_J}) \, \delta^{d-2}(\vec{\mathcal{P}}_{n_J\perp}) \, \chi_{n_J}^\beta \right],$$

$$O_g^{\mu\nu}(\omega_J n_J) = -\omega_J \frac{2(2\pi)^{d-1}}{N_c^2 - 1} \mathcal{B}_{n_J,\perp}^\mu |0\rangle\langle 0| \left[\delta(\omega_J - \overline{\mathcal{P}}_{n_J}) \, \delta^{d-2}(\vec{\mathcal{P}}_{n_J\perp}) \, \mathcal{B}_{n_J,\perp}^\nu \right], \qquad (3.99)$$

but involve only a single large label momentum $\omega_J n_J$ rather than a hard momentum transfer. The soft Wilson lines from the BPS redefinition cancel within each operator. (Note that in slightly unconventional notation, we included vacuum states and opened up the operators as we did for $\mathcal{O}_{ij}$.) Here the rightmost fields in the operators have continuous minus and perpendicular label momentum in the sense of eq. (2.139), and we used[12]

$$\sum_{n_J} \int \mathrm{d}\omega_J = \sum_{n_J} \int \mathrm{d}\omega_J \, \mathrm{d}^{d-2}\vec{\ell}_\perp \, \mathrm{d}(n_J \cdot \ell_J) \, \delta^{d-2}(\vec{\ell}_\perp) \, \delta(n_J \cdot \ell_J)$$

$$= 2 \int \mathrm{d}^d \ell_J \, \omega_J \, \delta_+(\ell_J^2) \, \delta^{d-2}(\vec{\ell}_\perp) \qquad (3.100)$$

to rewrite a sum over the possible directions and an integral over the support $\omega_J > 0$ of the operator as the phase-space measure of a continuous on-shell momentum $\ell_J^\mu = \omega_J n_J^\mu$, up to a conventional normalization of the operator and matching coefficient. (The constraint on additional perpendicular label momentum $\vec{\ell}_\perp$ relative to ℓ_J^μ is absorbed into the operators.) We left the label momentum of the second field in the effective operator unconstrained, anticipating that we will evaluate forward matrix elements of the $O_m(\omega_J n_J)$ and thus fix it by label momentum conservation. We can think of $O_m(\omega_J n_J)$ as describing, together with the n_J-collinear Lagrangian, the formation of a bunch of partons with angular spread $\sim R$ from a primary parton m. The matching on the first line of eq. (3.98) is illustrated in figure 3.11.

The second line in eq. (3.98) contains, apart from operators suppressed by powers of R, operators encoding configurations with $N \geq 2$ well-separated primary partons that each initiate a bunch of partons with spread $\sim R$. These operators appear under a sum over N distinct jet directions $n_J, n_J', \ldots$ and involve nontrivial soft Wilson lines with $p^\mu \sim p_T^{\mathrm{cut}}(R, R, R)$ along those directions. It is clear that the matching coefficients for these operators only start at $\mathcal{O}(\alpha_s^N)$ because they only overlap with $\mathcal{O}_{ij}$ for at least N hard partons in X, so at $\mathcal{O}(\alpha_s)$, the matching in eq. (3.98) is complete at leading power in R. We will argue below that higher multiplicites do not contribute to the leading clustering logarithms to all orders.

The first nontrivial states that have overlap with both the left and the right-hand side of eq. (3.98) are on-shell single particle states $|X\rangle = |m(k)\rangle$ with $m = q, g$ and $k^2 = 0$.

---

[12]Note that we are using different dimensional regularization schemes in the operator and the matching coefficient, where we analytically extend $\vec{p}_\perp$ and $\vec{p}_T$ to $d - 2$ dimensions, respectively. This is justified because the two contributions are factorized and only $\mathrm{d}^d \ell_J$ appears in eq. (3.98).

Implicitly summing over the helicity and color of m, we have at tree level

$$\delta_+(\ell_J^2)\,\langle q(k)|O_q^{\beta\alpha}(\ell_J)|q(k)\rangle^{(0)} = \delta^d(\ell_J - k)\,\frac{\slashed{n}_J^{\beta\alpha}}{2} + \mathcal{O}(\alpha_s)\,,$$

$$\delta_+(\ell_J^2)\,\langle g(k)|O_g^{\mu\nu}(\ell_J)|g(k)\rangle^{(0)} = \delta^d(\ell_J - k)\,g_\perp^{\mu\nu} + \mathcal{O}(\alpha_s) \tag{3.101}$$

Other combinations vanish. The full-theory matrix elements start at $\mathcal{O}(\alpha_s)$ and are precisely given by the one-loop spin-contracted amplitudes in eq. (3.69) before phase-space integration over k,

$$\langle m(k)|\mathcal{O}_{ij}(p,\omega)|m(k)\rangle = \delta_{m\,m(ij)}\,\theta(\omega)\,g^2\mathcal{A}_{ij}^{(1)}(p,k)\,\delta(p^- - k^- - \omega) + \mathcal{O}(\alpha_s^2)\,, \tag{3.102}$$

where $m(ij)$ is the parton type allowed by fermion number conservation in $j \to i^*m$. By comparing eqs. (3.101) and (3.102), we can extract the $\mathcal{O}(\alpha_s)$ hard matching coefficients summed over polarizations,

$$\frac{\slashed{n}_J^{\beta\alpha}}{2}H_{j\to i^*q}^{\alpha\beta}(p,\omega,\ell_J) = \delta_{q\,m(ij)}\,\theta(\omega)\,g^2\mathcal{A}_{ij}^{(1)}(p,\ell_J)\,\delta(p^- - \ell_J^- - \omega) + \mathcal{O}(\alpha_s^2)\,,$$

$$g_{\perp\mu\nu}H_{j\to i^*g}^{\mu\nu}(p,\omega,k) = \delta_{g\,m(ij)}\,\theta(\omega)\,g^2\mathcal{A}_{ij}^{(1)}(p,\ell_J)\,\delta(p^- - \ell_J^- - \omega) + \mathcal{O}(\alpha_s^2)\,. \tag{3.103}$$

Clustering master formula. We now consider the action of the beam function measurement operator $\hat{\mathcal{M}}_B$ on n_J-collinear states $|X_J\rangle$ that overlap with $O_q(\ell_J)$ and $O_g(\ell_J)$. All emissions in X_J have $(p\cdot n_J, p\cdot\bar{n}_J, \vec{p}_\perp) \sim \omega_J(R^2, 1, R)$, thus we can simplify

$$\mathcal{M}_B(p_T^{\text{cut}}, \eta_{\text{cut}}, R; X_J) = \theta\left(\max_{k\in\text{jets}(X_J,R):\,\eta_k<\eta_{\text{cut}}}|\vec{p}_{T,k}| < p_T^{\text{cut}}\right) \tag{3.104}$$

$$= \theta(\eta_J < \eta_{\text{cut}})\,\theta\left(\max_{k\in\text{jets}(X_J,R)}z_k|\vec{\ell}_{JT}| < p_T^{\text{cut}}\right) + \theta(\eta_J \geq \eta_{\text{cut}}) + \mathcal{O}(R)\,.$$

The expression on the first right-hand side is the full measurement on the overall n-collinear state, of which X_J is a subset, including the jet rapidity cut. On the second equality we have defined $n_J = (\cosh\eta_J, 1, 0, \sinh\eta_J)$ in the lab frame and used that at leading power in R, all subjets in the n_J-collinear final state X_J have the same rapidity η_J, so they all pass or fail the rapidity cut together. We have also defined the fraction z_k of the total transverse momentum $|\vec{\ell}_{JT}|$ carried by each subjet, exploiting that at leading power in R, all subjets lie in the same azimuthal direction in the transverse plane.

Importantly, the second line is simply the single-emission measurement $\mathcal{M}_B(p_T^{\text{cut}}, \eta_{\text{cut}}; k^\mu)$ in eq. (3.77) evaluated at $k^\mu = z_J\ell_J^\mu$, where z_J is the maximum of the z_k. It can be written as a convolution,

$$\mathcal{M}_B(p_T^{\text{cut}}, \eta_{\text{cut}}, R; X_J) = \int dz_J\,\mathcal{M}_B(p_T^{\text{cut}}, \eta_{\text{cut}}; z_J\ell^\mu)\,\delta\left(z_J - \max_{k\in\text{jets}(X,R)}z_k\right) + \mathcal{O}(R)\,. \tag{3.105}$$

In this form, the measurement is factorized, with all dependence on the dynamics at the scale R encoded in the δ function with the maximum, which only talks to the high-scale measurement through z_J.

Using the factorized form of the measurement, we are ready to evaluate the right-hand side of eq. (3.97) in the effective theory. The relevant low-energy matrix elements arise from tracing the n_J-collinear operators over hadronic radiation under the z_J measurement,

$$\sum_X \langle X|O_m(\omega_J n_J)\,\delta\Big(z_J - \max_{k\in\text{jets}(X,R)} z_k\Big)|X\rangle \equiv J_{m\,\text{lead}}(z_J,\omega_J,R)\,, \qquad (3.106)$$

where we have defined the spin-averaged operators

$$O_q(\ell) \equiv \frac{\slashed{n}_J^{\alpha\beta}}{4}\,O_q^{\beta\alpha}(\ell)\,, \qquad O_g(\ell) \equiv \frac{g_\perp^{\mu\nu}}{d-2}\,O_g^{\mu\nu}(\ell)\,. \qquad (3.107)$$

The matrix element in eq. (3.106) is known as the (bare) leading jet function, which was introduced in a different context in ref. [329]. It returns the probability to produce the leading jet at momentum fraction z_J from a primary parton m. In the EFT, only the low-energy matrix elements $J_{m\,\text{lead}}$ depend on R and other details of the jet algorithm. The leading logarithms $\alpha_s^{n+1}\ln^n R$ in the beam function matching coefficient therefore arise from the cross terms of the $\mathcal{O}(\alpha_s)$ hard matching coefficients with the tower of clustering logarithms $\alpha_s^n\ln^n R$ in the leading jet function, which in turn are predicted by iterating the one-loop renormalization of the $J_{m\,\text{lead}}$. In particular, the highest logarithms must be proportional to the tree-level result in eq. (3.101). This justifies taking matrix elements of the spin-averaged operators in eq. (3.107).[13] It also implies that the leading logarithms are independent of ω_J and the precise choice of clustering algorithm, which only enter at the level of the $\mathcal{O}(\alpha_s)$ finite term.

Inserting eq. (3.106) and the result for the matching coefficient into eq. (3.97) and picking out the leading clustering logarithms, we find

$$\langle j_n(p)|\mathcal{O}_i(p_T^{\text{cut}},\eta_{\text{cut}},R,\omega)|j_n(p)\rangle^{(n+1,\ln^n R)}$$

$$= \theta(z)\int \frac{\mathrm{d}^d\ell_J}{(2\pi)^{d-1}}\,\delta_+(\ell_J^2)\,\delta(p^- - \ell_J^- - \omega)\,g^2\mathcal{A}_{ij}^{(1)}(p,\ell_J)\,,$$

$$\times \int \mathrm{d}z_J\,\mathcal{M}_B(p_T^{\text{cut}},\eta_{\text{cut}};z_J\ell_J^\mu)\Big(\frac{\alpha_s}{4\pi}\Big)^n J_{m(ij)\,\text{lead}}^{(n,\ln^n R)}(z_J)\,. \qquad (3.108)$$

We can further refine this by going through the manipulations in section 3.4.1, where we use n-collinear label momentum conservation and the fact that ℓ_J is on shell to eliminate all but the final ℓ_J^+ and z_J integral. This leads to our main, all-order result in this section for the leading jet clustering logarithms arising from (collinear) initial-state radiation under a jet veto,

$$\boxed{\begin{aligned} &\langle j_n(p)|\mathcal{O}_i(p_T^{\text{cut}},\eta_{\text{cut}},R,\omega)|j_n(p)\rangle^{(n+1,\ln^n R)} \\ &= \theta(z)\theta(1-z)\Big(\frac{\alpha_s}{4\pi}\Big)^{n+1} A_{ij}^{(1)}(z,\omega/\nu) \\ &\quad \times \int_0^\infty \frac{\mathrm{d}\ell_J^+}{\ell_J^+}\int \mathrm{d}z_J\,\mathcal{M}_B(p_T^{\text{cut}},\eta_{\text{cut}};z_J\ell_J^\mu)\,J_{m(ij)\,\text{lead}}^{(n,\ln^n R)}(z_J)\,. \end{aligned}} \qquad (3.109)$$

---

[13]Beyond the leading $\ln R$ terms there are indeed nontrivial spin correlations already at $\mathcal{O}(\alpha_s)\times\mathcal{O}(\alpha_s)$, see appendix D of ref. [313].

We stress that while we performed the steps in eq. (3.104) for the jet p_T veto with a jet rapidity cut for definiteness, they go through for any measurement that is only sensitive to the kinematics of the leading jet (with respect to the z_k), and eq. (3.109) holds in all of these cases. In eq. (3.109) it is understood that in the argument of the single-emission measurement,

$$\ell_J^- = \frac{1-z}{z}\omega\,, \qquad \ell_{JT} = \sqrt{\ell_J^- \ell_J^+}\,, \tag{3.110}$$

and we remind the reader that in pure dimensional regularization, the matrix element in eq. (3.109) is in one-to-one correspondence to the coefficient $\mathcal{I}_{ij}^{(n+1,\ln^n R)}(z,\zeta_{\rm cut})$ of the leading clustering logarithms in the n-loop bare beam function matching coefficient. In eq. (3.109) we dropped several corrections of $\mathcal{O}(\epsilon)$ which are not required since the $\ln R$ terms in the jet function are finite as $\epsilon \to 0$ and the amplitudes (in SCET$_{\rm II}$) only exhibit poles in η.[14] On this point, note that the rapidity regulator acting on the primary emission's ℓ_J^- is precisely the correct regulator for the corresponding full theory diagram since all emissions in X_J arise from the same primary emission and therefore are part of the same connected web. Also note that the jet function in eq. (3.109) is the bare one expanded in renormalized couplings at the scale $\mu \sim p_T^{\rm cut}$, so there will in general be β function cross terms at higher orders.

When evaluating eq. (3.109) for a concrete measurement, it is useful to note that the probability to detect the leading jet at any momentum fraction is unity [329],

$$\int {\rm d}z_J \, J_{m\,\rm lead}(z_J,\omega_J,R) = 1\,. \tag{3.111}$$

This is already satisfied by the tree-level result $J_{m\,\rm lead}^{(0)}(z_J,\omega_J,R) = \delta(1-z_J)$. It follows that the integral of all radiative corrections to $J_{m\,\rm lead}$ vanishes, e.g. for the $\ln^n R$ terms,

$$\int {\rm d}z_J \, J_{m\,\rm lead}^{(n,\ln^n R)}(z_J) = 0\,. \tag{3.112}$$

This implies that any region in ℓ_J^+ where the z_J integral is unconstrained does not contribute clustering logarithms. For example, for the jet veto with a jet rapidity cut, with the single-emission measurement decomposed as in eq. (3.77), we find that the contribution from $\eta_J > \eta_{\rm cut}$ vanishes by eq. (3.112),

$$\int {\rm d}z_J \, \mathcal{M}^{(\eta > \eta_{\rm cut})}(p_T^{\rm cut},\eta_{\rm cut};z_J \ell_J^\mu) \, J_{m\,\rm lead}^{(n,\ln^n R)}(z_J)$$
$$= \mathcal{M}^{(\eta > \eta_{\rm cut})}(p_T^{\rm cut},\eta_{\rm cut};z_J \ell_J^\mu) \int {\rm d}z_J \, J_{m(ij)\,\rm lead}^{(n,\ln^n R)}(z_J) = 0 \tag{3.113}$$

---

[14]Note that in the SCET$_{\rm I}$ beam functions for smoothly rapidity-dependent jet vetoes in ref. [313], where the full R dependence at two loops is known, the leading clustering terms in the flavor-diagonal channels that are predicted by our setup at two loops have the form $\ln^2 R$, and arise from cross terms of an explicit pole $1/\epsilon$ from the ℓ_J^+ integral with the expansion of the bare leading jet function to subleading order in ϵ. Accounting for this, we agree with the leading $\ln^2 R$ terms in the flavor-diagonal and the $\ln R$ terms in the off-diagonal channels.

because in this region the measurement is only sensitive to the total rapidity of the n_J-collinear sector, so the dependence on z_J drops out.

Our derivation of eq. (3.109) is not yet complete because we still need to argue that the higher multiplicity terms in the hard matching in eq. (3.98), which are also leading-power SCET operators, do not give rise to terms $\propto \alpha_s^{n+1} \ln^n R$. This is not a priori obvious because the low-energy matrix elements at higher multiplicity $N \geq 2$ contain soft dynamics and could develop Sudakov double logarithms $\propto \alpha_s^n \ln^{2n} R$. For $N = 2$, these would overcome the suppression by the matching coefficient $\propto \alpha_s^2$ already at the combined $\mathcal{O}(\alpha_s^3 \ln^2 R)$. To see that this is not the case, note that at the lowest nontrivial order, we add a soft emission to a configuration with N partons (jets) carrying a momentum fraction $z_k = z_k' = \cdots = 1$ of their respective $n_J, n_J', \ldots$ collinear sector, so the hardest jet is the one initiated by the hardest primary emission. The soft emission is either clustered separately, in which case the resulting jet is parametrically softer than all the N collinear jets and does not affect the veto, or clustered with one of the N collinear jets. In the latter case, the transverse momentum of that jet is only affected by an $\mathcal{O}(R)$ amount, so at leading power in R the hardest jet is the same one as in the configuration without the soft emission. Thus the measurement is insensitive to soft radiation with $p^\mu \sim p_T^{\text{cut}}(R, R, R)$ at the relative $\mathcal{O}(\alpha_s)$ and we can exclude the presence of a tower of Sudakov logarithms in the higher-multiplicity terms, which would have to start at this order.[15]

Previous results for clustering logarithms at higher orders in color singlet jet veto cross sections include the explicit calculation of the leading clustering logarithms in the three-loop rapidity anomalous dimension [352] and the all-order resummation of clustering logarithms in what corresponds to γ_ν^i in our notation [353]. Eq. (3.109) extends those results to the full matching coefficient for jet veto beam functions. An analogous factorization can be derived for the soft function finite terms. The RGE of the leading jet function, which is in close correspondence to the hardest microjet function of ref. [353], has recently been derived and solved recursively in ref. [329]. It is a rather complicated nonlinear DGLAP-like equation and it would be interesting to apply it here to explicitly resum the leading clustering terms in the leading jet function that we left symbolic in eq. (3.109). We note, however, that the resummation of the higher-order clustering terms even in the rapidity anomalous dimension has only a minor phenomenological effect [71].

Finally, we like to point out that the result in eq. (3.109) may equivalently be derived by explicitly factorizing the phase space and the full-theory amplitude for $j \to i^* k_1 \cdots k_n$ into a primary emission $j \to i^* m$ and a subsequent collinear splitting $m \to k_1 \cdots k_n$, see e.g. refs. [354, 355] for the required ingredients at two and three loops. Again, the key physical insight is that the primary emission is approximately on shell at the scale p_T^{cut}, which in

---

[15]Note that we have not excluded the possible presence of nonglobal logarithms in the low-energy matrix elements, which are beyond the scope of this discussion. These may be connected to the physical scenario where for more than one collinear particle in a given sector, an additional soft emission affects their clustering history such that the set of $\{z_k\}$ is affected by an $\mathcal{O}(1)$ amount. This could happen e.g. if the soft particle is clustered with one of the subjets first and displaces it by an $\mathcal{O}(R)$ amount in the perpendicular plane, causing it to be merged with another subjet down the line.

our setup is encoded in the label momentum dependence of the hard matching. To recover the formal result in terms of the SCET leading jet function in this approach, it is useful to note that jet functions can be represented in terms of collinear phase space and splitting functions [356].

Two-loop results. We now turn to evaluating eq. (3.109) at two loops. As discussed above, clustering logarithms arise exclusively from the region $\eta_J < \eta_{\text{cut}}$. In this region, the jet veto is active and sensitive to the precise distribution of subjets within the n_J-collinear sector, which changes depending on the perturbative order. At $\mathcal{O}(\alpha_s)$, the leading jet function is particularly simple and related to the semi-inclusive jet function $J_m(z, \omega, R)$ [357] by

$$J^{(1)}_{m\,\text{lead}}(z_J, \omega_J, R) = \theta\big(z_J - \tfrac{1}{2}\big)\, J^{(1)}_m(z_J, \omega_J, R)\,. \tag{3.114}$$

The semi-inclusive jet function encodes the rate at which *any* jet is observed in the n_J-collinear final state at a momentum fraction z_J. Since at $\mathcal{O}(\alpha_s)$ there can be at most two jets in the final state, the jet with $z_k > 1/2$ is always the hardest one, leading to the simple relation in eq. (3.114). In particular, the leading jet function at this order only has support for $z > 1/2$.[16] The coefficients of the one-loop clustering logarithm in the semi-inclusive jet function are [357]

$$
\begin{aligned}
J^{(1,\ln R)}_q(z_J) &= -2\big[P^{(0)}_{qq}(z_J) + P^{(0)}_{gq}(z_J)\big]\,, \\
J^{(1,\ln R)}_g(z_J) &= -2\big[P^{(0)}_{gg}(z_J) + 2n_f P^{(0)}_{qg}(z_J)\big]\,,
\end{aligned}
\tag{3.115}
$$

It is instructive to first consider the relevant integral without a rapidity cut $\eta_{\text{cut}} \to \infty$,

$$\int_0^\infty \frac{\mathrm{d}\ell_J^+}{\ell_J^+} \int \mathrm{d}z_J\, \mathcal{M}_B(p_T^{\text{cut}}; z_J k_T)\, J^{(1,\ln R)}_{m\,\text{lead}}(z_J) \tag{3.116}$$

The p_T^{cut} translates to $p_{\text{cut}}^+ = (p_T^{\text{cut}})^2/\ell_J^-$. For $\ell_J^+ < p_{\text{cut}}^+$, the primary emission has $\ell_{J,T} < p_T^{\text{cut}}$, therefore the whole range of z_J is included and the integral vanishes by eq. (3.112). In other words, the event passes the jet veto independent of how the two final-state partons are clustered, and there are no clustering logarithms.[17] On the other hand, for $p_{\text{cut}}^+ < \ell_J^+ < 4p_{\text{cut}}^+$, corresponding to $p_T^{\text{cut}} < \ell_{J,T} < 2p_T^{\text{cut}}$, there is a nonzero contribution because the two emissions can pass the veto if clustered separately, but fail the veto if clustered together. Changing variables to $z' = \sqrt{p_{\text{cut}}^+/\ell_J^+}$, inserting the expressions in eqs. (3.74) and (3.75) for the primary splitting amplitudes and the clustering coefficients in eq. (3.115), and

---

[16]Note that in the original calculation of the $\mathcal{O}(\alpha_s^2)$ clustering logarithms in ref. [2], the all-order relation to the leading jet function, defined only later in ref. [329], was not yet understood. Instead, the semi-inclusive jet function restricted to $1/2 < z_J < 1$ was inserted directly, following the above considerations.

[17]This can also be understood by breaking the veto down into a global veto e.g. on the transverse energy $E_T < p_T^{\text{cut}}$ of all emissions, and corrections to the global veto from clustering the emissions into jets [62]. In this picture the region $\ell_{J,T} < p_T^{\text{cut}}$ is precisely the region where the global and the jet veto coincide.

comparing to eq. (E.14) yields the compact result

$$c_{ij}^R = \int_{1/2}^1 \frac{\mathrm{d}z'}{z'} \int_{1/2}^{z'} \mathrm{d}z_J \, J_m^{(1,\ln R)}(z_J) \,, \qquad (3.117)$$

for the $\eta_{\mathrm{cut}} \to \infty$ clustering coefficients c_{ij}^R. Note that renormalizing the pole in η in the primary emission amplitudes recovers the clustering logarithm in the rapidity anomalous dimension with coefficient c_{ii}^R, see eq. (C.16).

The physical picture is very similar if a finite η_{cut} is retained. As discussed, the only integration region contributing clustering logarithms is $\eta_J < \eta_{\mathrm{cut}}$. Within this region it is again only the range $p_T^{\mathrm{cut}} < \ell_{J,T} < 2p_T^{\mathrm{cut}}$ that is sensitive to how the two partons are clustered. Comparing to eq. (3.21), we find the very compact expressions in eq. (3.22) for the two-loop $\ln R$ coefficient functions $c_{ij}^{R,\mathrm{cut}}(x)$,

$$c_{ij}^{(R,\mathrm{cut})}(x) = \int_{1/2}^x \frac{\mathrm{d}z'}{z'} \int_{1/2}^{z'} \mathrm{d}z_J \, J_m^{(1,\ln R)}(z_J) \,. \qquad (3.118)$$

Note that restricting to the region $\eta_J < \eta_{\mathrm{cut}}$ leads to a competing constraint on ℓ_J^+, which cuts off the z' integral at $z' \leq x = z/[\zeta_{\mathrm{cut}}(1-z)]$ rather than at $z' \leq 1$, where z is the overall partonic momentum fraction in the convolution against the PDF. This means that in the presence of a rapidity cut, the jet veto ties up the momentum distributions inside the proton and the sample of small-R subjets in a nontrivial way by probing different, truncated moments of the leading jet function at different points in partonic phase space. This conclusion also holds generally to higher orders in α_s by eq. (3.109), and should be contrasted with the clustering coefficients in the rapidity anomalous dimension (that were resummed or computed in refs. [352, 353]) and the $\eta_{\mathrm{cut}} \to \infty$ beam function, which are simple numbers given by a fixed moment of the leading jet function, and multiply a standard primary splitting amplitude in z.

3.4.5 Analytic consistency relations between regimes 2 and 3

We checked explicitly that the above results obey the consistency constraint in eq. (3.30), which at one loop reads

$$\mathcal{I}_{ij}^{(1)} + \Delta\mathcal{I}_{ij}^{(1)} = \mathcal{I}_{ij}^{(\mathrm{cut},1)} + \delta(1-z)\delta_{ij}\,\mathcal{S}_i^{(\mathrm{cut},1)} + \mathcal{O}\Big(\frac{1}{\zeta_{\mathrm{cut}}}\Big)\,. \qquad (3.119)$$

To verify eq. (3.119), note that eq. (3.19) becomes distribution valued in $(1-z)$ when taking the limit $\zeta_{\mathrm{cut}} \gg 1$. Specifically, the following distributional identities are required,

$$\theta\Big(z < \frac{\zeta_{\mathrm{cut}}}{1+\zeta_{\mathrm{cut}}}\Big) r(z) = r(z) + \mathcal{O}\Big(\frac{1}{\zeta_{\mathrm{cut}}}\Big)\,,$$

$$\theta\Big(z < \frac{\zeta_{\mathrm{cut}}}{1+\zeta_{\mathrm{cut}}}\Big) \mathcal{L}_0(1-z) = \mathcal{L}_0(1-z) + \ln\zeta_{\mathrm{cut}}\delta(1-z) + \mathcal{O}\Big(\frac{1}{\zeta_{\mathrm{cut}}}\Big)\,,$$

$$\theta\Big(z < \frac{\zeta_{\mathrm{cut}}}{1+\zeta_{\mathrm{cut}}}\Big) \mathcal{L}_0(1-z) \ln\big[\zeta_{\mathrm{cut}}(1-z)\big] = \mathcal{L}_1(1-z) + \ln\zeta_{\mathrm{cut}}\,\mathcal{L}_0(1-z)$$

$$+ \frac{1}{2}\ln^2\zeta_{\mathrm{cut}}\delta(1-z) + \mathcal{O}\Big(\frac{1}{\zeta_{\mathrm{cut}}}\Big)\,, \qquad (3.120)$$

where $r(z) = \mathcal{O}[(1-z)^0]$ is at most logarithmically divergent in the limit $z \to 1$. To derive eq. (3.120), we compared the left and right-hand sides in the bulk, $z < \zeta_{\mathrm{cut}}/(1 + \zeta_{\mathrm{cut}})$, and integrated over the full range of z.

For the terms multiplying $\ln R$ at two loops, the consistency relation reads

$$\mathcal{I}_{ij}^{(2,\ln R)} + \Delta \mathcal{I}_{ij}^{(2,\ln R)} = \delta_{ij}\delta(1-z)\,\mathcal{S}_i^{(\mathrm{cut},2,\ln R)} + \mathcal{O}\Big(\frac{1}{\zeta_{\mathrm{cut}}}\Big), \qquad (3.121)$$

since the unmeasured beam function is independent of R and the NGL contribution will only depend on it at the next order. Including the $\ln R$ piece from the rapidity anomalous dimension, the left-hand side evaluates to

$$
\begin{aligned}
&\mathcal{I}_{ij}^{(2,\ln R)} + \Delta \mathcal{I}_{ij}^{(2,\ln R)} \\
&= -\frac{1}{2}\gamma_{\nu 1}^{i,\ln R}\delta_{ij}\delta(1-z)\ln\frac{\nu}{\omega} + c_{ij}^R\Big[2P_{ij}^{(0)}(z) - \gamma_{B\,0}^i\,\delta_{ij}\delta(1-z)\Big] \\
&\quad + 2P_{ij}^{(0)}(z)\,\theta\Big(\frac{\zeta_{\mathrm{cut}}}{1+\zeta_{\mathrm{cut}}} > z\Big)\Big[-c_{ij}^R + \theta\Big(z > \frac{\zeta_{\mathrm{cut}}}{2+\zeta_{\mathrm{cut}}}\Big)c_{ij}^{R,\mathrm{cut}}\Big(\frac{z}{\zeta_{\mathrm{cut}}(1-z)}\Big)\Big] \\
&= \delta_{ij}\delta(1-z)\Big[-\frac{1}{2}\gamma_{\nu 1}^{i,\ln R}\ln\frac{\nu}{\omega} - 8C_i c_{ij}^R\ln\zeta_{\mathrm{cut}} + C_i\,\#+\mathcal{O}\Big(\frac{1}{\zeta_{\mathrm{cut}}}\Big)\Big] \qquad (3.122)
\end{aligned}
$$

where the first term in square brackets simply goes through, the second term is left over from the cancellation between the two c_{ij}^R pieces, and the third term arises as the distributional limit of $8C_i\,\mathcal{L}_0(1-z)\,\theta(z > \cdots)\,\theta(z < \cdots)$ as the arguments of both θ functions approach unity for $\zeta_{\mathrm{cut}} \to \infty$. (Nondiagonal splittings no longer contribute when taking both integration boundaries $\to 1$, whereas the flavor-diagonal splitting functions reduce to their leading eikonal limit.) The coefficient $\#$ is fixed by expanding the integral of the left-hand side as

$$
\begin{aligned}
&8\int \mathrm{d}z\,\mathcal{L}_0(1-z)\,\theta\Big(\frac{\zeta_{\mathrm{cut}}}{1+\zeta_{\mathrm{cut}}} > z\Big)\,\theta\Big(z > \frac{\zeta_{\mathrm{cut}}}{2+\zeta_{\mathrm{cut}}}\Big)c_{ij}^{R,\mathrm{cut}}\Big(\frac{z}{\zeta_{\mathrm{cut}}(1-z)}\Big) \\
&= 8\int_{1/2}^{1}\mathrm{d}x\,\frac{\zeta_{\mathrm{cut}}}{1+\zeta_{\mathrm{cut}}x}\,c_{ij}^{R,\mathrm{cut}}(x) = 8\int_{1/2}^{1}\frac{\mathrm{d}x}{x}\,c_{ij}^{R,\mathrm{cut}}(x) + \mathcal{O}\Big(\frac{1}{\zeta_{\mathrm{cut}}}\Big) = \#+\mathcal{O}\Big(\frac{1}{\zeta_{\mathrm{cut}}}\Big), \quad (3.123)
\end{aligned}
$$

where the integral in the first line covers the whole support of the integrand. On the second line we changed variables to $x = z/[\zeta_{\mathrm{cut}}(1-z)]$ and expanded over $\zeta_{\mathrm{cut}} \to \infty$. With this we confirm the consistency of the RG predicted terms in the soft-collinear function and arrive at the very simple relation in eq. (3.35) for the clustering coefficient in the soft-collinear finite term.

3.5 Numerical results

In section 3.2 we discussed in detail how to incorporate the jet rapidity cut into the resummed 0-jet cross section. In particular, in the regime $p_T^{\mathrm{cut}}/Q \sim e^{-\eta_{\mathrm{cut}}}$ (regime 2), the dependence on η_{cut} is incorporated into the resummation via the RG evolution of the η_{cut} dependent beam functions. In this section, we illustrate these results by presenting numerical predictions for the resummed cross section at NLL$'$+NLO.

In section 3.5.1, we outline how the resummed results are combined with the full QCD results, as well as our estimation of perturbative uncertainties. In section 3.5.2, we assess the impact of the additional perturbative ingredients by comparing the different treatments of $\eta_{\rm cut}$. In section 3.5.3, we show the predictions for selected $\eta_{\rm cut}$ as a function of $p_T^{\rm cut}$.

In the following, we consider the four cases of gluon-fusion Higgs production $gg \to H$ at $m_H = 125\,{\rm GeV}$, gluon fusion to a generic heavy scalar $gg \to X$ with $m_X = 1\,{\rm TeV}$, and Drell-Yan production at $Q = m_Z$ and $Q = 1\,{\rm TeV}$, with the same setup and inputs as described in section 3.2.3. The numerical results for the resummed predictions for all processes are obtained from our implementation in `SCETlib` [8]. The NLO results in full QCD are obtained from `MCFM 8.0` [330–332].

3.5.1 Fixed-order matching and perturbative uncertainties

The resummed cross section obtained from eq. (3.10) describes the 0-jet cross section up to power corrections in $p_T^{\rm cut}/Q$, which become relevant when $p_T^{\rm cut} \sim Q$. We account for them by the usual additive matching,

$$\sigma_0(p_T^{\rm cut}, \eta_{\rm cut}) = \sigma_0^{\rm res}(p_T^{\rm cut}, \eta_{\rm cut}) + \left[\sigma_0^{\rm FO}(p_T^{\rm cut}, \eta_{\rm cut}) - \sigma_0^{\rm sing}(p_T^{\rm cut}, \eta_{\rm cut})\right]. \tag{3.124}$$

Here, $\sigma_0^{\rm res}$ is the resummed singular cross section obtained from eq. (3.10), $\sigma_0^{\rm sing}$ is its fixed-order expansion, and $\sigma_0^{\rm FO}$ is the fixed-order result in full QCD. By construction, the difference in square brackets is nonsingular and vanishes as $p_T^{\rm cut} \to 0, \eta_{\rm cut} \to \infty$ and can therefore be included at fixed order even at small $p_T^{\rm cut}$. The dominant corrections at small $p_T^{\rm cut}$ are resummed in $\sigma_0^{\rm res}$. At large $p_T^{\rm cut}$, fixed-order perturbation theory is the appropriate description, so eq. (3.124) should recover $\sigma_0^{\rm FO}$. This is achieved by turning off the resummation in $\sigma_0^{\rm res}$ as a function of $p_T^{\rm cut}$, and by constructing $\sigma_0^{\rm res}$ such that it precisely reproduces $\sigma^{\rm sing}$ when the resummation is fully turned off.

To smoothly turn off the resummation as $p_T^{\rm cut} \to Q$, we use profile scales [203, 209], following the setup developed in ref. [67]. We stress that the profile scales for regime 2 are in one-to-one correspondence with the standard treatment in regime 1, since both regimes have the same RG structure. Similarly, our treatment of perturbative uncertainties is based on profile scale variations following ref. [67]. We distinguish an overall yield uncertainty $\Delta_{\mu 0}$, which is determined by a collective variation of all scales up and down, and a resummation (jet bin migration) uncertainty $\Delta_{\rm resum}$ from varying individual scales in the beam and soft functions. For the gluon-induced processes, we follow ref. [1] and include an additional uncertainty Δ_φ from varying the complex phase of the hard scale, which was not considered in ref. [67]. The total uncertainty is then obtained by considering the different uncertainty sources as independent, and hence uncorrelated, and adding them in quadrature,

$$\Delta_{\rm total} = \Delta_{\mu 0} \oplus \Delta_\varphi \oplus \Delta_{\rm resum} \equiv \left(\Delta_{\mu 0}^2 + \Delta_\varphi^2 + \Delta_{\rm resum}^2\right)^{1/2}. \tag{3.125}$$

3.5.2 Comparing different treatments of the jet rapidity cut

It is interesting to consider the impact of the additional perturbative ingredients in the $\eta_{\rm cut}$ dependent beam function on the prediction, e.g. compared to treating the rapidity cut
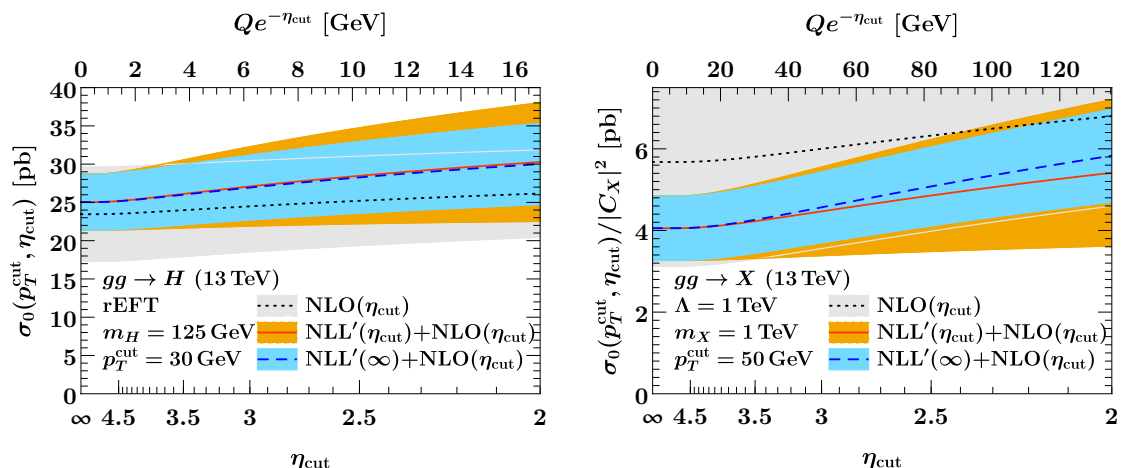
Figure 3.12: The 0-jet cross section for $gg \to H$ at $m_H = 125\,\mathrm{GeV}$ for $p_T^{\mathrm{cut}} = 30\,\mathrm{GeV}$ (left) and $gg \to X$ at $m_X = 1\,\mathrm{TeV}$ and $p_T^{\mathrm{cut}} = 50\,\mathrm{GeV}$ (right) as a function of η_{cut}. The same observable (σ_0) is calculated in three different ways, shown by the different bands, as described in the text.

effects purely at fixed order. In figures 3.12 and 3.13, we plot the results for fixed p_T^{cut} as a function of η_{cut} starting at $\eta_{\mathrm{cut}} = \infty$ on the left and decreasing toward the right. The corresponding values of the $Qe^{-\eta_{\mathrm{cut}}}$ scale are shown at the top.

Our result for the 0-jet cross section using the matching in eq. (3.124) is shown as orange bands. We refer to this prediction as NLL$'(\eta_{\mathrm{cut}})$+NLO(η_{cut}), because both the NLL$'$ resummed singular cross section and the fixed-order matching are exact in η_{cut}. To highlight the effect of the additional η_{cut} dependence in the regime 2 beam function, we consider two more alternative treatments of η_{cut}. For the regime 1 result, shown by the blue bands and denoted by NLL$'(\infty)$+NLO(η_{cut}), the η_{cut} dependence in the resummed cross section is dropped,

$$\sigma_0(p_T^{\mathrm{cut}}, \eta_{\mathrm{cut}}) = \sigma_0^{\mathrm{res}}(p_T^{\mathrm{cut}}, \infty) + \left[\sigma_0^{\mathrm{FO}}(p_T^{\mathrm{cut}}, \eta_{\mathrm{cut}}) - \sigma_0^{\mathrm{sing}}(p_T^{\mathrm{cut}}, \infty)\right]. \qquad (3.126)$$

The resummation then only acts on the singular cross section for $\eta_{\mathrm{cut}} = \infty$, while all η_{cut} effects are included purely at fixed order via the matching term in square brackets. Note that the matching term is now no longer nonsingular, i.e., it no longer vanishes like a power in p_T^{cut} as $p_T^{\mathrm{cut}} \to 0$, as we saw in figures 3.4 and 3.5. The plain fixed-order calculation without any resummation,

$$\sigma_0(p_T^{\mathrm{cut}}, \eta_{\mathrm{cut}}) = \sigma_0^{\mathrm{FO}}(p_T^{\mathrm{cut}}, \eta_{\mathrm{cut}}), \qquad (3.127)$$

is denoted by NLO(η_{cut}) and shown by the gray bands. In this case, the uncertainties are evaluated using the procedure of ref. [315].

We first consider gluon-fusion Higgs production shown in the left panel of figure 3.12, where we set $p_T^{\mathrm{cut}} = 30\,\mathrm{GeV}$. The NLO($\eta_{\mathrm{cut}}$) prediction (gray band) exhibits a slight, physical rise in the cross section as η_{cut} decreases towards the right. This is not surprising as at fixed order, decreasing η_{cut} simply amounts to accumulating the squared LO_1 matrix

element over a larger part of phase space. The rise is less pronounced than for the re-summed results (orange and blue bands), but still compatible with them within each others' uncertainties. Comparing NLL$'(\eta_{\rm cut})$+NLO$(\eta_{\rm cut})$ (orange) to NLL$'(\infty)$+NLO$(\eta_{\rm cut})$ (blue) we find that the additional tower of logarithms predicted by NLL$'(\eta_{\rm cut})$ on top of the fixed NLO $\eta_{\rm cut}$ dependence barely affects the central value of the prediction down to $\eta_{\rm cut} = 2$. This is perhaps not surprising since $Qe^{-\eta_{\rm cut}}$ is at most half of $p_T^{\rm cut}$, which means we are not far from regime 1. However, we do observe a noticeable increase in the perturbative uncertainty estimate. This is mainly due to the resummation uncertainty, which is reason-able: $\Delta_{\rm resum}$ probes the unknown higher-order finite terms (the RGE boundary condition) and is therefore sensitive to a change of the beam function boundary condition by the $\eta_{\rm cut}$ correction $\Delta I_{ij}^{(1)}$ (see section 3.2.3). On the other hand, $\Delta I_{ij}^{(1)}$ must be large enough to accommodate — up to power corrections — the fixed-order difference to $\eta_{\rm cut} = \infty$ (roughly 2 pb at $\eta_{\rm cut} = 2.5$, as can be read off from the gray line), so we expect an impact on $\Delta_{\rm resum}$ of similar size. Hence, the conclusion is not that the NLL$'(\infty)$+NLO$(\eta_{\rm cut})$ result is more precise, but rather that its uncertainty is potentially underestimated because it cannot capture the $\eta_{\rm cut}$ dependence.

In the right panel of figure 3.12, we show the same results for a hypothetical color-singlet scalar resonance $gg \to X$ at $m_X = 1$ TeV using $p_T^{\rm cut} = 50$ GeV. [The dimension-five operator mediating the production of X is given in eq. (3.27).] The NLO$(\eta_{\rm cut})$ result (gray) is now off by a large amount already at $\eta_{\rm cut} = \infty$, where it is not covered by the resummed predictions. This is expected because the high production energy of 1 TeV implies we are deep in the resummation region, even for the larger value of $p_T^{\rm cut} = 50$ GeV. The central values of the two resummed treatments start to differ below $\eta_{\rm cut} = 3$ or above $Qe^{-\eta_{\rm cut}} \simeq 50$ GeV, where we are now fully in regime 2. However, the main difference is again the larger and likely more reliable uncertainty estimate in the NLL$'(\eta_{\rm cut})$ prediction.

In figure 3.13 we show the analogous results for Drell-Yan production at $Q = m_Z$ using $p_T^{\rm cut} = 20$ GeV (left panel) and $Q = 1$ TeV using $p_T^{\rm cut} = 25$ GeV (right panel). For better readability, these results are normalized to the resummed 0-jet cross section at $\eta_{\rm cut} = \infty$. While all predictions agree in the slope of the cross section with respect to $\eta_{\rm cut}$, the NLO$(\eta_{\rm cut})$ result has a constant offset and an unrealistically small uncertainty estimate. At the lower $Q \sim 100$ GeV, we find practically no difference between the NLL$'(\eta_{\rm cut})$ and NLL$'(\infty)$ calculations, so here the effects of the jet rapidity cut can safely be included via the fixed-order matching corrections to the regime 1 resummation. At higher production energies, the intrinsic NLL$'(\eta_{\rm cut})$ ingredients become more relevant, similar to gluon-fusion, as shown by the increasing uncertainty estimates as $\eta_{\rm cut}$ decreases. Note that below $\eta_{\rm cut} = 2.5$, $Qe^{-\eta_{\rm cut}} \gtrsim 80$ GeV becomes large compared to this choice of $p_T^{\rm cut} = 25$ GeV, so resumming logarithms of $p_T^{\rm cut}/(Qe^{-\eta_{\rm cut}})$ using the regime 3 factorization given in section 3.2.4 might help reduce the uncertainties.
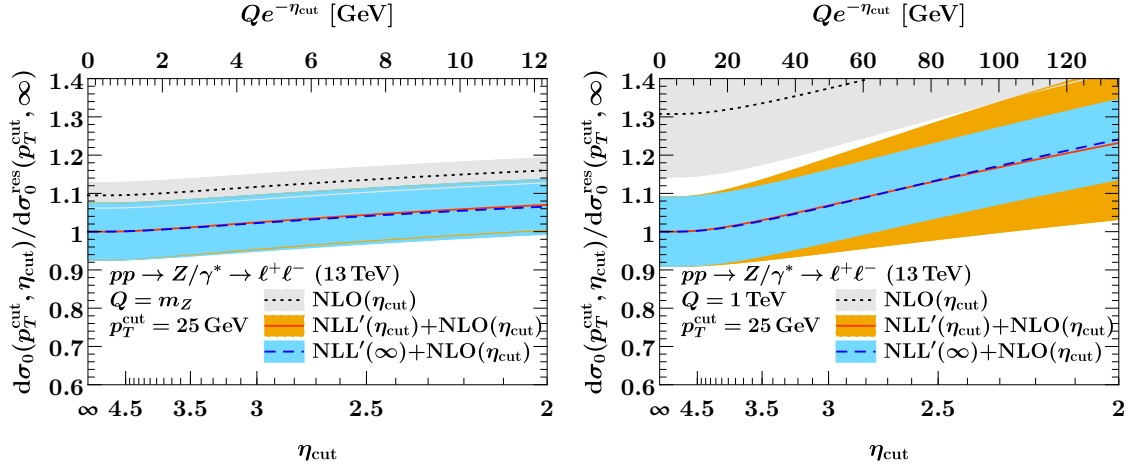
Figure 3.13: The 0-jet cross section for Drell-Yan at $Q = m_Z$ and $p_T^{\text{cut}} = 20\,\text{GeV}$ (left) and $Q = 1\,\text{TeV}$ and $p_T^{\text{cut}} = 25\,\text{GeV}$ (right) as a function of η_{cut}. The same observable (σ_0) is calculated in three different ways, shown by the different bands, as described in the text. For better readability, all results are normalized to the resummed central value at $\eta_{\text{cut}} = \infty$.
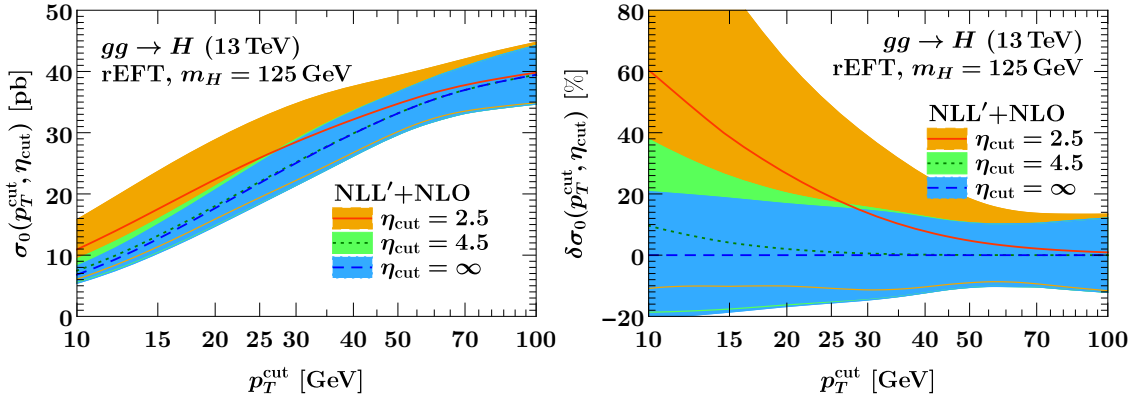
Figure 3.14: 0-jet cross section $\sigma_0(p_T^{\text{cut}}, \eta_{\text{cut}})$ for $gg \to H$ for $m_H = 125\,\text{GeV}$ at NLL$'$+NLO for different values of η_{cut}. The bands indicate the total uncertainty $\Delta_{\mu 0} \oplus \Delta_\varphi \oplus \Delta_{\text{res}}$. The absolute cross section is shown on the left. On the right, the same results are shown as the percent difference relative to the 0-jet cross section at $\eta_{\text{cut}} = \infty$.

3.5.3 Resummed predictions with a sharp rapidity cut

Here, we compare predictions for different values of η_{cut} as a function of p_T^{cut}. Our working order is NLL$'(\eta_{\text{cut}})$+NLO(η_{cut}) in the notation of the previous section, which from now on we simply refer to as NLL$'$+NLO, i.e., the η_{cut} dependence is always included in the resummation. We stress that the differences we observe between predictions in this subsection are physical differences due to the different jet rapidity cuts, and *not* due to different theoretical treatments as in the previous subsection.

In figure 3.14 and table 3.1 we present results for $gg \to H$. Going from $\eta_{\text{cut}} = \infty$ to $\eta_{\text{cut}} = 4.5$ we find a 1% increase of the cross section for the typical values of $p_T^{\text{cut}} = 25\,\text{GeV}$

$\sigma_0(p_T^{\text{cut}}, \eta_{\text{cut}})$ [pb], $gg \to H$ (13 TeV), rEFT, $m_H = 125$ GeV		
η_{cut}	$p_T^{\text{cut}} = 25$ GeV	$p_T^{\text{cut}} = 30$ GeV
2.5	$25.9 \pm 3.8_{\mu 0} \pm 1.5_{\varphi} \pm 5.0_{\text{res}}$ (25.0%)	$28.5 \pm 4.0_{\mu 0} \pm 1.6_{\varphi} \pm 4.6_{\text{res}}$ (22.0%)
4.5	$22.0 \pm 2.0_{\mu 0} \pm 1.0_{\varphi} \pm 2.8_{\text{res}}$ (16.2%)	$25.2 \pm 2.2_{\mu 0} \pm 1.2_{\varphi} \pm 2.8_{\text{res}}$ (15.0%)
∞	$21.8 \pm 1.9_{\mu 0} \pm 1.0_{\varphi} \pm 2.7_{\text{res}}$ (15.6%)	$25.0 \pm 2.2_{\mu 0} \pm 1.2_{\varphi} \pm 2.7_{\text{res}}$ (14.7%)

Table 3.1: 0-jet cross section for $gg \to H$ for $m_H = 125$ GeV at NLL′+NLO for different values of p_T^{cut} and η_{cut} with a breakdown of the uncertainties.
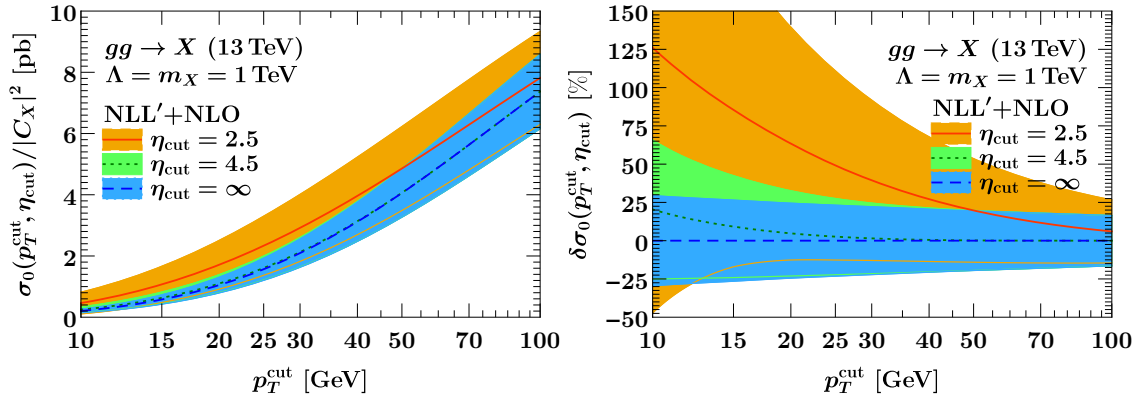
Figure 3.15: 0-jet cross section $\sigma_0(p_T^{\text{cut}}, \eta_{\text{cut}})$ for $gg \to X$ for $m_X = 1$ TeV at NLL′+NLO for different values of η_{cut}. The bands indicate the total uncertainty $\Delta_{\mu 0} \oplus \Delta_{\varphi} \oplus \Delta_{\text{res}}$. The absolute cross section is shown on the left. On the right, the same results are shown as the percent difference relative to the 0-jet cross section at $\eta_{\text{cut}} = \infty$.

$\sigma_0(p_T^{\text{cut}}, \eta_{\text{cut}})/|C_X|^2$ [pb], $gg \to X$ (13 TeV), $\Lambda = m_X = 1$ TeV		
η_{cut}	$p_T^{\text{cut}} = 50$ GeV	$p_T^{\text{cut}} = 100$ GeV
2.5	$4.9 \pm 0.7_{\mu 0} \pm 0.1_{\varphi} \pm 1.2_{\text{res}}$ (28.3%)	$7.8 \pm 0.8_{\mu 0} \pm 0.1_{\varphi} \pm 1.3_{\text{res}}$ (19.4%)
4.5	$4.1 \pm 0.3_{\mu 0} \pm 0.1_{\varphi} \pm 0.7_{\text{res}}$ (19.6%)	$7.4 \pm 0.6_{\mu 0} \pm 0.1_{\varphi} \pm 1.1_{\text{res}}$ (16.4%)
∞	$4.1 \pm 0.3_{\mu 0} \pm 0.1_{\varphi} \pm 0.7_{\text{res}}$ (19.5%)	$7.4 \pm 0.6_{\mu 0} \pm 0.1_{\varphi} \pm 1.1_{\text{res}}$ (16.4%)

Table 3.2: 0-jet cross section for $gg \to X$ for $m_X = 1$ TeV at NLL′+NLO for different values of p_T^{cut} and η_{cut} with a breakdown of the uncertainties.

and 30 GeV. At $\eta_{\text{cut}} = 2.5$ the increase becomes more sizable, 14% (19%) for $p_T^{\text{cut}} = 30$ GeV (25 GeV). The differences vanish as the cross section saturates around $p_T^{\text{cut}} \sim 100$ GeV.

The analogous results for $gg \to X$ for $m_X = 1$ TeV are shown in figure 3.15 and table 3.2. At such a high hard scale, the uncertainties for $\eta_{\text{cut}} = 2.5$ become essentially beyond control for very tight vetoes $p_T^{\text{cut}} \lesssim 25$ GeV, which would make an additional resummation
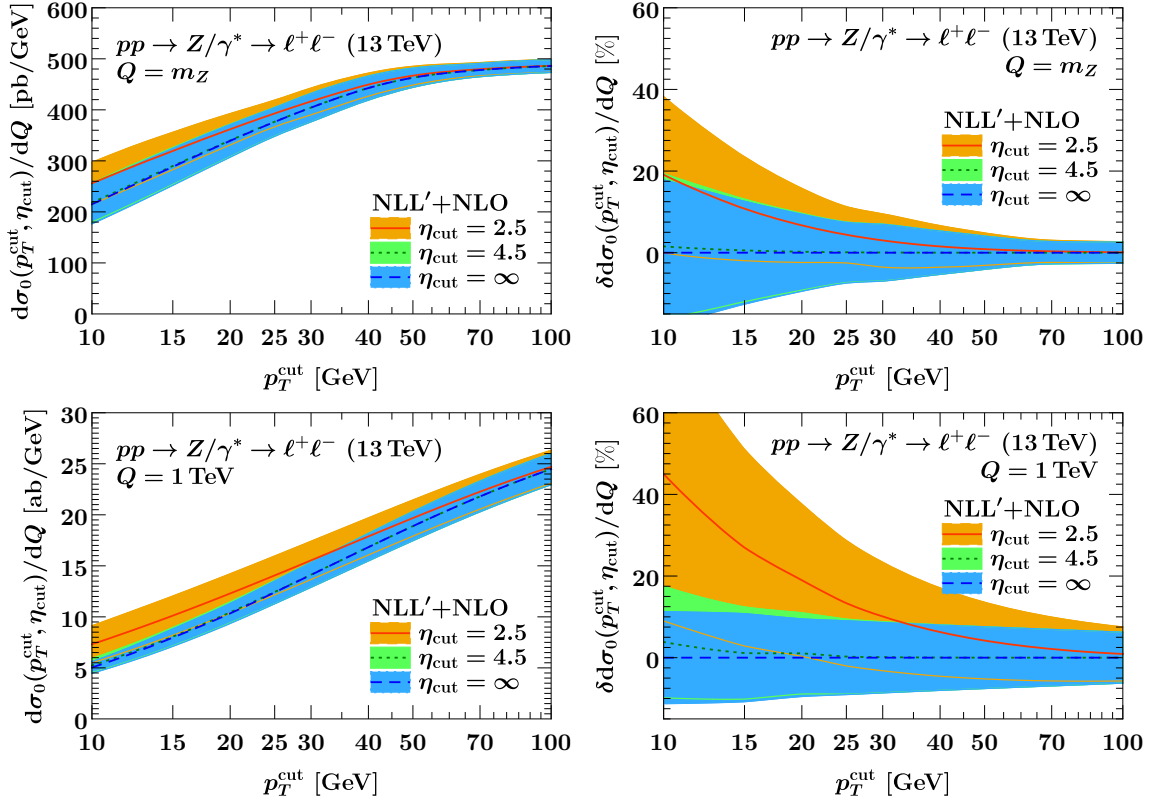
Figure 3.16: The 0-jet cross section $\mathrm{d}\sigma_0(p_T^{\mathrm{cut}}, \eta_{\mathrm{cut}})/\mathrm{d}Q$ for Drell-Yan production at the Z pole $Q = m_Z$ (top row) and at $Q = 1\,\mathrm{TeV}$ (bottom row) at NLL′+NLO for different values of η_{cut}. The bands indicate the total uncertainty $\Delta_{\mu 0} \oplus \Delta_{\mathrm{res}}$. The absolute cross section is shown on the left. On the right, the same results are shown as the percent difference relative to the 0-jet cross section at $\eta_{\mathrm{cut}} = \infty$.

of $\ln p_T^{\mathrm{cut}}/(Qe^{-\eta_{\mathrm{cut}}})$ as outlined in section 3.2.4 necessary. As we will see in the next subsection, this effect can be tamed by replacing the sharp rapidity cut by a step in the jet veto. However, for any choice of η_{cut} the cross section is very strongly Sudakov suppressed for such small values of p_T^{cut}. At more realistic values of the veto, the jet rapidity cut for $\eta_{\mathrm{cut}} = 2.5$ compared to $\eta_{\mathrm{cut}} = \infty$ still leads to a sizable increase of 20% (5%) for $p_T^{\mathrm{cut}} = 50\,\mathrm{GeV}$ ($p_T^{\mathrm{cut}} = 100\,\mathrm{GeV}$). In contrast, the effect for $\eta_{\mathrm{cut}} = 4.5$ is very small.

The results for Drell-Yan production are given in figure 3.16 and table 3.3. For $Q = m_Z$ (top rows), we find a $5-7\%$ increase in the cross section at $\eta_{\mathrm{cut}} = 2.5$ for $p_T^{\mathrm{cut}} = 20-25\,\mathrm{GeV}$. Here the uncertainty for $\eta_{\mathrm{cut}} = 2.5$ is under good control even down to $p_T^{\mathrm{cut}} \sim 10\,\mathrm{GeV}$. For $Q = 1\,\mathrm{TeV}$ (bottom rows), the cross section for $\eta_{\mathrm{cut}} = 2.5$ increases by 14% (4%) for $p_T^{\mathrm{cut}} = 25\,\mathrm{GeV}$ (50 GeV) compared to $\eta_{\mathrm{cut}} = \infty$. The Sudakov suppression and the accompanying increase in relative uncertainty at small p_T^{cut} are weaker than for $gg \to X$ due to the smaller color factor (C_F vs. C_A) in the Sudakov exponent, but are still substantial for a quark-induced process. The effect of the rapidity cut at $\eta_{\mathrm{cut}} = 4.5$ is negligible.

$\mathrm{d}\sigma_0(p_T^{\mathrm{cut}}, \eta_{\mathrm{cut}})/\mathrm{d}Q$ [pb/GeV], $pp \to Z/\gamma^* \to \ell^+\ell^-$ (13 TeV), $Q = m_Z$	
η_{cut}	$p_T^{\mathrm{cut}} = 20\,\mathrm{GeV}$ $\qquad\qquad$ $p_T^{\mathrm{cut}} = 25\,\mathrm{GeV}$

η_{cut}	$p_T^{\mathrm{cut}} = 20\,\mathrm{GeV}$	$p_T^{\mathrm{cut}} = 25\,\mathrm{GeV}$
2.5	$362\pm22_{\mu 0}\pm21_{\mathrm{res}}\ (8.5\%)$	$393\pm22_{\mu 0}\pm14_{\mathrm{res}}\ (6.6\%)$
4.5	$340\pm24_{\mu 0}\pm22_{\mathrm{res}}\ (9.4\%)$	$377\pm24_{\mu 0}\pm15_{\mathrm{res}}\ (7.4\%)$
∞	$339\pm24_{\mu 0}\pm22_{\mathrm{res}}\ (9.5\%)$	$376\pm24_{\mu 0}\pm15_{\mathrm{res}}\ (7.4\%)$

$\mathrm{d}\sigma_0(p_T^{\mathrm{cut}}, \eta_{\mathrm{cut}})/\mathrm{d}Q$ [ab/GeV], $pp \to Z/\gamma^* \to \ell^+\ell^-$ (13 TeV), $Q = 1\,\mathrm{TeV}$		
η_{cut}	$p_T^{\mathrm{cut}} = 25\,\mathrm{GeV}$	$p_T^{\mathrm{cut}} = 50\,\mathrm{GeV}$
2.5	$14.1\pm0.8_{\mu}\pm1.7_{\mathrm{res}}\ (13.6\%)$	$19.7\pm0.6_{\mu}\pm1.7_{\mathrm{res}}\ (9.0\%)$
4.5	$12.4\pm0.4_{\mu}\pm1.1_{\mathrm{res}}\ (9.2\%)$	$18.9\pm0.4_{\mu}\pm1.4_{\mathrm{res}}\ (7.6\%)$
∞	$12.4\pm0.4_{\mu}\pm1.1_{\mathrm{res}}\ (9.1\%)$	$18.9\pm0.4_{\mu}\pm1.4_{\mathrm{res}}\ (7.6\%)$

Table 3.3: The 0-jet cross section for Drell-Yan production at the Z pole $Q = m_Z$ (top) and at $Q = 1\,\mathrm{TeV}$ (bottom) at NLL$'$+NLO for different values of p_T^{cut} and η_{cut} with a breakdown of the uncertainties.

3.5.4 Resummed predictions with a step in the jet veto

In the previous subsection we have seen that a sharp rapidity cut at $\eta_{\mathrm{cut}} = 2.5$ can lead to a substantial loss of precision in the theory predictions, especially for gluon-induced processes and at high production energies.

In figure 3.17 we show the resummed 0-jet cross section for $gg \to H$ and $gg \to X$ with a step in the jet veto at $\eta_{\mathrm{cut}} = 2.5$ as a function of the second jet veto parameter $\tilde{p}_T^{\mathrm{cut}}$ that is applied beyond η_{cut}. The central jet veto below η_{cut} is fixed to $p_T^{\mathrm{cut}} = 25\,\mathrm{GeV}$. On the left of the plot $\tilde{p}_T^{\mathrm{cut}} = p_T^{\mathrm{cut}}$, which is equivalent to having no rapidity cut, in which case the uncertainties are well under control. In the limit $\tilde{p}_T^{\mathrm{cut}} \to \infty$ (towards the right) the step becomes a sharp cut, corresponding to the results of the previous subsection. While the step in the jet veto still leads to an increase in the uncertainties, this can now be controlled by the choice of $\tilde{p}_T^{\mathrm{cut}}$. At this order, a small step from $p_T^{\mathrm{cut}} = 25\,\mathrm{GeV}$ to $\tilde{p}_T^{\mathrm{cut}} = 30\,\mathrm{GeV}$ only leads to a small increase in uncertainty. For a larger step to $\tilde{p}_T^{\mathrm{cut}} = 50\,\mathrm{GeV} = 2p_T^{\mathrm{cut}}$, the uncertainties already increase substantially but are still much smaller than for a sharp cut.

3.6 Summary

We have developed a systematic framework to seamlessly incorporate a cut on the rapidity of reconstructed jets, $|\eta_{\mathrm{jet}}| < \eta_{\mathrm{cut}}$, into the theoretical description of jet-vetoed processes at the LHC. We have shown that the standard jet veto resummation, which neglects the rapidity cut, is correct up to power corrections of $\mathcal{O}(Qe^{-\eta_{\mathrm{cut}}}/p_T^{\mathrm{cut}})$, with Q the hard-interaction scale
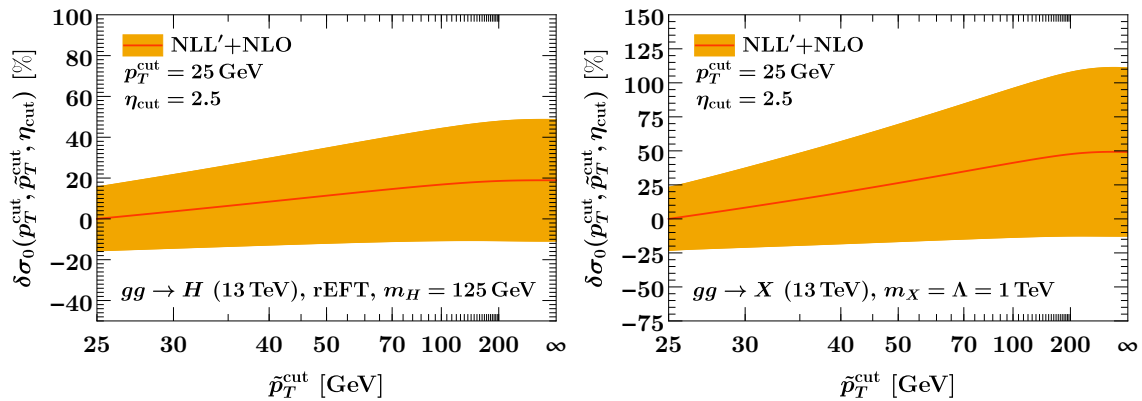
Figure 3.17: 0-jet cross section $\sigma_0(p_T^{\mathrm{cut}}, \tilde{p}_T^{\mathrm{cut}}, \eta_{\mathrm{cut}})$ with a step at $\eta_{\mathrm{cut}} = 2.5$ for $gg \to H$ (left panel) and $gg \to X$ (right panel) at NLL$'$+NLO. The results are shown for a fixed central veto at $p_T^{\mathrm{cut}} = 25\,\mathrm{GeV}$ as a function of the jet veto $\tilde{p}_T^{\mathrm{cut}}$ that is applied beyond η_{cut}. We show the percent differences relative to the result for a uniform veto $\tilde{p}_T^{\mathrm{cut}} = p_T^{\mathrm{cut}}$. The bands indicate the total uncertainty $\Delta_{\mu 0} \oplus \Delta_\varphi \oplus \Delta_{\mathrm{res}}$.

Figure replotted after ref. [2] on larger vertical range for aesthetic reasons.

and p_T^{cut} the jet veto cut.

We calculated the necessary η_{cut}-dependent corrections at one loop as well as all logarithmic contributions to them at two loops (including both small-R clustering logarithms and all jet veto logarithms predicted by the RGE; see section 3.2.3). We also derived a factorized expression for the leading clustering logarithms in the beam function, including the jet rapidity cut, to all orders in perturbation theory in terms of the $\mathcal{O}(\alpha_s)$ amplitudes for a primary collinear emission and the recently introduced leading jet function. In addition, we considered for the first time the case of a step in the jet veto, i.e., an increase in the veto parameter to $\tilde{p}_T^{\mathrm{cut}} > p_T^{\mathrm{cut}}$ beyond η_{cut}, and showed how to similarly incorporate it into the jet veto resummation (see section 3.3.2).

We also considered the jet veto cross section in the limit $p_T^{\mathrm{cut}} \ll Q e^{-\eta_{\mathrm{cut}}}$, corresponding to either very tight vetoes or very central rapidity cuts (see section 3.2.4). In this regime, the jet veto resummation becomes impaired by the presence of nonglobal logarithms, requiring a refactorization of the cross section. However, we have argued that this parametric region will most likely not play a role for typical jet binning analyses at the LHC. If experimentally necessary, it can be avoided by replacing the sharp rapidity cut by a moderate step in the jet veto, which is free of nonglobal logarithms (see section 3.3.4).

Chapter 4

Joint two-dimensional resummation in q_T and 0-jettiness at NNLL

In this chapter we consider the simultaneous measurement of the Z-boson transverse momentum q_T and the 0-jettiness event shape $\mathcal{T}_0$ in Drell-Yan production. Since both observables resolve the initial-state QCD radiation, the double-differential cross section in q_T and $\mathcal{T}_0$ contains Sudakov double logarithms of both q_T/Q and $\mathcal{T}_0/Q$. We simultaneously resum the logarithms in q_T and $\mathcal{T}_0$ to next-to-next-to-leading logarithmic order (NNLL) matched to next-to-leading fixed order (NLO), providing the first genuinely two-dimensional analytic Sudakov resummation for initial-state radiation.

This chapter is based on ref. [3], where work in close collaboration with the author of ref. [358] was presented, and some of the results have also appeared in ref. [358]. Compared to the published version in ref. [3], the discussion in section 4.3 has been expanded.

4.1 Motivation

Many analytic methods for the higher-order resummation of infrared-sensitive observables are available. These include the CSS formalism [105, 106, 359], seminumerical methods based on the coherent-branching formalism [360–363], and the methods based on renormalization group evolution (RGE) in effective field theories (EFTs) of QCD that we reviewed in chapter 2. A common drawback of these methods is that they only apply after a sufficient amount of emissions have been integrated over, which is why they have been primarily used for the resummation of single-differential observables. Their crucial advantage is that they can be systematically extended to higher orders, and that theoretical uncertainties can be addressed in a reliable way.

As discussed in the introduction, the resummation for measurements sensitive to infrared (soft and/or collinear) physics can, in part, also be achieved through the use of parton-shower Monte Carlo event generators; popular examples include `Pythia` [364, 365], `Herwig` [366, 367], or `Sherpa` [368]. Unlike analytic resummation methods, parton showers provide fully exclusive final states so that in principle, any desired measurements or cuts can be imposed on the generated events. The disadvantage of existing implementations of parton showers

is that they are only formally accurate at about leading-logarithmic (LL) level, depending on the shower's evolution variable (and other implementation details) and the observable in question.[1] Furthermore, estimating the perturbative uncertainties of parton showers is challenging, which is in part due to their limited perturbative accuracy.

There has been much progress in extending analytic resummation methods to cases involving multiple resummation variables. Examples include the joint resummation of transverse momentum q_T and threshold (large x) logarithms [375–381], q_T and high-energy (small x) logarithms [382], N-jettiness (or jet mass) together with dijet invariant masses [194, 383], two angularities [384, 385], jet mass and jet radius [345], threshold and jet radius logarithms in inclusive jet production [386, 387], as well as the work presented in chapter 3. Most of these examples either involve different variables that effectively resolve different subsequent emissions, or involve a primary resummation variable that is modified by an auxiliary measurement or constraint. Another well-understood case is when an infrared-sensitive measurement is separated into its contributions from mutually exclusive regions of phase space [291, 388, 389].[2]

In contrast, in this chapter we are interested in resolving emissions at the same level by simultaneously measuring two independent infrared-sensitive observables. Extending analytic resummation to such genuinely multi-dimensional resolution variables is of key theoretical concern, as it allows for a more complete description of the emission pattern beyond LL, effectively filling a gap between analytic resummations and parton showers. So far, this has been achieved only for the case of simultaneously measuring two angularities in e^+e^- collisions [385].[3]

We consider neutral-current Drell-Yan production, $pp \to Z/\gamma^* \to \ell^+\ell^-$, with a simultaneous measurement of (1) the transverse momentum q_T of the lepton pair and (2) the hadronic resolution variable 0-jettiness $\mathcal{T}_0$. We will refer to $\mathcal{T} \equiv \mathcal{T}_0$ in this chapter and write $pp \to Z$ for the Drell-Yan process for short, with the decay to leptons and the photon interference contribution understood. Achieving the combined resummation of q_T and $\mathcal{T}$ is important conceptually because as we reviewed in sections 2.4.3 and 2.4.4, q_T and $\mathcal{T}$ are prototypes for two large classes of infrared-sensitive observables: q_T constrains the transverse momentum of initial-state radiation, while $\mathcal{T}$ constrains its virtuality. These different behaviors lead to very different logarithmic structures already at LL, which in SCET is reflected in the different RGE structures of SCET$_\mathrm{I}$ and SCET$_\mathrm{II}$, respectively. (For parton showers, these correspond to evolution variables based on either transverse momentum or virtuality, respectively.)

Beyond providing a prototype for combining SCET$_\mathrm{I}$ and SCET$_\mathrm{II}$ resummations, the

---

[1] A recent detailed analysis can be found in ref. [369]. See also refs. [370–374] for work striving to improve the formal accuracy of the shower.

[2] Yet another case, which will not be relevant here, arises when different infrared-sensitive measurements are performed in different regions of phase space, which may require the resummation of nonglobal logarithms [341–343, 390–392].

[3] Since the original publication of these results in ref. [3], the simultaneous resummation of q_T and jet veto logarithms in pp collisions has been achieved in ref. [393] using the coherent branching formalism, and phenomenological results for W^+W^- production have been given in ref. [394].
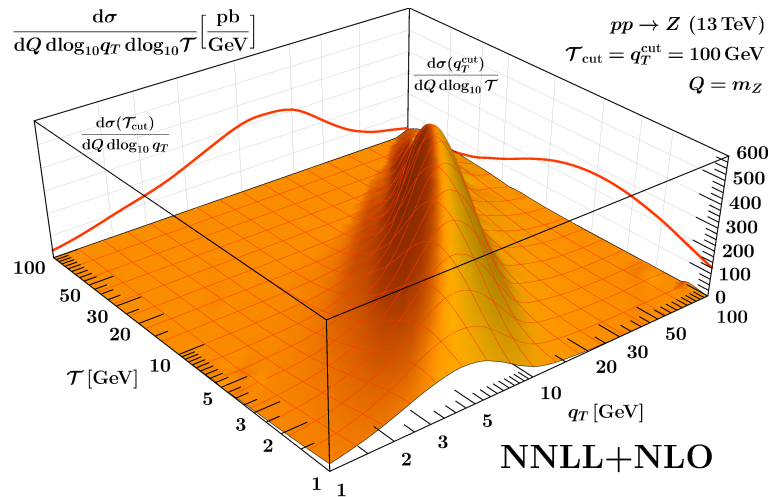
Figure 4.1: The Drell-Yan cross section double-differential in the transverse momentum q_T of the Z boson and the 0-jettiness event shape $\mathcal{T}$ at NNLL+NLO. For better visibility, the spectrum is plotted with respect to $\log_{10} q_T$ and $\log_{10} \mathcal{T}$. On the two side walls we show the corresponding single-differential spectra in q_T and $\mathcal{T}$ obtained by integrating the double-differential spectrum up to $\mathcal{T}_{\text{cut}} = 100\,\text{GeV}$ and $q_T^{\text{cut}} = 100\,\text{GeV}$, respectively.

joint resummation of q_T and $\mathcal{T}$ is also of direct phenomenological interest. First, they are important variables individually. The measurement of $\mathcal{T}$ in bins of q_T [395] can probe the so-called underlying event in hadronic collisions. Furthermore, the `Geneva` Monte Carlo event generator [122, 396] uses $\mathcal{T}$ as the underlying resolution variable for the event generation, achieving NNLL′+NNLO accuracy in $\mathcal{T}$ in conjunction with fully showered and hadronized events. While other observables, such as q_T, benefit from the underlying high resummation order, they do not enjoy the same level of formal accuracy in `Geneva` as $\mathcal{T}$ itself. The joint resummation of $\mathcal{T}$ and q_T to a given order enables extending the event generation in `Geneva` to also be accurate in q_T to the same order.

The double-differential factorization for q_T and $\mathcal{T}$ was first considered in ref. [195]. There, the regions of phase space where q_T (SCET$_{\text{II}}$) and $\mathcal{T}$ (SCET$_{\text{I}}$) determine the resummation structure were identified, together with the appropriate intermediate effective theory SCET$_+$ [194, 195] that connects them. Here, we develop an explicit matching procedure that combines the three different theories, SCET$_{\text{I}}$, SCET$_+$, and SCET$_{\text{II}}$, such that the resummation structure of each is recovered in its respective region of phase space. In particular, our method ensures that the single-differential resummation in one variable is recovered upon integration over the other. We discuss in detail the technical challenges involved. These include the construction of appropriate two-dimensional profile scales to combine the SCET$_{\text{II}}$ resummation for q_T, which is performed in position (impact-parameter) space, with the SCET$_{\text{I}}$ resummation for $\mathcal{T}$, which is performed in momentum space, the estimation of perturbative uncertainties, and the matching to full QCD at large q_T and/or $\mathcal{T}$ in a flexible way and consistent with the corresponding single-differential cases. We obtain explicit numerical predictions for the double-differential $(q_T, \mathcal{T})$ spectrum, achieving

its complete and fully two-dimensional Sudakov resummation at NNLL+NLO. Our main result is shown in figure 4.1, featuring a nice two-dimensional Sudakov peak structure.

We like to stress that our methods are completely general and can be applied to any color-singlet production process and at any order for which the relevant perturbative ingredients are available. (Some of the double-differential ingredients required at NNLL′ and N³LL are already known [397].) Furthermore, our matching procedure is generic and can be applied to any type of two-dimensional resummation for which the relevant EFTs on the boundaries and in the bulk are known.

The chapter is organized as follows. In section 4.2, we discuss the three different parametric regimes and the factorization and resummation for each individually. In section 4.4, we discuss in detail our method for consistently combining them to obtain a complete description of the two-dimensional $(q_T, \mathcal{T})$ plane. Our numerical results for the double-differential spectrum at NNLL+NLO are presented in section 4.5. We summarize our results in section 4.6.

4.2 Resummation framework

4.2.1 Overview of parametric regimes

We consider color-singlet production at hadron colliders. Although the process dependence is not important for our discussion, we consider the example of neutral-current Drell-Yan production as described in section 2.1.3 for concreteness. We measure the total invariant mass Q and rapidity Y of the color-singlet final state (the lepton pair). The two resolution variables we measure are the transverse momentum q_T of the color-singlet final state and the 0-jettiness $\mathcal{T}$ introduced in section 2.4.4.

We are interested in the contribution of initial-state radiation (ISR) to the simultaneous measurement of $q_T, \mathcal{T} \ll Q$, where $Q \gg \Lambda_{\text{QCD}}$ sets the scale of the hard interaction. The dynamics of perturbative ISR is then governed by three distinct momentum scales set by the measurement of q_T and $\mathcal{T}$. First, the typical transverse momentum of emissions that recoil against the lepton pair is set by q_T. Second, isotropic (soft) emissions at central rapidities can contribute to $\mathcal{T}$ via either of the projections onto q_a^μ and q_b^μ in eq. (2.211). This implies that their characteristic transverse momentum is $\sim \mathcal{T}$. Third, ISR with typical energy $\sim Q$ can contribute to $\mathcal{T}$ as long as it is collinear to either of the incoming beams, such that its contribution to $\mathcal{T}$ in eq. (2.211) is small. These collinear emissions then have a typical transverse momentum $\sim \sqrt{Q\mathcal{T}}$. The factorization and resummation structure of the cross section for $q_T, \mathcal{T} \ll Q$ depends on the parametric hierarchy between these scales. There are three relevant parametric regimes [195], which are illustrated in figure 4.2 and are discussed in the following.

In the first (blue) regime, $\mathcal{T} \ll q_T \sim \sqrt{Q\mathcal{T}}$, soft emissions with transverse momentum $\sim \mathcal{T}$ and collinear emissions with transverse momentum $\sim \sqrt{Q\mathcal{T}}$ both contribute to the $\mathcal{T}$ measurement. Due to the separation in transverse momentum, the q_T measurement is determined by collinear emissions, while soft emissions do not contribute to it. The
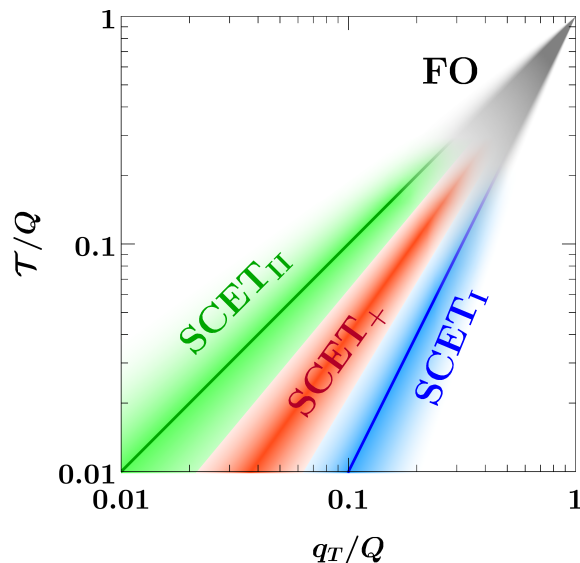
Figure 4.2: Parametric regimes in the $(q_T, \mathcal{T})$ plane and their SCET description. The solid lines correspond to the phase-space boundaries $q_T = \mathcal{T}$ (green) and $q_T = \sqrt{Q\mathcal{T}}$ (blue).

appropriate EFT description for this regime is SCET_I. It has the same RG structure as the single-differential $\mathcal{T}$ spectrum, with q_T acting as an auxiliary variable. The SCET_I regime is discussed in more detail in section 4.2.2.

In the opposite (green) regime, $\mathcal{T} \sim q_T \ll \sqrt{Q\mathcal{T}}$, both soft and collinear emissions have transverse momentum $\sim q_T$ and thus contribute to q_T. On the other hand, only soft radiation at central rapidities contributes to $\mathcal{T}$, while the contribution from collinear radiation is suppressed. This regime is described by SCET_II, whose RG structure is analogous to that of the single-differential q_T spectrum, with $\mathcal{T}$ as the auxiliary variable. The SCET_II regime is discussed in more detail in section 4.2.3.

Third, the intermediate (orange) regime in the bulk, $\mathcal{T} \ll q_T \ll \sqrt{Q\mathcal{T}}$, shares features with both boundary cases. As in the SCET_I regime, central soft radiation contributes to $\mathcal{T}$, while as in the SCET_II regime, collinear radiation contributes to q_T. In addition, this regime requires a distinct collinear-soft mode at an intermediate rapidity scale that can contribute to both measurements [195]. The relevant EFT description is provided by SCET_+, which in this case shares elements of both SCET_I and SCET_II. The SCET_+ regime, as well as its relation to the regimes on the two boundaries, is discussed in section 4.2.4. We briefly comment on the regions beyond the phase-space boundaries (left blank in figure 4.2) in section 4.2.5.

All numerical results for the SCET predictions in the following are obtained from our implementation in `SCETlib` [8]. All fixed NLO results in full QCD are obtained from `MCFM 8.0` [330–332]. Throughout this chapter we use `MMHT2014nnlo68cl` [110] NNLO PDFs with $\alpha_s(m_Z) = 0.118$ and five active quark flavors.

4.2.2 SCET$_{\mathrm{I}}$: $\mathcal{T} \ll q_T \sim \sqrt{Q\mathcal{T}}$

In this regime, both soft and collinear modes are constrained by $\mathcal{T}$, while only collinear modes can contribute to q_T, whose characteristic transverse momentum $\sqrt{Q\mathcal{T}}$ coincides parametrically with q_T. The scaling of the relevant EFT modes reads

$$
\begin{aligned}
n_a\text{-collinear:} \quad p^\mu &\sim \left(\mathcal{T}, Q, \sqrt{Q\mathcal{T}}\right) \sim \left(\tfrac{q_T^2}{Q}, Q, q_T\right), \\
n_b\text{-collinear:} \quad p^\mu &\sim \left(Q, \mathcal{T}, \sqrt{Q\mathcal{T}}\right) \sim \left(Q, \tfrac{q_T^2}{Q}, q_T\right), \\
\text{soft:} \quad p^\mu &\sim \left(\mathcal{T}, \mathcal{T}, \mathcal{T}\right).
\end{aligned}
\tag{4.1}
$$

Notably, these are the same modes as for the single-differential case in eq. (2.213), except that the collinear modes are now sensitive to q_T. This leads to the following factorization formula for the cross section [57, 398],[4]

$$
\frac{\mathrm{d}\sigma_{\mathrm{I}}}{\mathrm{d}Q^2\,\mathrm{d}Y\,\mathrm{d}q_T\,\mathrm{d}\mathcal{T}} = \sum_{i,j} H_{ij}(Q^2, \mu) \int \mathrm{d}t_a \int \mathrm{d}^2\vec{k}_a\, B_i(t_a, x_a, \vec{k}_a, \mu) \int \mathrm{d}t_b \int \mathrm{d}^2\vec{k}_b\, B_j(t_b, x_b, \vec{k}_b, \mu)
$$

$$
\times \int \mathrm{d}k\, S_i(k, \mu)\, \delta\!\left(q_T - |\vec{k}_a + \vec{k}_b|\right) \delta\!\left(\mathcal{T} - \frac{t_a}{Q_a} - \frac{t_b}{Q_b} - k\right),
\tag{4.2}
$$

which holds up to power corrections of the form[5]

$$
\frac{\mathrm{d}\sigma}{\mathrm{d}Q\,\mathrm{d}Y\,\mathrm{d}q_T\,\mathrm{d}\mathcal{T}} = \frac{\mathrm{d}\sigma_{\mathrm{I}}}{\mathrm{d}Q\,\mathrm{d}Y\,\mathrm{d}q_T\,\mathrm{d}\mathcal{T}} \left[1 + \mathcal{O}\!\left(\frac{\mathcal{T}}{Q}, \frac{q_T^2}{Q^2}, \frac{\mathcal{T}^2}{q_T^2}\right)\right].
\tag{4.3}
$$

The hard and soft function in eq. (4.2) are the same as in eq. (2.214), and the momentum fractions $x_{a,b}$ are as defined in eq. (2.62). The crucial difference is the appearance of *double-differential* beam functions $B_q(t, x, \vec{k}_T, \mu)$. They describe the extraction of a quark (or antiquark) from the proton with momentum fraction x and virtuality t like the inclusive beam function $B_q(t, x, \mu)$, but in addition measure the transverse momentum $\vec{k}_T$ of the extracted parton.[6] Formally, the bare double-differential quark beam function is defined as

$$
B_q\!\left(t, \frac{\omega}{P_n^-}, \vec{k}_T\right) = \theta(\omega)\langle p_n|\bar{\chi}_{qn}\left[\delta(\omega - \overline{\mathcal{P}})\,\delta(t + \omega\hat{p}^+)\,\delta(\vec{k}_T - \vec{\mathcal{P}})\,\frac{\slashed{\bar{n}}}{2}\chi_{qn}\right]|p_n\rangle,
\tag{4.4}
$$

which should be contrasted with the first line of eq. (2.215). The t and $\vec{k}_T$ translate into the contribution of collinear radiation to the $\mathcal{T}$ and q_T measurement, as captured by the

---

[4] We note that as in the single-differential case, Glauber effects are not included in eq. (4.2). We refer to the discussion in section 2.4.4 for details.

[5] Lorentz invariance suggests that power corrections in q_T always appear in terms of q_T^2. The distinction is irrelevant for the purposes of this chapter because we work to leading power in each respective regime. In chapter 7 we will formally show for power corrections in q_T/Q that the linear order vanishes as long as, like in this case, the individual decay products of the Z are not resolved.

[6] Here "double-differential" refers to the number of properties probed by IR-sensitive resolution variables, which in this case are $q_T \leftrightarrow k_T$ and $\mathcal{T} \leftrightarrow t$. Of course, like any beam function, the double-differential beam function in addition depends on the longitudinal momentum fraction x set by the Born kinematics. For this reason it is also referred to as "fully-differential" in the literature since it measures all components of the active parton's momentum.

Figure 4.3: Left: Comparison of singular and nonsingular contributions to the fixed $\mathcal{O}(\alpha_s)$ double spectrum as a function of $\mathcal{T}$, with $q_T = \sqrt{Q\mathcal{T}}$ kept fixed. The orange solid line shows the full QCD result and the dashed blue line the singular contributions contained in the SCET$_\mathrm{I}$ result eq. (4.2). The dotted green line shows their difference, which corresponds to the power corrections indicated in eq. (4.3). Right: SCET$_\mathrm{I}$ profile scales and their associated variations. The dotted lines (and the yellow band) indicate common up/down variations of μ_S^I and μ_B^I from varying α. The dashed lines (and the green band) are variations of β that only act on μ_B^I. In both plots, the thin vertical lines correspond to the transition points (x_0, x_1, x_2, x_3) given in the text.

δ functions on the last line of eq. (4.2). For $t \sim k_T^2 \gg \Lambda_{\mathrm{QCD}}^2$, the double-differential beam function can be matched onto PDFs [57, 293, 398],

$$B_q(t, x, \vec{k}_T, \mu) = \sum_j \int \frac{\mathrm{d}z}{z} \mathcal{I}_{qj}(t, z, \vec{k}_T, \mu) \, f_j\Big(\frac{x}{z}, \mu\Big) \left[1 + \mathcal{O}\Big(\frac{\Lambda_{\mathrm{QCD}}^2}{t}, \frac{\Lambda_{\mathrm{QCD}}^2}{k_T^2}\Big)\right]. \qquad (4.5)$$

Because the hard and soft function in eq. (4.2) are the same as in the single-differential case, the RG consistency of the cross section implies that the RGE of the double-differential beam functions cannot depend on q_T, such that the overall RG structure of the cross section is equivalent to the single-differential case, i.e., q_T takes the role of an auxiliary measurement in the SCET$_\mathrm{I}$ resummation, with no large logarithms of q_T appearing in the cross section as long as $q_T \sim \sqrt{Q\mathcal{T}}$ is satisfied. In particular, the canonical scales μ_X^I that achieve the resummation of all large logarithms of $\mathcal{T}/Q \sim q_T^2/Q^2$ in the SCET$_\mathrm{I}$ regime are the same as for the single-differential case,

$$\mu_H^\mathrm{I} \sim Q, \qquad \mu_B^\mathrm{I} \sim \sqrt{Q\mathcal{T}}, \qquad \mu_S^\mathrm{I} \sim \mathcal{T}. \qquad (4.6)$$

We stress that eq. (4.2) nevertheless provides a nontrivial and genuinely double-differential extension of the single-differential case. This is already visible from the structure of power corrections in eq. (4.3). Furthermore, the q_T dependence does affect and is affected by the $\mathcal{T}$ resummation because the double-differential beam functions enter in a convolution with the beam and soft renormalization group kernels; some technical challenges in evaluating these convolutions are addressed in section 4.3. Physically, the convolutions account for the total q_T recoil from all collinear emissions that are being resummed in $\mathcal{T}$.

Scale setting and fixed-order matching. To extend the description of the cross section to large $\mathcal{T} \sim q_T^2/Q \lesssim Q$, we have to reinstate the power corrections dropped in eq. (4.3). This is achieved by matching to the full fixed-order result, for which we use the standard additive matching,

$$d\sigma_{\mathrm{I}}^{\mathrm{match}} = d\sigma_{\mathrm{I}}\big|_{\mu^{\mathrm{I}}} + \big[d\sigma_{\mathrm{FO}} - d\sigma_{\mathrm{I}}\big]_{\mu_{\mathrm{FO}}} . \tag{4.7}$$

Here we abbreviated $d\sigma \equiv d\sigma/(dQ^2\, dY\, dq_T\, d\mathcal{T})$, and $d\sigma_{\mathrm{FO}}$ denotes the fixed-order cross section in full QCD. The scale subscripts on the right-hand side indicate whether $d\sigma_{\mathrm{I}}$ is RG evolved using the SCET$_{\mathrm{I}}$ resummation scales μ^{I}, with their precise choices given below, or whether it is evaluated with all scales set to a common fixed-order scale μ_{FO}.

By construction, $d\sigma_{\mathrm{I}}$ evaluated at common scales μ_{FO} exactly reproduces the singular limit of $d\sigma_{\mathrm{FO}}$, such that the term in square brackets in eq. (4.7) is a pure nonsingular power correction at small $\mathcal{T}$, which we can simply add to the resummed cross section. In the left panel of figure 4.3, we explicitly check that this is satisfied at fixed $\mathcal{O}(\alpha_s)$, and numerically assess the size of the power corrections. We compare the full QCD result (solid orange) to the SCET$_{\mathrm{I}}$ singular limit (dashed blue) as a function of $\mathcal{T}$, while keeping $q_T = \sqrt{Q\mathcal{T}}$ fixed to ensure that all classes of power corrections in eq. (4.3) uniformly vanish as $\mathcal{T} \to 0$. This is indeed satisfied, as the difference (dotted green) vanishes like a power.

For $\mathcal{T} \sim Q$, the SCET$_{\mathrm{I}}$ singular contribution and the power corrections are of the same size, implying that the resummation must be turned off to not upset the $\mathcal{O}(1)$ cancellation between them and correctly reproduce the fixed-order result. As discussed in section 2.3.3 this can be achieved by using profile scales, i.e., by having $\mu_B^{\mathrm{I}} \equiv \mu_B^{\mathrm{I}}(\mathcal{T})$ and $\mu_S^{\mathrm{I}} \equiv \mu_S^{\mathrm{I}}(\mathcal{T})$ transition from their canonical values eq. (4.6) at small $\mathcal{T}$ to a common high scale for large $\mathcal{T}$, schematically,

$$\mu_B^{\mathrm{I}}(\mathcal{T}), \mu_S^{\mathrm{I}}(\mathcal{T}) \to \mu_H^{\mathrm{I}} = \mu_{\mathrm{FO}} \quad \text{for} \quad \mathcal{T} \to Q . \tag{4.8}$$

As a result, the first and third term in eq. (4.7) exactly cancel in this limit, so the matched result reproduces $d\sigma_{\mathrm{FO}}$ as desired.

For the concrete choices of μ_B^{I}, μ_S^{I} we can rely on those used for the single-differential spectrum due to the equivalent RG structure. We use the profile scale setup developed for the closely related case of SCET$_{\mathrm{I}}$-like jet vetoes in ref. [70] and used for the $\mathcal{T}$ resummation in `Geneva` [122]. The profile scales are chosen as

$$\mu_S^{\mathrm{I}} = \mu_{\mathrm{FO}}\, f_{\mathrm{run}}^{\mathrm{I}}\Big(\frac{\mathcal{T}}{Q}\Big), \qquad \mu_B^{\mathrm{I}} = \mu_{\mathrm{FO}} \Big[f_{\mathrm{run}}^{\mathrm{I}}\Big(\frac{\mathcal{T}}{Q}\Big)\Big]^{1/2}, \qquad \mu_H^{\mathrm{I}} = \mu_{\mathrm{FO}} , \tag{4.9}$$

with the profile function $f_{\mathrm{run}}^{\mathrm{I}}$ given by [67]

$$f_{\mathrm{run}}^{\mathrm{I}}(x) = \begin{cases} x_0\Big(1 + \frac{x^2}{4x_0^2}\Big) & x \leq 2x_0 , \\ x & 2x_0 < x \leq x_1 , \\ x + \frac{(2-x_2-x_3)(x-x_1)^2}{2(x_2-x_1)(x_3-x_1)} & x_1 < x \leq x_2 , \\ 1 - \frac{(2-x_1-x_2)(x-x_3)^2}{2(x_3-x_1)(x_3-x_2)} & x_2 < x \leq x_3 , \\ 1 & x_3 < x . \end{cases} \tag{4.10}$$

Based on figure 4.3, we take $(x_1, x_2, x_3) = (0.2, 0.5, 0.8)$ for the transition points towards the fixed-order region $x \sim 1$. In addition, eq. (4.10) turns off the resummation in the nonperturbative region $x \lesssim 2x_0$, where we set $x_0 = 1\,\text{GeV}/Q$. This cuts off the nonperturbative region and ensures that RG running induced by perturbative anomalous dimensions always starts from a perturbative boundary condition. For μ_{FO} itself we use $\mu_{\text{FO}} = Q$ as the central scale. Our central scale choices are illustrated as solid lines in the right panel of figure 4.3.

Perturbative uncertainties. We estimate perturbative uncertainties in $\mathrm{d}\sigma_{\text{I}}^{\text{match}}$ by considering two different sources. The first uncertainty contribution Δ_{I} is inherent to the SCET$_{\text{I}}$ resummation. It is estimated by varying the individual SCET$_{\text{I}}$ scales while keeping μ_{FO} fixed, effectively probing the tower of higher-order logarithms that are being resummed. For this we use the profile scale variations [70]

$$
\mu_S^{\text{I}} = \mu_{\text{FO}} \left[f_{\text{vary}}\!\left(\frac{\mathcal{T}}{Q}\right) \right]^{\alpha} f_{\text{run}}^{\text{I}}\!\left(\frac{\mathcal{T}}{Q}\right),
$$

$$
\mu_B^{\text{I}} = \mu_{\text{FO}} \left\{ \left[f_{\text{vary}}\!\left(\frac{\mathcal{T}}{Q}\right) \right]^{\alpha} f_{\text{run}}^{\text{I}}\!\left(\frac{\mathcal{T}}{Q}\right) \right\}^{1/2-\beta}, \tag{4.11}
$$

where $\alpha = \beta = 0$ corresponds to the central scale choice in eq. (4.9), and the variation factor is defined as

$$
f_{\text{vary}}(x) = \begin{cases} 2(1 - x^2/x_3^2) & 0 \leq x < x_3/2\,, \\ 1 + 2(1 - x/x_3)^2 & x_3/2 \leq x < x_3\,, \\ 1 & x_3 \leq x\,. \end{cases} \tag{4.12}
$$

It approaches a factor of two in the resummation region at small x and reduces to unity toward the fixed-order regime at $x = x_3$, where the resummation is turned off. The estimate for Δ_{I} is obtained by computing $\mathrm{d}\sigma_{\text{match}}^{\text{I}}$ for each of the four profile scale variations

$$
(\alpha, \beta) = \{(+1, 0), (-1, 0), (0, +1/6), (0, -1/6)\}\,, \tag{4.13}
$$

and taking the maximum absolute deviation from the central result. These variations are also indicated in the right panel of figure 4.3. Note that for simplicity we do not perform explicit variations of the transition points since they are known to have a subdominant effect, and the uncertainty in the fixed-order matching is not essential to the results in this chapter. Also note that independent variations of μ_H need not be considered as part of resummation uncertainties because the corresponding change in the argument of the resummed logarithms is already covered by varying the low scales.

For the second uncertainty contribution, Δ_{FO}, we consider common variations of μ_{FO} up and down by a factor of two in all pieces of eq. (4.7). Since μ_{FO} enters all μ^{I} scales as a common overall factor, they inherit the same variation, which keeps all resummed logarithms invariant. Hence, the μ_{FO} variation effectively probes the effect of missing

higher-order corrections in the fixed-order contributions. The final uncertainty estimate for $d\sigma_I^{\text{match}}$ is obtained by adding both contributions in quadrature,

$$\Delta_{\text{total}}^{I} = \Delta_I \oplus \Delta_{\text{FO}} \equiv \left(\Delta_I^2 + \Delta_{\text{FO}}^2\right)^{1/2}. \tag{4.14}$$

The matched result $d\sigma_I^{\text{match}}$ in eq. (4.7) on its own constitutes a prediction for the double-differential spectrum that covers the part of phase space where $q_T \sim \sqrt{Q\mathcal{T}}$.

4.2.3 SCET$_{\text{II}}$: $\mathcal{T} \sim q_T \ll \sqrt{Q\mathcal{T}}$

In this regime, both soft and collinear emissions are constrained by q_T. Only soft radiation is constrained by the $\mathcal{T}$ measurement, while collinear radiation at transverse momenta $\sim q_T \ll \sqrt{Q\mathcal{T}}$ is not affected by it. The relevant EFT modes scale as

$$
\begin{aligned}
n_a\text{-collinear:} \quad p^\mu &\sim \left(\tfrac{q_T^2}{Q}, Q, q_T\right), \\
n_b\text{-collinear:} \quad p^\mu &\sim \left(Q, \tfrac{q_T^2}{Q}, q_T\right), \\
\text{soft:} \quad p^\mu &\sim \left(q_T, q_T, q_T\right) \sim \left(\mathcal{T}, \mathcal{T}, \mathcal{T}\right).
\end{aligned}
\tag{4.15}
$$

In this case, the cross section factorizes as [195]

$$
\frac{d\sigma_{\text{II}}}{dQ^2\, dY\, dq_T\, d\mathcal{T}} = \sum_{i,j} H_{ij}(Q^2, \mu) \int d^2\vec{k}_a\, B_i(x_a, \vec{k}_a, \mu, \nu/\omega_a) \int d^2\vec{k}_b\, B_j(x_b, \vec{k}_b, \mu, \nu/\omega_b)
$$
$$
\times \int dk \int d^2\vec{k}_s\, S_i(k, \vec{k}_s, \mu, \nu)\, \delta\big(q_T - |\vec{k}_a + \vec{k}_b + \vec{k}_s|\big)\, \delta(\mathcal{T} - k). \tag{4.16}
$$

The factorization receives power corrections of the form

$$
\frac{d\sigma}{dQ\, dY\, dq_T\, d\mathcal{T}} = \frac{d\sigma_{\text{II}}}{dQ\, dY\, dq_T\, d\mathcal{T}} \left[1 + \mathcal{O}\left(\frac{\mathcal{T}}{Q}, \frac{q_T^2}{\mathcal{T}Q}\right)\right]. \tag{4.17}
$$

We see that in this case the factorization has a form closely analogous to the single-differential q_T spectrum in eqs. (2.192) and (2.193), with hard and beam functions being the same this time. The difference in this case is the presence of a double-differential soft function $S_i(k, \vec{k}_s, \mu, \nu)$ that encodes the contribution of soft radiation to both $\mathcal{T}$ and q_T. The RG consistency of the cross section implies that its μ and ν RGEs do not depend on $\mathcal{T}$, and are the same as for the single-differential soft function in eq. (2.193a). Hence, the overall RG structure of the double-differential cross section is equivalent to the single-differential q_T spectrum, including the evolution in rapidity, with $\mathcal{T}$ acting as an auxiliary measurement. As for the single-differential spectrum, it is challenging to carry out the resummation in momentum space, and we will instead carry out the resummation in b_T space, turning the vectorial convolutions in eq. (4.16) into products of functions evaluated at $b_T \equiv |\vec{b}_T|$. (Details on the Fourier transform of the double-differential soft function are given in section 4.3.) The canonical SCET$_{\text{II}}$ scales in b_T-space are as in eq. (2.209),

$$
\begin{aligned}
\mu_H^{\text{II}} &\sim Q\,, & \mu_B^{\text{II}} &\sim b_0/b_T\,, & \mu_S^{\text{II}} &\sim b_0/b_T\,, & \mu_0 &\sim b_0/b_T\,, \\
\nu_B^{\text{II}} &\sim Q\,, & \nu_S^{\text{II}} &\sim b_0/b_T\,.
\end{aligned}
\tag{4.18}
$$

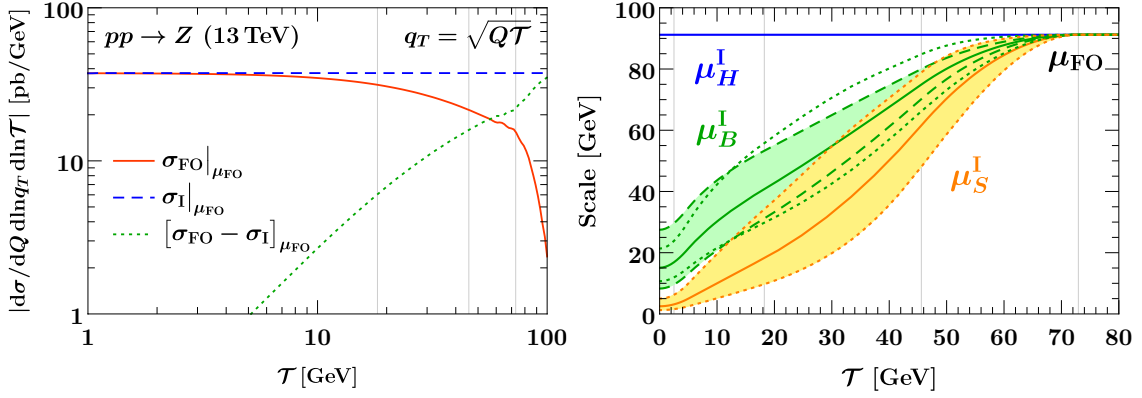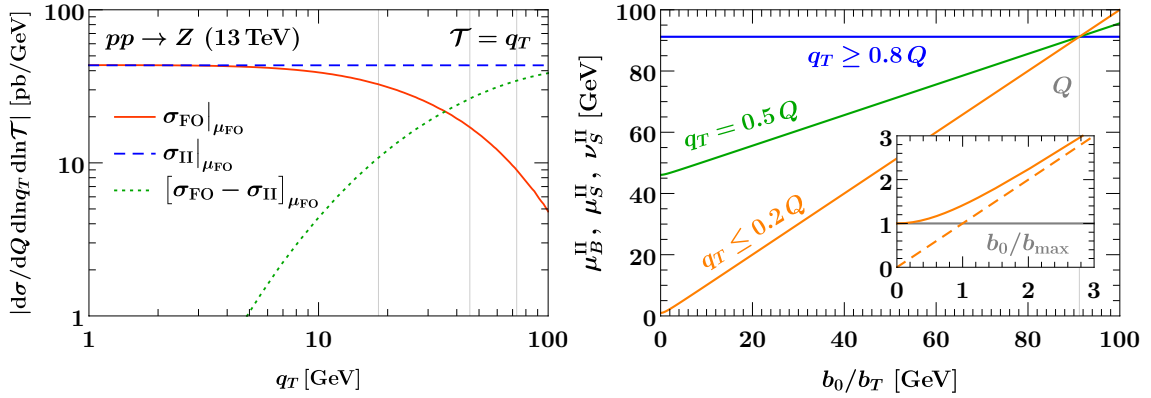**Figure 4.4:** Left: Comparison of singular and nonsingular contributions to the fixed $\mathcal{O}(\alpha_s)$ double spectrum as a function of q_T, with $\mathcal{T} = q_T$ kept fixed. The orange solid line shows the full QCD result and the dashed blue line the singular contributions contained in the SCET_{II} result eq. (4.16). The dotted green line shows their difference, which corresponds to the power corrections indicated in eq. (4.17). The thin vertical lines correspond to the transition points (x_1, x_2, x_3) given in the text. Right: SCET_{II} hybrid profile scales as a function of b_0/b_T for representative values of q_T. The thin vertical line in the main plot corresponds to Q. The inset shows the behavior of the profile in the nonperturbative region $b_0/b_T \sim \Lambda_{\text{QCD}}$, where the gray horizontal line indicates the scale $b_0/b_{\max}$ at which we freeze out the resummation. The dashed orange line in the inset indicates the canonical value of $\mu_B^{\text{II}}, \mu_S^{\text{II}}, \nu_S^{\text{II}}$.

In our profile scale construction in the next paragraph we will require that for $q_T \ll Q$, eq. (4.18) is exactly satisfied, such that the resummed q_T spectrum in this region is obtained from the inverse Fourier transform of the canonical b_T-space result, ensuring the formal equivalence to the q_T-space solution [263]. The rapidity evolution of the beam and double-differential soft function is driven by the resummed rapidity anomalous dimension in eq. (2.202), where we set the nonperturbative component to zero, $\tilde{\gamma}_{\nu,\text{np}}^i(b_T) = 0$, since it is not the focus of this work. We similarly ignore nonperturbative effects of $\mathcal{O}(\Lambda_{\text{QCD}}/q_T)$ in the SCET_{II} beam and soft function boundary conditions. To extend the perturbative contribution we will make the boundary scales $\mu = \{\mu_S, \mu_B, \mu_0\}$ asymptote to a fixed value at large b_T in our profile scale construction such that $\alpha_s(\mu)$ remains perturbative.[7]

Scale setting and fixed-order matching. We again extend the description of the cross section to the fixed-order region $q_T \sim \mathcal{T} \lesssim Q$ by an additive matching,

$$\mathrm{d}\sigma_{\text{II}}^{\text{match}} = \mathrm{d}\sigma_{\text{II}}\big|_{\mu^{\text{II}}} + \big[\mathrm{d}\sigma_{\text{FO}} - \mathrm{d}\sigma_{\text{II}}\big]_{\mu_{\text{FO}}} . \tag{4.19}$$

Here the subscript μ^{II} indicates that we evaluate $\mathrm{d}\sigma_{\text{II}}$ at the SCET_{II} resummation scales μ^{II} (given below) in b_T space, and take a numerical inverse Fourier transform in the end.

---

[7]We note that in addition, this leaves fixed-order logarithms of $\mu_0 b_T$ in $\tilde{\gamma}_{\nu,\text{FO}}^i$ that lead to an exponential suppression of the b_T space cross section as $b_T \to \infty$. This increases the numerical stability of the inverse Fourier transform.

The subscript μ_{FO} indicates that it is instead evaluated at common fixed-order scales μ_{FO}, which can be done directly in momentum space.

Analogous to the discussion for $\mathrm{SCET_I}$, the term in square brackets in eq. (4.19) is by construction a pure nonsingular power correction at small q_T. This is illustrated in the left panel of figure 4.4, which shows that the difference (green dotted) between the full QCD result (solid orange) and the $\mathrm{SCET_{II}}$ singular result (dashed blue) indeed vanishes like a power as $q_T \to 0$ along the line of fixed $\mathcal{T} = q_T$.

Approaching $q_T \sim \mathcal{T} \sim Q$, the q_T resummation must again be turned off to ensure the delicate cancellations between singular and nonsingular contributions and to properly recover the correct fixed-order result for the spectrum. We achieve this by constructing hybrid profile scales that depend on both b_T and q_T, and undergo a continuous deformation away from the canonical b_T scales in eq. (4.18) as a function of the target q_T value,

$$\mu_{B,S}^{\mathrm{II}}(q_T, b_T)\,, \nu_{B,S}^{\mathrm{II}}(q_T, b_T) \to \mu_H^{\mathrm{II}} = \mu_{\mathrm{FO}} \quad \text{for} \quad q_T \to Q\,. \tag{4.20}$$

We note that μ_0 does not need to asymptote to μ_{FO} towards large q_T because its effect on the matched result is already turned off as $\nu_S^{\mathrm{II}} \to \nu_B^{\mathrm{II}}$. In this limit, the first and last term in eq. (4.19) exactly cancel, leaving the fixed-order result $\mathrm{d}\sigma_{\mathrm{FO}}$.

We strive to achieve eq. (4.20) and the perturbativity requirements in the simplest possible way. We choose central scales as

$$\mu_H^{\mathrm{II}} = \nu_B^{\mathrm{II}} = \mu_{\mathrm{FO}}\,, \quad \mu_B^{\mathrm{II}} = \mu_S^{\mathrm{II}} = \nu_S^{\mathrm{II}} = \mu_{\mathrm{FO}}\, f_{\mathrm{run}}^{\mathrm{II}}\!\left(\frac{q_T}{Q}, \frac{b_0}{b^*(b_T)\, Q}\right)\,, \quad \mu_0 = \frac{b_0}{b^*(b_T)}\,, \tag{4.21}$$

where $f_{\mathrm{run}}^{\mathrm{II}}$ is a hybrid profile function given by

$$f_{\mathrm{run}}^{\mathrm{II}}(x, y) = 1 + g_{\mathrm{run}}(x)(y - 1)\,. \tag{4.22}$$

It controls the amount of resummation by adjusting the slope of the scales in b_T space as a function of q_T/Q via the function

$$g_{\mathrm{run}}(x) = \begin{cases} 1 & 0 < x \le x_1\,, \\ 1 - \frac{(x-x_1)^2}{(x_2-x_1)(x_3-x_1)} & x_1 < x \le x_2\,, \\ \frac{(x-x_3)^2}{(x_3-x_1)(x_3-x_2)} & x_2 < x \le x_3\,, \\ 0 & x_3 \le x\,. \end{cases} \tag{4.23}$$

As a result, for $q_T \le x_1 Q$, the slope is unity yielding the canonical resummation, while for $q_T \ge x_3 Q$, the slope vanishes so the resummation is fully turned off. In between, the slope smoothly transitions from one to zero, which transitions the resummation from being canonical to being turned off. This is illustrated in the right panel of figure 4.4. We use the same transition points $(x_1, x_2, x_3) = (0.2, 0.5, 0.8)$ as for $\mathrm{SCET_I}$, which is supported by figure 4.4.

We note that our approach differs from the hybrid profile scales introduced in ref. [399]. While the latter also satisfy the requirement in eq. (4.20), they do not reproduce the exact

canonical b_T-space scales for $q_T \ll Q$ because they introduce a profile shape directly in b_T space.

As discussed below eq. (2.207), we require a nonperturbative prescription when the canonical value of μ_0 (or μ_S^{II}, or μ_B^{II}) approaches the Landau pole $b_0/b_T \sim \Lambda_{\mathrm{QCD}}$. This is encoded in evaluating the hybrid scales at $b^*(b_T)$ rather than b_T itself,

$$b^*(b_T) = \frac{b_T}{\sqrt{1 + b_T^2/b_{\mathrm{max}}^2}} \,, \tag{4.24}$$

where $b_0/b_{\mathrm{max}} \gtrsim \Lambda_{\mathrm{QCD}}$ ensures that all scales are canonical for small $b_T \approx b^*$, but remain perturbative for large b_T where $b^* \to b_{\mathrm{max}}$, as shown in the inset in the right panel of figure 4.4. In practice we pick

$$b_0/b_{\mathrm{max}} = 1\,\mathrm{GeV} \,, \tag{4.25}$$

in keeping with our choice of nonperturbative turn-off parameter in the SCET$_{\mathrm{I}}$ case. The functional form of eq. (4.24) is the same as in the standard b^* prescription [185, 251], although any other functional form with the same asymptotic behavior is also viable. We stress, however, that a key difference in our case is that b^* only affects the scales, so it essentially serves the same purpose as the x_0 nonperturbative cutoff in the SCET$_{\mathrm{I}}$ scales in eq. (4.10). By contrast, the standard b^* prescription corresponds to a *global* replacement of b_T by b^*, including the measurement itself. For the single-differential q_T spectrum, this global replacement induces power corrections $\mathcal{O}(b_T^2/b_{\mathrm{max}}^2)$ that scale like a generic nonperturbative contribution. While they might complicate the extraction of nonperturbative model parameters from data [400], they are not a critical issue.

For the double-differential case, we find that a standard b^* prescription does in fact not work. This is because substituting b^* for b_T in the physical measurement renders Fourier integrals of the double-differential SCET$_{\mathrm{II}}$ soft function divergent, at least at fixed order (i.e., without Sudakov suppression). This can be seen from eqs. (4.59) and (4.60), which only depend on $x = b_T \mathcal{T}$. Substituting b^* for b_T makes them asymptote to a constant for any given $\mathcal{T}$, which upsets their required asymptotic behavior $\sim 1/x^2$. Physically this means that the deformation of the measurement at large b_T also deforms the observable of interest, i.e., the dependence on $\mathcal{T}$.

Perturbative uncertainties. To estimate the resummation uncertainty for $\mathrm{d}\sigma_{\mathrm{II}}^{\mathrm{match}}$, we adopt the set of profile scale variations introduced for the SCET$_{\mathrm{II}}$-like jet veto in ref. [67]. They are given by

$$\mu_S^{\mathrm{II}} = \mu_{\mathrm{FO}} \left[f_{\mathrm{vary}}\left(\frac{q_T}{Q}\right) \right]^{v_{\mu_S}} f_{\mathrm{run}}^{\mathrm{II}}\left(\frac{q_T}{Q}, \frac{b_0}{b^*Q}\right) ,$$

$$\nu_S^{\mathrm{II}} = \mu_{\mathrm{FO}} \left[f_{\mathrm{vary}}\left(\frac{q_T}{Q}\right) \right]^{v_{\nu_S}} f_{\mathrm{run}}^{\mathrm{II}}\left(\frac{q_T}{Q}, \frac{b_0}{b^*Q}\right) ,$$

$$\mu_B^{\mathrm{II}} = \mu_{\mathrm{FO}} \left[f_{\mathrm{vary}}\left(\frac{q_T}{Q}\right) \right]^{v_{\mu_B}} f_{\mathrm{run}}^{\mathrm{II}}\left(\frac{q_T}{Q}, \frac{b_0}{b^*Q}\right) ,$$

$$\nu_B^{\mathrm{II}} = \mu_{\mathrm{FO}} \left[f_{\mathrm{vary}}\left(\frac{q_T}{Q}\right) \right]^{v_{\nu_B}} , \tag{4.26}$$
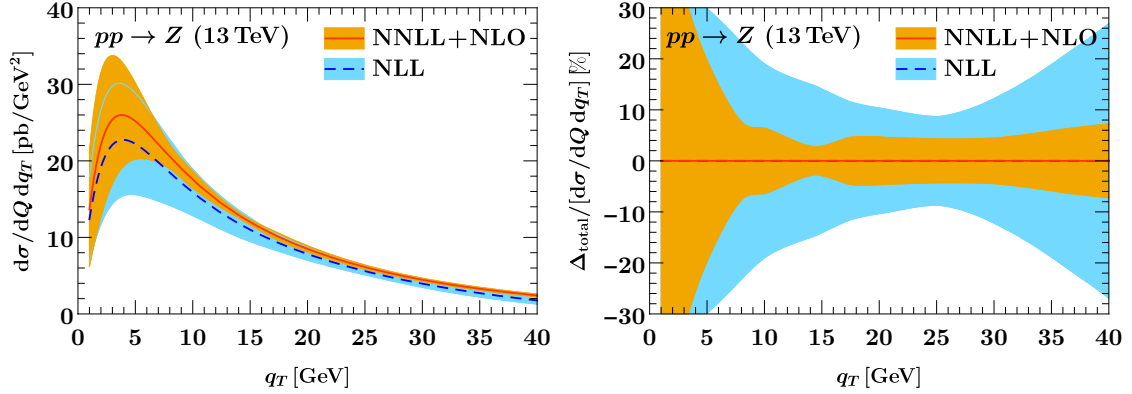
Figure 4.5: The single-differential q_T spectrum at NLL (blue) and NNLL+NLO (orange), using the q_T resummation method described in the text. The bands indicate $\Delta_{\mathrm{II}} \oplus \Delta_{\mathrm{FO}}$. In the right panel, the uncertainties are shown as percent differences relative to the central result at each order.

where each of the four variation exponents can be $v_i = \{+1, 0, -1\}$, and f_{vary} was given in eq. (4.12). The central scale choice corresponds to $(v_{\mu_S}, v_{\nu_S}, v_{\mu_B}, v_{\nu_B}) = (0, 0, 0, 0)$, and a priori there are 80 possible different combinations of the v_i. Since the arguments of the resummed logarithms are ratios of scales, some combinations of scale variations will lead to variations of these arguments that are larger than a factor of two, and therefore should be excluded [67]. After dropping these combinations we are left with 36 different scale variations for the SCET$_{\mathrm{II}}$ regime. We add two independent variations of $b_0/b_{\max} = \{0.5\,\mathrm{GeV}, 2\,\mathrm{GeV}\}$ to probe the uncertainty in our nonperturbative prescription. The SCET$_{\mathrm{II}}$ resummation uncertainty Δ_{II} is then determined as the maximum absolute deviation from the central result among all 38 variations. For simplicity we again refrain from variations of the transition points. As for SCET$_{\mathrm{I}}$, Δ_{FO} is estimated by overall variations of μ_{FO} by a factor of two, which is inherited by all SCET$_{\mathrm{II}}$ scales, so it probes the fixed-order uncertainties while leaving the resummed logarithms invariant. The total uncertainty estimate for $\mathrm{d}\sigma_{\mathrm{II}}^{\mathrm{match}}$ is then obtained as

$$\Delta_{\mathrm{total}}^{\mathrm{II}} = \Delta_{\mathrm{II}} \oplus \Delta_{\mathrm{FO}} \,. \tag{4.27}$$

The matched result $\mathrm{d}\sigma_{\mathrm{II}}^{\mathrm{match}}$ in eq. (4.19) provides a prediction for the double-differential spectrum that covers the part of phase space where $\mathcal{T} \sim q_T$.

Results for the single-differential spectrum. Since we are using a new method to perform the q_T resummation, we also briefly consider the single-differential q_T spectrum as a sanity check of our setup. The setup described in this section immediately carries over to the single-differential spectrum. In figure 4.5 we show the q_T spectrum at the NNLL+NLO order we are aiming for in the double-differential spectrum, as well as one order lower at NLL, and with the uncertainties estimated as described above. The results look very reasonable, providing us with confidence in our q_T resummation procedure. Note that there is a slight pinch in the uncertainty bands around $q_T = 15\,\mathrm{GeV}$, indicating that

the uncertainties there are likely a bit underestimated. This is an artifact of scale variations that is not unusual to be seen in resummed spectrum predictions.

4.2.4 SCET$_+$: $\mathcal{T} \ll q_T \ll \sqrt{Q\mathcal{T}}$

This regime is characterized by the presence of intermediate collinear-soft modes that contribute both to the q_T and the $\mathcal{T}$ measurement, which uniquely fixes their scaling. Central soft modes only contribute to $\mathcal{T}$ as in SCET$_I$, while the energetic collinear modes only contribute to q_T as in SCET$_{II}$,

$$
\begin{aligned}
n_a\text{-collinear:} \quad & p^\mu \sim \left(\tfrac{q_T^2}{Q}, Q, q_T\right), & n_a\text{-collinear-soft:} \quad & p^\mu \sim \left(\mathcal{T}, \tfrac{q_T^2}{\mathcal{T}}, q_T\right), \\
n_b\text{-collinear:} \quad & p^\mu \sim \left(Q, \tfrac{q_T^2}{Q}, q_T\right), & n_b\text{-collinear-soft:} \quad & p^\mu \sim \left(\tfrac{q_T^2}{\mathcal{T}}, \mathcal{T}, q_T\right), \\
\text{soft:} \quad & p^\mu \sim \left(\mathcal{T}, \mathcal{T}, \mathcal{T}\right). &&
\end{aligned}
\tag{4.28}
$$

The collinear-soft modes have the same virtuality as the collinear modes, $p^2 \sim q_T^2$, but live at more central rapidity $e^{|y|} \sim q_T/\mathcal{T}$, which is small compared to the rapidity $e^{|y|} \sim Q/q_T$ of the collinear modes. Hence, the two have a SCET$_{II}$-like relation and become a single collinear mode in the SCET$_I$ limit $q_T \sim \sqrt{Q\mathcal{T}}$. At the same time, the collinear-soft and soft modes have a SCET$_I$-like relation, being separated in virtuality, and become a single soft mode in the SCET$_{II}$ limit $\mathcal{T} \sim q_T$. In this way, SCET$_+$ is able to connect the SCET$_I$ and SCET$_{II}$ regimes. This is similar to the collinear-soft mode originally introduced in ref. [194], which instead connected two SCET$_I$ theories.

The cross section in SCET$_+$ factorizes as [195]

$$
\frac{\mathrm{d}\sigma_+}{\mathrm{d}Q\,\mathrm{d}Y\,\mathrm{d}q_T\,\mathrm{d}\mathcal{T}} = \sum_{i,j} H_{ij}(Q,\mu) \int \mathrm{d}^2\vec{k}_a\, B_i(x_a, \vec{k}_a, \mu, \nu/\omega_a) \int \mathrm{d}^2\vec{k}_b\, B_j(x_b, \vec{k}_b, \mu, \nu/\omega_b) \tag{4.29}
$$

$$
\times \int \mathrm{d}\ell_a^+ \int \mathrm{d}^2\vec{\ell}_a\, \mathcal{S}_i(\ell_a^+, \vec{\ell}_a, \mu, \nu) \int \mathrm{d}\ell_b^- \int \mathrm{d}^2\vec{\ell}_b\, \mathcal{S}_j(\ell_b^-, \vec{\ell}_b, \mu, \nu)
$$

$$
\times \int \mathrm{d}k\, S_i(k,\mu)\, \delta\big(q_T - |\vec{k}_a + \vec{k}_b + \vec{\ell}_a + \vec{\ell}_b|\big)\, \delta\Big(\mathcal{T} - \frac{\omega_a \ell_a^+}{Q_a} - \frac{\omega_b \ell_b^-}{Q_b} - k\Big),
$$

which holds up to power corrections

$$
\frac{\mathrm{d}\sigma}{\mathrm{d}Q\,\mathrm{d}Y\,\mathrm{d}q_T\,\mathrm{d}\mathcal{T}} = \frac{\mathrm{d}\sigma_+}{\mathrm{d}Q\,\mathrm{d}Y\,\mathrm{d}q_T\,\mathrm{d}\mathcal{T}} \left[1 + \mathcal{O}\Big(\frac{q_T^2}{\mathcal{T}Q}, \frac{\mathcal{T}^2}{q_T^2}\Big)\right]. \tag{4.30}
$$

The hard function is the same as before. The beam functions are the q_T-dependent ones from SCET$_{II}$, while the soft function is the $\mathcal{T}$-dependent one from SCET$_I$. The new ingredient is the double-differential collinear-soft function $\mathcal{S}_i(k, \vec{k}_T, \mu, \nu)$, which encodes the contributions of the collinear-soft modes to both q_T and $\mathcal{T}$. Like the soft function it is defined as a matrix element of eikonal Wilson lines, but like the beam functions it describes radiation that goes into a definite hemisphere.

Equation (4.29) can be interpreted as a refactorization of the double-differential SCET_{I} and SCET_{II} cross sections [195], which precisely reflects the relation between the EFT modes described above. Expanding the SCET_{I} double-differential beam function in the limit $q_T \ll \sqrt{Q\mathcal{T}}$, it factorizes into the SCET_{II} beam function and the collinear-soft function,

$$B_q(\omega k, x, \vec{k}_T, \mu) = \int \mathrm{d}^2 \vec{\ell}_T \, B_q(x, \vec{k}_T - \vec{\ell}_T, \mu, \nu/\omega) \, \mathcal{S}_\kappa(k, \vec{\ell}_T, \mu, \nu) \left[1 + \mathcal{O}\left(\frac{k_T^2}{\omega k}\right) \right]. \quad (4.31)$$

The ν dependence of the two terms on the right-hand side must cancel, while their μ dependence must combine into that of the left-hand side. This allows us to completely fix the RGE of the collinear-soft function, where in b_T space we have

$$\mu \frac{\mathrm{d}}{\mathrm{d}\mu} \tilde{\mathcal{S}}_i(k, b_T, \mu, \nu) = \int \mathrm{d}k' \, \gamma_{\mathcal{S}}^i(k - k', \mu, \nu) \, \tilde{\mathcal{S}}_i(k', b_T, \mu, \nu) \,,$$

$$\nu \frac{\mathrm{d}}{\mathrm{d}\nu} \tilde{\mathcal{S}}_i(k, b_T, \mu, \nu) = \frac{1}{2} \tilde{\gamma}_\nu^i(b_T, \mu) \, \tilde{\mathcal{S}}_i(k, b_T, \mu, \nu) \,,$$

$$\gamma_{\mathcal{S}}^i(k, \mu, \nu) = -2\Gamma_{\text{cusp}}^i(\alpha_s) \, \mathcal{L}_0\left(k, \frac{\mu^2}{\nu}\right) + \gamma_{\mathcal{S}}^i[\alpha_s(\mu)]\delta(k) \,, \quad (4.32)$$

and all anomalous dimensions can be inferred from consistency,[8]

$$-\gamma_S^i(\alpha_s) = \gamma_{\mathcal{S}}^i(\alpha_s) = \tilde{\gamma}_S^i(\alpha_s) \,, \qquad -\gamma_{S\,n}^i = \gamma_{\mathcal{S}\,n}^i = \tilde{\gamma}_{S\,n}^i \,. \quad (4.33)$$

Similarly, expanding the SCET_{II} double-differential soft function in the limit $\mathcal{T} \ll q_T$, it factorizes into the SCET_{I} soft function and the two n_a-collinear-soft and n_b-collinear-soft functions,

$$S_\kappa(k, \vec{k}_T, \mu, \nu) = \int \mathrm{d}^2 \vec{\ell}_T \int \mathrm{d}\ell_a^+ \, \mathcal{S}_\kappa(\ell_a^+, \vec{\ell}_T, \mu, \nu) \int \mathrm{d}\ell_b^- \, \mathcal{S}_\kappa(\ell_b^-, \vec{k}_T - \vec{\ell}_T, \mu, \nu)$$

$$\times S_\kappa\left(k - \frac{\omega_a \ell_a^+}{Q_a} - \frac{\omega_b \ell_b^-}{Q_b}\right) \left[1 + \mathcal{O}\left(\frac{k^2}{k_T^2}\right) \right]. \quad (4.34)$$

Since the left-hand side does not depend on $\omega_{a,b}$ and $Q_{a,b}$, this dependence must also drop out on the right-hand side, and therefore in the whole SCET_+ cross section in eq. (4.29). To see this explicitly, first recall that the large label momenta and the distance measures satisfy $\omega_a \omega_b = Q_a Q_b = Q^2$. In addition, boost invariance at the level of the collinear-soft matrix element implies that $\mathrm{d}\ell_a^+ \, \mathcal{S}_\kappa(\ell_a^+, \vec{k}_T, \mu, \nu)$ can only depend on the product $\ell_a^+ \nu$ (and

---

[8] We note that ref. [195] incorrectly did not distinguish between $\gamma_B^i(\alpha_s)$ and $\tilde{\gamma}_B^i(\alpha_s)$. This lead to the noncusp contribution to the collinear-soft anomalous dimension being missing in their eq. (3.26), whereas the difference is in fact nonzero already at two loops, c.f. eq. (C.11).

analogously for ℓ_b^-).[9] Hence, we can rewrite

$$
\mathrm{d}\ell_a^+ \, \mathcal{S}_\kappa(\ell_a^+, \vec{\ell}_a, \mu, \nu) \, \mathrm{d}\ell_b^- \, \mathcal{S}_\kappa(\ell_b^-, \vec{\ell}_b, \mu, \nu) \, \delta\Big(\mathcal{T} - \frac{\omega_a \ell_a^+}{Q_a} - \frac{\omega_b \ell_b^-}{Q_b} - k\Big)
$$
$$
= \mathrm{d}k_a^+ \, \mathcal{S}_\kappa\Big(k_a^+, \vec{\ell}_a, \mu, \frac{Q_a \nu}{\omega_a}\Big) \, \mathrm{d}k_b^- \, \mathcal{S}_\kappa\Big(k_b^-, \vec{\ell}_b, \mu, \frac{Q_b \nu}{\omega_b}\Big) \, \delta(\mathcal{T} - k_a^+ - k_b^- - k)
$$
$$
= \mathrm{d}k_a^+ \, \mathcal{S}_\kappa(k_a^+, \vec{\ell}_a, \mu, \nu) \, \mathrm{d}k_b^- \, \mathcal{S}_\kappa(k_b^-, \vec{\ell}_b, \mu, \nu) \, \delta(\mathcal{T} - k_a^+ - k_b^- - k)\,, \tag{4.35}
$$

where in the first step we changed variables from $\ell_{a,b}^\pm$ to $k_a^+ = \omega_a \ell_a^+ / Q_a$ and $k_b^- = \omega_b \ell_b^- / Q_b$. In the second step we performed the rapidity evolution from $\nu_{a,b} \equiv Q_{a,b} \nu / \omega_{a,b}$ back to a common ν at fixed μ [see eq. (D.5)], for which the rapidity evolution factors exactly cancel because

$$
\ln \frac{\nu_a}{\nu} + \ln \frac{\nu_b}{\nu} = \ln \frac{Q_a Q_b}{\omega_a \omega_b} = 0 \,. \tag{4.36}
$$

The SCET$_+$ factorization in eq. (4.29) fully disentangles the physics at the following SCET$_+$ canonical energy and rapidity scales:

$$
\mu_H^+ \sim Q\,, \qquad \mu_B^+ \sim q_T\,, \qquad \mu_\mathcal{S}^+ \sim q_T\,, \qquad \mu_S^+ \sim \mathcal{T}\,,
$$
$$
\nu_B^+ \sim Q\,, \qquad \nu_\mathcal{S}^+ \sim q_T^2/\mathcal{T}\,. \tag{4.37}
$$

As for SCET$_\mathrm{II}$, we perform the q_T resummation in b_T space, transforming the vectorial convolutions in eq. (4.29) into simple products. In b_T space, the canonical scales are

$$
\mu_H^+ \sim Q\,, \qquad \mu_B^+ \sim b_0/b_T\,, \qquad \mu_\mathcal{S}^+ \sim b_0/b_T\,, \qquad \mu_S^+ \sim \mathcal{T}\,,
$$
$$
\nu_B^+ \sim Q\,, \qquad \nu_\mathcal{S}^+ \sim (b_0/b_T)^2/\mathcal{T}\,. \tag{4.38}
$$

By evaluating all functions at their natural scales and evolving them to common scales, all logarithms of large scale ratios in the problem are resummed, e.g.,

$$
\frac{(b_0/b_T)^2}{Q\mathcal{T}} \sim \frac{\nu_\mathcal{S}^+}{\nu_B^+}\,, \qquad \frac{\mathcal{T}}{b_0/b_T} \sim \frac{\mu_S^+}{\mu_\mathcal{S}^+}\,, \qquad \frac{b_0/b_T}{Q} \sim \frac{\mu_B^+}{\mu_H^+} \sim \frac{\mu_\mathcal{S}^+}{\mu_H^+}\,, \qquad \frac{\mathcal{T}}{Q} \sim \frac{\mu_S^+}{\mu_H^+}\,. \tag{4.39}
$$

The logarithms of the first ratio appear in the double-differential SCET$_\mathrm{I}$ beam function in the limit $q_T \ll \sqrt{Q\mathcal{T}}$, and are resummed in SCET$_+$ by the additional ν evolution in the refactorization in eq. (4.31). Similarly, logarithms of the second ratio appear in the double-differential SCET$_\mathrm{II}$ soft function in the limit $\mathcal{T} \ll q_T$, and are resummed in SCET$_+$ by the additional μ evolution in eq. (4.34). Our framework to match between the rich logarithmic structure predicted by eq. (4.29) and the two boundary regimes is the subject of section 4.4.

---

[9]More specifically, the rapidity regulator softly breaks the RPI-III invariance of SCET, see section 2.2.3 and the implementation of the regulator for collinear-soft Wilson lines in eq. (2.163). To restore it, ν must transform under RPI-III like $\bar{n} \cdot p$ in each n-collinear-soft sector. The RPI-III transformation of the explicit measurement δ function in the matrix element is canceled by the corresponding integration measure in eqs. (4.29) and (4.34). Therefore, RPI-III invariance implies that each collinear-soft function can only depend on the RPI-III invariant combination $\nu \, n \cdot k$.

4.2.5 Outer space

We now briefly discuss the outer phase-space regions left blank in figure 4.2. The region above the SCET$_{\mathrm{II}}$ regime is characterized by the hierarchy $q_T \ll \mathcal{T} \ll \sqrt{Q\mathcal{T}}$, while the region to the right of the SCET$_{\mathrm{I}}$ regime corresponds to $\mathcal{T} \ll \sqrt{Q\mathcal{T}} \ll q_T$. Both regions are power suppressed.

As we have discussed in section 4.2.3, only the soft function contributes to $\mathcal{T}$ in SCET$_{\mathrm{II}}$, as the collinear contribution is power suppressed. However, for $q_T \ll \mathcal{T}$, even the soft contribution to $\mathcal{T}$ becomes power suppressed. In particular, for a single real emission at fixed $\mathcal{O}(\alpha_s)$, the region $\mathcal{T} > q_T$ is kinematically forbidden both in SCET$_{\mathrm{II}}$ as well as in full QCD. At higher orders only (soft) emissions that are mostly back-to-back such that their transverse momenta largely cancel can fill out this region. The cross section in this region is power suppressed by $\mathcal{O}(q_T^2/\mathcal{T}^2)$. Equivalently, expanding the SCET$_{\mathrm{II}}$ factorization of the double-differential cross section in the limit $q_T \ll \mathcal{T}$ reduces it to the single-differential q_T spectrum with an overall $\delta(\mathcal{T})$, which we exploit in our numerical implementation, cf. eq. (4.52). Physically this means that by integrating the double spectrum in SCET$_{\mathrm{II}}$ up to some $\mathcal{T}_{\mathrm{cut}} \gg q_T$, we recover the single-differential q_T spectrum, while the effect of the cut is power suppressed in this limit. Note that there is also a contribution from double-parton scattering [401–404] in this region, where the two jets produced in the second interaction alongside the Z boson are naturally back to back and not power suppressed. This contribution is still not expected to much exceed the single-parton scattering contribution because double-parton scattering itself is power suppressed by $\mathcal{O}(\Lambda_{\mathrm{QCD}}^2/\mathcal{T}^2)$, with $\mathcal{T}$ setting the scale of the second hard scatter producing the back-to-back jets.

Similarly, in the limit $\sqrt{Q\mathcal{T}} \ll q_T$, even the contribution from collinear radiation to q_T becomes power suppressed in SCET$_{\mathrm{I}}$ [cf. eq. (4.41)], and at leading power we recover the single-differential $\mathcal{T}$ spectrum with an overall $\delta(q_T)$. This is analogous to the relation between the regimes 1 and 2 for a jet veto with a jet rapidity cut in ref. [2], where the effect of a very forward jet rapidity cut (the auxiliary measurement) on collinear radiation becomes power suppressed. An additional subtlety for $\sqrt{Q\mathcal{T}} \ll q_T$ is that very energetic forward radiation with energy $\sim q_T^2/\mathcal{T}$ can theoretically contribute [195], pushing the hard scale up to $q_T^2/\mathcal{T} \gg Q$. However, the cross section in this kinematic configuration is very strongly suppressed by the PDFs, so we choose to describe it at fixed order.

The above analysis justifies focusing on the shaded regions of phase space in figure 4.2, corresponding to the main SCET$_{\mathrm{I}}$, SCET$_{\mathrm{II}}$, and SCET$_+$ regimes.

4.3 RG evolution of double-differential matrix elements

A specific challenge in evaluating the resummed SCET$_{\mathrm{I}}$ and SCET$_{\mathrm{II}}$ cross sections is that they involve the action of the renormalization group evolution on the double-differential beam or soft function that have a more intricate structure than their single-differential counterparts. In particular, the matrix elements have an a priori arbitrary dependence on certain dimensionless combinations of their arguments and do not admit a straightforward

evaluation in terms of powers of logarithms or a basis of plus distributions.

4.3.1 Double-differential beam function

For the double-differential SCET$_{\mathrm{I}}$ beam function, the task at hand is to analytically evaluate convolutions of the form

$$Q_i \int \mathrm{d}k' \, \mathcal{V}_\eta(k - k', \mu) \, \mathcal{I}_{qj}(Q_i k', z, \vec{k}_T, \mu^2) \,, \tag{4.40}$$

between the distribution-valued RG evolution kernel and the double-differential matching coefficient, i.e., *before* performing the numerical convolution with the PDF to maximize evaluation speed. What is more, the outcome of eq. (4.40) is again a distribution in k, $\vec{k}_T$, and (potentially) in z, and in full generality we need either its value at finite $\mathcal{T} = k$ or its integral over $k \leq \mathcal{T}_{\mathrm{cut}}$, and similarly for $q_T = |\vec{k}_T|$ and $|\vec{k}_T| \leq q_T^{\mathrm{cut}}$. (There is no nontrivial cross term with the opposite beam function at this order.)

To evaluate eq. (4.40), it is convenient to decompose the matching coefficients as

$$\mathcal{I}_{qj}(t, z, \vec{k}_T, \mu) = \delta(\vec{k}_T) \, \mathcal{I}_{qj}(t, z, \mu) + \Delta \mathcal{I}_{qj}(t, z, \vec{k}_T, \mu) \,, \tag{4.41}$$

where $\mathcal{I}_{qj}(t, z, \mu)$ is the matching coefficient for the inclusive quark beam function, whose contribution to eq. (4.40) can be evaluated in a straightforward way. The $\Delta \mathcal{I}_{qj}$ piece can be interpreted as a correction over the limit $t \ll k_T^2$, where recoil from collinear radiation is power suppressed and the double-differential beam function becomes proportional to $\delta(\vec{k}_T)$. Specifically, it scales as

$$\Delta \mathcal{I}_{qj}(t, z, \vec{k}_T, \mu) \sim \frac{1}{t} \frac{1}{k_T^2} \, \mathcal{O}\!\left(\frac{t}{k_T^2}\right) \quad \text{for} \quad t \ll k_T^2 \,, \tag{4.42}$$

and by construction satisfies

$$\int \mathrm{d}^2\vec{k}_T \, \Delta \mathcal{I}_{qj}(t, z, \vec{k}_T, \mu) = 0 \,. \tag{4.43}$$

At one loop it can be extracted from the full calculation of $\mathcal{I}_{qj}(t, z, \vec{k}_T, \mu)$ [398, 405],

$$\Delta \mathcal{I}_{qj}(t, z, \vec{k}_T, \mu) = \frac{\alpha_s(\mu)}{4\pi} \Delta I_{qj}^{(1)}(t, z, \vec{k}_T) + \mathcal{O}(\alpha_s^2) \,,$$
$$\Delta I_{qj}^{(1)}(t, z, \vec{k}_T) = \frac{\theta(t)}{t} \tilde{P}_{qj}^{(0)}(z) \left[\frac{1}{\pi}\delta\!\left(k_T^2 - \frac{1-z}{z}t\right) - \delta(\vec{k}_T)\right] \,, \tag{4.44}$$

using the shorthand

$$\tilde{P}_{qj}^{(0)}(z) \equiv P_{qj}^{(0)}(z) - \delta_{qj}\delta(1-z)\frac{\gamma_{B\,0}^q}{2} = \begin{cases} 2C_F \mathcal{L}_0(1-z)(1+z^2)\,, & j = q\,, \\ 2T_F\left[(1-z)^2 + z^2\right]\,, & j = g\,. \end{cases}$$

The second line in eq. (4.44) is regular in t because the term in square brackets vanishes as $t \to 0$. After accumulating over the transverse plane up to $q_T^{\mathrm{cut}} > 0$, we have

$$\int \mathrm{d}^2\vec{k}_T \, \theta(q_T^{\mathrm{cut}} - |\vec{k}_T|) \, \Delta I_{qj}^{(1)}(t, z, \vec{k}_T) = -\frac{\theta(t)}{t}\tilde{P}_{qj}^{(0)}(z)\,\theta\!\left[(q_T^{\mathrm{cut}})^2 < \frac{1-z}{z}t\right] \,. \tag{4.45}$$

So far, these are the fixed-order results for $\eta = 0$ in eq. (4.40). The key insight allowing for an efficient organization of the result also at finite $\eta \neq 0$ is that also *after* performing the convolution with the measurement inserted, the final result can only depend on a certain dimensionless combination r of the final measured quantities that is dictated by the power counting, e.g. $r = (q_T^2)/(Q_i \mathcal{T})$ for the double spectrum. This is because ΔI_{qj} is independent of μ, and we can shift the explicit boundary condition μ of the evolution kernel $\propto \mathcal{V}_\eta(k', \mu)$ e.g. to $\mu = \mathcal{T}$ (or $\mathcal{T}_{\rm cut}$) using eq. (A.19) and pull out the resulting factor of $(\mu/\mathcal{T})^{-\eta}$. Depending on the measurement, we distinguish the following four cases for the resulting Mellin kernel in z:

1. cumulant up to $\mathcal{T}_{\rm cut} > 0$, cumulant up to $q_T^{\rm cut} > 0$, $r \equiv (q_T^{\rm cut})^2/(Q_i \mathcal{T}_{\rm cut})$:

$$Q_i \int \mathrm{d}k \int \mathrm{d}^2 \vec{k}_T \, \theta(\mathcal{T}_{\rm cut} - k) \, \theta(q_T^{\rm cut} - |\vec{k}_T|) \int \mathrm{d}k' \, \mathcal{V}_\eta(k - k', \mathcal{T}_{\rm cut}) \, \Delta I_{qj}^{(1)}(Q_i k', z, \vec{k}_T)$$

$$= \theta\Big(r > \frac{1-z}{z}\Big) P_{qj}^{(0)}(z) \frac{e^{-\gamma_E \eta}}{\Gamma(1+\eta)} \Big[-B_{1 - rz/(1-z)}(1+\eta, 0)\Big], \quad (4.46)$$

where $B_x(a, b)$ is the incomplete Beta function,

$$B_x(a, b) = \int_0^x \mathrm{d}t \, t^{a-1}(1-t)^{b-1}. \quad (4.47)$$

2. spectrum at $\mathcal{T} > 0$, cumulant up to $q_T^{\rm cut} > 0$, $r \equiv (q_T^{\rm cut})^2/(Q_i \mathcal{T})$:

$$Q_i \int \mathrm{d}k \int \mathrm{d}^2 \vec{k}_T \, \delta(\mathcal{T} - k) \, \theta(q_T^{\rm cut} - |\vec{k}_T|) \int \mathrm{d}k' \, \mathcal{V}_\eta(k - k', \mathcal{T}) \, \Delta I_{qj}^{(1)}(Q_i k', z, \vec{k}_T) \quad (4.48)$$

$$= \frac{1}{\mathcal{T}} \theta\Big(r > \frac{1-z}{z}\Big) P_{qj}^{(0)}(z) \frac{e^{-\gamma_E \eta}}{\Gamma(1+\eta)} \Big[-\eta B_{1-rz/(1-z)}(1+\eta, 0) - \Big(1 - \frac{rz}{1-z}\Big)^\eta\Big].$$

3. cumulant up to $\mathcal{T}_{\rm cut}$, spectrum at $q_T > 0$, $r \equiv (q_T)^2/(Q_i \mathcal{T}_{\rm cut})$:

$$Q_i \int \mathrm{d}k \int \mathrm{d}^2 \vec{k}_T \, \theta(\mathcal{T}_{\rm cut} - k) \, \delta(q_T - |\vec{k}_T|) \int \mathrm{d}k' \, \mathcal{V}_\eta(k - k', \mathcal{T}_{\rm cut}) \, \Delta I_{qj}^{(1)}(Q_i k', z, \vec{k}_T)$$

$$= \frac{2}{q_T} \theta\Big(r > \frac{1-z}{z}\Big) P_{qj}^{(0)}(z) \frac{e^{-\gamma_E \eta}}{\Gamma(1+\eta)} \Big(1 - \frac{rz}{1-z}\Big)^\eta. \quad (4.49)$$

4. spectrum at $\mathcal{T} > 0$, spectrum at $q_T > 0$, $r \equiv (q_T)^2/(Q_i \mathcal{T})$:

$$Q_i \int \mathrm{d}k \int \mathrm{d}^2 \vec{k}_T \, \delta(\mathcal{T} - k) \, \delta(q_T - |\vec{k}_T|) \int \mathrm{d}k' \, \mathcal{V}_\eta(k - k', \mathcal{T}) \, \Delta I_{qj}^{(1)}(Q_i k', z, \vec{k}_T)$$

$$= \frac{2}{q_T} \frac{1}{\mathcal{T}} P_{qj}^{(0)}(z) \, \mathcal{V}_\eta\Big(1 - \frac{rz}{1-z}\Big) \quad (4.50)$$

In the first three cases the overall θ function cuts off the final PDF integral at

$$z < z_{\rm cut} \equiv \frac{1}{1+r}, \quad (4.51)$$

and the Mellin kernel is regular up to and including z_{cut}. In the last case we instead find a singularity at $z = z_{\text{cut}}$, i.e., the subtraction from $\mathcal{V}_\eta$ now acts directly on the PDF integral. This highlights the richer structure of the double-differential resummation compared to the single-differential case, where the RG evolution that encodes the dependence on the measurement only multiplies fixed functions $I_{ij}^{(n)}(z)$ of the longitudinal momentum fraction, but never acts on the z integral directly. We have also exploited that terms proportional to $\delta(1 - z)$ are cut off since $r > 0$, so we could replace $\tilde{P}_{qj}^{(0)}$ back by $P_{qj}^{(0)}$. Note that the right-hand side depends only on the dimensionless parameters r and η as expected, up to an overall dimensionful Jacobian. It is straightforward to check that for $\eta \to 0$ (at fixed order), the above results reduce to cumulants (spectra) of $\Delta I_{qj}^{(1)}$ itself.

4.3.2 Double-differential soft function

For the double-differential SCET$_{\text{II}}$ soft function, which has been computed in momentum space in ref. [195], the task is to analytically evaluate its Fourier transform to b_T space for a fixed value of $k = \mathcal{T}$ and integrated over $k \leq \mathcal{T}_{\text{cut}}$, respectively. With the result in b_T space at hand, the multiplicative RG evolution can be trivially performed. It is again convenient to decompose the double-differential soft function into separate pieces with distinct power counting,

$$S_i(k, \vec{k}_T, \mu, \nu) = \delta(k)\, S_i(\vec{k}_T, \mu, \nu) + \Delta S_i(k, \vec{k}_T, \mu, \nu)\,. \tag{4.52}$$

Here $S_i(\vec{k}_T, \mu, \nu)$ is the standard single-differential q_T soft function. The second term in eq. (4.52) can again be interpreted as a correction, in this case over the limit $k \gg \vec{k}_T$ where the contribution of soft radiation to the $\mathcal{T} = k$ measurement becomes power suppressed. In momentum space this term satisfies

$$\int dk\, \Delta S_i(k, \vec{k}_T, \mu, \nu) = 0\,, \qquad \Delta S_i(k, \vec{k}_T, \mu, \nu) \ \sim \ \frac{1}{k}\frac{1}{k_T^2}\mathcal{O}\!\left(\frac{k_T^2}{k^2}\right) \quad \text{for} \quad k_T^2 \ll k^2\,. \tag{4.53}$$

Equivalently, in position space we have

$$\int dk\, \Delta \tilde{S}_i(k, b_T, \mu, \nu) = 0\,, \qquad \Delta \tilde{S}_i(k, b_T, \mu, \nu) \ \sim \ \frac{1}{k}\mathcal{O}\!\left(\frac{1}{b_T^2 k^2}\right) \quad \text{for} \quad \frac{1}{b_T^2} \ll k^2\,. \tag{4.54}$$

At one loop, ΔS_i is given by

$$\Delta S_i(k, \vec{k}_T, \mu, \nu) = \frac{\alpha_s(\mu)}{4\pi}\Delta S_{i,1}(k, \vec{k}_T) + \mathcal{O}(\alpha_s^2)\,,$$

$$\Delta S_{i,1}(k, \vec{k}_T) = 4C_i\left[\frac{2}{\pi\mu^3}\mathcal{L}_\Delta\!\left(\frac{k}{\mu}, \frac{k_T^2}{\mu^2}\right) - \delta(k)\mathcal{L}_1(\vec{k}_T, \mu)\right]\,. \tag{4.55}$$

Here we used a two-dimensional plus distribution originally defined in ref. [195],

$$\mathcal{L}_\Delta(x_1, x_2) \equiv \lim_{\beta \to 0} \frac{d}{dx_1}\frac{d}{dx_2}\left[\theta(x_2 - x_1^2)\theta(x_1 - \beta)\ln x_1\,(\ln x_2 - \ln x_1)\right.$$

$$\left. + \frac{1}{4}\,\theta(x_1^2 - x_2)\theta(x_2 - \beta^2)\ln^2 x_2\right]\,. \tag{4.56}$$

The second line in eq. (4.55) is not yet manifestly independent of μ, but can be simplified noting that

$$\mathcal{L}_\Delta(x_1, x_2) - \delta(x_1)\mathcal{L}_1(x_2) = \frac{\mathrm{d}}{\mathrm{d}x_1} \frac{\mathrm{d}}{\mathrm{d}x_2} \theta(x_2 - x_1^2) \left[-\frac{1}{2} \ln^2 \frac{x_1^2}{x_2} \right]. \qquad (4.57)$$

It is straightforward to show this by writing all three distributions in terms of $\theta(x_1 - \beta)$ and $\theta(x_2 - \beta^2)$ for infinitesimal β, collecting terms, and noting that the result is finite as $\beta \to 0$. From eq. (4.57) we can immediately read off the fixed-order double cumulant of $\Delta S_{i,1}$ for $\mathcal{T}_{\mathrm{cut}} > 0$, $q_T^{\mathrm{cut}} > 0$,

$$\int^{\mathcal{T}_{\mathrm{cut}}} \mathrm{d}k \int \mathrm{d}^2\vec{k}_T \, \theta(q_T^{\mathrm{cut}} - |\vec{k}_T|) \, \Delta S_{i,1}(k, \vec{k}_T) = 4C_F \, \theta(q_T^{\mathrm{cut}} - \mathcal{T}_{\mathrm{cut}}) \left[-2 \ln^2 \frac{\mathcal{T}_{\mathrm{cut}}}{q_T^{\mathrm{cut}}} \right], \qquad (4.58)$$

where the dependence on μ drops out as expected. Inserting eq. (4.57) and integrating by parts also yields the cumulant up to $\mathcal{T}_{\mathrm{cut}} > 0$ in position space,

$$\int^{\mathcal{T}_{\mathrm{cut}}} \mathrm{d}k \, \Delta \tilde{S}_{i,1}(k, b_T) = 4C_F \left[\frac{1}{4} x^2 \, {}_3F_4\left(1, 1, 1; 2, 2, 2, 2; -\frac{x^2}{4}\right) - 2 \ln^2 \frac{x e^{\gamma_E}}{2} \right], \qquad (4.59)$$

where $x \equiv b_T \mathcal{T}_{\mathrm{cut}}$ and $_iF_j(x_1, \ldots, x_i; y_1, \ldots, y_j; z)$ is the generalized hypergeometric function. The right hand side of eq. (4.59) asymptotes to $1/x^2$ as $x \to \infty$, as required by the scaling law in eq. (4.54). We also need the spectrum of $\Delta \tilde{S}_{i,1}$ at $\mathcal{T} > 0$ in position space,

$$\Delta \tilde{S}_{i,1}(\mathcal{T}, b_T) = 4C_F \frac{1}{\mathcal{T}} \left[\frac{1}{2} x^2 \, {}_2F_3\left(1, 1; 2, 2, 2; -\frac{x^2}{4}\right) - 4 \ln \frac{x e^{\gamma_E}}{2} \right], \qquad (4.60)$$

where this time $x \equiv b_T \mathcal{T}$ and the term in square brackets again asymptotes to $1/x^2$ as $x \to \infty$. It is interesting to note that an important physical feature of the resummed spectrum we already presented in figure 4.1, namely the smooth suppression towards the intrinsic two-emission region $\mathcal{T} > q_T$, is entirely encoded in eq. (4.60) weighted with the Sudakov evolution factor in b_T space.

4.4 Matching effective theories

4.4.1 Structure of power corrections

An important feature of our EFT setup is that the factorized cross section in SCET_+ differs from the ones in SCET_I and $\mathrm{SCET}_\mathrm{II}$ only by a subset of the power corrections it receives relative to the full QCD result,

$$\frac{\mathrm{d}\sigma_\mathrm{I}}{\mathrm{d}Q \, \mathrm{d}Y \, \mathrm{d}q_T \, \mathrm{d}\mathcal{T}} = \frac{\mathrm{d}\sigma_+}{\mathrm{d}Q \, \mathrm{d}Y \, \mathrm{d}q_T \, \mathrm{d}\mathcal{T}} \left[1 + \mathcal{O}\left(\frac{q_T^2}{\mathcal{T}Q}\right) \right],$$

$$\frac{\mathrm{d}\sigma_\mathrm{II}}{\mathrm{d}Q \, \mathrm{d}Y \, \mathrm{d}q_T \, \mathrm{d}\mathcal{T}} = \frac{\mathrm{d}\sigma_+}{\mathrm{d}Q \, \mathrm{d}Y \, \mathrm{d}q_T \, \mathrm{d}\mathcal{T}} \left[1 + \mathcal{O}\left(\frac{\mathcal{T}^2}{q_T^2}\right) \right]. \qquad (4.61)$$
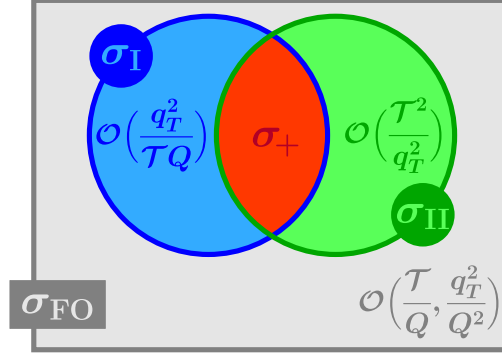
Figure 4.6: Venn diagram of power corrections to the factorized double-differential spectrum. $\mathrm{SCET_I}$ (blue) and $\mathrm{SCET_{II}}$ (green) each capture a set of power corrections that is expanded away in the $\mathrm{SCET_+}$ factorization (red) and the opposite boundary regime. A third class of power corrections to the overall soft-collinear limit is captured by the fixed-order calculation in full QCD (gray).

This is illustrated in figure 4.6, and follows from comparing eq. (4.30) to eq. (4.3) and eq. (4.17), respectively. Crucially, eq. (4.61) also holds when the cross sections are evaluated at common (but not necessarily fixed-order) scales.

For example, both σ_I and σ_+ share a logarithmic singularity with respect to $\mathcal{T}/Q$, which can be resummed by running between the scales of the hard, soft, and (refactorized) beam functions. In $\mathrm{SCET_+}$ this amounts to setting the μ^+ scales to be equal to their μ^I counterparts,

$$\mu_B^+ = \mu_{\mathcal{S}}^+ = \mu_B^\mathrm{I}\,, \qquad \nu_B^+ = \nu_{\mathcal{S}}^+ = \mu_\mathrm{FO}\,, \qquad \mu_S^+ = \mu_S^\mathrm{I}\,, \tag{4.62}$$

such that any large logarithms inside the refactorized beam function in eq. (4.31) are treated at fixed order. We write $\mathrm{d}\sigma_+\big|_{\mu^\mathrm{I}}$ to indicate that $\mathrm{d}\sigma_+$ is evaluated at scales that satisfy eq. (4.62). A natural way to judge the size of the power corrections in eq. (4.61) then is to compare $\mathrm{d}\sigma_+\big|_{\mu^\mathrm{I}}$ to $\mathrm{d}\sigma_\mathrm{I}\big|_{\mu^\mathrm{I}}$, with our choices for μ^I as given in section 4.2.2, i.e., including the whole set of all-order terms from the $\mathcal{T}$ resummation in both of them. This comparison is shown in figure 4.7 for representative choices of fixed $\mathcal{T}$ and q_T at NNLL. We can clearly read off a power-like behavior of the difference $\big[\mathrm{d}\sigma_\mathrm{I}-\mathrm{d}\sigma_+\big]_{\mu^\mathrm{I}}$ (dotted green) as either $q_T \to 0$ for fixed $\mathcal{T}$ (left panel) or $\mathcal{T} \to \infty$ for fixed q_T (right panel). This also provides a nontrivial check on our implementation of σ_I and σ_+. This comparison in figure 4.7 is analogous to the usual procedure of comparing the full-theory result for a cross section with its singular EFT limit at a common scale μ_FO. Here, $\mathrm{SCET_I}$ takes on the role of the full theory, while $\mathrm{SCET_+}$ provides the singular limit, and the comparison is performed at common scales μ^I.

Similarly, both σ_II and σ_+ have a common singular structure as $q_T/Q \to 0$. In this case, resumming the shared logarithmic terms requires running between the hard, beam, and (refactorized) soft function. In $\mathrm{SCET_+}$ this amounts to setting the μ^+ scales to be equal to their μ^II counterparts,

$$\mu_{\mathcal{S}}^+ = \mu_S^+ = \mu_S^\mathrm{II}\,, \qquad \nu_{\mathcal{S}}^+ = \nu_S^\mathrm{II}\,, \tag{4.63}$$

which treats the large logarithms in the refactorized double-differential soft function in
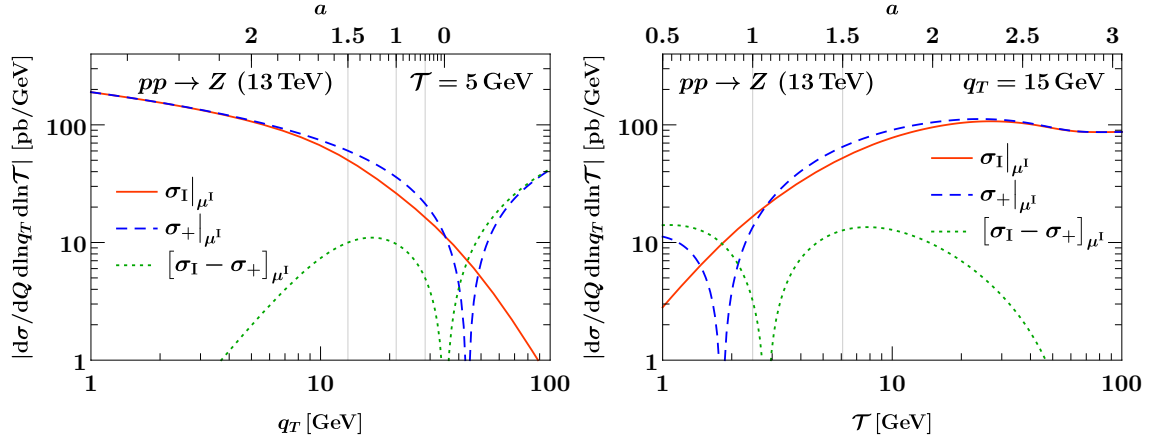
Figure 4.7: Singular/nonsingular comparison between SCET_I and SCET_+ at NNLL as a function of q_T for fixed $\mathcal{T} = 5\,\text{GeV}$ (left) and as a function of $\mathcal{T}$ for fixed $q_T = 15\,\text{GeV}$ (right). The orange solid lines show the full SCET_I result including resummation. The dashed blue lines show the corresponding SCET_+ singular limit with *only* SCET_I resummation. The dotted green lines show their difference, corresponding to the power corrections indicated in eq. (4.61). The thin vertical lines indicate our choice of transition points (a_1, a_2, a_3) with respect to the regime parameter a (upper horizontal axis), as discussed in section 4.4.3.
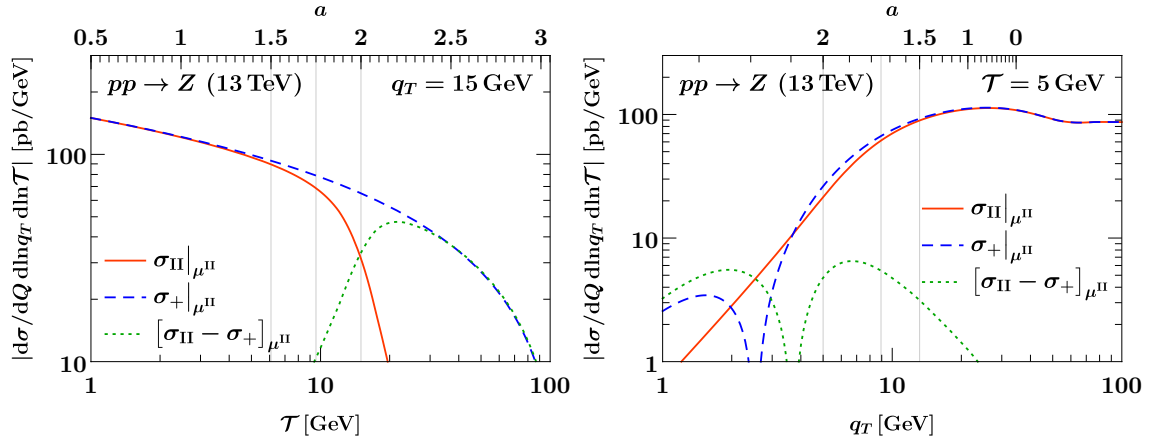
Figure 4.8: Singular/nonsingular comparison between SCET_II and SCET_+ at NNLL as a function of $\mathcal{T}$ for fixed $q_T = 15\,\text{GeV}$ (left) and as a function of q_T for fixed $\mathcal{T} = 5\,\text{GeV}$ (right). The orange solid lines show the full SCET_II result including resummation. The dashed blue lines show the corresponding SCET_+ singular limit with *only* SCET_II resummation. The dotted green lines show their difference, corresponding to the power corrections indicated in eq. (4.61). The thin vertical lines indicate our choice of transition points (a_4, a_5, a_6) with respect to the regime parameter a (upper horizontal axis), as discussed in section 4.4.3.
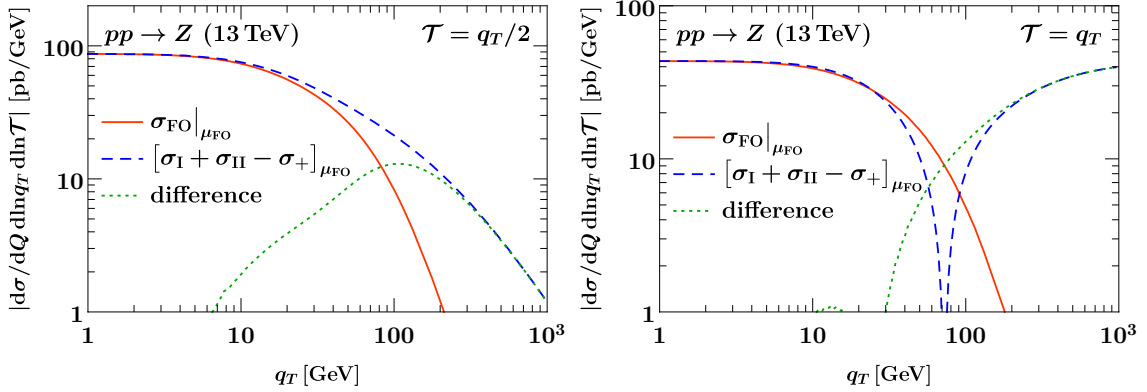
Figure 4.9: Singular/nonsingular comparison between the matched SCET descriptions and QCD at fixed $\mathcal{O}(\alpha_s)$ as a function of q_T for $\mathcal{T} = q_T/2$ (left) and $\mathcal{T} = q_T$ (right). The orange solid line shows the fixed-order QCD double spectrum, the dashed blue the matched SCET result in eq. (4.64), and the dotted green the difference.

eq. (4.34) at fixed order. We denote this choice of scales by $\mathrm{d}\sigma_+\big|_{\mu^{\mathrm{II}}}$, with scale setting in b_T space and the inverse Fourier transform understood as in section 4.2.3. In figure 4.8 we compare $\mathrm{d}\sigma_+\big|_{\mu^{\mathrm{II}}}$ to $\mathrm{d}\sigma^{\mathrm{II}}\big|_{\mu^{\mathrm{II}}}$ at NNLL as a function of $\mathcal{T}$ at fixed q_T (left) and vice versa (right). It is clear that even when evaluated at its intrinsic scales, $\mathrm{d}\sigma_{\mathrm{II}}\big|_{\mu^{\mathrm{II}}}$ (solid orange) exhibits an unresummed singularity as $\mathcal{T}/q_T \ll 1$, which, as expected, is captured by $\mathrm{d}\sigma_+\big|_{\mu^{\mathrm{II}}}$ (dashed blue) up to power corrections (dotted green). This check is highly nontrivial as it involves an additional Fourier transform on both sides of the comparison. We note that the strong kinematic suppression of the double spectrum for $\mathcal{T} \gtrsim q_T$ is correctly captured by SCET$_{\mathrm{II}}$, where central soft modes resolve the phase-space boundary. In SCET$_+$, soft modes have too little energy and collinear-soft modes are too forward to resolve it, leading to large power corrections in this region.

As a final important consequence of figure 4.6, the complete infrared structure of the double-differential spectrum for $q_T \ll Q$ and $\mathcal{T} \ll Q$, i.e., for any hierarchy between q_T and $\mathcal{T}$, is described by adding the SCET$_{\mathrm{I}}$ and SCET$_{\mathrm{II}}$ cross sections and removing the overlap between the two by subtracting the SCET$_+$ cross section,

$$\frac{\mathrm{d}\sigma}{\mathrm{d}Q\,\mathrm{d}Y\,\mathrm{d}q_T\,\mathrm{d}\mathcal{T}} = \left[\frac{\mathrm{d}\sigma_{\mathrm{I}}}{\mathrm{d}Q\,\mathrm{d}Y\,\mathrm{d}q_T\,\mathrm{d}\mathcal{T}} + \frac{\mathrm{d}\sigma_{\mathrm{II}}}{\mathrm{d}Q\,\mathrm{d}Y\,\mathrm{d}q_T\,\mathrm{d}\mathcal{T}} - \frac{\mathrm{d}\sigma_+}{\mathrm{d}Q\,\mathrm{d}Y\,\mathrm{d}q_T\,\mathrm{d}\mathcal{T}} \right]$$
$$\times \left[1 + \mathcal{O}\left(\frac{q_T^2}{Q^2}, \frac{\mathcal{T}}{Q}\right) \right]. \tag{4.64}$$

In figure 4.9 we numerically check this relation at fixed $\mathcal{O}(\alpha_s)$, which requires setting all scales equal to a common μ_{FO}. We plot the comparison as a function of q_T along lines of fixed $\mathcal{T}/q_T = 1/2$ (left) and $\mathcal{T}/q_T = 1$ (right), finding excellent agreement between the full result (solid orange) and the first line on the right-hand side of eq. (4.64) (dashed blue), as evident from the power-like behavior of their difference (dotted green) as $q_T, \mathcal{T} \to 0$.

This singular/nonsingular comparison is qualitatively different from the structure of power corrections in either SCET$_{\mathrm{I}}$ or SCET$_{\mathrm{II}}$ alone, which we already verified in figure 4.3

and figure 4.4. Because $SCET_I$ and $SCET_{II}$ both involve an additional expansion about a specific hierarchy between q_T and $\mathcal{T}$, they incur power corrections $\mathcal{O}(\mathcal{T}^2/q_T^2)$ or $\mathcal{O}(q_T^2/(Q\mathcal{T}))$, respectively. Accordingly, they only recover the singular limit of full QCD when approaching it along specific lines in the $(q_T, \mathcal{T})$ plane. This is different from figure 4.9, where the combined expression in eq. (4.64) (dashed blue) describes the singular limit $q_T, \mathcal{T} \to 0$ along an arbitrary line of approach, with the ratio $q_T/\mathcal{T}$ effectively controlling the "admixture" of power corrections $\mathcal{O}(q_T^2/Q^2)$ and $\mathcal{O}(\mathcal{T}/Q)$, respectively. We have verified that also for other fixed ratios of q_T and $\mathcal{T}$, the singular behavior of full QCD is correctly described.

As a final remark, as noted in ref. [50], this property actually qualifies the expression $d\sigma_I + d\sigma_{II} - d\sigma_+$ for use as a double-differential subtraction term to treat infrared divergences in fixed-order calculations.

4.4.2 Matching formula

The structure of power corrections discussed in the previous section, together with the all-order resummation shared between $SCET_+$ and $SCET_I$ or $SCET_{II}$, suggests the following matching formula to describe all regions of the double-differential spectrum:

$$
d\sigma^{\text{match}} = d\sigma_+\big|_{\mu^+} + \big[d\sigma_I - d\sigma_+\big]_{\mu^I} + \big[d\sigma_{II} - d\sigma_+\big]_{\mu^{II}}
$$
$$
+ \big[d\sigma_{\text{FO}} - d\sigma_I - d\sigma_{II} + d\sigma_+\big]_{\mu_{\text{FO}}} . \tag{4.65}
$$

The only ingredient in this matching formula we have not yet discussed is $d\sigma_+\big|_{\mu^+}$, for which all ingredients in the $SCET_+$ factorization are evaluated at the $SCET_+$ scales μ^+, such that the full RGE of $SCET_+$ is in effect. In the following we describe the requirements on μ^+ to ensure the best possible prediction across phase space. Our precise construction of μ^+ to satisfy all requirements is the subject of section 4.4.3.

In the simplest case, i.e., when the power corrections in eq. (4.30) are small, and thus the $SCET_+$ parametric assumptions are satisfied, μ^+ is given by the canonical $SCET_+$ scales in eq. (4.38). As for μ^{II}, these scales are set in b_T space, followed by an inverse Fourier transform.

As we approach the $SCET_I$ region, the resummation inside the refactorization of the beam function in eq. (4.31) must be turned off,

$$
\left.\begin{array}{l}
\mu_B^+(q_T, \mathcal{T}, b_T) \to \mu_B^I(\mathcal{T}) \\
\mu_S^+(q_T, \mathcal{T}, b_T) \to \mu_B^I(\mathcal{T}) \\
\nu_S^+(q_T, \mathcal{T}, b_T) \to \nu_B^+(q_T, \mathcal{T}, b_T)
\end{array}\right\} \quad \text{for} \quad q_T \to \sqrt{Q\mathcal{T}} . \tag{4.66}
$$

In addition we can identify the soft scales in $SCET_I$ and $SCET_+$ because the soft functions are identical,

$$
\mu_S^+(q_T, \mathcal{T}, b_T) \to \mu_S^I(\mathcal{T}) \quad \text{for} \quad q_T \to \sqrt{Q\mathcal{T}} . \tag{4.67}
$$

These relations must hold for every value of the b_T argument of the scale.

Similarly, as we approach the SCET_{II} region, the scales inside the refactorized soft function eq. (4.34) must become equal

$$
\left.
\begin{array}{l}
\mu_S^+(q_T, \mathcal{T}, b_T) \to \mu_S^{\text{II}}(q_T, b_T) \\[4pt]
\mu_{\mathcal{S}}^+(q_T, \mathcal{T}, b_T) \to \mu_{\mathcal{S}}^{\text{II}}(q_T, b_T) \\[4pt]
\nu_{\mathcal{S}}^+(q_T, \mathcal{T}, b_T) \to \nu_{\mathcal{S}}^{\text{II}}(q_T, b_T)
\end{array}
\right\}
\quad \text{for} \quad q_T \to \mathcal{T}, \tag{4.68}
$$

and we can identify the scales of the common beam function in SCET_{II} and SCET_+,

$$
\left.
\begin{array}{l}
\mu_B^+(q_T, \mathcal{T}, b_T) \to \mu_B^{\text{II}}(q_T, b_T) \\[4pt]
\nu_B^+(q_T, \mathcal{T}, b_T) \to \nu_B^{\text{II}}(q_T, b_T)
\end{array}
\right\}
\quad \text{for} \quad q_T \to \mathcal{T}. \tag{4.69}
$$

Some of the above requirements for the behavior at the boundary are already satisfied by the canonical SCET_+ scales, e.g., the canonical soft scales in SCET_+ and SCET_{I} are simply equal. The challenge in these cases is to extend the scale choice onto the opposite boundary, where they are constrained in a nontrivial way. The nontrivial all-order information in SCET_+ is mostly encoded in the canonical choice of

$$
\nu_{\mathcal{S}}^+(q_T, \mathcal{T}, b_T) = \frac{(b_0/b_T)^2}{\mathcal{T}} \quad \text{for} \quad \mathcal{T} \ll q_T \ll \sqrt{Q\mathcal{T}}, \tag{4.70}
$$

which does not coincide with any scale on either boundary.

It is instructive to explicitly consider the behavior of eq. (4.65) on the SCET_{I} and SCET_{II} phase-space boundaries, as well as in the fixed-order region. By construction, for any choice of μ^+ scales satisfying eqs. (4.66) and (4.67) we have

$$
\mathrm{d}\sigma_+\big|_{\mu^+} \to \mathrm{d}\sigma_+\big|_{\mu^{\text{I}}} \quad \text{for} \quad q_T \to \sqrt{Q\mathcal{T}}. \tag{4.71}
$$

It follows that

$$
\begin{aligned}
\mathrm{d}\sigma^{\text{match}} \to \mathrm{d}\sigma_{\text{I}}\big|_{\mu^{\text{I}}} &+ \big[\mathrm{d}\sigma_{\text{FO}} - \mathrm{d}\sigma_{\text{I}}\big]_{\mu_{\text{FO}}} \\
&+ \big[\mathrm{d}\sigma_{\text{II}} - \mathrm{d}\sigma_+\big]_{\mu^{\text{II}}} - \big[\mathrm{d}\sigma_{\text{II}} - \mathrm{d}\sigma_+\big]_{\mu_{\text{FO}}} \quad \text{for} \quad q_T \to \sqrt{Q\mathcal{T}}. \tag{4.72}
\end{aligned}
$$

This mostly coincides with the result in eq. (4.7) of matching $\mathrm{d}\sigma_{\text{I}}$ to the fixed-order result $\mathrm{d}\sigma_{\text{FO}}$, and is guaranteed to capture all large logarithms of $\mathcal{T}/Q$ captured by the SCET_{I} RGE. It improves over eq. (4.7) by also resumming logarithms of q_T/Q in the power corrections $\mathcal{O}(\mathcal{T}^2/q_T^2)$, encoded in $\big[\sigma_{\text{II}} - \sigma_+\big]_{\mu^{\text{II}}}$. This is not a numerically large effect and cannot be exploited to achieve the resummation of $\mathcal{T}$ at next-to-leading power, as it is only a subset of all power corrections.

Similarly, eqs. (4.68) and (4.69) imply that

$$
\mathrm{d}\sigma_+\big|_{\mu^+} \to \mathrm{d}\sigma_+\big|_{\mu^{\text{II}}} \quad \text{for} \quad q_T \to \mathcal{T}, \tag{4.73}
$$

and consequently

$$
\begin{aligned}
\mathrm{d}\sigma^{\text{match}} \to \mathrm{d}\sigma_{\text{II}}\big|_{\mu^{\text{II}}} &+ \big[\mathrm{d}\sigma_{\text{FO}} - \mathrm{d}\sigma_{\text{II}}\big]_{\mu_{\text{FO}}} \\
&+ \big[\mathrm{d}\sigma_{\text{I}} - \mathrm{d}\sigma_+\big]_{\mu^{\text{I}}} - \big[\mathrm{d}\sigma_{\text{I}} - \mathrm{d}\sigma_+\big]_{\mu_{\text{FO}}} \quad \text{for} \quad q_T \to \mathcal{T}. \tag{4.74}
\end{aligned}
$$

Scale	SCET$_\mathrm{I}$	SCET$_+$	SCET$_\mathrm{II}$
μ_H	Q	Q	Q
μ_B	$\sqrt{\mathcal{T}Q}$	b_0/b_T	b_0/b_T
ν_B		Q	Q
$\mu_\mathcal{S}$		b_0/b_T	
$\nu_\mathcal{S}$		$(b_0/b_T)^2/\mathcal{T}$	
μ_S	$\mathcal{T}$	$\mathcal{T}$	b_0/b_T
ν_S			b_0/b_T

Table 4.1: Summary of canonical scales in SCET$_\mathrm{I}$, SCET$_+$, and SCET$_\mathrm{II}$ [see eq. (4.6), (4.18) and (4.38)]. For SCET$_+$ and SCET$_\mathrm{II}$ we give the canonical scales in b_T space.

This mostly coincides with the result in eq. (4.19) of matching $\mathrm{d}\sigma_\mathrm{II}$ to the fixed-order result $\mathrm{d}\sigma_\mathrm{FO}$, and thus captures all large logarithms of q_T/Q captured by the SCET$_\mathrm{II}$ RGE. In addition, it resums logarithms of $\mathcal{T}/Q$ in the $\mathcal{O}(q_T^2/(\mathcal{T}Q))$ power corrections encoded in $[\mathrm{d}\sigma_\mathrm{I} - \mathrm{d}\sigma_+]_{\mu^\mathrm{I}}$.

Finally, in the fixed-order region, all μ^+, μ^I, and μ^II scales become equal to μ_FO. Thus as desired, the matched prediction reduces to the fixed-order result,

$$\mathrm{d}\sigma^\mathrm{match} \to \mathrm{d}\sigma_\mathrm{FO}\big|_{\mu_\mathrm{FO}} \quad \text{for} \quad q_T, \mathcal{T} \to Q\,. \tag{4.75}$$

4.4.3 Profile scales

In this section, we describe our choice of the central μ^+ scales for the various ingredients in the SCET$_+$ factorized cross section, taking into account the transition to the SCET$_\mathrm{I}$ and SCET$_\mathrm{II}$ boundary theories as well as the transition to the fixed-order region. The SCET$_+$ scales are obtained using a regime parameter that selects the appropriate combination of scales from the boundary theories in each region of phase space, and selects a third, independent choice in the SCET$_+$ "bulk" when necessary. The profile functions that handle the transition to fixed order can conveniently be reused from SCET$_\mathrm{I}$ and SCET$_\mathrm{II}$.

We start by summarizing the canonical scales for SCET$_\mathrm{I}$, SCET$_\mathrm{II}$, SCET$_+$ in table 4.1. At these scales, the arguments of logarithms in the ingredients of the factorized cross section are order one, i.e., all large logarithms are resummed by RG evolution. To interpolate between the canonical scales in different regimes, we find it convenient to introduce the regime parameter

$$a = 3 - \frac{|\ln(\mathcal{T}/Q)|}{|\ln(q_T/Q)|}\,. \tag{4.76}$$

Its definition is carefully chosen such that $a = 1$ when the SCET$_\mathrm{I}$ parametric relation is exactly satisfied, $q_T = \sqrt{\mathcal{T}Q}$, and $a = 2$ on the SCET$_\mathrm{II}$ boundary of phase space,
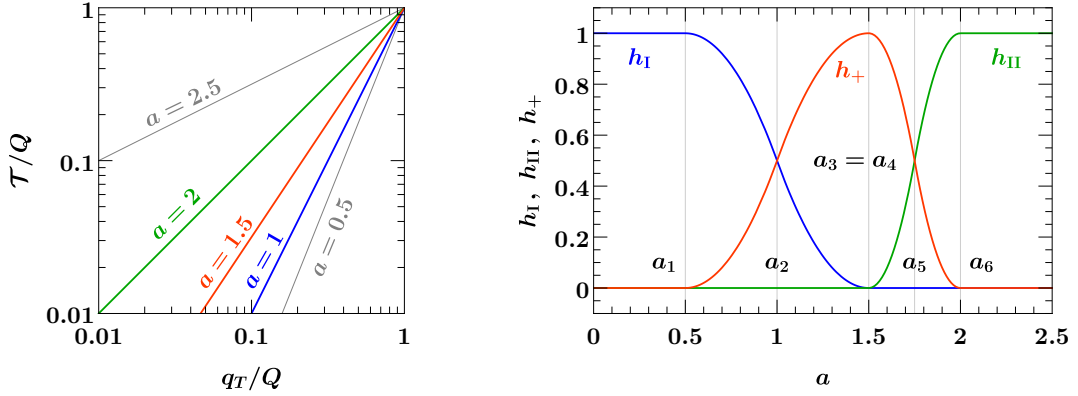
Figure 4.10: Left: Illustration of the regime parameter a that governs the matching between EFTs. We show lines of constant a in the $(q_T, \mathcal{T})$ plane. For $a = 1$ the SCET$_\mathrm{I}$ parametric relation is exactly satisfied, $q_T = \sqrt{Q\mathcal{T}}$, whereas for $a = 2$, the SCET$_\mathrm{II}$ parametric relation is exactly satisfied, $q_T = \mathcal{T}$. Right: Helper functions used to interpolate between scales on the boundaries (SCET$_\mathrm{I}$, SCET$_\mathrm{II}$) and in the bulk (SCET$_+$). The helper functions have continuous derivatives and always sum to one. The individual helper functions are exactly one in their respective canonical regions. See the text for a detailed discussion.

$q_T = \mathcal{T}$. As illustrated in the left panel of figure 4.10, the canonical SCET$_+$ region lies at intermediate $a \sim 1.5$. The requirements on the SCET$_+$ scales were given in eqs. (4.66) and (4.67) for the transition to SCET$_\mathrm{I}$, and in eqs. (4.68) and (4.69) for SCET$_\mathrm{II}$. To satisfy these requirements, we take weighted products of scales on the boundary and in the bulk, schematically,

$$\mu^+ = \left[\mu^\mathrm{I}\right]^{h_\mathrm{I}(a)} \left[\mu^+_\mathrm{bulk}\right]^{h_+(a)} \left[\mu^\mathrm{II}\right]^{h_\mathrm{II}(a)} . \tag{4.77}$$

The weights in the exponent are given by helper functions that depend on a, as illustrated in the right panel of figure 4.10. They satisfy

$$h_\mathrm{I}(a) + h_+(a) + h_\mathrm{II}(a) = 1 , \tag{4.78}$$

for any a and are given explicitly in eq. (4.82) below. The helper functions ensure that the appropriate scales are used in each region, e.g., $h_\mathrm{II}(a)$ is one in the vicinity of $a = 2$ and vanishes for $a < 1.5$, with a smooth transition between regions.

For the soft and collinear-soft scales, eq. (4.77) takes the following concrete form:

$$\begin{aligned} \mu^+_\mathcal{S} &= \left[\mu^\mathrm{I}_B\right]^{h_\mathrm{I}(a)} \left[\mu^+_{\mathcal{S},\mathrm{bulk}}\right]^{h_+(a)} \left[\mu^\mathrm{II}_S\right]^{h_\mathrm{II}(a)} , \\ \nu^+_\mathcal{S} &= \left[\nu\right]^{h_\mathrm{I}(a)} \left[\nu^+_{\mathcal{S},\mathrm{bulk}}\right]^{h_+(a)} \left[\nu^\mathrm{II}_S\right]^{h_\mathrm{II}(a)} , \\ \mu^+_S &= \left[\mu^\mathrm{I}_S\right]^{h_\mathrm{I}(a)} \left[\mu^+_{S,\mathrm{bulk}}\right]^{h_+(a)} \left[\mu^\mathrm{II}_S\right]^{h_\mathrm{II}(a)} . \end{aligned} \tag{4.79}$$

The most nontrivial of these cases is $\nu_\mathcal{S}$, which must be equal to the overall ν in the SCET$_\mathrm{I}$ region to turn off the rapidity resummation there, has a distinct canonical value in the SCET$_+$ bulk, and must asymptote to yet another value on the SCET$_\mathrm{II}$ boundary. We note

that μ_S^+ also requires a distinct treatment in the bulk to ensure that the hierarchy $\mu_S^+ < \mu_S^+$ inside the refactorized soft function, as implied by the SCET$_+$ power counting, is not upset by variations (see next subsection). Our central choices for the above scales in the bulk are

$$\mu_{\mathcal{S},\text{bulk}}^+ = \mu_{\text{FO}}\, f_{\text{run}}^{\text{II}}\left(\frac{q_T}{Q}, \frac{b_0}{b^*(b_T)\, Q}\right), \quad \nu_{\mathcal{S},\text{bulk}}^+ = \mu_{\text{FO}}\, \frac{\left[f_{\text{run}}^{\text{II}}\left(\frac{q_T}{Q}, \frac{b_0}{b^*(b_T)Q}\right)\right]^2}{f_{\text{run}}^{\text{I}}\left(\frac{\mathcal{T}}{Q}\right)},$$

$$\mu_{S,\text{bulk}}^+ = \mu_{\text{FO}}\, f_{\text{run}}^{\text{I}}\left(\frac{\mathcal{T}}{Q}\right). \tag{4.80}$$

The profile function $f_{\text{run}}^{\text{I}}$ was introduced for the transition between SCET$_{\text{I}}$ and fixed-order QCD in eq. (4.10), and similarly for the hybrid profile $f_{\text{run}}^{\text{II}}$ in eq. (4.22) and the nonperturbative $b^*(b_T)$ prescription in eq. (4.24). These functions turn off the resummation of logarithms involving q_T (b_T) and $\mathcal{T}$, respectively, as the fixed-order regime is approached, and also ensure that scales are frozen in the nonperturbative regime to avoid the Landau pole. It is straightforward to check that away from the nonperturbative region, the above bulk scales all assume their canonical values for $q_T, \mathcal{T} \ll Q$ as given in table 4.1, and asymptote to μ_{FO} when simultaneously taking $q_T, \mathcal{T} \to Q$. The beam function scales in the bulk can simply be associated with their SCET$_{\text{II}}$ counterparts and only require a transition towards the SCET$_{\text{I}}$ boundary,

$$\mu_B^+ = \left[\mu_B^{\text{I}}\right]^{h_{\text{I}}(a)} \left[\mu_B^{\text{II}}\right]^{h_+(a)+h_{\text{II}}(a)},$$

$$\nu_B^+ = \left[\nu\right]^{h_{\text{I}}(a)} \left[\nu_B^{\text{II}}\right]^{h_+(a)+h_{\text{II}}(a)}. \tag{4.81}$$

In our numerical implementation, we choose the helper functions $h_{\text{I,II},+}$ as

$$h_{\text{I}}(a) \equiv \begin{cases} 1 & a < a_1, \\ 1 - c_{123}(a) & a_1 \leq a < a_2, \\ c_{312}(a) & a_2 \leq a < a_3, \\ 0 & a_3 \leq a, \end{cases} \qquad h_{\text{II}}(a) \equiv \begin{cases} 0 & a < a_4, \\ c_{456}(a) & a_4 \leq a < a_5, \\ 1 - c_{645}(a) & a_5 \leq a < a_6, \\ 1 & a_6 \leq a, \end{cases}$$

$$h_+(a) \equiv 1 - h_{\text{I}}(a) - h_{\text{II}}(a), \tag{4.82}$$

where the polynomials governing the interpolation between zero and one are

$$c_{ijk}(a) = \frac{(a - a_i)^2}{(a_i - a_j)(a_i - a_k)}. \tag{4.83}$$

The transition points $a_{1,\ldots,6}$ determine the transition between the different regions, as can be seen from the helper functions in figure 4.10: For values $a_3 \leq a < a_4$, the exact canonical SCET$_+$ scales are selected, implying that the resummation of logarithms of both q_T and $\mathcal{T}$ is fully turned on. For lower values $a_1 \leq a < a_3$, the additional q_T resummation is smoothly turned off and for $a < a_1$, SCET$_{\text{I}}$ scales are used so that only logarithms of $\mathcal{T}$ are resummed. Conversely, for higher values of the regime parameter $a_4 \leq a < a_6$, the

resummation of $\mathcal{T}$ logarithms is smoothly turned off. At values $a_6 \leq a$, SCET$_\text{II}$ scales are selected by the helper functions, and the additional resummation of logarithms of $\mathcal{T}$ is completely turned off.

In practice we use $(a_1, a_2, a_3, a_4, a_5, a_6) = (0.5, 1.0, 1.5, 1.5, 1.75, 2.0)$. This choice ensures that for $a \geq a_6 = 2$, we fully recover SCET$_\text{II}$ resummation and faithfully describe the kinematic edge at $q_T \sim \mathcal{T}$ by preserving the $\mathcal{O}(1)$ cancellation between $\sigma_+\big|_{\mu^\text{II}}$ and the SCET$_\text{II}$ nonsingular contribution visible at $a \sim 2$ in the left panel of figure 4.8. (In both figures 4.7 and 4.8, corresponding values of a are indicated on the horizontal axis at the top of the panels.) On the other hand, from figure 4.7 we observe that power corrections from SCET$_\text{I}$ are smaller and tend to set in at values of a lower than the naively expected $a = 1$. E.g., an $\mathcal{O}(1)$ cancellation between $\sigma_+\big|_{\mu^\text{I}}$ and the SCET$_\text{I}$ nonsingular only is in effect around $a \sim 0.5$ in the right panel of figure 4.7, leaving more room for slowly turning off the SCET$_+$ resummation down towards $a_1 = 0.5$. This is expected because the SCET$_\text{I}$ nonsingular encodes the suppression of collinear recoil beyond the naive phase-space boundary at $a \sim 1$ ($q_T \sim \sqrt{Q\mathcal{T}}$) that is washed out by the PDFs, unlike the sharp kinematic edge at $q_T \sim \mathcal{T}$ encoded in the SCET$_\text{II}$ nonsingular. For simplicity we set $a_3 = a_4$ for our central prediction, i.e., we shrink the canonical SCET$_+$ region to a point at $a = 1.5$, and fix a_2 (a_5) to be the midpoint between a_1 and a_3 (a_4 and a_6). Variations of the transition points, including independent variations of a_3 and a_4, are considered as part of our uncertainty estimate described in the next section.

4.4.4 Perturbative uncertainties

In this section we describe how we assess perturbative uncertainties by varying the scales entering the matched prediction in eq. (4.65). Following the same approach as for SCET$_\text{I}$ and SCET$_\text{II}$ on their own (see sections 4.2.2 and 4.2.3), we distinguish between resummation uncertainties and a fixed-order uncertainty. The fixed-order uncertainty Δ_FO is estimated by varying μ_FO up and down by a factor of two, i.e., by setting $\mu_\text{FO} = \{Q/2, 2Q\}$. Since all scales (in any piece of the matching formula) include an overall factor of μ_FO, the ratios between the various scales remain unchanged and the same logarithms are resummed. The fixed-order uncertainty Δ_FO is then taken to be the maximum deviation from the central cross section.

We consider several sources of resummation uncertainty entering the matched prediction in eq. (4.65). To probe the tower of logarithms of $\mathcal{T}/Q$ predicted by the SCET$_\text{I}$ RGE, we perform variations of μ_B^I and μ_S^I parametrized by α and β as in eq. (4.11). This directly affects the resummed power corrections $\big[\mathrm{d}\sigma_\text{I} - \mathrm{d}\sigma_+\big]_{\mu_\text{I}}$ captured by SCET$_\text{I}$. In addition, however, $\mathrm{d}\sigma_+\big|_{\mu_+}$ near the SCET$_\text{I}$ boundary also undergoes variations because for large h_I, the SCET$_+$ scales in eqs. (4.79) and (4.81) strongly depend on their SCET$_\text{I}$ counterparts and inherit their variations. Our setup thus ensures that in (or near) the SCET$_\text{I}$ region, variations probing resummed logarithms of $\mathcal{T}/Q$ are properly treated as correlated between the SCET$_+$ cross section and the SCET$_\text{I}$ matching correction. When referring to the matched prediction in eq. (4.65), we take Δ_I to be the maximum deviation of $\mathrm{d}\sigma_\text{match}$ from

its central value under these correlated variations of α, β.

In complete analogy, we define Δ_{II} as the maximum deviation under correlated variations of μ_{II} as described in section 4.2.3. These variations act on both $\left[d\sigma_{\text{II}} - d\sigma_+\right]_{\mu_{\text{II}}}$ and $d\sigma_+\big|_{\mu_+}$, where now the SCET$_+$ scales inherit variations from μ_{II} near the SCET$_{\text{II}}$ boundary (where h_{II} is large). As a result, Δ_{II} probes an all-order set of logarithms of $(b_0/b_T)/Q$ predicted and resummed by the SCET$_{\text{II}}$ RGE, and properly captures the correlated tower of logarithms in SCET$_+$. We like to stress that our setup is fully general with respect to the method chosen to perform scale variations for the boundary theories, as any variation will automatically be inherited by SCET$_+$.

As a final source of uncertainty, we consider the uncertainty inherent in our matching procedure and in our choice of SCET$_+$ scales in the bulk. To estimate this we perform the following 8 variations of the (in principle arbitrary) transition points (a_1, a_3, a_4, a_6),

$$
\begin{aligned}
&(\uparrow, -, -, -), \quad &&(-, \downarrow, -, -), \quad &&(-, -, -, \downarrow), \quad &&(-, \uparrow, \uparrow, -), \\
&(\downarrow, -, -, -), \quad &&(-, -, \uparrow, -), \quad &&(-, -, -, \uparrow), \quad &&(-, \downarrow, \downarrow, -),
\end{aligned} \tag{4.84}
$$

where $\uparrow$ ($\downarrow$) indicates a variation by $+0.2$ (-0.2), a dash indicates keeping the transition point fixed, and we always maintain $a_2 = (a_1 + a_3)/2$ and $a_5 = (a_4 + a_6)/2$. In addition, we perform the following two variations of the SCET$_+$ bulk scales,

$$
\begin{aligned}
\mu_{\mathcal{S},\text{bulk}}^+ &= \mu_{\text{FO}} \left(\frac{q_T}{\mathcal{T}}\right)^{+\gamma/2} f_{\text{run}}^{\text{II}}\left(\frac{q_T}{Q}, \frac{b_0}{b^* Q}\right), \\
\mu_{S,\text{bulk}}^+ &= \mu_{\text{FO}} \left(\frac{q_T}{\mathcal{T}}\right)^{-\gamma/2} f_{\text{run}}^{\text{I}}\left(\frac{\mathcal{T}}{Q}\right), \qquad \gamma = \{+1/6, -1/6\}, \tag{4.85}
\end{aligned}
$$

where $\gamma = 0$ corresponds to the central scales in eq. (4.80). Similarly to the role of β in the SCET$_{\text{I}}$ variations [see eq. (4.11)], making the strength of the γ variations depend on the ratio $q_T/\mathcal{T}$ ensures that the hierarchy $\mu_S < \mu_{\mathcal{S}}$ implied by the SCET$_+$ power counting is not upset by variations, counting $b_0/b_T \sim q_T$. We note that the third independent bulk scale $\nu_{\mathcal{S},\text{bulk}}^+$ does not require independent variation because it only enters through rapidity logarithms of $\nu_B^+/\nu_{\mathcal{S}}^+$, which are already being probed by variations of ν_B^+ inherited from SCET$_{\text{II}}$. Taking the envelope of the eight transition point variations and the two bulk scale variations, we obtain a third contribution to the resummation uncertainty denoted by Δ_+. The total uncertainty assigned to the matched prediction is then given by adding all contributions in quadrature,

$$
\Delta_{\text{total}} = \Delta_+ \oplus \Delta_{\text{I}} \oplus \Delta_{\text{II}} \oplus \Delta_{\text{FO}}. \tag{4.86}
$$

4.5 Results

In this section we present our results for Drell-Yan production $pp \to Z/\gamma^* \to \ell^+\ell^-$ at the LHC, with a simultaneous measurement of the transverse momentum q_T of the lepton pair and the 0-jettiness event shape $\mathcal{T}$. The center-of-mass energy is taken to be $E_{\text{cm}} = 13\,\text{TeV}$.

We assume that in addition, the invariant mass Q of the lepton pair is measured, and write $pp \to Z$ for short if $Q = m_Z$, and $pp \to Z^*$ otherwise.

To obtain numerical results for the SCET$_\mathrm{I}$, SCET$_\mathrm{II}$, and SCET$_+$ contributions, we have implemented all pieces of the relevant double-differential factorized cross sections to $\mathcal{O}(\alpha_s)$ and their RGEs to NNLL in `SCETlib` [8]. The fixed NLO contributions in full QCD are obtained from `MCFM 8.0` [330–332]. We make use of the `MMHT2014nnlo68cl` [110] NNLO PDFs with five-flavor running and $\alpha_s(m_Z) = 0.118$. Since we focus on the perturbative calculation and do not include any nonperturbative effects, we provide the results down to $1\,\mathrm{GeV}$ in q_T and $\mathcal{T}$.

The outline of this section is as follows: In section 4.5.1 we present our fully resummed prediction for the double-differential spectrum, both as surface plots over the $(q_T, \mathcal{T})$ plane and for selected slices along lines of constant q_T or $\mathcal{T}$. We demonstrate that our prediction smoothly interpolates between the SCET$_\mathrm{I}$ and SCET$_\mathrm{II}$ boundary theories, i.e., we show that our matching formula in eq. (4.65) recovers the matched predictions on either boundary and improves over them by an additional resummation of power-suppressed terms. Finally, in section 4.5.2 we present our predictions for the single-differential spectra $\mathrm{d}\sigma(q_T^\mathrm{cut})/\mathrm{d}\mathcal{T}$ and $\mathrm{d}\sigma(\mathcal{T}_\mathrm{cut})/\mathrm{d}q_T$ with a cut on the other variable, and show how they recover the inclusive single-differential $\mathcal{T}$ and q_T spectra for large values of q_T^cut and $\mathcal{T}_\mathrm{cut}$, respectively.

4.5.1 Double spectrum and comparison with boundary theories

To highlight the necessity of the simultaneous resummation of large logarithms of both q_T and $\mathcal{T}$, we start by showing results for the double spectrum (the cross section double-differential in q_T and $\mathcal{T}$) where only some of the logarithms are resummed. These results are shown as surface plots in figure 4.11, where we plot the double-differential spectrum with respect to $\log_{10} q_T$ and $\log_{10} \mathcal{T}$ for better visibility. In each case the left rear wall of the surface plot shows the result of integrating the double-differential spectrum up to $\mathcal{T}_\mathrm{cut} = 100\,\mathrm{GeV}$, but staying differential in $\log_{10} q_T$. Similarly, the right rear wall shows the projection onto the single-differential spectrum in $\log_{10} \mathcal{T}$, with a cut at $q_T^\mathrm{cut} = 100\,\mathrm{GeV}$.[10]

The top left panel of figure 4.11 shows the spectrum evaluated at fixed $\mathcal{O}(\alpha_s)$, without any resummation. The double-differential fixed-order spectrum diverges logarithmically for small $\mathcal{T}$ at any value of q_T, while its projections onto the single-differential spectra in q_T and $\mathcal{T}$ feature double-logarithmic singularities. Notably, the double-differential spectrum has a sharp kinematic edge along $q_T = \mathcal{T}$. This sharp edge is unphysical because it only reflects the kinematics of a single on-shell emission with transverse momentum k_T at rapidity η, which contributes at most $\mathcal{T} = k_T\, e^{-|\eta|} \leq k_T = q_T$. Due to the vectorial nature of q_T, however, back-to-back emissions can populate the region $\mathcal{T} > q_T$ at higher orders, and the kinematic edge must be smeared out.

Next, we consider the cases in which only logarithms of one variable are resummed, while logarithms involving the auxiliary variable are treated at fixed order. In the middle panel of figure 4.11, we show the result of resumming logarithms of $\mathcal{T}$ using the SCET$_\mathrm{I}$ matched

---

[10]We refer the reader to appendix G.1 for the precise way we perform these integrals.
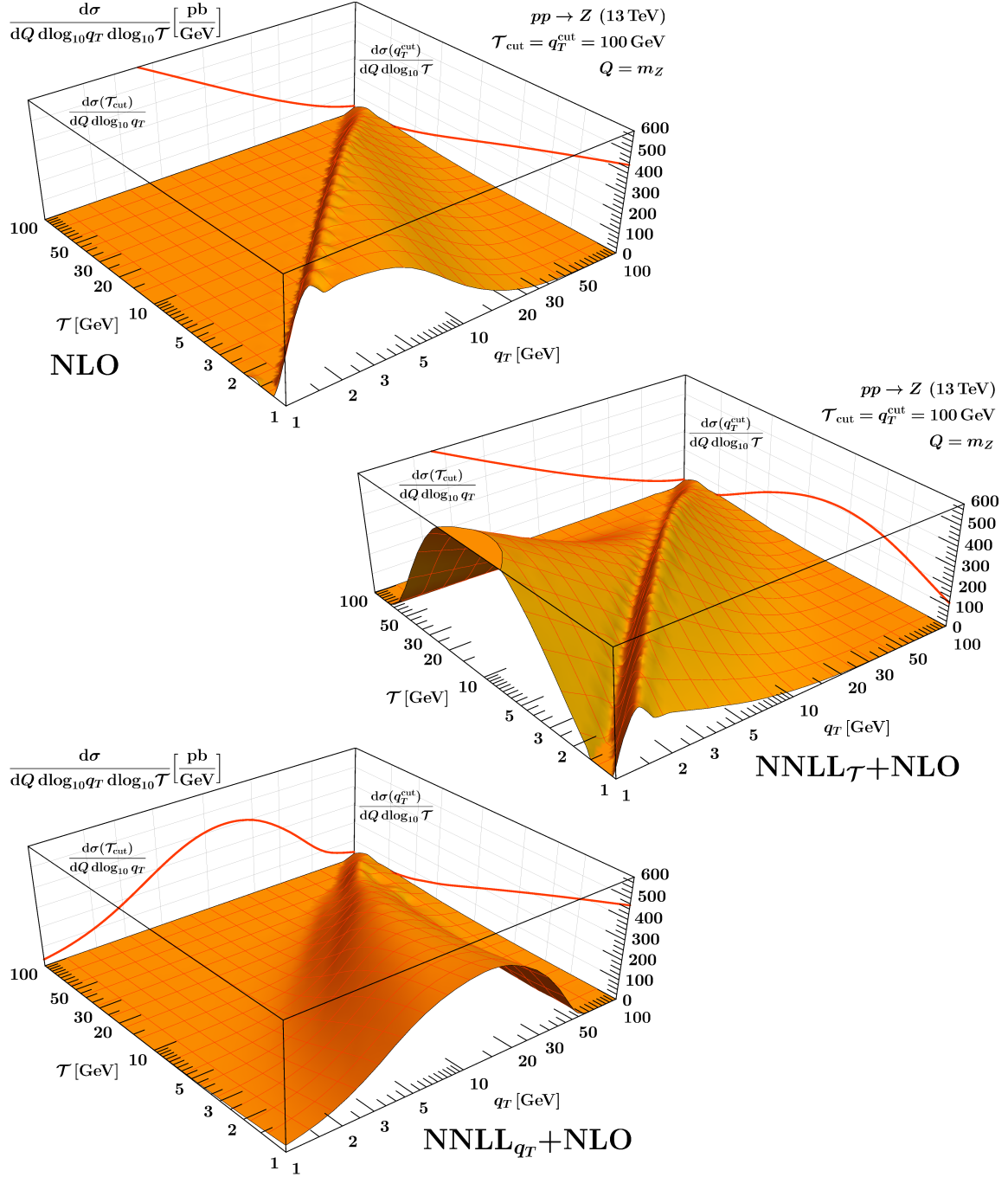
Figure 4.11: The double-differential Drell-Yan cross section at fixed NLO (top), resummed NNLL$_{\mathcal{T}}$+NLO (center), and NNLL$_{q_T}$+NLO (bottom). The resummed predictions are obtained by using only SCET$_\mathrm{I}$ (SCET$_\mathrm{II}$) renormalization group evolution to resum logarithms of $\mathcal{T}$ (q_T), as outlined in section 4.2.2 (section 4.2.3), and matching the result to the fixed-order cross section. For better visibility we show the spectrum with respect to $\log_{10} q_T$ and $\log_{10} \mathcal{T}$. On the rear walls we show the result of integrating the double spectrum over either variable up to a cut at 100 GeV.

result in eq. (4.7). The resummation is performed at NNLL and is matched to full NLO, which we refer to as $\text{NNLL}_{\mathcal{T}}+\text{NLO}$. As discussed in section 4.2.2, this prediction is valid as long as the parametric relation $\mathcal{T} \ll q_T \sim \sqrt{Q\mathcal{T}}$ is satisfied. This corresponds to the SCET_I phase-space boundary (blue) in figure 4.2, running from the region of small $\mathcal{T}$ and intermediate q_T towards the fixed-order region where $q_T \sim \mathcal{T} \sim Q$. It is clear that away from its region of validity, the $\text{NNLL}_{\mathcal{T}}+\text{NLO}$ result contains unresummed logarithms of q_T because at any point in $\mathcal{T}$, the prediction diverges for very small q_T. In particular, power corrections of $\mathcal{O}(\mathcal{T}^2/q_T^2)$ are only captured by the fixed-order matching. They become $\mathcal{O}(1)$ as one approaches the diagonal $\mathcal{T} = q_T$ (the green line in figure 4.2), and encode the phase-space boundary at $q_T \sim \mathcal{T}$. As in the NLO case, treating this phase-space boundary at fixed order leads to the sharp kinematic edge along the diagonal; physically, the all-order tower of collinear emissions that contribute to q_T in SCET_I cannot resolve the boundary because it arises from the dynamics at central rapidities. The projections onto the rear walls highlight that only $\mathcal{T}$ is resummed. The single-differential q_T spectrum still diverges as $q_T \to 0$, while the $\mathcal{T}$ spectrum features a physical Sudakov peak.

In the bottom panel of figure 4.11, we show the result of resumming logarithms of (the b_T variable conjugate to) q_T to NNLL and matching to fixed NLO, using the SCET_II matched result in eq. (4.19). We denote this order by $\text{NNLL}_{q_T}+\text{NLO}$. This result is valid for $\mathcal{T} \sim q_T \ll \sqrt{Q\mathcal{T}}$, i.e., around the SCET_II phase-space boundary (green) in figure 4.2, where we find the onset of a Sudakov peak from the q_T resummation and a smooth kinematic suppression towards $\mathcal{T} \gg q_T$. However, the $\text{NNLL}_{q_T}+\text{NLO}$ result diverges for smaller values of $\mathcal{T}$. This is due to unresummed logarithms of $\mathcal{T}$ in both the factorized cross section in SCET_II and terms of $\mathcal{O}(q_T^2/(Q\mathcal{T}))$ that are treated at fixed order as part of the matching correction. In this case the single-differential projections show a Sudakov peak in q_T, but a logarithmic divergence at small $\mathcal{T}$.

Our final results for the Drell-Yan double spectrum are shown in figure 4.12, as given by the fully matched prediction in eq. (4.65). Here all resummed contributions are evaluated at NNLL, and we match to fixed NLO. This achieves, for the first time, the complete resummation of all large logarithms in the double spectrum, so we simply refer to this order as NNLL+NLO. The top row of plots is for $Q = m_Z$, i.e., for Drell-Yan production at the Z pole. In the bottom row we consider $Q = 300\,\text{GeV}$ as a representative phase-space point at higher production energies. Our matched and fully resummed double spectrum features a two-dimensional Sudakov peak that is situated between the two parametric phase-space boundaries (cf. figure 4.2), is smoothly suppressed beyond, and shifts towards higher values of q_T and $\mathcal{T}$ for $Q = 300\,\text{GeV}$, as expected. Integrating the double spectrum over either variable also results in a physical Sudakov peak, as can be seen from the projections onto the rear walls. Up to small differences in scale setting discussed in appendix G.1, the left and right rear walls agree with the result of integrating the $\text{NNLL}_{q_T}+\text{NLO}$ and $\text{NNLL}_{\mathcal{T}}+\text{NLO}$ results in figure 4.11 over $\mathcal{T}$ and q_T, respectively. The contour plots in figure 4.12 show the total perturbative uncertainties Δ_total as percent deviations from the central result for the double spectrum. As described in section 4.4.4, Δ_total combines estimates of all sources of resummation uncertainty in the prediction.
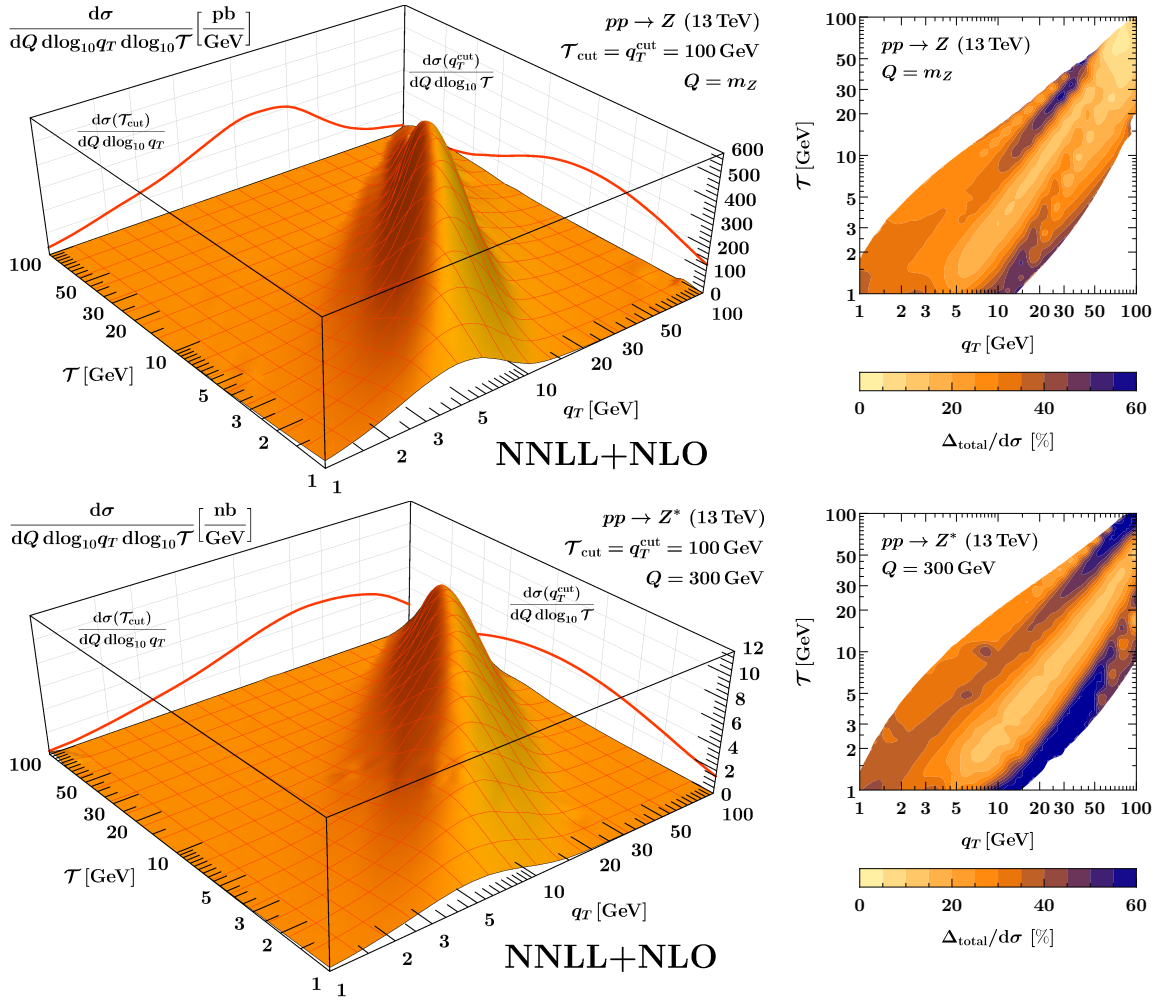
Figure 4.12: The double-differential Drell-Yan cross section at NNLL+NLO, at $Q = m_Z$ (top) and $Q = 300\,\text{GeV}$ (bottom), with respect to $\log_{10} q_T$ and $\log_{10} \mathcal{T}$. On the rear walls we show the result of integrating the double spectrum over either variable up to a cut at $100\,\text{GeV}$. The contour plots indicate total perturbative uncertainties relative to the cross section, $\Delta_{\text{total}} = \Delta_+ \oplus \Delta_{\text{I}} \oplus \Delta_{\text{II}} \oplus \Delta_{\text{FO}}$. The contour plots are left blank in the region where $d\sigma/(dQ\,d\log_{10} q_T\,d\log_{10} \mathcal{T})$ is less than 3% of its peak height.

In figure 4.13, we break down the uncertainty for the Drell-Yan double-differential spectrum at $Q = m_Z$ into its contributions from SCET_{I}, SCET_{II} and SCET_+ resummation uncertainties, respectively. As expected, the SCET_{I} resummation uncertainty dominates in the SCET_{I} region of phase space, and similarly for SCET_{II}. The SCET_+ resummation uncertainty is largest along the phase-space boundaries, indicating that it is mostly sensitive to variations of the transition points, i.e., the points where the intrinsic SCET_+ resummation is turned off in our matched prediction.

To further highlight the differences between our fully double-differential resummation and the single-differential resummation at either NNLL_{q_T} or $\text{NNLL}_{\mathcal{T}}$, we take slices of the
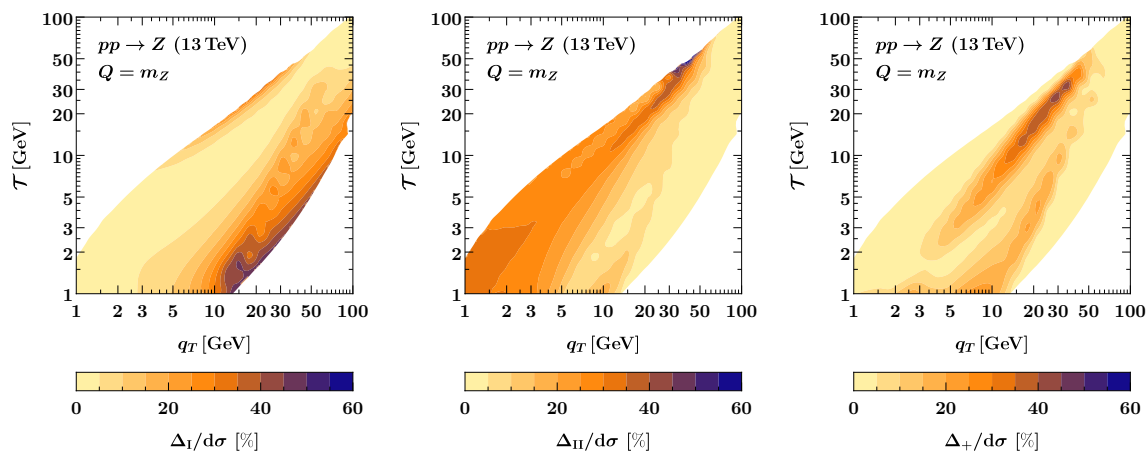
Figure 4.13: Breakdown of resummation uncertainties contributing to the relative uncertainty in the top right panel of figure 4.12, showing (from left to right) Δ_{I}, Δ_{II}, and Δ_{+}. As in figure 4.12 we leave regions blank where the cross section is small.

surface plots and overlay them in figure 4.14, keeping q_T (left) or $\mathcal{T}$ (right) fixed. The solid red curve corresponds to the matched and fully resummed cross section in eq. (4.65), with the uncertainty band given by the total perturbative uncertainty Δ_{total}, see eq. (4.86). The matched SCET$_{\mathrm{I}}$ (dashed blue) and SCET$_{\mathrm{II}}$ (dotted green) predictions correspond to the middle and bottom panel of figure 4.11, respectively. Their uncertainty bands are given by $\Delta_{\mathrm{total}}^{\mathrm{I}}$ and $\Delta_{\mathrm{total}}^{\mathrm{II}}$, which only probe a subset of higher-order terms as predicted by the respective RGE, see eqs. (4.14) and (4.27). The SCET$_{\mathrm{I}}$ prediction features an unphysical sharp edge at $\mathcal{T} = q_T$, cf. the middle panel of figure 4.11, and for this reason is cut off at $\mathcal{T} = 0.8\,q_T$.

All panels in figure 4.14 show that our final prediction smoothly interpolates between the SCET$_{\mathrm{I}}$ and SCET$_{\mathrm{II}}$ boundary theories, both for the central values and for the uncertainties. Specifically, the matched prediction tends towards SCET$_{\mathrm{I}}$ (SCET$_{\mathrm{II}}$) for small (large) values of $\mathcal{T}$ and large (small) values of q_T. In the left column one clearly sees that SCET$_{\mathrm{II}}$ only captures logarithms of $\mathcal{T}$ at fixed order, leading to a diverging spectrum as $\mathcal{T} \to 0$, while the complete NNLL result features a physical Sudakov peak. Conversely, the SCET$_{\mathrm{I}}$ result diverges as $q_T \to 0$, but is rendered physical by the additional q_T resummation at NNLL.

We would like to stress that our fully resummed prediction does not exactly agree with either boundary theory, even beyond the final transition points a_1 and a_6 where the intrinsic SCET$_{+}$ resummation is turned off. The reason for this is that even in these limits, the matched cross section in eq. (4.65) improves over the matched SCET$_{\mathrm{I}}$ and SCET$_{\mathrm{II}}$ cross sections in eq. (4.7) and eq. (4.19) by an additional resummation of power-suppressed terms, cf. eqs. (4.72) and (4.74). To assess the size of this effect, we again compare both single-differential resummations (dashed blue and dotted green) to our matched prediction (solid red) in figure 4.15, but for reference include the case where σ_+ in the matched prediction is evaluated at μ^{I} (solid blue) or μ^{II} (solid green) directly. One can easily verify from
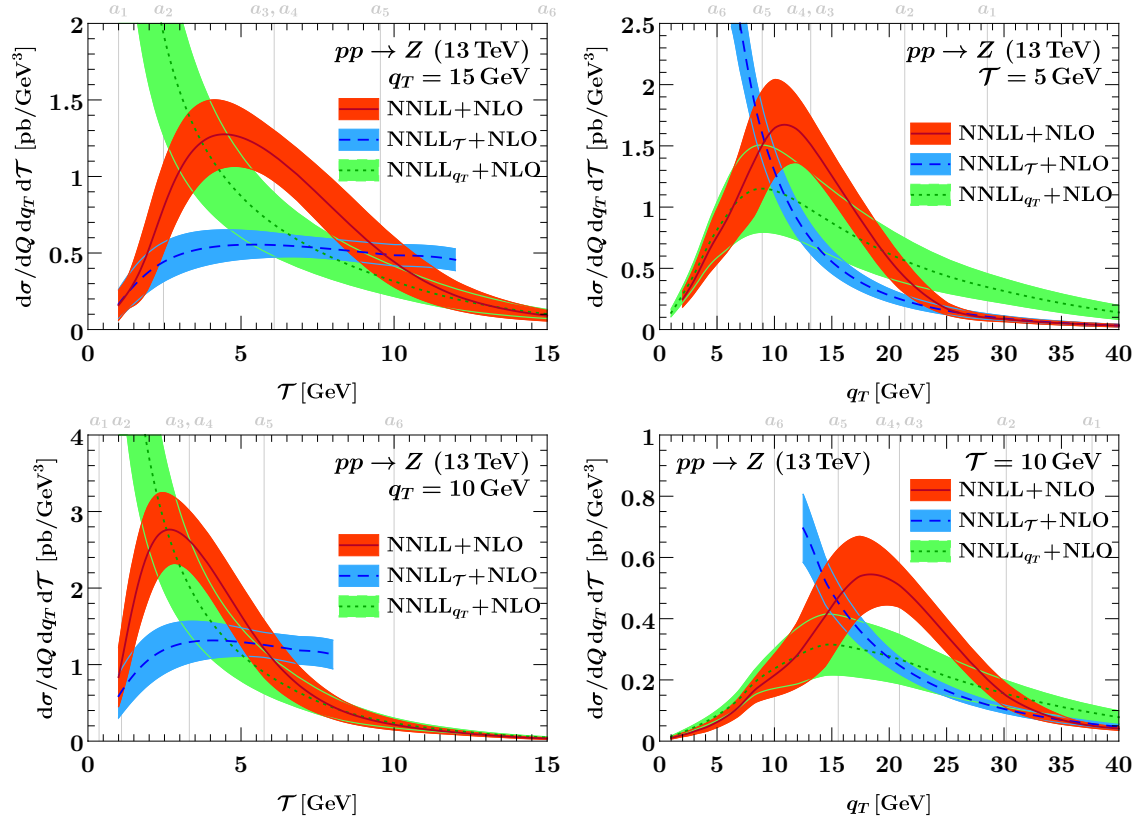
Figure 4.14: The double-differential Drell-Yan cross section for fixed q_T, as a function of $\mathcal{T}$ (left) and for fixed $\mathcal{T}$, as a function of q_T (right). The solid red curves are slices of the surface plots shown in the top left panel in figure 4.12, up to Jacobians. The blue dashed (green dotted) curve corresponds to the middle (bottom) panel of figure 4.11. The thin vertical lines indicate the transition points a_i described in section 4.4.3. The SCET$_\text{I}$ prediction (dashed blue) has an unphysical edge at $\mathcal{T} = q_T$, see figure 4.11, and is not shown beyond $\mathcal{T} = 0.8\, q_T$ to avoid distraction. See the text for details on the uncertainty bands.

e.g. the right panel that for q_T above the right-most vertical line (where $a < a_1$), the difference between the solid blue and the dashed blue curves indeed amounts to a small power-suppressed set of higher-order terms, while our best prediction (solid red) recovers the solid blue curve as it must. Similarly, for q_T below the left-most vertical line (where $a > a_6$), the difference between the solid green (and solid red) and dashed green curves can be seen to be a small correction, reflecting the size of power-suppressed higher-order terms predicted by the SCET$_\text{I}$ RGE in this region. The asymptotic limits are interchanged in the left panel, where $a < a_1$ towards the left and $a > a_6$ towards the very right of the plot.

4.5.2 Single-differential spectra with a cut on the other variable

So far we have turned our attention to the cross section differential in both q_T and $\mathcal{T}$. In addition to this double spectrum, our setup also predicts the fully matched and resummed
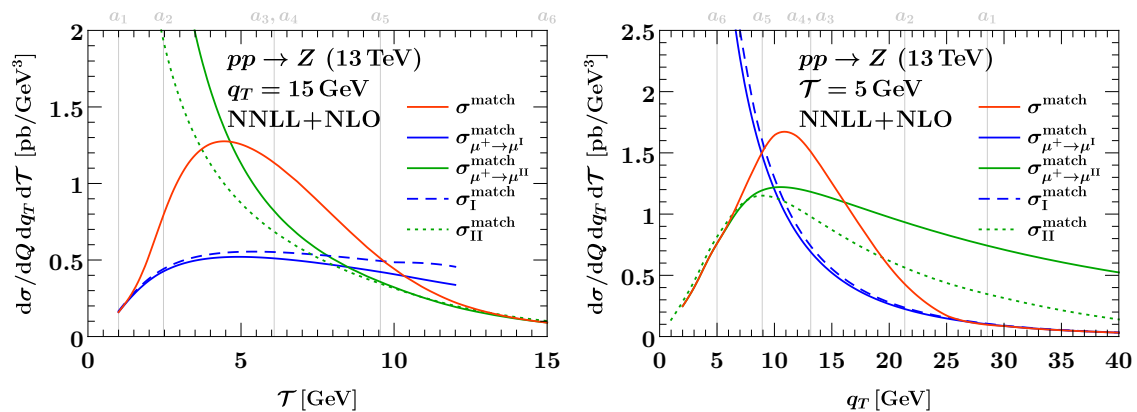
Figure 4.15: Slices of the double-differential Drell-Yan cross section at $q_T = 15\,\mathrm{GeV}$ (left) and $\mathcal{T} = 5\,\mathrm{GeV}$ (right). The solid red, dashed blue, and dotted green curves are identical to the central results in figure 4.14. The solid blue and green curves depict the $\mathrm{SCET_I}$ and $\mathrm{SCET_{II}}$ limits of our fully resummed result, given in eqs. (4.72) and (4.74). The thin vertical lines indicate the transition points a_i described in section 4.4.3.

double cumulant cross section, and the single-differential q_T (or $\mathcal{T}$) spectrum with a cut on the other variable; selected results for these observables are also discussed in appendix G.1 from a more technical point of view. In figure 4.16, we show some more detailed results for the single-differential spectra with an additional cut, where the left panel shows $\mathrm{d}\sigma(q_T^{\mathrm{cut}})/\mathrm{d}\mathcal{T}$ as a function of $\mathcal{T}$ for various values of q_T^{cut}, and the right panel shows $\mathrm{d}\sigma(\mathcal{T}_{\mathrm{cut}})/\mathrm{d}q_T$ as a function of q_T for various values of $\mathcal{T}_{\mathrm{cut}}$. By increasing the value of the cut, they can be seen to approach the inclusive single-differential spectra (orange solid), with which they must agree when sending $q_T^{\mathrm{cut}} \to \infty$ or $\mathcal{T}_{\mathrm{cut}} \to \infty$, respectively. This is by construction because we employ cumulant scale setting as appropriate for this prediction, cf. appendix G.1. We observe that cuts on the other variable shape either spectrum in a very nontrivial way. Tight cuts $\lesssim 10\,\mathrm{GeV}$ push the peak to lower values and suppress the tail, where the q_T spectrum is somewhat more resilient to cuts on $\mathcal{T}$ than vice versa. Intermediate cuts $\sim 10 - 15\,\mathrm{GeV}$ keep the peak and mostly lead to a suppression in the tail, while the effect of cuts $\gtrsim 40\,\mathrm{GeV}$ is almost negligible in the q_T and $\mathcal{T}$ ranges of interest.

4.6 Summary

In this chapter we calculated the Drell-Yan cross section double-differential in the transverse momentum q_T of the lepton pair and the 0-jettiness $\mathcal{T}$. Both $\mathcal{T}$ and q_T probe the initial state radiation, leading to Sudakov double logarithms of $\mathcal{T}/Q$ and q_T/Q in the cross section. We performed, for the first time, the simultaneous resummation of both kinds of logarithms, achieving next-to-next-to-leading logarithmic accuracy and matching the result to next-to-leading fixed order. We accomplish this resummation by using $\mathrm{SCET_I}$ and $\mathrm{SCET_{II}}$ to describe the regions $\mathcal{T} \ll q_T \sim \sqrt{\mathcal{T}Q}$ and $\mathcal{T} \sim q_T \ll \sqrt{\mathcal{T}Q}$, respectively, and $\mathrm{SCET_+}$ to describe the bulk of phase space in between these boundaries [195].
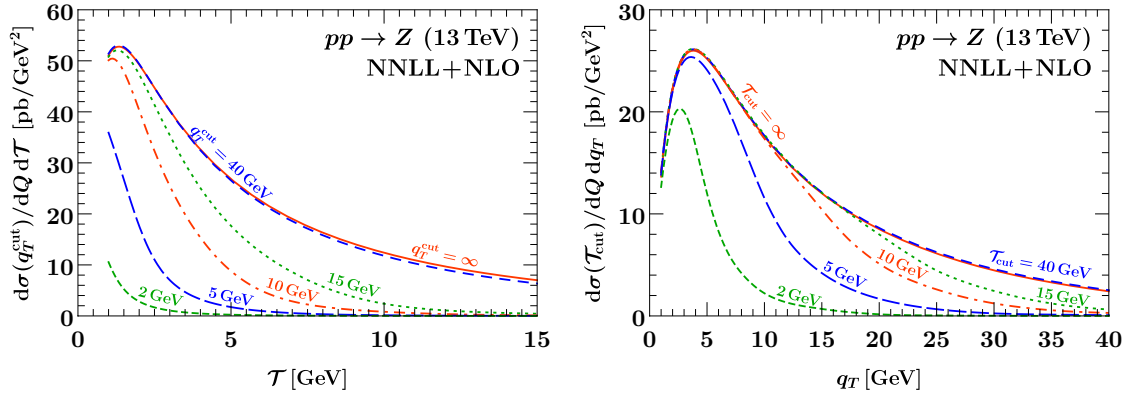
Figure 4.16: The single-differential $\mathcal{T}$ (left) and q_T (right) spectrum with a cut on the other variable at NNLL+NLO. The different curves represent different values of the cut. The solid orange lines correspond to the inclusive single-differential spectrum obtained by lifting the cut.

Obtaining reliable numerical predictions required several nontrivial steps: (1) Matching several factorized cross sections for the different regions of phase space, for which we use a Venn-diagram method to avoid double counting. (2) Choosing appropriate profile scales for the various ingredients in the factorization formulas that respect all relevant canonical scaling relations and at the same time smoothly interpolate between the different regions of phase space, and varying these scales to estimate perturbative uncertainties. This is significantly more involved than in the usual single-differential case, and is further complicated by the requirement to choose scales in impact parameter (b_T) space for SCET$_{\rm II}$. For example, the rapidity scale for the collinear-soft function in SCET$_+$ has a canonical scaling that does not coincide with any scale on the SCET$_{\rm I}$ and SCET$_{\rm II}$ boundaries. (3) Ensuring that scales and scale variations are still, to the extent possible, inherited from the single-differential resummation of $\mathcal{T}$ and q_T. This makes our setup flexible enough to incorporate other procedures for estimating the uncertainty in the individual resummations. (4) To handle the transition between SCET$_{\rm I}$, SCET$_+$ and SCET$_{\rm II}$, we introduced profile scales in terms of a regime parameter a, designed such that $a = 1$ for SCET$_{\rm I}$ and $a = 2$ for SCET$_{\rm II}$. The precise transition points in a were chosen by comparing the various singular and nonsingular cross section, and are varied as part of the uncertainty estimate. (5) We also introduced a new hybrid (i.e., q_T and b_T dependent) scale choice for q_T resummation, allowing the resummation to strictly take place in b_T space, while turning the resummation on and off using q_T.

We demonstrated that our simultaneous resummation of $\mathcal{T}$ and q_T yields the correct resummed single-differential cross sections after integrating over either $\mathcal{T}$ or q_T. This requires choosing scales at the level of the differential or integrated (cumulative) cross section as appropriate, which we discuss in more detail in appendix G.1.

Chapter 5

Generalized threshold factorization with full collinear dynamics

In this chapter we present and prove a generalized threshold factorization theorem for color-singlet production processes. It holds in the weaker limit of only $x_a \to 1$ for generic x_b (or vice versa), whereas the well-known soft threshold factorization theorem in eq. (2.186) holds only when $x_a \to 1$ *and* $x_b \to 1$ simultaneously. As a first illustrative application of the new factorization theorem, we use it to predict a nontrivial set of the N^{3}LO corrections to the Drell-Yan rapidity spectrum.

This chapter is based on ref. [4], where work in close collaboration with the author of ref. [358] was presented, and some of the results have also appeared in ref. [358]. Compared to ref. [4], the detailed proof in section 5.3 has been added, and the discussion has been deepened throughout.

5.1 Motivation

The soft threshold factorization theorem in eq. (2.186) has been widely used in QCD collider physics for decades. The utility of its partonic version in eq. (2.188) in particular lies in the fact that while taking $\tau = Q^2/E_{\rm cm}^2 \to 1$ forces the partonic momentum fraction $z \to 1$, even for typical LHC values of $\tau \ll 1$, the $z \sim 1$ region often numerically dominates the cross section.

   Eq. (2.186) enables the all-order resummation of the leading terms in $1-z$, see for example refs. [210, 211, 219–240]. The resummation at next-to-leading power (NLP) in $1-z$ has also received recent interest [206, 207, 406–410]. Another important use is to approximate the fixed-order cross section by expanding in $1-z$, e.g. at N^{3}LO [241, 242, 244–246, 248–250]. However, its applicability is limited by requiring that both partonic momentum fractions in the proton approach 1, which neglects a tower of singular terms in each momentum fraction. In particular, all off-diagonal partonic channels are power suppressed in this limit.

   In this chapter, we present, derive, and apply the factorization theorem that generalizes eqs. (2.186) and (2.188) to the weaker limit where only one of

$$x_a = \frac{Q}{E_{\rm cm}}e^{+Y}\,, \quad x_b = \frac{Q}{E_{\rm cm}}e^{-Y}\,, \tag{5.1}$$
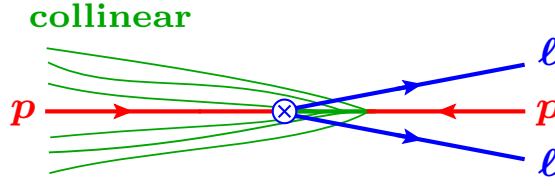
Figure 5.1: Illustration of the inclusive production of a Drell-Yan pair (blue) at large rapidity. The right-moving proton (red) is probed at large momentum fraction. The hadronic final state (green) by momentum conservation becomes collimated in the direction opposite to the color-singlet final state, and predominantly consists of collinear initial-state radiation emitted from the active parton in the left-moving proton.

or the corresponding partonic momentum fraction, approaches 1, while keeping the exact dependence on the other variable. This corresponds to the kinematic limit $|Y| \to Y_{\text{max}} = \ln(E_{\text{cm}}/Q)$ for generic (including small) Q values.

This chapter is structured as follows: In section 5.2, we present the new factorization theorem and introduce the relevant ingredients in nontechnical terms. A formal proof of the factorization theorem using soft-collinear effective theory is given in section 5.3. The extraction of a new beam function matching coefficient to $\mathcal{O}(\alpha_s^2)$ that arises in the theorem is described in section 5.4. In section 5.5, we perform an extensive validation of the factorization against known fixed-order results in full QCD through NNLO. In section 5.6, we present some illustrative applications of the new factorization theorem, including color-singlet rapidity spectra at N^{3}LO. We summarize our results in section 5.7.

5.2 Generalized threshold factorization theorem

We use light-cone coordinates $p^\mu \equiv (n \cdot p, \bar{n} \cdot p, \vec{p}_\perp) \equiv (p^+, p^-, \vec{p}_\perp)$ with respect to lightlike vectors $n^\mu \equiv (1, \hat{z})$ and $\bar{n}^\mu \equiv (1, -\hat{z})$ along the beam axis $\hat{z}$.[1] We first consider the observables $q^\mp$ instead of Q and Y, with corresponding momentum fractions

$$x_\mp \equiv \frac{q^\mp}{P_{a,b}^\mp} = \frac{\sqrt{Q^2 + q_T^2}}{E_{\text{cm}}} e^{\pm Y} . \tag{5.2}$$

We consider the generalized threshold limit

$$\lambda_{\text{QCD}}^2 \ll \lambda^2 \sim 1 - x_- \ll 1 \quad \text{for generic } x_+ , \tag{5.3}$$

where $\lambda_{\text{QCD}} \equiv \Lambda_{\text{QCD}}/Q$ and λ are power-counting parameters. In this limit, illustrated in figure 5.1, the leptonic final state L has large Y while the emissions in X become collimated

---

[1]Note that at variance with our conventions in section 2.2, we start out with n^μ and $\bar{n}^\mu$ defined in the hadronic center-of-mass frame (the lab frame) for the purposes of this section, so that in general $q^+ \neq q^-$. In the next section we will explicitly transition to the leptonic frame and recover our standard choice of $n^\mu, \bar{n}^\mu \equiv n_{a,b}^\mu = (1, \pm \hat{z})_{\text{lep}}$. The boost-invariant ratios $x_\pm$ are independent of this choice in any case.

in the opposite direction with typical momenta

$$p_X^\mu \sim (q^+, P_a^- - q^-, \vec{p}_{X\perp}) \sim (q^+, \lambda^2 q^-, \lambda\sqrt{q^+ q^-}) \,. \tag{5.4}$$

In this situation, the following factorization theorem holds to leading power in $1 - x_-$,

$$\frac{\mathrm{d}\sigma}{\mathrm{d}x_- \mathrm{d}x_+} = \sum_{i,j} H_{ij}(q^+ q^-, \mu) \int \mathrm{d}t \, f_i^{\mathrm{thr}}\left[x_- \left(1 + \frac{t}{q^+ q^-}\right), \mu\right] B_j(t, x_+, \mu) \,. \tag{5.5}$$

To derive eq. (5.5), we use the soft-collinear effective theory (SCET) reviewed in section 2.2. The key element in the derivation are the necessary degrees of freedom (modes) in the effective theory. Here we go through the terms in eq. (5.5) and briefly introduce the corresponding modes and the physics they describe. A detailed technical derivation of the factorization theorem, including modes whose contributions cancel and the formal definitions of all ingredients, is given in section 5.3 below.

In eq. (5.5), $B_j(t, x, \mu)$ is the inclusive beam function that also appears in the factorization for N-jettiness, e.g. for $N = 0$ as given in eq. (2.214). It describes the QCD final state at the scale λQ, whose scaling by eq. (5.4) is constrained to be

$$\bar{n}\text{-collinear:} \quad p^\mu \sim (q^+, \lambda^2 q^-, \lambda\sqrt{q^- q^+}) \,. \tag{5.6}$$

The beam function depends on the transverse virtuality t and momentum fraction x of the colliding parton j. Since $t \sim p_X^2 \sim \lambda^2 Q^2 \gg \Lambda_{\mathrm{QCD}}^2$, the beam function can be calculated perturbatively in terms of standard PDFs using the beam function OPE in eq. (2.217).

The hard function H_{ij} encodes hard virtual corrections $p^\mu \sim Q(1, 1, 1)$ that are integrated out in SCET, and arises from matching the electroweak current for L onto the corresponding SCET current. It is the same universal hard function as for all other factorization results for color-singlet production in this thesis.

The threshold PDF $f_i^{\mathrm{thr}}(x, \mu)$ describes the extraction of a parton i from the proton at large values $x \to 1$ of the momentum fraction,

$$f_i(x, \mu) = f_i^{\mathrm{thr}}(x, \mu)\left[1 + \mathcal{O}(1 - x)\right] \,. \tag{5.7}$$

It combines contributions from two modes,

$$\begin{aligned}
n\text{-collinear:} \quad & p^\mu \sim \left(\tfrac{\Lambda_{\mathrm{QCD}}^2}{q^-}, q^-, \Lambda_{\mathrm{QCD}}\right), \\
n\text{-collinear-soft:} \quad & p^\mu \sim \left(\tfrac{\Lambda_{\mathrm{QCD}}^2}{\lambda^2 q^-}, \lambda^2 q^-, \Lambda_{\mathrm{QCD}}\right).
\end{aligned} \tag{5.8}$$

The n-collinear modes are the active constituents of the proton that initiate the hard scattering. The n-collinear-soft modes mostly describe the low-energy remnant of the proton after converting a large fraction $x \to 1$ of its energy into the leptonic final state. As we will see in detail in section 5.3, the threshold PDF is in fact the same as in the standard endpoint DIS, eq. (2.179), and soft threshold factorization theorems, eq. (2.186).

Next, we consider also measuring $\vec{q}_T$. From eq. (5.4), it follows that generically $\vec{q}_T \sim \vec{p}_{X\perp} \sim \lambda Q$, so the $\vec{q}_T$ dependence is entirely described by the $p_{\bar{n}}$ modes, which yields the factorization theorem

$$\frac{\mathrm{d}\sigma}{\mathrm{d}x_-\mathrm{d}x_+\,\mathrm{d}\vec{q}_T} = \sum_{i,j} H_{ij}(q^+q^-,\mu) \int \mathrm{d}t\, f_i^{\mathrm{thr}}\Big[x_-\Big(1+\frac{t}{q^+q^-}\Big),\mu\Big]\, B_j(t, x_+, \vec{q}_T, \mu)\,. \quad (5.9)$$

Here, $B_j(t, \vec{k}_T, x, \mu)$ is the double-differential beam function [397, 398] that we also encountered in the joint resummation of q_T and 0-jettiness in chapter 4.

So far we have been working with the momentum fractions $x_\mp$, which are not in direct correspondence to Q and Y, i.e., the inclusive rapidity spectrum. However, since we have full control over the transverse momentum $\vec{q}_T$ in eq. (5.9), we can change variables to $x_{a,b}$, using eq. (5.2) and expanding in λ, which yields

$$\frac{\mathrm{d}\sigma}{\mathrm{d}x_a\mathrm{d}x_b\,\mathrm{d}\vec{q}_T} = \sum_{i,j} H_{ij}(Q^2,\mu) \int \mathrm{d}t\, f_i^{\mathrm{thr}}\Big[x_a\Big(1+\frac{q_T^2}{2Q^2}+\frac{t}{Q^2}\Big),\mu\Big]\, B_j(t, x_b, \vec{q}_T, \mu)\,. \quad (5.10)$$

Crucially, when expanding $x_- = x_a[1+q_T^2/(2Q^2)+\mathcal{O}(\lambda^4)]$, we have to keep the $q_T^2/(2Q^2) \sim \lambda^2$ term in the PDF argument because it is of the same order as $t/Q^2 \sim \lambda^2$. Integrating eq. (5.10) over $\vec{q}_T$, we obtain

$$\frac{\mathrm{d}\sigma}{\mathrm{d}x_a\mathrm{d}x_b} = \sum_{i,j} H_{ij}(Q^2,\mu) \int \mathrm{d}\tilde{t}\, f_i^{\mathrm{thr}}\Big[x_a\Big(1+\frac{\tilde{t}}{Q^2}\Big),\mu\Big]\, \tilde{B}_j(\tilde{t}, x_b, \mu)\,. \quad (5.11)$$

The factorization theorems in eqs. (5.10) and (5.11) hold at leading power in the generalized threshold limit $\lambda^2 \sim 1 - x_a \ll 1$ for generic x_b. They are our key new results. In eq. (5.11) we changed variables to $\tilde{t} = t + q_T^2/2$, and defined the new modified beam function

$$\tilde{B}_j(\tilde{t}, x, \mu) = \int \mathrm{d}^2\vec{k}_T\, B_j\Big(\tilde{t} - \frac{k_T^2}{2}, x, \vec{k}_T, \mu\Big)\,. \quad (5.12)$$

It has the same μ evolution as $B_j(t, x, \mu)$ but different constant terms. It obeys a matching relation analogous to eq. (2.217),[2]

$$\tilde{B}_i(\tilde{t}, x, \mu) = \sum_j \int \frac{\mathrm{d}z}{z}\, \tilde{\mathcal{I}}_{ij}(\tilde{t}, z, \mu)\, f_j\Big(\frac{x}{z}, \mu\Big)\,. \quad (5.13)$$

Using the known results for $B_j(t, \vec{k}_T, x, \mu)$ [397, 398], we have calculated the matching coefficients $\tilde{\mathcal{I}}_{jk}(\tilde{t}, z, \mu)$ to $\mathcal{O}(\alpha_s^2)$ for $j = q$ and $\mathcal{O}(\alpha_s)$ for $j = g$, see section 5.4.[3]

---

[2]In this chapter we reserve the symbol $\tilde{\mathcal{I}}_{ij}$ for the matching coefficients of the above modified virtuality-dependent beam function, not to be confused with the b_T-space matching coefficients of the q_T beam function in eq. (2.210) as used in the rest of this thesis. The two are also distinguished by their arguments.

[3]Since the original publication of these results in ref. [4], the double-differential gluon beam function and the finite terms of the modified beam function introduced here have been calculated to $\mathcal{O}(\alpha_s^2)$ [411].

5.2.1 RG consistency and relation to DIS near endpoint

A nontrivial consistency check for Eqs. (5.5), (5.9), (5.10), (5.11) is that they must satisfy RGE consistency, i.e., the μ dependence must cancel between the different functions on the right-hand side, since the cross section on the left-hand side does not depend on μ. It is instructive to see explicitly how this happens, picking out eq. (5.5) as an example. The hard function satisfies the RGE

$$\mu \frac{\mathrm{d}}{\mathrm{d}\mu} H_{ij}(q^+ q^-, \mu) = \gamma_H^i(q^+ q^-, \mu) \, H_{ij}(q^+ q^-, \mu) \,,$$

$$\gamma_H^i(q^+ q^-, \mu) = 2\Gamma_{\mathrm{cusp}}^i[\alpha_s(\mu)] \ln \frac{q^+ q^-}{\mu^2} + \gamma_H^i[\alpha_s(\mu)] \,. \tag{5.14}$$

Here and below, the superscript i on the cusp and noncusp anomalous dimensions denotes the relevant color channel $i = q$ or $i = g$. The beam function is renormalized as in eq. (2.216). The RGE for the threshold PDF can be read off from that of the full PDF in eq. (2.164). Taking the limit $x \to 1$, which implies $z \to 1$, and changing variables to $\xi = 1 - z$ yields the RGE for the threshold PDF,

$$\mu \frac{\mathrm{d}}{\mathrm{d}\mu} f_i^{\mathrm{thr}}(x, \mu) = \int \mathrm{d}\xi \, \gamma_f^i[\alpha_s(\mu), \xi] \, f_i^{\mathrm{thr}}[x(1+\xi), \mu] \,,$$

$$\gamma_f^i(\alpha_s, \xi) = 2\Gamma_{\mathrm{cusp}}^i(\alpha_s) \, \mathcal{L}_0(\xi) + \gamma_f^i(\alpha_s) \, \delta(\xi) \,, \tag{5.15}$$

which becomes a Fourier convolution diagonal in flavor with the threshold anomalous dimension $\gamma_f^i(\alpha_s, \xi)$ given by the $z \to 1$ limit of the full splitting functions,

$$2P_{ij}(\alpha_s, z) = \delta_{ij} \gamma_f^i(\alpha_s, 1 - z) + \mathcal{O}[(1-z)^0] \,. \tag{5.16}$$

The RGE in eq. (5.15) was also confirmed by direct calculation [214, 216].

Requiring the μ derivative of eq. (5.23) to vanish leads to the following consistency condition for the anomalous dimensions, after pulling them under a single convolution,

$$0 = \delta(t) \, \gamma_H^i(q^- q^+, \mu) + \frac{1}{q^+ q^-} \, \gamma_f^i\Big[\alpha_s(\mu), \frac{t}{q^+ q^-}\Big] + \gamma_B^i(t, \mu)$$

$$= 2\Gamma_{\mathrm{cusp}}^i[\alpha_s(\mu)] \bigg[\delta(t) \ln \frac{q^+ q^-}{\mu^2} + \frac{1}{q^+ q^-} \mathcal{L}_0\Big(\frac{t}{q^+ q^-}\Big) - \frac{1}{\mu^2} \mathcal{L}_0\Big(\frac{t}{\mu^2}\Big)\bigg]$$

$$+ \Big\{\gamma_H^i[\alpha_s(\mu)] + \gamma_f^i[\alpha_s(\mu)] + \gamma_B^i[\alpha_s(\mu)]\Big\} \delta(t) \,. \tag{5.17}$$

The terms proportional to Γ_{cusp}^i can easily be seen to vanish by rescaling the plus distributions to a common argument. For the noncusp terms, the endpoint DIS factorization in eq. (2.179) implies the relation $\gamma_H^i(\alpha_s) + \gamma_f^i(\alpha_s) + \gamma_J^i(\alpha_s) = 0$, where $\gamma_J^i(\alpha_s)$ is the jet-function noncusp anomalous dimension. Hence, requiring the noncusp terms to vanish is equivalent to the statement that the beam and jet anomalous dimensions are equal to all orders, $\gamma_B^i(\alpha_s) = \gamma_J^i(\alpha_s)$ [293]. The existence of our new factorization theorems provides an independent confirmation of this fact. The above discussion also shows that to be fully
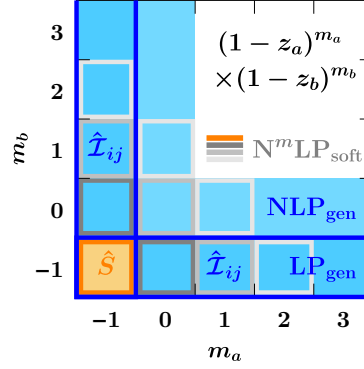
Figure 5.2: Terms in the partonic cross section $\hat{\sigma}(z_a, z_b)$ captured by the soft and generalized threshold expansions. The leading-power factorization theorems without matching are indicated by the dark blue and filled orange boxes, respectively. Terms captured by the generalized threshold expansion at different orders are indicated by successively lighter shades of blue. (The $\mathrm{LP}_{\mathrm{gen}}$ includes the soft orange box.) Terms captured by the soft expansion at different orders are indicated by boxes with successively lighter gray edges.

consistent, the factorization theorem has to contain the threshold PDFs. Using the full PDFs, the RGE consistency would only hold up to power corrections in $1 - x$.

The equivalence of RG consistency in the two cases underlines the close physical connection to inclusive DIS near endpoint, which, roughly speaking, is related to our new factorization theorem by crossing, with the jet function J_j describing collimated *final-state* radiation. The key differences to endpoint DIS, allowing for a richer perturbative structure, are the additional dependence on x_b, the presence of off-diagonal partonic channels at leading power, and the nontrivial dependence on q_T. The latter in particular allows for the subtle distinction between the factorization theorems for $x_{\mp}$ and $x_{a,b}$, which bears some resemblance to different 1-jettiness definitions in exclusive DIS [292].[4]

5.2.2 Matching and partonic factorization theorem

Since eq. (5.11) is valid for $x_a \to 1$ and arbitrary x_b, it must contain the soft threshold factorization in eq. (2.186) for $x_b \to 1$ as a special case. Stripping off common ingredients, this implies

$$\tilde{B}_j(\omega k^-, x_b, \mu) = \int \frac{\mathrm{d}k^+}{\omega} \, S_j(k^-, k^+, \mu) \, f_j^{\mathrm{thr}}\Big[x_b\Big(1 + \frac{k^+}{\omega}\Big), \mu\Big] \tag{5.18}$$

to leading power in $1-x_b$. Identical results hold for $x_\pm$, i.e., for the standard inclusive beam function $B_j(t, x, \mu)$ on the left-hand side, as well as differential in transverse momentum.

---

[4]We note that some of the factorization theorems in ref. [292] could also be marginalized over the transverse momentum of collinear ISR, giving rise to projections of the double-differential beam function similar to eq. (5.12). In the case of ref. [292], however, the factor multiplying k_T^2 in the first argument of the beam function would be -1 rather than $-1/2$, so our explicit results for $\tilde{\mathcal{I}}_{ij}$ computed in this chapter unfortunately do not carry over immediately. We thank C. Lee and D. Kang for discussion on this point.

A formal derivation of eq. (5.18) is given in section 5.3.5, with particular attention to the possible issue of noncommuting limits in x_a and x_b.

With the relation to the soft limit at hand, we can ask what terms are captured by our new factorization theorem at the level of the partonic cross section. Expanding $f_i(x/z)/z = f_i^{\text{thr}}[x(1 + 1 - z)] \times [1 + \mathcal{O}(1 - z)]$ in eq. (2.64) and comparing to eq. (5.11), we find

$$\hat{\sigma}_{ij}(z_a, z_b, Q, \mu = Q) = \sum_k \hat{H}_{ik} \hat{\mathcal{I}}_{kj}(z_a, z_b) \big[1 + \mathcal{O}(1 - z_a)\big], \tag{5.19}$$

where we changed variables to $z_{a,b}$ and defined

$$\hat{H}_{ij} \equiv H_{ij}(Q^2, \mu = Q),$$
$$\hat{\mathcal{I}}_{ij}(z_a, z_b) \equiv Q^2 \tilde{\mathcal{I}}_{ij}\big[Q^2(1 - z_a), z_b, \mu = Q\big]. \tag{5.20}$$

Here we focus on the partonic cross section at a fixed scale for simplicity and suppress the residual dependence on Q through $\alpha_s(Q)$. From eq. (5.19), we see that all singular terms $\sim (1 - z_a)^{-1}$ are captured by the beam function coefficient, including their exact dependence on z_b and across partonic channels. This is illustrated by the vertical blue box with $m_a = -1$ in figure 5.2. The overlap with the opposite limit $z_b \to 1$, indicated by the horizontal blue box with $m_b = -1$, is precisely given by the soft function (the filled orange box at $m_a = m_b = -1$),

$$\hat{\mathcal{I}}_{ij}(z_a, z_b) = \delta_{ij} \, \hat{S}_i(z_a, z_b) \big[1 + \mathcal{O}(1 - z_b)\big], \tag{5.21}$$

where $\hat{S}_i(z_a, z_b)$ was defined in eq. (2.189). This is the partonic version of eq. (5.18).

Combining the leading terms encoded in $\hat{\mathcal{I}}_{ij}(z_a, z_b)$ and $\hat{\mathcal{I}}_{ij}(z_b, z_a)$ and removing the soft overlap, we obtain, at the partonic level, the generalized threshold factorization theorem

$$\hat{\sigma}_{ij}(z_a, z_b, Q, \mu = Q) = \sum_{k,\ell} \hat{H}_{k\ell} \Big[\delta_{ki} \hat{\mathcal{I}}_{\ell j}(z_a, z_b) + \hat{\mathcal{I}}_{ki}(z_b, z_a) \, \delta_{\ell j} - \delta_{ki} \, \delta_{\ell j} \, \hat{S}_i(z_a, z_b)\Big]$$
$$+ \mathcal{O}\big[(1 - z_a)^0 (1 - z_b)^0\big]. \tag{5.22}$$

As written, all remaining power corrections to this expression are integrable in $z_{a,b}$ in all possible limits, with $m_a, m_b \geq 0$. Thus we see that eq. (5.22) isolates all singularities in color-singlet rapidity spectra in a fully process-independent way, with the process-dependent virtual corrections captured by the overall hard function. This should be contrasted with eq. (2.188), which only captures the doubly singular terms in $z_{a,b}$, but drops *relative* power corrections of both $\mathcal{O}(1 - z_a)$ and $\mathcal{O}(1 - z_b)$, i.e., the boxes immediately adjacent to the soft orange box in figure 5.2. An analogous expression to eq. (5.22) holds at hadronic level by directly matching the hadronic factorization theorems.

Mode	Lab frame $(+, -, \perp)$	Leptonic $(\hat{Y} = 0)$ frame $(+, -, \perp)$
$p_{\bar{n}}$	$(q^+, \lambda^2 q^-, \lambda\sqrt{q^- q^+})$	$Q\,(1, \lambda^2, \lambda)$
$P_{\bar{n}}$	$\left(q^+, \dfrac{\Lambda_{\mathrm{QCD}}^2}{q^+}, \Lambda_{\mathrm{QCD}}\right)$	$Q\,(1, \lambda_{\mathrm{QCD}}^2, \lambda_{\mathrm{QCD}})$
P_n	$\left(\dfrac{\Lambda_{\mathrm{QCD}}^2}{q^-}, q^-, \Lambda_{\mathrm{QCD}}\right)$	$Q\,(\lambda_{\mathrm{QCD}}^2, 1, \lambda_{\mathrm{QCD}})$
P_{cs}	$\left(\dfrac{1}{\lambda^2}\dfrac{\Lambda_{\mathrm{QCD}}^2}{q^-}, \lambda^2 q^-, \Lambda_{\mathrm{QCD}}\right)$	$Q\left(\dfrac{\lambda_{\mathrm{QCD}}^2}{\lambda^2}, \lambda^2, \lambda_{\mathrm{QCD}}\right)$
P_{us}	$\left(\dfrac{\Lambda_{\mathrm{QCD}}^2}{q^-}, \dfrac{\Lambda_{\mathrm{QCD}}^2}{q^+}, \dfrac{\Lambda_{\mathrm{QCD}}^2}{\sqrt{q^+ q^-}}\right)$	$Q\,(\lambda_{\mathrm{QCD}}^2, \lambda_{\mathrm{QCD}}^2, \lambda_{\mathrm{QCD}}^2)$
P_G	$\left(\dfrac{\Lambda_{\mathrm{QCD}}^2}{q^-}, \dfrac{\Lambda_{\mathrm{QCD}}^2}{q^+}, \Lambda_{\mathrm{QCD}}\right)$	$Q\,(\lambda_{\mathrm{QCD}}^2, \lambda_{\mathrm{QCD}}^2, \lambda_{\mathrm{QCD}})$

Table 5.1: Relevant EFT modes in the limit $\lambda_{\mathrm{QCD}} \sim \lambda^2 \sim 1 - x^- \ll 1$ in the lab (hadronic center-of-mass) frame and the leptonic frame where $\hat{Y} = 0$. Lowercase p (uppercase P) indicates that a mode is perturbative (nonperturbative). In the right column we used that in the leptonic frame, $q^\pm \to \hat{q}^\pm = \sqrt{q^+ q^-} \sim Q$.

5.3 Proof of the factorization theorem

In this section we give a detailed derivation of the factorization theorem in eq. (5.9), from which all the other factorization theorems follow. We repeat it here for easy reference:

$$\frac{\mathrm{d}\sigma}{\mathrm{d}x_- \mathrm{d}x_+ \,\mathrm{d}\vec{q}_T} = H_{ij}(q^+ q^-, \mu) \int \mathrm{d}t\, f_i^{\mathrm{thr}}\Big[x_-\Big(1 + \frac{t}{q^+ q^-}\Big), \mu\Big] B_j(t, x_+, \vec{q}_T, \mu)\,. \qquad (5.23)$$

For definiteness, and because it provides some additional insight on the spin dynamics as $x^- \to 1$, we focus on the Drell-Yan process, described in detail in section 2.1.3. Our results readily generalize to other color-singlet process.

Equation (5.23) is valid up to power corrections in λ^2 in the generalized threshold limit

$$\lambda^2 \sim 1 - x_- \ll 1 \qquad \text{for generic } x_+\,, \qquad \lambda_{\mathrm{QCD}} \equiv \Lambda_{\mathrm{QCD}}/Q \sim \lambda^2 \ll \lambda\,. \qquad (5.24)$$

We require $\lambda_{\mathrm{QCD}} \ll \lambda$ for reasons that will be apparent soon. Without loss of generality we can then consider $\lambda_{\mathrm{QCD}} \sim \lambda^2$. This relation is to be interpreted as follows: First, in our context, λ_{QCD} denotes the scale of the PDFs, which is generically allowed to be as large as λ^2 and does not necessarily have to be nonperturbative. If it happens to be a perturbative scale, then the physics below λ_{QCD} is simply described by the PDF evolution. Conversely, it also means that λ^2 is in principle allowed to be as small as λ_{QCD} including being nonperturbative, i.e., it is only relevant that $\lambda \gg \lambda_{\mathrm{QCD}}$ is perturbative.

5.3.1 Degrees of freedom and Glauber cancellation

The key step in deriving eq. (5.23) is to identify the relevant degrees of freedom (modes) in the effective field theory (EFT) that describe the physical situation. They are defined by the relative scaling of their light-cone momentum components and are summarized in table 5.1.

The $p_{\bar{n}}$ modes describe the hadronic final state of the collision. Their scaling is determined by the fact that in the limit of eq. (5.24), there is only $p_{\bar{n}}^- \sim \lambda^2 E_{\rm cm} \sim \lambda^2 q^-$ minus momentum available. On the other hand, their plus momentum is unconstrained, which means it has generic scaling set by the hard interaction, $p_{\bar{n}}^+ \sim \xi_b E_{\rm cm} \sim x_b E_{\rm cm} \sim q^+$. Since $p_{\bar{n}}^2 \sim \lambda^2 q^+ q^- \sim \lambda^2 Q^2 \gg \Lambda_{\rm QCD}^2$, the $p_{\bar{n}}$ modes are perturbative. Therefore, they describe the perturbative QCD final state produced in the partonic collision in addition to L (but excluding the beam remnant). The P_n and $P_{\bar{n}}$ modes describe the incoming protons, or more precisely, the partons in the proton with the typical momentum fractions required to produce the hard final state. This means their scaling is determined by $P_n^- \sim q^-$ and $P_{\bar{n}}^+ \sim \xi_b E_{\rm cm} \sim x_b E_{\rm cm} \sim q^+$ and $P_n^2 \sim P_{\bar{n}}^2 \sim \Lambda_{\rm QCD}^2$.

The collinear-soft P_{cs} modes describe the interactions between the $p_{\bar{n}}$ and P_n modes.[5] Their scaling is thus determined by $P_{cs}^- \sim p_{\bar{n}}^- \sim \lambda^2 Q$ and $P_{s\perp} \sim P_{n\perp} \sim \Lambda_{\rm QCD}$ or equivalently $P_{cs}^2 \sim P_n^2 \sim \Lambda_{\rm QCD}^2$. Hence, they keep the $p_{\bar{n}}$ modes on shell and have a SCET$_{\rm I}$-like relation to them. Their interactions with the $p_{\bar{n}}$ modes in the leading-power SCET Lagrangian are decoupled and moved into collinear-soft Wilson lines $V_n(x)$ in the SCET current via the BPS field redefinition. At the same time, the P_{cs} modes have a SCET$_{\rm II}$-like relation to the P_n modes, i.e., they have the same virtuality but are parametrically separated in rapidity. Hence, their interactions with the P_n modes, which take the P_n modes off shell, are described by collinear-soft Wilson lines $X_n(x)$ in the SCET current that are generated during the matching onto SCET. The distinction of the P_{cs} modes relies on $\lambda_{\rm QCD} \ll \lambda$, while for $\lambda_{\rm QCD} \sim \lambda$, they would become degenerate with the $p_{\bar{n}}$ and $P_{\bar{n}}$ modes.

The power counting and the relations between the modes are most transparent in the leptonic frame, which is the frame where the color-singlet final state has total rapidity $\hat{Y} = 0$. Boosting from the lab frame to the leptonic frame by Y, we have $\hat{q}^\pm = q^\pm e^{\pm Y} = \sqrt{q^+ q^-} \sim Q$. In the leptonic frame, the $p_{\bar{n}}$ modes are genuinely $\bar{n}$-collinear with $p_{\bar{n}}^- \sim \lambda^2 p_{\bar{n}}^+$, and the collinear-soft modes become isotropic when we take $\lambda^2 \sim \lambda_{\rm QCD}$, $P_s \sim \lambda^2 Q \sim \lambda_{\rm QCD} Q$. By contrast, in the lab frame we must separately keep track of q^+ and q^-, i.e., we cannot count them as $q^+ \sim q^-$, because we want to take the limit of large q^- for generic q^+. As a result, the $p_{\bar{n}}$ modes do not necessarily appear to be $\bar{n}$-collinear in the lab frame because $q^+ \sim \lambda^2 q^-$ is allowed. However, the key requirement for their factorization is that they are collinear *relative* to the collinear-soft modes, which in the lab frame are boosted in the n-collinear direction i.e., they are n-collinear-soft.

---

[5]Note that e.g. in ref. [216], these collinear-soft modes were referred to as soft since one can take $\lambda_{\rm QCD} \sim \lambda^2$ without loss of generality as discussed, in which case they indeed become isotropic central soft modes in the lab frame (or Breit frame, for DIS). Here we refer to them as collinear-soft to highlight that they have simultaneous SCET$_{\rm I}$ and SCET$_{\rm II}$ relations with neighboring collinear modes, and to avoid confusion with the perturbative soft modes contributing to the soft threshold factorization theorem.

Finally, the ultrasoft (usoft) P_{us} and Glauber P_G modes describe the interactions between the P_n and $P_{\bar{n}}$ modes that are possible without pushing either of them off shell, which requires $P_{us}^- \sim P_{\bar{n}}^-$ and $P_{us}^+ \sim P_n^+$. The $\perp$ component of the usoft modes is fixed by requiring them to be on-shell modes, $P_{us\perp}^2 \sim P_{us}^+ P_{us}^-$. The corresponding Glauber modes are allowed to be off shell, so their $\perp$ component can be as large as $P_{G\perp} \sim P_{n\perp} \sim P_{\bar{n}\perp} \sim \Lambda_{\text{QCD}}$. The effects of the usoft and Glauber modes cancel, so we do not need to consider them further. To see this, note that we are still in the domain of applicability of the general collinear factorization theorem in eq. (2.65) because in the limit we consider, the lowest scale probed by the measurement is $\Lambda_X \sim q_T \sim Q\sqrt{1-x_-} \gg \lambda_{\text{QCD}} Q$, and the measurement is still fully inclusive over transverse momenta at the scale $\lambda_{\text{QCD}} Q \ll \Lambda_X$. Thus the cancellation of the P_{us} and P_G degrees of freedom follows in the same way as in the original proof of eq. (2.65) in refs. [104–106]. This is another reason why we require $\lambda_{\text{QCD}} \ll \lambda$.

Importantly, there is only a single collinear sector at the scale λQ, so Glauber modes with the other possible parametric scaling $Q(\lambda^2, \lambda^2, \lambda)$ are absent in the EFT and cannot spoil factorization; while interactions with them would keep the $p_{\bar{n}}$ modes on shell, there is no other collinear sector at that scale that they could couple to.

5.3.2 Fields and hard matching

With the modes at hand, we can write down the leading-power EFT operators. All light-cone momenta from now on are given in the leptonic frame, returning to our standard conventions, and we drop the hat. The relevant n-collinear operator building block reads

$$\chi_{q\,n,\tilde{\omega}_n}(x) = \left[\delta_{\overline{\mathcal{P}}_n \tilde{\omega}_n} \chi_{q\,n}(x) \right], \tag{5.25}$$

where we pick out a *discrete* large label momentum $\tilde{\omega}_n$ as indicated by the Kronecker δ, i.e., the field on the left-hand side depends on all residual spacetime directions, $\chi_{q\,n,\tilde{\omega}_n}(x) = \chi_{q\,n,\tilde{\omega}_n}(x^+, x^-, \vec{x}_\perp)$. Working with discrete label momentum on n-collinear fields will turn out to be a convenient choice to describe the physics and disentangle n-collinear and collinear-soft contributions. To further reduce the risk of confusion, we indicate the discreteness of $\tilde{\omega}_n$ by a tilde.

The building blocks in the $\bar{n}$-collinear sector read

$$\chi_{q\,\bar{n},p_{\bar{n}}}(x) = \left[\delta(\omega_{\bar{n}} - \overline{\mathcal{P}}_{\bar{n}}) \, \delta^2(\vec{p}_{\bar{n}\perp} - \vec{\mathcal{P}}_{\bar{n}\perp}) \, \chi_{q\,n}(x) \right], \qquad p_{\bar{n}}^\mu = \omega_{\bar{n}} \frac{n^\mu}{2} + p_{\bar{n}\perp}, \tag{5.26}$$

and have continuous label momentum in all three directions in the sense of eq. (2.139), so they only depend on $\chi_{q\,\bar{n},p_{\bar{n}}}(x) = \chi_{q\,\bar{n},p_{\bar{n}}}(x^+)$, where $x^+ = \bar{n} \cdot x$ is conjugate to a small residual momentum $k_{\bar{n}}^-$. The indicated relation between $p_{\bar{n}}^\mu$ and its components is always understood in the following. Analogous definitions hold for $\mathcal{B}_{n,\tilde{\omega}_n\perp}^\mu$ and $\mathcal{B}_{\bar{n},p_{\bar{n}}\perp}^\mu$.

Collinear-soft fields always appear in the combination

$$O_{cs}(x) \equiv V_n^\dagger(x) X_n(x), \qquad \mathcal{O}_{cs}(x) \equiv \mathcal{V}_n^\dagger(x) \mathcal{X}_n(x), \tag{5.27}$$

as dictated by invariance under collinear-soft gauge transformations. Whether $O_{cs}(x)$ or $O_{cs}^\dagger(x)$ appears in the leading-power hard operators below is determined by the neighboring

n and $\bar{n}$-collinear fields that induced the Wilson lines during the BPS redefinition or the matching, respectively.

In terms of the above building blocks, the leading-power hard operators read

$$O_{q'\bar{q}}^{\alpha\beta}(\tilde{\omega}_n, p_{\bar{n}}; x) = \bar{\chi}_{q'\,n,-\tilde{\omega}_n}^{\alpha j}(x)\, \mathrm{T}\big[O_{cs}^\dagger(x)\big]^{jk} \chi_{q\,\bar{n},p_{\bar{n}}}^{\beta k}(x)\,,$$

$$O_{\bar{q}q'}^{\alpha\beta}(\tilde{\omega}_n, p_{\bar{n}}; x) = \bar{\chi}_{q'\,\bar{n},-p_{\bar{n}}}^{\alpha j}(x)\, \mathrm{T}\big[O_{cs}(x)\big]^{jk} \chi_{q\,n,\tilde{\omega}_n}^{\beta k}(x)\,,$$

$$O_{gg}^{\mu\nu}(\omega_n, p_{\bar{n}}; x) = \sqrt{\omega_n \omega_{\bar{n}}}\Big\{ \mathcal{B}_{n,-\tilde{\omega}_n\perp}^{\mu,a}(x)\, \mathrm{T}\big[\mathcal{O}_{cs}^\dagger(x)\big]^{ab} \mathcal{B}_{\bar{n},-p_{\bar{n}}\perp}^{\nu,b}(x)$$
$$+ \mathcal{B}_{\bar{n},-p_{\bar{n}}\perp}^{\mu,a}(x)\, \mathrm{T}\big[\mathcal{O}_{cs}(x)\big]^{ab} \mathcal{B}_{n,-\tilde{\omega}_n\perp}^{\nu,b}(x)\Big\}\,. \qquad (5.28)$$

These are very similar to the hard operators in eq. (2.154), with an obvious replacement of ultrasoft by collinear-soft Wilson lines and a relabelling of flavor indices. The more important difference is that in our current setup, n and $\bar{n}$-collinear modes are distinguished not just by their directions, but also by their virtualities and by the fact that only one of them (n) is accompanied by collinear-soft modes at the same virtuality. Therefore instead of the generic directions in eq. (2.154), which would allow for permutations $n_1 \leftrightarrow n_2$, we should directly pick up the combinations $n_1 \equiv n, n_2 \equiv \bar{n}$ and vice versa that are allowed by label momentum conservation with the external proton states, and dress each with the appropriate Wilson line.

In terms of these operators, the leading-power current reads

$$J_V^{(0)\mu}(x) = \sum_{\tilde{\omega}_n} \int \mathrm{d}\omega_{\bar{n}}\, \mathrm{d}^2\vec{p}_{\bar{n}\perp}\, e^{-\mathrm{i}(\tilde{\omega}_n n\cdot x/2 + p_{\bar{n}}\cdot x)}$$

$$\times \bigg[\sum_{q,q'} C_{V\,q'\bar{q}}^{\mu\,\alpha\beta}(n,\bar{n};\tilde{\omega}_n,\omega_{\bar{n}})\, O_{q'\bar{q}}^{\alpha\beta}(\tilde{\omega}_n, p_{\bar{n}}; x) + C_{V\,\bar{q}q'}^{\mu\,\alpha\beta}(n,\bar{n};\tilde{\omega}_n,\omega_{\bar{n}})\, O_{\bar{q}q'}^{\alpha\beta}(\tilde{\omega}_n, p_{\bar{n}}; x)$$

$$+ C_{V\,gg\,\rho\sigma}^{\mu}(n,\bar{n};\tilde{\omega}_n,\omega_{\bar{n}})\, O_{gg}^{\rho\sigma}(\tilde{\omega}_n, p_{\bar{n}}; x) \bigg] \quad + \text{other directions}\,. \qquad (5.29)$$

We drop the superscript (0) on the right-hand side because we always work to leading power. The matching coefficients C_V^μ are exactly the same as when matching QCD onto SCET$_\mathrm{I}$ in eq. (2.144). To see this, note that we can perform the matching using the fully factorized operators to compute the relevant matrix elements in the EFT, in which case the result is independent of the precise relation between the modes and only depends on the number of collinear sectors (two) and soft or collinear-soft Wilson lines (two, with matching orientation and charges). In addition, the leading-power Wilson coefficients can only depend on the large label components $\tilde{\omega}_n$, $\omega_{\bar{n}}$, but not on $\vec{p}_{\bar{n}\perp} \sim \lambda Q$, and are independent of whether the label momenta are discrete or continuous. The matching coefficient in the second quark term in eq. (5.29), where we interchanged the directions, is related to the first by

$$C_{V\,q'\bar{q}}^{\mu\,\alpha\beta}(n,\bar{n};\tilde{\omega}_n,\omega_{\bar{n}}) = C_{V\,\bar{q}q'}^{\mu\,\alpha\beta}(\bar{n},n;\omega_{\bar{n}},\tilde{\omega}_n)\,. \qquad (5.30)$$

The two terms in the gluon operator in eq. (5.28) have the same matching coefficient $C_{V\,gg\,\rho\sigma}^{\mu}(n,\bar{n};\tilde{\omega}_n,\omega_{\bar{n}})$ due to Bose symmetry [57]. We note that rather than matching QCD directly onto these modes, one may also perform a multi-stage matching, as was done for endpoint DIS in ref. [216], which yields the same end result.

5.3.3 Factorizing the effective operator matrix element

Our starting point for factorizing the cross section is the hadronic tensor for inclusive Drell-Yan production in eq. (2.55) integrated over any hadronic observables $\mathcal{O}_X$,

$$
W_{VV'}^{\mu\nu}(q, P_n, P_{\bar{n}}) = \sum_X \langle pp | J_V^{\dagger\mu} | X \rangle \langle X | J_{V'}^\nu | pp \rangle \, \delta^4(P_n + P_{\bar{n}} - q - p_X)
$$

$$
= \int \frac{\mathrm{d}^4 x}{(2\pi)^4} \, e^{-iq\cdot x} \langle pp | J_V^{\dagger\mu}(x) \, J_{V'}^\nu(0) | pp \rangle \,. \tag{5.31}
$$

On the second line we have used momentum conservation in the first matrix element to translate the current to x, and used the completeness relation in eq. (2.33) to eliminate the sum over final states. After inserting eq. (5.28), the relevant matrix elements in the EFT take the form $\langle pp | O^\dagger(x) \, O'(0) | pp \rangle$, where O and O' are any of $O_{q'\bar{q}}, O_{\bar{q}q'}, O_{gg}$. We first consider the interference $O_{\bar{q}q'}^{\dagger\beta\alpha}(\tilde{\omega}_n, p_{\bar{n}}; x) \, O_{\bar{q}q'}^{\alpha'\beta'}(\tilde{\omega}_n', p_{\bar{n}}'; 0)$ of $O_{\bar{q}q'}$ with itself for identical flavors, but potentially different label momenta, spin, and color indices indicated by a prime. Since the interactions between different sectors are fully factorized at the level of the Lagrangian and Glauber and usoft interactions cancel as discussed above, the matrix element factorizes into individual forward matrix elements in each sector,

$$
\langle pp | O_{\bar{q}q'}^{\dagger\beta\alpha}(\tilde{\omega}_n, p_{\bar{n}}; x) \, O_{\bar{q}q'}^{\alpha'\beta'}(\tilde{\omega}_n', p_{\bar{n}}'; 0) | pp \rangle
$$

$$
= \theta(\tilde{\omega}_n)\theta(\tilde{\omega}_n') \langle p_n | \bar{\chi}_{qn,\tilde{\omega}_n}^{\beta k}(x) \, \bar{\mathrm{T}}\big[O_{cs}^\dagger(x)\big]^{kj} \, \mathrm{T}\big[O_{cs}(0)\big]^{j'k'} \chi_{qn,\tilde{\omega}_n'}^{\beta'k'}(0) | p_n \rangle
$$

$$
\times \theta(\omega_{\bar{n}})\theta(\omega_{\bar{n}}') \langle p_{\bar{n}} | \chi_{q'\bar{n},-p_{\bar{n}}}^{\alpha j}(x) \, \bar{\chi}_{q'\bar{n},-p_{\bar{n}}'}^{\alpha'j'}(0) | p_{\bar{n}} \rangle
$$

$$
= \frac{1}{N_c} \delta_{\tilde{\omega}_n \tilde{\omega}_n'} \theta(\tilde{\omega}_n) \langle p_n | \bar{\chi}_{qn}^\beta(x) \, \bar{\mathrm{T}}\big[O_{cs}^\dagger(x)\big] \, \mathrm{T}\big[O_{cs}(0)\big] \chi_{qn,\tilde{\omega}_n}^{\beta'}(0) | p_n \rangle
$$

$$
\times \delta(\omega_{\bar{n}} - \omega_{\bar{n}}') \, \delta^2(\vec{p}_{\bar{n}\perp} - \vec{p}_{\bar{n}\perp}') \, \theta(\omega_{\bar{n}}) \langle p_{\bar{n}} | \chi_{q'\bar{n}}^\alpha(x) \, \bar{\chi}_{q'\bar{n},-p_{\bar{n}}}^{\alpha'}(0) | p_{\bar{n}} \rangle \,. \tag{5.32}
$$

Note that the proton state $|p_n\rangle$ moving in the n-collinear direction must in general contain collinear-soft degrees of freedom, as discussed in more detail in section 5.3.6, so the collinear-soft Wilson lines cannot a priori be moved into a separate vacuum matrix element. The θ functions in front of the matrix elements encode the constraint that the fields in the operators must annihilate positive-energy states in the proton. On the second equality we used label momentum conservation in each matrix element to eliminate the primed label momenta, and the QCD Fierz identity for fields in the fundamental representation to eliminate primed color indices,

$$
\delta_{j\ell} \, \delta_{j'\ell'} = \frac{1}{N_c} \delta_{jj'} \delta_{\ell\ell'} - 2(T^a)_{jj'}(T^a)_{\ell\ell'} \,. \tag{5.33}
$$

Only the first term survives because matrix elements of color-octet operators between the color-singlet proton states vanish. We will deal with the spin structure later on.

There are analogous contributions from the square of $O_{q'\bar{q}}$ and O_{gg}. The matching coefficient $C_{V\,gg}^\mu$ of O_{gg} is proportional to q^μ [57], so this contribution vanishes when dotted into the conserved leptonic tensor for inclusive Drell-Yan in eq. (2.59). We will give final

results for the square of $O_{q'\bar{q}}$ in the end. The contributions from the interference of different operators vanish because forward matrix elements $\langle p|\chi\chi|p\rangle = \langle p|\bar{\chi}\bar{\chi}|p\rangle = \langle p|\chi\mathcal{B}_\perp|p\rangle = 0$ due to fermion number conservation. Similarly, the interference of quark operators with flavors that do not match up vanishes, i.e., $\langle p|\bar{\chi}_q\chi_{q'}|p\rangle = \langle p|\chi_q\bar{\chi}_{q'}|p\rangle = 0$ due to the flavor symmetry of QCD.

We next translate all fields in the EFT matrix element back from x to 0 using the residual momentum operator $\hat{p}^\mu = \mathrm{i}\partial^\mu$, where we have $\hat{p}^\mu$ act on the fields to its right (in the same set of square brackets) using overall momentum conservation,

$$\langle p_n p_{\bar{n}}|O_{\bar{q}q'}^{\dagger\beta\alpha}(\tilde{\omega}_n, p_{\bar{n}}; x)\, O_{\bar{q}q'}^{\alpha'\beta'}(\tilde{\omega}'_n, p'_{\bar{n}}; 0)|p_n p_{\bar{n}}\rangle \tag{5.34}$$

$$= \frac{1}{N_c}\delta_{\tilde{\omega}_n \tilde{\omega}'_n}\theta(\tilde{\omega}_n)\langle p_n|\bar{\chi}_{qn}^\beta\,\bar{\mathrm{T}}[O_{cs}^\dagger]\big[e^{\mathrm{i}\hat{p}\cdot x}\,\mathrm{T}[O_{cs}]\chi_{qn,\tilde{\omega}_n}^{\beta'}\big]|p_n\rangle$$

$$\times\, \delta(\omega_{\bar{n}} - \omega'_{\bar{n}})\,\delta^2(\vec{p}_{\bar{n}\perp} - \vec{p}'_{\bar{n}\perp})\,\theta(\omega_{\bar{n}})\langle p_{\bar{n}}|\chi_{q'\bar{n}}^{\alpha j}\big[e^{\mathrm{i}\hat{p}\cdot x}\chi_{q'\bar{n},-p_{\bar{n}}}^{\alpha' j}\big]|p_{\bar{n}}\rangle$$

$$= \frac{1}{N_c}\delta_{\tilde{\omega}_n \tilde{\omega}'_n}\theta(\tilde{\omega}_n)\int\mathrm{d}^4k_{cs}\,e^{\mathrm{i}k_{cs}\cdot x}\,\langle p_n|\bar{\chi}_{qn}^\beta\,\bar{\mathrm{T}}[O_{cs}^\dagger]\big[\delta^4(k_{cs} - \hat{p})\,\mathrm{T}[O_{cs}]\chi_{qn,\tilde{\omega}_n}^{\beta'}\big]|p_n\rangle$$

$$\times\, \delta(\omega_{\bar{n}} - \omega'_{\bar{n}})\,\delta^2(\vec{p}_{\bar{n}\perp} - \vec{p}'_{\bar{n}\perp})\,\theta(\omega_{\bar{n}})\int\mathrm{d}k_{\bar{n}}^-\,e^{\mathrm{i}k_{\bar{n}}^- x^+/2}\,\langle p_{\bar{n}}|\chi_{q'\bar{n}}^\alpha\big[\delta(k_{\bar{n}}^- - \hat{p}^-)\bar{\chi}_{q'\bar{n},-p_{\bar{n}}}^{\alpha'}\big]|p_{\bar{n}}\rangle\,.$$

On the second equality we have rewritten the exponentials of $\hat{p}^\mu$ in terms of its eigenvalues, i.e., the residual momenta k_{cs}^μ and $k_{\bar{n}}^-$ as measured on the fields by the δ functions. Note that when acting on the $\bar{n}$-collinear fields in the last line, the $\hat{p}^\mu$ only picks up a minus component $k_{\bar{n}}^-$ because the fields have continuous label momentum and only depend on residual x^+. Also note that k_{cs}^μ arises from the action of $\hat{p}^\mu$ on both n-collinear and collinear-soft fields, but we will see shortly that the name is justified.

Taking the x integral of the forward matrix element as in eq. (5.31), including the label momentum phases from the translated EFT operator, leads to three δ functions that encode the overall momentum conservation for the q^+, q^-, and $\vec{q}_\perp$ component, respectively,

$$\int\frac{\mathrm{d}^4x}{(2\pi)^4}\,e^{-\mathrm{i}q\cdot x}\,e^{+\mathrm{i}(\tilde{\omega}_n n\cdot x/2 + p_{\bar{n}}\cdot x)}\,\langle p_n p_{\bar{n}}|O_{\bar{q}q'}^{\dagger\beta\alpha}(\tilde{\omega}_n, p_{\bar{n}}; x)\, O_{\bar{q}q'}^{\alpha'\beta'}(\tilde{\omega}'_n, p'_{\bar{n}}; 0)|p_n p_{\bar{n}}\rangle$$

$$= \frac{2}{N_c}\int\mathrm{d}^4k_{cs}\int\mathrm{d}k_{\bar{n}}^-\,\delta(\tilde{\omega}_n + k_{cs}^- + k_{\bar{n}}^- - q^-)\,\delta(\omega_{\bar{n}} + k_{cs}^+ - q^+)\,\delta^2(\vec{p}_{\bar{n}\perp} + \vec{k}_{cs\perp} - \vec{q}_\perp)$$

$$\times\, \delta_{\tilde{\omega}_n \tilde{\omega}'_n}\theta(\tilde{\omega}_n)\langle p_n|\bar{\chi}_{qn}^\beta\,\bar{\mathrm{T}}[O_{cs}^\dagger]\big[\delta^4(k_{cs} - \hat{p})\,\mathrm{T}[O_{cs}]\chi_{qn,\tilde{\omega}_n}^{\beta'}\big]|p_n\rangle$$

$$\times\, \delta(\omega_{\bar{n}} - \omega'_{\bar{n}})\,\delta^2(\vec{p}_{\bar{n}\perp} - \vec{p}'_{\bar{n}\perp})\,\theta(\omega_{\bar{n}})\langle p_{\bar{n}}|\chi_{q'\bar{n}}^\alpha\big[\delta(k_{\bar{n}}^- - \hat{p}^-)\bar{\chi}_{q'\bar{n},-p_{\bar{n}}}^{\alpha'}\big]|p_{\bar{n}}\rangle \tag{5.35}$$

We now arrive at the key point of this derivation. Since every term in the momentum-conserving δ functions has definite power counting, we can expand, to leading power,

$$\delta(\tilde{\omega}_n + k_{cs}^- + k_{\bar{n}}^- - q^-)\,\delta(\omega_{\bar{n}} + k_{cs}^+ - q^+)\,\delta^2(\vec{p}_{\bar{n}\perp} + \vec{k}_{cs\perp} - \vec{q}_\perp)$$

$$= \delta_{\tilde{\omega}_n q^-}\,\delta(k_{cs}^- + k_{\bar{n}}^-)\,\delta(\omega_{\bar{n}} - q^+)\,\delta^2(\vec{p}_{\bar{n}\perp} - \vec{q}_\perp)\big[1 + \mathcal{O}(\lambda, \lambda_{\mathrm{QCD}})\big]\,. \tag{5.36}$$

In the δ functions involving the q^+ and $\vec{q}_\perp$ components we have expanded away the sub-leading contributions from k_{cs}^μ. Importantly, we cannot do so for the δ function involving

q^- because the difference between q^- and $\tilde{\omega}_n$, which is bounded by $\tilde{\omega}_n \leq P_a^-$ due to the support of the matrix element, is itself of $\mathcal{O}(\lambda^2)$. Instead, label and residual momentum in the q^- direction (that together make up the argument of the first δ function on the first line) are separately conserved in the EFT. Here the Kronecker δ function on the second line is to be interpreted as having *aligned* the label momentum grid with the Born kinematics such that q^- exactly coincides with a grid point $\tilde{\omega}_n$, while any additional residual momentum is subject to the continuous constraint $\delta(k_{cs}^- + k_{\bar{n}}^-)$. (Being able to make this distinction transparent was the reason we chose discrete label momenta for n-collinear modes.) Note that in the derivation of an exclusive factorization formula away from the endpoints, one would have expanded away all residual momenta in this step, such that the large label momenta would simply be set to $\omega_{n,\bar{n}} = q^{\mp}$ and nontrivial convolutions between matrix elements would only arise from the factorized measurement.

Plugging eq. (5.36) into eq. (5.35) allows us to perform the integrals over the k_{cs}^+ and $\vec{k}_{cs\perp}$ components that are now unconstrained,

$$
\int \frac{\mathrm{d}^4 x}{(2\pi)^4}\, e^{-iq\cdot x}\, e^{+i(\tilde{\omega}_n n\cdot x/2 + p_{\bar{n}}\cdot x)}\, \langle p_n p_{\bar{n}}| O_{\bar{q}q'}^{\dagger\beta\alpha}(\tilde{\omega}_n, p_{\bar{n}}; x)\, O_{\bar{q}q'}^{\alpha'\beta'}(\tilde{\omega}_n', p_{\bar{n}}'; 0)|p_n p_{\bar{n}}\rangle
$$

$$
= \frac{2}{N_c} \int \mathrm{d}k_{cs}^- \int \mathrm{d}k_{\bar{n}}^-\, \delta_{\tilde{\omega}_n q^-}\delta(k_{cs}^- + k_{\bar{n}}^-)\,\delta(\omega_{\bar{n}} - q^+)\,\delta^2(\vec{p}_{\bar{n}\perp} - \vec{q}_\perp)
$$

$$
\times\, \delta_{\tilde{\omega}_n \tilde{\omega}_n'}\theta(\tilde{\omega}_n)\langle p_n|\bar{\chi}_{q\,n}^{\beta}\bar{\mathrm{T}}[O_{cs}^{\dagger}]\big[\delta(k_{cs}^- - \hat{p}^-)\,\mathrm{T}[O_{cs}]\big]\chi_{q\,n,\tilde{\omega}_n}^{\beta'}|p_n\rangle
$$

$$
\times\, \delta(\omega_{\bar{n}} - \omega_{\bar{n}}')\,\delta^2(\vec{p}_{\bar{n}\perp} - \vec{p}_{\bar{n}\perp}')\,\theta(\omega_{\bar{n}})\langle p_{\bar{n}}|\chi_{q'\,\bar{n}}^{\alpha}\big[\delta(k_{\bar{n}}^- - \hat{p}^-)\bar{\chi}_{q'\,\bar{n},-p_{\bar{n}}}^{\alpha'}\big]|p_{\bar{n}}\rangle
$$

$$
\equiv \frac{2}{N_c} \int \mathrm{d}t\, \delta_{\tilde{\omega}_n q^-}\,\delta(\omega_{\bar{n}} - q^+)\,\delta^2(p_{\bar{n}\perp} - \vec{q}_\perp)
$$

$$
\times\, \delta_{\tilde{\omega}_n \tilde{\omega}_n'}\, M_{q\,n}^{\beta'\beta}\Big(\frac{\tilde{\omega}_n + t/\omega_{\bar{n}}}{P_n^-}\Big)\,\delta(\omega_{\bar{n}} - \omega_{\bar{n}}')\,\delta^2(\vec{p}_{\bar{n}\perp} - \vec{p}_{\bar{n}\perp}')\, M_{q'\,\bar{n}}^{\alpha\alpha'}\Big(t, \frac{\omega_{\bar{n}}}{P_{\bar{n}}^-}, \vec{p}_{\bar{n}\perp}\Big), \qquad (5.37)
$$

where we used that the dominant contribution to k_{cs}^- indeed comes from the collinear-soft modes to move the n-collinear field out of the square brackets on the third line,

$$
\big[\delta(k_{cs}^- - \hat{p}^-)\,\mathrm{T}[O_{cs}]\chi_{q\,n,\tilde{\omega}_n}^{\beta'}\big] = \big[\delta(k_{cs}^- - \hat{p}^-)\,\mathrm{T}[O_{cs}]\big]\chi_{q\,n,\tilde{\omega}_n}^{\beta'}\Big[1 + \mathcal{O}\Big(\frac{\lambda_{\mathrm{QCD}}^2}{\lambda}\Big)\Big] \qquad (5.38)
$$

On the second equality we performed the k_{cs}^- integral and changed variables to $t = -\omega_{\bar{n}}k_{\bar{n}}^- > 0$. Making all δ functions explicit, the $\bar{n}$-collinear matrix element $M_{\bar{q}'\,\bar{n}}$ is defined as

$$
M_{\bar{q}'\,\bar{n}}^{\alpha\alpha'}\Big(t, \frac{\omega_{\bar{n}}}{P_{\bar{n}}^+}, \vec{p}_{\bar{n}\perp}\Big) = \theta(\omega_{\bar{n}})\langle p_{\bar{n}}|\chi_{q'\,\bar{n}}^{\alpha}\big[\delta(t + \omega_{\bar{n}}\hat{p}^-)\,\delta(\omega_{\bar{n}} - \overline{\mathcal{P}}_{\bar{n}})\,\delta(\vec{p}_{\bar{n}\perp} - \vec{\mathcal{P}}_{\bar{n}\perp})\,\bar{\chi}_{q'\,\bar{n}}^{\alpha'}\big]|p_{\bar{n}}\rangle,
$$

$$
(5.39)
$$

where we used that the matrix element can only depend on the RPI-III invariant quantities t, $\vec{p}_{\bar{n}\perp}$, and $\omega_{\bar{n}}/P_{\bar{n}}^+$. Note that RPI-III invariance of the matrix elements is not yet manifest due to the open spin indices. However, the possible spin structures for the n ($\bar{n}$) collinear matrix element all involve $\not{n}$ ($\not{\bar{n}}$), see eq. (5.44), so the open spin indices count as n ($\bar{n}$) in an RPI-III transformation.

The combined n-collinear and collinear-soft matrix element is defined as

$$M_{q\,n}^{\beta'\beta}\left(\frac{\omega_n}{P_n^-}\right) = \theta(\omega_n)\langle p_n|\bar{\chi}_{q\,n}^\beta \bar{\mathrm{T}}[O_{cs}^\dagger]\big[\delta(\omega_n - \tilde{\omega}_n - \hat{p}^-)\,\mathrm{T}[O_{cs}]\big]\big[\delta_{\tilde{\omega}_n \overline{\mathcal{P}}_n}\chi_{q\,n}^{\beta'}\big]|p_n\rangle . \tag{5.40}$$

Here the unique combination of partonic light-cone momenta that the matrix element can depend on is $\omega_n \equiv \tilde{\omega}_n + k_{cs}^-$ due to the freedom in the split between label and residual momentum.[6] By RPI-III it then follows that the proton matrix element depends only on ω_n/P_n^-.

Inserting eq. (5.37) into eq. (5.31) yields the following contribution from the square of $O_{\bar{q}q'}$ to the hadronic tensor, including the hard matching and after performing the now trivial integrals and sums over the various label momenta,

$$W_{VV'\,\bar{q}q'}^{\mu\nu}(q, P_n, P_{\bar{n}}) = \frac{2}{N_c}\bar{C}_{V\,\bar{q}q'}^{\mu\,\beta\alpha}(n,\bar{n};q^-,q^+)\,C_{V'\,\bar{q}q'}^{\nu\,\alpha'\beta'}(n,\bar{n};q^-,q^+)$$
$$\times \int \mathrm{d}t\,M_{q\,n}^{\beta'\beta}\left(\frac{q^- + t/q^+}{P_n^-}\right)M_{\bar{q}'\,\bar{n}}^{\alpha\alpha'}\left(t, \frac{q^+}{P_{\bar{n}}^+}, \vec{q}_\perp\right). \tag{5.41}$$

Note that this result already has the convolution structure in eq. (5.23), where

$$\frac{q^- + t/q^+}{P_n^-} = x^-\left(1 + \frac{t}{q^+q^-}\right), \qquad \frac{q^+}{P_{\bar{n}}^+} = x^+ . \tag{5.42}$$

While eq. (5.41) is formally derived in the leptonic frame, it has exactly the same form in the lab frame. This is because the measured observables $x_\mp$ and $\vec{q}_T$ are boost invariant along the beam axis, and RPI-III forces all functions to only depend on quantities that are likewise invariant under longitudinal boosts.

5.3.4 Spin structure

We next deal with the spin structure of eq. (5.41). We already used in the derivation of the leading-power collinear quark Lagrangian in section 2.2.4 that $\not{n}, \not{n}\gamma_5$, and $\not{n}\gamma_\perp^\mu$ form a complete basis of bilinears in ξ_n because the collinear quark field ξ_n has only two components and satisfies $\not{n}\xi_n = 0$. It follows that for any spin structure Γ, the following trace formula holds when inserted in a bilinear of ξ_n fields [171],

$$\bar{\xi}_n\Gamma\xi_n: \quad \Gamma = \frac{\not{n}}{8}\,\mathrm{tr}\big[\not{n}\Gamma\big] - \frac{\not{n}\gamma_5}{8}\,\mathrm{tr}\big[\not{n}\gamma_5\Gamma\big] - \frac{\not{n}\gamma_\perp^\mu}{8}\,\mathrm{tr}\big[\not{n}\gamma_{\perp\mu}\Gamma\big] \tag{5.43}$$

A similar trace formula holds for bilinears of n and $\bar{n}$ fields [171]. Eq. (5.43) implies that matrix elements $M_n^{\alpha\alpha'} = \langle \bar{\xi}_n^\alpha \cdots \xi_n^{\alpha'}\rangle$ of a collinear quark bilinear, with additional Wilson lines and measurements indicated by $\cdots$, may be decomposed as

$$M_n^{\alpha\alpha'} = \frac{(\not{n})^{\alpha\alpha'}}{4}\,\mathrm{tr}\Big[M_n\frac{\not{n}}{2}\Big] - \frac{(\not{n}\gamma_5)^{\alpha\alpha'}}{4}\,\mathrm{tr}\Big[M_n\frac{\not{n}\gamma_5}{2}\Big] - \frac{(\not{n}\gamma_{\perp\mu})^{\alpha\alpha'}}{4}\,\mathrm{tr}\Big[M_n\frac{\not{n}\gamma_\perp^\mu}{2}\Big],$$
$$\equiv \frac{(\not{n})^{\alpha\alpha'}}{4}M_n^{(f)} - \frac{(\not{n}\gamma_5)^{\alpha\alpha'}}{4}M_n^{(g)} - \frac{(\not{n}\gamma_{\perp\mu})^{\alpha\alpha'}}{4}M_n^{(h)\,\mu} , \tag{5.44}$$

---

[6]For the $\bar{n}$-collinear matrix element, where only one set of modes contribute, this was built in by using continuous label momenta, which is why we use this suggestive notation also for ω_n. Note, however, that in this case the dominant residual momentum dependence is carried by a different set of modes.

and analogously for $n \leftrightarrow \bar{n}$. In the case where the spin indices $\beta' \beta$ ($\alpha \alpha'$) of n ($\bar{n}$) quark bilinears are directly contracted with each other, this implies the SCET spin Fierz identity

$$\delta^{\beta \alpha} \delta^{\alpha' \beta'} = \frac{1}{2} \left[\frac{(\not{n})^{\beta' \beta}}{2} \frac{(\not{n})^{\alpha \alpha'}}{2} - \frac{(\not{n} \gamma_5)^{\beta' \beta}}{2} \frac{(\not{n} \gamma_5)^{\alpha \alpha'}}{2} - \frac{(\not{n} \gamma_\perp^\mu)^{\beta' \beta}}{2} \frac{(\not{n} \gamma_{\perp \mu})^{\alpha \alpha'}}{2} \right]. \tag{5.45}$$

This identity is useful when working with SCET helicity operators that, like their matching coefficients, are overall Dirac scalars [177].

We are instead interested in the case of open spin indices contracted with the hard matching coefficients, and therefore will directly apply eq. (5.44), using constraints from the possible Lorentz four-vectors that the matrix elements depend on. Suppressing all but the vector-valued arguments relevant for the spin structure, our result in eq. (5.41) reads

$$\frac{2}{N_c} \bar{C}_{V \bar{q} q'}^{\mu \beta \alpha}(n, \bar{n}) \, C_{V' \bar{q} q'}^{\nu \alpha' \beta'}(n, \bar{n}) \, M_{q n}^{\beta' \beta} \, M_{\bar{q}' \bar{n}}^{\alpha \alpha'}(\vec{p}_{\bar{n} \perp})$$

$$= \frac{2}{N_c} \text{tr} \left[\bar{C}_{V \bar{q} q'}^{\mu}(n, \bar{n}) \, M_{\bar{q}' \bar{n}}(\vec{p}_{\bar{n} \perp}) \, C_{V' \bar{q} q'}^{\nu}(n, \bar{n}) \, M_{q n} \right]. \tag{5.46}$$

We remind the reader that $n, \bar{n}$ were chosen along the proton directions, so the momenta of the external states do not provide additional reference vectors. We will also need the fact that the leading-power hard matching coefficients are linear combinations of [see eq. (7.93)]

$$C_{V \bar{q} q'}^{\mu}(n, \bar{n}) \propto \gamma_\perp^\mu, \gamma_\perp^\mu \gamma_5 \tag{5.47}$$

Applying the decomposition in eq. (5.44) to our matrix elements at hand, we find that the combinations involving γ_5 vanish,

$$M_{q n}^{(g)} = 0, \qquad M_{\bar{q}' \bar{n}}^{(g)}(\vec{p}_{\bar{n} \perp}) = 0 \tag{5.48}$$

because they measure the difference of the number densities of quarks with positive and negative helicity along the n ($\bar{n}$) direction, which must be zero for an unpolarized proton. This can most easily be seen when working in the helicity basis for Dirac spinors, where $\gamma_5 = \text{diag}(1, -1)$ on the subspace on nonvanishing components of ξ_n [171].

Importantly, by rotational invariance in the perpendicular plane, we can also eliminate

$$M_{q n}^{(h) \mu} = 0, \tag{5.49}$$

because $M_{q n}$ only depends on the single vector n^μ. On the other hand, $M_{\bar{q}' \bar{n}}^{(h) \mu}(\vec{p}_{\bar{n} \perp})$ is nonzero in general due to the explicit measurement on perpendicular momenta. However, it only contributes to the hadronic tensor through

$$M_{q n}^{(f)} M_{\bar{q}' \bar{n}}^{(h) \mu} \text{tr} \left[\bar{C}_{V \bar{q} q'}^{\mu} \not{n} \gamma_{\perp \mu} C_{V' \bar{q} q'}^{\nu} \not{n} \right] = 0, \tag{5.50}$$

which due to eq. (5.47) contains an odd number of $\gamma_\perp$ matrices and therefore vanishes.

We thus find only a single nonvanishing contribution to the hadronic tensor proportional to the product of unpolarized proton matrix elements,

$$\frac{2}{N_c}\,\mathrm{tr}\big[\bar{C}^\mu_{V\,\bar{q}q'}(n,\bar{n})\,M_{\bar{q}'\,\bar{n}}(\vec{p}_{\bar{n}\perp})\,C^\nu_{V'\,\bar{q}q'}(n,\bar{n})\,M_{q\,n}\big]$$

$$= \frac{1}{2N_c}\,\mathrm{tr}\Big[\bar{C}^\mu_{V\,\bar{q}q'}(n,\bar{n})\,\frac{\slashed{\bar{n}}}{2}C^\nu_{V'\,\bar{q}q'}(n,\bar{n})\,\frac{\slashed{n}}{2}\Big]M^{(f)}_{q\,n}M^{(f)}_{\bar{q}'\,\bar{n}}(\vec{p}_{\bar{n}\perp})$$

$$\equiv H^{\mu\nu}_{VV'\,\bar{q}q'}(n,\bar{n})\,M^{(f)}_{q\,n}M^{(f)}_{\bar{q}'\,\bar{n}}(\vec{p}_{\bar{n}\perp}) \tag{5.51}$$

The unpolarized n-collinear matrix element $M^{(f)}_{q\,n}(x)=\mathrm{tr}\big[M_{q\,n}(x)\frac{\slashed{n}}{2}\big]\equiv f^{\mathrm{thr}}_q(x)$ defines the bare quark threshold PDF of flavor q, with $P^\mu_n=P^-_n n^\mu/2$,

$$f^{\mathrm{thr}}_q\Big(\frac{\omega_n}{P^-_n}\Big)\equiv\theta(\omega_n)\langle p_n|\bar{\chi}_{q\,n}\bar{\mathrm{T}}[O^\dagger_{cs}]\big[\delta(\omega_n-\tilde{\omega}_n-\hat{p}^-)\,\mathrm{T}[O_{cs}]\big]\big[\delta_{\tilde{\omega}_n\overline{\mathcal{P}}_n}\frac{\slashed{n}}{2}\chi_{q\,n}\big]|p_n\rangle\,, \tag{5.52}$$

while $M^{(f)}_{\bar{q}'\,\bar{n}}(t,\vec{p}_{\bar{n}\perp},x)=\mathrm{tr}\big[M_{\bar{q}'\,\bar{n}}(t,\vec{p}_{\bar{n}\perp},x)\frac{\slashed{n}}{2}\big]=B_{\bar{q}'}(t,\vec{p}_{\bar{n}\perp},x)$ precisely recovers the definition of the bare double-differential antiquark beam function of flavor q', with $P^\mu_{\bar{n}}=P^+_{\bar{n}}\bar{n}^\mu/2$,

$$B_{\bar{q}'}\Big(t,\frac{\omega_{\bar{n}}}{P^+_{\bar{n}}},\vec{p}_{\bar{n}\perp}\Big)=\theta(\omega_{\bar{n}})\langle p_{\bar{n}}|\mathrm{tr}\Big\{\frac{\slashed{\bar{n}}}{2}\chi_{q'\,\bar{n}}\big[\delta(t+\omega_{\bar{n}}\hat{p}^-)\delta(\omega_{\bar{n}}-\overline{\mathcal{P}}_{\bar{n}})\delta(\vec{p}_{\bar{n}\perp}-\vec{\mathcal{P}}_{\bar{n}\perp})\bar{\chi}_{q'\,\bar{n}}\big]\Big\}|p_{\bar{n}}\rangle\,, \tag{5.53}$$

which should be compared with the quark beam function definition in eq. (4.4). With this, our final result for the contribution to the hadronic tensor from the $O_{\bar{q}q'}$ operator reads

$$W^{\mu\nu}_{VV'\,\bar{q}q'}(q,P_n,P_{\bar{n}})=H^{\mu\nu}_{VV'\,\bar{q}q'}(n,\bar{n};q^-,q^+)\int\mathrm{d}t\,f^{\mathrm{thr}}_q\Big(\frac{q^-+t/q^+}{P^-_n}\Big)B_{\bar{q}'}\Big(t,\frac{q^+}{P^+_{\bar{n}}},\vec{p}_{\bar{n}\perp}\Big) \tag{5.54}$$

The contribution from the $O_{q'\bar{q}}$ operator can be worked out in full analogy and yields a product of $f^{\mathrm{thr}}_{\bar{q}'}$ and B_q. Summing both over quark flavors and contracting with the inclusive leptonic tensor proves the factorization theorem in eq. (5.23), where the hard function is given by the contraction of the squared matching coefficient with the inclusive leptonic tensor summed over all contributing vector bosons, see appendix B. The above expression for the hadronic tensor can serve as a starting point for the straightforward extension of the factorization theorem to a fully differential description of the decay products using the results of chapter 7.

As a final comment on the spin structure, we note that the spin Fierzing steps leading to inclusive beam functions in the derivation of the single-differential $\mathcal{T}_0$ factorization, eq. (2.214), were not made explicit in ref. [57], but the result nevertheless holds because the measurement on the collinear sectors is scalar. The restriction to unpolarized matrix elements actually breaks down for the double-differential SCET$_\mathrm{I}$ factorization for $(q_T,\mathcal{T}_0)$ in eq. (4.2) due to the explicit vectorial measurements, and to all orders a contribution analogous to the double Boer-Mulders effect, proportional to two so-called Boer-Mulders functions parametrizing matrix elements of the form $M^{(h)}_n$, must be expected also in SCET$_\mathrm{I}$. As discussed in chapter 7 below eq. (7.89), however, the Boer-Mulders functions are suppressed for $\Lambda_{\mathrm{QCD}}\ll q_T$ and therefore do not affect our results in chapter 4, where we were concerned with the perturbative domain. In addition, the double Boer-Mulders effect drops out when the decay products are not resolved, see also chapter 7.

5.3.5 Formal relation to the soft threshold limit

We now show that the generalized threshold limit contains the soft threshold limit in the sense of eq. (5.18) In particular, the limits $x_- \to 1$ and $x_+ \to 1$ commute, so taking one limit after the other is equivalent to taking $x_-, x_+ \to 1$ simultaneously. To see this, consider the hierarchy $\lambda_-^2 \sim 1 - x_- \ll \lambda_+^2 \sim 1 - x_+ \ll 1$, which we can interpret as taking $x_+ \to 1$ after having already taken $x_- \to 1$. In this limit, the $p_{\bar{n}}$ modes factorize into perturbative $\bar{n}$-collinear-soft modes $p_{\bar{n},cs} \sim Q(\lambda_+^2, \lambda_-^2, \lambda_+ \lambda_-)$ and $\bar{n}$-collinear-soft modes $P_{\bar{n},cs} \sim Q(\lambda_+^2, \lambda_{\rm QCD}^2/\lambda_+^2, \lambda_{\rm QCD})$. Including λ_+, the condition $\lambda_{\rm QCD} \ll \lambda$ becomes $\lambda_{\rm QCD} \ll \lambda_- \lambda_+$ and without loss of generality we can consider $\lambda_{\rm QCD} \sim \lambda_-^2 \lambda_+^2$. This also implies that the P_{cs} modes now get boosted in the n direction and become n-collinear-soft modes $P_{n,cs}$. The beam function matching onto PDFs in this limit takes the form

$$ B_j(\omega_{\bar{n}} k^-, x_+, \vec{k}_T, \mu) = \int \frac{dk^+}{\omega_{\bar{n}}} \mathcal{S}_j(k^-, k^+, \vec{k}_T, \mu) \, f_j^{\rm thr}\left[x_+\left(1 + \frac{k^+}{\omega_{\bar{n}}}\right), \mu\right] \left[1 + \mathcal{O}(\lambda_+)\right], \quad (5.55) $$

where the combined $P_{\bar{n},cs}$ and $P_{\bar{n}}$ modes yield another threshold PDF, and $\mathcal{S}_j(k^-, k^+, \vec{k}_T)$ is the matrix element of the perturbative $p_{\bar{n},cs}$ modes. It has the same Wilson line structure as the soft function appearing in eq. (2.186), and thus upon integration over $\vec{k}_T$ becomes equal to it to all orders by reparametrization invariance. We now have $k_T^2/Q^2 \sim \lambda_-^2 \lambda_+^2 \ll t/Q^2 \sim \lambda_-^2$, so B_j and $\tilde{B}_j$ become the same and integrating eq. (5.55) over $\vec{k}_T$ yields eq. (5.18) for either of them.

5.3.6 Comment on the threshold PDF

To close the formal discussion of eq. (5.23), we briefly return to the definition of the bare quark threshold PDF in eq. (5.52), which reads, for a proton with momentum $P_n^\mu = P_n^- n^\mu/2$,

$$ f_q^{\rm thr}\left(\frac{\omega_n}{P_n^-}\right) \equiv \theta(x) \langle p_n | \bar{\chi}_{q\,n} \bar{\rm T}[O_{cs}^\dagger] \left[\delta(\omega_n - \tilde{\omega}_n - \hat{p}^-) \, {\rm T}[O_{cs}]\right] \left[\delta_{\tilde{\omega}_n \overline{\mathcal{P}}_n} \frac{\not{n}}{2} \chi_{q\,n}\right] | p_n \rangle, \quad (5.56) $$

and discuss its precise relation to other expressions in the literature on the DIS endpoint and soft threshold factorization theorems, where it also appears. We focus on refs. [214, 216], which are the most explicit recent references in terms of their formal EFT construction.

As a first comment, we tend to disagree with the assertion that the threshold PDF can be factorized into a collinear-soft vacuum matrix element and a collinear proton matrix element because on physical grounds, we expect collinear-soft degrees of freedom to be part of the proton wave function when probed at large x. Specifically, if the proton wave function has any overlap with a collinear parton field with label momentum $\tilde{\omega}_n \to P_n^-$ at all, as required for the concept of a threshold PDF to make sense in the first place, then by momentum conservation it cannot contain additional collinear partons that could form an overall color singlet, and hence must contain collinear-soft partons whose presence is parametrically still allowed to make up for this. After the collision, the collinear-soft degrees of freedom form the proton remnant radiated into the final state. This picture receives additional support from comparing to the case of a heavy quark, where the analogous

threshold fragmentation function can explicitly be computed by matching onto (boosted) heavy quark effective theory [412]. In this case the collinear-soft "brown muck" that forms the observed color-singlet heavy meson together with the heavy quark does have a matrix element in isolation, the (fragmentation) shape function, but it still involves a nontrivial external bound state.

On a second, related note, we stress that residual momentum conservation, leading to the physical support of the threshold PDF $\omega_n/P_n^- \leq 1$, is an $\mathcal{O}(1)$ effect. To see this, note that $P_n^- = q^-[1 + \mathcal{O}(\lambda)^2]$, so the discrete large label component $\tilde{P}_n^-$ of P_n^- is equal to q^-, as also noted in ref. [214]. Thus the residual momentum $P_n^- - q^- = P_n^- - \tilde{P}_n^- \equiv K_n^-$ available from the proton in addition is of $\mathcal{O}(\lambda^2 Q)$, which is precisely the scaling of the residual momentum carried by the collinear-soft operators. Expanding $k_n^-/K_n^- \ll 1$, or equivalently taking $K_n^- \to \infty$ when factoring off a vacuum collinear-soft matrix element, is therefore not justified.

Third, turning to the argument of the threshold PDF and the way it enters in factorization theorems, recall that due to the freedom in the split between label and residual momentum, the threshold PDF can only depend on $\tilde{\omega}_n + k_{cs}^- = q^- + t/q^+$ and $P_n^- = \tilde{P}_n^- + K_n^-$, and by RPI-III must exclusively depend on their ratio,

$$\frac{\tilde{\omega}_n + k_{cs}^-}{P_n^-} = x^-\left(1 + \frac{t}{q^+ q^-}\right). \tag{5.57}$$

The analogous expressions are $x(1 + s/Q^2)$ for endpoint DIS and $x_{a,b}(1 + k^\mp/\omega_{a,b})$ for the soft threshold factorization theorem, which we already used in our review in sections 2.4.1 and 2.4.2. In ref. [216], the argument of the threshold PDF (for DIS) instead involved the combination $x + s/Q^2 = q^-/P_n^- + k_{cs}^-/q^-$. This is an RPI-III invariant, but it does not reflect the freedom in the label/residual split. While the difference to eq. (5.57) is power suppressed, we stress that the form of the threshold PDF in eq. (5.56) is the unique way to split the single continuous argument ξ into the momenta carried by the fields and the external state in a way compatible with the symmetries.

We hasten to add that the important physics conclusions reached in refs. [214, 216] about the properties of the threshold PDF are unaffected by the above subtleties, and that we have in fact made repeated use of those results already. A first important point is the renormalization of f_i^{thr}, which was explicitly computed in refs. [214, 216] based on the operator definition and compared to the full DGLAP kernels. This result continues to hold because the renormalization is performed at the level of the composite operator that defines the threshold PDF. To determine the counterterm, one may use the simplest (factorized) external state with nontrivial overlap, which is indeed the product of a collinear-soft vacuum and a collinear single-parton state carrying label momentum $\tilde{\omega}_n$, as used in refs. [214, 216]. The combined counter term, after the cancellation of rapidity divergences between the two contributions [214], contains a cusp term proportional to $\mathcal{L}_0(k_{cs}^-/\tilde{\omega}_n)$, and the partonic threshold PDF is renormalized by a convolution in $\xi = k_{cs}^-/\tilde{\omega}_n$. This result goes through for the hadronic matrix element of the operator and yields the RGE of the threshold PDF in eq. (5.15) that we already used to check consistency, where the factor of

x in the argument under the convolution accounts for eq. (5.57).

Another important property of the threshold PDF is that it is indeed, like the full PDF, universal to both the DIS and Drell-Yan process. This is not a priori obvious because in DIS, the operator $O_{cs}(x)$ contains a future-pointing collinear-soft Wilson line along the path $x + s\bar{n}, 0 \leq s < \infty$, and no explicit time ordering is required as it coincides with the path ordering of the Wilson lines. In ref. [214] it was shown that the direction of the Wilson line can be flipped and that the two definitions are equivalent. These manipulations were also done at operator level, and therefore remain valid when the external collinear-soft state is not the vacuum.

5.4 Calculation of two-loop beam function boundary terms

In this section we describe the computation of the matching coefficients $\tilde{\mathcal{I}}_{ij}(t, z, \mu)$ of the modified virtuality-dependent beam function defined in eq. (5.58). (We drop the tilde on $\tilde{t}$ for the purposes of this section for brevity.) Since the renormalization of $\tilde{B}_i(t, x, \mu)$ and of the double-differential beam function is the same as for the inclusive beam function, the two only differ in their boundary terms $I_{ij}^{(n)}(z) \neq \tilde{I}_{ij}^{(n)}(z)$ at each order, with an otherwise identical structure given in appendix E.1. The definition in eq. (5.12) implies, at the level of the matching coefficients,

$$\tilde{\mathcal{I}}_{ij}(t, z, \mu) = \int \mathrm{d}^2 \vec{k}_T \, \mathcal{I}_{ij}\Big(t - \frac{k_T^2}{2}, z, \vec{k}_T, \mu \Big),\tag{5.58}$$

which we use to calculate $\tilde{I}_{ij}^{(n)}(z)$ from the one-loop result for $i = g$ [398] and from the two-loop result for $i = q$ [397, 398].[7] Note that for $i = g$, the integral over all $\vec{k}_T$ leaves behind only the polarization-independent piece of the double-differential gluon beam function. We have also verified that the μ-dependent pieces $\propto \mathcal{L}_n(t, \mu)$ obtained from eq. (5.58) agree with the RGE prediction in appendix E.1, i.e., we have explicitly checked that the projection and the RGE commute.

Analytic structure. All terms in the double-differential beam function belong to one of the following three categories,

$$T_{n,m}^{\uparrow}(t, z, k_T^2, \mu) \equiv \mathcal{L}_n(t, \mu^2) \frac{1}{\pi t} \mathcal{L}_m\Big(\frac{1-z}{z} - \frac{k_T^2}{t} \Big),$$

$$T_{n,m}^{\downarrow}(t, z, k_T^2, \mu) \equiv \mathcal{L}_n(t, \mu^2) \frac{1}{\pi t} \mathcal{L}_m\Big(\frac{k_T^2}{t} \Big) \theta\Big(\frac{1-z}{z} t - k_T^2 \Big),$$

$$T_n^R(t, z, k_T^2, \mu) \equiv \mathcal{L}_n(t, \mu^2) \frac{1}{\pi t} \theta(k_T^2) \, R\Big(\frac{k_T^2}{t}, z \Big) \theta\Big(\frac{1-z}{z} t - k_T^2 \Big),\tag{5.59}$$

typically multiplied with a regular or distribution-valued function of z. The overall factors of $\mathcal{L}_n(t, \mu^2)/t$ are dictated by the power counting and dimensional analysis, and are only

---

[7]We thank M. Stahlhofen for providing us with the results of ref. [397] in machine-readable form.

superficially divergent because the $1/t$ simply rescales the neighboring terms to be dimensionless. The θ functions of $t(1-z)/z - k_T^2$, partially implicit in the plus distributions, encode the maximum amount of recoil the collinear final state can kinematically provide. The terms in eq. (5.59) are classified by the order of the plus distributions involved, where we take $\mathcal{L}_{-1}(x) = \delta(x)$ for short, and by whether the range in k_T^2 has a singularity at the lower edge ($\downarrow$), the upper edge ($\uparrow$), or is regular, i.e., $R(s,z)$ is integrable as $s \to 0$ and $s \to (1-z)/z$. The overall transcendental weight at $\mathcal{O}(\alpha_s^2)$ is bounded by $n + m + 2 = 4$.

To project structures like eq. (5.59) onto the modified beam function, it is convenient to split up the double-differential beam function as in eq. (4.41). In this way the inclusive beam function $\mathcal{I}_{ij}(t, z, \mu)$ projects onto itself, and we only require the projection of $\Delta \mathcal{I}_{ij}(t, z, \vec{k}_T, \mu)$ as an additive correction. In particular, we can exploit that all singular terms as $z \to 1$ cancel in $\Delta \mathcal{I}_{ij}(t, z, \vec{k}_T, \mu)$, as we saw explicitly at NLO in eq. (4.44), and can therefore treat all functions of z as regular. Many terms at higher weight also drop out during this step. With this, the task is to compute, for $T = \{T_{n,m}^{\uparrow}, T_{n,m}^{\downarrow}, T_n^R\}$ any of the structures above,

$$S(t, z, \mu^2) = \int dk_T^2 \left[T\left(t - \frac{k_T^2}{2}, z, k_T^2, \mu\right) - T(t, z, k_T^2, \mu) \right]. \tag{5.60}$$

By careful repeated application of plus distribution identities in the bulk, i.e., at finite values of t and integrated over t up to μ^2, we find the following dictionary: For terms that are singular as $k_T^2 \to 0$, we have

$$S_{n,-1}^{\downarrow}(t, z) = 0,$$

$$S_{0,0}^{\downarrow}(t, z) = \delta(t) \operatorname{Li}_2\left(-\frac{1-z}{2z} + i0\right),$$

$$S_{0,1}^{\downarrow}(t, z) = \delta(t) \left[-\operatorname{Li}_3\left(-\frac{1-z}{2z} + i0\right) + \operatorname{Li}_2\left(-\frac{1-z}{2z} + i0\right) \ln\left(\frac{1-z}{z}\right)\right], \tag{5.61}$$

where the branch cuts of polylogarithms are chosen as indicated, and cancel in final results. Terms with a singularity as $k_T^2 \to t(1-z)/z$ are more intricate,

$$S_{2,-1}^{\uparrow}(t, z) = \mathcal{L}_1(t, \mu^2) 2\ln\left(\frac{2z}{1+z}\right) + \mathcal{L}_0(t, \mu^2) \ln^2\left(\frac{2z}{1+z}\right) + \delta(t) \frac{1}{3} \ln^3\left(\frac{2z}{1+z}\right), \tag{5.62}$$

$$S_{1,-1}^{\uparrow}(t, z) = \mathcal{L}_0(t, \mu^2) \ln\left(\frac{2z}{1+z}\right) + \delta(t) \frac{1}{2} \ln^2\left(\frac{2z}{1+z}\right),$$

$$S_{0,-1}^{\uparrow}(t, z) = \delta(t) \ln\left(\frac{2z}{1+z}\right),$$

$$S_{0,0}^{\uparrow}(t, z) = \delta(t) \left[\operatorname{Li}_2\left(\frac{1-z}{1+z}\right) + \ln\left(\frac{2z}{1+z}\right) \ln\left(\frac{1-z}{z}\right)\right],$$

$$S_{0,1}^{\uparrow}(t, z) = \delta(t) \left[-\operatorname{Li}_3\left(\frac{1-z}{1+z}\right) + \operatorname{Li}_2\left(\frac{1-z}{1+z}\right) \ln\left(\frac{1-z}{z}\right) + \frac{1}{2} \ln\left(\frac{2z}{1+z}\right) \ln^2\left(\frac{1-z}{z}\right)\right].$$

The rule for $T_{0,-1}^{\uparrow}$ is already relevant at $\mathcal{O}(\alpha_s)$. For regular terms, we have

$$S_0^R(t, z) = \delta(t) \int_0^{\frac{1-z}{z}} ds \ln\left(\frac{2}{2+s}\right) R(s). \tag{5.63}$$

Results. In the following we summarize the results we obtained using the above projections. At one loop, we find that the following simple relation holds for all partonic channels,

$$
\tilde{\mathcal{I}}_{ij}^{(1)}(t, z, \mu) = \mathcal{I}_{ij}^{(1)}(t, z, \mu) + \delta(t)\, P_{ij}^{(0)}(z) \ln \frac{2z}{1+z}\,, \tag{5.64}
$$

where $\mathcal{I}_{ij}^{(1)}$ is the one-loop matching coefficient for the inclusive beam function. Explicitly, the one-loop finite terms in the flavor decomposition in eq. (A.29) are given by

$$
\begin{aligned}
\tilde{I}_{qqV}^{(1)}(z) &= 2C_F\,\theta(z)\Big[\mathcal{L}_1(1-z)(1+z^2) - \frac{\pi^2}{6}\delta(1-z) + \theta(1-z)(1-z) + P_{qq}(z)\ln\frac{2}{1+z}\Big], \\
\tilde{I}_{qg}^{(1)}(z) &= 2T_F\,\theta(z)\Big[P_{qg}(z)\ln\frac{2(1-z)}{1+z} + \theta(1-z)\,2z(1-z)\Big], \\
\tilde{I}_{gg}^{(1)}(z) &= 2C_A\,\theta(z)\Big[\mathcal{L}_1(1-z)\frac{2(1-z+z^2)^2}{z} - \frac{\pi^2}{6}\delta(1-z) + P_{gg}(z)\ln\frac{2}{1+z}\Big], \\
\tilde{I}_{gq}^{(1)}(z) &= 2C_F\,\theta(z)\Big[P_{gq}(z)\ln\frac{2(1-z)}{1+z} + \theta(1-z)\,z\Big].
\end{aligned} \tag{5.65}
$$

The P_{ij} are given in eq. (C.7). At two loops, we find it convenient to pull common rational factors out of recurring terms with transcendental weight three $(\tilde{S}_3, \tilde{T}_3, \tilde{U}_3, \tilde{V}_3, \tilde{R}_{...})$, as was done for the $I_{ij}^{(2)}(z)$ in refs. [294, 295], and group terms of lower transcendental weight separately by color factor and flavor structure $(\tilde{C}_{...})$. We also pull out a conventional factor of four:

$$
\begin{aligned}
\tilde{I}_{qqV}^{(2)}(z) &= 4C_F^2\Big\{ D_{qqV,C_F}(z) - \frac{2}{1-z}\tilde{T}_3(z) + \frac{1+z^2}{1-z}\big[\tilde{V}_3(z) - 2\tilde{U}_3(z)\big] + \tilde{C}_{qqV,C_F}(z)\Big\} \\
&\quad + 4C_F C_A\Big\{ D_{qqV,C_A}(z) + \frac{1+z^2}{1-z}\big[\tilde{U}_3(z) + \tilde{R}_{qqV}(z)\big] + \tilde{C}_{qqV,C_A}(z)\Big\} \\
&\quad + 4C_F\beta_0\Big[D_{qqV,\beta_0}(z) + \tilde{C}_{qqV,\beta_0}(z)\Big], \\
\tilde{I}_{q\bar{q}V}^{(2)}(z) &= 4C_F(2C_F - C_A)\Big[\frac{1+z^2}{1+z}\tilde{S}_3(z) + \tilde{C}_{q\bar{q}V}(z)\Big], \\
\tilde{I}_{qqS}^{(2)}(z) &= 4C_F T_F\Big[-2(1+z)\,\tilde{T}_3(z) + \tilde{C}_{qqS}(z)\Big], \\
\tilde{I}_{qg}^{(2)}(z) &= 4T_F C_F\Big\{-2(1-z)^2\,\tilde{T}_3(z) + P_{qg}(z)\big[\tilde{V}_3(z) + \tilde{R}_{qg,C_F}(z)\big] + \tilde{C}_{qg,C_F}(z)\Big\} \\
&\quad + 4T_F C_A\Big\{-2(1+4z)\,\tilde{T}_3(z) - P_{qg}(z)\big[\tilde{U}_3(z) + \tilde{R}_{qg,C_A}(z)\big] \\
&\qquad\qquad + P_{qg}(-z)\,\tilde{S}_3(z) + \tilde{C}_{qg,C_A}(z)\Big\}.
\end{aligned} \tag{5.66}
$$

Here, overall factors of $\theta(z)\,\theta(1-z)$ are understood, but omitted for brevity. The $D_{qqV,...}(z)$ contain all distributional terms in $1-z$ and are the same as for the standard inclusive beam function [294], cf. the eikonal three-loop result in eq. (6.17),

$$
D_{qqV,C_F}(z) = (1+z^2)\Big[\mathcal{L}_3(1-z) - \frac{5\pi^2}{6}\mathcal{L}_1(1-z) + 4\zeta_3\mathcal{L}_0(1-z)\Big] + \frac{7\pi^4}{120}\delta(1-z),
$$

$$D_{qqV,C_A}(z) = (1 + z^2)\Big[\Big(\frac{2}{3} - \frac{\pi^2}{6}\Big)\mathcal{L}_1(1 - z) + \Big(-\frac{8}{9} + \frac{7\zeta_3}{2}\Big)\mathcal{L}_0(1 - z)\Big]$$
$$+ \Big(\frac{52}{27} - \frac{\pi^2}{6} - \frac{\pi^4}{36}\Big)\delta(1 - z),$$
$$D_{qqV,\beta_0}(z) = (1 + z^2)\Big[-\frac{1}{4}\mathcal{L}_2(1 - z) + \frac{5}{6}\mathcal{L}_1(1 - z) + \Big(-\frac{7}{9} + \frac{\pi^2}{12}\Big)\mathcal{L}_0(1 - z)\Big]$$
$$+ \Big(\frac{41}{27} - \frac{5\pi^2}{24} - \frac{5\zeta_3}{6}\Big)\delta(1 - z). \tag{5.67}$$

All remaining terms in eq. (5.66) are integrable for $z \to 1$. Their full expressions are lengthy and are available in machine-readable form upon request. As an example of the structures that occur, we give

$$\tilde{S}_3(z) = 2G\big(-1, -1, -\tfrac{1}{2}; z\big) - 3G\big(-1, 0, -\tfrac{1}{2}; z\big) - 3G\big(0, -1, -\tfrac{1}{2}; z\big) + 4G\big(0, 0, -\tfrac{1}{2}; z\big)$$
$$- 2H(-1, -1, 0; z) + 2H(-1, 0, -1; z) - 3H(-1, 0, 0; z)$$
$$- 2H(-1, 1, 0; z) + H(0, -1, 0; z) - H(0, 0, -1; z)$$
$$- H(0, 0, 1; z) - 2H(1, -1, 0; z) - \frac{\ln^3(z)}{12} - 2H(-1, 0; z)\ln(1 - z)$$
$$+ \ln(2)\Big[-\frac{\pi^2}{6} + G\big(-1, -\tfrac{1}{2}; z\big) - G\big(0, -\tfrac{1}{2}; z\big) - 2H(-1, 0; z) + \frac{\ln^2(z)}{2}\Big]$$
$$+ \ln(1 + z)\Big[-\frac{5\pi^2}{12} - G\big(-1, -\tfrac{1}{2}; z\big) + G\big(0, -\tfrac{1}{2}; z\big)\Big]$$
$$+ \ln(z)\Big[\frac{\pi^2}{4} + 2G\big(-1, -\tfrac{1}{2}; z\big) - 2G\big(0, -\tfrac{1}{2}; z\big) + 2H(-1, 0, z)\Big] + \frac{9\zeta_3}{4}. \tag{5.68}$$

Here, we have used the recent `PolyLogTools` package [413] to convert all polylogarithms of rational functions of z to standard harmonic polylogarithms $H(a_1, \ldots, a_n; z)$ as well as multiple polylogarithms $G(a_1, \ldots, a_n; z)$ of $z \in [0, 1]$. The latter are as defined in ref. [413], and for all $a_i = 0, \pm 1$ reduce to standard harmonic polylogarithms up to a sign. We find no evidence for a simple generalization of the one-loop relation eq. (5.64) at two loops. Finally, we note that the two-loop $\tilde{I}_{ij}^{(2)}(z)$ for the modified beam function are substantially more complicated than those for the standard inclusive beam function. For example, the latter does not involve polylogarithms with fractional weights, which only arise from the projection integral in eq. (5.58). We expect that similarly the three-loop cross section in terms of (q^+, q^-) will have a much simpler structure than in terms of (Q, Y), and will provide an easier target for an expansion in the generalized threshold limit.[8]

5.5 Validation

A first, necessary check of eq. (5.11) is consistency with the known soft limit. At the level of the perturbative ingredients, the relevant relation is given in eq. (5.21), which we verified

---

[8]In fact, the full leading-power term is already available after the recent complete calculation of the inclusive beam function at $\mathcal{O}(\alpha_s^3)$ [299].

analytically to two loops.[9] Details on this check can be found in section 6.2, where we extend the calculation to three loops and turn it around to predict the beam function finite terms in the eikonal limit at three loops.

A much more nontrivial check is to validate eq. (5.22) against the full fixed-order result for the partonic cross section in QCD. Because the soft limit checks out, it suffices to verify that eq. (5.19) is satisfied in the limit $z_a \to 1$, and we perform this check in the following.

5.5.1 Analytic validation at NLO

At NLO, we perform an analytic check for Drell-Yan and $gg \to H$ in the EFT limit [see eq. (2.73)] against the results of refs. [113, 414], which are given as distributions in $z = z_a z_b$ and a variable $y(z_a, z_b)$. Their translation to (z_a, z_b) is nontrivial, and is described in detail in the remainder of this subsection. We find complete agreement for all partonic channels. We also combined all singular terms from eq. (5.22) with the regular terms from refs. [113, 414] to reconstruct the full $\hat{\sigma}_{ij}(z_a, z_b)$ in terms of the more convenient variables $z_{a,b}$ at NLO. The results are given in appendix F and agree with refs. [219, 415, 416], where results were given in terms of $x_{a,b}$ and $z_{a,b}$ as well, but subtractions were written out in full at the level of the hadronic cross section.[10]

Plus distribution identities. In refs. [113, 114, 414], the partonic cross section for (Q, Y) is given in terms of partonic variables (z, y), defined as

$$z = z_a z_b, \qquad y = \frac{z_b(1 - z_a^2)}{(1 - z_a z_b)(z_a + z_b)}, \qquad 1 - y = \frac{z_a(1 - z_b^2)}{(1 - z_a z_b)(z_a + z_b)} = y|_{a \leftrightarrow b}, \quad (5.69)$$

where $z_{a,b}$ are defined by eq. (2.64), and the integration limits $0 \leq z_{a,b} \leq 1$ correspond to $0 \leq z \leq 1$ and $0 \leq y \leq 1$. The inverse relations and the Jacobian read

$$z_a = \sqrt{\frac{z[1 - y(1 - z)]}{z + y(1 - z)}}, \quad z_b = z_a|_{y \leftrightarrow 1 - y}, \quad \frac{\mathrm{d}z\,\mathrm{d}y}{\mathrm{d}z_a \mathrm{d}z_b} = \frac{2[1 - y(1 - z)][1 - (1 - y)(1 - z)]}{1 - z^2}, \tag{5.70}$$

The parametrization of the (z_a, z_b) plane in terms of (z, y) is illustrated in figure 5.3. In the following, we derive relations between plus distributions in (z, y) and (z_a, z_b).

In general, the two-dimensional plus distributions are uniquely defined by their functional form in the bulk, i.e. for $z_{a,b} < 1$ away from any singularity, and their integrals (against unit test functions) over arbitrary integration regions that include the singularities. In a first step, the functional form in the bulk is easily obtained by plugging in eq. (5.70). Next, the correct boundary terms at $z_a = 1$ as a function of z_b, at $z_b = 1$ as a function of z_a, and at $z_a = z_b = 1$ are determined by comparing integrals over the integration region $x_a \leq z_a(z, y) \leq 1$ and $x_b \leq z_b(z, y) \leq 1$ for generic x_a and x_b. This integration region is

---

[9] As discussed further in section 5.5.3, several soft threshold factorizations differential in rapidity [232–236] differ from eq. (2.186) and do not reproduce the correct soft limit already at NLO.

[10] We thank P. Mathews and V. Ravindran for help in comparing with refs. [219, 416].
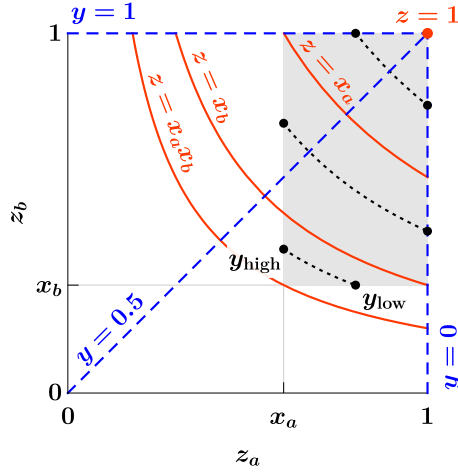
Figure 5.3: The (z_a, z_b) plane as parametrized by (z, y). The gray area shows the integration region $x_a \leq z_a \leq 1$ and $x_b \leq z_b \leq 1$ (for the case of $x_a > x_b$) used to derive the distribution identities. The dotted black lines indicate integration paths over y at representative fixed values of z. The solid red lines indicate the edge cases in z. The dashed blue lines are lines of constant y.

indicated by the gray box in the (z_a, z_b) plane in figure 5.3. It is sufficiently general to fix all boundary terms and precisely corresponds to the relevant integration region for the physical cross section in (Q, Y). In terms of (z, y), the integration region is given by

$$\theta\big[z_a(z,y) \geq x_a\big]\,\theta\big[z_b(z,y) \geq x_b\big]$$
$$= \theta\big[x_a x_b \leq z < \min\{x_a, x_b\}\big]\,\theta\big[y_{\text{low}}(z) \leq y \leq y_{\text{high}}(z)\big] + \theta\big[\max\{x_a, x_b\} \leq z\big]$$
$$+ \theta\big[x_b \leq z < x_a\big]\,\theta\big[y \leq y_{\text{high}}(z)\big] + \theta\big[x_a \leq z < x_b\big]\,\theta\big[y_{\text{low}}(z) \leq y\big]\,, \tag{5.71}$$

where the integration bounds in y, also illustrated in figure 5.3, are given by

$$y_{\text{high}}(z) = \frac{z(1 - x_a^2)}{(1 - z)(x_a^2 + z)}\,, \qquad y_{\text{low}}(z) = \frac{x_b^2 - z^2}{(1 - z)(z + x_b^2)}\,. \tag{5.72}$$

In table 5.2, we collect the resulting distribution identities at leading power in $1 - z_a$ and arbitrary z_b that are required for validating eq. (5.11) at NLO. Our conventions for one-dimensional plus distributions are summarized in appendix A.3. The relations are derived by integrating each structure in the left column in terms of (z, y) over the region in eq. (5.71), expanding the result to leading power in $1 - x_a$, and comparing to the corresponding (straightforward) integral over the same region in terms of $z_{a,b}$ of each structure in the right column.

The last entry in table 5.2 has the most intricate structure. Its exact integral without any expansion is given by

$$\int \mathrm{d}z\,\mathrm{d}y\,\theta\big[z_a(z,y) - x_a\big]\,\theta\big[z_b(z,y) - x_b\big]\,\mathcal{L}_0(1 - z)\big[\mathcal{L}_0(y) + \mathcal{L}_0(1 - y)\big]$$
$$= F_a(x_a) + F_b(x_b) - F_a(x_a x_b) - F_b(x_a x_b)\,, \tag{5.73}$$

$\mathrm{d}z\,\mathrm{d}y \times (\text{left-hand side})$	$= \mathrm{d}z_a\mathrm{d}z_b \times (\text{right-hand side})$
$f(z)\,\delta(y)$	$f(z_b)\,\delta(1-z_a)$
$r(z)\,\mathcal{L}_0(y)$	$r(z_b)\Big[\mathcal{L}_0(1-z_a) + \delta(1-z_a)\,\ln\dfrac{2z_b}{(1+z_b)(1-z_b)}\Big] + \mathcal{O}(1)$
$f(z)\,\delta(1-y)$	$f(z_a)\delta(1-z_b)$
$r(z)\,\mathcal{L}_0(1-y)$	$\mathcal{O}(1)$
$r(z)\,\mathcal{O}[y^0(1-y)^0]$	$\mathcal{O}(1)$
$\mathcal{L}_0(1-z)\big[\mathcal{L}_0(y) + \mathcal{L}_0(1-y)\big]$	$-\mathcal{L}_1(1-z_a)\,\delta(1-z_b) + \mathcal{L}_0(1-z_a)\,\mathcal{L}_0(1-z_b)$
	$-\delta(1-z_a)\,\mathcal{L}_1(1-z_b) + \dfrac{\pi^2}{6}\delta(1-z_a)\,\delta(1-z_b)$
	$+\delta(1-z_a)\,\dfrac{1}{1-z_b}\ln\dfrac{2z_b}{1+z_b} + \mathcal{O}(1)$

Table 5.2: Translation identities of two-dimensional plus distributions between the (z,y) and (z_a, z_b) parametrizations. Here, $f(x)$ is an arbitrary function of x, potentially distribution-valued for $x \to 1$, while $r(x) = \mathcal{O}[(1-x)^0]$ has at most an integrable singularity for $x \to 1$. When indicated, the relations receive power corrections in $1 - z_a$ starting at $\mathcal{O}(1) \equiv \mathcal{O}[(1-z_a)^0]$. Overall factors of $\theta(1-z)\,\theta(y)\,\theta(1-y) = \theta(1-z_a)\,\theta(1-z_b)$ are understood on both sides.

with $\qquad F_{a,b}(z) = -\ln(1-z)\ln(-z+\mathrm{i}0) - \mathrm{Li}_2\Big(\dfrac{1-z}{1+x_{a,b}}\Big) - \mathrm{Li}_2\Big(\dfrac{1-z}{1-x_{a,b}} - \mathrm{i}0\Big) - \mathrm{Li}_2(z)\,,$

where the imaginary parts from the branch cuts cancel between the different terms. Matching this with the exact distribution in the bulk, we obtain the distributional identity

$$\mathrm{d}z\,\mathrm{d}y\,\mathcal{L}_0(1-z)\big[\mathcal{L}_0(y) + \mathcal{L}_0(1-y)\big] \tag{5.74}$$

$$= \mathrm{d}z_a\mathrm{d}z_b\bigg[\frac{\pi^2}{6}\delta(1-z_a)\,\delta(1-z_b) - \mathcal{L}_1(1-z_a)\,\delta(1-z_b) + \mathcal{L}_0(1-z_a)\,\mathcal{L}_0(1-z_b) - \delta(1-z_a)\,\mathcal{L}_1(1-z_b)$$

$$+ \delta(1-z_a)\,\frac{1}{1-z_b}\ln\frac{2z_b}{1+z_b} + \delta(1-z_b)\,\frac{1}{1-z_a}\ln\frac{2z_a}{1+z_a} + \frac{1}{(1+z_a)(1+z_b)}\bigg]\,.$$

Expanding the right-hand side to leading power in $1 - z_a$ yields the result given in the last line of table 5.2. The way to think of eq. (5.74) is as a two-dimensional version of a typical distribution identity like

$$\left[\frac{1+z^2}{1-z}\right]_+ = 2\mathcal{L}_0(1-z) + \frac{3}{2}\delta(1-z) - (1+z)\,. \tag{5.75}$$

Namely, it expresses plus distributions of a function $y(z_a, z_b)$ in terms of simpler plus distributions of $1 - z_{a,b}$ plus regular terms. Moving the regular terms out of the plus distribution incurs additional boundary terms.

A key property of the left-hand side of eq. (5.74) is that it vanishes when integrated over all of y. It is instructive to see how this is reproduced by the right-hand side by projecting

onto z via $\int \mathrm{d}z_a \mathrm{d}z_b \, \delta(z - z_a z_b)$. The only nontrivial projection integral involved is

$$\int \mathrm{d}z_a \mathrm{d}z_b \, \delta(z - z_a z_b) \, \mathcal{L}_0(1 - z_a) \, \mathcal{L}_0(1 - z_b) = 2\mathcal{L}_1(1 - z) - \frac{\pi^2}{6}\delta(1 - z) - \frac{\ln z}{1 - z} \,. \quad (5.76)$$

These terms are precisely the ones required to cancel contributions from the other terms upon projecting onto z.

5.5.2 Numerical validation at NNLO

At NNLO, we numerically validate our own implementation of eq. (5.11) in `SCETlib` [8] against `Vrap` [114]. We use flat PDFs, $f_i^{\mathrm{thr}}(x) = f_i(x) = \theta(1 - x)$, which amounts to taking cumulant integrals of the partonic cross section with a cutoff at $1 - x_{a,b}$, and ensures the check covers the complete singular structure of the partonic cross section. In figure 5.4, we compare the $\mathcal{O}(\alpha_s^2)$ contributions for Drell-Yan as a function of $1 - x_a$ at fixed $x_b = 10^{-2}$. We find perfect agreement in the singular limit $x_a \to 1$, with the difference vanishing like a power in $1 - x_a$. We also find similar agreement for other x_b and for $pp \to Z/\gamma^*$ on the resonance.

We next consider the breakdown of figure 5.4 by partonic channel. Following `Vrap` [114], we take the $ij = q\bar{q}$ channel to include all topologies where i and j are part of the same quark line. The leading-power limit of these diagrams corresponds to the qqV beam function matching coefficient in the decomposition in eq. (A.29). In addition, the $q\bar{q}$ channel also includes purely nonsingular contributions with topologies $q\bar{q} \to g \to q\bar{q}V$. We then take the qq' channel to include the remaining quark-initiated processes, which at leading power reduces to the sum of the qqS and $q\bar{q}V$ beam function contributions in eq. (A.29). The qg channel maps onto the qg beam function contribution at leading power, while the gq and gg channels are purely nonsingular.

The results are shown in figure 5.5. In all cases, the prediction of eq. (5.11) is in excellent agreement with the singular limit of the full calculation, with their difference vanishing as a power of $1 - x_a$ as it should. The excellent numerical stability of `Vrap` for the off-diagonal channels allows us to extend the check down to $1 - x_a = 10^{-5}$, where it becomes limited by Monte Carlo statistics. For the $q\bar{q}$ channel, we start to see a systematic deviation at the 10^{-4} level below $1 - x_a \lesssim 10^{-4}$. We observe a similar deviation already at NLO, where the partonic cross sections agree analytically, and thus tend to attribute this to a systematic effect in the PDF integrations in `Vrap`.

5.5.3 Comment on soft threshold results in the literature

As we have discussed, the soft threshold limit is fully contained in the generalized threshold limit. Our results thus provide an independent confirmation that eq. (2.186) is the correct soft threshold factorization for the cross section differential in both Q and Y, or equivalently eq. (2.188) for the two-dimensional partonic cross section in (z_a, z_b).

Several results in the literature [232–236] considering the soft threshold factorization differential in rapidity differ from eq. (2.186). The difference is manifest already at fixed
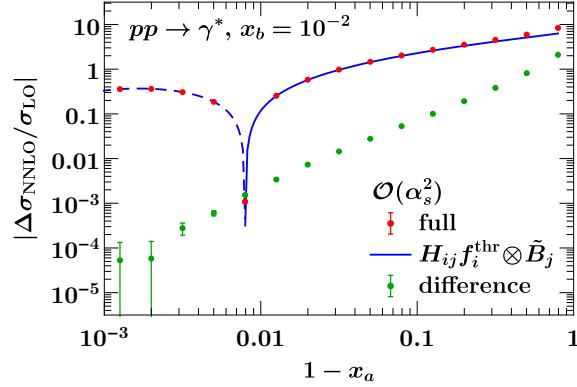
Figure 5.4: Numerical validation of the $\mathcal{O}(\alpha_s^2)$ contribution to $\mathrm{d}\sigma/\mathrm{d}x_a\mathrm{d}x_b$ predicted for $x_a \to 1$ by eq. (5.11) (blue) against the full result from Vrap (red). Their difference (green) vanishes like a power as $1 - x_a \to 0$, as it must. The error bars indicate the integration uncertainties.
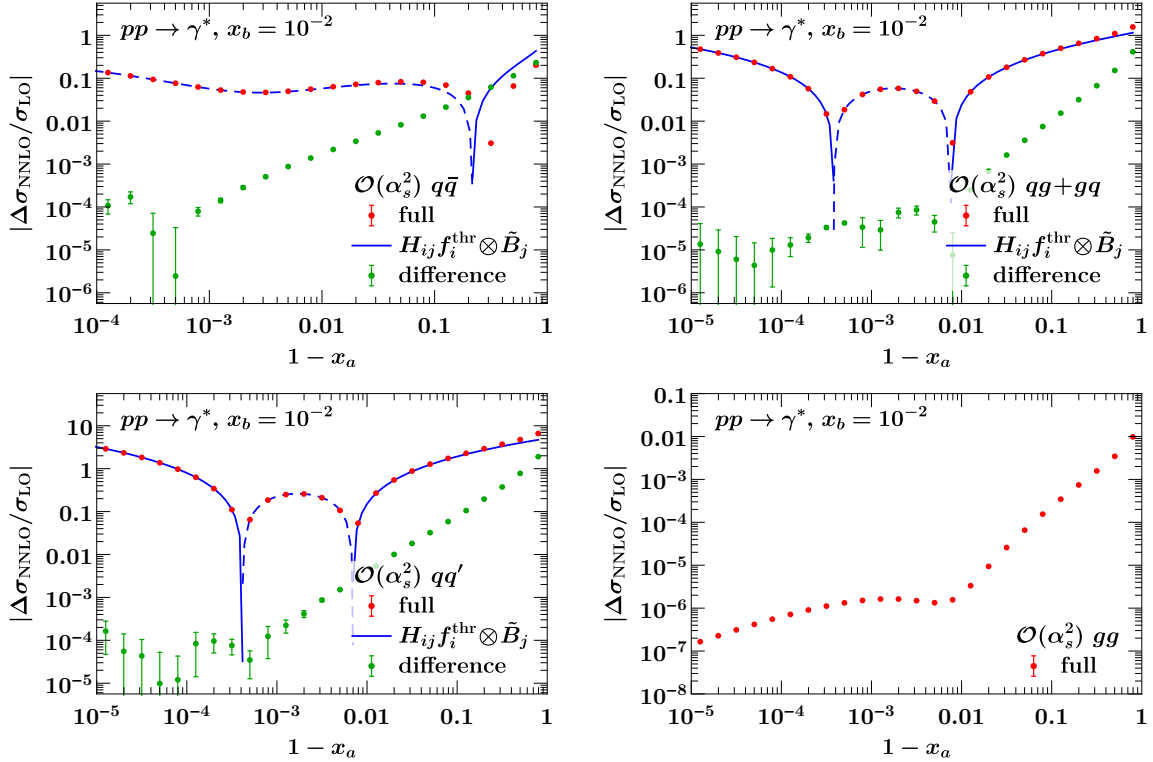
Figure 5.5: Breakdown of figure 5.4 by partonic channel. Shown are the $\mathcal{O}(\alpha_s^2)$ contributions to $\sigma \equiv \mathrm{d}\sigma/\mathrm{d}x_a\mathrm{d}x_b$ predicted for $x_a \to 1$ by eq. (5.11) (blue), and the full result from Vrap (red). In all cases, their difference (green) vanishes like a power as $1 - x_a \to 0$, as it must. The gg channel is power suppressed, so its full result by itself vanishes like a power. The error bars indicate the integration uncertainties. Dashing in the blue line indicates negative sign.

NLO in the term $\mathcal{L}_0(1-z)[\mathcal{L}_0(y) + \mathcal{L}_0(1-y)]$, which appears in the flavor-diagonal partonic cross sections. The distributional identity in eq. (5.74) unambiguously shows that this term has a double singularity in the limit $z_a \to 1$ and $z_b \to 1$, which means it contributes a priori at leading power in the soft limit $z = z_a z_b \to 1$, i.e., it contributes to the $m_a = m_b = -1$ term in eq. (5.88). This can already be seen just by considering the distribution in the bulk since

$$\mathrm{d}z\,\mathrm{d}y\,\frac{1}{1-z}\Big(\frac{1}{y} + \frac{1}{1-y}\Big) = \mathrm{d}z_a\mathrm{d}z_b\,\frac{1}{(1-z_a)(1-z_b)}\big[1 + \mathcal{O}(1-z_a, 1-z_b)\big]. \qquad (5.77)$$

Moreover, eq. (5.74) shows that it contributes at leading-logarithmic order. The soft function in eqs. (2.186) and (2.188) precisely contains the leading-power contribution of this term, which is given by the first four terms on the right-hand side of eq. (5.74).

By contrast, this term and analogous ones at higher order are missing in the leading-power resummed results in refs. [232–236]. There, it is effectively argued that the contribution of such terms to the rapidity spectrum is power-suppressed in $1 - z$, leading to the incorrect conclusion that the rapidity dependence in the soft threshold limit can be included simply by taking $\hat{\sigma}_{ij}(z_a, z_b)$ to be $\hat{\sigma}_{ij}(z)\,[\delta(y) + \delta(1-y)]/2$ or, depending on the reference, $\hat{\sigma}_{ij}(z)\,\delta(y - 1/2)$, where $\hat{\sigma}_{ij}(z)$ is the inclusive, rapidity-integrated, partonic cross section in eq. (2.71) evaluated in the soft limit $z \to 1$. In the following, we give a critical appraisal of the arguments used to support this conclusion and show why they are flawed.

This replacement first appeared in ref. [417], where it was conjectured to provide an approximation to the threshold-resummed rapidity spectrum at small Y. The phenomenological impact of the correct convolution structure on PDF determinations relying on soft threshold resummation was discussed in ref. [220]. A detailed numerical study of the difference at the level of the resummed Drell-Yan rapidity spectrum was performed in ref. [222]. The different forms of soft threshold factorization differential in rapidity have led to considerable confusion and debate in the literature. We hope that with the evidence collected here, the debate can be considered resolved.

Argument based on PDF momentum fractions What makes the $\mathcal{L}_0(1-z)[\mathcal{L}_0(y) + \mathcal{L}_0(1-y)]$ term subtle is that it vanishes upon integration over y, so it drops out in the inclusive cross section. This fact alone is of course insufficient to argue that it is power suppressed at each point in the spectrum. It simply means that different leading-power terms conspire to cancel upon integration, which is clear in terms of (z_a, z_b), as discussed below eq. (5.74).

The argument in ref. [234] rests on the observation that the PDF arguments, $x_a/z_a(z, y)$ and $x_b/z_b(z, y)$, in the two-dimensional convolution integral are independent of y at $z = 1$, from which it is concluded that the y dependence of the PDF arguments is power suppressed in $1 - z$ and can be dropped. If this is done, the y integral becomes unconstrained and can be carried out freely, which eliminates this term. More generally, one could then replace $\hat{\sigma}_{ij}(z, y) = \hat{\sigma}_{ij}(z)\,\delta(y - 1/2)[1 + \mathcal{O}(1-z)]$ underneath the convolution integral.

However, a closer inspection of the PDF arguments in terms of (z, y) reveals that

$$\frac{x_a}{z_a(z,y)} = x_a \Big\{ 1 + y(1-z) + \mathcal{O}[(1-z)^2] \Big\},$$
$$\frac{x_b}{z_b(z,y)} = x_b \Big\{ 1 + (1-y)(1-z) + \mathcal{O}[(1-z)^2] \Big\}. \tag{5.78}$$

Hence, the y dependence is not power suppressed but multiplies the *leading* dependence of the PDF arguments on z itself, and so it cannot be dropped. This becomes even clearer in terms of (z_a, z_b),

$$y(1-z) = 1 - z_a + \mathcal{O}[(1-z)^2], \qquad (1-y)(1-z) = 1 - z_b + \mathcal{O}[(1-z)^2], \tag{5.79}$$

which are precisely the $\mathcal{O}(\lambda^2)$ convolution variables $k^{\mp}/(Qe^{\pm Y})$ in eq. (2.186).

To illustrate explicitly that the y dependence has a leading-power effect, consider the hadronic soft threshold limit $1 - x_a \sim 1 - x_b \ll 1$ and a simple toy PDF with a power-law behavior near the endpoint, with $\alpha > 0$,

$$f(x) \equiv \theta(1-x)(1-x)^\alpha. \tag{5.80}$$

Using eq. (5.74), it is straightforward to show that $\mathcal{L}_0(1-z)[\mathcal{L}_0(y) + \mathcal{L}_0(1-y)]$ gives rise to double logarithms of $1 - x_{a,b}$, but performing the integral directly in terms of (z, y) is tedious, essentially as tedious as deriving eq. (5.74) itself. Instead, to disprove the above argument and show that the y dependence is not power suppressed, it suffices to consider two terms that have the same y integral,

$$A(z,y) \equiv \mathcal{L}_0(1-z) \frac{\delta(y) + \delta(1-y)}{2}, \qquad B(z,y) \equiv \mathcal{L}_0(1-z)\, \delta\Big(y - \frac{1}{2}\Big), \tag{5.81}$$

and show that they give different results at leading power, while the above argument would imply that they do not. Convolving $A(z,y)$ and $B(z,y)$ against the toy PDFs over the domain shown in figure 5.3 yields, up to relative power corrections of $\mathcal{O}(1 - x_a, 1 - x_b)$,

$$\int \mathrm{d}z\,\mathrm{d}y\, A(z,y)\, f\Big[\frac{x_a}{z_a(z,y)}\Big] f\Big[\frac{x_b}{z_b(z,y)}\Big] = f(x_a)f(x_b)\Big[\frac{1}{2}\ln\big(1 - x_a\big) + \frac{1}{2}\ln\big(1 - x_b\big) - H_\alpha\Big],$$
$$\int \mathrm{d}z\,\mathrm{d}y\, B(z,y)\, f\Big[\frac{x_a}{z_a(z,y)}\Big] f\Big[\frac{x_b}{z_b(z,y)}\Big] = f(x_a)f(x_b)\Big[\ln\big(1 - \max\{x_a, x_b\}\big) - H_\alpha\Big], \tag{5.82}$$

where H_α is the harmonic number. To evaluate the integrals it is convenient to already expand at integrand level, e.g. $1 - x_a/z_a = 1 - x_a + y(1-z)$ up to higher powers in $1 - z$ and $1 - x_a$. The maximum in the second case arises because the integration region in z along fixed $y = 1/2$ is cut off by the square of the larger of the two momentum fractions. (The order of expanding in $1 - x_a$ and $1 - x_b$ also needs to be picked accordingly.) Clearly, the two results only coincide for $Y = 0$, where $x_a = x_b$. Away from $Y = 0$, the logarithmic dependence on $x_{a,b}$ and thus on Y differs at leading power.

Fourier-transform argument   An alternative line of argument [232, 233, 235] relies on taking the Fourier transform of the partonic cross section to also argue that the y dependence is trivial. A first step is to change variables from y to

$$u \equiv \frac{1}{2} \ln \frac{z_a}{z_b}\,, \qquad -u_{\mathrm{max}} \le u \le u_{\mathrm{max}}\,, \qquad u_{\mathrm{max}} \equiv \ln \frac{1}{\sqrt{z}}\,. \tag{5.83}$$

(Note that the variables u and y are precisely interchanged in the notation used in ref. [235].) One then considers the Fourier transform of the partonic cross section $C(z,u)$ with respect to u,

$$\tilde{C}(z,M) \equiv \int \mathrm{d}u\, e^{\mathrm{i}Mu}\, C(z,u) \overset{?}{=} \int \mathrm{d}u\, C(z,u)\big[1 + \mathcal{O}(1-z)\big]\,. \tag{5.84}$$

The second equality, which is in question, is based on observing that $C(z,u)$ only has support on an interval bounded by $u_{\mathrm{max}} \sim 1 - z$, and concluding that the Fourier kernel can be expanded in $u \sim 1 - z$ as $e^{\mathrm{i}Mu} \overset{?}{=} 1 + \mathcal{O}(1-z)$, and so $\tilde{C}(z,M)$ is independent of M at leading power. Thus, taking the inverse Fourier transform, the partonic cross section may be approximated as

$$C(z,u) = \int \frac{\mathrm{d}M}{2\pi}\, e^{-\mathrm{i}Mu}\, \tilde{C}(z,M) \overset{?}{=} \delta(u) \int \mathrm{d}u'\, C(z,u')\big[1 + \mathcal{O}(1-z)\big]\,. \tag{5.85}$$

This argument is flawed because in order to satisfy the Fourier inversion theorem, one must count $M \sim (1-z)^{-1}$ if one wants to count $u \sim 1 - z$. In particular, one is not allowed to count $M \sim 1$ when taking the limit $z \to 1$ (or equivalently $N \to \infty$ for the Mellin conjugate N of z). This is essential because $C(z,u)$ contains distributional terms in u that cancel the suppression by the integration domain.

To disprove eq. (5.85), it again suffices to consider the distributions $A(z,y)$ and $B(z,y)$ defined in eq. (5.81). Changing variables to u, we have

$$\mathrm{d}y\, A(z,y) = \mathrm{d}u\, \mathcal{L}_0(1-z)\, \frac{\delta(u + u_{\mathrm{max}}) + \delta(u - u_{\mathrm{max}})}{2}\,, \qquad \mathrm{d}y\, B(z,y) = \mathrm{d}u\, \mathcal{L}_0(1-z)\, \delta(u)\,. \tag{5.86}$$

Both terms satisfy the assumptions of the above argument, i.e., they only have support for $|u| \le u_{\mathrm{max}}$. Changing variables back to y, eq. (5.85) would imply that up to power corrections in $1 - z$,

$$A(z,y) = \mathcal{L}_0(1-z)\, \frac{\delta(y) + \delta(1-y)}{2} \overset{?}{=} \mathcal{L}_0(1-z)\, \delta\!\left(y - \frac{1}{2}\right) = B(z,y)\,. \tag{5.87}$$

In fact, the overall factor found in ref. [235] is $\delta(y - 1/2)$, while it is $[\delta(y) + \delta(1-y)]/2$ in ref. [234], and the above argument was used in ref. [235] to argue that the two are equivalent. As a distributional identity, this is obviously incorrect. The only thing that is equal between $A(z,y)$ and $B(z,y)$ are their y integrals, and as demonstrated before, this is insufficient because the y dependence of the PDF arguments is a leading-power effect and cannot be neglected.

Discussion We conclude that for pp production processes in general, to correctly describe the soft threshold limit of differential observables that are sensitive to the total rapidity of the Born system, one must maintain the two-dimensional dependence on z_a and z_b in the convolutions against the PDFs. Equivalently, in Mellin space one must maintain two Mellin fractions N_a and N_b as in the original ref. [211]. In terms of the Mellin conjugate N of z and the Fourier conjugate M of another variable like u, one has to keep the dependence on $M \sim |N_a - N_b| \sim N$. In particular, reducing the two-dimensional convolution structure to one dimension, such that the rapidity dependence is only carried by the luminosity function, amounts to making an additional assumption that is not justified by taking the soft limit.

5.6 Applications

5.6.1 Fixed-order approximants at leading power

The immediate question arises how well the generalized threshold limit approximates the full fixed-order result for physical PDFs, particularly in comparison to the soft limit. We work with the `MMHT2014nnlo68cl` PDFs [110] and use `Vrap 0.9` [114] to obtain full NNLO results for the cross section,[11] and `SCETlib` [8] to implement eq. (5.22). In figure 5.6 we compare the $\mathcal{O}(\alpha_s)$ (top) and $\mathcal{O}(\alpha_s^2)$ (center) contributions to the Drell-Yan rapidity spectrum at $Q = m_Z$, separated into quark channels ($q\bar{q} + qq'$) and channels involving a gluon ($qg + gq + gg$). We also show results for the relative $\mathcal{O}(\alpha_s)$ contribution to the $gg \to H$ rapidity spectrum (bottom) in the (r)EFT limit, see eq. (2.74). In both cases we include results at $\mu = Q$ (left) and $\mu = Q/2$ (right), where $Q = m_H$ in the case of Higgs production.

We note that when performing any threshold expansion for different scale choices, there are several options how to treat the terms in the partonic cross section that are predicted by the running of the PDFs or α_s. One option is to expand these terms to the working order in the threshold expansion. This ensures that the partonic cross section has homogeneous power counting at any scale, but leaves the running of the PDFs and the coupling uncanceled beyond the working order. Another option is to threshold-expand the partonic cross section at a given reference scale and treat the running exactly. This leads to a privileged scale where the expansion was performed, but ensures the cancellation of α_s and PDF running to all powers (up to higher orders in α_s). For the results in figure 5.6, we choose the first option for definiteness. The difference between the two approaches could serve as a way to estimate the size of power corrections in phenomenological applications.

We find that the generalized threshold limit approximates the full result for Drell-Yan well for all channels, at both orders considered, and at all Y. As expected, it works particularly well toward large Y and correctly captures the divergent behavior (with opposite sign) of the different partonic channels in this region, suggesting that resummation based on the generalized threshold factorization theorem could greatly improve the prediction. The

---

[11] The public `Vrap 0.9` assumes $f_q(x) = f_{\bar{q}}(x)$ for $q = s, c, b$. We modified it to allow for different sea quark and antiquark PDFs.
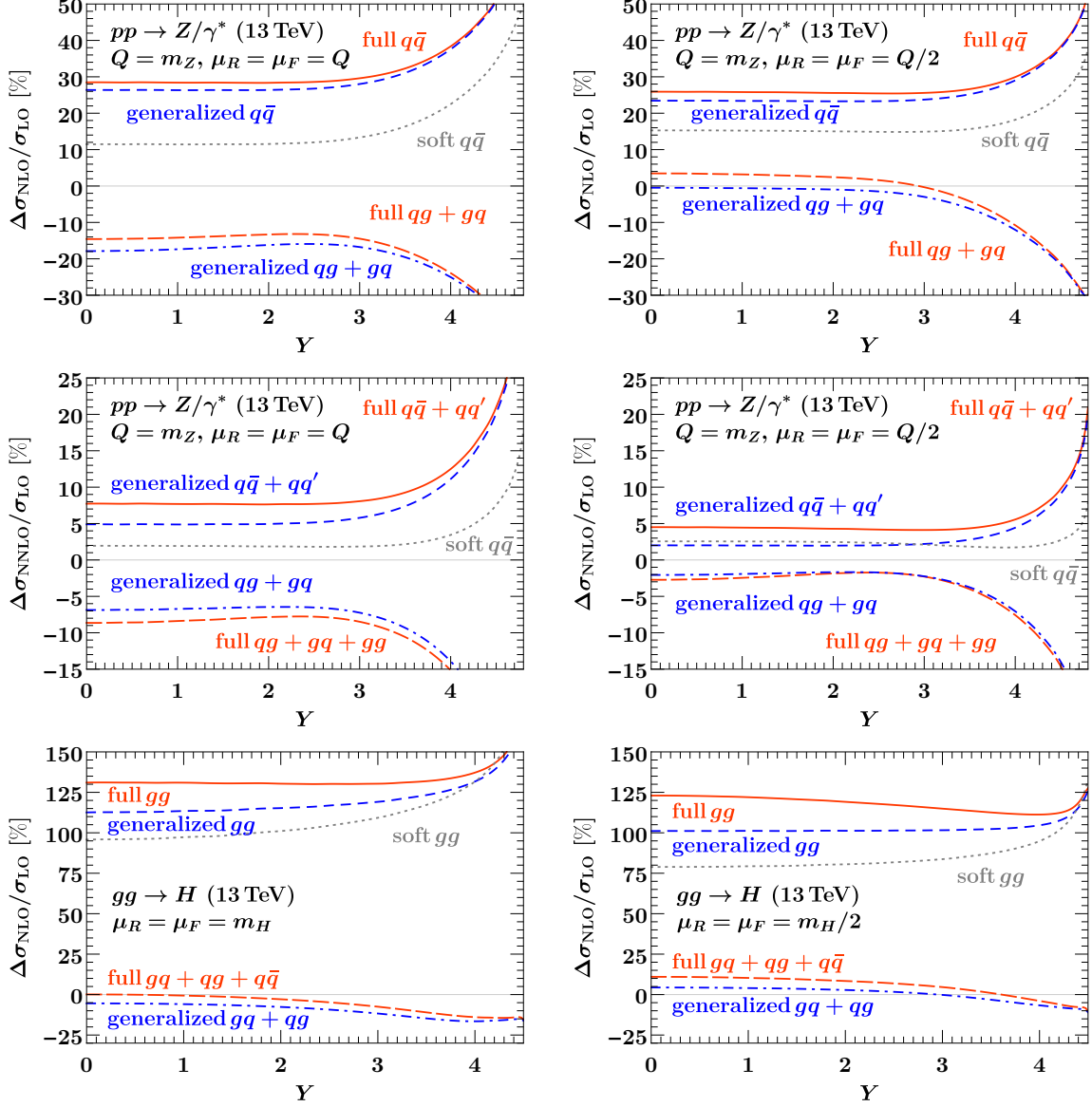
Figure 5.6: Generalized threshold approximation of the $\mathcal{O}(\alpha_s)$ (top) and $\mathcal{O}(\alpha_s^2)$ contribution (center) to the Drell-Yan rapidity spectrum $\sigma \equiv \mathrm{d}\sigma/(\mathrm{d}Q\mathrm{d}Y)$, and of the $\mathcal{O}(\alpha_s)$ contribution to the $gg \to H$ rapidity spectrum $\sigma \equiv \mathrm{d}\sigma/\mathrm{d}Y$ (bottom). We show the full result (red), the generalized threshold approximation (blue), and the soft threshold approximation (gray) for different partonic channels, at $\mu = Q$ (left column) and $\mu = Q/2$ (right column) normalized to the respective total LO result.

generalized threshold limit works significantly better than the soft limit, which only provides a poor approximation for the $q\bar{q}$ channel and none for the others.

For $gg \to H$ at $\mathcal{O}(\alpha_s)$, the generalized threshold expansion again performs in a manner clearly superior to the soft one. Here, the increment from the leading-power soft to the leading-power generalized approximation of the gg channel at NLO is roughly comparable to the piece still missing to the full result; either contribution amounts to $\mathcal{O}(20\%)$ in units of the Born cross section. This is consistent with the expectation that for a gluon-induced process, hard central radiation plays a larger role than for Drell-Yan. The shape of the NLO contributions at large Y is well captured by the leading-power generalized approximation for both the gg and $gq + qg$ channel. The leading-power soft approximation for the gg channel (on close inspection) turns out to be off at large Y, and in both channels there is barely any convergence beyond leading power in the soft expansion at any Y.

5.6.2 Convergence of the expansion

Next, we may ask how well the power expansion around the generalized threshold limit works and how it relates to the soft expansion. Consider the double expansion in $1 - z_a$ and $1 - z_b$, also illustrated in figure 5.2,

$$\hat{\sigma}_{ij}(z_a, z_b) = \sum_{m_a, m_b} \hat{\sigma}_{ij}^{(m_a, m_b)}(z_a, z_b), \tag{5.88}$$

where $\hat{\sigma}_{ij}^{(m_a, m_b)}(z_a, z_b) \sim (1 - z_a)^{m_a}(1 - z_b)^{m_b}$. Expanding around the soft $z = z_a z_b \to 1$ limit corresponds to counting powers of $(1 - z)^{m_a + m_b + 1}$, as indicated by successively lighter shades of gray in figure 5.2. The leading-power result in eq. (2.188) gives the $m_a = m_b = -1$ term. At the mth order, $\mathrm{N}^m\mathrm{LP}_{\mathrm{soft}}$, we keep all terms with $m_a + m_b + 2 \leq m$. At leading power in the generalized expansion, eq. (5.22) includes all terms with $\min\{m_a, m_b\} = -1$. Similarly, at the mth order, $\mathrm{N}^m\mathrm{LP}_{\mathrm{gen}}$, we keep all terms with $\min\{m_a, m_b\} = m - 1$, so the *missing* corrections at $\mathrm{N}^m\mathrm{LP}_{\mathrm{gen}}$ are $\mathcal{O}[(1 - z_a)^m(1 - z_b)^m]$.

In figure 5.7, we show the deviation from the exact result at various orders in both expansions for Drell-Yan and Higgs production at NLO, where we have full analytic control. The generalized expansion performs significantly better than the soft one for both flavor-diagonal and off-diagonal partonic channels. We expect this to hold in general, since expanding a two-dimensional function along a one-dimensional boundary is superior to expanding it in a single point on that boundary.

In fact, as seen in figure 5.2, each order in the generalized expansion fully contains two orders in the soft expansion, and in particular, the $\mathrm{LP}_{\mathrm{gen}}$ result eq. (5.22) contains the entire $\mathrm{NLP}_{\mathrm{soft}}$ contribution. This does not mean it can be used to perform the $\mathrm{NLP}_{\mathrm{soft}}$ resummation because the μ evolution of $B_i(t, x)$ does not predict its x dependence. It does, however, show that H_{ij} factorizes for all partonic channels and reduces the problem to deriving the $\mathrm{NLP}_{\mathrm{soft}}$ factorization for eq. (5.18).
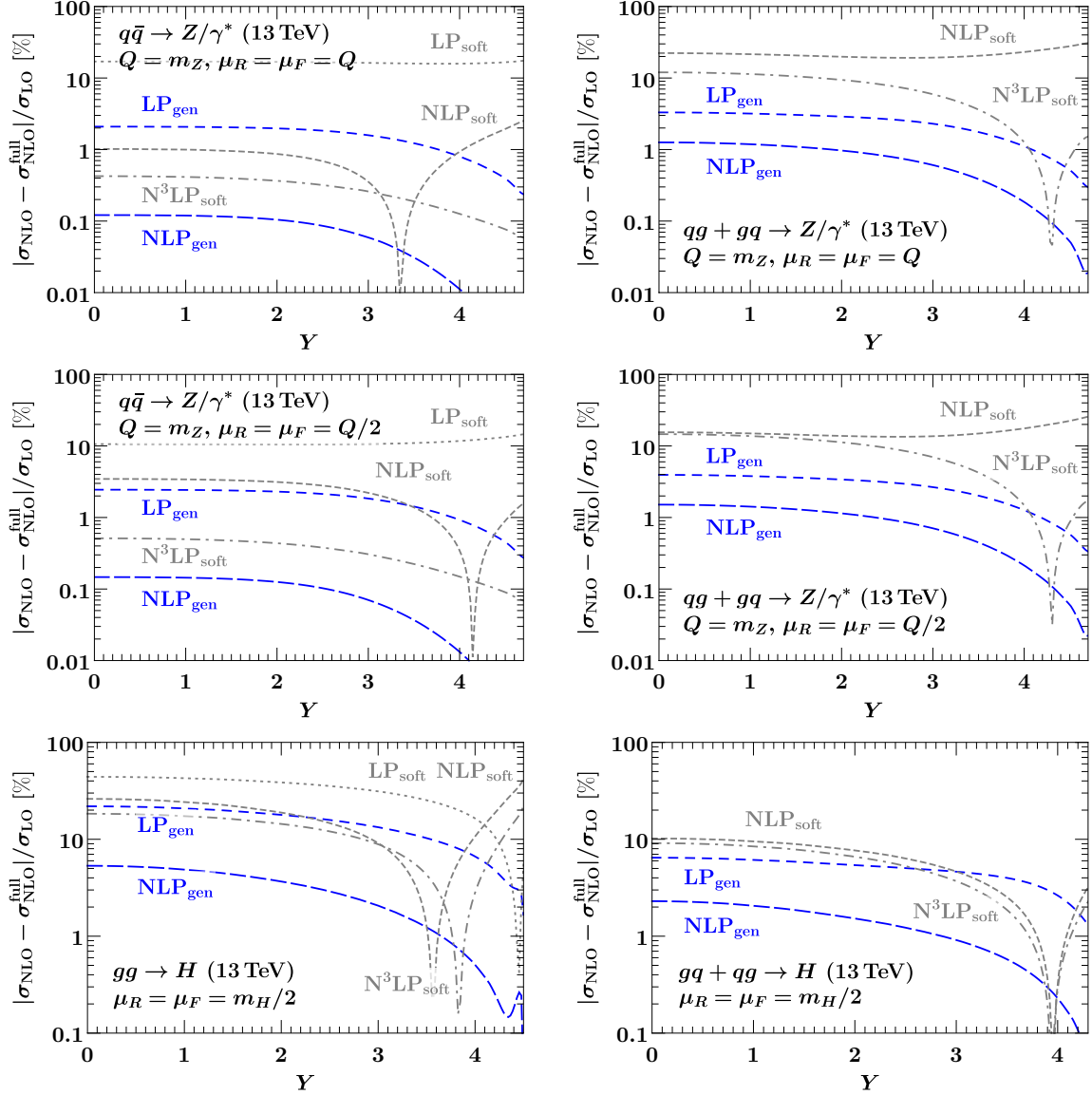
Figure 5.7: Convergence of the generalized (blue) and soft (gray) threshold expansions. Shown are the deviations from the full NLO result normalized to the total LO result for the flavor-diagonal $q\bar{q}$ or gg channel (left) and the off-diagonal $qg + gq$ contribution (right). We show results for the rapidity spectrum for Drell-Yan production at $\mu = Q = m_Z$ (top) and $\mu = Q/2$ (center), and for $gg \to H$ at $\mu = m_H/2$ (bottom).

5.6.3 Towards the Drell-Yan rapidity spectrum at N³LO

At N³LO, eq. (5.22) predicts a highly nontrivial set of terms for any color-singlet process, since all terms $\sim \mathcal{L}_n(1 - z_a)$ in $\hat{\mathcal{I}}_{ij}(z_a, z_b)$ are known from its μ evolution, where $\mathcal{L}_n(y) \equiv [\ln^n(y)/y]_+$. In particular, their coefficients are predicted including their exact z_b dependence and all possible contributions from off-diagonal channels. This also provides a powerful tools to organize future calculations and check intermediate results. To illustrate this, the terms with $n \geq 3$ in the N³LO partonic rapidity spectrum for any color-singlet process are predicted to be

$$
\hat{\sigma}_{ij}^{(3)}(z_a, z_b) = \mathcal{L}_5(1 - z_a)\hat{H}_{ij}^{(0)}\delta(1 - z_b)\frac{(\Gamma_0^i)^3}{8} \tag{5.89}
$$
$$
+ \mathcal{L}_4(1 - z_a)\hat{H}_{ik}^{(0)}\left[\delta_{kj}\delta(1 - z_b)\left(-\frac{2\beta_0}{3} - \frac{\gamma_{B\,0}^i}{2}\right) + P_{kj}^{(0)}(z_b)\right]\frac{5}{8}(\Gamma_0^i)^2
$$
$$
+ \mathcal{L}_3(1 - z_a)\left\{\hat{H}_{ij}^{(1)}\delta(1 - z_b)\frac{\Gamma_0^i}{2} + \hat{H}_{ik}^{(0)}\left[\delta_{kj}\delta(1 - z_b)\left(\Gamma_1^i - \frac{\pi^2}{6}(\Gamma_0^i)^2 + \frac{\beta_0^2}{3}\right.\right.\right.
$$
$$
\left.+ \frac{(\gamma_{B\,0}^i)^2}{4} + \frac{5}{6}\beta_0\gamma_{B\,0}^i\right) - P_{kj}^{(0)}(z_b)\left(\frac{5\beta_0}{3} + \gamma_{B\,0}^i\right)
$$
$$
\left.\left.+ \left(P^{(0)} \otimes P^{(0)}\right)_{kj}(z_b) + \tilde{I}_{kj}^{(1)}(z_b)\frac{\Gamma_0^i}{2}\right]\right\}\Gamma_0^i + \cdots .
$$

Note the appearance of the modified beam function finite term, which is specific to the (Q, Y) measurement, already at this high logarithmic order, and that none of these terms are predicted by the running of the PDFs or the coupling since we are given a prediction for the *boundary terms* of the cross section at $\mu = Q$. Instead, these terms are predicted by the RG evolution of the beam function between $\sqrt{t}$ and Q in the context of our new factorization theorem, which exposes for the first time that even at fixed Q, the partonic cross section is sensitive to the lower scale $\sqrt{t} \sim Q\sqrt{1 - z_a}$ of collinear radiation in the limit $z_a \to 1$. The extension down to $\mathcal{L}_0(1 - z_a)$, indicated by the ellipses, and to the full z_a dependence for $z_b \to 1$ is straightforward, see ref. [5]. The relevant pieces of the beam function entering eq. (5.89) are also given in appendix E.1. The $\delta(1 - z_a)$ coefficient requires the still unknown $\mathcal{O}(\alpha_s^3)$ finite terms of the (modified) virtuality-dependent beam function. For Drell-Yan, eq. (5.89) significantly extends the current knowledge at $\mathcal{O}(\alpha_s^3)$ [219, 244], providing the full z_b dependence for all partonic channels. For $gg \to H$, the extension to $\mathcal{L}_0(1 - z_a)$ would also provide additional information beyond what is currently known [250].

5.7 Summary

In this chapter we presented and derived a factorization theorem that generalizes the often-used soft threshold factorization by including the full collinear dynamics, and demonstrated that it has much wider applicability. The new factorization theorem describes all kinematic limits in (x_a, x_b) or (Q, Y), including in particular $|Y| \to Y_{\max}$ at generic Q, which is directly accessible at the LHC. We gave a proof of the theorem that draws on many

aspects of soft-collinear effective theory and improves the formal understanding of the foundations of leading-power threshold factorization in general. We extensively validated the perturbative content of the factorization theorem against exact calculations. As a corollary to the theorem, we have been able to resolve a long-standing issue in the description of rapidity spectra in the soft limit. At the partonic level, the new factorization theorem captures all singularities of $\hat{\sigma}_{ij}(z_a, z_b)$, including off-diagonal partonic channels. It can be used to predict a rich set of terms at higher fixed order or to resum them to all orders. As a first illustrative application, we have demonstrated that the factorization theorem predicts a highly nontrivial set of previously unknown terms in the N^3LO Drell-Yan rapidity spectrum.

Chapter 6

N³LO beam functions in the eikonal limit

In this chapter, we show that the matching coefficients for the q_T and $\mathcal{T}_0$ beam functions in the limit of large partonic momentum fraction $z \to 1$ satisfy all-order relations to known soft matrix elements, and use these relations to extract the previously unknown complete three-loop results for the beam functions in the $z \to 1$ limit.

This chapter is based on ref. [5], reflecting the author's contribution. Compared to ref. [5], the discussion in section 6.3.3 has been added.

6.1 Motivation

Beam functions B_i describe the collinear emission pattern from an incoming parton i. In SCET, they can formally be defined as proton matrix elements of renormalized quark and gluon operators. They are universal objects that do not depend on the details of the hard process. When the scale of collinear emissions resolved by the measurement constraint is perturbative, the associated beam function can be matched onto standard PDFs to isolate its perturbative content in perturbative matching coefficients.

The beam and soft functions appearing in the factorization for q_T and $\mathcal{T}_0$ in eqs. (2.192) and (2.214) are the most basic of their kind, measuring the total transverse momentum or the small light-cone momentum of the inclusive sum of all collinear emissions, respectively. For this reason, they are important objects in their own right, encoding fundamental properties of the singular structure of QCD, and also appear in a variety of other contexts. Among these are the generalizations of the pp color-singlet factorization for q_T and $\mathcal{T}_0$ to the case of (semi-inclusive) DIS and to pp collisions with identified jets in the final state, see e.g. refs. [57, 259–262, 292, 293, 418]. In addition, they often serve as building blocks for constructing the beam and soft functions necessary for more complicated scenarios or observables, see e.g. refs. [66, 67, 195, 291, 313, 349, 389, 397, 398, 419, 420]. Finally, as we showed in chapter 5 above, the $\mathcal{T}_0$ beam function and its variants also describe *inclusive* color-singlet production in a generalized threshold limit.

In these applications, knowledge of the beam function matching coefficients to high perturbative orders is key. Percent-level predictions for color-singlet spectra in particular mandate a full N³LO calculation of the beam functions. The most challenging part are

the nonlogarithmic boundary coefficients at $\mathcal{O}(\alpha_s^3)$ that are not predicted by the RGE, require a dedicated three-loop calculation, and are in general nontrivial functions of the partonic momentum fraction z. However, they simplify in the limit $z \to 1$. In this limit, the energy of collinear emissions is constrained to be small which means their interactions with the primary collinear parton can be described in the eikonal approximation where they only resolve its color charge and direction. This was already pointed out and exploited at NNLO in refs. [294, 295]. In this chapter, we derive the explicit relations between the beam function matching coefficients in the $z \to 1$ limit to known soft matrix elements, and use these relations to extract the leading terms in the eikonal limit at three loops.[1]

6.2 $\mathcal{T}_0$ beam function

6.2.1 Consistency relation

We first consider the matching coefficients $I_{ij}^{(n)}(z)$ of the $\mathcal{T}_0$ beam function in the $z \to 1$ limit. In this case, the relevant consistency relation with an eikonal matrix element is a byproduct of the generalized threshold factorization theorem presented in chapter 5. It involves the double-differential threshold soft function and reads at the hadronic level, as given in eq. (5.18),

$$B_i(t, x, \mu) = \int \frac{\mathrm{d}k}{\omega} S_i^{\mathrm{thr}}\left(\frac{t}{\omega}, k, \mu\right) f_i^{\mathrm{thr}}\left[x\left(1 + \frac{k}{\omega}\right), \mu\right] \left[1 + \mathcal{O}(1-x)\right]. \qquad (6.1)$$

Eq. (6.1) follows from comparing one of the main results of chapter 5, eq. (5.5), with the standard soft threshold factorization for color-singlet rapidity spectra in eq. (2.186).

The threshold soft function is defined as a vacuum matrix element of Wilson lines that are invariant under longitudinal boosts, and therefore satisfies the rescaling property

$$S_i^{\mathrm{thr}}(k^-, k^+, \mu) = S_i^{\mathrm{thr}}(e^{+y}k^-, e^{-y}k^+, \mu). \qquad (6.2)$$

More specifically, in the context of SCET, the soft function is invariant under RPI-III transformations, see section 2.2.3. Exploiting this property, the soft function can be extracted [192, 219, 244, 250, 265] from the soft-virtual limit of the total color-singlet production cross section $\mathrm{d}\sigma/\mathrm{d}Q^2$, which is known to $\mathcal{O}(\alpha_s^3)$ [241, 246]. In section 6.2.2, we review this procedure and give explicit results for $S_i^{\mathrm{thr}}(k^-, k^+, \mu)$ to three loops.

Replacing $f_i^{\mathrm{thr}}[x(1 + 1 - z)]$ by $f_i(x/z)/z$, which is justified at leading power in $1 - z$, yields the corresponding relation for the matching coefficient,

$$\mathcal{I}_{ij}(t, z, \mu) = \delta_{ij}\, S_i^{\mathrm{thr}}\left[\frac{t}{\omega}, \omega(1-z), \mu\right] \left[1 + \mathcal{O}(1-z)\right]. \qquad (6.3)$$

---

[1]At the time of the original publication of the results of this chapter in ref. [5], only a few master integrals for selected topologies in the $\mathcal{T}_0$ beam function at $\mathcal{O}(\alpha_s^3)$ were known [296, 297]. Since the appearance of ref. [5], results for the three-loop $\mathcal{T}_0$ quark beam function in the generalized large-N_c approximation have appeared in ref. [298], and the complete three-loop beam functions have been calculated in refs. [287, 288] for the q_T quark and q_T quark and gluon cases, respectively, and in ref. [299] for the $\mathcal{T}_0$ quark and gluon cases. In these works, the eikonal terms derived in this work were used as an important cross check, finding full agreement.

This relation captures all terms in $\mathcal{I}_{ij}(t, z, \mu)$ that are singular for $z \to 1$, while power corrections have at most an integrable singularity for $z \to 1$. Notably, the beam function becomes flavor diagonal as $z \to 1$, while off-diagonal channels are $\mathcal{O}(1 - z)$ suppressed. By eq. (6.3), the matching coefficients also inherit the rescaling property in eq. (6.2), i.e., in the limit $z \to 1$, they become invariant under a simultaneous rescaling $t \mapsto e^{+y}t$ and $1 - z \mapsto e^{-y}(1 - z)$. In other words, they are symmetric in t/ω and $\omega(1 - z)$ such that the dependence on ω cancels on the right-hand side.

6.2.2 Threshold soft function to three loops

In this section we discuss the double-differential threshold soft function $S_i^{\mathrm{thr}}(k^-, k^+, \mu)$, which determines the eikonal limit of the $\mathcal{T}_0$ beam function in eq. (6.3). We give a compact, complete N³LO expression in terms of a convenient plus distribution basis defined below, and discuss how the three-loop coefficients are extracted from the known three-loop results for the closely-related inclusive threshold soft function.

Plus distribution basis. A key property of the threshold soft function is that is invariant under the simultaneous rescaling $k^- \mapsto k^- e^{+y}$ and $k^+ \mapsto k^+ e^{-y}$, see eq. (6.2). To make this property manifest, we define a basis of plus distributions in $k^{\pm}$ that individually have this property,

$$\frac{\theta(k^-)\theta(k^+)}{\mu^2}\left(\frac{k^- k^+}{\mu^2}\right)^{-1+a} = \left[\frac{\delta(k^-)}{a} + \sum_{n=0}^{\infty}\frac{a^n}{n!}\mathcal{L}_n(k^-, \mu)\right]\left[\frac{\delta(k^+)}{a} + \sum_{m=0}^{\infty}\frac{a^m}{m!}\mathcal{L}_m(k^+, \mu)\right]$$

$$\equiv \frac{\delta(k^-, k^+)}{a^2} + \sum_{n=0}^{\infty}\frac{a^{n-1}}{n!}\mathcal{L}_n(k^-, k^+, \mu)\,. \tag{6.4}$$

Note that the leading $\delta(k^-, k^+)$ term multiplies a double pole in a. The second line implicitly defines the $\mathcal{L}_n(k^-, k^+, \mu)$ by the expansion of the first line in powers of a. They are by construction invariant under rescaling, because the left-hand side is. Explicitly, they are given by

$$\delta(k^-, k^+) = \delta(k^-)\,\delta(k^+)\,,$$
$$\mathcal{L}_n(k^-, k^+, \mu) = \delta(k^-)\,\mathcal{L}_n(k^+, \mu) + \mathcal{L}_n(k^-, \mu)\,\delta(k^+)$$
$$+ n\sum_{m=0}^{n-1}\binom{n-1}{m}\mathcal{L}_m(k^-, \mu)\,\mathcal{L}_{n-1-m}(k^+, \mu)\,. \tag{6.5}$$

Three-loop structure. The threshold soft function satisfies the all-order RGE

$$\mu\frac{\mathrm{d}}{\mathrm{d}\mu}S_i^{\mathrm{thr}}(k^-, k^+, \mu) = \int\mathrm{d}\ell^-\,\mathrm{d}\ell^+\,\gamma_{\mathrm{thr}}^i(k^- - \ell^-, k^+ - \ell^+, \mu)\,S_i^{\mathrm{thr}}(\ell^-, \ell^+, \mu)\,,$$
$$\gamma_{\mathrm{thr}}^i(k^-, k^+, \mu) = -2\Gamma_{\mathrm{cusp}}^i[\alpha_s(\mu)]\,\mathcal{L}_0(k^-, k^+, \mu) + \gamma_{\mathrm{thr}}^i[\alpha_s(\mu)]\,\delta(k^-, k^+)\,. \tag{6.6}$$

213

Expanding the threshold soft function in α_s as

$$S_i^{\text{thr}}(k^-, k^+, \mu) = \sum_{n=0}^{\infty} S_i^{\text{thr}(n)}(k^-, k^+, \mu) \left[\frac{\alpha_s(\mu)}{4\pi}\right]^n , \qquad (6.7)$$

and suppressing all arguments for brevity, $S_i^{\text{thr}(n)} \equiv S_i^{\text{thr}(n)}(k^-, k^+, \mu)$, $\mathcal{L}_n \equiv \mathcal{L}_n(k^-, k^+, \mu)$, $\delta \equiv \delta(k^-, k^+)$, the three-loop solution of eq. (6.6) takes the very compact form

$$S_i^{\text{thr}(0)} = \delta \,,$$

$$S_i^{\text{thr}(1)} = \mathcal{L}_1 \Gamma_0^i - \mathcal{L}_0 \frac{\gamma_{\text{thr}\,0}^i}{2} + \delta\, s_i^{\text{thr}(1)} \,,$$

$$S_i^{\text{thr}(2)} = \mathcal{L}_3 \frac{(\Gamma_0^i)^2}{2} - \mathcal{L}_2 \frac{\Gamma_0^i}{2}\left(\beta_0 + \frac{3}{2}\gamma_{\text{thr}\,0}^i\right)$$

$$+ \mathcal{L}_1\left[-2\zeta_2(\Gamma_0^i)^2 + \left(\beta_0 + \frac{\gamma_{\text{thr}\,0}^i}{2}\right)\frac{\gamma_{\text{thr}\,0}^i}{2} + \Gamma_1^i + \Gamma_0^i s_i^{\text{thr}(1)}\right]$$

$$+ \mathcal{L}_0\left[\Gamma_0^i(2\zeta_3\Gamma_0^i + \zeta_2\gamma_{\text{thr}\,0}^i) - \frac{\gamma_{\text{thr}\,1}^i}{2} - \left(\beta_0 + \frac{\gamma_{\text{thr}\,0}^i}{2}\right)s_i^{\text{thr}(1)}\right] + \delta\, s_i^{\text{thr}(2)} \,,$$

$$S_i^{\text{thr}(3)} = \mathcal{L}_5 \frac{(\Gamma_0^i)^3}{8} - \mathcal{L}_4 \frac{5}{8}(\Gamma_0^i)^2\left(\frac{2}{3}\beta_0 + \frac{\gamma_{\text{thr}\,0}^i}{2}\right)$$

$$+ \mathcal{L}_3 \Gamma_0^i\left[-2\zeta_2(\Gamma_0^i)^2 + \frac{\beta_0^2}{3} + \left(\frac{5}{3}\beta_0 + \frac{\gamma_{\text{thr}\,0}^i}{2}\right)\frac{\gamma_{\text{thr}\,0}^i}{2} + \Gamma_1^i + \frac{\Gamma_0^i}{2}s_i^{\text{thr}(1)}\right]$$

$$+ \mathcal{L}_2\left\{(\Gamma_0^i)^2\left[5\zeta_3\Gamma_0^i + 3\zeta_2(\beta_0 + \gamma_{\text{thr}\,0}^i)\right] - \left(\beta_0 + \frac{3}{4}\gamma_{\text{thr}\,0}^i\right)\left(\beta_0\frac{\gamma_{\text{thr}\,0}^i}{2} + \Gamma_1^i\right)\right.$$

$$\left. - \frac{(\gamma_{\text{thr}\,0}^i)^3}{16} - \frac{\Gamma_0^i}{2}\left[\beta_1 + \frac{3}{2}\gamma_{\text{thr}\,1}^i + \left(4\beta_0 + \frac{3}{2}\gamma_{\text{thr}\,0}^i\right)s_i^{\text{thr}(1)}\right]\right\}$$

$$+ \mathcal{L}_1\left\{(\Gamma_0^i)^2\left[4\zeta_4\Gamma_0^i - \zeta_3(6\beta_0 + 4\gamma_{\text{thr}\,0}^i)\right] - \zeta_2\Gamma_0^i\left[(3\beta_0 + \gamma_{\text{thr}\,0}^i)\gamma_{\text{thr}\,0}^i + 4\Gamma_1^i\right]\right.$$

$$+ \beta_0\gamma_{\text{thr}\,1}^i + \frac{\gamma_{\text{thr}\,0}^i}{2}(\beta_1 + \gamma_{\text{thr}\,1}^i) + \Gamma_2^i$$

$$\left. + \left[-2\zeta_2(\Gamma_0^i)^2 + 2\beta_0^2 + \left(3\beta_0 + \frac{\gamma_{\text{thr}\,0}^i}{2}\right)\frac{\gamma_{\text{thr}\,0}^i}{2} + \Gamma_1^i\right]s_i^{\text{thr}(1)} + \Gamma_0^i s_i^{\text{thr}(2)}\right\}$$

$$+ \mathcal{L}_0\left\{(\Gamma_0^i)^2\left[-\Gamma_0^i(8\zeta_2\zeta_3 - 6\zeta_5) + 2\zeta_4(\beta_0 - \gamma_{\text{thr}\,0}^i)\right] + \zeta_3\Gamma_0^i\left[\left(\beta_0 + \frac{\gamma_{\text{thr}\,0}^i}{2}\right)\gamma_{\text{thr}\,0}^i\right.\right.$$

$$\left. + 4\Gamma_1^i\right] + \zeta_2\left(\gamma_{\text{thr}\,0}^i\Gamma_1^i + \Gamma_0^i\gamma_{\text{thr}\,1}^i\right) - \frac{\gamma_{\text{thr}\,2}^i}{2} + \left[(\Gamma_0^i)^2 2\zeta_3 + \Gamma_0^i\zeta_2(2\beta_0 + \gamma_{\text{thr}\,0}^i)\right.$$

$$\left.\left. - \left(\beta_1 + \frac{\gamma_{\text{thr}\,1}^i}{2}\right)\right]s_i^{\text{thr}(1)} - \left(2\beta_0 + \frac{\gamma_{\text{thr}\,0}^i}{2}\right)s_i^{\text{thr}(2)}\right\} + \delta\, s_i^{\text{thr}(3)} \,. \qquad (6.8)$$

Anomalous dimensions. The noncusp threshold anomalous dimension $\gamma_{\text{thr}}^i(\alpha_s)$ appearing in eq. (6.6) is not an independent quantity, but strongly constrained by consistency relations. Drawing on the RG consistency of several factorization theorems we already encountered or derived, namely eqs. (2.186), (2.214), and (5.5), we have, in this order,

$$2\gamma_f^i(\alpha_s) + \gamma_{\text{thr}}^i(\alpha_s) = 2\gamma_B^i(\alpha_s) + \gamma_S^i(\alpha_s) = \gamma_f^i(\alpha_s) + \gamma_B^i(\alpha_s) \,, \qquad (6.9)$$

because the hard function is the same in all cases. Here, $\gamma_f^i(\alpha_s)$ is the coefficient of $\delta(1-z)$ in the PDF anomalous dimension eq. (2.164), see eqs. (5.15) and (5.16). Solving eq. (6.9) for $\gamma_{\mathrm{thr}}^i(\alpha_s)$, we find

$$\gamma_{\mathrm{thr}}^i(\alpha_s) = -\gamma_S^i(\alpha_s), \qquad \gamma_{\mathrm{thr}\,n}^i = -\gamma_{S\,n}^i, \tag{6.10}$$

where the (beam)thrust soft anomalous dimension coefficients $\gamma_{S\,n}^i$ are given in eq. (C.11). We are not aware of any reference pointing out the very simple relation eq. (6.10), even though the ingredients would have been at hand already without the results of chapter 5 by combining the DIS endpoint factorization in eq. (2.179), which involves the jet function, and the factorization theorem for thrust in e^+e^- collisions, which involves γ_S^i and two jet anomalous dimensions.

Extracting the finite terms. The double-differential threshold soft function depends on the total light-cone momentum components $k^\pm$ of the soft hadronic final state. Equivalently, its Fourier transform

$$\hat{S}_i^{\mathrm{thr}}(b^+, b^-, \mu) = \int \mathrm{d}k^- \mathrm{d}k^+ \, e^{+\mathrm{i}(k^- b^+ + k^+ b^-)/2} \, S_i^{\mathrm{thr}}(k^-, k^+, \mu), \tag{6.11}$$

depends on the time-like separation $(b^- n^\mu + b^+ \bar{n}^\mu)/2$ between the Wilson lines in the soft matrix element.

Importantly, $\hat{S}_i^{\mathrm{thr}}(b^+, b^-, \mu)$ only depends on the product $b^+ b^-$ by the rescaling relation eq. (6.2), and thus only depends on $b^+ b^- \mu^2$ by dimensional analysis. On the other hand, the dependence on μ is fully predicted by the RGE eq. (6.6), which in position space reads

$$\mu \frac{\mathrm{d}}{\mathrm{d}\mu} \hat{S}_i^{\mathrm{thr}}(b^+, b^-, \mu) = \left\{ 2\Gamma_{\mathrm{cusp}}^i[\alpha_s(\mu)] \, L_{\mathrm{thr}}(b^+, b^-, \mu) + \gamma_{\mathrm{thr}}^i[\alpha_s(\mu)] \right\} \hat{S}_i^{\mathrm{thr}}(b^+, b^-, \mu). \tag{6.12}$$

This implies that at any order in perturbation theory, $\hat{S}_i^{\mathrm{thr}}(b^+, b^-, \mu)$ is a polynomial in

$$L_{\mathrm{thr}}(b^+, b^-, \mu) \equiv \ln\left(-\frac{b^+ b^- \mu^2 e^{2\gamma_E}}{4} - \mathrm{i}0 \right). \tag{6.13}$$

The relevant Fourier transforms between L_{thr}^n and $\mathcal{L}_n(k^-, k^+, \mu)$ follow from the one-dimensional Fourier transforms in appendix B of ref. [263], accounting for the relative factors of $-1/2$ in the Fourier exponent in eq. (6.11).

A factorization analogous to eq. (2.186) holds for the inclusive cross section $\mathrm{d}\sigma/\mathrm{d}Q^2$ in eq. (2.69), where the corresponding inclusive threshold soft function $S_i^{\mathrm{thr}}(k^0, \mu)$ only depends on the total energy k^0 of soft radiation. In particular, $S_i^{\mathrm{thr}}(k^0, \mu)$ is the process-independent soft contribution to the inclusive partonic cross section $\hat{\sigma}_{ij}(z)$ in eq. (2.71) in the soft-virtual limit $z \to 1$, where $1 - z = 2k^0/Q$. In position space, the inclusive threshold soft function $\hat{S}_i^{\mathrm{thr}}(b^0, \mu)$ is defined in terms of Wilson lines separated by $b^0(n^\mu + \bar{n}^\mu)/2$, i.e., strictly along the time axis. This is a special case of eq. (6.11), so the two position-space threshold soft functions are simply related by

$$\hat{S}_i^{\mathrm{thr}}(b^0, b^0, \mu) = \hat{S}_i^{\mathrm{thr}}(b^0, \mu). \tag{6.14}$$

This is of course equivalent to integrating over the longitudinal momentum k^3 of soft radiation. We stress that eq. (6.14) cannot be used to approximate $\hat{S}_i^{\mathrm{thr}}(b^+, b^-, \mu)$ by taking $b^+ = b^-$ in general. This is because in eq. (2.186) the soft function is separately convolved in its k^+ and k^- arguments with the two different PDFs, and thus the rescaling property eq. (6.2) is lost at the level of the cross section. We refer the reader to section 5.5.3 for further discussion of this point.

Inserting eq. (6.14) into eq. (6.12) implies that both threshold soft functions have the same noncusp anomalous dimension given by eq. (6.10). Moreover, the position-space boundary coefficients of the double-differential soft function at $L_{\mathrm{thr}} = 0$, i.e., at $\mu = \mu_* \equiv +\mathrm{i}2e^{-\gamma_E}/b^0$, are equal to the inclusive ones at the same scale. Hence, the double-differential threshold soft function can be constructed from the inclusive one.

The inclusive threshold soft function was calculated to three loops in refs. [241, 246]. Here we use the results of ref. [246], where the three-loop soft function for $i = g$ is reported in exponentiated form,

$$\hat{S}_i^{\mathrm{thr}}(b^0, \mu_*) = \exp\left\{\frac{C_i}{C_A}\left[\frac{\alpha_s(\mu_*)}{4\pi}c_{1\,\mathrm{ref.}\,[246]}^H + \frac{\alpha_s^2(\mu_*)}{(4\pi)^2}\Delta c_{2\,\mathrm{ref.}\,[246]}^H + \frac{\alpha_s^3(\mu_*)}{(4\pi)^3}\Delta c_{3\,\mathrm{ref.}\,[246]}^H\right] + \mathcal{O}(\alpha_s^4)\right\}. \tag{6.15}$$

We have also exploited Casimir scaling to three loops to restore the dependence on C_i. Comparing eq. (6.15) to the position-space solution of eq. (6.12) at $L_{\mathrm{thr}} = 0$, and comparing the inverse Fourier transform of the outcome to eq. (6.8), we find the following momentum-space boundary coefficients:[2]

$$s_i^{\mathrm{thr}(1)} = -C_i\,2\zeta_2\,,$$

$$s_i^{\mathrm{thr}(2)} = C_i\left[C_i\,21\zeta_4 + C_A\left(\frac{208}{27} - 4\zeta_2 - 10\zeta_4\right) + \beta_0\left(\frac{164}{27} - 5\zeta_2 - \frac{10\zeta_3}{3}\right)\right],$$

$$\begin{aligned}
s_i^{\mathrm{thr}(3)} = C_i\Bigg[&C_i^2\left(\frac{640}{3}\zeta_3^2 - \frac{499}{6}\zeta_6\right) + C_iC_A\left(-\frac{416}{27}\zeta_2 - \frac{512}{9}\zeta_3 + \frac{188}{3}\zeta_4 + 224\zeta_3^2 - 77\zeta_6\right) \\
&+ C_i\beta_0\left(-\frac{328}{27}\zeta_2 - \frac{448}{9}\zeta_3 + \frac{235}{3}\zeta_4 + \frac{308}{3}\zeta_2\zeta_3 - 64\zeta_5\right) \\
&+ C_A^2\left(\frac{115895}{324} - \frac{45239}{486}\zeta_2 - \frac{23396}{81}\zeta_3 - \frac{334}{3}\zeta_4 + 240\zeta_2\zeta_3 - 224\zeta_5 + \frac{1072}{9}\zeta_3^2 + \frac{4348}{27}\zeta_6\right) \\
&+ C_A\beta_0\left(-\frac{363851}{2916} + \frac{1043}{486}\zeta_2 - \frac{140}{81}\zeta_3 + \frac{230}{9}\zeta_4 - \frac{164}{3}\zeta_2\zeta_3 + \frac{632}{9}\zeta_5\right) \\
&+ \beta_0^2\left(-\frac{64}{729} - \frac{34}{3}\zeta_2 - \frac{20}{27}\zeta_3 + \frac{31}{3}\zeta_4\right) \\
&+ \beta_1\left(\frac{42727}{972} - \frac{275}{18}\zeta_2 - \frac{1636}{81}\zeta_3 - \frac{76}{9}\zeta_4 + \frac{40}{3}\zeta_2\zeta_3 - \frac{112}{9}\zeta_5\right)\Bigg].
\end{aligned} \tag{6.16}$$

---

[2]We note that the coefficient of C_iC_A in the two-loop finite term disagrees with the $\vec{b}_T \to 0$ limit of the fully-differential soft function as reported in terms of $k^\pm$ and $\vec{b}_T$ in ref. [421]. This color structure only enters at two loops and thus is unaffected by nonabelian exponentiation. We were unable to resolve this difference, but tend to attribute it to a typographical error in ref. [421] because refs. [192, 265] agreed with the pure position-space result of ref. [421] in terms of $b^\pm$ and $\vec{b}_T$.

We have checked that inserting the above coefficients into eq. (6.8) and expanding against the Drell-Yan hard function, we reproduce the three-loop soft-virtual partonic cross section in refs. [219, 244] in terms of $1 - z_a = k^-/(Qe^{+Y})$ and $1 - z_b = k^+/(Qe^{-Y})$.[3]

6.2.3 Results for the beam function

With the three-loop expressions for the threshold soft function at hand, we return to the consistency relation in eq. (6.3). At two loops, we explicitly verified eq. (6.3) by comparing the above results for the threshold soft function to the full results of refs. [294, 295]. We now use it to predict the beam function coefficients in the eikonal limit at three loops. They are given by the coefficient of $\delta(k^-)$ in the threshold soft function upon identifying $\delta(k^+) \mapsto \delta(1 - z)$ and $\mathcal{L}_n(k^+, \mu) \mapsto \mathcal{L}_n(1 - z)$. Including the one-loop and two-loop results for reference, we find

$$I_{ij}^{(1)}(z) = \delta_{ij}\Big[\mathcal{L}_1(1 - z)\,\Gamma_0^i + \delta(1 - z)\,s_i^{\mathrm{thr}(1)}\Big] + \mathcal{O}\big[(1 - z)^0\big],$$

$$I_{ij}^{(2)}(z) = \delta_{ij}\bigg\{\mathcal{L}_3(1 - z)\,\frac{(\Gamma_0^i)^2}{2} - \mathcal{L}_2(1 - z)\,\frac{\Gamma_0^i}{2}\beta_0 + \mathcal{L}_1(1 - z)\Big[-2\zeta_2(\Gamma_0^i)^2 + \Gamma_1^i + \Gamma_0^i\,s_i^{\mathrm{thr}(1)}\Big]$$

$$+ \mathcal{L}_0(1 - z)\Big[2\zeta_3(\Gamma_0^i)^2 + \frac{\gamma_{S1}^i}{2} - \beta_0\,s_i^{\mathrm{thr}(1)}\Big] + \delta(1 - z)\,s_i^{\mathrm{thr}(2)}\bigg\} + \mathcal{O}\big[(1 - z)^0\big],$$

$$I_{ij}^{(3)}(z) = \delta_{ij}\bigg\{\mathcal{L}_5(1 - z)\,\frac{(\Gamma_0^i)^3}{8} - \mathcal{L}_4(1 - z)\,\frac{5}{12}(\Gamma_0^i)^2\beta_0$$

$$+ \mathcal{L}_3(1 - z)\,\Gamma_0^i\Big[-2\zeta_2(\Gamma_0^i)^2 + \frac{\beta_0^2}{3} + \Gamma_1^i + \frac{\Gamma_0^i}{2}s_i^{\mathrm{thr}(1)}\Big]$$

$$+ \mathcal{L}_2(1 - z)\,\Big[(\Gamma_0^i)^2(5\zeta_3\Gamma_0^i + 3\zeta_2\beta_0) - \beta_0\Gamma_1^i - \frac{\Gamma_0^i}{2}\Big(\beta_1 - \frac{3}{2}\gamma_{S1}^i + 4\beta_0\,s_i^{\mathrm{thr}(1)}\Big)\Big]$$

$$+ \mathcal{L}_1(1 - z)\,\Big[(\Gamma_0^i)^2(4\zeta_4\Gamma_0^i - 6\zeta_3\beta_0) - 4\zeta_2\Gamma_0^i\Gamma_1^i - \beta_0\gamma_{S1}^i + \Gamma_2^i$$

$$+ \big(-2\zeta_2(\Gamma_0^i)^2 + 2\beta_0^2 + \Gamma_1^i\big)s_i^{\mathrm{thr}(1)} + \Gamma_0^i\,s_i^{\mathrm{thr}(2)}\Big]$$

$$+ \mathcal{L}_0(1 - z)\,\Big[(\Gamma_0^i)^2\big(-\Gamma_0^i(8\zeta_2\zeta_3 - 6\zeta_5) + 2\zeta_4\beta_0\big) + \Gamma_0^i(4\zeta_3\Gamma_1^i - \zeta_2\gamma_{S1}^i) + \frac{\gamma_{S2}^i}{2}$$

$$+ \Big((\Gamma_0^i)^2 2\zeta_3 + \Gamma_0^i 2\zeta_2\beta_0 - \beta_1 + \frac{\gamma_{S1}^i}{2}\Big)s_i^{\mathrm{thr}(1)} - 2\beta_0\,s_i^{\mathrm{thr}(2)}\Big]$$

$$+ \delta(1 - z)\,s_i^{\mathrm{thr}(3)}\bigg\} + \mathcal{O}\big[(1 - z)^0\big]. \tag{6.17}$$

The boundary coefficients $s_i^{\mathrm{thr}(n)}$ of the threshold soft function are given in eq. (6.16). We have exploited that the noncusp anomalous dimension of the threshold soft function is given by the negative of the thrust soft anomalous dimension $-\gamma_S^i(\alpha_s)$, see eq. (6.10). For brevity, we also used that $\gamma_{S0}^i = 0$. The result for generic γ_{S0}^i can be read off from the full expression for the threshold soft function in eq. (6.8).

The three-loop result in eq. (6.17) is new and a genuine prediction of the consistency relation in eq. (6.3). We stress that the information provided by it goes beyond the three-

---

[3]We thank V. Ravindran for providing us with the results of refs. [219, 244] in machine-readable form.

loop structure predicted by the RGE. The fact that the leading $z \to 1$ terms must be symmetric in t/ω and $\omega(1-z)$ allows one to directly determine (or check) the $\delta(t)\mathcal{L}_n(1-z)$ terms from the RGE-predicted $\mathcal{L}_n(t)\delta(1-z)$ terms, which was already noted in refs. [294, 347]. However, the $\delta(t)\delta(1-z)$ coefficient cannot be predicted in this way, and eq. (6.3) explicitly identifies it with the threshold soft function coefficients $s_i^{\text{thr}(3)}$.

We remind the reader that the modified virtuality-dependent beam function defined in eq. (5.12) in the eikonal limit $x \to 1$ (or $z \to 1$) coincides with the standard inclusive beam function $B_i(t, x, \mu)$, see the discussion below eq. (5.55). For this reason, the $z \to 1$ limit of the modified $\tilde{I}_{ij}^{(n)}$ matching coefficients at three loop is also given by eq. (6.17), and could e.g. be used to predict N³LO color-singlet rapidity spectra with all finite terms correct in the soft limit $z_{a,b} \to 1$, and all logarithmically enhanced terms correct in all singular limits, as predicted by the beam function RGE.

6.3 q_T beam function

6.3.1 Consistency relations

We now proceed to extract the three-loop matching coefficients for the q_T beam function in the $z \to 1$ limit from consistency relations with known soft matrix elements. For the q_T beam function, these consistency relations arise from factorization theorems for the triple-differential cross section $\mathrm{d}\sigma_{pp \to L}/\mathrm{d}Q^2 \mathrm{d}Y \mathrm{d}q_T$ that enable the joint q_T and soft threshold resummation [375–378]. In terms of the momentum fractions $x_{a,b}$ defined in eq. (2.62), the soft threshold limit is equivalent to taking both $x_a \to 1$ and $x_b \to 1$. As $x_{a,b} \to 1$, initial state radiation is constrained to have energy $\lesssim \lambda_- \lambda_+ Q$, where

$$\lambda_-^2 \sim 1 - x_a \qquad \text{and} \qquad \lambda_+^2 \sim 1 - x_b \tag{6.18}$$

are power-counting parameters that encode the distance from the kinematic endpoint.

The all-order factorization relevant for different hierarchies in q_T/Q and the threshold constraint $\lambda_- \lambda_+$ was derived in refs. [192, 379]. Some consequences of the resulting consistency relations have already been explored in refs. [192, 379]. In fact, the exponential regulator is *defined* by its action on the refactorized pieces in these consistency relations. In the following, we briefly review the relevant factorization theorems and derive the all-order structure that arises for the q_T beam function in the eikonal limit.

$q_T/Q \ll \lambda_- \lambda_+ \sim 1$. In this regime, initial-state radiation is not yet subject to the threshold constraint, and the standard q_T factorization theorem eq. (2.192) holds. It receives power corrections $\mathcal{O}(q_T^2/Q^2)$, but captures the exact dependence on $x_{a,b}$ via the beam functions.

$q_T/Q \ll \lambda_- \lambda_+ \ll 1$. For this hierarchy, the factorization takes a form similar to eq. (2.192), but real collinear radiation into the final state is constrained in energy by $1 - x_{a,b} \ll 1$. The leftover radiation in this limit is described by intermediate collinear-soft

modes [194, 195] in terms of $n_{a,b}$-collinear-soft functions $\tilde{\mathscr{S}}_i(k, b_T, \mu, \nu)$. They are matrix elements of collinear-soft Wilson lines and depend on the additional momentum $k = k^{\mp}$ available from either one of the (threshold) PDFs and on the color charge of the colliding partons.[4] The factorization theorem in this regime reads [192, 379], working in b_T space for convenience,

$$\frac{\mathrm{d}\tilde{\sigma}(\vec{b}_T)}{\mathrm{d}Q^2\,\mathrm{d}Y} = \sum_{i,j} H_{ij}(Q^2, \mu) \int \mathrm{d}k^- \, \tilde{\mathscr{S}}_i(k^-, b_T, \mu, \nu) \, f_i^{\mathrm{thr}}\Big[x_a\Big(1 + \frac{k^-}{\omega_a}\Big), \mu\Big]$$

$$\times \int \mathrm{d}k^+ \, \tilde{\mathscr{S}}_j(k^+, b_T, \mu, \nu) \, f_j^{\mathrm{thr}}\Big[x_b\Big(1 + \frac{k^+}{\omega_b}\Big), \mu\Big] \, \tilde{S}_i(b_T, \mu, \nu)$$

$$\times \Big[1 + \mathcal{O}\Big(\frac{1}{b_T^2 \lambda_-^2 \lambda_+^2 Q^2}, \lambda_-^2, \lambda_+^2\Big)\Big]. \tag{6.19}$$

Collinear-soft emissions do not contribute angular momentum, so the polarization indices for gluon-induced processes [left implicit in eq. (2.192)] become trivial in this limit. The formal definition of the threshold PDF and a discussion of the way it enters in the convolution above are given in section 5.3.6.

$q_T/Q \sim \lambda_-\lambda_+ \ll 1$. In this regime, the threshold constraint dominates and all radiation is forced to be soft. The recoil against soft radiation with transverse momentum $\vec{k}_T = -\vec{q}_T$ is encoded in the fully-differential threshold soft function $S_i^{\mathrm{thr}}(k^-, k^+, \vec{k}_T)$. In terms of its Fourier transform $\tilde{S}_i^{\mathrm{thr}}(k^-, k^+, b_T)$ with respect to $\vec{k}_T$, the factorization theorem reads

$$\frac{\mathrm{d}\tilde{\sigma}(\vec{b}_T)}{\mathrm{d}Q^2\,\mathrm{d}Y} = \sum_{i,j} H_{ij}(Q^2, \mu) \int \mathrm{d}k^-\mathrm{d}k^+ f_i^{\mathrm{thr}}\Big[x_a\Big(1 + \frac{k^-}{\omega_a}\Big), \mu\Big] f_j^{\mathrm{thr}}\Big[x_b\Big(1 + \frac{k^+}{\omega_b}\Big), \mu\Big]$$

$$\times \tilde{S}_i^{\mathrm{thr}}(k^-, k^+, b_T, \mu) \left[1 + \mathcal{O}(\lambda_-^2, \lambda_+^2)\right]. \tag{6.20}$$

Notably, the fully-differential threshold soft function is free of rapidity divergences because they are regulated by the threshold constraint. (This is the starting point of the exponential regularization procedure.) The fully-differential soft function was calculated to $\mathcal{O}(\alpha_s^2)$ in ref. [421], albeit in a different context, and to $\mathcal{O}(\alpha_s^3)$ in ref. [265]. By construction, it satisfies

$$\int \mathrm{d}^2\vec{k}_T \, S_i^{\mathrm{thr}}(k^-, k^+, \vec{k}_T, \mu) = \tilde{S}_i^{\mathrm{thr}}(k^-, k^+, b_T = 0, \mu) = S_i^{\mathrm{thr}}(k^-, k^+, \mu), \tag{6.21}$$

where $S_i^{\mathrm{thr}}(k^-, k^+, \mu)$ is the double-differential threshold soft function in eq. (2.186).

Consistency between eqs. (2.192) and (6.19) implies that the $x \to 1$ limit of the q_T beam function is captured by the collinear-soft function [192, 379],

$$\tilde{B}_i(x, \vec{b}_T, \mu, \nu/\omega) = \int \mathrm{d}k \, \tilde{\mathscr{S}}_i(k, b_T, \mu, \nu) \, f_i^{\mathrm{thr}}\Big[x\Big(1 + \frac{k}{\omega}\Big), \mu\Big] \left[1 + \mathcal{O}(1-x)\right]. \tag{6.22}$$

---

[4]Note that the collinear-soft function $\tilde{\mathscr{S}}_i(k, b_T, \mu, \nu)$ is distinct from the $\tilde{\mathcal{S}}_i(k, b_T, \mu, \nu)$ considered in chapter 4; see section 6.3.3 for their precise relation. Also note that in ref. [5] that this chapter is based on, our $\tilde{\mathscr{S}}_i$ was indicated by $\tilde{\mathcal{S}}_i$.

This is the analog of eq. (6.1) for q_T, but this time relates the eikonal limit of the beam function to an exclusive collinear-soft matrix element instead of the inclusive threshold soft function. At the partonic level, eq. (6.22) implies [192, 379]

$$\tilde{\mathcal{I}}_{ij}(z, b_T, \mu, \nu/\omega) = \delta_{ij}\, \omega\, \tilde{\mathscr{S}}_i\big[\omega(1-z), b_T, \mu, \nu\big] \big[1 + \mathcal{O}(1-z)\big]. \tag{6.23}$$

Note that eq. (6.23) is true for any rapidity regulator as long as the same regulator is used on both sides. The consistency between eqs. (6.19) and (6.20) implies [192, 379]

$$\tilde{S}_i^{\mathrm{thr}}(k^-, k^+, b_T, \mu) = \tilde{\mathscr{S}}_i(k^-, b_T, \mu, \nu)\, \tilde{\mathscr{S}}_i(k^+, b_T, \mu, \nu)\, \tilde{S}_i(b_T, \mu, \nu) \left[1 + \mathcal{O}\Big(\frac{1}{b_T^2 k^- k^+}\Big)\right], \tag{6.24}$$

which again holds for any choice of rapidity regulator. In particular, the left-hand side has no rapidity divergences, so the dependence on the rapidity regulator cancels between the terms on the right-hand side. Together, eqs. (6.22) and (6.24) uniquely determine the eikonal limit of the beam function in any given rapidity regulator scheme in terms of the fully-differential soft function (which is independent of the scheme) and the q_T soft function $\tilde{S}_i(b_T, \mu, \nu)$ (which determines the scheme). Furthermore, the scheme ambiguity amounts to moving terms from the soft function boundary coefficients into the coefficient of $\delta(1-z)$ in the beam function coefficients. Since $\delta(1-z)$ is a leading-power contribution as $z \to 1$, it follows that up to lower-order cross terms, all scheme-dependent terms in the beam function are contained in the leading eikonal terms predicted by eq. (6.23).

6.3.2 All-order result for the collinear-soft function

We next derive a simple all-order expression for the collinear-soft function for the specific case of the exponential regulator. We start by defining the complete Fourier transform of the fully-differential threshold soft function

$$\hat{S}_i^{\mathrm{thr}}(b^+, b^-, b_T, \mu) = \int \mathrm{d}^4 k\, e^{+ib\cdot k}\, S_i^{\mathrm{thr}}(k^-, k^+, k_T, \mu), \tag{6.25}$$

where $b^\mu = (b^+, b^-, \vec{b}_T)$ is the four-vector Fourier conjugate of $k^\mu = (k^+, k^-, \vec{k}_T)$ with $b \cdot k = b^+ k^-/2 + b^- k^+/2 - \vec{b}_T \cdot \vec{k}_T$. Correspondingly, we define the Fourier transform of $\tilde{\mathscr{S}}_i(k^\pm, b_T, \mu, \nu)$ with respect to its light-cone momentum argument $k^\pm$ as

$$\hat{\mathscr{S}}_i(b^+, b_T, \mu, \nu) = \int \mathrm{d}k^-\, e^{+ik^- b^+/2}\, \tilde{\mathscr{S}}_i(k^-, b_T, \mu, \nu), \tag{6.26}$$

and analogously for $b^- \leftrightarrow b^+$ and $k^+ \leftrightarrow k^-$. Fully in position space, the consistency relation eq. (6.24) reads

$$\hat{S}_i^{\mathrm{thr}}(b^+, b^-, b_T, \mu) = \hat{\mathscr{S}}_i(b^+, b_T, \mu, \nu)\, \hat{\mathscr{S}}_i(b^-, b_T, \mu, \nu)\, \tilde{S}_i(b_T, \mu, \nu) \left[1 + \mathcal{O}\Big(\frac{b^+ b^-}{b_T^2}\Big)\right]. \tag{6.27}$$

In the exponential regulator scheme, the regulated q_T soft function is *defined* as [192, 265][5]

$$\tilde{S}_i(b_T, \mu, \nu') = \lim_{\nu' \to \infty} \hat{S}_i^{\text{thr}}\left(\frac{\mathrm{i}b_0}{\nu'}, \frac{\mathrm{i}b_0}{\nu'}, b_T, \mu\right),$$ (6.28)

where we use ν' to distinguish it from the scale at which we later wish to evaluate the collinear-soft function. The prescription for taking the limit is to keep all nonvanishing terms. In particular, a logarithmic dependence of the right-hand side on ν' is to be kept. Inserting eq. (6.27), we have

$$\begin{aligned}
\tilde{S}_i(b_T, \mu, \nu') &= \lim_{\nu' \to \infty}\left[\hat{\mathscr{S}}_i\left(\frac{\mathrm{i}b_0}{\nu'}, b_T, \mu, \nu\right)\hat{\mathscr{S}}_i\left(\frac{\mathrm{i}b_0}{\nu'}, b_T, \mu, \nu\right)\tilde{S}_i(b_T, \mu, \nu) + \mathcal{O}\left(\frac{1}{\nu'^2 b_T^2}\right)\right] \\
&= \tilde{S}_i(b_T, \mu, \nu)\lim_{\nu' \to \infty}\left[\hat{\mathscr{S}}_i\left(\frac{\mathrm{i}b_0}{\nu'}, b_T, \mu, \nu\right)\hat{\mathscr{S}}_i\left(\frac{\mathrm{i}b_0}{\nu'}, b_T, \mu, \nu\right)\right] \\
&= \tilde{S}_i(b_T, \mu, \nu)\hat{\mathscr{S}}_i\left(\frac{\mathrm{i}b_0}{\nu'}, b_T, \mu, \nu\right)\hat{\mathscr{S}}_i\left(\frac{\mathrm{i}b_0}{\nu'}, b_T, \mu, \nu\right).
\end{aligned}$$ (6.29)

In the second line we moved the q_T soft function out of the limit, since it does not depend on ν', and dropped the power corrections. On the third line we used that all dependence of the $\hat{\mathscr{S}}_i$ on ν' is logarithmic, so the limit is trivial. Because the exponential regulator is symmetric under an interchange of collinear-soft directions, we find

$$\hat{\mathscr{S}}_i^2\left(\frac{\mathrm{i}b_0}{\nu'}, b_T, \mu, \nu\right) = \frac{\tilde{S}_i(b_T, \mu, \nu')}{\tilde{S}_i(b_T, \mu, \nu)} = \exp\left[\tilde{\gamma}_\nu^i(b_T, \mu)\ln\frac{\nu'}{\nu}\right],$$ (6.30)

where the second equality follows from solving the rapidity RGE of the soft function between ν and ν' at fixed μ. Assuming we are dealing with the n_a-collinear-soft function that depends on b^+, we can analytically continue back to $\nu' = \mathrm{i}b_0/b^+ = 2\mathrm{i}/(b^+ e^{\gamma_E})$, leaving

$$\hat{\mathscr{S}}_i(b^+, b_T, \mu, \nu) = \exp\left[-\frac{1}{2}\tilde{\gamma}_\nu^i(b_T, \mu)\ln(-\mathrm{i}b^+ \nu e^{\gamma_E}/2)\right].$$ (6.31)

Evaluating the inverse Fourier transform using eq. (A.21), we find the following all-order relation for the momentum-space n_a-collinear-soft function in the exponential regulator scheme,

$$\tilde{\mathscr{S}}_i(k^-, b_T, \mu, \nu) = \mathcal{V}_{\tilde{\gamma}_\nu^i(b_T, \mu)/2}(k^-, \nu),$$ (6.32)

and identically for the n_b-collinear one as a function of k^+. In other words, the collinear-soft function in the exponential regulator scheme is simply given by the rapidity RG evolution between its canonical rapidity scale $\nu_{\mathscr{S}} \sim k^-$ and ν, with trivial boundary condition at $\nu_{\mathscr{S}}$.

6.3.3 Relation to the collinear-soft function for $(q_T, \mathcal{T}_0)$ resummation

Here we briefly clarify the relation of $\tilde{\mathscr{S}}_i$ to the collinear-soft function $\tilde{\mathcal{S}}_i(k, b_T, \mu, \nu)$ relevant for the two-dimensional $(q_T, \mathcal{T}_0)$ resummation considered in chapter 4. The two functions

---

[5]Comparing eq. (2) in ref. [265] to eq. (33) in ref. [192] suggests that the latter has a spurious factor of 2 in the denominator, noting that their $\tau = 1/\nu$.

are distinct because $\tilde{\mathscr{S}}_i(k, b_T, \mu, \nu)$ measures the large rather than the small light-cone momentum of collinear-soft radiation. However, the two are related to each other by a factor of the standard q_T soft function [155, 379],

$$\tilde{\mathcal{S}}_i(k, b_T, \mu, \nu) = \tilde{\mathscr{S}}_i(k, b_T, \mu, \nu) \, \tilde{S}_i(b_T, \mu, \nu) \,. \tag{6.33}$$

This relation holds independently of the regulator and can be interpreted as a (soft) zero-bin subtraction in the computation of $\tilde{\mathscr{S}}_i$ when the η regulator is not expanded to leading power in the collinear-soft mode scaling [379]. It can be proven using the rapidity renormalization group and the RPI-III properties of the three matrix elements, accounting for soft RPI-III breaking by the η rapidity regulator [155].[6] The most straightforward way to see that eq. (6.33) holds is to use a rapidity regulator that always regulates the same light-cone component, e.g. the analytic or α regulator [422] or the pure rapidity regulator [193]. In this case the soft function is scaleless, $\tilde{S}_i(b_T, \mu, \nu) = 1$, and the two collinear-soft functions are manifestly equal.

Specifying to the exponential regulator and inserting the result in eq. (6.32), we have

$$\tilde{\mathcal{S}}_i(k, b_T, \mu, \nu) = \mathcal{V}_{\tilde{\gamma}_\nu^i(b_T, \mu)/2}(k, \nu) \, \tilde{S}_i(b_T, \mu, \nu) \,. \tag{6.34}$$

It is straightforward to check this relation at one loop, where the $\tilde{\mathcal{S}}_i$ is known explicitly. Beyond one loop, it can be used to extract the $(q_T, \mathcal{T}_0)$ collinear-soft function $\tilde{\mathcal{S}}_i$ to the order that the soft function is known, i.e., currently to three loops. It also holds nonperturbatively and can serve as a starting point for nonperturbative modeling in the double-differential $(q_T, \mathcal{T}_0)$ spectrum.

6.3.4 Results for the beam function

As we saw, the relation between the fully-differential and standard TMD soft function is particularly simple for the exponential regulator, leading to an all-order result for the collinear-soft function in terms of the rapidity anomalous dimension in eq. (6.32). Inserting this result into eq. (6.23), we find for the eikonal limit of the b_T-space beam function matching coefficient $\tilde{\mathcal{I}}_{ij}$ in the exponential regulator scheme,

$$\tilde{\mathcal{I}}_{ij}(z, b_T, \mu, \nu/\omega) = \delta_{ij} \frac{\omega}{\nu} \mathcal{V}_{\tilde{\gamma}_\nu^i(b_T, \mu)/2}\Big[\frac{\omega}{\nu}(1 - z)\Big] \big[1 + \mathcal{O}(1 - z)\big] \,, \tag{6.35}$$

where the plus distribution $\mathcal{V}_a(x)$ is defined in eq. (A.17). The simplicity of this result is a direct consequence of the specific rapidity regulator, i.e., one may equally well have imposed this form of the eikonal limit as the renormalization condition. Nonetheless, when combined with the soft function to a given order, the scheme dependence cancels and leaves

---

[6]Note that the $S'(\vec{k}_T, k, \mu, \nu)$ of ref. [155] is equal to the Fourier transform of our $\tilde{\mathcal{S}}_i$ in the transverse plane; while defined as a soft matrix element there, the two are related by a simple boost. This can be seen explicitly from the refactorization relation for the double-differential beam function in eq. (4.31) in terms of $\tilde{\mathcal{S}}_i$, and noting that the factorization theorem in eq. (3.26) of ref. [155] that contains $\tilde{S}'(k, b_T, \mu, \nu)$ is the refactorization limit of the generalized threshold factorization theorem in eq. (5.9), which involves the double-differential beam function.

behind a unique set of terms that capture the threshold limit of the singular cross section in eq. (2.192). We note that a close relation between the rapidity anomalous dimension and the eikonal limit of the beam function is a scheme-independent feature [379], and was also conjectured for the δ-regulator in ref. [284].

It is straightforward to expand eq. (6.35) in α_s to obtain the finite terms in the matching coefficient at any given fixed order using eqs. (2.205) and (A.20). Up to two loops we have

$$
\tilde{I}_{ij}^{(1)}(z) = \mathcal{O}\big[(1-z)^0\big]\,,
$$
$$
\tilde{I}_{ij}^{(2)}(z) = \delta_{ij}\,\frac{\tilde{\gamma}_{\nu\,1}^i}{2}\,\mathcal{L}_0(1-z) + \mathcal{O}\big[(1-z)^0\big]\,, \tag{6.36}
$$

in agreement with the full two-loop result [264], and where we have used that $\tilde{\gamma}_{\nu\,0}^i = 0$. Including terms up to six loops for illustration, we find

$$
\tilde{I}_{ij}^{(3)}(z) = \delta_{ij}\,\frac{\tilde{\gamma}_{\nu\,2}^i}{2}\,\mathcal{L}_0(1-z) + \mathcal{O}\big[(1-z)^0\big]\,,
$$
$$
\tilde{I}_{ij}^{(4)}(z) = \delta_{ij}\,\frac{\tilde{\gamma}_{\nu\,3}^i}{2}\,\mathcal{L}_0(1-z) + \frac{(\tilde{\gamma}_{\nu\,1}^i)^2}{4}\Big[\mathcal{L}_1(1-z) - \frac{\zeta_2}{2}\delta(1-z)\Big] + \mathcal{O}\big[(1-z)^0\big]\,,
$$
$$
\tilde{I}_{ij}^{(5)}(z) = \delta_{ij}\,\frac{\tilde{\gamma}_{\nu\,4}^i}{2}\,\mathcal{L}_0(1-z) + \frac{\tilde{\gamma}_{\nu\,1}^i\tilde{\gamma}_{\nu\,2}^i}{2}\Big[\mathcal{L}_1(1-z) - \frac{\zeta_2}{2}\delta(1-z)\Big] + \mathcal{O}\big[(1-z)^0\big]\,,
$$
$$
\tilde{I}_{ij}^{(6)}(z) = \delta_{ij}\,\frac{\tilde{\gamma}_{\nu\,5}^i}{2}\,\mathcal{L}_0(1-z) + \frac{(\tilde{\gamma}_{\nu\,2}^i)^2 + 2\tilde{\gamma}_{\nu\,1}^i\tilde{\gamma}_{\nu\,3}^i}{4}\Big[\mathcal{L}_1(1-z) - \frac{\zeta_2}{2}\delta(1-z)\Big]
$$
$$
+ \frac{(\tilde{\gamma}_{\nu\,1}^i)^3}{8}\Big[\frac{\mathcal{L}_2(1-z)}{2} - \frac{\zeta_2}{2}\mathcal{L}_0(1-z) + \frac{\zeta_3}{3}\delta(1-z)\Big] + \mathcal{O}\big[(1-z)^0\big]\,. \tag{6.37}
$$

We again stress that these expressions are a direct consequence of the renormalization condition in the exponential regulator scheme and must be combined with the soft function in the same scheme to obtain a scheme-independent result. It is interesting to note that starting at four loops, eq. (6.35) does in fact predict a term proportional to $\delta(1-z)$ in the beam function matching coefficient due to the inverse Fourier transform to $k^\pm$ back from the conjugate $b^\pm$ space, where the regularization procedure is applied.

6.4 Summary

We have studied the three-loop structure of the beam functions relevant for N-jettiness $\mathcal{T}_N$ and transverse momentum-dependent factorization. These functions are defined as collinear proton matrix elements that measure the small light-cone momentum (for $\mathcal{T}_0$) or total transverse momentum (for q_T) of all collinear emissions, and thus are universal objects describing the infrared structure of QCD.

We considered the previously unknown scale-independent boundary coefficients $I_{ij}^{(3)}(z)$ of the N³LO beam functions and employed consistency relations between different factorization limits to derive their leading eikonal limit $I_{ij}^{(3)}(z \to 1)$, i.e. the full singular limit of the beam functions as $z \to 1$. These results were a step towards, and are an important check on, the full calculation of the three-loop beam functions, which will enable three-loop predictions in resummed and fixed-order perturbation theory in the future.

Chapter 7

Resumming fiducial power corrections at N³LL

In this chapter we consider Drell-Yan production $pp \to VX \to LX$ at small $q_T \ll Q$. We point out that experimental measurements that resolve the details of L in general introduce enhanced, linear power corrections in q_T/Q, and show that they can be unambiguously predicted from factorization and resummed to the same order as the leading-power contribution. Matching to full NNLO (α_s^2), we find that the linear power corrections are indeed the dominant ones, and once included by factorization, the remaining fixed-order corrections become almost negligible below $q_T \lesssim 40\,\mathrm{GeV}$. We also discuss the implications for more complicated observables, provide predictions for the fiducial ϕ^* and the lepton p_T spectrum at N³LL+NNLO, and compare to ATLAS and CMS data for the q_T and ϕ^* spectrum.

This chapter is based on ref. [6], reflecting the author's contribution.

7.1 Motivation

The neutral and charged-current Drell-Yan processes, $pp \to Z/\gamma^* \to \ell\ell$ and $pp \to W \to \ell\nu$, are important benchmark processes at the LHC. We are interested in the kinematic region where the vector boson is produced with small or moderate transverse momentum q_T, which contains the bulk of the total cross section. As discussed in the introduction, differential distributions in this region can be measured to sub-percent precision [31–33, 35, 36, 423–432], allowing for high-precision tests of the electroweak sector of the SM, including the precise measurement of the W boson mass [36] and the weak mixing angle [425, 432].

For small transverse momentum $q_T \ll Q$, the differential cross section admits an expansion in q_T/Q

$$\frac{\mathrm{d}\sigma}{\mathrm{d}q_T^2} = \frac{\mathrm{d}\sigma^{(0)}}{\mathrm{d}q_T^2} \;+\; \frac{\mathrm{d}\sigma^{(1)}}{\mathrm{d}q_T^2} \;+\; \frac{\mathrm{d}\sigma^{(2)}}{\mathrm{d}q_T^2} \;+\; \cdots$$
$$\sim \; \frac{1}{q_T^2}\left[1 \;+\; \mathcal{O}\!\left(\frac{q_T}{Q}\right) \;+\; \mathcal{O}\!\left(\frac{q_T^2}{Q^2}\right) + \; \cdots \right]. \tag{7.1}$$

The dominant term scales as $\mathrm{d}\sigma^{(0)}/\mathrm{d}q_T^2 \sim 1/q_T^2$ and is referred to as the leading-power (LP) contribution. The additional terms $\mathrm{d}\sigma^{(n)}$ are suppressed by $(q_T/Q)^n$ relative to $\mathrm{d}\sigma^{(0)}$, and are referred to as power corrections or subleading-power contributions.

At small $q_T \ll Q$, the fixed-order expansion contains logarithmically enhanced terms $\alpha_s^n \ln^m(q_T/Q)$ caused by soft and collinear emissions. These series of logarithms need to be resummed to all orders in perturbation theory to obtain precise and reliable perturbative predictions. For the LP term, this resummation is possible thanks to the q_T-dependent (TMD) factorization theorem for $d\sigma^{(0)}$ in eqs. (2.192) and (2.193), originally derived in refs. [185, 251, 252], with several equivalent formulations [188, 189, 191, 192, 253, 257] based on different regularization methods. A large variety of approaches for the resummation exist [258, 263, 276, 399, 433–443] and by now have reached N³LL precision [267, 268, 363, 394, 444–447], the inclusion of quark-mass effects [420] and of QED corrections [448–450].

The power corrections $d\sigma^{(n)}$ in eq. (7.1) are classified by their relative $(q_T/Q)^n$ suppression, and we refer to $d\sigma^{(1)}$ as the next-to-leading power (NLP) term, $d\sigma^{(2)}$ as NNLP etc. Due to their suppression, they are less relevant at small $q_T \ll Q$, and are included by matching to the full fixed-order calculations, which amounts to numerically extracting the complete set of power-suppressed terms at a given fixed order in α_s. They are in principle known to $\mathcal{O}(\alpha_s^3)$ from the NNLO $V + 1$-parton calculations [49, 451–457].

Nevertheless, the subleading-power terms also contain logarithms $\alpha_s^n \ln^m(q_T/Q)$, and so in principle should be resummed as well to maintain their power suppression relative to the resummed LP term. Hence, given the high precision reached at LP, it is important to investigate the resummation of the subleading-power corrections to avoid them limiting the theoretical precision. First progress towards this direction has been made in ref. [193], where the power corrections were explicitly calculated at NLO, and in ref. [208], where the resummation at subleading power in a related, simpler context was studied. In ref. [193], it was explicitly shown that the linear NLP corrections for the inclusive q_T spectrum are absent, i.e. $d\sigma^{(1)} = 0$, consistent with earlier numerical observations, see e.g. ref. [458]. On the other hand, in ref. [459], it was shown explicitly that linear corrections do generically arise once fiducial cuts on the final-state leptons are applied.[1]

In this work, we consider the generic Drell-Yan process $pp \to VX \to LX$, with the intermediate vector boson decaying to the leptonic (color-singlet) final state L. We study the origin and resummation of power corrections that arise from applying fiducial cuts or performing measurements on L, to which we will refer as *fiducial power corrections*. While our primary application will be to $Z/\gamma^* \to \ell\ell$ and $W \to \ell\nu$, most of our general analysis, which is carried out in section 7.2, will be for generic L. Our analysis and general results also immediately apply to the simpler case of an intermediate color-singlet scalar, such as Higgs production, though we will not consider this case explicitly here.

We encounter two classes of fiducial power corrections in our analysis:

1. *Linear fiducial* power corrections in q_T/Q arise when azimuthal symmetry is preserved by the leptonic measurement at leading power, but is broken at $\mathcal{O}(q_T/Q)$. For such measurements, the linear fiducial power corrections constitute the *complete* NLP corrections $d\sigma^{(1)}$, and can be unambiguously predicted from factorization, and resummed to the same logarithmic order as the LP term $d\sigma^{(0)}$.

---

[1]In case of isolation cuts, the power corrections can be even further enhanced [459].

The prototypical example is the q_T spectrum in the presence of fiducial cuts on L, which generically break azimuthal symmetry and induce linear power corrections. It also applies to other more complicated q_T-like observables, that resolve the recoil of the leptonic final state and vanish at Born level, e.g. the ϕ^* observable or the scalar p_T-imbalance $p_{T1}^\ell - p_{T2}^\ell$.

2. *Leptonic fiducial* power corrections in q_T/p_L arise when the leptonic measurement is sensitive to the edge of Born phase space, with p_L corresponding to the distance to the Born edge. In the bulk of the leptonic phase space $p_L \sim Q$, and the discussion in point 1) applies. As p_L gets smaller, the leptonic power corrections become enhanced, and for $q_T \sim p_L$ they become $\mathcal{O}(1)$ and must be retained exactly to all powers to obtain the *actual* LP result.

   The prototypical example is the lepton p_T^ℓ spectrum close to the Jacobian peak $p_T^\ell = Q/2$, with $p_L = Q - 2p_T^\ell$. Close to the Jacobian peak $q_T \sim p_L \ll Q$, fixed-order predictions are not reliable, which is a well-known effect. The resummation at strict LP is also not sufficient as it neglects the $\mathcal{O}(1)$ corrections in q_T/p_L. Hence, in this limit the resummation including all leptonic power corrections is required.

The inclusion of the fiducial power corrections in the q_T factorization is derived in section 7.2. As we will see, the fiducial power corrections are a property of the leptonic decay and are independent of the underlying production of the decaying vector boson. This allows one to include them in the factorization theorem by treating the leptonic vector-boson decay exactly in q_T and consequently makes it possible to resum them at the same level of precision as the singular cross section $d\sigma^{(0)}$. In particular, this yields a resummation of the NLP terms $d\sigma^{(1)}$ to N³LL.

Our derivation in section 7.2 is general and independent of the specific method to perform the actual resummation, and of whether q_T is treated as a perturbative scale or not. It is based on performing a Lorentz decomposition of the hadronic and leptonic tensors, which encode the production and decay of the intermediate vector boson. The basic idea of Lorentz-decomposing the hadronic tensor is of course not new and has been used before, typically to analyze the angular dependence for lepton pair production, see e.g. [456, 460–463]. Here, we use it for both hadronic and leptonic tensors to discuss the power counting at small q_T. Some preparatory remarks on current conservation relations that constrain the structure of the leptonic and hadronic tensor are made in section 7.2.1. The tensor decomposition is discussed in section 7.2.2. It is constructed in a fully Lorentz-covariant way based on minimal requirements on symmetry and to make the small-q_T limit maximally transparent, which leads to a direct equivalence with the Collins-Soper (CS) frame.

Our tensor decomposition holds for any leptonic final state L. In section 7.2.3, we show that for the specific cases of $Z/\gamma^* \to \ell\ell$ and $W \to \ell\nu$ it directly maps onto the angular decomposition of the fully differential cross section in terms of CS angles. In section 7.2.3, we discuss that Born leptons have a well-defined theoretical interpretation as a Born projection of the full leptonic final state, and that in this case an analogous angular decomposition in terms of generalized angular coefficients also holds for generic L, in particular when

including QED final-state radiation. This implies that the use of so-defined Born leptons is theoretically preferred over other lepton definitions in this context.

Our main power-counting analysis of both linear and leptonic fiducial corrections and their inclusion in the factorization is given in section 7.2.4. Some of the more technical details, such as the required power-counting of the hadronic tensor, are derived in using the soft-collinear effective theory reviewed in section 2.2. Our analysis does not rely on the precise formalism to factorize $d\sigma^{(0)}$, and thus provides formal justification for existing approaches in the literature that include the exact lepton kinematics in the factorized cross section [267, 268, 433–435, 439, 440], as discussed in section 7.2.6.

In section 7.3, we summarize our specific q_T resummation setup, implemented in the `C++` library `SCETlib` [8], which we use to obtain numerical results for all factorized cross sections at fixed order and including resummation up to N³LL. Some additional details on the numerical inputs and computational setup can be found in section 7.4.1. In section 7.4, we discuss and illustrate in more detail the different sources of fiducial power corrections and the mechanism for their resummation. We consider three concrete examples, the q_T spectrum with fiducial cuts (section 7.4.2), the p_T^ℓ distribution near the Jacobian peak (section 7.4.3), and the ϕ^* distribution (section 7.4.4). In all cases, we validate numerically that the fiducial power corrections are indeed captured by the q_T factorization, that their resummation significantly improves their perturbative stability, and that the size of remaining fixed-order power corrections is significantly reduced. In addition, we provide for the first time the resummed p_T^ℓ spectrum at N³LL+NNLO accuracy.

In section 7.5 we compare our resummed predictions at N³LL+NNLO for the fiducial q_T and ϕ^* distributions in $pp \to Z/\gamma^* \to \ell^+\ell^-$ with measurements by ATLAS [426] and CMS [31]. We compare the results both with the fiducial power corrections included at fixed order as well as resummed, illustrating the improvement from resumming the fiducial power corrections and the fact that this significantly reduces the impact of the remaining fixed-order matching corrections.

In short, the outline of this chapter is as follows: Our general analysis is given in section 7.2, with a discussion of current conservation relations in section 7.2.1, the hadronic tensor decomposition in section 7.2.2, the leptonic tensor and relation to angular coefficients in section 7.2.3, the main power-counting analysis in section 7.2.4, some of the more technical details in section 7.2.5, and the relation to other approaches in section 7.2.6. In section 7.3, we specify the q_T resummation setup used in this chapter. In section 7.4, we provide a detailed analysis of fiducial power corrections for the fiducial q_T spectrum, the p_T^ℓ distribution, and the ϕ^* observable. In section 7.5, we compare our resummed N³LL+NNLO results for q_T and ϕ^* to ATLAS and CMS measurements. We summarize our results in section 7.6.

7.2 Theory

Our goal is to compute the differential Drell-Yan cross section with an arbitrary measurement on the leptonic final state, but inclusive over hadronic radiation,

$$\frac{\mathrm{d}\sigma(\Theta)}{\mathrm{d}^4 q \, \mathrm{d}\mathcal{O}} = \frac{1}{2E_{\mathrm{cm}}^2} L_{\mu\nu}(q, \mathcal{O}, \Theta) \, W^{\mu\nu}(q, P_a, P_b) \,, \qquad (7.2)$$

Compared to the more general eq. (2.53), we have integrated $W^{\mu\nu}$ over the hadronic observable $\mathcal{O}_X$. We write the leptonic observable as $\mathcal{O} = \mathcal{O}_L$ and, to stay explicit, allow for a set of fiducial cuts Θ to be applied to the leptonic final state in addition. (This is of course equivalent to integrating a more differential measurement over a suitable region.) As in eq. (2.53) we keep the sum over the intermediate vector bosons implicit most of the time.

Importantly, the hadronic tensor in this setup only depends on the four-momenta q, P_a, P_b, which strongly constrains its structure. For a simple example, consider the cross section integrated over the leptonic measurement as in eq. (2.60), which now takes the form

$$\frac{\mathrm{d}\sigma}{\mathrm{d}^4 q} = \frac{1}{2E_{\mathrm{cm}}^2} \, L(q^2) \, W_{\mathrm{incl}}(q^2, s_{aq}, s_{bq}) \,. \qquad (7.3)$$

Here we have used that by Lorentz invariance, the scalar function $W_{\mathrm{incl}} = (q^\mu q^\nu / q^2 - g^{\mu\nu}) W_{\mu\nu}$ can only depend on the six independent kinematic invariants of q, P_a, P_b. Three of these contain nontrivial kinematic information, which we choose as (recall $m_T^2 = Q^2 + q_T^2$)

$$q^2 = Q^2 \,, \qquad s_{aq} \equiv 2q \cdot P_a = E_{\mathrm{cm}} \, m_T \, e^{-Y} \,, \qquad s_{bq} \equiv 2q \cdot P_b = E_{\mathrm{cm}} \, m_T \, e^{+Y} \,. \qquad (7.4)$$

These are in one-to-one correspondence to the three kinematic variables $Q, Y, q_T^2 = \vec{q}_T^2$. In particular, since $L(q^2)$ only depends on q^2, the entire dependence on Y and q_T^2 in eq. (7.3) is carried by W_{incl}, so W_{incl} encodes the *inclusive* (without fiducial cuts) q_T distribution for fixed Q, Y. The three remaining invariants, which we suppress in the arguments of W_{incl}, only encode the beam parameters, and two of them are trivial due to our assumption of massless protons,

$$P_{a,b}^2 = 0 \,, \qquad s_{ab} \equiv 2P_a \cdot P_b = E_{\mathrm{cm}}^2 \,. \qquad (7.5)$$

Expanding the inclusive hadronic tensor and factorizing the leading term leads to the factorization theorem for the inclusive q_T spectrum in eq. (2.192), which receives corrections that are suppressed by powers of q_T/Q relative to the leading term. As indicated in eq. (2.192), the leading corrections scale as $(q_T/Q)^2$, while linear power corrections are absent. This can be understood intuitively from the azimuthal symmetry of W_{incl}, i.e., the fact that it only depends on the Lorentz invariants in eq. (7.4), which in turn only depend on q_T^2. The absence of linear power corrections in W_{incl} has been verified explicitly by analytic $\mathcal{O}(\alpha_s)$ calculations at next-to-leading power [193]. More formally, an argument for their absence to all orders in the inclusive case is presented in section 7.2.5. In the remainder of this section, we discuss how eq. (2.192) is extended to the case where the decay products are resolved and, notably, linear power corrections arise.

We note that there are various approaches in the literature on how to perform the resummation that eq. (2.192) gives rise to. While they all aim to describe the same inclusive hadronic tensor W_{incl}, they can differ in practice, e.g., due to differences in the rapidity regularization scheme, the different equivalent forms of eq. (2.193), different mathematical methods of performing the actual resummation, and different choices for the precise form of the logarithms that are being resummed. Crucially, all our results in this section are general and hold *independently* of how the resummation is carried out, and thus immediately apply to all formulations in the literature.[2] This is because they only rely on general arguments, such as Lorentz invariance and power counting, and the general structure of the hadronic and leptonic tensors.

7.2.1 Constraints on tensor structure from current conservation

In this section we apply current conservation to identify the possible tensor structures in $W^{\mu\nu}$ that are nonzero, or give nonzero contributions to the cross section. The relevant hadronic currents were given in eqs. (2.30), (2.50), and (2.52). The conservation of the vector current in QCD, $\partial_\mu J_\gamma^\mu = 0$, implies

$$q_\mu W_{\gamma\gamma}^{\mu\nu} = q_\nu W_{\gamma\gamma}^{\mu\nu} = 0 \,. \tag{7.6}$$

The same relation for $V = Z$ does not automatically follow from gauge invariance, because the axial-vector current is not conserved in QCD due to finite quark masses and because of the Adler-Bell-Jackiw axial anomaly [464–466]. In the unbroken electroweak theory, the axial anomaly cancels in all gauge currents thanks to the anomaly cancellation in the SM. Since the anomaly coefficient is mass independent, it also does not contribute to the divergence of J_Z^μ after electroweak symmetry breaking, namely it still cancels between up-type and down-type quarks due to their opposite $T_3^{u,d} = \pm 1/2$. However, the nonzero quark masses now explicitly break the axial-vector current conservation. Therefore, we have the non-conservation relation[3]

$$-\mathrm{i}\partial_\mu J_Z^\mu = |e| \sum_f a_f\, 2m_f\, \bar{q}_f \gamma_5 q_f \,. \tag{7.7}$$

In practice, neglecting all but the top-quark masses, we thus have the chiral Ward identity

$$q_\mu \langle X | J_Z^\mu | pp \rangle = |e| a_t\, 2m_t\, \langle X | \bar{t}\gamma_5 t | pp \rangle \,. \tag{7.8}$$

At the partonic level, the leading contribution to this relation (without explicit top quarks in the final state) is the gluon-fusion top-quark triangle diagram. To isolate these non-conserved contributions, we write the hadronic matrix element as

$$\left[\langle X | J_V^\mu | pp \rangle - \frac{q^\mu q_\nu}{q^2} \langle X | J_V^\nu | pp \rangle \right]_{\mathrm{cons}} + \frac{q^\mu q_\nu}{q^2} \langle X | J_V^\nu | pp \rangle \,, \tag{7.9}$$

---

[2]This of course only holds to the extent that an approach itself does not induce new power corrections.

[3]As discussed, this relation is *not* anomalous. It also holds after suitable renormalization that preserves the non-renormalization of the axial anomaly [466], see e.g. refs. [467, 468] for a detailed discussion.

where the first term is "conserved" by construction, i.e., it vanishes when contracted with q_μ, while the second term $\sim q^\mu$ contains the non-conserved pieces in eq. (7.8). Similarly, we can write the hadronic tensor as

$$W^{\mu\nu} = W^{\mu\nu}_{\text{cons}} + (\text{terms} \propto q^\mu \text{ or } q^\nu),$$
$$q_\mu W^{\mu\nu}_{\text{cons}} = q_\nu W^{\mu\nu}_{\text{cons}} = 0, \tag{7.10}$$

where the conserved part $W^{\mu\nu}_{\text{cons}}$ arises from squaring the conserved parts of the currents.

In practice, the non-conserved pieces rarely matter for various reasons: First, for a real, on-shell massive vector boson with physical polarization ε, they vanish due to $q \cdot \varepsilon = 0$. As a result, for an off-shell vector boson near the resonance, they are suppressed by $1 - q^2/m_V^2$. This is easy to see in unitary gauge, where all Goldstone bosons have been eaten up and the vector-boson propagator is proportional to $g^{\mu\nu} - q^\mu q^\nu/m_V^2$. (In 't Hooft-Feynman gauge, the second term is generated by the exchange of Goldstone bosons.) Second, we can repeat the analogous discussion on the leptonic decay side, and split the leptonic tensor into conserved parts, $q_\mu L^{\mu\nu}_{\text{cons}} = q_\nu L^{\mu\nu}_{\text{cons}} = 0$, and non-conserved parts. The non-conserved parts of $W^{\mu\nu}$ are $\propto q^{\mu,\nu}$, and thus they only survive when contracted with the non-conserved parts of the leptonic tensor. However, considering leptonic decays (i.e., with the intermediate vector boson coupling to a leptonic current) the non-conserved leptonic parts are proportional to the lepton masses and can thus be neglected.[4] Therefore, for simplicity, we will ignore the non-conserved contributions for the most part, though we emphasize that they do not pose any additional conceptual problems and could be straightforwardly included in our analysis.

7.2.2 Hadronic tensor decomposition

We now return to the generic, fiducial cross section in eq. (7.2), and bring it into a form suitable for factorization at small q_T. The manipulations of this section are exact in q_T, i.e., we do not yet expand in $q_T \ll Q$. For the purposes of this section only, we consider the collision of generic hadrons $h_a(P_a)$ and $h_b(P_b)$ with nonzero, possibly distinct masses m_a and m_b. This is relevant for treating proton or ion mass corrections in $pp \to XL$, $pA \to XL$, or $AA' \to XL$, where A and A' are ions with these atomic numbers. We will find that retaining the masses exposes interesting subtleties in the decomposition that were not previously considered. Allowing for finite masses and arbitrary beam velocities $v_{a,b}$, the proton momenta in the lab-frame are given by

$$P_a^\mu = E_a(1,0,0,v_a), \qquad P_b^\mu = E_b(1,0,0,-v_b), \qquad v_{a,b} = \frac{1}{E_{a,b}}\sqrt{E_{a,b}^2 - m_{a,b}^2}, \tag{7.11}$$

---

[4]A notable exception is associated Higgs production, which has a $gg \to Z^* \to ZH$ contribution. As a consequence of Yang's theorem, the ggZ vertex vanishes if all three bosons are real and on shell. Therefore, for real, on-shell gluons, the effective $gg \to Z$ contribution via a top-quark triangle is purely $\propto q^\mu$ and thus the $gg \to Z^* \to ZH$ process proceeds entirely via the non-conserved parts in eq. (7.8). Starting at $\mathcal{O}(\alpha_s^2)$, one or both gluons are off shell, and the ggZ vertex also contributes to the conserved parts, and therefore also to the Drell-Yan process $Z \to \ell\ell$ [144, 469].

the three kinematic invariants containing nontrivial kinematic information become

$$q^2 = Q^2 \, ,$$
$$s_{aq} \equiv 2q \cdot P_a = 2E_a \, m_T \left(\cosh Y - v_a \sinh Y \right) ,$$
$$s_{bq} \equiv 2q \cdot P_b = 2E_b \, m_T \left(\cosh Y + v_b \sinh Y \right) . \tag{7.12}$$

As before, the three remaining invariants only encode the beam parameters,

$$P_{a,b}^2 = m_{a,b}^2 \, , \qquad s_{ab} \equiv 2P_a \cdot P_b = 2E_a E_b (1 + v_a v_b) \, . \tag{7.13}$$

The key idea is to decompose the hadronic tensor $W^{\mu\nu}(q, P_a, P_b)$ into Lorentz-scalar projections with respect to four orthogonal unit four-vectors that are constructed from the four-vectors $P_{a,b}^\mu$ and q^μ and their invariants, and by imposing reasonable symmetry constraints. For the tensor decomposition to be complete, we should pick one timelike vector t^μ and three spacelike vectors x^μ, y^μ, z^μ,

$$t^2 = 1 \, , \qquad x^2 = y^2 = z^2 = -1 \, . \tag{7.14}$$

Motivated by eq. (7.10), we take the timelike vector to be

$$t^\mu = \frac{q^\mu}{\sqrt{q^2}} \, , \tag{7.15}$$

such that the conserved and non-conserved parts of $W^{\mu\nu}$ will get projected onto orthogonal components. The spacelike vectors must be given by linear combinations of $P_{a,b}^\mu$ and q^μ. It will prove convenient to take z^μ to lie in the plane spanned by P_a^μ and P_b^μ,

$$z^\mu = \lambda_a P_a^\mu + \lambda_b P_b^\mu \, , \tag{7.16}$$

where λ_a and λ_b are scalar functions of the kinematic invariants. Imposing $t \cdot z = 0$ and $z^2 = -1$ then uniquely fixes z^μ to

$$z^\mu = \frac{s_{bq} P_a^\mu - s_{aq} P_b^\mu}{(s_{ab} s_{aq} s_{bq} - m_b^2 s_{aq}^2 - m_a^2 s_{bq}^2)^{1/2}} \, , \tag{7.17}$$

up to a conventional overall sign. The s_{ij} are all positive definite, as can be seen from their explicit expressions in eqs. (7.12) and (7.13), and $s_{ab} s_{aq} s_{bq} - m_b^2 s_{aq}^2 - m_a^2 s_{bq}^2 = [2E_a E_b (v_a + v_b) \, m_T]^2 > 0$, so z^μ is real. Interchanging $P_a \leftrightarrow P_b$, eq. (7.17) satisfies $z^\mu \mapsto -z^\mu$. The choice for the remaining x^μ and y^μ is degenerate in principle. To reflect the fact that interchanging the initial-state hadrons is equivalent to a 180° rotation about an axis in the transverse plane, we require x^μ to be invariant under $P_a \leftrightarrow P_b$ and y^μ to only change sign. All together we then have

$$P_a \leftrightarrow P_b : \qquad x^\mu \mapsto +x^\mu \, , \qquad y^\mu \mapsto -y^\mu \, , \qquad z^\mu \mapsto -z^\mu \, . \tag{7.18}$$

We can write x^μ as a linear combination of q^μ and $P_{a,b}^\mu$,

$$x^\mu = \frac{c_x}{\sqrt{q^2}} \left(q^\mu - \kappa_a P_a^\mu - \kappa_b P_b^\mu \right) , \tag{7.19}$$

where we chose the q^μ coefficient to be positive to fix the overall sign of x^μ. Imposing $t \cdot x = z \cdot x = 0$ and $x^2 = -1$, we find for the scalar coefficients and normalization factor

$$
\begin{aligned}
\kappa_a &= \frac{q^2(s_{ab}s_{bq} - 2m_b^2 s_{aq})}{s_{ab}s_{aq}s_{bq} - m_a^2 s_{bq}^2 - m_b^2 s_{aq}^2} = \frac{Q^2}{m_T E_a} \frac{v_b \cosh Y + \sinh Y}{v_a + v_b} \,, \\
\kappa_b &= \frac{q^2(s_{ab}s_{aq} - 2m_a^2 s_{bq})}{s_{ab}s_{aq}s_{bq} - m_a^2 s_{bq}^2 - m_b^2 s_{aq}^2} = \frac{Q^2}{m_T E_b} \frac{v_a \cosh Y - \sinh Y}{v_a + v_b} \,, \\
c_x^2 &= \frac{s_{ab}s_{aq}s_{bq} - m_b^2 s_{aq}^2 - m_a^2 s_{bq}^2}{s_{ab}s_{aq}s_{bq} - q^2 s_{ab}^2 - m_b^2 s_{aq}^2 - m_a^2 s_{bq}^2 + 4m_a^2 m_b^2 q^2} = 1 + \frac{Q^2}{q_T^2} = \frac{m_T^2}{q_T^2} \,.
\end{aligned}
\tag{7.20}
$$

Finally, y^μ is chosen to complete a right-handed coordinate system

$$
y^\mu = \epsilon^{\mu\nu\rho\sigma} t_\nu x_\rho z_\sigma \,,
\tag{7.21}
$$

where we use the convention $\epsilon^{0123} = +1$. For completeness, the results for the unit vectors in the massless limit are

$$
\begin{aligned}
t^\mu &= \frac{q^\mu}{\sqrt{q^2}} \,, &\qquad x^\mu &= \frac{s_{aq}s_{bq}\, q^\mu - s_{bq}q^2\, P_a^\mu - s_{aq}q^2\, P_b^\mu}{[s_{aq}s_{bq}q^2(s_{aq}s_{bq} - s_{ab}q^2)]^{1/2}} \\
z^\mu &= \frac{s_{bq}\, P_a^\mu - s_{aq}\, P_b^\mu}{(s_{ab}s_{aq}s_{bq})^{1/2}} \,, &\qquad y^\mu &= \epsilon^{\mu\nu\rho\sigma} t_\nu x_\rho z_\sigma \,.
\end{aligned}
\tag{7.22}
$$

Reference frame interpretation

The four-vectors $t^\mu, x^\mu, y^\mu, z^\mu$ are orthogonal and normalized, and thus uniquely define a reference frame, namely the frame in which they have components $t^\mu = (1,0,0,0)$, $x^\mu = (0,1,0,0)$, $y^\mu = (0,0,1,0)$, and $z^\mu = (0,0,0,1)$. Since $t^\mu = q^\mu/\sqrt{q^2}$, this frame is automatically a frame where the vector boson is at rest, i.e., where $q^\mu = (\sqrt{q^2},0,0,0)$. A goal of this section is to show that this frame turns out to be the well-known Collins-Soper (CS) frame [470]. We will also find and discuss some subtleties in the massive case due to the fact that different CS-frame definitions that are equivalent in the massless case are no longer equivalent in the massive case.

Let us first remind the reader that the vector-boson rest frame is not unique in itself because different rest frames can still differ by spatial rotations, i.e., by their orientation of the x, y, z-axes. There are many ways to perform a sequence of pure boosts to go from a given frame, say the lab frame, to the rest frame, and the difference between them precisely corresponds to an overall spatial rotation in the rest frame. Hence, a unique way to define a specific vector-boson rest frame is to specify the precise boost sequence to go from the lab frame to the rest frame. We will show how to rotate between different rest frames during the discussion leading up to eq. (7.105).

Intuitively, the CS frame is defined such that its z-axis points into the same direction as in the lab frame and its x-axis points in the direction of $\vec{q}_T$ in the lab frame. In terms of boosts from the lab frame, the CS frame is defined by performing two boosts (see figure 7.4):

1. A longitudinal boost by Y in the beam direction (taken to be the z-axis) that takes us to the *leptonic frame* in which $\tilde{Y} = 0$ and $\tilde{q}^z = 0$. Here and in the following, the tilde denotes the same physical quantity but evaluated in the leptonic frame.

2. A transverse boost in the direction of $\vec{q}_T$ (taken to be the x-axis) with boost parameters

$$\beta\gamma = \epsilon = \frac{q_T}{Q}, \qquad \gamma = \sqrt{1 + \epsilon^2} = \frac{m_T}{Q}, \tag{7.23}$$

which takes us from the leptonic frame to the rest frame.

Under these boosts a generic four-vector p^μ transforms as

$$
\begin{aligned}
p^\mu &= (p^0, p^x, p^y, p^z)_{\text{lab}} \\
&= (p^0 \cosh Y - p^z \sinh Y, p^x, p^y, p^z \cosh Y - p^0 \sinh Y)_{\text{lep}} \equiv (\tilde{p}^0, \tilde{p}^x, \tilde{p}^y, \tilde{p}^z)_{\text{lep}} \\
&= (\gamma \tilde{p}^0 - \epsilon \tilde{p}^x, \gamma \tilde{p}^x - \epsilon \tilde{p}^0, \tilde{p}^y, \tilde{p}^z)_{\text{CS}},
\end{aligned}
\tag{7.24}
$$

where we explicitly indicated by a subscript in which frame the component-form is given, with $p^{0,x,y,z}$ always denoting the lab-frame components and $\tilde{p}^{0,x,y,z}$ always denoting the leptonic-frame components. To illustrate the boosts, applying them to q^μ itself, we obtain

$$q^\mu = Q(\gamma \cosh Y, \epsilon, 0, \gamma \sinh Y)_{\text{lab}} = Q(\gamma, \epsilon, 0, 0)_{\text{lep}} = Q(1, 0, 0, 0)_{\text{CS}}. \tag{7.25}$$

Hence, we indeed arrive in the vector-boson rest frame, which is of course how eq. (7.23) was chosen in the first place.

We can now use this definition of the CS frame to make contact with our unit vectors $t^\mu, x^\mu, y^\mu, z^\mu$. To do so, we perform the same exercise for them, i.e., evaluate them in the lab frame and then boost them to the CS frame. For $t^\mu = q^\mu/Q$, this would just repeat eq. (7.25). For z^μ, evaluating its general covariant expression in eq. (7.17) in the lab frame and applying the two boosts to the CS frame, we obtain

$$
\begin{aligned}
z^\mu &= \lambda_a P_a^\mu + \lambda_b P_b^\mu \\
&= \frac{1}{v_a + v_b} \left(\frac{\cosh Y + v_b \sinh Y}{E_a} P_a^\mu - \frac{\cosh Y - v_a \sinh Y}{E_b} P_b^\mu \right) \\
&= (\sinh Y, 0, 0, \cosh Y)_{\text{lab}} = (0, 0, 0, 1)_{\text{lep}} = (0, 0, 0, 1)_{\text{CS}}.
\end{aligned}
\tag{7.26}
$$

Similarly, starting from the expression for x^μ in eq. (7.19), we obtain

$$
\begin{aligned}
x^\mu &= \frac{c_x}{\sqrt{q^2}} \left(q^\mu - \kappa_a P_a^\mu - \kappa_b P_b^\mu \right) \\
&= \frac{\gamma}{\epsilon} \frac{q^\mu}{Q} - \frac{1}{\epsilon(v_a + v_b)} \left(\frac{v_b \cosh Y + \sinh Y}{E_a} P_a^\mu + \frac{v_a \cosh Y - \sinh Y}{E_b} P_b^\mu \right) \\
&= (\epsilon \cosh Y, \gamma, 0, \epsilon \sinh Y)_{\text{lab}} = (\epsilon, \gamma, 0, 0)_{\text{lep}} = (0, 1, 0, 0)_{\text{CS}}.
\end{aligned}
\tag{7.27}
$$

This shows explicitly that the frame defined by $t^\mu, x^\mu, y^\mu, z^\mu$ is equivalent to the CS frame (in its boost definition), and that this equivalence also holds in the general massive case.

It is quite pleasing to see that the CS frame naturally appears in a covariant way only by imposing eq. (7.16) and the symmetry constraints in eq. (7.18).

Another definition of the CS frame [470], which is also often used in practice, is to consider $\vec{P}_a$ and $\vec{P}_b$ in the vector-boson rest frame, and to define the z-axis to bisect the angle between $\vec{P}_a$ and $-\vec{P}_b$, while the x-axis is chosen to lie in the plane defined by $\vec{P}_a$ and $\vec{P}_b$. Denoting individual components in the CS frame (defined via the above boosts) by hats, we have

$$
\begin{aligned}
P_a^\mu &= E_a(1, 0, 0, +v_a)_{\text{lab}} = (\hat{P}_a^0, \hat{P}_a^x, 0, \hat{P}_a^z)_{\text{CS}}, \\
P_b^\mu &= E_b(1, 0, 0, -v_b)_{\text{lab}} = (\hat{P}_b^0, \hat{P}_b^x, 0, \hat{P}_b^z)_{\text{CS}},
\end{aligned}
\tag{7.28}
$$

where explicit expressions for the components can be straightforwardly obtained from eq. (7.24). The angles $\gamma_{a,b}$ between $\vec{P}_{a,b}$ and the z-axis (see figure 7.1 right) are given by

$$
\begin{aligned}
\tan\gamma_a &= +\frac{\hat{P}_a^x}{\hat{P}_a^z} = \epsilon \frac{v_a \sinh Y - \cosh Y}{v_a \cosh Y - \sinh Y}, \\
\tan\gamma_b &= -\frac{\hat{P}_b^x}{\hat{P}_b^z} = -\epsilon \frac{v_b \sinh Y + \cosh Y}{v_b \cosh Y + \sinh Y}.
\end{aligned}
\tag{7.29}
$$

The bisector criterion amounts to requiring these two angles to be equal, i.e.,

$$
\tan\gamma_a - \tan\gamma_b = \epsilon \frac{(v_a - v_b)\cosh(2Y) - (1 - v_a v_b)\sinh(2Y)}{(v_a \cosh Y - \sinh Y)(v_b \cosh Y + \sinh Y)} \overset{!}{=} 0.
\tag{7.30}
$$

This can only be satisfied for generic Y if and only if $v_a = v_b = 1$, i.e., both hadrons are massless. This means the bisector definition of the CS frame is only equivalent to the above boost definition for massless hadrons, for which both definitions where originally introduced in ref. [470], while for nonzero hadron masses the two definitions are *no longer equivalent*.[5] The key advantage of our construction of t^μ, x^μ, y^μ, z^μ and the corresponding boost definition of the CS frame is that they are symmetric under interchanging the beams [see eq. (7.18)] and furthermore are manifestly independent of the beam parameters, i.e., they only depend on q^μ without reference to the beam momenta beyond the beam direction itself. In the rest of the chapter, we will always use this definition, unless stated otherwise.

Helicity decomposition

Using $t^\mu, x^\mu, y^\mu, z^\mu$, we can define polarization vectors for the vector boson in a fully covariant way as

$$
\varepsilon_\pm^\mu = \frac{1}{\sqrt{2}}\big(x^\mu \mp \mathrm{i}y^\mu\big), \qquad \varepsilon_0^\mu = z^\mu,
\tag{7.31}
$$

---

[5]In some of the literature, the equivalence of the two definitions for the massive case seems to be incorrectly assumed. For example, in ref. [463] expressions for the proton momenta in the CS frame are given that would suggest the equivalence to also hold in the massive case, but can be easily seen to contradict the explicit expression for the Lorentz boost.

which correspond to positive/negative helicity and longitudinal polarization with respect to z^μ. Using these, we project the hadronic tensor onto the entries of a helicity density matrix [461],

$$W_{\lambda\lambda'}(q, P_a, P_b) \equiv \varepsilon_\lambda^\mu \varepsilon_{\lambda'}^{*\nu} \, W_{\mu\nu}(q, P_a, P_b) \qquad \text{with} \qquad \lambda = \{+, -, 0\} \,. \tag{7.32}$$

Since the $\varepsilon_{\pm,0}^\mu$ span the space orthogonal to $t^\mu = q^\mu/Q$, this decomposition fully captures the conserved part of the hadronic tensor, see eq. (7.10). (To also account for the non-conserved parts, we would just have to include the fourth time-like polarization t^μ.)

From its definition in eq. (2.55), it is clear that $W^{\mu\nu}$ is hermitian, $W^{*\mu\nu} = W^{\nu\mu}$, so its symmetric (antisymmetric) components are purely real (imaginary). Therefore, the nine helicity components $W_{\lambda\lambda'}$ are fully specified by a total of nine real-valued, Lorentz-scalar hadronic structure functions. We will use the following linear combinations:

$$
\begin{aligned}
W_{-1} &= W_{++} + W_{--} & &= (x_\mu x_\nu + y_\mu y_\nu)\, W^{\mu\nu}\,, \\
W_0 &= 2 W_{00} & &= 2\, z_\mu z_\nu\, W^{\mu\nu}\,, \\
W_1 &= -\frac{1}{\sqrt{2}}\big(W_{+0} + W_{0+} + W_{-0} + W_{0-}\big) & &= -(x_\mu z_\nu + x_\nu z_\mu)\, W^{\mu\nu}\,, \\
W_2 &= -2\big(W_{+-} + W_{-+}\big) & &= 2\,(y_\mu y_\nu - x_\mu x_\nu)\, W^{\mu\nu}\,, \\
W_3 &= -\sqrt{2}\big(W_{+0} + W_{0+} - W_{-0} - W_{0-}\big) & &= 2\mathrm{i}\,(y_\mu z_\nu - y_\nu z_\mu)\, W^{\mu\nu}\,, \\
W_4 &= 2\big(W_{++} - W_{--}\big) & &= 2\mathrm{i}\,(x_\mu y_\nu - x_\nu y_\mu)\, W^{\mu\nu}\,, \\
W_5 &= -\mathrm{i}\big(W_{+-} - W_{-+}\big) & &= -(x_\mu y_\nu + x_\nu y_\mu)\, W^{\mu\nu}\,, \\
W_6 &= -\frac{\mathrm{i}}{\sqrt{2}}\big(W_{+0} - W_{0+} - W_{-0} + W_{0-}\big) & &= -(y_\mu z_\nu + y_\nu z_\mu)\, W^{\mu\nu}\,, \\
W_7 &= -\mathrm{i}\sqrt{2}\big(W_{+0} - W_{0+} + W_{-0} - W_{0-}\big) & &= -2\mathrm{i}\,(x_\mu z_\nu - x_\nu z_\mu)\, W^{\mu\nu}\,.
\end{aligned}
\tag{7.33}
$$

The reason for the somewhat odd numbering and normalization will become apparent shortly. In the second equality, we have given the projections in terms of x^μ, y^μ, z^μ, corresponding to linear vector-boson polarizations. The inclusive structure function from eq. (2.61) is given by

$$W_{\text{incl}} \equiv W_{++} + W_{--} + W_{00} = W_{-1} + \frac{1}{2} W_0 \,. \tag{7.34}$$

Since the projections of $W^{\mu\nu}$ that define the W_i are orthogonal, we can easily invert them and write $W^{\mu\nu}$ in terms of the W_i as

$$W^{\mu\nu} = \sum_{i=-1}^{7} P_i^{\mu\nu} W_i \qquad (+ \text{ terms} \propto q^\mu \text{ or } q^\nu)\,, \tag{7.35}$$

where the $P_i^{\mu\nu}$ are the same projections as in eq. (7.33) up to a trivial difference in normal-

ization, for example,

$$
\begin{aligned}
P_{-1}^{\mu\nu} &= \frac{1}{2}\left(\varepsilon_+^{*\mu}\varepsilon_+^\nu + \varepsilon_-^{*\mu}\varepsilon_-^\nu\right) = \frac{1}{2}\left(x^\mu x^\nu + y^\mu y^\nu\right),\\
P_0^{\mu\nu} &= \frac{1}{2}\,\varepsilon_0^{*\mu}\varepsilon_0^\nu \hspace{2.2cm} = \frac{1}{2}\,z^\mu z^\nu,\\
P_4^{\mu\nu} &= \frac{1}{4}\left(\varepsilon_+^{*\mu}\varepsilon_+^\nu - \varepsilon_-^{*\mu}\varepsilon_-^\nu\right) = \frac{1}{4\mathrm{i}}\left(x^\mu y^\nu - x^\nu y^\mu\right).
\end{aligned}
\tag{7.36}
$$

Contracting the leptonic tensor $L_{\mu\nu}$ with $W^{\mu\nu}$ decomposed as in eq. (7.35), we have

$$
L_{\mu\nu}W^{\mu\nu} = \sum_i L_{\mu\nu}P_i^{\mu\nu}W_i \equiv \sum_i L_i W_i\,,
\tag{7.37}
$$

with the corresponding leptonic structure functions defined as

$$
L_i(q,\mathcal{O},\Theta) = \int \mathrm{d}\Phi_L(q)\,P_i^{\mu\nu}L_{\mu\nu}(\Phi_L)\,\delta[\mathcal{O}-\hat{\mathcal{O}}(q,\Phi_L)]\,\hat{\Theta}(q,\Phi_L)\,.
\tag{7.38}
$$

The cross section in eq. (7.2) in terms of the scalar structure functions now becomes

$$
\frac{\mathrm{d}\sigma(\Theta)}{\mathrm{d}^4q\,\mathrm{d}\mathcal{O}} \equiv \frac{1}{2E_{\mathrm{cm}}^2}\sum_i L_i(q,\mathcal{O},\Theta)\,W_i(q^2,s_{aq},s_{bq})\,,
\tag{7.39}
$$

which generalizes the inclusive cross section in eq. (7.3) to arbitrary leptonic observables and fiducial cuts. Here and in the following we return to the limit of center-of-mass collisions of approximately massless hadrons as relevant for the LHC, cf. the flux factor in eq. (7.39). As for W_{incl} before, Lorentz invariance implies that the hadronic structure functions W_i only depend on the three kinematic invariants q^2, s_{aq}, s_{bq}, or equivalently the three kinematic variables Q^2, Y, q_T^2, see eq. (7.4). In particular, they do not depend on the orientation of $\vec{q}_T$. Since the x^μ, y^μ, z^μ reduce to the spatial coordinate axes in the CS frame, the structure functions correspond to the individual tensor components of the hadronic tensor $\hat{W}^{\mu\nu}$ evaluated in the CS frame, e.g., $W_{-1} = \hat{W}^{xx} + \hat{W}^{yy}$, $W_0 = 2W^{zz}$, etc. We will refer to eqs. (7.33) and (7.35) as the *CS tensor decomposition.*

We note that one may also decompose the hadronic tensor in terms of Lorentz structures directly formed out of $g^{\mu\nu} - q^\mu q^\nu/q^2$ and its contractions with $P_{a,b}^\mu$, see e.g. refs. [456, 460, 462, 463]. This automatically ensures that the projectors are covariant combinations of q^μ and $P_{a,b}^\mu$ and that the corresponding coefficients are Lorentz-scalar functions. This is usually not manifest when one considers the individual tensor components in the CS frame (or any other rest frame). However, as we have seen, the CS-frame components are reproduced by the CS tensor decomposition in a manifestly covariant manner as the Lorentz-scalar structure functions W_i that only depend on Lorentz invariants. Hence, there is no formal preference for either decomposition and the two are related by a straightforward change of basis. We will see in the following sections that the physics at small $q_T \ll Q$ becomes particularly transparent when using the CS tensor decomposition.
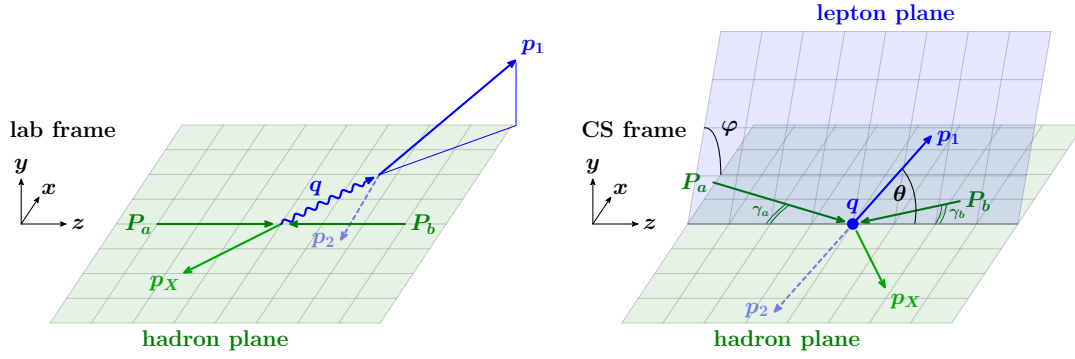
Figure 7.1: Kinematics in the lab frame (left) and the Collins-Soper frame (right). In the lab frame, the incoming hadron momenta are head-to-head (assuming the lab frame and hadronic center-of-mass frame coincide), while the vector boson has nonvanishing three-momentum $\vec{q}$. The scattering $p(P_a)\,p(P_b) \to V(q)\,X(p_X)$ defines the hadron plane (green). In the CS frame (right), the vector boson is at rest. The leptons are produced back to back in the lepton plane (blue). The magnitudes of the hadron momenta in general differ for $Y \neq 0$, but their angles $\gamma_{a,b}$ with respect to the z axis (indicated by the double arcs) become equal in the limit of vanishing hadron masses. The Collins-Soper angles θ and φ are defined as indicated.

7.2.3 Leptonic decomposition and relation to angular coefficients

In this subsection, we discuss the leptonic decay in more detail. For the most part, we specifically consider the leading-order Drell-Yan decays

$$
\begin{aligned}
Z/\gamma^*(q) &\to \ell^-(p_1)\,\ell^+(p_2)\,, & Z &\to \nu(p_1)\,\bar{\nu}(p_2)\,, \\
W^+(q) &\to \nu_\ell(p_1)\,\ell^+(p_2)\,, & W^-(q) &\to \ell^-(p_1)\,\bar{\nu}_\ell(p_2)\,,
\end{aligned}
\tag{7.40}
$$

neglecting lepton masses, $m_{1,2} = 0$, and summing over lepton polarizations. These are the primary application we are eventually interested in. The kinematics of the process in the lab and CS frames are illustrated in the left and right panels of figure 7.1.

In section 7.2.3, we discuss the extension to more complicated leptonic final states, e.g. including QED final-state radiation, which is important at the precision of current Drell-Yan measurements. In particular, there we show to what extent the LO discussion carries over for measurements that are performed in terms of suitably defined Born leptons.

Definition of CS angles

It is convenient to introduce spherical coordinates $(\cos\theta, \varphi)$ in the CS frame, in terms of which we can parametrize $p_{1,2}$, as illustrated in the right panel of figure 7.1, as

$$
p_{1,2}^\mu = \frac{Q}{2}\left(t^\mu \pm x^\mu \sin\theta\cos\varphi \pm y^\mu \sin\theta\sin\varphi \pm z^\mu \cos\theta\right).
\tag{7.41}
$$

The angles θ, φ are known as Collins-Soper angles.[6] From eq. (7.41), one can easily derive their explicit expressions in terms of lab-frame quantities $E_{1,2}$, $p_{1,2}^{x,y,z}$,

$$\cos\theta = \frac{1}{Qm_T}\left[(E_1 + p_1^z)(E_2 - p_2^z) - (E_1 - p_1^z)(E_2 + p_2^z)\right],$$

$$\cos\varphi = \frac{1}{\sin\theta}\frac{p_{1T}^2 - p_{2T}^2}{q_T m_T}, \qquad \sin\varphi = \frac{2}{\sin\theta}\frac{p_1^y p_2^x - p_2^y p_1^x}{q_T Q}, \qquad (7.42)$$

Note that we have arbitrarily chosen the positive orientation of the z axis by having hadron a move in the z direction in the lab frame. As a result, the negatively charged lepton moves into the same rest-frame hemisphere as hadron a for $\cos\theta > 0$. In experimental measurements at the LHC, where the choice of a and b is arbitrary, hadron b is often taken to be the one closer to the vector boson in rapidity to ensure that angular distributions do not average out when integrating over rapidity, see e.g. refs. [425, 427, 430, 432]. The resulting angles θ^* and φ^*, which are often also referred to as Collins-Soper angles, are then related to eq. (7.42) by

$$\cos\theta^* = \frac{Y}{|Y|}\cos\theta, \qquad \varphi^* = \frac{Y}{|Y|}\varphi. \qquad (7.43)$$

On the other hand, eq. (7.42) does not depend on the chosen orientations of the x and y axes in the lab frame as long as they form a right-handed coordinate system.

The advantage of eq. (7.41), or equivalently the boost definition to define the CS frame, is that it stays true regardless of whether hadron masses are included or neglected, and thus also any relations like eq. (7.42) that are derived from it are independent of any beam parameters. On the other hand, with the bisector construction including hadron masses, eq. (7.42) no longer holds, see the discussion below eq. (7.30).

Leptonic decay parametrization by angles

The fully-differential leptonic tensor for the $1 \to 2$ Drell-Yan decays in eq. (7.40) at tree level has the form

$$L^{\mu\nu}(p_1, p_2) = \frac{24\pi}{q^2}\left[L_+(q^2)\left(p_1^\mu p_2^\nu + p_1^\nu p_2^\mu - g^{\mu\nu}p_1\cdot p_2\right) + iL_-(q^2)\,\epsilon^{\mu\nu\rho\sigma}p_{1\rho}p_{2\sigma}\right]. \qquad (7.44)$$

Only the contribution proportional to L_+ (L_-) survives the contraction with the symmetric (antisymmetric) $P_i^{\mu\nu}$ corresponding to the parity-even (parity-odd) hadronic structure functions $W_{-1,0,1,2,5,6}$ $(W_{3,4,7})$. The normalization is chosen such that $L_+(q^2) = L(q^2)$ agrees with the inclusive coefficient in eq. (2.59), and such that $L_-(q^2) = L_+(q^2)$ for W decays, where parity is maximally violated. Explicit expressions for the $L_\pm(q^2)$ are given in appendix B.

---

[6]To be precise, here we have defined the CS angles by $\theta \equiv \theta_1$ and $\varphi \equiv \varphi_1$, where (θ_1, φ_1) are the spherical coordinates of p_1. Since at LO in QED p_1 and p_2 are back-to-back, the spherical coordinates for p_2 are then $(\pi - \theta, \pi + \varphi)$.

It is convenient to parametrize the 2-body decay phase space using the CS angles θ, φ, in terms of which the phase-space measure is isotropic,

$$\mathrm{d}\Phi_L(q) = \frac{\mathrm{d}\cos\theta\,\mathrm{d}\varphi}{32\pi^2}\,. \tag{7.45}$$

Applying this parametrization to eq. (7.38), we find

$$L_i(q, \mathcal{O}, \Theta) = \int_{-1}^{1} \mathrm{d}\cos\theta \int_{0}^{2\pi} \mathrm{d}\varphi\, L_i(q^2, \theta, \varphi)\, \delta[\mathcal{O} - \hat{\mathcal{O}}(q, \theta, \varphi)]\, \hat{\Theta}(q, \theta, \varphi)\,, \tag{7.46}$$

$$L_i(q^2, \theta, \varphi) = \frac{3}{16\pi} L_{\pm(i)}(q^2)\, g_i(\theta, \varphi) \qquad \text{with} \qquad \pm(i) = \begin{cases} +\,, & i \in \{-1, 0, 1, 2, 5, 6\}\,, \\ -\,, & i \in \{3, 4, 7\}\,, \end{cases}$$

where the angular dependence arises from contracting $P_i^{\mu\nu}$ with the Lorentz structures in eq. (7.44), and is encoded in nine (real combinations of) spherical harmonics

$$\begin{aligned}
g_{-1}(\theta, \varphi) &= 1 + \cos^2\theta\,, & g_2(\theta, \varphi) &= \tfrac{1}{2}\sin^2\theta\cos(2\varphi)\,, & g_5(\theta, \varphi) &= \sin^2\theta\sin(2\varphi)\,, \\
g_0(\theta, \varphi) &= 1 - \cos^2\theta\,, & g_3(\theta, \varphi) &= \sin\theta\cos\varphi\,, & g_6(\theta, \varphi) &= \sin(2\theta)\sin\varphi\,, \\
g_1(\theta, \varphi) &= \sin(2\theta)\cos\varphi\,, & g_4(\theta, \varphi) &= \cos\theta\,, & g_7(\theta, \varphi) &= \sin\theta\sin\varphi\,.
\end{aligned} \tag{7.47}$$

Putting everything together, we obtain

$$\frac{\mathrm{d}\sigma(\Theta)}{\mathrm{d}^4 q\,\mathrm{d}\mathcal{O}} = \int_{-1}^{1} \mathrm{d}\cos\theta \int_{0}^{2\pi} \mathrm{d}\varphi\, \frac{\mathrm{d}\sigma}{\mathrm{d}^4 q\,\mathrm{d}\cos\theta\,\mathrm{d}\varphi}\, \delta[\mathcal{O} - \hat{\mathcal{O}}(q, \theta, \varphi)]\, \hat{\Theta}(q, \theta, \varphi)\,,$$

$$\frac{\mathrm{d}\sigma}{\mathrm{d}^4 q\,\mathrm{d}\cos\theta\,\mathrm{d}\varphi} = \frac{1}{2E_{\mathrm{cm}}^2} \sum_{i=-1}^{7} L_i(q^2, \theta, \varphi)\, W_i(q^2, s_{aq}, s_{bq}) \equiv \frac{3}{16\pi} \sum_{i=-1}^{7} \frac{\mathrm{d}\sigma_i}{\mathrm{d}^4 q}\, g_i(\theta, \varphi)\,, \tag{7.48}$$

where in the last step we defined the so-called helicity cross sections

$$\frac{\mathrm{d}\sigma_i}{\mathrm{d}^4 q} = \frac{1}{2E_{\mathrm{cm}}^2} L_{\pm(i)}(q^2)\, W_i(q^2, s_{aq}, s_{bq})\,. \tag{7.49}$$

Integrating over $\mathcal{O}$ and setting $\hat{\Theta} = 1$, we recover the inclusive cross section in eq. (2.60),

$$\frac{\mathrm{d}\sigma}{\mathrm{d}^4 q} = \frac{\mathrm{d}\sigma_{-1}}{\mathrm{d}^4 q} + \frac{1}{2}\frac{\mathrm{d}\sigma_0}{\mathrm{d}^4 q}\,, \qquad W_{\mathrm{incl}} = W_{-1} + \frac{W_0}{2}\,. \tag{7.50}$$

Relation to angular coefficients

From eq. (7.48), we can write the fully-differential cross section in the CS angles as

$$\frac{\mathrm{d}\sigma}{\mathrm{d}^4 q\,\mathrm{d}\cos\theta\,\mathrm{d}\varphi} = \frac{3}{16\pi}\frac{\mathrm{d}\sigma}{\mathrm{d}^4 q}\left[1 + \cos^2\theta + \frac{A_0}{2}\left(1 - 3\cos^2\theta\right) + \sum_{i=1}^{7} A_i\, g_i(\theta, \varphi)\right]\,, \tag{7.51}$$

where the *angular coefficients* A_i are given in terms of the helicity cross sections or the hadronic structure functions as

$$A_i = \frac{\mathrm{d}\sigma_i}{\mathrm{d}\sigma_{-1} + \frac{1}{2}\mathrm{d}\sigma_0} = \frac{L_{\pm(i)}(q^2)\, W_i(q^2, s_{aq}, s_{bq})}{L_+(q^2)\,(W_{-1} + \frac{1}{2}W_0)(q^2, s_{aq}, s_{bq})}\,. \tag{7.52}$$

We deliberately chose the numbering and normalization of the W_i in eq. (7.33) to match the often used form of the cross section in eq. (7.51). The only exception is the inclusive cross section, which is split into orthogonal contributions from W_0 and W_{-1}. For the same reason, we refrained from normalizing the spherical harmonics in eq. (7.47). We remind the reader that both numerator and denominator in eq. (7.52) in general involve a sum over the intermediate vector bosons, $L_\pm W_i \equiv \sum_{V,V'} L_{\pm VV'} W_{iVV'}$ so for neutral-current Drell-Yan ($V = Z, \gamma$), the parity-even leptonic prefactors $L_+(q^2) \equiv L_{+VV'}(q^2)$ do not in general cancel in the ratio in eq. (7.52).

A priori, eq. (7.48) or eq. (7.51) simply provide a convenient way to parametrize the fully-differential Drell-Yan cross section for massless 2-body decays. For this purpose, it is irrelevant whether or not the CS angles can be reconstructed experimentally. Similarly, the choice of the CS tensor decomposition is a priori arbitrary, and we could have used another decomposition. Of course, the combination of using the CS tensor decomposition for the hadronic tensor together with using the CS angles to parametrize the leptonic tensor is what leads to the simple angular dependence in eq. (7.48). If we were to choose a different tensor decomposition W_i', we would also choose polar coordinates $\cos\theta'$, φ' with respect to its corresponding rest frame, and arrive at eqs. (7.51) and (7.52) in terms of $\cos\theta'$, φ', A_i', and W_i'. On the other hand, when $\cos\theta$ and φ are explicitly measured, or when eq. (7.51) is used as a template to measure the A_i, it obviously does matter with respect to which frame they are defined. It is also straightforward to relate the W_i or A_i for different frames, see section 7.2.5 below.

Extension to more complicated leptonic final states

Up to now, our discussion in this subsection assumed the leading-order dilepton final states in eq. (7.40), and so in particular eq. (7.51) is derived in this limit. For a generic leptonic final state L, e.g. when including QED final-state radiation (FSR) or for more complicated electroweak decays like $V^* \to VH$ or $V^* \to V_1 V_2$, there is a priori no reason that the L_i are proportional to spherical harmonics $g_i(\theta, \varphi)$ any longer, in which case one cannot use eq. (7.51) to define the A_i beyond this LO.

On the other hand, as we saw in eq. (7.52), the A_i are in one-to-one correspondence with the underlying hadronic structure functions W_i. The W_i are by construction independent of L (apart from its total momentum q^μ) and thus well-defined for arbitrary L. The physical reason for the appearance of nine independent structures in both cases is exactly the same, namely the spin-1 nature of the intermediate vector boson (and the fact that we ignore the non-conserved parts). Hence, the cross section in the CS tensor decomposition in eq. (7.39) should be considered as the generalization of the LO angular decomposition in eq. (7.51) to arbitrary leptonic final states and measurements. One could also use eq. (7.52) as the all-order definition of the A_i in terms of the W_i and conventional LO weak couplings and propagators included in the $L_\pm(q^2)$. One could then easily rewrite eq. (7.39) in terms of the so-defined A_i multiplied by generic leptonic coefficients $L_i(q, \mathcal{O}, \Theta)$, which in the simplest case reduce to $L_\pm(q^2) g_i(\theta, \varphi)$ as in eq. (7.46), but in general can also be more complicated.

Although at that point, it is easier and perhaps less confusing to directly work in terms of the W_i and eq. (7.39) as it is.

Nevertheless, in the context of Drell-Yan measurements, the LO relation in eq. (7.51) is very useful in practice because the g_i are orthogonal spherical harmonics. This allows one to directly measure the A_i (or W_i) by performing a fit to the angular dependence of the (θ, φ) distribution or by projecting out different terms by taking suitably weighted angular integrals of it [427, 430]. This procedure has received some criticism, since it seemingly relies on a LO QED interpretation of the angular dependence, while QED final-state radiation can be relevant at the level of precision reached by Drell-Yan measurements. In fact, even the definition of the CS angles (θ, φ) themselves becomes nonobvious, because with additional QED radiation in the final state, the lepton momenta generically no longer add to the full vector-boson momentum q^μ. Instead, we now have

$$q^\mu = p_1^\mu + p_2^\mu + k^\mu \,, \tag{7.53}$$

where $p_{1,2}^\mu$ are the measured lepton momenta, which depend on the lepton definition, and k^μ is the remaining momentum not included in the definitions of $p_{1,2}$. We stress that here we are *not* concerned with the experimental methods to reconstruct and calibrate the leptons or to recover photon radiation. The "measured" lepton momenta $p_{1,2}^\mu$ refer to the *truth-level* lepton definition to which the raw reconstructed momenta are corrected or unfolded. This truth-level definition must be theoretically well-defined to have a meaningful measurement that can be compared to theoretical calculations, and one can consider the question whether certain truth-level definitions are theoretically preferred or not.[7]

Obviously, the (θ_1, φ_1) angles describing the orientation of p_1 now depend on the lepton definition and also on whether they are defined in the full *vector-boson* rest frame (where q^μ or equivalently the full L is at rest) or the *dilepton* rest frame (where only $p_1^\mu + p_2^\mu$ is at rest). Especially in the latter case, there is no guarantee (in fact it seems quite unlikely) that the angular distribution in (θ_1, φ_1) will still admit a decomposition in terms of the nine spherical harmonics $g_i(\theta_1, \varphi_1)$.

For "bare" leptons, $p_{1,2}^\mu$ are defined without including any FSR photons. This means infrared QED singularities are regulated by the lepton mass leading to potentially large logarithms of the lepton mass. This effect is reduced by defining "dressed" leptons, which include all photons radiated within a cone of some size around the leptons, and hence can be theoretically thought of as QED "lepton jets". With either definition, the remaining momentum k^μ in eq. (7.53) is nonzero and so the dilepton and vector-boson rest frames are no longer equivalent.

Another option is to include all k^μ into $p_{1,2}^\mu$, i.e., the lepton momenta are (partially) defined by the condition $q^\mu = p_1^\mu + p_2^\mu$. This is basically what "Born" leptons are. Their full definition corresponds to defining an IR-safe projection of the full leptonic final state

---

[7]On the other hand, whether a specific truth-level definition receives more or less associated experimental uncertainties is a separate, experimental question, to which we have nothing to say here. While these two questions are not entirely unrelated, they should nevertheless be kept well separated. We thank Daniel Froidevaux for discussions on this issue.

L onto a Born-like 2-body final state. In principle there are many ways to do so, but as long as the Born projection is well defined so are the Born leptons.

To illustrate this, let us consider an explicit example: We start by defining the leptonic thrust axis $\vec{n}_L$ of the full leptonic final state L in its rest frame. The thrust axis $\vec{n}_L$ is defined in the usual way as the axis $\vec{n}$, with $\vec{n}^2 = 1$, that minimizes

$$\vec{n}_L : \qquad \min_{\vec{n}} \sum_{i \in L} (E_i - |\vec{n} \cdot \vec{p}_i|) = Q - \max_{\vec{n}} \sum_i |\vec{n} \cdot \vec{p}_i| \,, \qquad (7.54)$$

where the sum runs over all particles in L, including in particular all QED FSR, and E_i, $\vec{p}_i$ are defined in the rest frame of L. The overall positive (negative) orientation of $\vec{n}_L$ can be fixed by convention, e.g., to point into the hemisphere that contains the lepton (antilepton).[8] Imposing the condition $p_1^\mu + p_2^\mu = q^\mu$, requiring massless on-shell momenta, $p_{1,2}^2 = 0$, and using $\vec{n}_L$ to define the direction of $\vec{p}_1 = -\vec{p}_2$, then uniquely determines (recall $Q = \sqrt{q^2}$)

$$p_{1,2}^\mu = \frac{Q}{2}\,(1, \pm\vec{n}_L)_{\mathrm{CS}} \equiv \frac{Q}{2}(t^\mu \pm n_L^\mu)\,. \qquad (7.55)$$

In the second step we defined the unit vectors

$$t^\mu = \frac{q^\mu}{Q} = (1, \vec{0})_{\mathrm{CS}}\,, \qquad n_L^\mu = (0, \vec{n}_L)_{\mathrm{CS}}\,, \quad n_L^2 = -1\,, \qquad t \cdot n_L = 0\,, \qquad (7.56)$$

where t^μ is the same as before, and n_L^μ describes the overall orientation of L.

More generally, we can also carry out the construction in two steps, first constructing $q^\mu = P_1^\mu + P_2^\mu$ with massive $P_{1,2}^2 \neq 0$ and then projecting them onto massless $p_{1,2}$. Here, we first cluster all emissions with either the lepton or antilepton based on whose hemisphere they are in, which yields the massive hemisphere momenta $P_{1,2}^\mu$,

$$P_{1,2}^\mu = \frac{Q}{2}\Big[x_{1,2}\,t^\mu \pm \lambda(q^2, P_1^2, P_2^2)\,n_L^\mu\Big]\,,$$
$$x_{1,2} = 1 + \frac{P_{1,2}^2 - P_{2,1}^2}{q^2}\,, \qquad \lambda(q^2, P_1^2, P_2^2) = \frac{1}{q^2}\sqrt{(q^2 - P_1^2 - P_2^2)^2 - 4P_1^2 P_2^2}\,. \qquad (7.57)$$

Next, we project $P_{1,2}^\mu$ onto massless momenta $p_{1,2}^\mu$ by preserving the three-momentum direction, $\vec{p}_1/|\vec{p}_1| = \vec{P}_1/|\vec{P}_1| = \vec{n}_L$, and the total energy, $p_1^0 + p_2^0 = P_1^0 + P_2^0 = Q$, which yields eq. (7.55). The spherical coordinates (θ_L, φ_L) of $\vec{n}_L$ in the CS frame now provide a unique, all-order definition of the CS angles $(\theta, \varphi) \equiv (\theta_L, \varphi_L)$, i.e.,

$$n_L^\mu = x^\mu \sin\theta \cos\varphi + y^\mu \sin\theta \sin\varphi + z^\mu \cos\theta\,. \qquad (7.58)$$

This is the generalization of eq. (7.41), where the CS angles now describe the overall orientation of L in the CS frame, as illustrated in figure 7.2.

It is easy to see that the above definitions are IR safe and reduce to the respective LO definitions. In principle, any other IR-safe way of clustering the emissions into $P_{1,2}^\mu$ is

---

[8]In practice, one would use a flavor-aware minimization or clustering procedure to exclude minima or solutions for $\vec{n}_L$ for which lepton and antilepton are clustered into the same hemisphere.
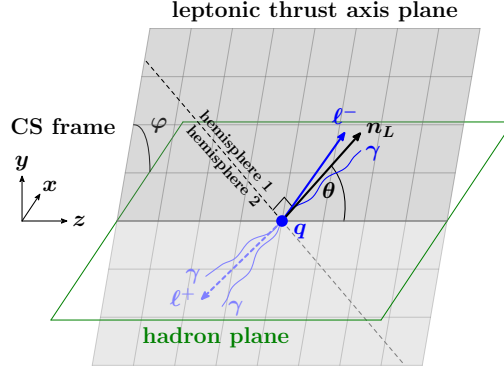
Figure 7.2: Definition of the Collins-Soper angles θ, φ for a generic leptonic final state including FSR (blue) in terms of the leptonic thrust axis n_L. The leptonic thrust axis plane in the CS frame is spanned by the z axis and n_L and generalizes the lepton plane in figure 7.1. Beyond LO in QED, the decay products do no longer have to lie in this plane. The hadronic scattering in the hadron plane (green) is as in figure 7.1 and omitted for clarity. The hemisphere boundary (dashed line) is perpendicular to the thrust axis and separates the emissions into hemisphere 1 (clustered with the lepton) and hemisphere 2 (clustered with the antilepton).

possible. Other ways to project them onto massless $p^{\mu}_{1,2}$ are also possible, as long as the projection is IR safe and preserves the total leptonic momentum $q^{\mu} = P^{\mu}_1 + P^{\mu}_2 = p^{\mu}_1 + p^{\mu}_2$. In practice, defining the projection by keeping the orientation fixed is the most natural and also the easiest, as it avoids any confusion about which particular direction is used to define the CS angles.

The advantage of Born leptons is that they *do admit* an analogous LO-like angular decomposition as we will now show. More generally, it is sufficient to restrict to leptonic measurements that can be written in terms of $P^{\mu}_{1,2}$,

$$\hat{\mathcal{O}}(q, \Phi_L) \equiv \hat{\mathcal{O}}(q, P_1, P_2) = \hat{\mathcal{O}}(q, \theta, \varphi, P_1^2, P_2^2),$$
$$\hat{\Theta}(q, \Phi_L) \equiv \hat{\Theta}(q, P_1, P_2) = \hat{\Theta}(q, \theta, \varphi, P_1^2, P_2^2). \tag{7.59}$$

For such measurements we can write the general leptonic tensor in eq. (2.57) as

$$L^{\mu\nu}(q, \mathcal{O}, \Theta) = \int \frac{\mathrm{d}^4 P_1}{(2\pi)^3} \frac{\mathrm{d}^4 P_2}{(2\pi)^3} (2\pi)^4 \delta^4(q - P_1 - P_2) F^{\mu\nu}(P_1, P_2)$$
$$\times \delta[\mathcal{O} - \hat{\mathcal{O}}(q, P_1, P_2)] \hat{\Theta}(q, P_1, P_2), \tag{7.60}$$

where $F^{\mu\nu}(P_1, P_2)$ is the projection of the full leptonic decay $L^{\mu\nu}(\Phi_L)$ onto the massive 2-body (P_1, P_2) phase space,

$$F^{\mu\nu}(P_1, P_2) = (2\pi)^2 \int \mathrm{d}\Phi_L(P_1 + P_2) L^{\mu\nu}(\Phi_L) \delta^4[P_1 - \hat{P}(\Phi_L)], \tag{7.61}$$

where $\hat{P}^{\mu}(\Phi_L)$ implements the clustering of Φ_L into P^{μ}_1, and P^{μ}_2 is implicitly defined via $q^{\mu} = P^{\mu}_1 + P^{\mu}_2$. For the LO decays in eq. (7.40), we have $\Phi_L = (p_1, p_2)$ and $\hat{P}(\Phi_L) = p_1$

such that

$$F_{\text{LO}}^{\mu\nu}(P_1, P_2) = L^{\mu\nu}(P_1, P_2)\, \delta(P_1^2)\, \delta(P_2^2)\,, \tag{7.62}$$

with $L^{\mu\nu}(p_1, p_2)$ given by the LO result in eq. (7.44).

The key point is that $F^{\mu\nu}(P_1, P_2)$ is defined in a Lorentz-covariant way, and therefore obeys the following Lorentz decomposition (ignoring as before the non-conserved parts)

$$F^{\mu\nu}(P_1, P_2) = 12\pi \left[(t^\mu t^\nu - g^{\mu\nu} - n_L^\mu n_L^\nu)\, F_+ + (t^\mu t^\nu - g^{\mu\nu})\, F_0 + i\epsilon^{\mu\nu\rho\sigma} n_{L\rho} t_\sigma\, F_- \right]$$
$$(+ \text{ terms} \propto q^\mu \text{ or } q^\nu)\,, \tag{7.63}$$

where $F_{\pm,0} \equiv F_{\pm,0}(q^2, P_1^2, P_2^2)$ are Lorentz-scalar functions that can only depend on three independent invariants formed out of $P_{1,2}$, which we chose as $q^2 = (P_1 + P_2)^2$ and $P_{1,2}^2$. The decomposition in eq. (7.63) is chosen so that at LO, comparing to eq. (7.44), we have

$$F_\pm(q^2, P_1^2, P_2^2) = L_\pm(q^2)\, \delta(P_1^2)\delta(P_2^2) + \mathcal{O}(\alpha_{\text{em}})\,, \qquad F_0(q^2, P_1^2, P_2^2) = \mathcal{O}(\alpha_{\text{em}})\,. \tag{7.64}$$

The leptonic structure functions are now obtained as defined in eq. (7.38), by contracting eq. (7.63) with the projectors $P_i^{\mu\nu}$ and performing the phase-space integrals in eq. (7.60),

$$L_i(q, \mathcal{O}, \Theta) = \int \mathrm{d}\cos\theta\, \mathrm{d}\varphi\, \mathrm{d}P_1^2\, \mathrm{d}P_2^2\, \lambda(q^2, P_1^2, P_2^2)\, L_i(q^2, \theta, \varphi, P_1^2, P_2^2)$$
$$\times\, \delta\!\left[\mathcal{O} - \hat{\mathcal{O}}(q, \theta, \varphi, P_1^2, P_2^2)\right] \hat{\Theta}(q, \theta, \varphi, P_1^2, P_2^2)\,, \tag{7.65}$$

with the underlying leptonic structure functions given by

$$L_{-1}(q^2, \theta, \varphi, P_1^2, P_2^2) = \frac{3}{16\pi}\left[F_+(q^2, P_1^2, P_2^2)\, g_{-1}(\theta, \varphi) + 2F_0(q^2, P_1^2, P_2^2)\right]\,,$$
$$L_0(q^2, \theta, \varphi, P_1^2, P_2^2) = \frac{3}{16\pi}\left[F_+(q^2, P_1^2, P_2^2)\, g_0(\theta, \varphi) + F_0(q^2, P_1^2, P_2^2)\right]\,,$$
$$L_{1,2,5,6}(q^2, \theta, \varphi, P_1^2, P_2^2) = \frac{3}{16\pi} F_+(q^2, P_1^2, P_2^2)\, g_{1,2,5,6}(\theta, \varphi)\,,$$
$$L_{3,4,7}(q^2, \theta, \varphi, P_1^2, P_2^2) = \frac{3}{16\pi} F_-(q^2, P_1^2, P_2^2)\, g_{3,4,7}(\theta, \varphi)\,. \tag{7.66}$$

Eqs. (7.65) and (7.66) are the generalization of eq. (7.46) to an arbitrary Born-projected leptonic final state L. The (θ, φ) dependence is still completely described by the same $g_i(\theta, \varphi)$ in eq. (7.47). The L_i for $i \geq 1$ are still given by their own respective g_i times a common leptonic form factor F_+ for $i = 1, 2, 5, 6$ and F_- for $i = 3, 4, 7$. On the other hand, the angular dependence of L_{-1} and L_0 now gets mixed up by F_0, which enters with a flat (θ, φ) dependence corresponding to $g_{-1} + g_0 = 2$.

If the measurements are defined in terms of massless Born leptons, then they are also independent of $P_{1,2}^2$, such that the $P_{1,2}^2$ integrals in eq. (7.65) can be performed to give $L_i(q^2, \theta, \varphi)$ that are given by the same expressions as in eq. (7.66) but in terms of corresponding integrated

$$F_{\pm,0}(q^2) = \int \mathrm{d}P_1^2\, \mathrm{d}P_2^2\, \lambda(q^2, P_1^2, P_2^2)\, F_{\pm,0}(q^2, P_1^2, P_2^2)\,. \tag{7.67}$$

Removing all leptonic measurements, the inclusive q_T spectrum is now given by

$$\frac{\mathrm{d}\sigma}{\mathrm{d}^4 q} = \frac{1}{2E_{\mathrm{cm}}^2}\left[F_+(q^2) + \frac{3}{2}F_0(q^2)\right]W_{\mathrm{incl}}(q^2, s_{aq}, s_{bq})\,, \qquad W_{\mathrm{incl}} = W_{-1} + \frac{W_0}{2}\,, \qquad (7.68)$$

i.e., in terms of the *same* inclusive hadronic structure function multiplied by a generalized inclusive leptonic function. We remind the reader that also here there is always an implicit sum over intermediate vector bosons, $F_{\pm,0}W_i \equiv \sum_{V,V'} F_{\pm,0\,VV'}W_{i\,VV'}$. The cross section differential in the CS angles becomes

$$\frac{\mathrm{d}\sigma}{\mathrm{d}^4 q\,\mathrm{d}\cos\theta\,\mathrm{d}\varphi} = \frac{1}{2E_{\mathrm{cm}}^2}\frac{3}{16\pi}\left[2F_0\,W_{\mathrm{incl}} + \sum_{i=-1}^{7} F_{\pm(i)}W_i\,g_i(\theta,\varphi)\right] \qquad (7.69)$$

$$= \frac{1}{2E_{\mathrm{cm}}^2}\frac{3}{16\pi}\left[\left(F_+ + \frac{3}{2}F_0\right)W_{\mathrm{incl}}(1+\cos^2\theta) + \frac{F_+ W_0 + F_0\,W_{\mathrm{incl}}}{2}\left(1 - 3\cos^2\theta\right)\right.$$

$$\left. + \sum_{i=1}^{7} F_{\pm(i)}W_i\,g_i(\theta,\varphi)\right]$$

$$\equiv \frac{\mathrm{d}\sigma}{\mathrm{d}^4 q}\left[1 + \cos^2\theta + \frac{\tilde{A}_0}{2}\left(1 - 3\cos^2\theta\right) + \sum_{i=1}^{7}\tilde{A}_i\,g_i(\theta,\varphi)\right],$$

where we suppressed the arguments of the structure functions for brevity, and the analogous expression also holds differential in $P_{1,2}^2$. To make contact with eq. (7.51), in the second step we split the flat contribution from F_0 as $(3/2)(1 + \cos^2\theta) + (1/2)(1 - 3\cos^2\theta) = 2$, and in the last step we factored out the inclusive cross section in eq. (7.68), denoting the resulting normalized coefficients of the angular dependence as $\tilde{A}_i$,

$$\tilde{A}_0 = \frac{F_+ W_0 + F_0\,W_{\mathrm{incl}}}{\left(F_+ + \frac{3}{2}F_0\right)W_{\mathrm{incl}}}\,, \qquad \tilde{A}_{i\geq 1} = \frac{F_{\pm(i)}W_i}{\left(F_+ + \frac{3}{2}F_0\right)W_{\mathrm{incl}}}\,. \qquad (7.70)$$

These are the generalization of the A_i in eq. (7.52) for an arbitrary Born-projected final state. They implicitly depend on the specific Born projection used because the CS angles (θ,φ) implicitly depend on it. The $\tilde{A}_i$ are the angular coefficients that are measured by decomposing or projecting the (θ,φ) dependence defined in terms of Born-projected leptons. It would be interesting to precisely identify the underlying Born projection that is effectively used in the measurements [427, 430].

Generically, the QED corrections to F_+, F_-, and F_0 will differ and thus not cancel in eq. (7.70). In other words, even though Born-projected leptons admit a well-defined LO-like angular decomposition as shown in eq. (7.69), the resulting $\tilde{A}_i$ in eq. (7.70) still differ by QED FSR corrections from the LO A_i in eq. (7.52). These corrections should be of generic $\mathcal{O}(\alpha_{\mathrm{em}})$ size, i.e., neither enhanced by soft or collinear photon emissions nor suppressed near the Z pole. In the limit of an on-shell Z boson, they would produce the QED corrections to the Z decay rate to leptons. For $i \geq 1$, the hadronic contributions to A_i and $\tilde{A}_i$ are the same. As we will discuss below, W_0 is suppressed by $\mathcal{O}(q_T^2/Q^2)$ relative to W_{incl} at small q_T, such that at LO in QED A_0 vanishes like q_T^2 for $q_T \to 0$. Interestingly, $\tilde{A}_0$ receives an

additional contribution $F_0 W_{\text{incl}}$, and therefore it no longer vanishes for $q_T \to 0$ but goes to a calculable $\mathcal{O}(\alpha_{\text{em}})$ constant.

Ref. [471] considered QED radiation off massive final-state leptons, and found linear power corrections even in the inclusive case. Since their massive leptons correspond to bare leptons, this is not entirely surprising. It would be interesting to identify the precise source of linear power corrections, i.e, whether the bare leptons induce linear corrections in the leptonic tensor itself, or populate additional leptonic structure functions that come with linearly suppressed hadronic structure functions, or both.

Finally, while most of the above discussion was phrased in terms of QED FSR corrections to Drell-Yan, it applies to an arbitrary Born-projected final state L. For example, keeping the $P_{1,2}^2$ dependence, it applies to Drell-Yan-like electroweak diboson production $V^* \to VH$ or $V^* \to V_1 V_2$ if one remains inclusive over the decays of the final-state bosons.

7.2.4 Factorization for fiducial power corrections

We now investigate the structure of power corrections in the limit $q_T \ll Q$ in the presence of measurements on the leptonic final state. To expand in $q_T \ll Q$, we introduce a formal power-counting parameter

$$\lambda \sim q_T/Q \,. \tag{7.71}$$

The leptonic measurements $\hat{\mathcal{O}}$ and $\hat{\Theta}$ in eq. (7.38) are functions of the total four-momentum q of the final state, and admit an expansion in λ as

$$\hat{\mathcal{O}}(q, \Phi_L) = \hat{\mathcal{O}}^{(0)}(q, \Phi_L)\big[1 + \mathcal{O}(\lambda)\big] \,,$$
$$\hat{\Theta}(q, \Phi_L) = \hat{\Theta}^{(0)}(q, \Phi_L)\big[1 + \mathcal{O}(\lambda)\big] \,. \tag{7.72}$$

We refer to the corrections in λ in these expansions as *fiducial power corrections*. For observables that exist at Born level, e.g., cuts on the lepton momenta, the leading-power (LP) observables $\hat{\mathcal{O}}^{(0)}$ and $\hat{\Theta}^{(0)}$ are simply obtained by taking the Born limit $q_T \to 0$. For q_T-like resolution variables like ϕ^* that scale like q_T itself and vanish at Born level, $\hat{\mathcal{O}}^{(0)}$ or $\hat{\Theta}^{(0)}$ are given by the leading, nontrivial contribution in the $q_T \to 0$ limit.

Linear fiducial power corrections

We first assume that the leptonic measurement does not induce any additional nontrivial dynamic scale p_L, such that the power expansion in eq. (7.72) is genuinely an expansion in q_T/Q. We can then focus on the *linear* $\mathcal{O}(\lambda)$ fiducial power corrections.

Let us consider leptonic measurements that are *azimuthally symmetric at leading power*, which we will indicate by $L^{(0)}(\not\phi)$ and define more precisely in a moment. We will show that for such measurements the only linear $\mathcal{O}(\lambda)$ power corrections that arise are due to the linear fiducial power corrections in eq. (7.72). As a result, the $\mathcal{O}(\lambda)$ power corrections can be uniquely predicted and resummed in terms of leading-power hadronic structure functions.

W_i	Scaling	$\pm(i)$	$g_i(\theta,\varphi)$	$L_i^{(0)}$
W_{-1}	$\sim \lambda^0$	$+$	$1 + \cos^2\theta$	✓
W_0	$\sim \lambda^2$	$+$	$1 - \cos^2\theta$	✓
W_1	$\sim \lambda^1$	$+$	$\sin(2\theta)\cos\varphi$	–
W_2	$\sim \lambda^0$	$+$	$\frac{1}{2}\sin^2\theta\cos(2\varphi)$	–
W_3	$\sim \lambda^{\geq 1}$	$-$	$\sin\theta\cos\varphi$	–
W_4	$\sim \lambda^0$	$-$	$\cos\theta$	✓
W_5	$\sim \lambda^0$	$+$	$\sin^2\theta\sin(2\varphi)$	–
W_6	$\sim \lambda^{\geq 1}$	$+$	$\sin(2\theta)\sin\varphi$	–
W_7	$\sim \lambda^{\geq 1}$	$-$	$\sin\theta\sin\varphi$	–

Table 7.1: Scaling of the hadronic structure functions W_i in the CS tensor decomposition in eq. (7.33) in the limit $\lambda \sim q_T/Q \ll 1$ relative to the leading $W_{-1,4} \sim 1/q_T^2$. In this table we generically count $\Lambda_{\mathrm{QCD}} \sim q_T$. In several cases we only derive bounds on the scaling, where $\sim \lambda^{\geq m}$ means the W_i is suppressed by at least λ^m. We group the structure functions by parity and whether they arise from the dispersive ($i = -1\ldots 4$) or absorptive parts ($i = 5\ldots 7$) of the production amplitude [472]. The second-to-last column shows the corresponding angular dependence $g_i(\theta,\varphi)$ on the Collins-Soper angles for 2-body decays, and in the last column we indicate whether there is a nonvanishing LP leptonic tensor $L_i^{(0)}$ for observables that are azimuthally symmetric at Born level.

For measurements that can be parameterized in terms of CS angles θ, φ, which includes our default Drell-Yan cases in eq. (7.40), azimuthal symmetry means that they do not depend on φ. Azimuthal symmetry at leading power then simply means that the LP measurements $\hat{\mathcal{O}}^{(0)}(q,\theta)$ and $\hat{\Theta}^{(0)}(q,\theta)$ are φ independent, which implies that they average out against $\cos(n\varphi)$ and $\sin(n\varphi)$,

$$L^{(0)}(\not\varphi) : \qquad \int_0^{2\pi} \mathrm{d}\varphi\, e^{in\varphi}\, \delta[\mathcal{O} - \hat{\mathcal{O}}^{(0)}(q,\theta)]\, \hat{\Theta}^{(0)}(q,\theta) = 0\,, \qquad (n \geq 1)\,. \tag{7.73}$$

In particular, the integration against all spherical harmonics $g_i(\theta,\varphi)$ in eqs. (7.46) and (7.47) vanishes, except for $i = -1, 0, 4$, which do not depend on φ. More generally, we *define* a generic leptonic measurement as azimuthally symmetric if it only contributes to $L_{-1,0,4}$, such that azimuthal symmetry at leading power is defined by

$$L^{(0)}(\not\varphi) : \qquad L_i^{(0)}(q,\mathcal{O},\Theta) = 0\,, \qquad i \neq -1,0,4\,. \tag{7.74}$$

Note that this definition is also natural from the point of view of the CS tensor decomposition in eq. (7.33). Azimuthal symmetry corresponds to symmetry under rotations of the x and y axes around the z axis. The projections for $i = -1, 0, 4$ are precisely those that are invariant under azimuthal rotations (corresponding to the norm and cross product, or are independent of x and y), which is the physical reason why their corresponding $g_i(\theta,\varphi)$ do not depend on φ.

A primary example is a fiducial cut on the lepton transverse momenta $p_{T1,2} \geq p_T^{\min}$, for which we have

$$\hat{\Theta}^{(0)}(Q, Y, \vec{q}_T, \theta) = \theta\left(p_T^{\min} \leq \frac{Q}{2}\sin\theta\right) = \hat{\Theta}(Q, Y, \vec{q}_T = 0, \theta, \varphi). \tag{7.75}$$

In words, the leptons are exactly back-to-back at leading power, and whether they pass the cut only depends on their rest-frame energy $Q/2$ and scattering angle θ. We discuss this case as well as a cut on the lepton rapidity in more detail in section 7.4.2. On the other hand, angular asymmetries that are designed to project out the $\cos\varphi$ or $\cos(2\varphi)$ dependence in the angular distribution (by construction) do not qualify under eq. (7.74).

Power expanding the leptonic structure functions, which includes the power expansion of the measurement, we have

$$L_i(q, \mathcal{O}, \Theta) = L_i^{(0)}(q, \mathcal{O}, \Theta) + L_i^{(1)}(q, \mathcal{O}, \Theta) + \cdots, \tag{7.76}$$

where with the assumption in eq. (7.74) only $L_i^{(0)}$ with $i = -1, 0, 4$ are nonzero. The $L_i^{(1)}$ contain the linear fiducial power corrections. They can be, and in general are, nonzero for other i, as our azimuthal symmetry assumption only concerns the leading-power $L_i^{(0)}$.

We also need to power-count the hadronic structure functions W_i,

$$W_i = \sum_{m=0}^{\infty} W_i^{(m)}, \qquad W_i^{(m)} \sim \frac{\lambda^m}{q_T^2}. \tag{7.77}$$

The λ scaling of the first nonzero contributions $W_i^{(m)}$ relative to the leading-power $W_{-1,4}^{(0)} \sim 1/q_T^2$ is summarized in table 7.1, and is derived more carefully using SCET in section 7.2.5. From table 7.1, we see that the only nonvanishing LP structure functions $W_i^{(0)}$ are for $i = -1, 2, 4, 5$. The physical reason is that at LP, angular momentum conservation works the same way as at tree level, i.e., as in the collision of two massless partons with $p_a + p_b = q$, $p_{Ta} = p_{Tb} = q_T = 0$. In this limit, the CS frame coincides with the leptonic frame, and the longitudinal polarization vector is given by

$$\varepsilon_0^\mu = \frac{p_a^\mu - p_b^\mu}{Q} \qquad \text{(tree level)}. \tag{7.78}$$

It is easy to see that projections of the tree-level partonic matrix element onto ε_0^μ vanish,

$$\varepsilon_{0\mu}^* \langle 0|J_\gamma^\mu|q(p_a, s_a)\bar{q}(p_b, s_b)\rangle \propto \bar{v}^{s_b}(p_b)(\not{p}_a - \not{p}_b)u^{s_a}(p_a) = 0 \tag{7.79}$$

for any polarization s_a (s_b) of the quark (antiquark), and similarly for the axial-vector current. It follows that structure functions W_i that involve contractions with ε_0^μ vanish at tree level. We will see in section 7.2.5 that to all orders, each contraction with ε_0^μ is in fact penalized by at least one power of λ.

Suppressing the arguments of L_i and W_i, the strict LP cross section is given by

$$L^{(0)}(\not\varphi): \qquad \frac{d\sigma^{(0)}(\Theta)}{d^4q\,d\mathcal{O}} = \frac{1}{2E_{cm}^2} \sum_{i=-1,4} L_i^{(0)} W_i^{(0)}. \tag{7.80}$$

Figure 7.3: Power counting of hadronic structure functions and their leptonic counterparts for $\lambda \sim q_T/Q \ll 1$, assuming azimuthal symmetry at leading power. Nonzero contributions to the hadronic and leptonic tensors are indicated by solid orange and blue filling, respectively. Nonzero contributions to the cross section are indicated by solid light orange filling. Hatched filling for $W_{2,5}^{(0)}$ indicates that this contribution does not match onto leading-twist collinear PDFs and is suppressed for $\Lambda_{\mathrm{QCD}} \ll q_T$. Gray boxes indicate contributions to the LP and linear NLP cross sections $\sigma^{(0)}$ and $\sigma^{(1)}$. The latter solely arise through the leptonic tensor as $L_i^{(1)} W_i^{(0)}$ while all contributions of the form $L_i^{(0)} W_i^{(1)}$ vanish. Dashes indicate that a contribution vanishes. In the bottom right panel, "rest" refers to structure functions $i = 1, 3, 6, 7$.

The $i = 2, 5$ contribution does not survive because $L_{2,5}^{(0)} = 0$ due to eq. (7.74), and the nonzero $L_0^{(0)}$ does not contribute because $W_0^{(0)} = 0$.

Next, the linear $\mathcal{O}(\lambda)$ power corrections to the cross section are given by

$$\frac{\mathrm{d}\sigma^{(1)}(\Theta)}{\mathrm{d}^4 q \, \mathrm{d}\mathcal{O}} = \frac{1}{2E_{\mathrm{cm}}^2} \sum_{i=-1}^{7} \left[L_i^{(1)} W_i^{(0)} + L_i^{(0)} W_i^{(1)} \right]. \tag{7.81}$$

In the first term, only $i = -1, 2, 4, 5$ contribute to the sum due to table 7.1. For the second term, assuming LP azimuthal symmetry, only $i = -1, 0, 4$ contribute. From table 7.1, $W_0 \sim \mathcal{O}(\lambda^2)$, and as we will argue in section 7.2.5, all power corrections to $W_{-1,4}$ are quadratic in λ, so we have

$$W_{-1}^{(1)} = 0, \qquad W_0^{(1)} = 0, \qquad W_4^{(1)} = 0. \tag{7.82}$$

For W_{-1} and W_0, this statement is equivalent to the absence of linear power corrections in the inclusive cross section $\propto W_{-1} + \frac{1}{2}W_0$. For W_4, it is equivalent to the absence of linear power corrections in the inclusive forward-backward asymmetry. Hence, the second term in eq. (7.81) vanishes, and we arrive at

$$L^{(0)}(\not\phi) : \qquad \frac{\mathrm{d}\sigma^{(1)}(\Theta)}{\mathrm{d}^4 q\,\mathrm{d}\mathcal{O}} = \frac{1}{2E_{\mathrm{cm}}^2} \sum_{i=-1,2,4,5} L_i^{(1)} W_i^{(0)}\,. \qquad (7.83)$$

We have thus shown that for leptonic measurements that are azimuthally symmetric at leading power, *all linear* power corrections uniquely arise from *linear fiducial* power corrections $L_i^{(1)}$ multiplying the leading-power hadronic structure functions $W_{-1,2,4,5}^{(0)}$. The power-counting logic leading to eq. (7.83) is summarized in figure 7.3.

Leptonic fiducial power corrections

We now turn to leptonic fiducial power corrections that arise from the presence of an additional, physical scale p_L induced by the leptonic measurement. In this case, the power expansion of the measurements a priori receives power corrections in both q_T/Q and q_T/p_L,

$$\hat{\mathcal{O}}(q,\Phi_L) = \hat{\mathcal{O}}^{(0)}(q,\Phi_L)\Big[1 + \mathcal{O}\Big(\frac{q_T}{Q}, \frac{q_T}{p_L}\Big)\Big]\,,$$
$$\hat{\Theta}(q,\Phi_L) = \hat{\Theta}^{(0)}(q,\Phi_L)\Big[1 + \mathcal{O}\Big(\frac{q_T}{Q}, \frac{q_T}{p_L}\Big)\Big]\,. \qquad (7.84)$$

The case of linear fiducial power corrections discussed above corresponds to $p_L \sim Q$. We refer to the q_T/p_L corrections as *leptonic* fiducial power corrections. For $q_T \ll p_L \ll Q$, they become enhanced compared to the q_T/Q corrections and for $q_T \sim p_L$ they become $\mathcal{O}(1)$ and cause the naive expansion in q_T to break down.

Generically this happens when the leptonic measurement is close to an edge of Born phase space that is sensitive to additional radiation, such that a nonzero q_T opens up new phase space beyond the Born edge, with $p_L \sim q_T$ parametrizing the distance from the Born edge. We will demonstrate this effect in detail in section 7.4.3 for the important example of the p_T^ℓ spectrum near the Jacobian peak $p_T^\ell \sim Q/2$, in which case $p_L = Q - 2p_T^\ell$.

To expand in such regions, it is necessary to count both

$$\frac{q_T}{Q} \sim \frac{p_L}{Q} \sim \lambda\,, \qquad (7.85)$$

which explicitly avoids expanding in $q_T/p_L \sim \mathcal{O}(1)$ and thereby retains all leptonic power corrections exactly to all powers. Expanding the leptonic measurements in this limit

$$\hat{\mathcal{O}}(q,\Phi_L) = \hat{\mathcal{O}}^{(0)}(q,\Phi_L; q_T/p_L)\Big[1 + \mathcal{O}\Big(\frac{q_T}{Q}, \frac{p_L}{Q}\Big)\Big]\,,$$
$$\hat{\Theta}(q,\Phi_L) = \hat{\Theta}^{(0)}(q,\Phi_L; q_T/p_L)\Big[1 + \mathcal{O}\Big(\frac{q_T}{Q}, \frac{p_L}{Q}\Big)\Big]\,, \qquad (7.86)$$

where with a slight abuse of notation the superscript (0) now refers to the leading-power term in λ with the modified power counting in eq. (7.85), and the q_T/p_L argument is meant to remind us that we have not expanded in this ratio.

The cross section at leading power in λ in this limit is given by

$$\frac{\mathrm{d}\sigma(\Theta)}{\mathrm{d}^4 q \, \mathrm{d}\mathcal{O}} = \frac{1}{2E_{\mathrm{cm}}^2} \sum_{i=-1,2,4,5} L_i^{(0)}(q_T/p_L) \, W_i^{(0)} \left[1 + \mathcal{O}\!\left(\frac{q_T}{Q}, \frac{p_L}{Q}\right)\right], \qquad (7.87)$$

where the $L_i^{(0)}(q_T/p_L)$ arise from the modified LP leptonic measurements in eq. (7.86). The hadronic tensor does not know anything about p_L, and so its power expansion is unaffected by eq. (7.85). However, as we are now keeping some terms in the leptonic measurement that we would otherwise drop in the strict $q_T \to 0$ limit, the azimuthal symmetry we might have in the strict $q_T \to 0$ limit is typically lost now, and so we do not require it. As a result, also the $W_{2,5}$ contribute at LP in eq. (7.87). Furthermore, there are now generically linear power corrections to eq. (7.87) from both $L_i^{(1)}$ and $W_i^{(1)}$.

Generic fiducial power corrections

Since eq. (7.87) relies on counting $p_L/Q \sim \lambda$ it is not valid for $p_L \sim Q$. Hence, to cover the full leptonic phase space, we have to satisfy two competing conditions from the different regions. For $q_T \ll p_L \sim Q$ we must not expand in p_L/Q, while for $q_T \sim p_L \ll Q$ we must count $q_T \sim p_L$ to avoid uncontrolled power corrections in q_T/p_L. The natural way to satisfy both requirements is to expand the leptonic measurements neither in q_T nor p_L and thus keep the exact leptonic tensor,

$$\boxed{\frac{\mathrm{d}\sigma^{(0+L)}(\Theta)}{\mathrm{d}^4 q \, \mathrm{d}\mathcal{O}} \equiv \frac{1}{2E_{\mathrm{cm}}^2} \sum_{i=-1,2,4,5} L_i(q, \mathcal{O}, \Theta) \, W_i^{(0)}(q^2, s_{aq}, s_{bq}).} \qquad (7.88)$$

Of course, we still need to expand the hadronic tensor in $q_T/Q \sim \lambda$, and all four LP hadronic structure functions in principle contribute. For $q_T \ll p_L \sim Q$, eq. (7.88) obviously captures the linear power corrections as in eq. (7.83), while for $q_T \sim p_L \ll Q$ it captures as required all leptonic power corrections as in eq. (7.87). In the following, we always use the notation $\mathrm{d}\sigma^{(0+L)}$ to denote the inclusion of the exact leptonic tensor as in eq. (7.88).

Eq. (7.88) is our final master formula. By treating the leptonic tensor exactly, it in fact incorporates *all* fiducial power corrections that multiply the leading-power hadronic structure functions. The leptonic tensor does not produce small-q_T logarithms, which solely arise from the hadronic tensor. Therefore, eq. (7.88) automatically resums all logarithms in fiducial power corrections to the same order as the resummation is included for the hadronic tensor. All further power corrections to $\mathrm{d}\sigma^{(0+L)}$ are obtained by working to subleading power in the hadronic structure functions, and arise purely from subleading-power QCD dynamics.

One might argue that we could have immediately kept the leptonic tensor exact from the start, just because there is no reason or benefit to expanding it, and so one should not. On the other hand, one might argue that by doing so one keeps a seemingly arbitrary set of power corrections in the cross section, and there is a priori no guarantee that doing so would make things better and not worse, and so one should expand the leptonic tensor in

order to have a consistent power expansion for the cross section at each order in the power expansion. Both arguments are found in the literature.

Our analysis provides several formal justifications for keeping the exact leptonic tensor. First, for the common case of leptonic measurements that are azimuthally symmetric at Born level (and generic $p_L \sim Q$), it uniquely predicts all linear $\mathcal{O}(\lambda)$ next-to-leading power corrections in the cross section. In other words, in this limit the retained power corrections are not arbitrary but provide an unambiguous, systematic improvement in the power expansion of the cross section, including their logarithmic resummation. Second, it retains all leptonic power corrections, which as argued is mandatory to correctly obtain the actual *leading-power* result for $q_T \sim p_L$. Third, the actual regions and relevant scales p_L depend on the leptonic measurement and identifying them can be quite involved. Keeping the exact leptonic tensor is by far the simplest (and perhaps only sensible) way to guarantee that all such possible regions are correctly treated. Finally, it ensures that any in-between regions $q_T \ll p_L \ll Q$ are smoothly covered.

The LP hadronic structure functions entering in eq. (7.88) are given by

$$
W_i^{(0)} = \sum_{a,b} H_{i\,ab}(Q^2, \mu) \begin{cases} [B_a B_b S_a](Q^2, x_a, x_b, \vec{q}_T, \mu), & i = -1, 4 \\ [h_{1a}^\perp h_{1b}^\perp](Q^2, x_a, x_b, \vec{q}_T, \mu), & i = 2, 5. \end{cases} \tag{7.89}
$$

The cases $i = -1, 4$ are a straightforward generalization of the standard inclusive factorization theorem in eqs. (2.192) and (2.193a), where $B_{a,b}$ and S_a are the same beam and soft functions, and only the hard functions $H_{i\,ab}$ depend on the projection i. They are collected in appendix B.1. Eq. (7.89) is summed over the contributing quark-antiquark combinations a, b. (We use a, b here to reserve i for numbering structure functions.)

The $W_{2,5}^{(0)}$ contribution, which corresponds to the $\cos(2\varphi)$ and $\sin(2\varphi)$ angular modulations of the cross section, are proportional to a (weighted) convolution of two Boer-Mulders functions $h_1^\perp$ in the transverse plane [473–475], where $h_{1a}^\perp$ measures the net transverse polarization of flavor a, longitudinal momentum fraction x, and given transverse momentum $\vec{k}_T$ within an unpolarized proton [476]. It does not match onto leading twist-2 collinear PDFs, i.e., for $\Lambda_{\mathrm{QCD}} \ll q_T$, each $h_1^\perp$ is suppressed by at least one power of $\Lambda_{\mathrm{QCD}}/q_T$ [477] relative to the leading-power beam functions B_a in $W_{-1,4}$, which do match onto leading twist-2 PDFs. The matching of $h_1^\perp$ onto subleading twist-3 PDFs was carried out in ref. [478]. On the other hand, the first contribution to $W_{2,5}$ that does match onto leading twist-2 PDFs is suppressed by q_T^2/Q^2 relative to $W_{-1,4}$ [462]. For these reasons, we will neglect the $i = 2, 5$ contributions in our numerical results. However, it should be stressed that for $q_T \sim \Lambda_{\mathrm{QCD}}$ they do become formally leading contributions.

Perturbatively, eqs. (7.88) and (7.89) allow us to resum fiducial power corrections to the same order to which the LP hadronic structure functions are known. We stress that due to the different sum over flavors with different weights $H_{i\,ab}$, the resummation effects do not in general cancel in the ratio $W_4^{(0)}/W_{-1}^{(0)}$. This is relevant when computing the angular coefficient A_4, corresponding to the forward-backward asymmetry, at small q_T.

7.2.5 Uniqueness of linear power corrections

There are several loose ends in the nontechnical discussion of the previous subsection that we now tie up to establish that eq. (7.83) uniquely and unambiguously captures all linear power corrections for LP-azimuthally symmetric observables.

1. We derive the power counting of the hadronic structure functions in table 7.1.

2. We argue that power corrections to $W_{-1,4}^{(0)}$ are quadratic, such that eq. (7.82) holds.

3. We show explicitly that the linear power corrections in eq. (7.83) are unique, i.e., that switching to a different basis induces only quadratic power corrections.

Power counting hadronic structure functions

To derive the λ scaling of the W_i in table 7.1, we use the soft-collinear effective theory reviewed in section 2.2. We choose the lightlike reference vectors $n_{a,b}^{\mu}$ and $\bar{n}_{a,b}^{\mu}$ along the proton directions as in eqs. (2.87) and (2.90). In addition, we need to distinguish a direction in the transverse plane, which we take to be

$$n_{\perp}^{\mu} = \frac{q_{\perp}^{\mu}}{(-q_{\perp}^2)^{1/2}} = (0,1,0,0)_{\text{lep}}, \qquad n_{\perp}^2 = -1, \qquad n_{\perp} \cdot n_a = n_{\perp} \cdot n_b = 0, \qquad (7.90)$$

where $q_{\perp}^{\mu} \equiv g_{\perp}^{\mu\nu} q_{\nu}$, and we remind the reader that we aligned the x axis in the leptonic frame with the transverse component of q^{μ}.

To discuss the power counting of the hadronic structure functions in SCET, we first write t^{μ}, x^{μ}, z^{μ} in terms of $n_{a,b}^{\mu}$ and $n_{\perp}^{\mu}$. From their explicit expressions in the leptonic frame in eqs. (7.26) and (7.27), we have

$$t^{\mu} = \gamma \frac{n_a^{\mu} + n_b^{\mu}}{2} + \epsilon\, n_{\perp}^{\mu}, \qquad y^{\mu} = \epsilon_{\perp}^{\mu\nu} n_{\perp\nu},$$

$$x^{\mu} = \epsilon \frac{n_a^{\mu} + n_b^{\mu}}{2} + \gamma\, n_{\perp}^{\mu}, \qquad z^{\mu} = \frac{n_a^{\mu} - n_b^{\mu}}{2}, \qquad (7.91)$$

where as before $\epsilon = q_T/Q \sim \lambda$ and $\gamma = \sqrt{1+\epsilon^2} = 1 + \mathcal{O}(\lambda^2)$. It is straightforward to expand eq. (7.91) in λ,

$$t^{\mu} = \frac{n_a^{\mu} + n_b^{\mu}}{2} + \epsilon\, n_{\perp}^{\mu} + \mathcal{O}(\lambda^2), \qquad y^{\mu} = \epsilon_{\perp}^{\mu\nu} n_{\perp\nu},$$

$$x^{\mu} = n_{\perp}^{\mu} + \epsilon \frac{n_a^{\mu} + n_b^{\mu}}{2} + \mathcal{O}(\lambda^2), \qquad z^{\mu} = \frac{n_a^{\mu} - n_b^{\mu}}{2}. \qquad (7.92)$$

Note that the relations for y^{μ} and z^{μ} are exact and do not receive power corrections, which is a direct consequence of the symmetry we imposed on z^{μ}. The simple form of eq. (7.92) motivates our choice of $n_{a,b}$ in the leptonic frame. If we had chosen $n_{a,b}$ as $(1,0,0,\pm 1)_{\text{lab}}$ in the lab frame instead, there would be additional factors of $e^{\pm Y}$ in eq. (7.92).

The power counting of the hadronic structure functions is determined by the order in λ at which contractions of eq. (7.92) with the hadronic current are populated when expanding

the hadronic currents J_V^μ in an explicit power expansion in λ in terms of the corresponding SCET currents, as in eq. (2.129).

The leading-power current for generic collinear directions $n_{1,2}$ was given in eq. (2.144). The matching coefficient of the leading-power gluon operator $O_{gg}^{(0)}$ in eq. (2.144) is proportional to q^μ [57]. It precisely captures the non-conserved part of the current, see eq. (7.8) and the discussion below it. It does not contribute to the (conserved) hadronic structure function in table 7.1, so we can focus on the quark operator $O_{q\bar{q}'}^{(0)}$. When evaluating proton matrix elements of $O_{q\bar{q}'}^{(0)}(n_1, n_2; \omega_1, \omega_2; x)$, momentum conservation requires $n_{2,1} = n_{a,b}$ and $\omega_{2,1} = \omega_{a,b}$ in the case where parton a is a quark. Making use of these identifications and the fact that $\omega_a \omega_b = q^2$, the hard matching coefficients for $V = \gamma, Z, W$ are given by [57, 177]

$$C_{\gamma q\bar{q}'}^{(0)\mu\,\alpha\beta}(n_b, n_a; \omega_b, \omega_a) = \delta_{qq'}|e|(\gamma_\perp^\mu)^{\alpha\beta}\Big[Q_q\, C_q(q^2) + \sum_f Q_f\, C_{vf}(q^2)\Big],$$

$$C_{Z q\bar{q}'}^{(0)\mu\,\alpha\beta}(n_b, n_a; \omega_b, \omega_a) = \delta_{qq'}(-|e|)\Bigg\{\big[\gamma_\perp^\mu(v_q - a_q\gamma_5)\big]^{\alpha\beta} C_q(q^2)$$
$$+ \sum_f \Big[(\gamma_\perp^\mu)^{\alpha\beta} v_f\, C_{vf}(q^2) - (\gamma_\perp^\mu\gamma_5)^{\alpha\beta} a_f\, C_{af}(q^2)\Big]\Bigg\},$$

$$C_{W^+ q\bar{q}'}^{(0)\mu\,\alpha\beta}(n_b, n_a; \omega_b, \omega_a) = -\frac{|e|V_{qq'}}{2\sqrt{2}\sin\theta_w}\big[\gamma_\perp^\mu(1 - \gamma_5)\big]^{\alpha\beta} C_q(q^2),$$

$$C_{W^- q\bar{q}'}^{(0)\mu\,\alpha\beta}(n_b, n_a; \omega_b, \omega_a) = -\frac{|e|V_{q'q}^*}{2\sqrt{2}\sin\theta_w}\big[\gamma_\perp^\mu(1 - \gamma_5)\big]^{\alpha\beta} C_q(q^2), \tag{7.93}$$

where the vector and axial-vector contributions have the same flavor-diagonal matching coefficient $C_q(q^2)$ because massless QCD preserves chirality, but in general have different singlet coefficients $C_{vf}(q^2)$ and $C_{af}(q^2)$. The latter arise from closed quark loops coupling to the vector boson, and thus involve an electroweak coupling different from the external quark flavors. Here, $V_{qq'}$ is the CKM-matrix element for $q \in \{u, c, t\}$ and $q' \in \{d, s, b\}$ (and we take it to vanish in all other cases).

Importantly, the spin structure of the leading-power hard matching coefficient is proportional to $\gamma_\perp^\mu = g_\perp^{\mu\nu}\gamma_\nu$, and therefore satisfies

$$n_a \cdot C_{V q\bar{q}'}^{(0)\alpha\beta}(n_b, n_a; \omega_b, \omega_a) = n_b \cdot C_{V q\bar{q}'}^{(0)\alpha\beta}(n_b, n_a; \omega_b, \omega_a) = 0. \tag{7.94}$$

Using eq. (7.92), it is easy to see that contractions with the longitudinal polarization vector $\varepsilon_0^\mu = z^\mu$ vanish to all orders at the level of the amplitude,

$$\varepsilon_{0\mu}^* \langle X|J_V^{(0)\mu}|pp\rangle = 0. \tag{7.95}$$

This is the all-order analogue of eq. (7.79) in the limit $\lambda \ll 1$. It follows that projections onto ε_0^μ in eq. (7.33) are only populated by matrix elements of the subleading-power currents $J_V^{(i)\mu}$ with $i \geq 1$ in eq. (2.130), and are penalized by at least one power of λ. This implies that only $W_{-1,2,4,5}$, which do not involve longitudinal polarizations, can scale as $\mathcal{O}(\lambda^0)$,

while $W_{1,3,6,7}$ are suppressed at least by $\mathcal{O}(\lambda)$, and $W_0 = 2W_{00}$ is suppressed by at least $\mathcal{O}(\lambda^2)$. This completes the derivation of table 7.1.

For $W_{-1,2,4,5}$, our power-counting argument agrees with the well-known scaling of the leading contributions given by eq. (7.89), while for W_0 and W_1 it reproduces the known scaling at fixed $\mathcal{O}(\alpha_s)$ [462]. For the remaining $W_{3,6,7}$, our argument provides a lower bound on the degree of power suppression. To our knowledge, this is the first time that the scaling of $W_{3,6,7}$ at small q_T has been explicitly considered for generic currents.

We also point out that starting from eq. (7.92), it is straightforward to identify the subleading-power SCET currents that populate a given W_i. For example, $W_{1,3,6,7}$ can only receive their leading contributions from the interference of $J_V^{(1)\mu}$ with the leading-power current $J_V^{(0)\mu}$, while the leading contribution to W_0 must arise from the interference of $J_V^{(1)\mu}$ with itself due to eq. (7.95). The hard-scattering operators to $\mathcal{O}(\lambda^2)$ relevant for color-singlet production have been constructed in refs. [179–181] using the approach of helicity operators [177, 178], and the list of operators contributing to $J_V^{(1)\mu}$ is fairly short. Due to the explicit power suppression from the current, it should be possible to derive factorization theorems for these W_i in the $q_T \ll Q$ limit using SCET. This would be relevant e.g. to understand the degree to which resummation effects are universal between W_i and W_{-1}, and hence to what extent they cancel in predictions for the angular coefficients A_i. A conjecture for the factorization of W_1 at small q_T was given in ref. [479], and it would be interesting to analyze it using the systematic organization of subleading operators in SCET.

Vanishing $\mathcal{O}(\lambda)$ corrections in $W_{-1,4}$

We next discuss the absence of linear power corrections in $W_{-1,4}$, cf. eq. (7.82). The projectors defining $W_{-1,4}$ involve x^μ, which in principle receives a linear power correction, see eq. (7.92). However, this $\mathcal{O}(\lambda)$ correction is proportional to $n_a + n_b$ and thus orthogonal to the leading-power SCET current in eq. (2.144) due to eq. (7.94), similar to the longitudinal polarization vector discussed above. We therefore have up to quadratic power corrections,

$$W_{-1} = -g_{\perp\mu\nu}W^{\mu\nu}\big[1 + \mathcal{O}(\lambda^2)\big], \qquad W_4 = 2\mathrm{i}\epsilon_{\perp\mu\nu}W^{\mu\nu}\big[1 + \mathcal{O}(\lambda^2)\big]. \qquad (7.96)$$

The question then reduces to why $-g_{\perp\mu\nu}W^{\mu\nu}$ and $2\mathrm{i}\epsilon_{\perp\mu\nu}W^{\mu\nu}$ do not receive linear power corrections relative to the contribution from the squared LP current.

It is well known that for $e^+e^- \to$ dijets event shapes such as thrust, the leading $\mathcal{O}(\lambda)$ corrections vanish [180, 480–483]. The explicit proof in refs. [180, 483] relies on invariance under rotations about the axis defined by the lightlike directions that parametrize the collinear sectors for the outgoing jets. The analogous statement here is that $-g_{\perp\mu\nu}W^{\mu\nu}$ and $2\mathrm{i}\epsilon_{\perp\mu\nu}W^{\mu\nu}$ are indeed invariant under rotations about $n_a^\mu - n_b^\mu$. To see that this implies the absence of linear power corrections, we discuss the possible sources of power corrections in turn:

1. Subleading hard-scattering operators were shown not to contribute to the thrust spectrum at $\mathcal{O}(\lambda)$ in ref. [180], using the rotational symmetry. While thrust is

described by SCET$_\mathrm{I}$ and q_T is a SCET$_\mathrm{II}$ observable, the operator basis involving only collinear fields is identical and has manifest crossing symmetry, so for these contributions the argument carries over to the case of Drell-Yan.

2. On the other hand, contributions involving soft fields differ between SCET$_\mathrm{I}$ and SCET$_\mathrm{II}$, and occur both through subleading hard-scattering operators and subleading Lagrangian insertions. For SCET$_\mathrm{I}$-like event shapes the vanishing of such terms at $\mathcal{O}(\lambda)$ was demonstrated in refs. [180, 483]. The analysis of $\mathcal{O}(\lambda)$ terms in SCET$_\mathrm{II}$ is more difficult due to the non-locality of the theory and existence of $\mathcal{O}(\lambda^{1/2})$ operators [484]. In ref. [485], subleading-power Lagrangians and hard-scattering operators involving soft fields in SCET$_\mathrm{II}$ are constructed, and it is demonstrated that soft $\mathcal{O}(\lambda)$ contributions are absent for the inclusive Drell-Yan small q_T spectrum, including the forward-backward asymmetry.

3. For our choice of $n_{a,b}$ in eq. (2.87), the measurement function for $\vec{q}_T$ is the vectorial sum of the perpendicular momenta of all particles in the hadronic final state. Unlike the case of e^+e^- event shapes, the sum factorizes into n_a-collinear, n_b-collinear, and soft contributions without approximation, so power corrections from the $\vec{q}_T$ measurement are absent. Since fundamentally the hadronic structure functions only depend on the Lorentz invariants in eq. (7.4), the measurement can be marginalized over the azimuthal angle of $\vec{q}_T$ and thus preserves the rotational symmetry.

4. A source of power corrections absent in the e^+e^- case are the Born measurements on Q and Y that set the arguments of the PDFs. As has been discussed in detail in refs. [193, 486], these give rise to new nonperturbative functions such as derivatives of the PDFs at subleading power in q_T. It can easily be seen from the exact result that these corrections are quadratic,

$$\frac{q^-}{P_a^-} = \frac{\sqrt{Q^2 + q_T^2}\, e^Y}{E_\mathrm{cm}} = \frac{Q e^Y}{E_\mathrm{cm}} \big[1 + \mathcal{O}(\lambda^2)\big] = x_a \big[1 + \mathcal{O}(\lambda^2)\big]. \tag{7.97}$$

Recall that $W_\mathrm{incl} = W_{-1} + W_0/2$ and we already showed that $W_0 \sim \lambda^2$, so the absence of linear power corrections for W_incl and W_{-1} is equivalent. We can thus conclude that W_{-1} and W_4 do not receive linear power corrections.

Choice of tensor decomposition is $\mathcal{O}(\lambda^2)$

In section 7.2.2, we defined a set of reference vectors $t^\mu, x^\mu, y^\mu, z^\mu$ to perform the tensor decomposition into hadronic structure functions, which turned out to be equivalent to the CS frame (using the boost definition). The x^μ, y^μ, z^μ were uniquely determined by imposing eqs. (7.16) and (7.18), but these constraints are not technically required. In general, we can also pick a different set x'^μ, y'^μ, z'^μ of orthonormal, spacelike reference vectors. These in turn define a vector-boson rest frame related to the CS frame by a rotation $r \in \mathrm{SO}(3)$
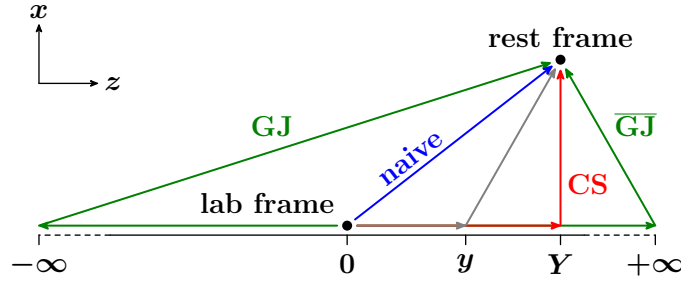
Figure 7.4: Sequence of boosts defining different vector-boson rest frames. In the general case (gray), we first boost by a rapidity y along the lab-frame beam axis, and then boost into the rest frame. Different choices of y lead to a relative Wigner rotation of the resulting rest frames. Relevant special cases are $y = Y$ (Collins-Soper frame, red), $y = 0$ (the naive rest frame, blue) and $y \to \pm\infty$, (Gottfried-Jackson frame, green).

that in general depends on q,

$$
\begin{pmatrix} x'^{\mu} \\ y'^{\mu} \\ z'^{\mu} \end{pmatrix} = r(q) \begin{pmatrix} x^{\mu} \\ y^{\mu} \\ z^{\mu} \end{pmatrix} .
\tag{7.98}
$$

The corresponding hadronic structure functions W_i' are related to the W_i by a corresponding orthogonal transformation

$$
W_i' = \sum_j R_{ij}(q) W_j .
\tag{7.99}
$$

In terms of the W_i', the fully differential cross section is given by

$$
\frac{\mathrm{d}\sigma(\Theta)}{\mathrm{d}^4 q \, \mathrm{d}\mathcal{O}} = \frac{1}{2E_{\mathrm{cm}}^2} \sum_i L_i(q, \mathcal{O}, \Theta) \sum_j R_{ij}^{-1}(q) \, W_j'(q^2, s_{aq}, s_{bq}) .
\tag{7.100}
$$

Note that the parametrization of the lepton phase space used to evaluate the L_i is irrelevant here. Of course, if corresponding angles θ', φ' are considered, the corresponding spherical harmonics are related by the same rotation $R_{ij}(q)$, such that their angular coefficients are given by ratios of the W_i'.

First, let us point out that there is never any frame ambiguity to the order in the power expansion we are working in, because to the working order different frame choices simply amount to a specific choice of basis or coordinate system, which the final result cannot depend on. An ambiguity can only arise in the higher-order terms that are partially retained and partially neglected, which in general do depend on the frame choice.

To remove the trivial effect from a mere basis choice at LP, we start from a common LP rest frame at $q_T = 0$, which is the leptonic frame. A convenient way to parametrize the different possible frames for nonzero q_T is by the sequence of boosts starting from the lab frame as shown in figure 7.4. Specifically, we first boost by a rapidity y along the beam

direction and then directly into the rest frame. Some cases of interest are the "naive" rest frame, obtained by performing a single direct boost from the lab frame ($y = 0$) into the rest frame, the CS frame ($y = Y$), the Gottfried-Jackson (GJ) frame defined by the limit $y \to -\infty$, or the $\overline{\text{GJ}}$ frame obtained by taking $y \to +\infty$. Another way to conceptualize these frames is through the angles between their respective z'^μ axes and the momenta of the incoming protons. In the CS frame, those angles become precisely equal for massless hadrons, see figure 7.1. In the GJ frame, the z axis is aligned with the direction of P_a, while the naive case falls in between for $Y > 0$.

It is easy to see that for $q_T \to 0$, the two boosts for any frame collapse into a single boost from the lab frame to the leptonic frame. Since for $q_T \to 0$ all frames coincide, we have

$$r(q) = \mathbf{1}_{3\times3} + \mathcal{O}(\lambda), \qquad R_{ij}(q) = \delta_{ij} + \mathcal{O}(\lambda). \tag{7.101}$$

Working at LP in the hadronic tensor, the $\mathcal{O}(\lambda)$ corrections in eq. (7.101) could in principle induce an $\mathcal{O}(\lambda)$ ambiguity in the hadronic power corrections. We now show that this is not the case, which means that the linear power corrections predicted by eq. (7.83) are unique. In other words, we have to show that the absence of additional linear corrections from the hadronic tensor that lead to eq. (7.83) was not just an accident of our particular choice of tensor decomposition.

Eq. (7.101) immediately implies that the new axes still satisfy

$$x'^\mu = n_\perp^\mu + \mathcal{O}(\lambda), \qquad y'^\mu = \epsilon_\perp^{\mu\nu} n_{\perp\nu} + \mathcal{O}(\lambda), \qquad z'^\mu = \frac{n_a^\mu - n_b^\mu}{2} + \mathcal{O}(\lambda), \tag{7.102}$$

so the scaling properties in table 7.1 also hold for the W_j'. Following our previous analysis, we would now discard all power-suppressed W_j' structure functions, evaluate the remaining ones ($j = -1, 2, 4, 5$) at leading power, and dress them with exact leptonic tensor components,

$$\frac{d\sigma^{(0+L)}(\Theta)}{d^4q \, d\mathcal{O}} = \frac{1}{2E_{\text{cm}}^2} \sum_i L_i(q, \mathcal{O}, \Theta) \sum_{j=-1,2,4,5} R_{ij}^{-1}(q) \, W_j'^{(0)}(q^2, s_{aq}, s_{bq}) \left[1 + \mathcal{O}(\lambda^2)\right]. \tag{7.103}$$

Since all $i = -1, \ldots, 7$ are now populated by R_{ij}^{-1}, one might think that the different choice of tensor decomposition amounts to a linear power correction compared to the left-hand side as given in eq. (7.88), because the R_{ij} differ from unity by $\mathcal{O}(\lambda)$, but as indicated it is only of $\mathcal{O}(\lambda^2)$.

To show that the induced difference is indeed only $\mathcal{O}(\lambda^2)$, first note that rotations around the z axis amount to a trivial shift in φ. This induces an $\mathcal{O}(\lambda^2)$ difference at cross-section level due to our assumption of azimuthal symmetry at leading power in eq. (7.74). Hence, it is sufficient to consider the SO(2) subgroup of rotations around the y axis parametrized by one remaining Euler angle α,

$$\begin{pmatrix} x'^\mu \\ z'^\mu \end{pmatrix} = \begin{pmatrix} c_\alpha & s_\alpha \\ -s_\alpha & c_\alpha \end{pmatrix} \begin{pmatrix} x^\mu \\ z^\mu \end{pmatrix}, \qquad y'^\mu = y^\mu, \tag{7.104}$$

with $c_\alpha \equiv \cos\alpha$ and $s_\alpha \equiv \sin\alpha$. By a straightforward calculation, the W_i can be shown to transform under the following representations of SO(2):

$$
\begin{pmatrix} W'_{-1} \\ W'_0 \\ W'_1 \\ W'_2 \end{pmatrix} = \begin{pmatrix} 1 - \frac{s_\alpha^2}{2} & \frac{s_\alpha^2}{2} & -s_\alpha c_\alpha & \frac{s_\alpha^2}{4} \\ s_\alpha^2 & 1 - s_\alpha^2 & 2s_\alpha c_\alpha & -\frac{s_\alpha^2}{2} \\ s_\alpha c_\alpha & -s_\alpha c_\alpha & 1 - 2s_\alpha^2 & -\frac{s_\alpha c_\alpha}{2} \\ s_\alpha^2 & -s_\alpha^2 & 2s_\alpha c_\alpha & 1 - \frac{s_\alpha^2}{2} \end{pmatrix} \begin{pmatrix} W_{-1} \\ W_0 \\ W_1 \\ W_2 \end{pmatrix}, \tag{7.105}
$$

$$
\begin{pmatrix} W'_3 \\ W'_4 \end{pmatrix} = \begin{pmatrix} c_\alpha & s_\alpha \\ -s_\alpha & c_\alpha \end{pmatrix} \begin{pmatrix} W_3 \\ W_4 \end{pmatrix}, \qquad \begin{pmatrix} W'_5 \\ W'_6 \end{pmatrix} = \begin{pmatrix} c_\alpha & s_\alpha \\ -s_\alpha & c_\alpha \end{pmatrix} \begin{pmatrix} W_5 \\ W_6 \end{pmatrix}, \qquad W'_7 = W_7.
$$

It is a simple exercise in special relativity to show that the resulting Wigner rotation of a generic frame defined by boost y relative to the CS frame with $y = Y$ is

$$
\tan\alpha = \frac{\epsilon \sinh(Y-y)\left[\gamma\cosh(Y-y) - 1\right]}{\gamma\sinh^2(Y-y) + \epsilon^2\cosh(Y-y)} = \epsilon\tanh\frac{Y-y}{2} + \mathcal{O}(\epsilon^3), \tag{7.106}
$$

where $\epsilon = q_T/Q \sim \lambda$ and $\gamma = \sqrt{1 + \epsilon^2}$. For any Y, y, eq. (7.106) turns out to be bounded by the leading term, $|\tan\alpha| \leq \epsilon|\tanh\frac{Y-y}{2}| \leq \epsilon$. In particular for the GJ frame we have $\tan\alpha_{\mathrm{GJ}} = \epsilon$, with which we recover the well-known result for the relation between $W_{-1,0,1,2}$ in the CS and GJ frames [462].

Eq. (7.106) shows explicitly that $\alpha \sim \lambda$. To see that eq. (7.103) indeed holds up to quadratic power corrections, we invert eq. (7.105) by taking $\alpha \mapsto -\alpha$, and expand in $\alpha \sim \lambda$ to find

$$
\begin{pmatrix} W_{-1} \\ W_0 \\ W_1 \\ W_2 \end{pmatrix} = \left[\mathbf{1}_{4\times 4} + \mathcal{O}\begin{pmatrix} \lambda^2 & \lambda^2 & \lambda & \lambda^2 \\ \lambda^2 & \lambda^2 & \lambda & \lambda^2 \\ \lambda & \lambda & \lambda^2 & \lambda \\ \lambda^2 & \lambda^2 & \lambda & \lambda^2 \end{pmatrix} \right] \begin{pmatrix} W'_{-1} \\ W'_0 \\ W'_1 \\ W'_2 \end{pmatrix},
$$

$$
\begin{pmatrix} W_3 \\ W_4 \end{pmatrix} = \left[\mathbf{1}_{2\times 2} + \mathcal{O}\begin{pmatrix} \lambda^2 & \lambda \\ \lambda & \lambda^2 \end{pmatrix} \right] \begin{pmatrix} W'_3 \\ W'_4 \end{pmatrix},
$$

$$
\begin{pmatrix} W_5 \\ W_6 \end{pmatrix} = \left[\mathbf{1}_{2\times 2} + \mathcal{O}\begin{pmatrix} \lambda^2 & \lambda \\ \lambda & \lambda^2 \end{pmatrix} \right] \begin{pmatrix} W'_5 \\ W'_6 \end{pmatrix}, \qquad W_7 = W'_7. \tag{7.107}
$$

We see that under the rotation, the leading structure functions mix into themselves and into each other only by an $\mathcal{O}(\lambda^2)$ amount. The subleading structure functions are populated precisely by an amount commensurate with their intrinsic scaling, see table 7.1. Combined with the scaling of the corresponding leptonic structure functions as in figure 7.3, we find that the effect of any $\mathcal{O}(\lambda)$ rotation on the cross section is indeed only of $\mathcal{O}(\lambda^2)$ for LP-azimuthally symmetric observables.

It is natural to ask whether a specific frame choice should be preferred in order to also capture an optimal set of terms at $\mathcal{O}(\lambda^2)$. It is well known that leading-logarithmic terms are absent in W_1 in the CS frame [462]. This is natural from the point of view that the CS z axis does not receive power corrections, reducing "spill-over" of terms from the leading-power currents. A reduced size of power corrections by a symmetric choice of frame has also been found for 0-jettiness $\mathcal{T}_0$ [486–488], albeit for a somewhat different physical reason. In section 7.4.4 we will find some numerical evidence that the CS decomposition also reduces the size of power corrections in the ϕ^* spectrum. Taken together, this suggests that the CS frame might indeed be the optimal choice, although the size of the frame-dependent $\mathcal{O}(\lambda^2)$ corrections should still be assessed.

7.2.6 Relation to the literature

Early approaches to resummation effects on the Drell-Yan cross section differential in the lepton kinematics [433–435] typically picked the CS angles to parametrize the decay phase-space integral, but did not discuss the ambiguity inherent in this choice or the relative size of power corrections. In these approaches, the CS frame primarily serves as a tool to enable generic lepton-differential observables. In ref. [462], the logarithmic structure of $W_{-1,0,1,2}$ at low q_T in collinear factorization was discussed in detail, but the implications for the structure of power corrections to e.g. the fiducial cross section were not explored.

An implementation of generic lepton-differential observables in q_T resummation was presented in ref. [439] and more recently in ref. [440] based on a parton-level Monte-Carlo generation of the leptonic final state. There, the choice of rest frame used in earlier results was recast as a q_T-recoil prescription for how to distribute the nonzero q_T between the colliding partons in the rest frame where the leptonic decay is evaluated. They also showed that the ambiguity in the q_T-recoil prescription is in one-to-one correspondence with the ambiguity of the rest-frame choice and that it vanishes for $q_T \to 0$. They thus argue that the recoil effects are $\mathcal{O}(q_T/Q)$ effects that cannot be unambiguously computed through the q_T resummation, but some recoil prescription is nevertheless required for practical purposes to satisfy transverse momentum conservation in the parton-level generation of the leptonic decay. (Note that similar recoil prescriptions to preserve momentum conservation are also commonly used in parton-shower Monte Carlos.)

Very recently, refs. [267, 268] used N³LL perturbative baselines to fit nonperturbative models for the rapidity anomalous dimension and TMDPDFs using fiducial Z q_T spectra among other data. They also retain the exact dependence of the fiducial phase space on q_T, with the analytic leptonic decay matrix element contracted against the LP hadronic tensor $\propto g_\perp^{\mu\nu}$ (see also ref. [489]).[9] This is essentially equivalent to an exact treatment of L_{-1} in our notation (up to an overall $\mathcal{O}(\lambda^2)$ difference in the projection itself), while L_4 does not contribute to the observables they consider. They also do not provide formal arguments for the exact treatment of the leptonic contributions.

---

[9] The leptonic q_T dependence is extrapolated across a given q_T bin in ref. [268] to simplify the q_T bin integral, which should give a good approximation of the exact bin integral, especially for small bin width.

If the fully-differential and flavor-channel dependent leptonic decay matrix element is evaluated in the vector-boson rest frame, including exact leptonic cuts, and contracted against the resummed LP hadronic tensor, either explicitly at the analytic level or during the parton-level generation via the recoil prescription, then this essentially amounts to retaining the exact q_T dependence of the leptonic tensor. To the best of our understanding this is the case in refs. [267, 268, 439, 440]. Our analysis thus provides formal justification for doing so, showing that the ambiguity is only of $\mathcal{O}(\lambda^2)$ and that for a large class of common measurements (those that are azimuthally symmetric at LP) it actually unambiguously predicts all linear power corrections along with their resummation. In addition, it is formally required in phase-space regions that exhibit leptonic power corrections.

In ref. [445], fiducial lepton cuts are implemented in the resummed cross section strictly on Born kinematics at $q_T = 0$, while fiducial power corrections are obtained through the fixed-order matching. Large power corrections from the fixed-order matching were observed in the fiducial case compared to the inclusive case. From our analysis, this is explained by the linear power corrections induced by the fiducial cuts.

Sometimes a multiplicative fixed-order matching procedure is employed, see for example refs. [394, 445], where in order to Sudakov-suppress the fixed-order matching corrections at small q_T they are multiplied by the ratio of the LP resummed contribution to its fixed-order expansion. While this procedure is unlikely to produce the correct Sudakov suppression for genuine hadronic power corrections, one might ask if it correctly "dresses" the fiducial power corrections with the LP resummation to achieve their resummation. For this to be the case, the multiplicative matching at minimum has to reproduce eq. (7.83) for the linear power corrections. Clearly, this can only happen if the multiplicative matching only involves a single (effective) hadronic structure function at a time and if it is performed fully differentially in q^2, Y, and q_T^2. This is typically not the case. For example, the multiplicative matching in refs. [394, 445] is performed at the cumulant level, and thus does not satisfy this requirement.

7.3 Resummation of leading-power hadronic tensor

In this section, we discuss our specific resummation setup for the leading-power hadronic structure functions $W_{-1,4}^{(0)}$ in eq. (7.89). The setup follows standard procedures as reviewed in section 2.4.3, and is deliberately kept simple, e.g., by ignoring nonperturbative corrections or quark-mass effects [420] at small q_T, allowing us to focus on the effect of resumming the fiducial power corrections in the following sections. As discussed in the previous section, the fact that their resummation can be obtained in terms of the leading-power hadronic structure functions, and that this captures all linear as well as leptonic power corrections, holds independently of how the LP resummation is performed.

7.3.1 Canonical scales and nonperturbative prescription

The canonical scales of the hard, beam, and soft functions, and the rapidity anomalous dimension in b_T were given in eq. (2.209), and we repeat them here for reference:

$$\mu_H \sim Q\,, \qquad \mu_B \sim b_0/b_T\,, \qquad \mu_S \sim b_0/b_T\,, \qquad \mu_0 \sim b_0/b_T\,,$$
$$\nu_B \sim Q\,, \qquad\qquad \nu_S \sim b_0/b_T\,. \tag{7.108}$$

For our resummed numerical results we evaluate the ingredients in eq. (2.196) at these scales, perform the RG evolution between them as described in appendix D, and take a numerical inverse Fourier transform in the end. Note that with the choice in eq. (7.108), the beam and soft functions and the rapidity anomalous dimension become sensitive to nonperturbative effects at large $b_T \gtrsim \Lambda_{\text{QCD}}^{-1}$. To extend the perturbative description into the nonperturbative domain, in chapter 4 we chose μ_0 (and μ_B, μ_S) as a function of b_T such that it asymptotes to a perturbative scale at large b_T. Alternatively, a global replacement of b_T by a suitable function $b^*(b_T)$ may be performed at the level of the cross section, where $b^*(b_T)$ itself is bounded by some perturbative value $b_{\max} \lesssim 1/\Lambda_{\text{QCD}}$ [185, 251]. Since nonperturbative effects in the region $q_T \sim \Lambda_{\text{QCD}}$ are not our main focus here, we use an even simpler prescription to ensure that α_s remains perturbative. Specifically, we freeze out both the running coupling and the PDFs entering the hadronic structure functions $W_{-1,4}^{(0)}$ at a perturbative scale by performing the replacement

$$\alpha_s(\mu) \mapsto \alpha_s^{\text{fr}}(\mu) \equiv \alpha_s\big[\mu_{\text{fr}}(\mu)\big]\,, \qquad f_i(\mu) \mapsto f_i^{\text{fr}}(\mu) \equiv f_i\big[\mu_{\text{fr}}(\mu)\big]\,. \tag{7.109}$$

We choose the smooth function $\mu_{\text{fr}}(\mu)$ governing the freeze-out as

$$\mu_{\text{fr}}(\mu) = \begin{cases} \Lambda_{\text{fr}} + \frac{\mu^2}{4\Lambda_{\text{fr}}} & \mu \leq 2\Lambda_{\text{fr}}\,, \\ \mu & \mu > 2\Lambda_{\text{fr}}\,. \end{cases} \tag{7.110}$$

In practice, we pick $\Lambda_{\text{fr}} = 1\,\text{GeV}$ for our central results. The behavior of α_s^{fr} at low scales is illustrated in the left panel of figure 7.5. This choice constitutes a (fairly crude) model for the large b_T behavior of $\tilde{\gamma}_\nu^i$ that is sufficient to regulate the large b_T region, and formally amounts to a power correction in $\Lambda_{\text{QCD}} \ll q_T$. We similarly ignore contributions of
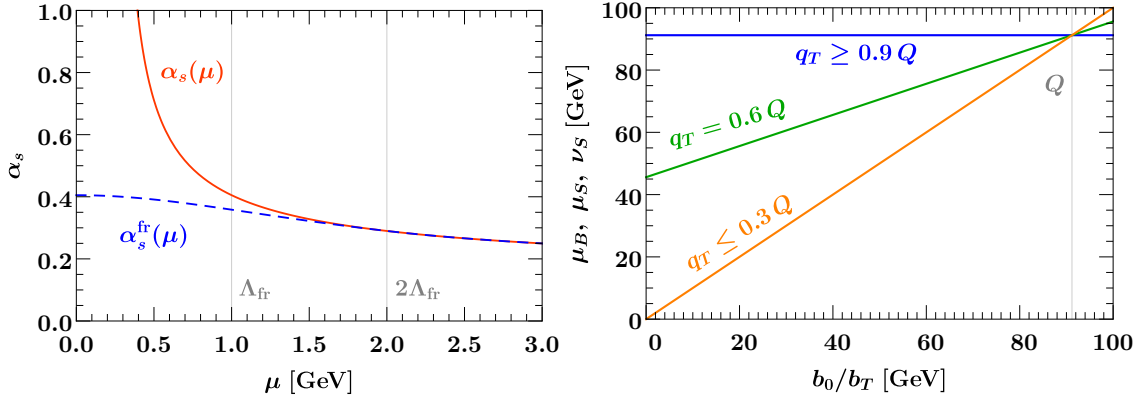
Figure 7.5: Left: Illustration of the freeze-out prescription used to ensure that α_s is evaluated at perturbative scales. Right: Hybrid profile scales as a function of b_0/b_T for representative values of q_T. The thin vertical line corresponds to $b_0/b_T = Q$, where $Q = m_Z$ for illustration purposes.

$\mathcal{O}(b_T \Lambda_{QCD})$ in the beam and soft function boundary conditions, beyond the ones encoded in our global choice of $\mu_{fr}(\mu)$. This is also consistent with neglecting the hadronic structure functions $W_{2,5}$ involving Boer-Mulders functions in the regime $\Lambda_{QCD} \ll q_T \ll Q$ altogether, see the discussion below eq. (7.89).

7.3.2 Fixed-order matching and profile scales

We extend the description of the cross section to the fixed-order region $q_T \sim Q$ by an additive matching to the fixed-order result via profile scales,

$$\mathrm{d}\sigma = \mathrm{d}\sigma^{(0+L)}\big|_{\mu_{res}} + \big[\mathrm{d}\sigma^{FO}\big|_{\mu_{FO}} - \mathrm{d}\sigma^{(0+L)}\big|_{\mu_{FO}}\big]. \qquad (7.111)$$

Here the subscript μ_{res} on the first term indicates that we evaluate the resummed LP hadronic structure functions in $\mathrm{d}\sigma^{(0+L)}$ using resummation (profile) scales in b_T space and numerically perform the inverse Fourier transform. The superscript μ_{FO} indicates that the structure functions are instead evaluated at common fixed-order scales μ_{FO}, which can be done directly in momentum space. The last term effectively acts as a differential subtraction term for the full fixed-order cross section $\mathrm{d}\sigma^{FO}$ in the second term, such that the difference in square brackets is a nonsingular power correction. We will refer to the outcome of eq. (7.111) as $N^3LL^{(0+L)}+NNLO_0$ when the resummed LP hadronic structure functions at N^3LL are combined with the exact leptonic tensor as discussed in section 7.2.4, and matched to the fixed $\mathcal{O}(\alpha_s^2)$ $NNLL_0$ result. When instead evaluating the leptonic tensor at strict LP, we refer to it as $N^3LL^{(0)}+NNLO_0$, in which case the fiducial power corrections are only included through the fixed-order matching. The analogous notation is used at lower orders.

Approaching $q_T \sim Q$, the q_T resummation must be turned off, while in the canonical region $q_T \ll Q$ the resummation scales should be exactly equal to the canonical b_T space scales in eq. (2.209). To achieve this, we use the hybrid profile scales constructed in

chapter 4. We choose central scales as

$$\mu_H = \nu_B = \mu_{\rm FO}\,, \qquad \mu_B = \mu_S = \nu_S = \mu_{\rm FO}\, f_{\rm run}\Big(\frac{q_T}{Q}, \frac{b_0}{b_T\, Q}\Big)\,, \qquad \mu_0 = \frac{b_0}{b_T}\,, \qquad (7.112)$$

where the hybrid profile function $f_{\rm run} \equiv f_{\rm run}^{\rm II}$ was given in eq. (4.22). It controls the amount of resummation by adjusting the slope of the scales in b_T space as a function of q_T/Q. Note that in contrast to chapter 4, we do not require a deformation away from the canonical scales to regulate the Landau pole at large b_T, but instead rely on the replacement in eq. (7.109), so the scales can stay canonical all the way down to $b_0/b_T \to 0$. For our central results, we use the transition points $(x_1, x_2, x_3) = (0.3, 0.6, 0.9)$. Our central profiles in b_T space as used in this chapter are illustrated for different values of q_T in figure 7.5.

7.3.3 Estimate of perturbative uncertainties

We identify several sources of perturbative uncertainties, which we estimate as follows. In the limit $q_T \ll Q$, the perturbative uncertainty is driven by the combined uncertainty from truncating the expansion of the soft, beam, and rapidity anomalous dimensions. To estimate them, we adopt the set of profile scale variations introduced for the SCET$_{\rm II}$-like jet veto in ref. [67] as applied to q_T resummation in chapter 4. The explicit variations for $\mu_X \equiv \mu_X^{\rm II}$ were given in eq. (4.26). Dropping combinations of scale variations that vary the resummed logarithm by a factor of four, we are left with 36 different scale variations. By taking their maximum envelope, we obtain an estimate of the resummation uncertainty $\Delta_{\rm res}$.

Second, we estimate the fixed-order perturbative uncertainty $\Delta_{\rm FO}$ from the maximum envelope of overall variations of $\mu_{\rm FO}$ by a factor of two. These variations are inherited by all the resummation scales in eq. (7.112), so they leave the resummed logarithms invariant. Third, we estimate the inherent uncertainty $\Delta_{\rm match}$ in our matching procedure eq. (7.111) by taking the maximum envelope of explicit variations of the transition points x_i,

$$(x_1, x_2, x_3) = \big\{(0.4, 0.75, 1.1),\, (0.2, 0.45, 0.7),\, (0.4, 0.55, 0.7),\, (0.2, 0.65, 1.1)\big\}\,. \qquad (7.113)$$

Finally, we consider two independent variations of $\Lambda_{\rm fr} = \{0.8, 1.5\}\,{\rm GeV}$ away from our central choice $\Lambda_{\rm fr} = 1\,{\rm GeV}$ as a rough estimate of the uncertainty Δ_Λ in our nonperturbative prescription. Note that at variance with chapter 4, where the variation of the nonperturbative parameter $b_{\rm max}$ entering the resummation scales was grouped with the overall resummation uncertainty (yielding a total of 38 variations), we keep variations of $\Lambda_{\rm fr}$ separate in this chapter because it amounts to a physical parameter that parametrizes our nonperturbative model rather than a resummation scale. For the same reason we only vary it in a reasonable physical range instead of the factor of two conventionally applied to resummation scales.

Combining all sources of uncertainty in quadrature, we take

$$\Delta_{\rm total} = \sqrt{\Delta_{\rm res}^2 + \Delta_{\rm FO}^2 + \Delta_{\rm match}^2 + \Delta_\Lambda^2} \qquad (7.114)$$

as an estimate of the total (perturbative) uncertainty on our results.

7.4 Resumming fiducial power corrections

As discussed in section 7.2.4, fiducial power corrections arise entirely from the leptonic tensors $L_i(q, \mathcal{O}, \Theta)$, and accordingly can be treated exactly in the factorization by keeping the L_i exact. In this section, we consider three applications to discuss this mechanism in more detail, namely the q_T spectrum with fiducial cuts (section 7.4.2), the lepton transverse momentum distribution (p_T^ℓ) (section 7.4.3), and the ϕ^* observable (section 7.4.4). In all cases, we consider our primary examples of $Z \to \ell^+\ell^-$ or $W \to \ell\nu$.

7.4.1 Numerical inputs and computational setup

All our numerical results in this and the following sections are obtained using the following setup. We use the `CT18NNLO` [112] PDF set, and correspondingly use the three-loop running to obtain the numerical value of α_s at any required scale with $\alpha_s(91.1870) = 0.118$ as starting point. We use the same PDF also at lower orders, which is consistent and allows us to exhibit the genuine size of perturbative corrections.

For the resonant W and Z propagators, we work in the fixed-width pole scheme. We use the following electroweak parameters [25][10]

$$
\begin{aligned}
m_Z &= 91.1535 \,\text{GeV}\,, & \Gamma_Z &= 2.4943 \,\text{GeV}\,, \\
m_W &= 80.3580 \,\text{GeV}\,, & \Gamma_W &= 2.0843 \,\text{GeV}\,, \\
G_F &= 1.1663787 \times 10^{-5} \,\text{GeV}^{-2}\,,
\end{aligned}
\tag{7.115}
$$

$$
V_{\text{CKM}} = \begin{pmatrix} V_{ud} & V_{us} & V_{ub} \\ V_{cd} & V_{cs} & V_{cb} \\ V_{td} & V_{ts} & V_{tb} \end{pmatrix} = \begin{pmatrix} 0.97446 & 0.22452 & 0.00365 \\ 0.22438 & 0.97359 & 0.04214 \\ 0.00896 & 0.04133 & 0.999105 \end{pmatrix}\,.
\tag{7.116}
$$

For the electroweak couplings, we use the G_μ scheme, with the values for α_{em} and $\sin^2\theta_w$ obtained from m_W, m_Z, and G_F as

$$
\sin^2\theta_w = 1 - \frac{m_W^2}{m_Z^2} = 0.22284\,,
$$

$$
\alpha_{\text{em}} \equiv \alpha_\mu = \frac{\sqrt{2}G_F}{\pi} m_W^2 \left(1 - \frac{m_W^2}{m_Z^2}\right) = \frac{1}{132.357}\,.
\tag{7.117}
$$

All factorized cross sections, both at fixed order and including resummation up to N^3LL accuracy as described in section 7.3 are obtained from the `C++` library `SCETlib` [8]. By default we use the CS tensor decomposition, and LP cross sections including fiducial power corrections are denoted as $\sigma^{(0+L)}$, while those at strict LP without fiducial power corrections

---

[10]The pole-scheme values are converted from the on-shell ones using

$$
m_V = m_V^{\text{OS}} \left[1 + (\Gamma_V^{\text{OS}}/m_V^{\text{OS}})^2\right]^{-1/2}\,, \qquad \Gamma_V = \Gamma_V^{\text{OS}} \left[1 + (\Gamma_V^{\text{OS}}/m_V^{\text{OS}})^2\right]^{-1/2}\,.
$$

are denoted by $\sigma^{(0)}$. We have also implemented alternative tensor decompositions using eq. (7.103), in particular the one that corresponds to the GJ frame, and will denote cross sections evaluated using this choice as $\sigma_{\mathrm{GJ}}^{(0+L)}$. `SCETlib` uses the `Cuba 4.2` library [490, 491] for adaptive multi-dimensional integration over Q and Y, combined with q_T integrals whenever they cannot be performed analytically. To perform oscillatory Bessel integrals for inverse Fourier transforms we use a double-exponential method for oscillatory integrals [492–494].

The integral over the leptonic phase space appearing in eq. (7.46),

$$\int_{-1}^{1} \mathrm{d}\cos\theta \int_{0}^{2\pi} \mathrm{d}\varphi \, g_i(\theta, \varphi) \, \delta[\mathcal{O} - \hat{\mathcal{O}}(q, \theta, \varphi)] \, \hat{\Theta}(q, \theta, \varphi) \,, \qquad (7.118)$$

is carried out semi-analytically as follows. We focus on binned observables $\hat{\Theta}(q, \theta, \varphi)$ and assume that the differential measurement $\mathcal{O}$ on the decay products is being integrated over. We assume that the measurement cuts and bins $\hat{\Theta}(q, \theta, \varphi)$ evaluate to 1 when all cuts are passed and 0 otherwise, i.e., we take it to be a product of θ functions. An explicit dependence on θ or φ, e.g. to apply angular projections, can also easily be accommodated, but this is not needed for our purposes here. For given values of q and φ, we first determine all intervals in $\cos\theta$ that pass the given cuts. Notably, for all observables considered here ($p_{T1,2}$, $\eta_{1,2}$, ϕ^*, and any of their combinations), the interval boundaries can be evaluated analytically even for nonzero q_T. The integral over $\cos\theta$ over these intervals is then carried out analytically. The remaining integral over φ is performed by adaptive numerical integration. In practice, the sum over hadronic structure functions i, see eq. (7.88), can be pulled under the integral in eq. (7.118) because the structure functions only depend on the given value of q, so the decay phase-space boundaries only have to be determined once. Typical evaluation times even for complicated phase-space volumes are in the few-millisecond range on a single Intel® Core™ `i5-7200U` CPU @ 2.50 GHz for a target relative numerical precision of 10^{-7}. The algorithm is not restricted to the leading-power structure functions, but can also be used standalone with generic hadronic structure functions that are provided.

Fixed-order results for q_T and ϕ^* at LO_1 and NLO_1 for the relevant Born+1-parton cross sections are obtained from `MCFM 8.0` [330, 332, 495]. These results are used in the fixed-order matching. In addition, they are used to obtain q_T (or ϕ^*) integrated cross sections at NLO_0 and NNLO_0 by combining them with q_T (or ϕ^*) subtractions including fiducial power corrections supplied by `SCETlib`. This setup is discussed in more detail in section 5 of ref. [6]. The inclusion of fiducial power corrections in the subtractions is essential to obtain numerically stable results down to very small q_T and ϕ^* and for p_T^ℓ near the Jacobian peak.

7.4.2 q_T spectrum with fiducial cuts

We first discuss the impact of fiducial cuts on the Drell-Yan q_T spectrum. We consider the standard kinematic selection cuts of requiring a minimum transverse momentum $p_T^{\min}$ and

maximum rapidity $\eta_{\max}$ of the final-state leptons,

$$\Theta: \qquad p_{T,i} \geq p_T^{\min}, \quad |\eta_i| \leq \eta_{\max}, \tag{7.119}$$

where $p_{T,i}$ and η_i with $i = 1, 2$ are the transverse momentum and pseudorapidity of the two leptons.

Origin of power corrections

The $p_T^{\min}$ cut was already discussed in detail in ref. [459]. Here, we briefly review the key steps and results, and in addition discuss the rapidity cut. A useful parametrization of the total momentum q^μ and the lepton momenta $p_{1,2}^\mu$ in the lab frame is

$$\begin{aligned}
q^\mu &= \left(m_T \cosh Y, \, q_T, \, 0, \, m_T \sinh Y \right), \\
p_1^\mu &= p_{T,1} \left(\cosh(Y + \Delta y), \, \cos\psi, \, \sin\psi, \, \sinh(Y + \Delta y) \right), \\
p_2^\mu &= q^\mu - p_1^\mu,
\end{aligned} \tag{7.120}$$

where $m_T = (Q^2 + q_T^2)^{1/2}$. As before, we neglect the lepton masses and align the total transverse momentum $\vec{q}_T$ with the x-axis. We denote the azimuthal angle of the first lepton in the lab frame as ψ to distinguish it from the CS angle φ, and write its rapidity as $y_1 = Y + \Delta y$. Momentum conservation determines p_2^μ, and fixes the transverse momenta and rapidities of the leptons to

$$\begin{aligned}
p_{T,1} &= \frac{Q^2/2}{m_T \cosh(\Delta y) - q_T \cos\psi}, & \eta_1 &= Y + \Delta y, \\
p_{T,2} &= \sqrt{p_{T,1}^2 - 2 q_T \, p_{T,1} \cos\psi + q_T^2}, & \eta_2 &= Y + \frac{1}{2} \ln \frac{m_T - p_{T,1} e^{+\Delta y}}{m_T - p_{T,1} e^{-\Delta y}}.
\end{aligned} \tag{7.121}$$

For compactness, here we do not substitute $p_{T,1}$ in the expressions for $p_{T,2}$ and η_2. The two-particle phase space defined in eq. (2.58) then takes the form

$$\mathrm{d}\Phi_L(q) = \frac{p_{T,1}^2}{8\pi^2 Q^2} \, \mathrm{d}\psi \, \mathrm{d}\Delta y. \tag{7.122}$$

The integrated phase space with the cuts in eq. (7.119) can now be written as

$$\begin{aligned}
\Phi_L(q, p_T^{\min}, \eta_{\max}) &= \int \mathrm{d}\Phi_L(q) \, \theta\!\left(p_{T,1} \geq p_T^{\min}\right) \theta\!\left(p_{T,2} \geq p_T^{\min}\right) \theta\!\left(|\eta_1| \leq \eta_{\max}\right) \theta\!\left(|\eta_2| \leq \eta_{\max}\right) \\
&= \int_0^{2\pi} \mathrm{d}\psi \int_{-\infty}^{\infty} \mathrm{d}\Delta y \, \frac{p_{T,1}^2}{8\pi^2 Q^2} \\
&\quad \times \theta\!\left(\min\{p_{T,1}, p_{T,2}\} \geq p_T^{\min}\right) \theta\!\left(\max\{|\eta_1|, |\eta_2|\} \leq \eta_{\max}\right).
\end{aligned} \tag{7.123}$$

The integrand in eq. (7.123) depends on q_T only through the combinations q_T^2 and $q_T \cos\psi$. Thus, the expansion of the integrand in the limit $q_T \ll Q$ can only yield linear fiducial corrections if the ψ integral does not average out. This is equivalent to requiring that the cuts break azimuthal symmetry, as otherwise the ψ integral can always be trivially carried

out, such that all odd powers of $q_T \cos \psi$ integrate to zero and only quadratic corrections in $(q_T/Q)^2$ arise. Inclusive measurements are a special case, as without cuts $\Phi_L(q)$ can only depend on q^2.

To see this mechanism explicitly for cuts on p_T and η, we expand the lepton transverse momenta and rapidities in eq. (7.121) in $q_T/Q \sim \lambda$,

$$
\begin{aligned}
p_{T,1} &= \frac{Q}{2\cosh \Delta y} \left[1 + \frac{q_T}{Q} \frac{\cos \psi}{\cosh \Delta y} + \mathcal{O}(q_T^2/Q^2) \right], \\
p_{T,2} &= p_{T,1} - q_T \cos \psi + \mathcal{O}(q_T^2/Q^2), \\
\eta_1 &= Y + \Delta y, \\
\eta_2 &= Y - \Delta y - 2\frac{q_T}{Q} \cos \psi \sinh \Delta y + \mathcal{O}(q_T^2/Q^2).
\end{aligned}
\tag{7.124}
$$

All observables in eq. (7.124) have a well-defined, nonvanishing LP limit as $q_T \to 0$, and the first correction is proportional to $q_T \cos \psi$. Since at $q_T = 0$, ψ and φ coincide, we immediately find that the fiducial q_T spectrum obeys azimuthal symmetry at leading power, so the discussion in section 7.2.4 applies.

Naively, one might also expect that all linear fiducial corrections vanish upon integration over ψ. However, this is spoiled by the minimum and maximum in the θ functions in eq. (7.123), as can be easily seen for the $p_T^{\min}$ cut. For $\cos \psi > 0$, one has $p_{T,1} > p_{T,2}$, and thus the θ function in eq. (7.123) only restricts $p_{T,2}$. Vice versa, for $\cos \psi < 0$ it is $p_{T,1}$ that is constrained. This leads to two different integrands of the ψ integral in the two integration regions, leading to a nonvanishing ψ integral. This shows that the azimuthal symmetry is explicitly broken at $\mathcal{O}(\lambda)$ leading to linear fiducial power corrections. However, it also shows that if one were to only apply cuts to one of the leptons while being fully inclusive in the other, no linear power corrections from the cuts would arise, since the ψ integral would average out when integrated against the $g_{-1,2,4,5}(\theta, \varphi)$ (using again that the difference between ψ and φ is itself of order q_T).

The situation is more complicated for the rapidity cut. Determining the transition point of the maximum in the corresponding θ function in eq. (7.123), i.e. the value ψ_{tp} for which $|\eta_1| = |\eta_2|$, we find that

$$
\cos \psi_{\mathrm{tp}} = \frac{Q}{2q_T} \frac{\sinh(2Y)}{\sinh(2Y + \Delta y)} \times \left[1 + \mathcal{O}(q_T^2/Q^2) \right].
\tag{7.125}
$$

If $|\cos \psi_{\mathrm{tp}}| \geq 1$, then the θ function in eq. (7.123) only restricts either $|\eta_1|$ or $|\eta_2|$ but not both for the whole ψ range. In this case, the rapidity cut does not break azimuthal symmetry.

For small but nonvanishing values of q_T, the Q/q_T scaling in eq. (7.125) can be overcome by a sufficiently small value of the vector-boson rapidity Y. To be precise, eq. (7.125) has a solution in the physical range $|\cos \psi_{\mathrm{tp}}| < 1$ when

$$
q_T > \frac{Q}{2} \left| \frac{\sinh(2Y)}{\sinh(2Y + \Delta y)} \right|.
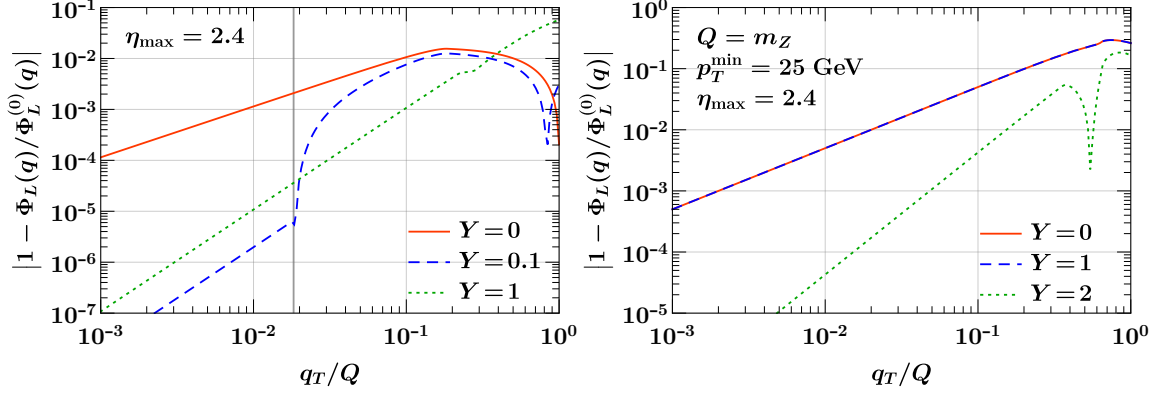\tag{7.126}
$$

Figure 7.6: Relative difference of the exact dilepton phase space with fiducial cuts to its LP (Born) limit, for various values of the total dilepton rapidity Y for a pure rapidity cut (left) and both rapidity and p_T cuts (right). The thick vertical line on the left shows transition point in eq. (7.126) for $Y = 0.1$.

Note that the η_1 constraint always requires that $|Y + \Delta y| \leq \eta_{\max}$. Furthermore, we are only interested in the $q_T \ll Q$ limit, which implies that eq. (7.126) only becomes important when $|Y| \ll 1$. Hence, linear fiducial corrections will only arise in the region

$$\frac{q_T}{Q} \gtrsim \frac{q_T^{\mathrm{tp}}}{Q} \equiv \frac{|Y|}{\sinh(\eta_{\max})}, \qquad |Y| \ll 1, \qquad (7.127)$$

while for $q_T \lesssim q_T^{\mathrm{tp}}$ only quadratic power corrections arise. Note that in the region $q_T \sim q_T^{\mathrm{tp}} \ll Q$ the standard power counting breaks down, as one has to simultaneously expand $|Y| \sim q_T/Q \ll 1$. This is an example of a leptonic fiducial power correction as discussed in section 7.2.4, where it is crucial to keep the lepton phase space exact to correctly account for both small scales q_T/Q and $|Y|$. In practice, the size of this region is of $\mathcal{O}(|Y|)$ and thus small by construction, and hence its contribution to the cross section when integrated over or binned in Y is suppressed as well.

To illustrate and validate our observations, we have numerically implemented the exact phase space with cuts in eq. (7.123). In figure 7.6, we show the relative difference of the dilepton phase space as a function of q_T/Q for the cut $\eta_{\max} = 2.4$ (left) and the combined cut $p_T^{\min} = 25$ GeV and $\eta_{\max} = 2.4$ (right), for different values of the total rapidity Y and fixed $Q = m_Z$. In the left plot, one can clearly see that for $Y = 0$ one has a linear power correction for small q_T up to $q_T/Q \sim 0.1$ (red solid line). For the slightly larger value $Y = 0.1$ (blue dashed line), we observe quadratic corrections up to the transition point $q_T^{\mathrm{tp}}/Q \approx 0.2$, indicated by the thick vertical line, while above this transition the correction has no simple scaling behavior. Finally, for the relatively large value $Y = 1$ one has quadratic corrections essentially throughout the whole q_T spectrum (green dotted line). Also note that, in general, the corrections to the phase space are rather small, as even for $Y = 0.1$ they do not exceed 1% for $q_T/Q < 0.1$.

In the right plot in figure 7.6, we apply both $\eta_{\max}$ and $p_T^{\min}$ cuts. For small values of Y,

the $p_T^{\min}$ cut is a stronger constraint on the phase space than the $\eta_{\max}$ cut. Hence, the two curves for $Y = 0$ (red solid) and $Y = 1$ (blue dashed) are equal, as the $p_T^{\min}$ constraint is independent of rapidity. For large $Y \sim \eta_{\max}$, the rapidity cut dominates over the p_T cut, as illustrated for $Y = 2$ (green dotted), and one only has quadratic power corrections.

Numerical results

Having explicitly demonstrated that linear power corrections to the q_T spectrum arise from fiducial cuts on the final-state leptons, we now verify that they can indeed be captured in the factorization theorem by keeping the lepton kinematics exact, as discussed in section 7.2.4. In the following, we will always consider the fiducial cut

$$p_T^\ell \geq 25 \text{ GeV}, \quad |\eta_\ell| \leq 2.4, \tag{7.128}$$

as employed in the CMS Drell-Yan measurement at 13 TeV [31].

In figure 7.7, we show the q_T spectrum for $Q = m_Z$ at NLO_0, both without (left) and with (right) fiducial cuts. In both figures, the red points illustrate the full NLO_0 result, while the solid blue line shows the result at $\sigma^{(0)}$ (left) and at $\sigma^{(0+L)}$ (right). The various dotted and dashed lines show the differences between the full result and different singular limits. In the inclusive case (left panel), there are no linear power corrections, and thus $\sigma - \sigma^{(0)}$ (green, dashed) scales quadratically in q_T, as expected. With fiducial cuts (right panel), $\sigma - \sigma^{(0)}$ (gray, dotted) clearly suffers from linear power corrections, and as explained before, these linear corrections can be accounted for by keeping the leptonic tensor exact. This is illustrated by the green-dashed line, which shows the difference $\sigma - \sigma^{(0+L)}$ between the exact and NLP result, and only depends quadratically on q_T. In particular, the size of these corrections is comparable to the quadratic corrections in the inclusive case. The orange, dot-dashed curve shows the difference $\sigma_{\mathrm{GJ}}^{(0+L)} - \sigma^{(0+L)}$ between two choices of the tensor decomposition, corresponding to the CS frame and the GJ frame. This difference scales quadratically in q_T, confirming that the ambiguity from the choice of tensor decomposition is quadratically suppressed. Moreover, we observe that this ambiguity is numerically much smaller than $\sigma^{(0+L)}$ itself, indicating that it may be completely negligible in practice.

It is also interesting to study the impact of the NLP corrections on the resummed q_T spectrum. In the top-left panel of figure 7.8, we show the difference between the LP and the exact q_T spectrum at NLO_0 (blue, short-dashed) and NNLO_0 (red, long-dashed). For reference, the gray line shows our best prediction σ_* at $\mathrm{N^3LL}^{(0+L)} + \mathrm{NNLO}_0$, scaled down to 5% of its original size. At both NLO_0 and NNLO_0, the power corrections diverge as $q_T \to 0$ due to the overall $1/q_T$ behavior (compared to $1/q_T^2$ at LP). The opposite signs at small q_T also illustrates the poor perturbative convergence in this regime.

In the top-right panel of figure 7.8, we show the difference between the LP q_T spectrum and the resummed and matched q_T spectrum, at $\mathrm{NLL}^{(0+L)}$ (green, dotted), $\mathrm{NNLL}^{(0+L)} + \mathrm{NLO}_0$ (blue, dashed) and $\mathrm{N^3LL}^{(0+L)} + \mathrm{NNLO}_0$ (red, solid). Since the resummation includes the linear power corrections, the divergence as $q_T \to 0$ is cured, and we observe very good perturbative convergence between the different resummed predictions.
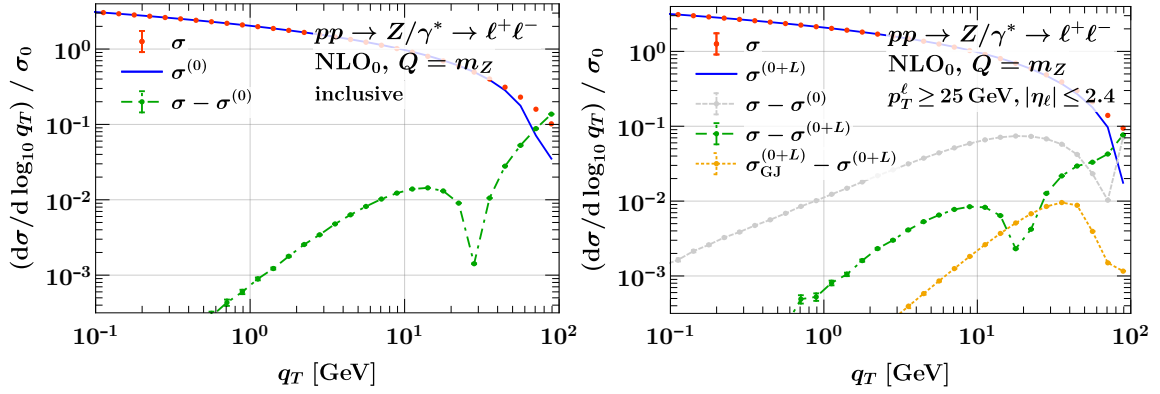
Figure 7.7: Power corrections for the q_T spectrum in Drell-Yan production, inclusive in the decay products (left) and with fiducial cuts (right).
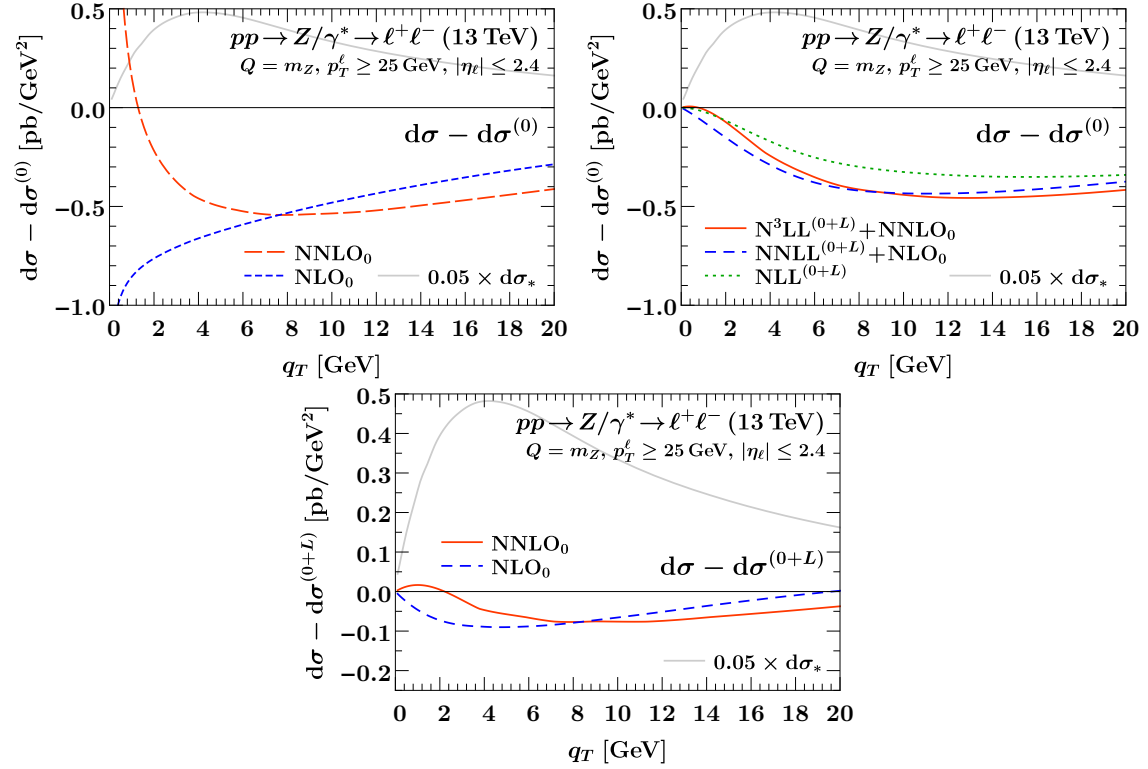
Figure 7.8: Breakdown of subleading-power contributions to the fiducial Drell-Yan q_T on the resonance, $Q = m_Z$. We compare the sum of all subleading power contributions, treating the linear fiducial power corrections at fixed order (top left) or resumming them (top right). Our best prediction $d\sigma_*$ for the total spectrum at $\mathrm{N^3LL}^{(0+L)}+\mathrm{NNLO_0}$ is indicated as a light gray line for reference, scaled down to 5% of its original size. In the bottom row we restrict to the remaining nonsingular (quadratic) power corrections, which are finite for $q_T \to 0$ (note the difference in vertical scale).

Finally, in the bottom panel of figure 7.8 we show the difference between the NLP and the exact q_T spectrum at NLO_0 (blue, short-dashed) and NNLO_0 (red, long-dashed), again including our best prediction σ_* for reference. Since all terms diverging as $1/q_T^2$ or $1/q_T$ are included in $\sigma^{(0+L)}$, this difference is finite as $q_T \to 0$, and the overall size is much smaller compared to the top left panel, indicating that corrections beyond the linear NLP limit can be safely included at fixed order.

Given the large effect that the resummation of fiducial power corrections has on the q_T spectrum at small q_T, it would be very interesting to investigate whether a net resummation effect on the *total* fiducial cross section remains after integration over q_T, as would be relevant for PDF determinations from fiducial Z and W rapidity spectra. It has been argued that recoil ambiguities might prevent a first-principle calculation of these effects [496], but since the ambiguity from the choice of tensor decomposition is fairly small, and vanishes as soon as the resummation is fully turned off, it is not unlikely that a surviving net effect is unambiguous and can be calculated.

7.4.3 Lepton p_T spectrum

We next study the distribution in the lepton transverse momentum p_T^ℓ. To be concrete, we consider $W^\pm \to \ell^\pm \nu_\ell$, for which p_T^ℓ is an essential observable. For simplicity, we do not consider any additional fiducial cuts. This serves as a prototypical example of the appearance of leptonic power corrections near a radiation-sensitive edge of Born phase space as discussed in section 7.2.4, which in this case happens near the Jacobian peak at $p_T^\ell \sim Q/2$.

Origin of power corrections

Using the parametrization of the lepton momenta in terms of CS angles in eq. (7.41), the lepton p_T^ℓ can be expressed as

$$p_T^\ell = \frac{Q}{2}\sqrt{(\gamma s_\theta c_\varphi + \epsilon)^2 + s_\theta^2 s_\varphi^2} \equiv \frac{Q}{2}\kappa, \qquad \epsilon = \frac{q_T}{Q}, \quad \gamma = \sqrt{1+\epsilon^2}, \tag{7.129}$$

where $s_\theta \equiv \sin\theta$, $s_\varphi \equiv \sin\varphi$, $c_\varphi \equiv \cos\varphi$. We also introduced the variable $\kappa = 2p_T^\ell/Q$ to parameterize the distance of p_T^ℓ from the Jacobian peak at $p_T^\ell = Q/2$, which will be useful in the following. Eq. (7.129) can be easily solved for s_θ, with physical solutions constrained by $0 \le s_\theta \le 1$. In the following, we restrict ourselves to the case $\kappa > \epsilon$, which will be the relevant region to describe large p_T^ℓ. In this case, the only physical solution for s_θ is given by

$$\sin(\theta_\varphi) = s(c_\varphi) = -\beta\gamma\,\epsilon c_\varphi + \sqrt{\Delta}\,, \tag{7.130}$$

where for brevity we introduced the abbreviations

$$\Delta = (\beta\gamma\,\epsilon c_\varphi)^2 + \beta(\kappa^2 - \epsilon^2)\,, \quad \beta = \frac{1}{1+(\epsilon c_\varphi)^2}\,. \tag{7.131}$$

The leptonic structure functions defined in eq. (7.46) are then given by

$$
\frac{L_i(q, p_T^\ell)}{L_{\pm(i)}(q^2)} = \frac{3p_T^\ell}{4\pi Q^2} \int_0^{2\pi} \mathrm{d}\varphi \, \frac{\beta}{\sqrt{\Delta}} \, \theta\Big(c_\varphi - \frac{\kappa - \gamma}{\epsilon}\Big) \int_0^\pi \mathrm{d}\theta \, s_\theta \, g_i(\theta, \varphi) \, \delta[s_\theta - s(c_\varphi)] . \qquad (7.132)
$$

Note that eq. (7.132) still shows the full dependence on φ and s_θ, such that one could easily reinstate fiducial cuts.

Eq. (7.130) yields two solutions for θ_φ, related by $\theta \to \pi - \theta$. Since the $g_i(\theta, \varphi)$ for $i = 1, 4, 6$ are odd under this transformation, eq. (7.132) immediately vanishes for these cases. In all other cases, the g_i are even under this transformation, such that we obtain

$$
\frac{L_i(q, p_T^\ell)}{L_{\pm(i)}(q^2)} = \frac{3p_T^\ell}{2\pi Q^2} \int_0^{2\pi} \mathrm{d}\varphi \, \frac{\beta}{\sqrt{\Delta}} \, \theta\Big(c_\varphi - \frac{\kappa - \gamma}{\epsilon}\Big) \frac{s(c_\varphi) \, g_i(\theta_\varphi, \varphi)}{[1 - s(c_\varphi)^2]^{1/2}} \qquad (i \neq 1, 4, 6), \quad (7.133)
$$

where θ_φ can be either of the two physical solutions defined by eq. (7.130).

It is now straightforward to expand in ϵ to study the $q_T \to 0$ limit, which yields

$$
\begin{aligned}
\frac{L_i(q, p_T^\ell)}{L_{\pm(i)}(q^2)} &= \frac{3p_T^\ell}{2\pi Q^2} \frac{\theta(1 - \kappa)}{\sqrt{1 - \kappa^2}} \int_0^{2\pi} \mathrm{d}\varphi \, g_i(\arcsin \kappa, \varphi) + \mathcal{O}(\epsilon) \\
&= \frac{3p_T^\ell}{Q^2} \frac{\theta(1 - \kappa)}{\sqrt{1 - \kappa^2}} \begin{cases} 2 - \kappa^2, & i = -1, \\ \kappa^2, & i = 0, \\ 0, & i = 1, \dots, 7. \end{cases}
\end{aligned} \qquad (7.134)
$$

The constraint $\kappa \leq 1$ reflects the strict bound $p_T^\ell \leq Q/2$ in the Born limit. We also recover that at LP only the $i = -1, 0$ contributions survive. The $i = 4$ contribution, which in principle can contribute at LP and gives rise to the forward-backward asymmetry, vanishes due to the symmetry of p_T^ℓ under $\theta \to \pi - \theta$.

Before proceeding, it is instructive to illustrate the phase space differential in p_T^ℓ, which is closely related to $L_i(q, p_T^\ell)$ and provides a bound on the $L_i(q, p_T^\ell)$ since all $g_i(\theta, \varphi)$ are bounded. It can be evaluated more easily using the parametrization of the lepton momenta given in eq. (7.120). After some effort, one obtains

$$
\begin{aligned}
\frac{\mathrm{d}\Phi_L(q)}{\mathrm{d}p_T^\ell} &= \int \mathrm{d}\Phi_L(q) \, \delta\big[p_T^\ell - p_T^\ell(\Phi_L)\big] \\
&= \begin{cases} \dfrac{1}{2\pi^2 Q} \dfrac{\alpha\kappa}{\sqrt{\alpha^2 - \kappa^2}} K\!\left[-\dfrac{(1 - \alpha^4)\kappa^2}{\alpha^2 - \kappa^2}\right] & 0 < \kappa \leq \alpha, \\[4mm] \dfrac{1}{2\pi^2 Q} \dfrac{\alpha\kappa}{\sqrt{\kappa^2 - \alpha^2}} K\!\left[\dfrac{\alpha^2(1 - \alpha^2\kappa^2)}{\alpha^2 - \kappa^2}\right], & \alpha < \kappa < 1/\alpha, \\[4mm] 0 & \kappa \geq 1/\alpha \end{cases}
\end{aligned} \qquad (7.135)
$$

Here, $\alpha = \sqrt{1 + \epsilon^2} - \epsilon$, and $K(x)$ is the complete elliptic integral of the first kind. The appearance of three distinct regions can easily be understood from eq. (7.133): For $\kappa > 1/\alpha$, the θ function in eq. (7.133) becomes incompatible with $c_\varphi \leq 1$, while for $\kappa < \alpha$ it imposes no constraint in addition to $c_\varphi \geq -1$.
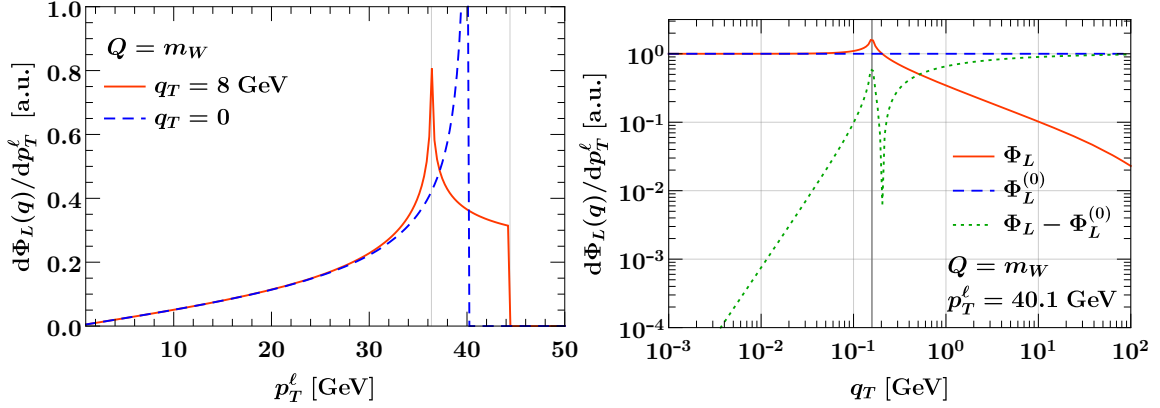
Figure 7.9: Leptonic phase space $\mathrm{d}\Phi_L(q)/\mathrm{d}p_T^\ell$, as a function of p_T^ℓ for fixed q_T (left) and as a function of q_T for fixed $p_T^\ell = 40.1\,\mathrm{GeV}$ (right). In both cases we fix $Q = m_W = 80.358\,\mathrm{GeV}$. Left: The red solid curve shows the exact result for $q_T = 8\,\mathrm{GeV}$, and the blue dashed curve shows the $q_T = 0$ Born limit. Right: The red solid curve shows the exact phase space, the blue dashed line the LP limit, and the green dotted curve their difference.

In figure 7.9, we show the differential phase space in p_T^ℓ in eq. (7.135) for $Q = m_W$. In the left panel, we show the exact phase space as a function of p_T^ℓ for fixed $q_T = 8\,\mathrm{GeV}$ (red solid), with the gray vertical lines indicating the edges of the different regions in eq. (7.135). In the $q_T = 0$ LP limit (blue dashed), they collapse to the kinematic Born limit $p_T^\ell \le Q/2$. In the right panel, we fix $p_T^\ell = 40.1\,\mathrm{GeV}$ very close to the Born edge, and show the phase space as a function of q_T. The exact result is shown by the red curve, the $q_T = 0$ LP limit by the blue dashed line, and their difference by the green dotted line. The thick vertical line at $q_T = Q - 2p_T^\ell \equiv p_L$ shows the transition to the second region of eq. (7.135). For sufficiently small $q_T \ll p_L$, we see a clear (quadratic) power suppression, while near and above this value the power corrections become $\mathcal{O}(1)$. (The sharp dip in the green line is just an artefact of the logarithmic scale and the green line changing its sign.)

Clearly, expanding in $\epsilon \sim \lambda$ is only well-defined if $\kappa \ll 1$, i.e., away from the Jacobian peak $p_T^\ell \ll Q/2$. This is already evident from the divergence of eq. (7.134) as $\kappa \to 1$. As long as $\kappa \ll 1$, ϵ is the only small scale in the problem, which justifies expanding in ϵ and leads to at most linear fiducial power corrections. On the other hand, close to the Jacobian peak, the distance $p_L = Q - 2p_T^\ell$ emerges as an additional small scale, and the naive expansion in q_T is actually an expansion in q_T/p_L, which is only allowed for $q_T \ll p_L$ but breaks down for $p_L \sim q_T$. To illustrate this explicitly, we can expand in the regime $p_L \sim q_T$ by simultaneously counting both scales as small. To do so, we take

$$p_L = Q - 2p_T^\ell \sim \lambda Q, \qquad 1 - \kappa = \frac{p_L}{Q} \sim \lambda, \tag{7.136}$$

where as before $\epsilon = q_T/Q \sim \lambda$, such that formally $q_T/(Q - 2p_T^\ell) \sim 1$. With this replacement,

we can expand eq. (7.133) in λ,

$$\frac{L_i(q, p_T^\ell)}{L_{\pm(i)}(q^2)} = \frac{3}{4\pi} \frac{1}{\sqrt{2Q}} \int_0^{2\pi} d\varphi \, \frac{\theta(q_T c_\varphi + p_L)}{\sqrt{q_T c_\varphi + p_L}} \, g_i\left(\pi/2, \varphi\right) \times \left[1 + \mathcal{O}(\lambda)\right]. \qquad (7.137)$$

This vanishes for all g_i odd in φ, which only leaves $i = -1, 0, 2, 3$. This should be contrasted with the naive LP result in eq. (7.134), which only receives contributions from $i = -1, 0$. The $i = 2$ contribution is proportional to the double Boer-Mulders effect, which we can neglect, see the discussion below eq. (7.89). For $i = 3$ we have $W_3 \sim \mathcal{O}(\lambda)$, see table 7.1, which thus yields a linear power correction. Hence, we find the interesting effect that the proximity to the Jacobian peak induces sensitivity to new hadronic structure functions at $\mathcal{O}(\lambda)$, which do not contribute at $\mathcal{O}(\lambda)$ away from the peak region.

From eq. (7.137) it is evident that naively expanding in q_T near the Jacobian peak would amount to expanding in q_T/p_L, which is not allowed. However, eq. (7.137) is only valid near the peak, because by counting $p_L/Q \sim \lambda$ we have expanded away the dependence on $\kappa = 1 + \mathcal{O}(\lambda)$, which is not allowed away from the peak. Hence, to cover the full range of p_T^ℓ, we must not expand in p_L, while near the peak we must count $q_T \sim p_L$ to avoid inducing uncontrolled leptonic power corrections in q_T/p_L. Clearly, the simplest way to satisfy both requirements is to not expand at all and keep the exact result corresponding to eq. (7.133).

Finally, note that the breakdown of the naive power expansion around $p_T^\ell = Q/2$ does not immediately affect the leptonic tensor if we only consider a fiducial cut $p_T^\ell \geq p_T^{\min}$, since we can evaluate it as

$$\Phi_L(q, p_T^{\min}) = \int_{p_T^{\min}} dp_T^\ell \frac{d\Phi_L(q)}{dp_T^\ell} = \frac{1}{8\pi} - \int_0^{p_T^{\min}} dp_T^\ell \frac{d\Phi_L(q)}{dp_T^\ell}. \qquad (7.138)$$

Thus, the leptonic power corrections in this case scale as $q_T/(Q - 2p_T^{\min})$, and so as long as $p_T^{\min} \ll Q/2$, the effect of $p_T^{\min}$ can be treated as a linear fiducial power correction as discussed for the q_T spectrum with fiducial cuts in section 7.4.2.

Numerical results

There are two key insights from our analysis of the differential p_T^ℓ phase space. First, the p_T^ℓ spectrum near the Jacobian peak is directly sensitive to the small transverse momentum q_T of the decaying vector boson. This causes fixed-order predictions to become unreliable in this region, which is a well-known effect. Second, the strict $q_T \to 0$ limit by itself cannot describe the p_T^ℓ spectrum in this region, which means the strict LP q_T resummation is also insufficient. Both problems are cured simultaneously by combining the exact leptonic tensor, which encodes the exact decay kinematics and automatically retains all leptonic power corrections, with the q_T-resummed hadronic tensor, thus allowing us to obtain physical predictions around the Jacobian peak.

We illustrate this in figure 7.10 for the p_T^ℓ spectrum in $W^+ \to \ell^+ \nu_\ell$ decays, where we show the spectrum both at fixed order (left) and after resummation including fiducial
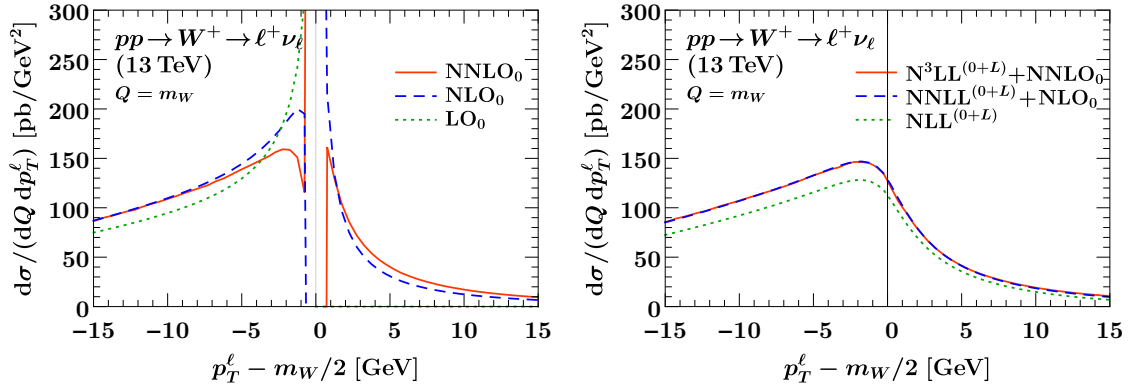
Figure 7.10: Lepton transverse momentum spectrum for on-resonance W^+ production at the LHC at fixed order (left) and including the resummation of fiducial power corrections to N^{3}LL (right). The horizontal axes shows the distance to the Jacobian peak at $p_T^\ell = m_W/2$.

power corrections (right). In both panels, the horizontal axis shows the distance of p_T^ℓ to the Jacobian peak at $p_T^\ell = m_W/2$, and to avoid smearing out the peak we consider the spectrum at a fixed point $Q = m_W$. The fixed-order spectrum (left) is shown at LO$_0$ (green dotted), NLO$_0$ (blue dashed), and NNLO$_0$ (red solid). The LO$_0$ result corresponds to Born kinematics and clearly shows the kinematic edge at $p_T^\ell = Q/2$. Starting at NLO$_0$, the W boson can have nonvanishing q_T, which opens up the phase space beyond the edge. However, in the vicinity of the edge, the fixed-order predictions become unstable due to the sensitivity to small q_T, which is clearly visible by the diverging NLO$_0$ and NNLO$_0$ curves, and in particular by the sign change between NLO$_0$ and NNLO$_0$ at $p_T^\ell \approx Q/2$.

In the right panel in figure 7.10, we show the resummed p_T^ℓ spectrum at NLL$^{(0+L)}$ (green dotted), NNLL$^{(0+L)}$+NLO$_0$ (blue dashed), and N^{3}LL$^{(0+L)}$+NNLO$_0$ (red solid). The resummation including leptonic power corrections cures the unphysical behaviour of the fixed-order results, yielding a well-behaved spectrum in the full p_T^ℓ range, with a resummed Sudakov shoulder at $p_T^\ell \approx m_W/2$. Note that the cross section beyond the edge is already populated at NLL$^{(0+L)}$ without any fixed-order matching. We stress that without including the exact leptonic tensor, the resummation would only affect the region $p_T^\ell < m_W/2$, and not cure the peak region. In fact, the results with strict LP resummation would look very similar to the pure fixed-order results, with the N^{3}LL$^{(0)}$+NNLO$_0$ essentially indistinguishable from the pure NNLO$_0$ result.

This is the first time that resummed N^{3}LL results for the p_T^ℓ spectrum are presented, and we observe extremely good perturbative convergence, with the results at NNLL$^{(0+L)}$+NLO$_0$ and N^{3}LL$^{(0+L)}$+NNLO$_0$ falling on top of each other. We leave a more detailed phenomenological analysis of the p_T^ℓ spectrum to future work.

7.4.4 ϕ^* spectrum

The ϕ^* observable was first proposed in ref. [497], extending earlier work on the a_T observable [498, 499]. Both observables are sensitive to small q_T, but promise better experimental

resolution than q_T itself due to being based on angular measurements, which are less susceptible to the momentum resolution of the individual lepton momenta than q_T itself.

The factorization and resummation for a_T was first studied in ref. [500] at NLL, and extended to both a_T and ϕ^* at NNLL+NLO in refs. [438, 501, 502], and also in refs. [503] including a study of nonperturbative contributions, and also more recently at N³LL+NNLO in refs. [363, 445]. None of these calculations incorporate the finite recoil of the dilepton system in the calculation of the ϕ^* observable, i.e. the employed definition of ϕ^* is only an approximation of the actually measured observable, as discussed below. The resummation with the exact definition of ϕ^* was considered in refs. [439, 446] at NNLL+NNLO and NNLL+NLO via parton-level MC integration of the leptonic final state.

Ref. [497] defines the two closely related observables ϕ^*_{CS} and ϕ^*_η. We only consider the latter, as it is more commonly used in experiments. It is defined as

$$\phi^* \equiv \phi^*_\eta = \tan(\phi_{\mathrm{acop}}/2)\,\sin\theta^*_\eta\,, \tag{7.139}$$

where the acoplanarity angle is $\phi_{\mathrm{acop}} = \pi - \Delta\varphi$, with $\Delta\varphi$ being the azimuthal opening angle between the leptons in the lab frame, and

$$\cos\theta^*_\eta = \tanh\frac{\eta_1 - \eta_2}{2}\,, \tag{7.140}$$

where $\eta_{1,2}$ are the two lepton rapidities.

Origin of power corrections

Using the parametrization of the lepton momenta in the Collins-Soper frame as given in eq. (7.41), eq. (7.139) can be written as

$$(\phi^*)^2 = \frac{8\kappa(\epsilon\sin\varphi\sin\theta)^2}{(\kappa - \epsilon^2 + \alpha^2)^2(\kappa + \epsilon^2 - \alpha^2 + 2)}\,,$$
$$\kappa^2 = (\epsilon^2 - \alpha^2)^2 + 4\epsilon^2\sin^2\theta\sin^2\varphi\,, \qquad \alpha^2 = \left(1 + \epsilon^2\cos^2\varphi\right)\sin^2\theta\,. \tag{7.141}$$

Note that ϕ^* is boost invariant and thus independent of Y, and can depend on q_T only through the dimensionless ratio $\epsilon = q_T/Q$. From eq. (7.141), one easily finds the special values

$$\phi^*|_{\theta=\pi/2} = \epsilon|\sin\varphi|\,, \qquad \lim_{\theta\to 0,\pi}\phi^* = \infty\,. \tag{7.142}$$

The singularity arises from the case where both momenta are parallel to each other in the transverse plane, such that $\phi_{\mathrm{acop}} = \pi$ and eq. (7.139) becomes ill-defined. Numerically, we have also tested that ϕ^* monotonically decreases with $|\sin\theta|$, such that ϕ^* can be uniquely inverted on the intervals $\theta \in [0, \pi/2]$ and $\theta \in [\pi/2, \pi]$, with the two solutions trivially related by $\theta_1 = \pi - \theta_2$.

Expanding eq. (7.141) in $\epsilon \ll 1$, one obtains the commonly employed approximation

$$\phi^{*\,(0)} = \epsilon\,|\sin\varphi|\,. \tag{7.143}$$

The monotonicity of ϕ^* with $|\sin\theta|$ implies that this is a lower bound to ϕ^*,[11] but from eq. (7.142) it follows that this bound is only saturated for $\theta = \pi/2$. It is thus natural to ask whether there is a better approximation of ϕ^*. From eq. (7.141), it is easy to see that ϕ^* only vanishes if either $\epsilon = 0$ or $\sin\varphi = 0$. Expanding eq. (7.141) in these limits, we find

$$
\begin{aligned}
(\phi^*)^2 &= \frac{\epsilon^2 \sin^2\varphi}{1 + \epsilon^2(1 - \sin^{-2}\theta)} + \mathcal{O}(\sin^4\varphi) \\
&= \epsilon^2 \sin^2\varphi \big[1 + \epsilon^2 \cot^2\theta + \mathcal{O}(\epsilon^4) \big] .
\end{aligned}
\tag{7.144}
$$

Note that the expansion in small ϵ in the second line can be recovered by reexpanding the small-$\sin\varphi$ limit, because in eq. (7.141) each term in ϵ either multiplies $\sin\varphi$ or is enhanced relative to $\epsilon \sin\varphi$. The first line in eq. (7.144) is ill-defined for $|\tan\theta| < \epsilon$ already at the leading $\mathcal{O}(\sin^2\varphi)$, while this singularity only appears at the second order in ϵ. Eq. (7.144) suggests that the fundamentally small quantity to be power counted is $\epsilon|\sin\varphi|$, not ϵ itself. In particular, any given value in ϕ^* can in principle receive contributions from arbitrarily large ϵ.

In figure 7.11, we compare the exact result for ϕ^* (red solid) to its leading expansions in small $\sin\varphi$ (blue dashed) and small ϵ (green dotted). We fix $\varphi = \pi/8$ and show results for $\epsilon = 0.25$ (left panel) and $\epsilon = 0.5$ (right panel). The gray vertical line shows the breakdown of the small-$\sin\varphi$ approximation at $\cos\theta = (1 + \epsilon^2)^{-1/2}$. Since ϕ^* is fairly insensitive to $\cos\theta$ in a rather large range of $\cos\theta$, the small-ϵ expansion is a fairly good approximation in that region. However, it quickly deteriorates for moderate to large $\cos\theta$. In contrast, the small-$\sin\varphi$ expansions follows the exact curve remarkably well, almost up to the point where it becomes ill-defined. At large $\cos\theta$, both approximations break down, as ϕ^* is driven by the small-θ behavior $\phi^* \sim 1/\theta^2$.

We find that the region $|\tan\theta| < \epsilon$ cannot be described by the expansion in small-$\sin\varphi$, which breaks down, or by the expansion small-ϵ, which assigns an artificially small value $\phi^{*(0)}$ in this region. However, this does not invalidate the LP description of ϕ^*, as this region of phase space is suppressed as $\mathcal{O}(\epsilon^2)$,

$$
\int \mathrm{d}\Phi_L(q)\, \theta(|\tan\theta| < \epsilon) = \frac{1}{8\pi}\big(1 - \sqrt{1 - \epsilon^2}\big) = \frac{\epsilon^2}{16\pi} + \mathcal{O}(\epsilon^4) .
\tag{7.145}
$$

Another important property of ϕ^* is that it is not azimuthally symmetric at LP due to its explicit dependence on φ. To identify which W_i contribute to ϕ^* at LP, we evaluate eq. (7.46) with the approximate observable in eq. (7.143), which yields

$$
\frac{\mathrm{d}\sigma}{\mathrm{d}Q^2 \mathrm{d}Y \mathrm{d}\cos\theta\, \mathrm{d}\phi^{*(0)}} = \frac{3Q}{16\pi E_{\mathrm{cm}}^2} \sum_{i=-1,0,2,4} L_{\pm(i)}(Q^2)\, g_i(\theta, 0)
$$
$$
\times \int_0^\infty \mathrm{d}b_T\, K_i(b_T Q \phi^{*(0)}) \tilde{W}_i(Q^2, Y, b_T) .
\tag{7.146}
$$

---

[11] This implies that a phase space generator producing events with $q_T \geq q_T^{\mathrm{min}}$ is guaranteed to correctly describe $\phi^* \geq q_T^{\mathrm{min}}/Q$.
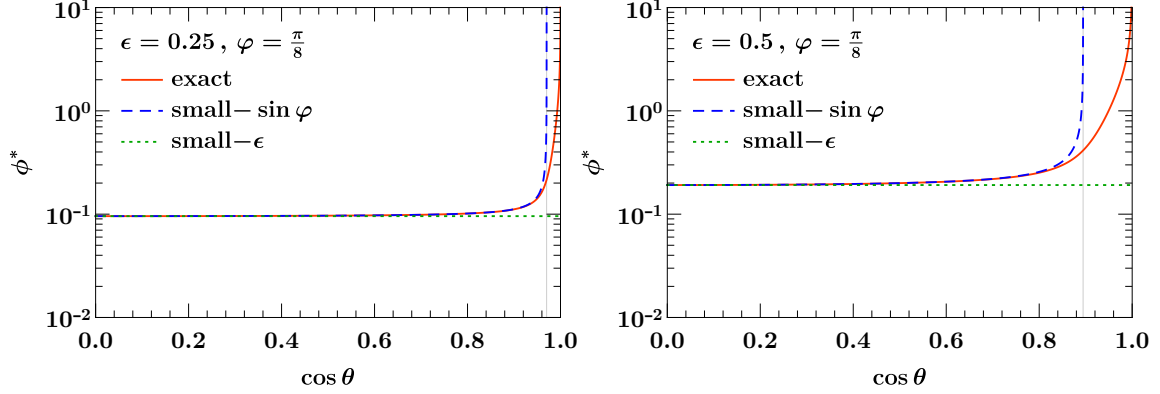
Figure 7.11: Comparison of the different expansions of ϕ^*, as given in eq. (7.144), as function of $\cos\theta$ for two different choices of ϵ and φ. The vertical gray line indicates the breakdown of the expansion in small $\sin\varphi$.

Here, the $\tilde{W}_i$ are the hadronic structure functions in Fourier space. In eq. (7.146), we have already carried out the integral over φ, which gives rise to kernels K_i, while we are still differential in $\cos\theta$. One can easily incorporate any LP fiducial cuts that depend on θ, but are independent of φ into eq. (7.146), which holds for most common cuts such as eq. (7.119).

The nonvanishing kernels entering eq. (7.146) are given by

$$K_{-1,0,4}(\beta) = \cos(\beta)\,, \qquad K_2(\beta) = \cos(\beta) + 2\beta\,\mathrm{si}(\beta)\,, \tag{7.147}$$

where $\mathrm{si}(\beta) = -\int_\beta^\infty \mathrm{d}t \, \sin t/t$ is the sine integral. The kernels for $i = 1, 3, 5, 6, 7$ vanish because the corresponding $g_i(\theta, \varphi)$ are odd in φ or under $\varphi \to \varphi + \pi$. Since $g_{-1,0,4}(\theta, \varphi)$ are independent of φ, they give rise to the same kernel $K_{-1,0,4}$. In contrast, W_2 is dressed with a different kernel K_2 due to the nontrivial φ dependence of $g_2(\theta, \varphi) \propto \cos(2\varphi)$. In particular, for $\beta \to \infty$ one has $K_2(\beta) \approx -\cos\beta = K_{-1,0,4}(\beta)$, and thus there is a relative phase shift of π.

Eq. (7.146) is convenient, as it effectively only reweights the (resummed) hadronic tensor in Fourier space with $K_i(b_T Q \phi^*)$, compared to $J_0(b_T q_T)$ appearing in q_T resummation. In momentum space, this is equivalent to the fact that the spectrum for the LP $\phi^{*(0)}$ in eq. (7.143) can be obtained by reweighting the (resummed) q_T distribution with the angle to the dilepton system. The convenient form of eq. (7.146) was first noticed in refs. [500, 501], where it was also noted that the $\cos(b_T Q \phi^*)$ gives rise to a plateau in the resummed ϕ^* spectrum, in contrast to the Sudakov peak encountered in q_T resummation. However, the form in eq. (7.146) has the distinct disadvantage that it does not allow one any longer to include fiducial power corrections due to additional fiducial cuts beyond the strict LP.

The above previous works did not consider the contribution from $W_2^{(0)}$, which involves the double Boer-Mulders contribution, see eq. (7.89). Comparing to table 7.1, W_2 does not contribute to azimuthally symmetric observables at LP, and thus is not encountered in
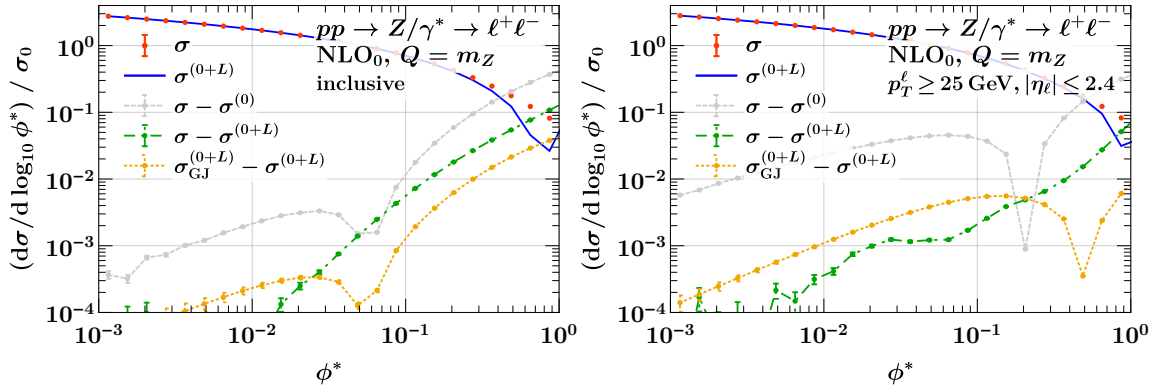
Figure 7.12: Power corrections for ϕ^* for inclusive (left) and fiducial (right) Drell-Yan production.

the LP $\vec{q}_T$ resummation. In practice, we expect this contribution to be rather small, as $h_1^\perp$ only matches onto subleading twist-3 collinear PDFs, and thus we will not consider it in our numerical study. Nevertheless, it is interesting to note that the ϕ^* spectrum may give direct access to the double Boer-Mulders effect, and we leave a more detailed study of this for future work. At leading twist-2, W_2 is suppressed as $\mathcal{O}(\lambda^2)$, such that our resummed spectrum $\sigma^{(0+L)}$ still fully captures all linear power corrections arising from small q_T with leading-twist collinear PDFs, and this also holds when including additional fiducial cuts.

Numerical results

We now turn to the numerical study of power corrections to ϕ^* at one loop. For simplicity, we work at fixed $Q = m_Z$, and normalize all results to the tree-level cross section. The results for inclusive and fiducial Drell-Yan are shown in the left and right panel of figure 7.12, respectively. In both plots, the exact results σ are shown by the red points, the factorized prediction including fiducial power corrections $\sigma^{(0+L)}$ by the blue line, and their difference by the green dot-dashed curve. This is contrasted by the gray-dashed curve which shows the difference $\sigma - \sigma^{(0)}$ between the exact and strict LP (i.e. employing $\phi^{*(0)}$) result. The orange, dot-dashed curve shows the difference $\sigma_{\mathrm{GJ}}^{(0+L)} - \sigma^{(0+L)}$ between our default CS tensor decomposition, and an alternative choice corresponding to the GJ frame.

In the inclusive case (left panel), $\sigma^{(0+L)}$ and $\sigma^{(0)}$ only differ by whether ϕ^* is implemented exactly or using $\phi^{*(0)}$. In this case, we observe large linear corrections to $\sigma^{(0)}$, whereas corrections to $\sigma^{(0+L)}$ appear to be quadratically suppressed. Interestingly, the $\sigma_{\mathrm{GJ}}^{(0+L)}$ seems to have linear corrections as can be seen from the linear scaling of the difference $\sigma_{\mathrm{GJ}}^{(0+L)} - \sigma^{(0+L)}$. Hence, $\sigma^{(0+L)}$ for a generic frame receives linear corrections, although they are roughly an order of magnitude suppressed compared to $\sigma^{(0)}$.

For fiducial Drell-Yan production (right panel), we observe linear power corrections for both $\sigma^{(0)}$ and $\sigma^{(0+L)}$, which are larger than the power corrections in the inclusive case, especially for $\sigma^{(0)}$. Nevertheless, we again see that $\sigma^{(0+L)}$ has significantly smaller corrections than $\sigma^{(0)}$, despite having the same linear scaling in ϕ^*. The ambiguity between
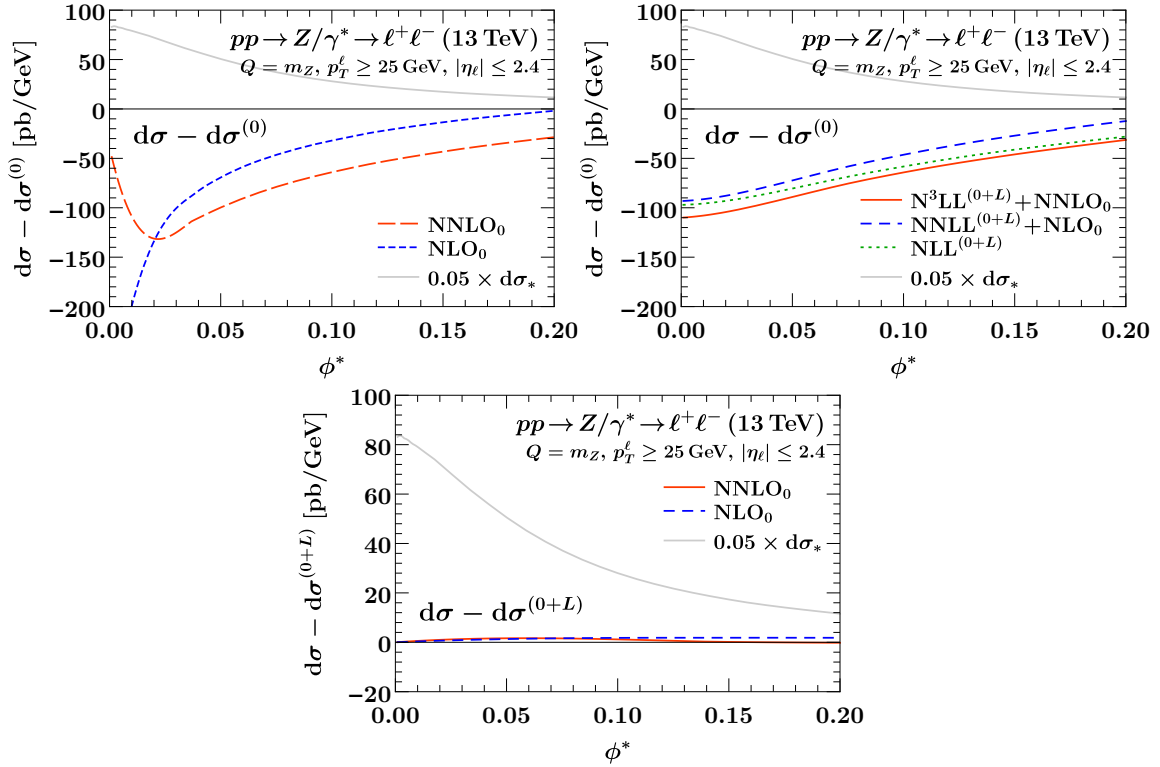
Figure 7.13: Subleading-power contributions to the fiducial ϕ^* spectrum for Drell-Yan on the resonance, $Q = m_Z$. We compare the sum of all subleading power contributions, treating the linear fiducial power corrections at fixed order (top left) or resumming them to all orders (top right). Our best prediction $d\sigma_*$ for the total spectrum at $\mathrm{N^3LL^{(0+L)}+NNLO_0}$ is indicated as a light gray line for reference, scaled down to 5% of its original size. The bottom panel shows the remaining fixed-order power corrections, which are finite for $\phi^* \to 0$ (note the difference in vertical scale).

the two choices of tensor decomposition is again a linear effect, but again at much smaller overall magnitude than the corrections beyond $\sigma^{(0)}$.

Overall, we find that ϕ^* generically receives linear power corrections. In addition to the common fiducial corrections, ϕ^* is affected by corrections from expanding the observable itself, and by the fact that even very small ϕ^* receives contributions from large q_T, as is apparent from eq. (7.143). Hence, *a priori* there is no reason to expect that corrections to ϕ^* are quadratically suppressed. Nevertheless, $\sigma^{(0+L)}$ includes all linear power corrections from small-q_T, which is reflected by the corrections to $\sigma^{(0+L)}$ being significantly reduced compared to $\sigma^{(0)}$. We also note that the choice of tensor decomposition strongly affects how well contributions from large q_T are captured. Empirically, we find that our default choice corresponding to the CS frame minimizes the size of power corrections, but we have not been able to identify an underlying reason for this observation.

We conclude this section by studying the impact of the fiducial power corrections on the resummed ϕ^* spectrum with fiducial cuts. In the top-left panel of figure 7.13, we show the difference between the strict LP and the exact ϕ^* spectrum at $\mathrm{NLO_0}$ (blue, short-dashed)

and $NNLO_0$ (red, long-dashed). For reference, the gray line shows our best prediction σ_* at $N^3LL^{(L)}+NNLO_0$, scaled down to 5% of its original size. We note a large discrepancy between NLO_0 and $NNLO_0$ as $\phi^* \to 0$, indicating large, unresummed logarithms in the power corrections and consequently poor perturbative convergence in this regime.

In the top-right panel of figure 7.13, we show the difference between the LP ϕ^* spectrum and the resummed and matched ϕ^* spectrum, at $NLL^{(0+L)}$ (green, dotted), $NNLL^{(0+L)}$ $+NLO_0$ (blue, dashed) and $N^3LL^{(0+L)}+NNLO_0$ (red, solid), which corresponds to the left panel but with the linear power corrections resummed. As a result, the divergence as $\phi^* \to 0$ is cured, and we observe very good perturbative convergence between the different resummed predictions. Note that in contrast to q_T, see figure 7.8, the resummed power corrections do not vanish as $\phi^* \to 0$, due to the different weighting of the Sudakov factor with $\cos(b_T Q \phi^*)$ rather than $J_0(b_T q_T)$, cf. eq. (7.146).

Finally, in the bottom panel of figure 7.13 we show the remaining fixed-order power corrections after including the fiducial power corrections in the resummation at NLO_0 (blue, short-dashed) and $NNLO_0$ (red solid), again including our best prediction σ_* for reference. Since all terms diverging as $\phi^* \to 0$ are included in $\sigma^{(0+L)}$, the remaining power corrections are well-behaved as $\phi^* \to 0$, which makes their overall size almost negligible.

7.5 Comparison to data

In this section, we compare our $N^3LL+NNLO_0$ resummed predictions for q_T and ϕ^* for Drell-Yan, $pp \to Z/\gamma^* \to \ell^+\ell^-$ ($\ell = e, \mu$), with the following precision LHC measurements:

- The ATLAS measurement from ref. [426] using 20.3 fb^{-1} of 8 TeV data. We consider the $m_{\ell^+\ell^-} \in [66, 116]$ GeV invariant mass bin. The fiducial lepton cuts are $p_T > 20$ GeV, $|\eta| < 2.4$ for both electrons and muons, with an additional exclusion region of $1.37 < |\eta| < 1.52$ for electrons. Separate results for the electron and muon channels are reported, in both cases we compare to the measurements using Born leptons.

- The CMS measurement from ref. [31] using 35.9 fb^{-1} of 13 TeV data in the $m_{\ell^+\ell^-} = m_Z \pm 15$ GeV invariant mass bin. The fiducial cuts are given by $p_T > 25$ GeV and $|\eta| < 2.4$ for both electrons and muons. We compare to the combined measurements of dressed electrons and muons.

We consider two sets of predictions: The strict LP resummation with fiducial power corrections only included via the fixed-order matching is denoted as $N^3LL^{(0)}+NNLO_0$, and analogously at lower orders. The resummation including fiducial power corrections is denoted as $N^3LL^{(0+L)}+NNLO_0$, and analogously at lower orders. In this case, the fixed-order matching only adds the remaining genuine (non-fiducial) power corrections.

By default we compare to the measured spectra that are normalized to the total cross section. We correspondingly normalize our predictions to the total fiducial cross section at the corresponding order obtained by integrating the central value for the spectrum to infinity. This effectively amounts to obtaining the total cross section via q_T or ϕ^* subtractions

including fiducial power corrections. Since the uncertainties for the total cross section are much smaller than for the spectrum, they are practically irrelevant for this purpose. We have also checked that treating the $\mu_{\rm FO}$ variation in a correlated fashion or treating it fully uncorrelated between spectrum and normalization and adding it in quadrature leads to essentially identical estimates of the total perturbative uncertainty. For completeness, we also provide analogous comparisons for the unnormalized CMS measurements in appendix G.2.

7.5.1 q_T spectrum

In figure 7.14, we compare our results to the CMS 13 TeV measurements for q_T. The top panels show the q_T spectrum at NLL (green), NNLL+NLO$_0$ (blue), and N³LL+NNLO$_0$ (orange). The bands show the estimated perturbative uncertainties as discussed in section 7.3.3. Note that the theory predictions are obtained for the measured binning, but are drawn as smooth curves for clearer visibility. The lower panels show the same results normalized to the respective highest-order prediction. The results using strict LP resummation are shown on the left (lighter shading), while those including the resummation of fiducial power corrections are shown on the right (darker shading). In both cases, we observe good convergence of the resummed predictions, with substantially reduced perturbative uncertainties at subsequent higher orders, as well as good agreement with the data. Nevertheless, resumming the fiducial power corrections on the right further improves the perturbative convergence and also yields a systematically better agreement with the data. The data agreement deteriorates in the first two bins, which can be attributed to small-q_T nonperturbative effects. These are expected to become important for $q_T \lesssim 2\,{\rm GeV}$, but the nonperturbative ingredients necessary to account for these effects are not included in our predictions. This is also reflected in the substantially increased perturbative uncertainties in this region.

To further illustrate the importance and impact of the fiducial power corrections, in figure 7.15 we show the analog of the bottom panel of figure 7.14 but comparing to the pure resummed results, i.e., without including the fixed-order matching corrections to the spectrum. (We still normalize to the same total cross section as in figure 7.14.) The strict LP resummation (left) completely fails to describe the data, showing that in this case the fixed-order matching corrections that supply the fiducial power corrections at fixed order are essential. On the other hand, upon resumming the fiducial power corrections (right), the excellent data agreement is restored even without the fixed-order matching. In other words, with the fiducial power corrections included in the resummation, the fixed-order matching becomes essentially unimportant for $q_T \lesssim 40\,{\rm GeV}$, both at NNLL and N³LL.

In figure 7.16, we show the analogous comparison for the ATLAS 8 TeV measurements [426] in the electron channel, with the top panel showing the q_T spectrum itself, while the bottom panel shows the relative differences to the respective highest-order prediction. As before, we see good perturbative convergence of the predictions, as well as good agreement with the data. The data agreement again improves when resumming the fiducial power corrections on the right, leading to an overall flatter shape and reduced size
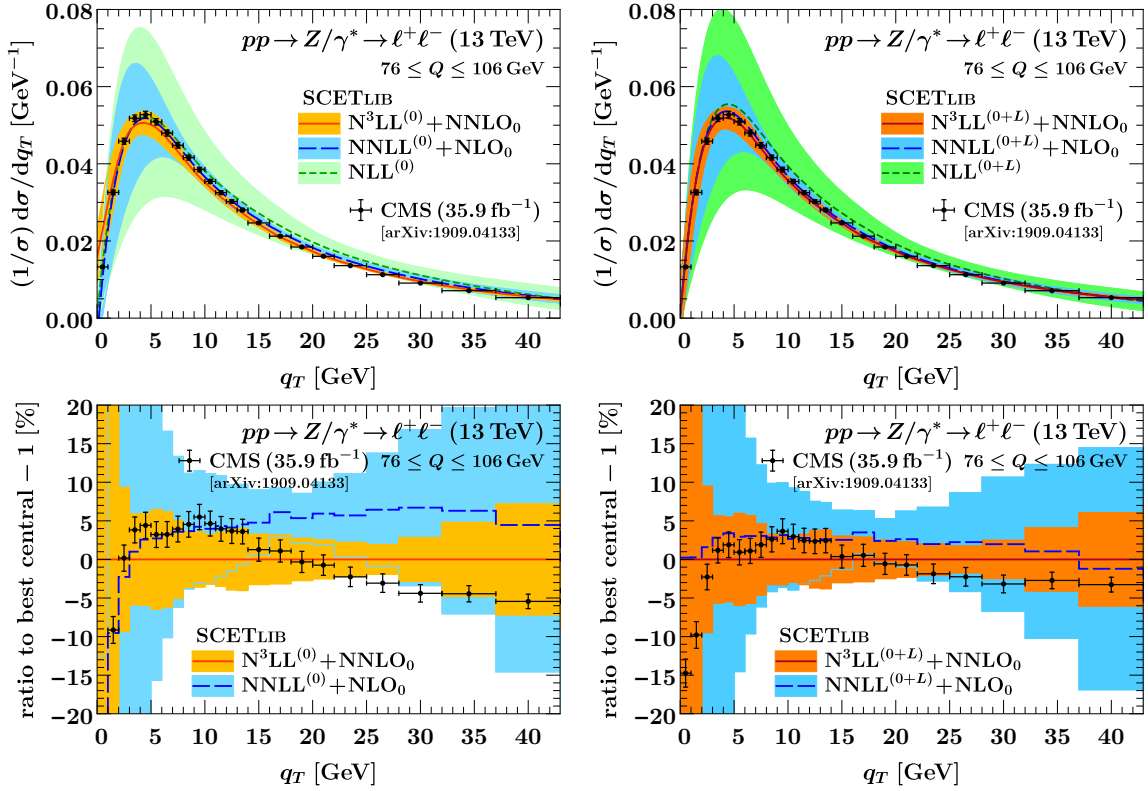
Figure 7.14: Predictions for the normalized Drell-Yan fiducial q_T spectrum without (left) and with (right) resummed fiducial power corrections compared to CMS 13 TeV measurements [31]. The top panels show the spectrum, with the theory predictions drawn as smooth curves for better visibility. The bottom panels show the percent differences to the respective highest-order prediction central value.
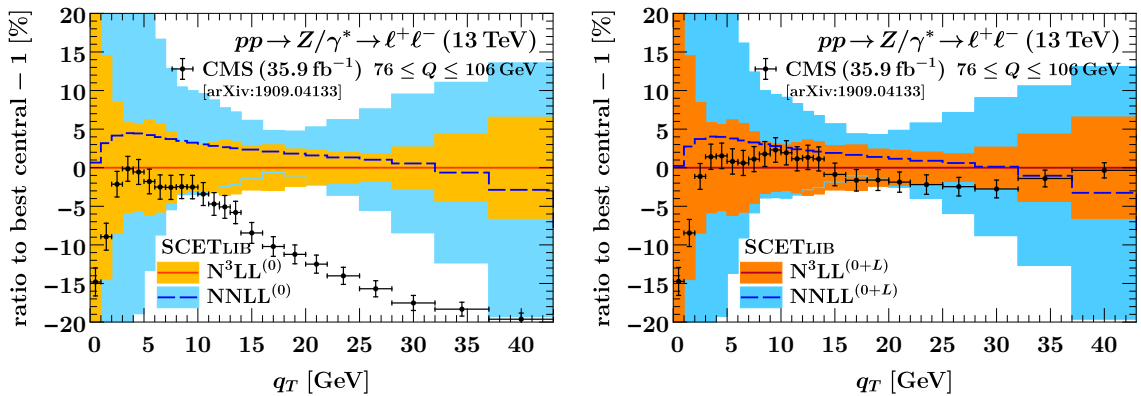

Figure 7.15: Same as the bottom row of figure 7.14, but without including power corrections from the fixed-order matching.
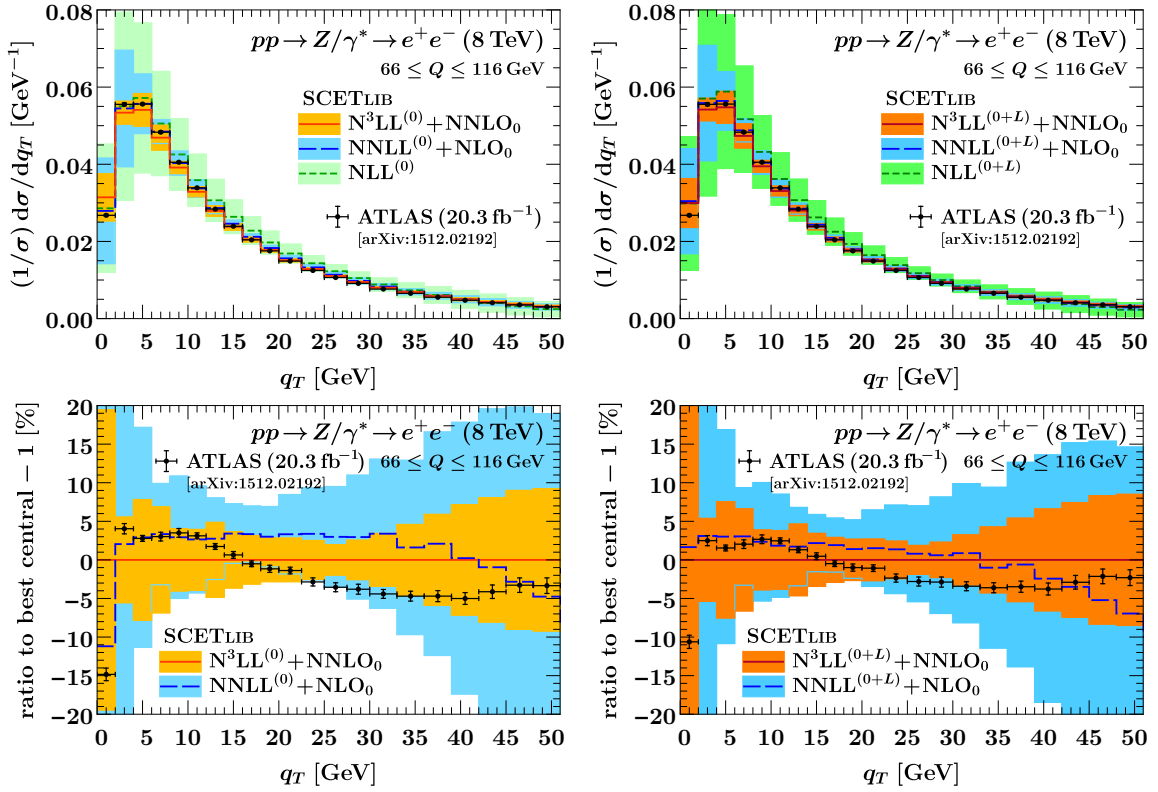
Figure 7.16: Predictions for the normalized Drell-Yan fiducial q_T spectrum without (left) and with (right) resummed fiducial power corrections compared to ATLAS 8 TeV measurements [426] in the e^+e^- channel. The top panels show the normalized spectrum. The bottom panels show the percent differences to the respective highest-order prediction central value. The analogous results for the $\mu^+\mu^-$ channel can be seen in appendix G.2 in figure G.7.

in the difference between predictions and measurement. The results in the muon channel are practically identical, and are provided for completeness in figure G.7 in appendix G.2.

7.5.2 ϕ^* distribution

In figure 7.17, we compare our results for the ϕ^* spectrum to the ATLAS 8 TeV measurements [426] in the electron channel. The analogous results in the muon channel are provided in appendix G.2 in figure G.8. The top panel shows the predictions at NLL (green), NNLL+NLO$_0$ (blue), and N^{3}LL+NNLO$_0$ (orange), with the bands showing the estimated perturbative uncertainties as discussed in section 7.3.3. The predictions are obtained with the experimental binning but are drawn as smooth curves for better visibility. The lower panels show the same results normalized to the respective highest-order predictions. The results using strict LP resummation for both the observable itself and the fiducial cuts are shown on the left (lighter shading), while those including the resummation of fiducial power corrections for observable and cuts are shown on the right (darker shading). In both cases we observe good convergence of the resummed predictions. For large $\phi^* \gtrsim 0.5$, the
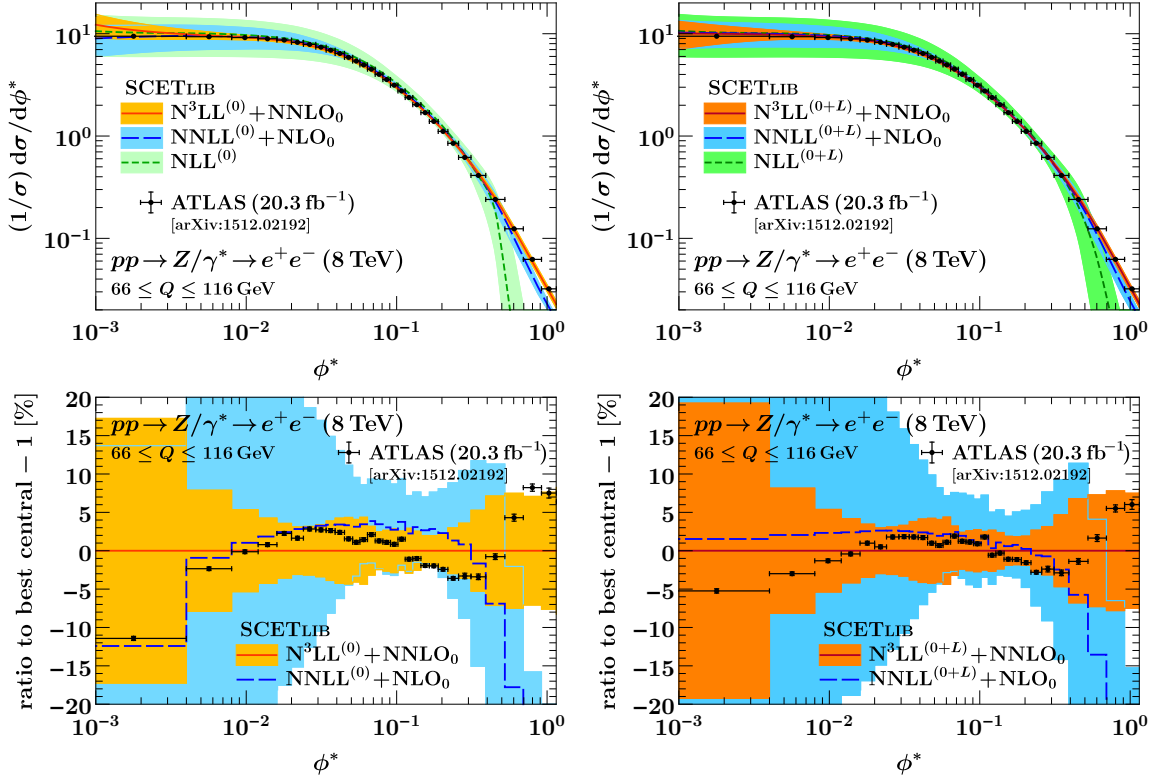
Figure 7.17: Predictions for the normalized Drell-Yan fiducial ϕ^* spectrum using the LP resummation (left) and including the resummation of fiducial power corrections (right) compared to ATLAS 8 TeV measurements [426] in the e^+e^- channel. The top panels show the spectrum, with the predictions drawn as smooth curves for better visibility. The bottom panels show the percent differences to the respective highest-order prediction central value. The analogous result for the $\mu^+\mu^-$ channel can be seen in appendix G.2 in figure G.8.

spectrum enters the fixed-order region and consequently the NLL (green) results start to deviate substantially, and to lesser extent also the NNLL+NLO_0 (blue) results. The first one or two bins are again sensitive to small-q_T nonperturbative effects, which is reflected in their increased perturbative uncertainties. As for the q_T spectrum, we find excellent agreement with the data, which is further improved on the right by resumming the fiducial power corrections, especially at NNLL+NLO_0 where the shape improves significantly.

In figure 7.18, we show the analogous comparison for the CMS 13 TeV ϕ^* measurements [31]. The top panels show the spectrum itself, and the bottom panels the relative difference to the respective highest-order prediction. The predictions show the same behaviour as at 8 TeV, and we again find good agreement with the data. Here, the improvements from resumming the fiducial power corrections are even more striking. While the strict LP resummation on the left shows a clear trend of overshooting the data at small ϕ^*, we find nigh-perfect agreement across the spectrum with resummed fiducial power corrections. To further highlight this, in figure 7.19 we show the analog of the bottom panel of figure 7.18 but comparing to the pure resummed results only, i.e., without including fixed-order match-
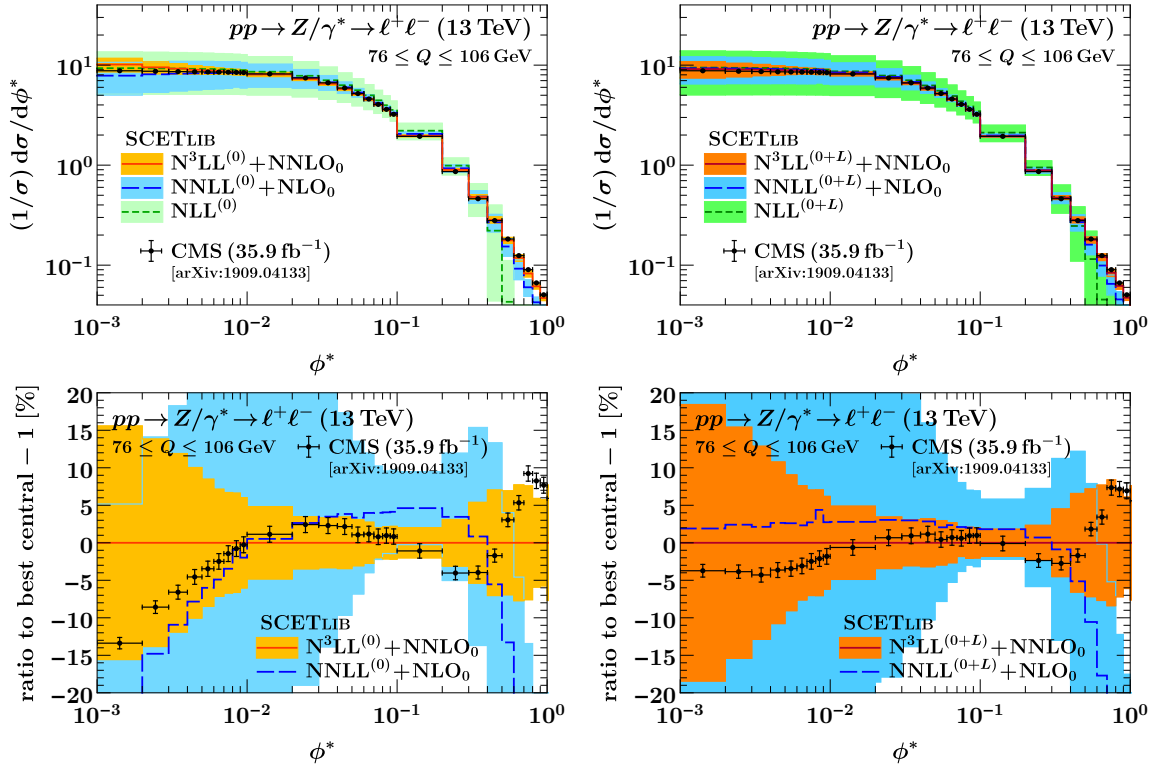
Figure 7.18: Predictions for the normalized Drell-Yan fiducial ϕ^* spectrum using the LP resummation (left) and including the resummation of fiducial power corrections (right) compared to CMS 13 TeV measurements [31]. The top panels show the spectrum, and the bottom panels show the percent differences to the respective highest-order prediction central value.
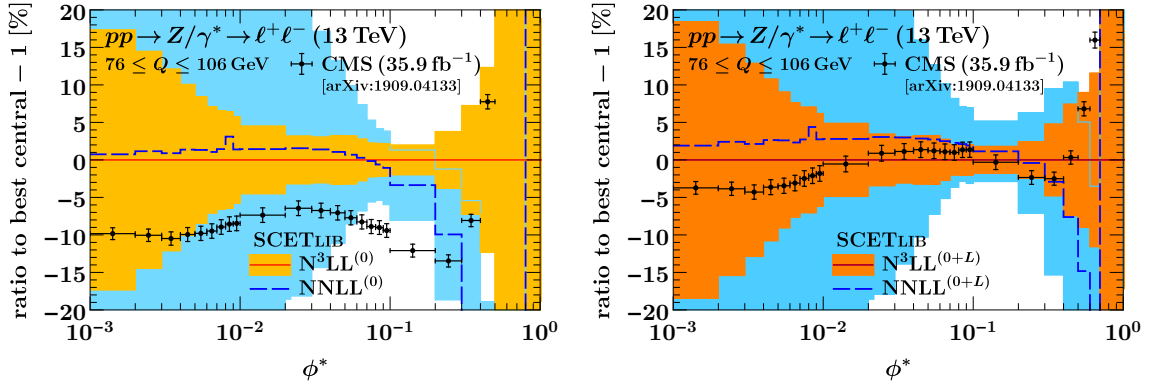
Figure 7.19: Same as the bottom row of figure 7.18, but without including power corrections from the fixed-order matching.

ing corrections. As we already saw for the q_T spectrum, the LP resummation alone (left) basically fails to describe the data, showing that in this case the fixed-order matching is necessary in order to supply the fiducial power corrections at least at fixed order. In contrast, when resumming the fiducial power corrections (right), we find the same excellent

data agreement as before up to $\phi^* \lesssim 0.5$. This shows that the ϕ^* spectrum has rather large sensitivity to power corrections throughout its spectrum and profits enormously from including them in the resummation. At the same time, the remaining fixed-order power corrections become almost negligible in this range. Beyond $\phi^* \gtrsim 0.5$, we enter the fixed-order region and as expected, the pure resummed results quickly deteriorate and matching to the fixed-order results becomes strictly necessary.

7.6 Summary

We have studied the impact of fiducial cuts and other generic leptonic measurements on the factorization of the Drell-Yan process at small transverse momentum $q_T \ll Q$. They generically induce fiducial power corrections in q_T/Q relative to the well-studied leading-power terms predicted by q_T (equivalently TMD) factorization, which are significantly larger than the quadratic power corrections arising for the inclusive q_T spectrum.

Using a Lorentz-covariant tensor decomposition of the leptonic and hadronic tensors combined with formal power-counting arguments in SCET, we have shown that for a large class of observables (those that are azimuthally symmetric at leading power), the fiducial power corrections are the only source of linear power corrections. Furthermore, by retaining the exact leptonic structure functions, the fiducial power corrections are unambiguously predicted from factorization and are correctly resummed to the same order as the leading-power terms.

We have also shown that the naive power expansion in $q_T/Q \ll 1$ can break down near the edge of Born phase space due to uncontrolled leptonic power corrections $\sim q_T/p_L$, where p_L is the distance from the edge of Born phase space. In such regions, it is strictly required to keep all leptonic power corrections $\sim q_T/p_L$ to correctly describe the actual *leading-power* limit. An important example is the p_T^ℓ spectrum near the Jacobian peak $p_T^\ell = Q/2$ with $p_L = Q - 2p_T^\ell$. This provides another formal reason to keep the exact leptonic structure functions, because doing so guarantees that all required leptonic power corrections are automatically retained. The kinematic recoil prescriptions used in practical implementations usually yield an exact description of the leptonic decay and measurements. Our analysis shows for the first time that this is not only justified, but even necessary to obtain a description that is formally valid across the entire leptonic phase space. These conclusions also immediately apply to scalar processes such as Higgs production.

The tensor decomposition can be interpreted as a specific choice of vector-boson rest frame, which naturally emerged to be the Collins-Soper frame as defined by boosting from the lab frame, even when keeping nonzero masses of the initial state hadrons. The CS tensor decomposition yields nine Lorentz-scalar hadronic structure functions, which are defined for an arbitrary leptonic final state, and for $Z/\gamma^* \to \ell\ell$ or $W \to \ell\nu$ decays directly map onto the commonly used angular coefficients for the cross section in the CS angles. We also discussed that Born leptons can be theoretically well defined in terms of an IR-safe Born projection of the full leptonic final state, including QED final-state radiation. We have shown that the cross section in the CS angles of the so-defined Born leptons admits a LO-like complete

angular decomposition in terms of spherical harmonics, with the corresponding generalized angular coefficients modified by QED corrections.

We have presented resummed predictions with and without the resummation of fiducial power corrections at N³LL. The comparison of our predictions to precision Drell-Yan q_T and ϕ^* measurements from ATLAS and CMS confirms the importance of fiducial power corrections and their resummation in a striking way: While the strict LP resummation is able to describe the data within (theory) uncertainties, it fails to do so without including the sizeable fixed-order corrections. On the other hand, including the fiducial power corrections in the resummation systematically improves the agreement with the data, particularly at very small q_T and ϕ^*. Furthermore, the fixed-order matching corrections now become very small and do not play much of a role below $q_T \lesssim 40\,\mathrm{GeV}$ and $\phi^* \lesssim 0.5$. We note that computationally, even at fixed order it is much cheaper to predict the fiducial power corrections via factorization instead of including them numerically through a full fixed-order calculation, since the latter becomes expensive quickly toward small q_T or may not even be available.

We have also considered the resummed p_T^ℓ spectrum, which plays a crucial role in the precision m_W measurement at the LHC, and have obtained the first N³LL predictions for it. We have demonstrated that a reliable prediction of the physical p_T^ℓ spectrum near the Jacobian peak is possible and that it relies in an essential way on the interplay between small-q_T resummation effects and the exact treatment of leptonic power corrections that describe the recoil of the leptonic system.

Chapter 8

Conclusion and outlook

In this thesis we derived new factorization results for hadronic collisions that extend and improve existing resummation methods, and applied them to the study of precisely measured differential distributions at the LHC. First-principle analytic theory predictions like these are important ingredients in the upcoming LHC precision program. The threefold aim of this program is (1) to thoroughly test the Standard Model at LHC energies, including the physics of the newly discovered Higgs boson, (2) to search for possible deviations pointing to new phenomena, and (3) to precisely determine universal ingredients for collider physics like the proton structure that will also shed light on strongly-bound physics. Differential distributions that are sensitive to emissions in the soft and collinear limits of QCD generically exhibit large Sudakov double logarithms that deteriorate the quality of a fixed-order perturbative expansion and require a resummation of the perturbative series to all orders. The results in this thesis extend the toolbox of analytic resummation methods, in particular to more realistic, or more differential, experimental measurements. We worked in the framework of soft-collinear-effective theory (SCET) that enables resummation through the renormalization group (RG) evolution of operators in the effective field theory (EFT).

We first discussed the extension of jet veto resummation to fully realistic experimental jet selection criteria involving a jet rapidity cut. We next considered the double-differential spectrum in color-singlet transverse momentum q_T and the 0-jettiness event shape $\mathcal{T}_0$, providing the first analytic prediction for a Sudakov peak in two dimensions. We then presented a generalized threshold factorization theorem that accounts for the full collinear dynamics of initial-state radiation and holds in a much weaker limit than the standard soft threshold factorization. Using consistency relations partly based on this new result, we derived the leading eikonal terms at third order in perturbation theory for the q_T and $\mathcal{T}_0$ beam functions. Finally we demonstrated how to perform the resummation of so-called fiducial power corrections that arise from experimental measurements on the decay products of a Z or W boson. We found an improved agreement with precision ATLAS and CMS measurements when including the resummation of these power corrections in cutting-edge N³LL+NNLO predictions, which also reduces the overall numerical cost. Using the same approach, we presented the first analytically resummed result for the p_T^ℓ spectrum near the Jacobian peak at N³LL+NNLO. In the following we go through each of these main research results in turn, summarizing their key outcomes and pointing out future applications, before closing with a general summary and outlook.

Jet veto resummation with jet rapidity cuts. We developed a systematic framework to incorporate a cut on the rapidity of reconstructed jets, $|\eta_{\mathrm{jet}}| < \eta_{\mathrm{cut}}$, into the theoretical description of jet-vetoed processes at the LHC. We showed that the standard jet veto resummation, which neglects the rapidity cut, is correct up to power corrections of $\mathcal{O}(Qe^{-\eta_{\mathrm{cut}}}/p_T^{\mathrm{cut}})$, with Q the hard-interaction scale and p_T^{cut} the jet veto cut, and demonstrated that these power corrections can be seamlessly incorporated into the resummed description by introducing more differential collinear matrix elements. The same holds true for a step in the jet veto selection, i.e., an increase in the veto parameter to $\tilde{p}_T^{\mathrm{cut}} > p_T^{\mathrm{cut}}$ beyond η_{cut}, which we considered in detail.

We calculated the necessary η_{cut}-dependent corrections at one loop as well as all logarithmic contributions to them at two loops. This includes in particular small-R clustering logarithms, for which we gave an all-order factorized result at the leading-logarithmic level by explicitly matching onto collinear modes at the scale $R\, p_T^{\mathrm{cut}}$ that form the final-state small-R jets. The remaining ingredients required for a full NNLL′ analysis with η_{cut} effects are finite nonlogarithmic pieces that could be either calculated explicitly or extracted numerically from the full-QCD results, which we leave to future work.

There are several important outcomes of our analysis. First, a jet rapidity cut at very forward rapidities due to the finite detector acceptance, $\eta_{\mathrm{cut}} \simeq 4.5$, is theoretically safe and unproblematic. The power counting that we introduced to arrive at this conclusion has already been picked up in the meantime in refs. [504–507] to estimate the effect of jet rapidity cuts on theory predictions for high-mass BSM signals under a jet veto. By contrast, restricting the jet veto to the more central region, with a sharp rapidity cut at the edge of the tracking detectors, $\eta_{\mathrm{cut}} \simeq 2.5$, leads to an increase in the perturbative uncertainties (which may not be captured if the jet rapidity cut is not included in the resummation). This loss in theoretical precision can become particularly severe for gluon-induced processes and for processes at high scales. It can however be mitigated by replacing the sharp rapidity cut by a moderate step in the jet veto. We expect this to be a generic feature that also holds at higher orders, and it will be interesting to extend our resummed predictions to the next order (NNLL′) to confirm this as well as to reduce the overall size of the theoretical uncertainties. We encourage our experimental colleagues to take full advantage of such step-like jet vetoes in order to benefit from suitably tight jet vetoes at central rapidities, while avoiding the increased pile-up contamination in the forward region.

Joint two-dimensional resummation in q_T and 0-jettiness at NNLL. We calculated the Drell-Yan cross section double-differential in the transverse momentum q_T of the lepton pair and the 0-jettiness event shape $\mathcal{T}_0$. Since both $\mathcal{T}_0$ and q_T probe the initial state radiation, the cross section contains Sudakov double logarithms of $\mathcal{T}_0/Q$ and q_T/Q. We performed, for the first time, the simultaneous resummation of both kinds of logarithms, achieving next-to-next-to-leading logarithmic accuracy and matching the result to next-to-leading fixed order.

The predictions we obtained are of some phenomenological interest, as $\mathcal{T}_0$ has been measured in bins of q_T [395], and constitute the perturbative baseline for a detailed study

of the various soft-QCD effects that this measurement is sensitive to. More importantly, our analysis is a key step towards precise *and* fully exclusive predictions for LHC cross sections in general. Specifically, the Monte Carlo event generator `Geneva` [122, 396] is based on a NNLL′ resummed prediction for the cross section differential in $\mathcal{T}_0$, and would benefit from the simultaneous resummation of q_T. Indeed, our NNLL results clearly indicate that only resumming the logarithms of either $\mathcal{T}_0$ or q_T gives a poor description of the double-differential cross section. Using our results, Monte Carlo event generators like `Geneva` can be pushed to higher formal accuracy for the q_T spectrum, while still maintaining full control over the hadronic final state through $\mathcal{T}_0$. High-precision event-level predictions for q_T spectra are of key experimental relevance, and we plan to address this in the future. Finally, the stability of fixed-order predictions may also be improved by using our matched result as a double-differential subtraction term [50], exploiting that it simultaneously describes all singular limits in the one-emission phase space in terms of $(q_T, \mathcal{T}_0)$. Our methods apply at any order and for any color-singlet production process, allowing for a straightforward extension once the relevant perturbative ingredients become available. We believe that our analysis, and our general strategy of matching bulk and boundary descriptions, can pave the way for going beyond single-differential resummations in many other contexts as well.

Generalized threshold factorization with full collinear dynamics. We presented and proved a generalization of the classic soft threshold factorization theorem. It notably includes the full collinear dynamics of hadronic radiation in the limit where a color-singlet final state is produced at large absolute rapidity $|Y| \to Y_{\max}$ at generic Q, which is directly accessible at the LHC. Combining it with the standard soft and the opposite collinear limit, we obtained a unified description of all singular limits in color-singlet rapidity spectra. The dependence on the hard process is manifestly factorized in terms of the purely virtual amplitudes contained in the hard function. The new factorization theorem enables the resummation of large logarithms of $1 - x_{a,b}$ in the limit where only one PDF is probed at large x, which is not captured by the soft limit. At the partonic level, it captures all singularities of $\hat{\sigma}_{ij}(z_a, z_b)$, including off-diagonal partonic channels. As a first application of the rich perturbative structure it predicts, we have derived a nontrivial set of terms in the N^{3}LO Drell-Yan rapidity spectrum.

We believe our results will have far-reaching impact on precision phenomenology on various fronts, which we now discuss in turn. (Each of the following bullet points amounts to one or several research projects in their own right.) For their most obvious application, our results will enable taking practical theory predictions for color-singlet spectra at the LHC to a new level of precision, as follows:

- As an immediate next step, the ingredients we calculated enable a complete resummation of endpoint logarithms in the Drell-Yan rapidity spectrum at N^{3}LL+NNLO, in particular accounting for the subtle cancellations between partonic channels that the soft threshold resummation is known to fail taking into account [222]. We plan to address this in upcoming work. These results will readily carry over to any color-singlet process for

which the two-loop virtual amplitudes are known.

- More generally, the leading-power factorization we derived, and the excellent convergence of the generalized threshold expansion that we demonstrated beyond the leading power, can guide the organization of a future N^3LO calculation of the Drell-Yan rapidity spectrum. In fact, the quality of the expansion has in the meantime been confirmed also for Higgs production at NNLO in ref. [508], and the methods in ref. [508] are tailored towards extensions to N^3LO. (The leading-power two-loop term for gluon-induced processes, given by the gluon threshold beam function up to the well-known form factor, has also been independently calculated in ref. [411] in the meantime as a byproduct of the two-loop calculation of the double-differential gluon beam function.) A calculation of the leading-power term in the generalized threshold expansion at three loops would be highly desirable, for both Drell-Yan production and gluon fusion, and the threshold beam function renormalization in the context of our factorization theorem will serve as a powerful cross check on these results. With the leading-power three-loop term at hand, the resummation can immediately be pushed to N^4LL using RG consistency and the results in ref. [509–511] for the required anomalous dimensions. Any available power corrections may then be incorporated by an additive matching to achieve an ultimate precision of N^4LL+N^3LO.

- The (Q,Y)-differential color-singlet production spectrum is also a key ingredient for applications of the projection-to-Born (P2B) method [51] at N^3LO, where an inclusive N^3LO_0 prediction differential in the Born phase space is combined with a fully-differential $NNLO_1$ calculation into a fully-differential N^3LO_0 prediction.[1] For future applications in P2B calculations, we stress that the N^3LO spectrum differential in (q^+, q^-) is an equally viable input because both (Q,Y) and (q^+, q^-) are viable parametrizations of the Born phase space. By one of the corollaries of our new factorization theorem, the (q^+, q^-) spectrum at leading power in the generalized threshold expansion is precisely given by the inclusive beam function that was calculated to $\mathcal{O}(\alpha_s^3)$ in ref. [299] in the meantime, and thus the full leading-power inputs for an N^3LO_0 P2B calculation *are already known*. Based on our explicit results at two loops, we also anticipate that the (q^+, q^-) spectrum will continue to have a simpler analytic structure than the (Q,Y) spectrum. Pending a thorough assessment of the size of next-lo-leading power terms in a generalized threshold expansion of the (q^+, q^-) spectrum at lower orders, which we expect to be similarly convergent as in the (Q,Y) case, this will put fully-differential N^3LO predictions for Drell-Yan production within reach.

- As a last note on applications to color-singlet production at the LHC, we stress that our results also make the dependence on the color-singlet transverse momentum at generalized threshold fully transparent in terms of the double-differential beam function. This makes it straightforward to also perform the generalized threshold resummation differential in

---

[1]For Higgs production this combination may already be performed using the results of ref. [250], but the soft expansion used for the Higgs N^3LO rapidity spectrum in that case manifestly fails for the Drell-Yan case. To restore the dependence on the decay products for Drell-Yan, note that at Born level the hadronic tensor only contains terms $\propto g_\perp^{\mu\nu}$ and $\propto \epsilon_\perp^{\mu\nu}$.

q_T and match it with q_T resummation using the approach of chapter 4 to reach the best possible precision for the triple-differential color-singlet cross section $d\sigma/(dQ\,dY\,dq_T)$. It also opens up a road to N^{3}LO predictions for $d\sigma/(dQ\,dY\,dq_T)$ that are correct at leading power in a generalized threshold expansion by calculating the double-differential $\mathcal{O}(\alpha_s^3)$ beam function only at *finite* q_T, which we expect to be much simpler than the full N^{3}LO result including the singularity at $q_T = 0$, and perform a q_T subtraction to recover the full result. In both cases, restoring the full dependence on the decay products poses no conceptional difficulty, and the leptonic phase space integration can be performed point by point in q_T using the methods of chapter 7.

We next turn to the impact that we expect the results of chapter 5 to have on the formal understanding of the behavior of QCD near kinematic endpoints:

• As discussed, our generalized threshold factorization theorem contains, after matching with the opposite limit, the complete next-to-soft contribution to the rapidity spectrum. Since the power suppression can only arise from either $1 - z_a$ or $1 - z_b$ at this power and the spectrum is symmetric under $z_a \leftrightarrow z_b$, these are in one-to-one correspondence to the next-to-soft terms in the inclusive partonic cross section $\hat{\sigma}_{ij}(z)$. For the latter, our results prove that only the leading-power SCET hard matching coefficient (corresponding to the form factor) arises even at next-to-leading power in the soft expansion for all partonic channels. This was later confirmed in ref. [408] as part of the full next-to-soft threshold factorization for $\hat{\sigma}_{ij}(z)$.

• Interestingly, the results of refs. [206, 207, 408] can be mapped back onto the rapidity spectrum using the above correspondence, and through our new factorization theorem also govern the factorization and resummation of next-to-eikonal terms *within* the beam function. It will be interesting to explore this connection further in the future.

Finally, we foresee rich applications of our general approach, i.e., of taking one momentum fraction to one at a time, beyond color-singlet production in pp collisions:

• For LHC phenomenology, we anticipate that similar factorization results can be derived for processes with top quarks, jets, or identified hadrons in the final state. (It will be interesting to determine the precise form that these factorizations take, given that perturbative soft radiation resolving all sectors should be present, but is absent in our color-singlet results.) For many of these processes, the standard soft threshold factorization has been applied to obtain fixed-order approximants or perform the resummation, and generalizing it will enable its extension to off-diagonal channels. We expect this to be particularly relevant for processes involving sizable contributions from initial-state quarks, which in turn can receive large corrections from gluon splittings. Important examples are single-top production (with an initial-state bottom quark) or highly boosted gluon-fusion Higgs production at $p_T^H \gg m_H$ with an identified hard jet. Deriving a factorized expression capturing the bulk of the large-p_T^H spectrum, which is a key place to look for the effect of new physics, is of particular interest because it may help explain why the NLO$_1$ spectrum in the full SM can

be surprisingly well approximated [512] by a roughly constant correction factor multiplying the NLO_1 result in the contact-operator approximation of eq. (2.73). There is no reason for this to happen in general because at these values of p_T^H, we are completely outside the validity region of the heavy-top expansion.

• Looking beyond LHC phenomenology, our approach readily generalizes to semi-inclusive DIS (SIDIS), which is characterized by the Bjorken fraction x and the light-cone momentum fraction z_h carried by the identified final-state hadron. So far, the threshold resummation for SIDIS is only available in the simultaneous limit $x, z_h \to 1$ [513], and our results generalize it to a weaker limit by either crossing the beam function into a final-state fragmenting jet function [347] ($x \to 1$) or the threshold PDF into a threshold fragmentation function ($z_h \to 1$). The latter is of particular phenomenological interest in the case of a fragmenting heavy quark, which naturally leads to a large amount of momentum being transferred into the resulting heavy meson.[2] Thus our results pave the way for turning the results of ref. [412] for heavy-quark fragmentation in single-inclusive e^+e^- annihilation (characterized by a single z_h, i.e., the crossed version of inclusive DIS near endpoint) into a possible precision observable at the future EIC [514], retaining the exact dependence on the Bjorken fraction x in the resummation. We expect that control over x and the associated off-diagonal beam function channels, which would be missed by the soft limit, will be crucial for a sensible description of heavy quark production in particular because there is an $\mathcal{O}(1)$ contribution from a gluon splitting at the beam scale. It should be possible to derive analogous results for the fragmentation into a jet (at large z_{jet}), another key process of interest at the EIC.

$\mathbf{N^3LO}$ beam functions in the eikonal limit. We considered the previously unknown scale-independent boundary coefficients $I_{ij}^{(3)}(z)$ of the $\mathrm{N^3LO}$ q_T and inclusive beam functions and employed consistency relations with known three-loop soft matrix elements to derive explicit expressions for the leading eikonal terms in $I_{ij}^{(3)}(z)$ as $z \to 1$. These consistency relations were already known in the literature for the case of q_T, but for the case of the inclusive ($\mathcal{T}_0$) beam function only follow as a nontrivial corollary from the new generalized threshold factorization theorem in chapter 5.

Since the original publication of these results in ref. [5], results for the three-loop $\mathcal{T}_0$ quark beam function in the generalized large-N_c approximation have appeared in ref. [298], and the complete three-loop beam functions have been calculated in refs. [287, 288] for the q_T quark and q_T quark and gluon cases, respectively, and in ref. [299] for the $\mathcal{T}_0$ quark and gluon cases. In these works, which enter the resummation of $\mathcal{T}_0$ and q_T at $\mathrm{N^3LL'}$ and $\mathrm{N^4LL}$ order and the application of $\mathcal{T}_0$ and q_T subtractions [46, 49, 50] at $\mathrm{N^3LO}_0$, the eikonal terms derived in this thesis were used as an important cross check, finding full agreement. The leading eikonal structure encoded in our results also enables estimating the four-loop contributions to beam functions as part of a completely thorough estimate of

---

[2]We thank D. Neill for discussion on this point, and F. Ringer for discussion on SIDIS threshold resummation in general.

missing higher-order uncertainties e.g. in a future high-precision N^4LL prediction for the q_T spectrum. This estimate will in particular capture the leading eikonal rapidity dependence.

Resumming fiducial power corrections at N^3LL. We studied the impact of fiducial acceptance cuts and other experimental measurements on the leptonic final state the factorization of the Drell-Yan process at small transverse momentum $q_T \ll Q$. Measurements that resolve the decay products generically lead to fiducial power corrections in q_T/Q relative to the well-studied leading-power terms predicted by q_T factorization. These corrections are significantly larger than the quadratic corrections that arise in the inclusive q_T spectrum.

We showed that for a large class of leptonic observables (those that exhibit azimuthal symmetry at leading power), the fiducial power corrections are the unique source of linear power corrections. By retaining the exact leptonic structure functions, we were able to unambiguously predict the fiducial power corrections from factorization and resum them to the same order as the leading-power terms. We also discussed in detail how keeping the leptonic structure functions exact ensures a correct treatment of another class of fiducial power corrections, which we dubbed leptonic power corrections. These scale as $\sim q_T/p_L$, where p_L is the distance from the edge of Born phase space, and cause a naive power expansion in $q_T/Q \ll 1$ to break down altogether in the limit of $p_L \to 0$. An important example is the p_T^ℓ spectrum near the Jacobian peak at $p_T^\ell = Q/2$ with $p_L = Q - 2p_T^\ell$. Our results provide formal justification for the kinematic recoil prescriptions that are commonly used in practical implementations of q_T resummation. Our conclusions also immediately apply to scalar processes such as Higgs production, which will be an interesting place to study the impact of fiducial power corrections in the future.[3]

Since the importance of unresummed, fixed-order power corrections is significantly reduced by resumming the dominant fiducial ones, our results have important implications for all phenomenological applications at small q_T, for example the extraction of nonperturbative inputs to TMD distributions from data.

There are many interesting avenues that our analysis opens up and that we were only able to briefly point out in chapter 7:

- For the lepton p_T spectrum in W decays, we made the interesting observation that at the first subleading power in $p_T^\ell - Q/2$ near the Jacobian peak, the p_T^ℓ spectrum is sensitive to an additional $\mathcal{O}(q_T/Q)$ hadronic structure functions (W_3, in the notation of chapter 7). We stress that these effects are suppressed in the q_T spectrum itself, where they only enter indirectly and at $\mathcal{O}(q_T^2/Q^2)$ through fiducial cuts. By contrast, they are directly exposed in the p_T^ℓ spectrum near the Jacobian peak, and can be expected to affect the shape of the peak at the level of precision required for m_W determinations at the LHC. We therefore encourage precise, unfolded measurements of the p_T^ℓ spectrum for both W and Z in this

---

[3]Very recently, results for fiducial Higgs, Drell-Yan, and diboson production at $N^3LL+NNLO_0$ were presented in ref. [515], achieving the resummation of fiducial power corrections through a standard recoil prescription. In ref. [515] it was observed that, in line with our expectations, the linear power corrections in the q_T spectrum uniquely arise from the fiducial cuts also for $H \to \gamma\gamma$.

region to further experimentally constrain these effects. Other interesting measurements sensitive to these effects would be the double-differential spectrum in the lepton momenta p_{T1}, p_{T2}, or measurements of the scalar difference $|p_{T1} - p_{T2}|$.

- On the theory side, we pointed out that W_3 and related $\mathcal{O}(q_T/Q)$ structure functions receive their power suppression exclusively from the subleading hard currents that they match on in SCET. This can be the starting point of a rigorous factorization analysis, which will further elucidate to which extent resummation effects can be considered to be correlated between hadronic structure functions, e.g. between W_3 and the leading-power unpolarized structure functions $W_{-1,4}$. Awaiting these improvements, we leave a more detailed phenomenological analysis of the p_T^ℓ spectrum for future work.

- As another intriguing observation, we found that the precisely measured ϕ^* spectrum receives a leading-power contribution from the so-called double Boer-Mulders effect, i.e., from intrinsically nonperturbative spin correlations in unpolarized protons, which so far have proven elusive at the LHC [516]. If the dominant contribution from the unpolarized structure function can be isolated, e.g. by using the equally precisely measured q_T spectrum, the ϕ^* spectrum could become a particularly clean probe of the double Boer-Mulders effect. We again leave a detailed study for future work.

- On the computational side, we found that it is numerically much cheaper to predict or obtain the fiducial power corrections via factorization instead of including (or extracting) them through full fixed-order calculations, since the latter quickly become expensive toward small q_T or may not even be available. As discussed in more detail in section 5 of ref. [6], this is also reflected in a significantly improved performance of the q_T subtraction method when the fiducial power corrections are included in the subtraction term. In particular, this extends the applicability of the popular q_T subtraction method to phase-space regions where it would otherwise break down due to uncontrolled leptonic power corrections, e.g. for the p_T^ℓ spectrum near $p_T^\ell = m_W/2$, or would deteriorate due to large linear power corrections, e.g. in the presence of symmetric lepton acceptance cuts. The latter in particular were previously considered to be a challenge for fixed-order subtractions methods [517, 518]. We have already made use of these improvements in chapter 7 to compute the necessary fixed-order matching pieces, but anticipate that they will be of wider utility in the future.

Closing remarks. The research in this thesis is part of an ongoing effort to produce theory predictions that can keep up with the impressive level of precision to which experimental observables are already being measured at the LHC, or will be measured in the near future. This involves pushing predictions to higher orders in perturbation theory, but in particular requires upgrading the tools used in theory predictions to handle realistic, multi-differential experimental observables. We hope that the new factorization and resummation methods we developed in this thesis will prove to be useful additions to the theory toolbox and will help maximize the potential of the LHC to discover even faint hints of new physics.

Appendix A

Notation and conventions

A.1 General notation

We use light-cone coordinates with respect to lightlike reference vectors n^μ and $\bar{n}^\mu$ that satisfy $n^2 = \bar{n}^2 = 0$ and $\boldsymbol{n \cdot \bar{n} = 2}$,

$$p^\mu = \bar{n} \cdot p \, \frac{n^\mu}{2} + n \cdot p \, \frac{\bar{n}^\mu}{2} + p_\perp^\mu \equiv (n \cdot p, \bar{n} \cdot p, \vec{p}_\perp) \equiv (p^+, p^-, \vec{p}_\perp) \,. \tag{A.1}$$

Unless otherwise noted, for color-singlet production in *pp* collisions we take

$$n \equiv n_a = (1, +\hat{z})_{\text{lep}} = e^{+Y}(1, +\hat{z})_{\text{lab}} \,, \qquad \bar{n} \equiv n_b = (1, -\hat{z})_{\text{lep}} = e^{-Y}(1, -\hat{z})_{\text{lab}} \,, \tag{A.2}$$

aligned with the beam and z axis in the *leptonic frame* where the longitudinal momentum of the color-singlet final state vanishes. As written, the leptonic frame is reached from the lab frame through a boost by the color-singlet rapidity Y. The metric, antisymmetric tensor, and Dirac matrices in the $\perp$ plane are

$$g_\perp^{\mu\nu} = g^{\mu\nu} - \frac{n^\mu \bar{n}^\nu}{2} - \frac{\bar{n}^\mu n^\nu}{2} \,, \qquad \epsilon_\perp^{\mu\nu} = \frac{1}{2} \epsilon^{\mu\nu}{}_{\rho\sigma} \, n^\rho \bar{n}^\sigma \,, \qquad \gamma_\perp^\mu = g_\perp^{\mu\nu} \gamma_\nu \,. \tag{A.3}$$

We write the phase-space measure for a particle with momentum k and mass m as

$$\frac{\mathrm{d}^d k}{(2\pi)^{d-1}} \, \delta_+(k^2 - m^2) \equiv \frac{\mathrm{d}^d k}{(2\pi)^{d-1}} \, \theta(k^0) \, \delta(k^2 - m^2) = \frac{\mathrm{d}^{d-1}\vec{k}}{(2\pi)^{d-1}} \frac{1}{2\sqrt{\vec{k}^2 + m^2}} \,, \tag{A.4}$$

where $d = 4 - 2\epsilon$ is the number of spacetime dimensions. In light-cone coordinates,

$$\frac{\mathrm{d}^d k}{(2\pi)^{d-1}} \, \delta_+(k^2 - m^2) = \frac{1}{2(2\pi)^{d-1}} \, \mathrm{d}k^- \, \mathrm{d}k^+ \, \theta(k^- + k^+) \, \mathrm{d}\Omega_{2-2\epsilon} \, \mathrm{d}|\vec{k}_\perp| \, |\vec{k}_\perp|^{1-2\epsilon}$$
$$\times \, \delta(k^+ k^- - |\vec{k}_\perp|^2 - m^2) \,. \tag{A.5}$$

We use the Einstein summation convention for Lorentz indices $(\mu, \nu, \dots)$, Dirac spin indices (superscript $\alpha, \beta, \dots$), fundamental color indices (superscript $j, k, \dots$, mostly implicit) and adjoint color indices (superscript $a, b, \dots$), but *not* for parton indices (subscript $i, j, k, \ell = q_f, \bar{q}_f, g$). We use uppercase Tr for traces over fundamental color indices and lowercase tr for traces over Dirac indices. Our convention for the antisymmetric tensor is

$$\epsilon^{0123} = +1 \,. \tag{A.6}$$

Throughout this thesis, we denote the perturbative expansion of renormalized functions $F(\ldots, \mu)$ in terms of the renormalized $\overline{\text{MS}}$ coupling $\alpha_s(\mu)$ by

$$F(\ldots, \mu) = \sum_{n=0}^{\infty} F^{(n)}(\ldots, \mu) \left[\frac{\alpha_s(\mu)}{4\pi} \right]^n. \tag{A.7}$$

We always expand in $\alpha_s/4\pi$.

A.2 Fourier transformation

Fourier-transformed quantities in one and d dimensions are explicitly introduced in the text. For the two-dimensional Fourier transform in the transverse plane, our convention is

$$\frac{\mathrm{d}f}{\mathrm{d}\vec{k}_T} = \int \frac{\mathrm{d}^2 \vec{b}_T}{(2\pi)^2} e^{+i\vec{k}_T \cdot \vec{b}_T} \tilde{f}(\vec{b}_T), \qquad \tilde{f}(\vec{b}_T) = \int \mathrm{d}^2 \vec{k}_T \, e^{-i\vec{k}_T \cdot \vec{b}_T} \frac{\mathrm{d}f}{\mathrm{d}\vec{k}_T}. \tag{A.8}$$

Here we make the differential $\mathrm{d}\vec{k}_T = \mathrm{d}k_x \, \mathrm{d}k_y$ explicit as e.g. in a cross section. (For transverse momentum dependent soft and beam functions the differential is implicit in the function.) If f is azimuthally symmetric, i.e., if for $k_T \equiv |\vec{k}_T|, b_T \equiv |\vec{b}_T|$,

$$\frac{\mathrm{d}f}{\mathrm{d}\vec{k}_T} = \frac{1}{2\pi k_T} \frac{\mathrm{d}f}{\mathrm{d}k_T}, \qquad \tilde{f}(\vec{b}_T) = \tilde{f}(b_T), \tag{A.9}$$

the azimuthal integral can be performed, leaving the Hankel transform pair

$$\frac{\mathrm{d}f}{\mathrm{d}k_T} = k_T \int_0^\infty \mathrm{d}b_T \, b_T \, J_0(b_T k_T) \, \tilde{f}(b_T), \qquad \tilde{f}(b_T) = \int_0^\infty \mathrm{d}k_T \, J_0(b_T k_T) \frac{\mathrm{d}f}{\mathrm{d}k_T}, \tag{A.10}$$

where $J_0(x)$ is the zeroth-order Bessel function of the first kind. Integrating the first expression in eq. (A.10) by parts, the cumulant in k_T is given by

$$\int^{k_T^{\text{cut}}} \mathrm{d}k_T \frac{\mathrm{d}f}{\mathrm{d}k_T} = k_T^{\text{cut}} \int_0^\infty \mathrm{d}b_T \, J_1(b_T k_T^{\text{cut}}) \, \tilde{f}(b_T), \tag{A.11}$$

where the integral includes a potential singularity at $\vec{k}_T = 0$ regulated by plus distributions and $J_1(x)$ is the first-order Bessel function of the first kind.

A.3 Plus distributions

Following ref. [209], we denote plus distributions with dimensionless arguments as

$$\mathcal{L}_n(x) \equiv \left[\frac{\theta(x) \ln^n x}{x} \right]_+ = \lim_{\beta \to 0} \left[\frac{\theta(x - \beta) \ln^n x}{x} + \delta(x - \beta) \frac{\ln^{n+1} \beta}{n+1} \right], \tag{A.12}$$

$$\mathcal{L}^a(x) \equiv \left[\frac{\theta(x)}{x^{1-a}} \right]_+ = \lim_{\beta \to 0} \left[\frac{\theta(x - \beta)}{x^{1-a}} + \delta(x - \beta) \frac{x^a - 1}{a} \right]. \tag{A.13}$$

They have the defining properties

$$\mathcal{L}_n(x > 0) = \frac{\ln^n x}{x}\,, \quad \mathcal{L}^a(x > 0) = \frac{1}{x^{1-a}}\,, \qquad \int^1 \mathrm{d}x\,\mathcal{L}_n(x) = \int^1 \mathrm{d}x\,\mathcal{L}^a(x) = 0\,, \quad \text{(A.14)}$$

where the integral includes the singularity. Their action on a test function $g(x)$ is

$$\int^1 \mathrm{d}x\,g(x)\,\mathcal{L}_n(x) = \int^1 \mathrm{d}x\,\big[g(x) - g(0)\big]\,\frac{\theta(x)\ln^n x}{x}\,,$$
$$\int^1 \mathrm{d}x\,g(x)\,\mathcal{L}^a(x) = \int^1 \mathrm{d}x\,\big[g(x) - g(0)\big]\,\frac{\theta(x)}{x^{1-a}} \qquad \text{(A.15)}$$

Our shorthands for distributions with dimensionful arguments in one spatial dimension are

$$\mathcal{L}_n(k, \mu) \equiv \frac{1}{\mu}\mathcal{L}_n\Big(\frac{k}{\mu}\Big)\,, \qquad \mathcal{L}_n(t, \mu^2) \equiv \frac{1}{\mu^2}\mathcal{L}_n\Big(\frac{t}{\mu^2}\Big)\,,$$
$$\mathcal{L}^a(k, \mu) \equiv \frac{1}{\mu}\mathcal{L}^a\Big(\frac{k}{\mu}\Big)\,, \qquad \mathcal{L}^a(t, \mu^2) \equiv \frac{1}{\mu^2}\mathcal{L}^a\Big(\frac{t}{\mu^2}\Big)\,. \qquad \text{(A.16)}$$

In terms of $\mathcal{L}^a$, we further define

$$\mathcal{V}_a(x) \equiv \frac{e^{-\gamma_E a}}{\Gamma(1+a)}\big[a\mathcal{L}^a(x) + \delta(x)\big]\,, \qquad \mathcal{V}_a(k, \mu) \equiv \frac{1}{\mu}\mathcal{V}_a\Big(\frac{k}{\mu}\Big)\,, \qquad \text{(A.17)}$$

with an analogous definition for $\mathcal{V}_a(t, \mu^2)$. The $\mathcal{V}_a$ satisfy a group property,

$$\int \mathrm{d}k'\,\mathcal{V}_a(k', \mu)\,\mathcal{V}_b(k - k', \mu) = \mathcal{V}_{a+b}(k, \mu)\,, \qquad \mathcal{V}_0(k, \mu) = \delta(k)\,. \qquad \text{(A.18)}$$

The μ dependence of $\mathcal{V}_a(k, \mu)$ is given by

$$\mathcal{V}_a(k, \mu) = \Big(\frac{\mu'}{\mu}\Big)^a \mathcal{V}_a(k, \mu')\,, \qquad \mu\frac{\mathrm{d}}{\mathrm{d}\mu}\mathcal{V}_a(k, \mu) = -a\mathcal{V}_a(k, \mu)\,. \qquad \text{(A.19)}$$

Expanding $\mathcal{V}_a(k, \mu)$ in powers of a we find

$$\mathcal{V}_a(k, \mu) = \delta(k) + a\,\mathcal{L}_0(k, \mu) + \frac{a^2}{2!}\big[2\mathcal{L}_1(k, \mu) - \zeta_2\delta(k)\big]$$
$$+ \frac{a^3}{3!}\big[3\mathcal{L}_2(k, \mu) - 3\zeta_2\mathcal{L}_0(k, \mu) + 2\zeta_3\delta(k)\big] + \mathcal{O}(a^4)\,. \qquad \text{(A.20)}$$

The Fourier transform of $\mathcal{V}_a(k, \mu)$ is given by

$$\int \mathrm{d}k\,e^{-\mathrm{i}ky}\,\mathcal{V}_a(k, \mu) = e^{-aL_y}\,, \qquad \int \frac{\mathrm{d}y}{2\pi}\,e^{\mathrm{i}ky}\,e^{-aL_y} = \mathcal{V}_a(k, \mu)\,, \quad L_y = \ln(\mathrm{i}y\mu e^{\gamma_E})\,. \quad \text{(A.21)}$$

For plus distributions in the transverse plane, we use the conventions from app. C of ref. [263]. With $k_T^2 \equiv \vec{k}_T^2 \geq 0$ understood, we define

$$\delta(\vec{k}_T) = \frac{1}{\pi}\delta(k_T^2)\,, \qquad \mathcal{L}_n(\vec{k}_T, \mu) \equiv \frac{1}{\pi\mu^2}\mathcal{L}_n\Big(\frac{k_T^2}{\mu^2}\Big)\,, \qquad \text{(A.22)}$$

L_b^n	$\int \frac{\mathrm{d}^2 \vec{b}_T}{(2\pi)^2} e^{+i\vec{k}_T \cdot \vec{b}_T} L_b^n$
1	$\delta^{(2)}(\vec{k}_T)$
L_b	$-\mathcal{L}_0(\vec{k}_T, \mu)$
L_b^2	$+2\mathcal{L}_1(\vec{k}_T, \mu)$
L_b^3	$-3\mathcal{L}_2(\vec{k}_T, \mu) - 4\zeta_3\delta^{(2)}(\vec{k}_T)$
L_b^4	$+4\mathcal{L}_3(\vec{k}_T, \mu) + 16\zeta_3\mathcal{L}_0(\vec{k}_T, \mu)$
L_b^5	$-5\mathcal{L}_4(\vec{k}_T, \mu) - 80\zeta_3\mathcal{L}_1(\vec{k}_T, \mu) - 48\zeta_5\delta^{(2)}(\vec{k}_T)$
L_b^6	$+6\mathcal{L}_5(\vec{k}_T, \mu) + 240\zeta_3\mathcal{L}_2(\vec{k}_T, \mu) + 288\zeta_5\mathcal{L}_0(\vec{k}_T, \mu) + 160\zeta_3^2\delta^{(2)}(\vec{k}_T)$

Table A.1: Fourier transform of $L_b^n = \ln^n(b_T^2\mu^2/b_0^2)$ to $\vec{k}_T$ space for $n \leq 6$ [263].

where $\mathcal{L}_n(x)$ is defined as above in eq. (A.12), such that

$$\int_{|\vec{k}_T| \leq \mu} \mathrm{d}^2\vec{k}_T\, \mathcal{L}_n(\vec{k}_T, \mu) = \pi \int_0^{\mu^2} \mathrm{d}q_T^2\, \frac{1}{\pi\mu^2} \mathcal{L}_n\left(\frac{q_T^2}{\mu^2}\right) = 0\,. \tag{A.23}$$

The cumulant for a generic cut $|\vec{k}_T| \leq k_T^{\mathrm{cut}}$ follows to be

$$\int_{|\vec{k}_T| \leq k_T^{\mathrm{cut}}} \mathrm{d}^2\vec{k}_T\, \mathcal{L}_n(\vec{k}_T, \mu) = \frac{\theta(k_T^{\mathrm{cut}})}{n+1} \ln^{n+1} \frac{(k_T^{\mathrm{cut}})^2}{\mu^2}\,. \tag{A.24}$$

Fourier transforms of $\mathcal{L}_n(\vec{k}_T, \mu)$ are most conveniently expressed in terms of

$$L_b \equiv \ln \frac{b_T^2\mu^2}{b_0^2}\,, \qquad b_0 \equiv 2e^{-\gamma_E}\,. \tag{A.25}$$

The inverse Fourier transforms of L_b^n with $n \leq 6$ are given in terms of the $\mathcal{L}_n(\vec{k}_T, \mu)$ in table A.1. (The general expression can be found in ref. [263].) These are in required to evaluate the fixed-order singular section in chapter 7 and the SCET_+ and $\mathrm{SCET}_{\mathrm{II}}$ cross sections in chapter 4 at fixed-order and μ_{I} scales.

A.4 Mellin convolution and flavor decomposition

We denote the Mellin convolution of z dependent functions $g(z), h(z)$ by

$$(g \otimes h)(z) \equiv \int \frac{\mathrm{d}z'}{z'}\, g\left(\frac{z}{z'}\right) h(z')\,. \tag{A.26}$$

For all concrete results in this thesis, we have used the MT package [519] to analytically evaluate convolutions of this kind before implementing them numerically in SCETlib [8]. We

have validated the implementation in `SCETlib` by a numerical implementation of eq. (A.26). If the Mellin kernels are tensors $G_{ij}(z)$, $H_{ij}(z)$ in flavor space in addition, we write

$$(G \otimes H)_{ij}(z) \equiv \sum_k (G_{ik} \otimes H_{kj})(z) = \sum_k \int \frac{\mathrm{d}z'}{z'} G_{ik}\left(\frac{z}{z'}\right) H_{kj}(z') . \qquad (A.27)$$

Note that for pure z dependent kernels, the product is commutative, $(g \otimes h)(z) = (h \otimes g)(z)$, whereas for tensor-valued kernels it is not. In appendix E we also make use of the corresponding identity element,

$$\mathbf{1}_{ij}(z) \equiv \delta_{ij}\, \delta(1-z) , \qquad (\mathbf{1} \otimes G)_{ij}(z) = G_{ij}(z) . \qquad (A.28)$$

Throughout the text, we decompose the flavor structure of Mellin kernels $G_{ij}(z)$ as

$$
\begin{aligned}
G_{q_i q_j}(z) &= G_{\bar{q}_i \bar{q}_j}(z) = \delta_{ij} G_{qqV}(z) + G_{qqS}(z) + G_{qq\Delta S}(z) , \\
G_{q_i \bar{q}_j}(z) &= G_{\bar{q}_i q_j}(z) = \delta_{ij} G_{q\bar{q}V}(z) + G_{qqS}(z) - G_{qq\Delta S}(z) , \\
G_{q_i g}(z) &= G_{\bar{q}_i g}(z) = G_{qg}(z) , \\
G_{gg}(z) &= G_{gg}(z) , \\
G_{g q_i}(z) &= G_{g \bar{q}_i}(z) = G_{gq}(z) .
\end{aligned}
\qquad (A.29)
$$

This decomposition is sufficient and unique to all orders by the flavor symmetry and charge conjugation invariance of massless QCD. We apply it to the perturbative coefficients $G = P^{(n)}$ of the DGLAP kernels in eq. (2.164) and to the finite terms $G = I^{(n)}$ of beam function matching coefficients at each order in α_s. The G_{qqV} and G_{gg} contributions are typically already present at tree level, the G_{qg} and G_{gq} channels start at one loop, the G_{qqS} and $G_{q\bar{q}V}$ channels open up at two loops, and the $G_{qq\Delta S}$ channel only receives contributions from topologies at three loops and beyond.

The decomposition in eq. (A.29) also makes it straightforward to evaluate and iterate sums over intermediate partons. For example, for the convolution in eq. (A.27), we have

$$
\begin{aligned}
(G \otimes H)_{gg}(z) &= (G_{gg} \otimes H_{gg})(z) + 2n_f (G_{gq} \otimes H_{qg})(z) , \\
(G \otimes H)_{qg}(z) &= \left[\left(G_{qqV} + G_{q\bar{q}V} + 2n_f G_{qqS}\right) \otimes H_{qg}\right](z) + (G_{qg} \otimes H_{gg})(z) , \\
(G \otimes H)_{gq}(z) &= \left[G_{gq} \otimes \left(H_{qqV} + H_{q\bar{q}V} + 2n_f H_{qqS}\right)\right](z) + (G_{gg} \otimes H_{gq})(z) , \\
(G \otimes H)_{qqV}(z) &= (G_{qqV} \otimes H_{qqV})(z) + (G_{q\bar{q}V} \otimes H_{q\bar{q}V})(z) , \\
(G \otimes H)_{q\bar{q}V}(z) &= (G_{qqV} \otimes H_{q\bar{q}V})(z) + (G_{q\bar{q}V} \otimes H_{qqV})(z) , \\
(G \otimes H)_{qqS}(z) &= \left[G_{qqS} \otimes \left(H_{qqV} + H_{q\bar{q}V}\right)\right](z) + \left[\left(G_{qqV} + G_{q\bar{q}V}\right) \otimes H_{qqS}\right](z) \\
&\quad + 2n_f \left(G_{qqS} \otimes H_{qqS}\right)(z) + \left(G_{qg} \otimes H_{gq}\right)(z) , \\
(G \otimes H)_{qq\Delta S}(z) &= \left[G_{qq\Delta S} \otimes \left(H_{qqV} - H_{q\bar{q}V}\right)\right](z) + \left[\left(G_{qqV} - G_{q\bar{q}V}\right) \otimes H_{qq\Delta S}\right](z) \\
&\quad + 2n_f \left(G_{qq\Delta S} \otimes H_{qq\Delta S}\right)(z) ,
\end{aligned}
\qquad (A.30)
$$

where n_f is the number of active flavors, and all products on the right-hand side only involve pure functions of z.

Appendix B

Hard scattering processes

In this appendix we collect expressions that are specific to the hard scattering process, but common to all factorized color-singlet cross sections. We use the notation of chapter 7, which explicitly separates the hard functions for different leading-power hadronic structure functions (appendix B.1) from the leptonic tensor (appendix B.2). The combined hard functions used at cross-section level in the rest of the text, which in addition include the flux factor and occasional Jacobians, are given in terms of these ingredients in appendix B.3. In appendix B.3 we also discuss how our notation generalizes to processes that are not mediated by a single hard current, e.g. diboson production.

B.1 Hard functions for hadronic structure functions

Drell-Yan production. At leading power in λ, the hard contribution to the hadronic tensor in the limit $\lambda \ll 1$ is given by [57],[1]

$$H^{\mu\nu}_{VV' q\bar{q}'}(n_a, n_b; \omega_a, \omega_b) = \frac{1}{2N_c} \operatorname{tr}\left[\frac{\not{n}_a}{2} \bar{C}^{(0)\mu}_{V q\bar{q}'}(n_b, n_a; \omega_b, \omega_a)\frac{\not{n}_b}{2} C^{(0)\nu}_{V' q\bar{q}'}(n_b, n_a; \omega_b, \omega_a)\right]$$
$$+ \left(\text{terms} \propto \operatorname{tr}\left[\not{n}_a \not{n}_{\perp a} \bar{C}^{(0)\mu}_{V q\bar{q}'} \not{n}_{\perp b} \not{n}_b C^{(0)\nu}_{V' q\bar{q}'}\right]\right), \tag{B.1}$$

where $C^{(0)\mu\,\alpha\beta}_{V,q\bar{q}'}$ are the hard matching coefficients in eq. (7.93), $\bar{C}^{\mu\beta\alpha} = [\gamma^0 C^{\dagger\mu}\gamma^0]^{\beta\alpha}$, and the trace is over the Dirac indices. The additional terms in parenthesis in the second line do not contribute to $H_{-1,4}$ but only to $H_{2,5}$ relevant for the Boer-Mulders effect, see eq. (7.89), where the $n_{\perp a,b}$ are transverse unit vectors associated with the Boer-Mulders functions $h^\perp_{1a,b}$.

We remind the reader that the VV' indices were largely left implicit in the main text. Using eq. (7.33), the hard functions $H_{i\,VV'\,q\bar{q}'}$ for $i = -1, 4$ are given by the projections onto $x_\mu x_\nu + y_\mu y_\nu = -g_{\perp\mu\nu} + \mathcal{O}(\lambda)$ and $2\mathrm{i}(x_\mu y_\nu - x_\nu y_\mu) = 2\mathrm{i}\epsilon_{\perp\mu\nu} + \mathcal{O}(\lambda)$,

$$H_{-1\,VV'\,q\bar{q}'}(q^2) = -g_{\perp\mu\nu}H^{\mu\nu}_{VV'\,q\bar{q}'}(n_a, n_b; \omega_a, \omega_b)\,,$$
$$H_{4\,VV'\,q\bar{q}'}(q^2) = 2\mathrm{i}\epsilon_{\perp\mu\nu}H^{\mu\nu}_{VV'\,q\bar{q}'}(n_a, n_b; \omega_a, \omega_b)\,. \tag{B.2}$$

Here we used that the projected hard function can only depend on the Lorentz-scalar product of the label momenta. Most commonly this is $\omega_a\omega_b = q^2 = Q^2$ as written here. In some occasions in chapter 5, the product evaluates to $\omega_a\omega_b = q^+q^- = Q^2 + q_T^2$ instead.

---

[1] An additional factor of 2 compared to ref. [57] is due to the fact that the hadronic tensor there is defined for $\mathrm{d}\sigma/\mathrm{d}Q^2\mathrm{d}Y\mathrm{d}^2\vec{q}_T$ whereas here it is defined for $\mathrm{d}\sigma/\mathrm{d}^4q = 2\,\mathrm{d}\sigma/\mathrm{d}Q^2\mathrm{d}Y\mathrm{d}^2\vec{q}_T$.

The case of an incoming antiquark in the a direction follows from $a \leftrightarrow b$,

$$H^{\mu\nu}_{VV'\,\bar{q}'q}(n_a, n_b; \omega_a, \omega_b) = H^{\mu\nu}_{VV'\,q\bar{q}'}(n_b, n_a; \omega_b, \omega_a)\,. \tag{B.3}$$

This implies

$$H_{-1\,VV'\,\bar{q}'q}(q^2) = +H_{-1\,VV'\,q\bar{q}'}(q^2)\,, \qquad H_{4\,VV'\,\bar{q}'q}(q^2) = -H_{4\,VV'\,q\bar{q}'}(q^2)\,, \tag{B.4}$$

as expected from parity. In the inclusive case we also use the shorthand

$$H_{VV'\,q\bar{q}'}(q^2) \equiv H_{-1\,VV'\,q\bar{q}'}(q^2)\,. \tag{B.5}$$

Inserting the expression in eq. (7.93) into eq. (B.1), and suppressing the q^2 argument for brevity, we find

$$H_{-1\,ZZ\,q\bar{q}'} = \frac{8\pi\alpha_{\rm em}}{N_c}\delta_{qq'}\Big\{(v_q^2 + a_q^2)|C_q|^2 + 2\,{\rm Re}\sum_f (v_q v_f C_q^* C_{vf} + a_q a_f C_q^* C_{af}) + \mathcal{O}(\alpha_s^4)\Big\}\,,$$

$$H_{-1\,\gamma\gamma\,q\bar{q}'} = \frac{8\pi\alpha_{\rm em}}{N_c}\delta_{qq'}\Big\{Q_q^2|C_q|^2 + 2\,{\rm Re}\sum_f Q_q Q_f C_q^* C_{vf} + \mathcal{O}(\alpha_s^6)\Big\}\,,$$

$$H_{-1\,Z\gamma\,q\bar{q}'} = \frac{8\pi\alpha_{\rm em}}{N_c}\delta_{qq'}\Big\{-v_q Q_q|C_q|^2 - \sum_f (v_f Q_q C_{vf}^* C_q + v_q Q_f C_q^* C_{vf}) + \mathcal{O}(\alpha_s^6)\Big\}$$

$$= H^*_{-1\,\gamma Z\,q\bar{q}'}\,, \tag{B.6}$$

where Re denotes the real part, the vector (v_f) and axial (a_f) couplings of a quark of flavor f to the Z boson were given in eq. (2.51). The terms denoted as $\mathcal{O}(\alpha_s^{4,6})$ are proportional to the square of the singlet matching coefficients, which only start at $C_{af} = \mathcal{O}(\alpha_s^2)$ and $C_{vf} = \mathcal{O}(\alpha_s^3)$, whereas the nonsinglet coefficient $C_q = 1 + \mathcal{O}(\alpha_s)$. In the parity-odd case, we have

$$H_{4\,ZZ\,q\bar{q}'} = \frac{16\pi\alpha_{\rm em}}{N_c}\delta_{qq'}\Big\{2v_q a_q|C_q|^2 + 2\,{\rm Re}\sum_f (v_q a_f C_q^* C_{af} + a_q v_f C_q^* C_{vf}) + \mathcal{O}(\alpha_s^5)\Big\}\,,$$

$$H_{4\,\gamma\gamma\,q\bar{q}'} = 0\,,$$

$$H_{4\,Z\gamma\,q\bar{q}'} = \frac{16\pi\alpha_{\rm em}}{N_c}\delta_{qq'}\Big\{-a_q Q_q|C_q|^2 - \sum_f (a_f Q_q C_{af}^* C_q + a_q Q_f C_q^* C_{vf}) + \mathcal{O}(\alpha_s^5)\Big\}$$

$$= H^*_{4\,\gamma Z\,q\bar{q}'}\,. \tag{B.7}$$

For $W^\pm$ exchange, we have

$$H_{-1\,W^+W^+\,q\bar{q}'} = \frac{2\pi\alpha_{\rm em}}{N_c}\frac{|V_{qq'}|^2}{\sin^2\theta_w}|C_q|^2\,, \qquad H_{4\,W^+W^+\,q\bar{q}'} = \frac{4\pi\alpha_{\rm em}}{N_c}\frac{|V_{qq'}|^2}{\sin^2\theta_w}|C_q|^2\,,$$

$$H_{-1\,W^-W^-\,q\bar{q}'} = \frac{2\pi\alpha_{\rm em}}{N_c}\frac{|V_{q'q}|^2}{\sin^2\theta_w}|C_q|^2\,, \qquad H_{4\,W^-W^-\,q\bar{q}'} = \frac{4\pi\alpha_{\rm em}}{N_c}\frac{|V_{q'q}|^2}{\sin^2\theta_w}|C_q|^2\,, \tag{B.8}$$

where $V_{qq'}$ denotes the CKM-matrix element for $q \in \{u, c, t\}$ and $q' \in \{d, s, b\}$ (and we take it to vanish in all other cases). The overall relative factor of 2 between H_{-1} and H_4 is due to the conventional normalization of $g_4(\theta, \varphi) = \cos\theta$ rather than $2\cos\theta$ in eq. (7.47).

The renormalized matching coefficients $C_q(q^2, \mu)$ and $C_{vf,af}(q^2, \mu)$ can be extracted from the IR-finite parts of the $q\bar{q}$ vector and axial-vector form factors, which admit the same flavor decomposition as eq. (7.93). The one-loop nonsinglet matching coefficient reads [212, 520]

$$C_q(q^2, \mu) = 1 + \frac{\alpha_s}{4\pi} C_F \left[-\ln^2 \frac{-q^2 - i0}{\mu^2} + 3 \ln \frac{-q^2 - i0}{\mu^2} - 8 + \zeta_2 \right] + \mathcal{O}(\alpha_s^2) \tag{B.9}$$

Explicit expressions for $C_q(q^2, \mu)$ to three loops in our notation can be found in ref. [1], including also its renormalization and running. The two-loop results which enter in our analysis in chapter 7 follow from the two-loop quark form factors [521–524]. In principle, there is an $\mathcal{O}(\alpha_s^2)$ contribution to the axial-vector singlet coefficient if the top quark is taken to be massive at the hard scale [57]. These contributions have however been found to be small at the level of the total cross section [144, 469], and we neglect them in this thesis.

Gluon-fusion Higgs production. For gluon-fusion Higgs production, the hadronic tensor is an overall scalar. For the case where the collinear matrix elements are scalar functions normalized to $f_g + \mathcal{O}(\alpha_s)$, the hard contribution to the hadronic tensor in the EFT approximation [see eq. (2.73)] reads

$$H_{HH\,gg}^{\mathrm{EFT}}(m_t^2, q^2, \mu^2) = \frac{|q^2|}{36\pi^2 v^2(N_c^2 - 1)} \, |\alpha_s C_t(m_t, \mu)|^2 \, |C_g(q^2, \mu)|^2 \,, \tag{B.10}$$

where $v^2 = 1/(\sqrt{2}G_F)$ is the square of the Higgs vacuum expectation value. The matching coefficient from integrating out the top quark reads [151–154],

$$C_t = 1 + \frac{\alpha_s}{4\pi}(5C_A - 3C_F) + \mathcal{O}(\alpha_s^2) \,. \tag{B.11}$$

In the rEFT scheme, eq. (B.10) is multiplied by an additional factor of $|F_0[m_H^2/(4m_t^2)]|^2$ as given in eq. (2.74), accordingly. The renormalized SCET matching coefficient $C_g(q^2, \mu)$ can be extracted from the IR-finite part of the gg scalar form factor. At one loop, the matching coefficient is given by [231, 525]

$$C_g(q^2, \mu) = 1 + \frac{\alpha_s}{4\pi} C_A \left[-\ln^2 \frac{-q^2 - i0}{\mu^2} + \zeta_2 \right] + \mathcal{O}(\alpha_s^2) \tag{B.12}$$

Explicit expressions for $C_g(q^2, \mu)$ to three loops can be found in ref. [1].

B.2 Leptonic tensors

Drell-Yan production. The leptonic scalar coefficients $L_{\pm VV'}(q^2)$ defined in eq. (7.44) encode the squared electroweak decay matrix element including the vector-boson propagator. In the inclusive case we also use the shorthand

$$L_{VV'}(q^2) \equiv L_{+VV'}(q^2) \,. \tag{B.13}$$

For $Z/\gamma^* \to \ell^+\ell^-$, the parity-even leptonic coefficients read

$$L_{+\,ZZ}(q^2) = \frac{2}{3}\frac{\alpha_{\rm em}}{q^2}\,(v_\ell^2 + a_\ell^2)\,\left|P_Z(q^2)\right|^2\,, \qquad L_{+\,\gamma\gamma}(q^2) = \frac{2}{3}\frac{\alpha_{\rm em}}{q^2}\,Q_\ell^2\,,$$

$$L_{+\,\gamma Z}(q^2) = \frac{2}{3}\frac{\alpha_{\rm em}}{q^2}\,(-v_\ell\,Q_\ell)\,P_Z(q^2)\,, \qquad L_{+\,Z\gamma}(q^2) = L_{+\,\gamma Z}^*(q^2)\,. \tag{B.14}$$

The parity-odd coefficients arise from the interference of axial and vector current contributions,

$$L_{-\,ZZ}(q^2) = \frac{2}{3}\frac{\alpha_{\rm em}}{q^2}\,(2v_\ell\,a_\ell)\,\left|P_Z(q^2)\right|^2\,, \qquad L_{-\,\gamma\gamma}(q^2) = 0\,,$$

$$L_{-\,\gamma Z}(q^2) = \frac{2}{3}\frac{\alpha_{\rm em}}{q^2}\,(-a_\ell Q_\ell)\,P_Z(q^2)\,, \qquad L_{-\,Z\gamma}(q^2) = L_{-\,\gamma Z}^*(q^2)\,. \tag{B.15}$$

Here, $Q_\ell = -1$, and the vector (v_ℓ) and axial couplings (a_ℓ) of the lepton ℓ to the Z boson have the same form as eq. (2.51) with $T_3^\ell = -1/2$. The $Z \to \nu\bar\nu$ process is obtained by the replacement $\ell \to \nu$ with $Q_\nu = 0$ and $T_3^\nu = +1/2$. The reduced propagator P_V is given by

$$P_V(q^2) = \frac{q^2}{q^2 - m_V^2 + {\rm i}\Gamma_V m_V}\,. \tag{B.16}$$

For $W \to \ell\nu$, the $L_\pm(q^2)$ are equal due to the current's $V - A$ structure, and are given by

$$L_{+\,W^\pm W^\pm}(q^2) = L_{-\,W^\pm W^\pm}(q^2) = \frac{1}{6}\frac{\alpha_{\rm em}}{q^2}\,\frac{1}{\sin^2\theta_w}\,\left|P_W(q^2)\right|^2\,. \tag{B.17}$$

Gluon-fusion Higgs production. For gluon-fusion Higgs production in the narrow-width approximation, the inclusive leptonic tensor for a given decay channel $H \to L$ reads

$$L_{HH}(q^2) = 2\pi\delta(q^2 - m_H^2)\,{\rm Br}_{H\to L}\,. \tag{B.18}$$

The scalar decay is isotropic in the Higgs rest frame, so a massless two-body decay like $H \to \gamma\gamma$ is simply flat in the Collins-Soper angles,

$$\mathrm{d}\cos\theta\,\mathrm{d}\varphi\,L_{HH}(q^2,\cos\theta,\varphi) = \frac{\mathrm{d}\cos\theta\,\mathrm{d}\varphi}{4\pi}\,L_{HH}(q^2)\,. \tag{B.19}$$

B.3 Combined hard functions

Throughout the main text we used the shorthand H_{ij} for the total contribution of the hard scattering process at the level of the total pp cross section. We used two distinct choices of normalization that differ by a Jacobian:

(A) In section 2.4.2 and chapter 5, we give the cross section differential in dimensionless momentum fractions like $x_{a,b}$ or $x_\mp$. In these cases the combined hard function is given in terms of the unpolarized hard function and the inclusive leptonic tensor as

$$H_{ij}^{(A)}(q^2,\mu) = \frac{1}{4}\sum_{V,V'} H_{VV'\,ij}(q^2,\mu)\,L_{VV'}(q^2)\,. \tag{B.20}$$

It includes the interference sum over all intermediate bosons, which for the Higgs is trivial due to the narrow-width approximation, $V = V' = H$. In section 2.4.1 we also used the DIS hard function, which is related to the above by crossing,

$$H_{q\bar{q}'}^{\text{DIS}}(-q^2, \mu) = H_{qq'}^{(\text{A})}(q^2, \mu) \,. \tag{B.21}$$

Note that in DIS, the SCET hard matching coefficients are evaluated at $q^2 = -Q^2 < 0$ and thus are purely real.

(B) In sections 2.4.3, 2.4.4, and 2.4.5 and chapters 3 and 4, we give the cross section differential in $\mathrm{d}Q^2 \, \mathrm{d}Y$, so the combined hard function differs from the above by an additional Jacobian $\mathrm{d}Q^2 \, \mathrm{d}Y = E_{\text{cm}}^2 \mathrm{d}x_a \, \mathrm{d}x_b$,

$$H_{ij}^{(\text{B})}(q^2, \mu) = \frac{1}{E_{\text{cm}}^2} H_{ij}^{(\text{A})}(q^2, \mu) \,. \tag{B.22}$$

We suppress the dependence on E_{cm} in this case.

The precise choice of (A) or (B) can always be read off from the left-hand side in factorization formulas, also on dimensional grounds, so we just dropped the superscripts in the main text. To account for more complicated final states produced from the decay of a single intermediate boson, one may simply adjust the leptonic tensor in the above.

Our notation for combined hard functions, and all our results for factorized cross sections in chapters 3, 4, and 5, also readily generalize to color-singlet production processes that are not mediated by a single electroweak current, e.g. to diboson production. In these cases it is tedious to factorize the cross section into high-rank hadronic and leptonic tensors. (As this is a requirement for the results in chapter 7, their extension to diboson processes, while desirable, is beyond the scope of this thesis.) Instead, it is more expedient to consider the combined hard function as a whole. For a general color-singlet production process $pp \to LX$, the hard function for normalization choice (A) is given by

$$H_{ij}^{(\text{A})}(Q^2, \mu) = \frac{1}{2Q^2} \int \mathrm{d}\Phi_L \, \delta^4 \Big(Q \frac{n^\mu + \bar{n}^\mu}{2} - p_L^\mu \Big) \big| \mathcal{M}_{\text{fin}}(ij \to L) \big|^2 \tag{B.23}$$

Here $\mathcal{M}_{\text{fin}}(ij \to L)$ is the all-order virtual amplitude for the partonic process $ij \to L$ computed in dimensional regularization (with $d-2$ helicities for internal gluon lines) and with the poles minimally subtracted [177]. As a check, this subtraction must be equivalent to applying the $\overline{\text{MS}}$ counterterm of the SCET quark/gluon matching coefficient $C_i(q^2)$. Our normalization of the matrix element is such that at leading order,

$$\frac{\mathrm{d}\sigma^{(0)}}{\mathrm{d}x_a \, \mathrm{d}x_b} = \sum_{i,j} f_i(x_a) \, f_j(x_b) \, \frac{1}{2Q^2} \int \mathrm{d}\Phi_L \, \delta^4(x_a P_a^\mu + x_b P_b^\mu - p_L^\mu) \, \big| \mathcal{M}^{(0)}(ij \to L) \big|^2 \,. \tag{B.24}$$

It is straightforward to make the calculation differential in the full color-singlet Born phase space Φ_L by inserting additional δ functions measuring e.g. the rapidity difference Δy of the diboson pair on the right-hand side of eq. (B.23). If fiducial cuts are applied on the

individual boson rapidities or that of their decay products, the hard function will also start to explicitly depend on the total rapidity Y of the diboson system, which drops out in the boost-invariant expression above. (Should fiducial cuts be applied, we remind the reader that $n^\mu, \bar{n}^\mu = (1, \pm\hat{z})_{\text{lep}}$ are chosen in the leptonic frame.)

Finally, note that the matrix element in eq. (B.23) is implicitly *averaged* over the spin and color of the i, j, i.e., this expression assumes unpolarized collinear matrix elements. This assumption is satisfied in chapters 3 and 5 and for quark production processes in the perturbative domain $\Lambda_{\text{QCD}} \ll q_T$, where Boer-Mulders effects are suppressed. More care is required if vectorial transverse momentum is measured on gluon collinear matrix elements. This would e.g. matter if the results of chapter 4 are applied to the $gg \to \gamma\gamma$ diphoton production channel. In this case there will be nontrivial spin correlations between the total $\vec{q}_T$ of the color-singlet system and its orientation in the transverse plane starting at $\mathcal{O}(\alpha_s^2)$ relative to the tree-level quark channel.

Appendix C

Anomalous dimensions

C.1 QCD anomalous dimensions

We expand the β function of QCD in $d = 4$ spacetime dimensions as

$$\mu \frac{\mathrm{d}\alpha_s(\mu)}{\mathrm{d}\mu} = \beta[\alpha_s(\mu)], \qquad \beta(\alpha_s) = -2\alpha_s \sum_{n=0}^{\infty} \beta_n \left(\frac{\alpha_s}{4\pi}\right)^{n+1}. \tag{C.1}$$

The coefficients up to three loops in the $\overline{\mathrm{MS}}$ scheme are [526, 527]

$$\beta_0 = \frac{11}{3} C_A - \frac{4}{3} T_F n_f, \tag{C.2}$$

$$\beta_1 = \frac{34}{3} C_A^2 - 2T_F n_f \left(\frac{10}{3} C_A + 2C_F\right),$$

$$\beta_2 = \frac{2857}{54} C_A^3 + 2T_F n_f \left(-\frac{1415}{54} C_A^2 - \frac{205}{18} C_F C_A + C_F^2\right) + 4T_F^2 n_f^2 \left(\frac{79}{54} C_A + \frac{11}{9} C_F\right).$$

The N³LL analysis in chapter 7 in addition uses the four-loop β function [526–529]. The cusp anomalous dimension and all noncusp anomalous dimensions are expanded as

$$\Gamma_{\mathrm{cusp}}^i(\alpha_s) = \sum_{n=0}^{\infty} \Gamma_n^i \left(\frac{\alpha_s}{4\pi}\right)^{n+1}, \qquad \gamma(\alpha_s) = \sum_{n=0}^{\infty} \gamma_n \left(\frac{\alpha_s}{4\pi}\right)^{n+1}. \tag{C.3}$$

The coefficients of the $\overline{\mathrm{MS}}$ cusp anomalous dimension to three loops are [199, 200, 530]

$$\Gamma_0^i = 4C_i,$$

$$\Gamma_1^i = 4C_i \left[C_A \left(\frac{67}{9} - 2\zeta_2\right) - \frac{20}{9} T_F n_f \right],$$

$$\Gamma_2^i = 4C_i \left\{ C_A^2 \left(\frac{245}{6} - \frac{268}{9}\zeta_2 + \frac{22}{3}\zeta_3 + 22\zeta_4\right) \right.$$

$$\left. + 2T_F n_f \left[C_A \left(-\frac{209}{27} + \frac{40}{9}\zeta_2 - \frac{28}{3}\zeta_3\right) + C_F \left(-\frac{55}{6} + 8\zeta_3\right) \right] - \frac{16}{27} T_F^2 n_f^2 \right\}, \tag{C.4}$$

where $C_i = C_F$ for $i = q$ and $C_i = C_A$ for $i = g$. For the N³LL analysis in chapter 7 we also need the four-loop coefficient [199–201, 511, 530–535]; see ref. [534] for a complete list of earlier references.

The PDF anomalous dimension in eq. (2.164) is expanded as

$$P_{ij}(\alpha_s, z) = \sum_{n=0}^{\infty} P_{ij}^{(n)}(z) \left(\frac{\alpha_s}{4\pi}\right)^{n+1}. \tag{C.5}$$

Note that we expand the PDF anomalous dimension in $\alpha_s/(4\pi)$ and not $\alpha_s/(2\pi)$ as is often done. We decompose the flavor dependence of the DGLAP kernels as in eq. (A.29). The one-loop coefficients of the PDF anomalous dimension read

$$P_{qqV}^{(0)}(z) = 2C_F\,\delta_{ij}\,\theta(z)P_{qq}(z)\,, \qquad\qquad P_{gg}^{(0)}(z) = 2C_A\,\theta(z)P_{gg}(z) + \beta_0\,\delta(1-z)\,,$$
$$P_{qg}^{(0)}(z) = 2T_F\,\theta(z)P_{qg}(z)\,, \qquad\qquad P_{gq}^{(0)}(z) = 2C_F\,\theta(z)P_{gq}(z)\,,$$
$$P_{qqS}^{(0)} = P_{q\bar{q}V}^{(0)} = P_{qq\Delta S}^{(0)} = 0\,, \tag{C.6}$$

in terms of the standard color-stripped one-loop QCD splitting functions

$$P_{qq}(z) = 2\mathcal{L}_0(1-z) - \theta(1-z)(1+z) + \frac{3}{2}\delta(1-z) \qquad = \left[\theta(1-z)\frac{1+z^2}{1-z}\right]_+,$$
$$P_{gg}(z) = 2\mathcal{L}_0(1-z) + \theta(1-z)\left[2z(1-z) + \frac{2(1-z)}{z} - 2\right] = 2\mathcal{L}_0(1-z)\frac{(1-z+z^2)^2}{z}\,,$$
$$P_{qg}(z) = \theta(1-z)\left[1 - 2z(1-z)\right],$$
$$P_{gq}(z) = \theta(1-z)\frac{1+(1-z)^2}{z}\,. \tag{C.7}$$

The DGLAP kernels have been calculated to two loops in refs. [536–538] and to three loops in refs. [199, 200]. Denoting the results of refs. [199, 200] by a calligraphic $\mathcal{P}$ to distinguish them from our $P_{ij}^{(n)}$, their results relate to our notation as

$$P_{qqV}^{(n)}(z) = \frac{1}{2}\left[\mathcal{P}_{ns}^{(n)+}(z) + \mathcal{P}_{ns}^{(n)-}(z)\right], \qquad P_{gg}^{(n)}(z) = \mathcal{P}_{gg}^{(n)}(z)\,,$$
$$P_{q\bar{q}V}^{(n)}(z) = \frac{1}{2}\left[\mathcal{P}_{ns}^{(n)+}(z) - \mathcal{P}_{ns}^{(n)-}(z)\right], \qquad P_{gq}^{(n)}(z) = \mathcal{P}_{gq}^{(n)}(z)\,,$$
$$P_{qqS}^{(n)}(z) = \frac{1}{2n_f}\mathcal{P}_{ps}^{(n)}(z)\,, \qquad\qquad P_{qg}^{(n)}(z) = \frac{1}{2n_f}\mathcal{P}_{qg}^{(n)}(z)\,,$$
$$P_{qq\Delta S}^{(n)}(z) = \frac{1}{2n_f}\mathcal{P}_{ns}^{(n)s}(z)\,. \tag{C.8}$$

C.2 Threshold and 0-jettiness factorization

The quark beam function noncusp anomalous dimension coefficients to three loops are [293]

$$\gamma_{B\,0}^q = 6C_F\,,$$
$$\gamma_{B\,1}^q = 2C_F\left[C_A\left(\frac{73}{9} - 40\zeta_3\right) + C_F\left(\frac{3}{2} - 12\zeta_2 + 24\zeta_3\right) + \beta_0\left(\frac{121}{18} + 2\zeta_2\right)\right],$$
$$\gamma_{B\,2}^q = 2C_F\left[C_A^2\left(\frac{52019}{162} - \frac{1682}{27}\zeta_2 - \frac{2056}{9}\zeta_3 - \frac{820}{3}\zeta_4 + \frac{176}{3}\zeta_2\zeta_3 + 232\zeta_5\right)\right.$$
$$+ C_A C_F\left(\frac{151}{4} - \frac{410}{3}\zeta_2 + \frac{844}{3}\zeta_3 - \frac{494}{3}\zeta_4 + 16\zeta_2\zeta_3 + 120\zeta_5\right)$$
$$+ C_F^2\left(\frac{29}{2} + 18\zeta_2 + 68\zeta_3 + 144\zeta_4 - 32\zeta_2\zeta_3 - 240\zeta_5\right)$$
$$+ C_A\beta_0\left(-\frac{7739}{54} + \frac{650}{27}\zeta_2 - \frac{1276}{9}\zeta_3 + \frac{617}{3}\zeta_4\right)$$

$$+ \beta_0^2 \Big(-\frac{3457}{324} + \frac{10}{3}\zeta_2 + \frac{16}{3}\zeta_3 \Big) + \beta_1 \Big(\frac{1166}{27} - \frac{16}{3}\zeta_2 + \frac{52}{9}\zeta_3 - \frac{82}{3}\zeta_4 \Big) \Big] . \quad \text{(C.9)}$$

They have been confirmed recently by an explicit three-loop calculation of the quark jet function [218], see also ref. [217]. The gluon beam function noncusp anomalous dimension coefficients to three loops are [59]

$$\gamma_{B\,0}^{g} = 2\beta_0 \,,$$

$$\gamma_{B\,1}^{g} = 2C_A \Big[C_A \Big(\frac{91}{9} - 16\zeta_3 \Big) + \beta_0 \Big(\frac{47}{9} - 2\zeta_2 \Big) \Big] + 2\beta_1 \,,$$

$$\gamma_{B\,2}^{g} = 2C_A \Big[C_A^2 \Big(\frac{49373}{162} - \frac{944}{27}\zeta_2 - \frac{2260}{9}\zeta_3 - 144\zeta_4 + \frac{128}{3}\zeta_2\zeta_3 + 112\zeta_5 \Big)$$

$$+ C_A \beta_0 \Big(-\frac{6173}{54} - \frac{376}{27}\zeta_2 + \frac{140}{9}\zeta_3 + 117\zeta_4 \Big) + \beta_0^2 \Big(-\frac{493}{81} - \frac{10}{3}\zeta_2 + \frac{28}{3}\zeta_3 \Big)$$

$$+ \beta_1 \Big(\frac{1765}{54} - 2\zeta_2 - \frac{152}{9}\zeta_3 - 8\zeta_4 \Big) \Big] + 2\beta_2 \,. \quad \text{(C.10)}$$

The (beam)thrust soft noncusp anomalous dimension coefficients to three loops follow from consistency by $\gamma_S^i(\alpha_s) = -2\gamma_B^i(\alpha_s) - 4\gamma_C^i(\alpha_s)$, where the $\gamma_C^i(\alpha_s)$ are taken from ref. [1]. They are the hard noncusp anomalous dimensions and are known up to three loops from the quark and gluon form factors [521–524, 539–541]. We obtain,

$$\gamma_{S\,0}^{i} = 0 \,,$$

$$\gamma_{S\,1}^{i} = 2C_i \Big[C_A \Big(-\frac{64}{9} + 28\zeta_3 \Big) + \beta_0 \Big(-\frac{56}{9} + 2\zeta_2 \Big) \Big] \,,$$

$$\gamma_{S\,2}^{i} = 2C_i \Big[C_A^2 \Big(-\frac{37871}{162} + \frac{620}{27}\zeta_2 + \frac{2548}{9}\zeta_3 + 144\zeta_4 - \frac{176}{3}\zeta_2\zeta_3 - 192\zeta_5 \Big)$$

$$+ C_A \beta_0 \Big(\frac{4697}{54} + \frac{484}{27}\zeta_2 + \frac{220}{9}\zeta_3 - 112\zeta_4 \Big) + \beta_0^2 \Big(\frac{520}{81} + \frac{10}{3}\zeta_2 - \frac{28}{3}\zeta_3 \Big)$$

$$+ \beta_1 \Big(-\frac{1711}{54} + 2\zeta_2 + \frac{152}{9}\zeta_3 + 8\zeta_4 \Big) \Big] . \quad \text{(C.11)}$$

The threshold soft noncusp anomalous dimension only differs from the thrust soft anomalous dimension by an overall sign as shown in the main text in eq. (6.10),

$$\gamma_{\text{thr}}^i(\alpha_s) = -\gamma_S^i(\alpha_s) \,, \qquad \gamma_{\text{thr}\,n}^i = -\gamma_{S\,n}^i \,. \quad \text{(C.12)}$$

C.3 Factorization at small q_T

In the exponential regulator, the noncusp anomalous dimension $\tilde{\gamma}_S^i$ of the q_T soft function is equal to that of the threshold soft function γ_{thr}^i, which in turn is the negative of the $\mathcal{T}_0$ soft anomalous dimension γ_S^i, see eq. (C.12). As a result, we have

$$\tilde{\gamma}_S^i(\alpha_s) = \gamma_{\text{thr}}^i(\alpha_s) = -\gamma_S^i(\alpha_s) \,, \qquad \tilde{\gamma}_{S\,n}^i = -\gamma_{S\,n}^i \,,$$

$$\tilde{\gamma}_B^i(\alpha_s) = \gamma_B^i(\alpha_s) + \gamma_S^i(\alpha_s) \,, \qquad \tilde{\gamma}_{B\,n}^i = \gamma_{B\,n}^i + \gamma_{S\,n}^i \,. \quad \text{(C.13)}$$

The result for $\tilde{\gamma}_B^i$ follows from RG consistency and the fact that the hard anomalous dimension is the same for q_T and $\mathcal{T}_0$. The $\gamma_{S\,n}^i$ and $\gamma_{B\,n}^i$ coefficients are given in eqs. (C.9), (C.10), and (C.11) above.

The rapidity anomalous dimensions coefficients, which enter the fixed-order expansion of $\tilde{\gamma}_\nu^i$ in eq. (2.205), are known up to three loops [264–266]. They are given by

$$
\tilde{\gamma}_{\nu\,0}^i = 0 \,,
$$
$$
\tilde{\gamma}_{\nu\,1}^i = 2C_i\left[C_A\left(-\frac{64}{9} + 28\zeta_3\right) - \frac{56}{9}\beta_0\right],
$$
$$
\tilde{\gamma}_{\nu\,2}^i = 2C_i\left[C_A^2\left(-\frac{37871}{162} + \frac{620}{27}\zeta_2 + \frac{2548}{9}\zeta_3 + 144\zeta_4 - \frac{176}{3}\zeta_2\zeta_3 - 192\zeta_5\right)\right.
$$
$$
+ C_A\beta_0\left(\frac{3865}{54} + \frac{412}{27}\zeta_2 + \frac{220}{9}\zeta_3 - 50\zeta_4\right)
$$
$$
\left. + \beta_0^2\left(-\frac{464}{81} - 8\zeta_3\right) + \beta_1\left(-\frac{1711}{54} + \frac{152}{9}\zeta_3 + 8\zeta_4\right)\right]. \tag{C.14}
$$

C.4 Jet veto factorization

The coefficients of the noncusp jet veto beam anomalous dimensions are [67, 322]

$$
\gamma_{B\,0}^q = 6C_F \,,
$$
$$
\gamma_{B\,1}^q = C_F\left[(3 - 4\pi^2 + 48\zeta_3)C_F + (-14 + 16(1 + \pi^2)\ln 2 - 96\zeta_3)C_A\right.
$$
$$
\left. + \left(\frac{19}{3} - \frac{4}{3}\pi^2 + \frac{80}{3}\ln 2\right)\beta_0\right],
$$
$$
\gamma_{B\,0}^g = 2\beta_0 \,,
$$
$$
\gamma_{B\,1}^g = 2\beta_1 + 8C_A\left[\left(-\frac{5}{4} + 2(1 + \pi^2)\ln 2 - 6\zeta_3\right)C_A + \left(\frac{5}{24} - \frac{\pi^2}{3} + \frac{10}{3}\ln 2\right)\beta_0\right] \tag{C.15}
$$

The coefficients of the rapidity noncusp anomalous dimension depend on the jet radius R. They read [67]

$$
\gamma_{\nu\,0}^i(R) = 0 \,, \tag{C.16}
$$
$$
\gamma_{\nu\,1}^i(R) = -16C_i\left[\left(\frac{17}{9} - (1 + \pi^2)\ln 2 + \zeta_3\right)C_A + \left(\frac{4}{9} + \frac{\pi^2}{12} - \frac{5}{3}\ln 2\right)\beta_0\right] + C_2^i(R) \,.
$$

Here $C_i = C_F\,(C_A)$ for $i = q\,(g)$ and $C_2^i(R)$ is the clustering correction due to the jet algorithm relative to a global E_T veto, as computed in refs. [62, 67],

$$
C_2^i(R) = 16C_i c_{ii}^R \ln R + 15.62\,C_i C_A - 9.17\,C_i\beta_0 + \mathcal{O}(R^2) \,. \tag{C.17}
$$

The small-R clustering coefficient $c_{ii} = c_{gg} = c_{qq}$ is given in eq. (3.25).

Appendix D

Renormalization group evolution

In this appendix we collect explicit expressions for the renormalization group evolution of various beam and soft functions in the main text. The renormalization and running of color-singlet hard functions can be found in our notation in ref. [1].

q_T **factorization.** The RG evolution factors for the q_T beam and soft functions $\tilde{B}_i$ and $\tilde{S}_i$ follow by solving the coupled systems of equations in eq. (2.197). Evolving first in ν and then in μ (from right to left), the solution of the beam function RGE in eq. (2.197) is

$$\tilde{B}_i(\omega, b_T, \mu, \nu) = \exp\left[2\eta_\Gamma^i(\mu_B, \mu)\ln\frac{\nu}{\omega} + K_{\tilde{\gamma}_B}^i(\mu_B, \mu)\right]$$
$$\times \exp\left[-\frac{1}{2}\ln\frac{\nu}{\nu_B}\,\tilde{\gamma}_\nu^i(b_T, \mu_B)\right]\tilde{B}_i(\omega, b_T, \mu_B, \nu_B)\,, \tag{D.1}$$

where the resummed rapidity anomalous dimension $\tilde{\gamma}_\nu^i(b_T, \mu_B)$ is given by eq. (2.202). Here we evolve first in ν and then in μ, where the final scale μ is ultimately set to the scale μ_H at which the hard function is evaluated. Any other path in the two-dimensional (μ, ν) space connecting $(\mu_H, \mu_B, \nu_B, \mu_S, \nu_S)$ is viable as well, and the path independence is ensured by exactly satisfying the RG consistency relations between all anomalous dimensions, in particular by using eq. (2.202). The definitions of η_Γ^i and K_γ^i for a generic noncusp anomalous dimension γ are given in eq. (D.6) below.

For the q_T soft function renormalized as in eq. (2.197), we have

$$\tilde{S}_i(b_T, \mu, \nu) = \exp\left[-4\eta_\Gamma^i(\mu_S, \mu)\ln\frac{\nu}{\mu_S} + 4K_\Gamma^i(\mu_S, \mu) + K_{\tilde{\gamma}_S}^i(\mu_S, \mu)\right]$$
$$\times \exp\left[\ln\frac{\nu}{\nu_S}\,\tilde{\gamma}_\nu^i(b_T, \mu_S)\right]\tilde{S}_i(b_T, \mu_S, \nu_S)\,. \tag{D.2}$$

The exponent K_Γ^i is defined in eq. (D.6) below. The evolution of the double-differential SCET$_{\mathrm{II}}$ soft function of chapter 4 in b_T space takes the exact same form with an additional argument k held fixed by the evolution on the left and right-hand side.

$\mathcal{T}_0$ **factorization.** The closed-form solution of eq. (2.216) is [209, 301]

$$B_i(t, x, \mu) = \exp\left[4K_\Gamma^i(\mu_B, \mu) + K_{\gamma_B}^i(\mu_B, \mu)\right]$$
$$\times \int dt'\, \mathcal{V}_{-2\eta_\Gamma^i(\mu_B, \mu)}(t - t', \mu_B^2)\, B_i(t', x, \mu_B)\,, \tag{D.3}$$

where $\mathcal{V}_\eta$ was defined in eq. (A.17). The evolution of the double-differential SCET$_\mathrm{I}$ beam function again takes the same form with an additional argument $\vec{k}_T$ held fixed in this case. t is straightforward to evaluate using results in app. B of ref. [209] for all terms in the inclusive beam function. The required nontrivial convolutions with the finite terms in the double-differential beam function are discussed in section 4.3. The solution of eq. (2.218) is

$$S_i(k,\mu) = \exp\left[-4K_\Gamma^i(\mu_S,\mu) + K_{\gamma_S}^i(\mu_S,\mu)\right] \int \mathrm{d}k'\, \mathcal{V}_{4\eta_\Gamma^i(\mu_S,\mu)}(k-k',\mu_S)\, S_i(k',\mu_S)\,. \quad \text{(D.4)}$$

Collinear-soft function in $(q_T, \mathcal{T}_0)$ resummation. Another nontrivial RG solution required in the main text is that of the collinear-soft SCET$_+$ function of chapter 4, which is multiplicative in b_T, but a convolution in k. Again evolving first in ν and then in μ, the solution of the collinear-soft RGE in eq. (4.32) in b_T space is given by

$$\tilde{S}_i(k,b_T,\mu,\nu) = \exp\left[4K_\Gamma^i(\mu_\mathcal{S},\mu) + K_{\gamma_\mathcal{S}}^i(\mu_\mathcal{S},\mu)\right] \int \mathrm{d}k'\, \mathcal{V}_{-2\eta_\Gamma^i(\mu_\mathcal{S},\mu)}\left(k-k',\frac{\mu_\mathcal{S}^2}{\nu}\right)$$

$$\times \exp\left[\frac{1}{2}\ln\frac{\nu}{\nu_\mathcal{S}}\,\tilde{\gamma}_\nu^i(b_T,\mu_\mathcal{S})\right] \tilde{S}_i(k',b_T,\mu_\mathcal{S},\nu_\mathcal{S})\,. \quad \text{(D.5)}$$

The rapidity evolution factor on the second line does not depend on k' and thus may be taken out of the convolution integral. Note the nontrivial boundary condition of the $\mathcal{V}_\eta$ plus distribution on the first line.

RG building blocks. The symbolic solutions above all make use of integrals over anomalous dimensions defined as

$$K_\Gamma^i(\mu_0,\mu) \equiv \int_{\mu_0}^\mu \frac{\mathrm{d}\mu'}{\mu'}\, \Gamma_\mathrm{cusp}^i[\alpha_s(\mu')] \ln\frac{\mu'}{\mu_0}\,, \quad \eta_\Gamma^i(\mu_0,\mu) \equiv \int_{\mu_0}^\mu \frac{\mathrm{d}\mu'}{\mu'}\, \Gamma_\mathrm{cusp}^i[\alpha_s(\mu')]\,,$$

$$K_\gamma^i(\mu_0,\mu) \equiv \int_{\mu_0}^\mu \frac{\mathrm{d}\mu'}{\mu'}\, \gamma^i[\alpha_s(\mu')]\,. \quad \text{(D.6)}$$

Different methods to numerically evaluate these integrals were analyzed in detail in ref. [450], which found that their numerical precision becomes relevant at N^{3}LL. Here we use the *approximate unexpanded analytic results* in the language of ref. [450], which provide sufficient numerical precision for our purposes. These solutions are obtained by changing variables from μ' to $\alpha_s(\mu')$ using the β function and recursively evaluating the integral in terms of the lower-order results. For K_Γ^i this requires rewriting the explicit logarithm as another nested integral over an α_s''. Through NNLL, the relevant expressions read, suppressing the indices i on the right hand side,

$$K_\Gamma^i(\mu_0,\mu) = -\frac{\Gamma_0}{4\beta_0^2}\left\{\frac{4\pi}{\alpha_s(\mu_0)}\left(1 - \frac{1}{r} - \ln r\right) + \left(\frac{\Gamma_1}{\Gamma_0} - \frac{\beta_1}{\beta_0}\right)(1-r+\ln r) + \frac{\beta_1}{2\beta_0}\ln^2 r\right.$$

$$+ \frac{\alpha_s(\mu_0)}{4\pi}\left[\left(\frac{\beta_1^2}{\beta_0^2} - \frac{\beta_2}{\beta_0}\right)\left(\frac{1-r^2}{2} + \ln r\right) + \left(\frac{\beta_1\Gamma_1}{\beta_0\Gamma_0} - \frac{\beta_1^2}{\beta_0^2}\right)(1-r+r\ln r)\right.$$

$$\left.\left. - \left(\frac{\Gamma_2}{\Gamma_0} - \frac{\beta_1\Gamma_1}{\beta_0\Gamma_0}\right)\frac{(1-r)^2}{2}\right]\right\}\,,$$

$$\eta_{\Gamma}^{i}(\mu_0, \mu) = -\frac{\Gamma_0}{2\beta_0}\left[\ln r + \frac{\alpha_s(\mu_0)}{4\pi}\left(\frac{\Gamma_1}{\Gamma_0} - \frac{\beta_1}{\beta_0}\right)(r-1)\right.$$

$$\left. + \frac{\alpha_s^2(\mu_0)}{16\pi^2}\left(\frac{\Gamma_2}{\Gamma_0} - \frac{\beta_1\Gamma_1}{\beta_0\Gamma_0} + \frac{\beta_1^2}{\beta_0^2} - \frac{\beta_2}{\beta_0}\right)\frac{r^2-1}{2}\right],$$

$$K_{\gamma}^{i}(\mu_0, \mu) = -\frac{\gamma_0}{2\beta_0}\left[\ln r + \frac{\alpha_s(\mu_0)}{4\pi}\left(\frac{\gamma_1}{\gamma_0} - \frac{\beta_1}{\beta_0}\right)(r-1)\right], \tag{D.7}$$

where $r = \alpha_s(\mu)/\alpha_s(\mu_0)$ and the running coupling is given by the three-loop expression

$$\frac{1}{\alpha_s(\mu)} = \frac{X}{\alpha_s(\mu_0)} + \frac{\beta_1}{4\pi\beta_0}\ln X + \frac{\alpha_s(\mu_0)}{16\pi^2}\left[\frac{\beta_2}{\beta_0}\left(1 - \frac{1}{X}\right) + \frac{\beta_1^2}{\beta_0^2}\left(\frac{\ln X}{X} + \frac{1}{X} - 1\right)\right], \tag{D.8}$$

with $X \equiv 1 + \alpha_s(\mu_0)\beta_0\ln(\mu/\mu_0)/(2\pi)$. At lower logarithmic accuracies, the expressions in eq. (D.7) are truncated after the term multiplied $\sim 1/\alpha_s(\mu_0)$ (LL) or $\sim [\alpha_s(\mu_0)]^0$ (NLL), respectively. The explicit N^{3}LL expressions entering our analysis in chapter 7 are given in ref. [450].

Appendix E

Fixed-order ingredients

In this appendix we collect expressions for various single-differential beam and soft functions in the main text to the order they are required for our analysis. The expressions are obtained by recursively solving the relevant RGEs order by order in perturbation theory, accounting for the running of the coupling and the PDFs, and we attempt to make the structure of the final results in terms of anomalous dimensions and the boundary conditions maximally explicit. Details on the recursive solution and the extension of many of these expressions to the full RG-predicted structure at N^3LO can be found in ref. [5].

E.1 Virtuality-dependent beam functions

The analysis in chapter 4, requires the matching coefficients $\mathcal{I}_{ij}(t, z, \mu)$ for the inclusive beam function $B_i(t, x, \mu)$ as a baseline to evaluate the double-differential beam function. In chapter 5 we need the matching coefficients $\tilde{\mathcal{I}}_{ij}(\tilde{t}, z, \mu)$ of the modified virtuality-dependent beam function $\tilde{B}_i(\tilde{t}, x, \mu)$ as introduced in that chapter to two loops, and partially at three loops. As discussed in chapter 5, B_i and $\tilde{B}_i$ have an identical RGE, so we only give results for $\mathcal{I}_{ij}(t, z, \mu)$ in the following. Results for $\tilde{\mathcal{I}}_{ij}(\tilde{t}, z, \mu)$ are obtained by replacing the boundary terms $I_{ij}^{(n)}(z)$ by the modified boundary terms $\tilde{I}_{ij}^{(n)}(z)$ calculated in section 5.4. Note that in this appendix we reserve the notation $\tilde{I}_{ij}^{(n)}(z)$ for the finite terms of the b_T-dependent $SCET_{II}$ beam function instead.

Combining the inclusive beam function matching relation and its RGE in eqs. (2.216) and (2.217), we find the following RGE for the matching coefficient [293],

$$
\mu \frac{\mathrm{d}}{\mathrm{d}\mu} \mathcal{I}_{ij}(t, z, \mu)
$$
$$
= \sum_k \int \mathrm{d}t' \int \frac{\mathrm{d}z'}{z'} \mathcal{I}_{ik}\Big(t - t', \frac{z}{z'}, \mu\Big) \Big\{ \mathbf{1}_{kj}(z') \, \gamma_B^i(t', \mu) - 2\delta(t') \, P_{kj}\big[\alpha_s(\mu), z'\big] \Big\}. \tag{E.1}
$$

Solving eq. (E.1) order by order in α_s, we obtain a general expression for $\mathcal{I}_{ij}^{(n)}(t, z, \mu)$,

$$
\mathcal{I}_{ij}^{(0)}(t, z, \mu) = \delta(t) \, \mathbf{1}_{ij}(z) \,,
$$
$$
\mathcal{I}_{ij}^{(1)}(t, z, \mu) = \mathcal{L}_1(t, \mu^2) \, \Gamma_0^i \, \mathbf{1}_{ij}(z) + \mathcal{L}_0(t, \mu^2) \Big[P_{ij}^{(0)}(z) - \frac{\gamma_{B\,0}^i}{2} \Big] + \delta(t) \, I_{ij}^{(1)}(z) \,,
$$
$$
\mathcal{I}_{ij}^{(2)}(t, z, \mu) = \mathcal{L}_3(t, \mu^2) \, \frac{(\Gamma_0^i)^2}{2} \, \mathbf{1}_{ij}(z)
$$

$$+ \mathcal{L}_2(t,\mu^2)\frac{\Gamma_0^i}{2}\left[-\left(\beta_0 + \frac{3}{2}\gamma_{B\,0}^i\right)\mathbf{1}_{ij}(z) + 3P_{ij}^{(0)}(z)\right]$$

$$+ \mathcal{L}_1(t,\mu^2)\left[\left(-\frac{\pi^2}{6}(\Gamma_0^i)^2 + \frac{\beta_0}{2}\gamma_{B\,0}^i + \frac{(\gamma_{B\,0}^i)^2}{4} + \Gamma_1^i\right)\mathbf{1}_{ij}(z)\right.$$

$$\left. - \left(\beta_0 + \gamma_{B\,0}^i\right)P_{ij}^{(0)}(z) + \left(P^{(0)}\otimes P^{(0)}\right)_{ij}(z) + \Gamma_0^i I_{ij}^{(1)}(z)\right]$$

$$+ \mathcal{L}_0(t,\mu^2)\left[\left(\zeta_3(\Gamma_0^i)^2 + \frac{\pi^2}{12}\Gamma_0^i\gamma_{B\,0}^i - \frac{\gamma_{B\,1}^i}{2}\right)\mathbf{1}_{ij}(z) - \frac{\pi^2}{6}\Gamma_0^i P_{ij}^{(0)}(z) + P_{ij}^{(1)}(z)\right.$$

$$\left. - \left(\beta_0 + \frac{\gamma_{B\,0}^i}{2}\right)I_{ij}^{(1)}(z) + \left(I^{(1)}\otimes P^{(0)}\right)_{ij}(z)\right]$$

$$+ \delta(t)\, I_{ij}^{(2)}(z)\,,$$

$$\mathcal{I}_{ij}^{(3)}(t,z,\mu) = \mathcal{L}_5(t,\mu^2)\frac{(\Gamma_0^i)^3}{8}\mathbf{1}_{ij}(z)$$

$$+ \mathcal{L}_4(t,\mu^2)\frac{5}{8}(\Gamma_0^i)^2\left[-\left(\frac{2}{3}\beta_0 + \frac{\gamma_{B\,0}^i}{2}\right)\mathbf{1}_{ij}(z) + P_{ij}^{(0)}(z)\right]$$

$$+ \mathcal{L}_3(t,\mu^2)\,\Gamma_0^i\left[\left(-\frac{\pi^2}{6}(\Gamma_0^i)^2 + \frac{\beta_0^2}{3} + \frac{5}{6}\beta_0\gamma_{B\,0}^i + \frac{(\gamma_{B\,0}^i)^2}{4} + \Gamma_1^i\right)\mathbf{1}_{ij}(z)\right.$$

$$\left. - \left(\frac{5}{3}\beta_0 + \gamma_{B\,0}^i\right)P_{ij}^{(0)}(z) + \left(P^{(0)}\otimes P^{(0)}\right)_{ij}(z) + \frac{\Gamma_0^i}{2}\,I_{ij}^{(1)}(z)\right]$$

$$+ \cdots + \delta(t)\, I_{ij}^{(3)}(z)\,, \tag{E.2}$$

where $I_{ij}^{(n)}(z)$ is the $\mathcal{O}(\alpha_s^n)$ boundary term multiplying $\delta(t)$ at the respective order. The ellipses in the three-loop result indicate terms proportional to $\mathcal{L}_n(t,\mu^2)$ with $0 \leq n \leq 2$ and are not needed for the results in this thesis. Expanding eq. (E.2) against the hard function yields eq. (5.89) in the main text. The one-loop boundary terms for the standard (inclusive) virtuality dependent quark beam function are [57, 293],

$$I_{qqV}^{(1)}(z) = 2C_F\,\theta(z)\left[\mathcal{L}_1(1-z)(1+z^2) - \frac{\pi^2}{6}\delta(1-z) + \theta(1-z)\left(1 - z - \frac{1+z^2}{1-z}\ln z\right)\right],$$

$$I_{qg}^{(1)}(z) = 2T_F\,\theta(z)\left[P_{qg}(z)\left(\ln\frac{1-z}{z} - 1\right) + \theta(1-z)\right]. \tag{E.3}$$

E.2 q_T soft function

The q_T soft function is most conveniently expressed in terms of

$$L_b = \ln\frac{b_T^2\mu^2}{b_0^2}\,, \quad b_0 = 2e^{-\gamma_E}\,, \qquad L_\nu = \ln\frac{\mu}{\nu}\,. \tag{E.4}$$

For our N³LL analysis in chapter 7, we require the two-loop expression

$$\tilde{S}_i^{(0)}(b_T,\mu,\nu) = 1\,,$$

$$\tilde{S}_i^{(1)}(b_T,\mu,\nu) = -L_b^2\frac{\Gamma_0^i}{2} + L_b\left(L_\nu\,2\Gamma_0^i + \frac{\tilde{\gamma}_{S\,0}^i}{2} + \frac{\tilde{\gamma}_{\nu\,0}^i}{2}\right) - L_\nu\tilde{\gamma}_{\nu\,0}^i + \tilde{s}_i^{(1)}\,,$$

$$\tilde{S}_i^{(2)}(b_T,\mu,\nu) = L_b^4 \frac{(\Gamma_0^i)^2}{8} - L_b^3 \Gamma_0^i\Big(L_\nu\Gamma_0^i + \frac{\beta_0}{3} + \frac{\tilde{\gamma}_{S0}^i}{4} + \frac{\tilde{\gamma}_{\nu0}^i}{4}\Big)$$

$$+ L_b^2\Big[L_\nu^2\, 2(\Gamma_0^i)^2 + L_\nu\Gamma_0^i\Big(\beta_0 + \tilde{\gamma}_{S0}^i + \frac{3}{2}\tilde{\gamma}_{\nu0}^i\Big)$$

$$+ \beta_0\Big(\frac{\tilde{\gamma}_{S0}^i}{4} + \frac{\tilde{\gamma}_{\nu0}^i}{2}\Big) + \frac{1}{8}(\tilde{\gamma}_{S0}^i + \tilde{\gamma}_{\nu0}^i)^2 - \frac{\Gamma_1^i}{2} - \frac{\Gamma_0^i}{2}\tilde{s}_i^{(1)}\Big]$$

$$+ L_b\Big\{-L_\nu^2\, 2\Gamma_0^i\tilde{\gamma}_{\nu0}^i + L_\nu\Big[-\Big(\beta_0 + \frac{\tilde{\gamma}_{S0}^i}{2} + \frac{\tilde{\gamma}_{\nu0}^i}{2}\Big)\tilde{\gamma}_{\nu0}^i + 2\Gamma_1^i + 2\Gamma_0^i\tilde{s}_i^{(1)}\Big]$$

$$+ \frac{\tilde{\gamma}_{S1}^i}{2} + \frac{\tilde{\gamma}_{\nu1}^i}{2} + \Big(\beta_0 + \frac{\tilde{\gamma}_{S0}^i}{2} + \frac{\tilde{\gamma}_{\nu0}^i}{2}\Big)\tilde{s}_i^{(1)}\Big\}$$

$$+ L_\nu^2 \frac{(\tilde{\gamma}_{\nu0}^i)^2}{2} - L_\nu\big(\tilde{\gamma}_{\nu1}^i + \tilde{\gamma}_{\nu0}^i\,\tilde{s}_i^{(1)}\big) + \tilde{s}_i^{(2)}\,. \tag{E.5}$$

The required anomalous dimension are given in appendix C.3. The boundary coefficients $s_i^{(n)}$ through two loops are [264, 265], with $C_i = C_F$ for $i = q$ and $C_i = C_A$ for $i = g$,

$$\tilde{s}_i^{(1)} = -C_i\, 2\zeta_2\,,$$

$$\tilde{s}_i^{(2)} = C_i\Big[C_i\, 5\zeta_4 + C_A\Big(\frac{208}{27} - 4\zeta_2 + 10\zeta_4\Big) + \beta_0\Big(\frac{164}{27} - 5\zeta_2 - \frac{14}{3}\zeta_3\Big)\Big]\,. \tag{E.6}$$

E.3 q_T beam function

The matching coefficients for the q_T beam functions can be written in terms of

$$L_b = \ln\frac{b_T^2\mu^2}{b_0^2}\,, \quad b_0 = 2e^{-\gamma_E}\,, \qquad L_\omega = \ln\frac{\nu}{\omega}\,. \tag{E.7}$$

Note that L_ω differs from the characteristic logarithm of the soft function in the previous section. For the N³LL analysis in chapter 7 and the NNLL analysis in chapter 4, we require the q_T quark beam function $i = q, \bar{q}$ up to two loops,

$$\tilde{\mathcal{I}}_{ij}^{(0)}(z,b_T,\mu,\nu/\omega) = \mathbf{1}_{ij}(z)\,,$$

$$\tilde{\mathcal{I}}_{ij}^{(1)}(z,b_T,\mu,\nu/\omega) = L_b\Big[\Big(L_\omega\Gamma_0^i + \frac{\tilde{\gamma}_{B0}^i}{2}\Big)\mathbf{1}_{ij}(z) - P_{ij}^{(0)}(z)\Big] - L_\omega\frac{\tilde{\gamma}_{\nu0}^i}{2}\mathbf{1}_{ij}(z) + \tilde{I}_{ij}^{(1)}(z)\,,$$

$$\tilde{\mathcal{I}}_{ij}^{(2)}(z,b_T,\mu,\nu/\omega) = L_b^2\Big\{\Big[L_\omega^2\frac{(\Gamma_0^i)^2}{2} + L_\omega\frac{\Gamma_0^i}{2}(\beta_0 + \tilde{\gamma}_{B0}^i) + \Big(\beta_0 + \frac{\tilde{\gamma}_{B0}^i}{2}\Big)\frac{\tilde{\gamma}_{B0}^i}{4}\Big]\mathbf{1}_{ij}(z)$$

$$- \Big(L_\omega\Gamma_0^i + \frac{\beta_0}{2} + \frac{\tilde{\gamma}_{B0}^i}{2}\Big)P_{ij}^{(0)}(z) + \frac{1}{2}\big(P^{(0)} \otimes P^{(0)}\big)_{ij}(z)\Big\}$$

$$+ L_b\Big\{\Big[-L_\omega^2\,\Gamma_0^i\frac{\tilde{\gamma}_{\nu0}^i}{2} + L_\omega\Big[-\Big(\beta_0 + \frac{\tilde{\gamma}_{B0}^i}{2}\Big)\frac{\tilde{\gamma}_{\nu0}^i}{2} + \Gamma_1^i\Big] + \frac{\tilde{\gamma}_{B1}^i}{2}\Big]\mathbf{1}_{ij}(z)$$

$$+ L_\omega\frac{\tilde{\gamma}_{\nu0}^i}{2}P_{ij}^{(0)}(z) - P_{ij}^{(1)}(z)$$

$$+ \Big(L_\omega\Gamma_0^i + \beta_0 + \frac{\tilde{\gamma}_{B0}^i}{2}\Big)\tilde{I}_{ij}^{(1)}(z) - \big(\tilde{I}^{(1)} \otimes P^{(0)}\big)_{ij}(z)\Big\}$$

$$+ \left[L_\omega^2 \frac{(\tilde{\gamma}_{\nu\,0}^i)^2}{8} - L_\omega \frac{\tilde{\gamma}_{\nu\,1}^i}{2} \right] \mathbf{1}_{ij}(z) - L_\omega \frac{\tilde{\gamma}_{\nu\,0}^i}{2} \tilde{I}_{ij}^{(1)}(z) + \tilde{I}_{ij}^{(2)}(z) \,. \qquad \text{(E.8)}$$

The matching coefficients $\mathcal{I}_{gj}$ for the unpolarized contribution to the gluon beam function have the same form. The $\tilde{I}_{ij}^{(n)}(z)$ up to $n = 2$ are given for the η regulator in ref. [264] in terms of the results of ref. [279], and up to that order are equal to the more compact expressions given in ref. [285, 286], where they were directly calculated using the exponential regulator. The one-loop results are

$$
\begin{aligned}
\tilde{I}_{qqV}^{(1)}(z) &= C_F\, \delta_{ij}\, \theta(z)\theta(1-z)\, 2(1-z)\,, \\
\tilde{I}_{qg}^{(1)}(z) &= T_F\, \theta(z)\theta(1-z)\, 4z(1-z)\,, \\
\tilde{I}_{gg}^{(1)}(z) &= 0\,, \\
\tilde{I}_{gq}^{(1)}(z) &= C_F\, \theta(z)\theta(1-z)\, 2z\,.
\end{aligned}
\qquad \text{(E.9)}
$$

Here we use a tilde to indicate that the $\tilde{I}_{ij}^{(n)}$ belong to the b_T-dependent beam function. (They are distinct from the modified SCET_I beam function finite terms calculated in section 5.4.) In general, the boundary terms as derived to all orders in α_s and to leading power in $1 - z$ in chapter 6 are related to the full $\tilde{\mathcal{I}}_{ij}^{(n)}$ by

$$\tilde{I}_{ij}^{(n)}(z) = \tilde{\mathcal{I}}_{ij}^{(n)}(z, b_T, \mu = b_0/b_T, \nu/\omega = 1)\,. \qquad \text{(E.10)}$$

E.4 Jet veto beam function for $\eta_\text{cut} \to \infty$

The matching coefficient $\mathcal{I}_{ij}(p_T^\text{cut}, R, \omega, z, \mu, \nu)$ of the $\eta_\text{cut} \to \infty$ beam functions satisfies an identical RGE to eq. (3.17). Solving it order by order in α_s yields, suppressing the arguments of $\mathcal{I}_{ij}^{(n)}(p_T^\text{cut}, R, \omega, z, \mu, \nu)$ on the left-hand side,

$$
\begin{aligned}
\mathcal{I}_{ij}^{(0)} &= \mathbf{1}_{ij}(1-z)\,, \\
\mathcal{I}_{ij}^{(1)} &= \mathbf{1}_{ij}(1-z)\, L_B^\mu (2\Gamma_0^i L_B^\nu + \gamma_{B\,0}^i) - 2L_B^\mu P_{ij}^{(0)}(z) + \tilde{I}_{ij}^{(1)}\,, \\
\mathcal{I}_{ij}^{(2)} &= \mathbf{1}_{ij}(1-z) \Bigg\{ (L_B^\mu)^2 \Big[2(\Gamma_0^i)^2 (L_B^\nu)^2 + L_B^\nu (2\beta_0 \Gamma_0^i + 2\Gamma_0^i \gamma_{B\,0}^i) + \beta_0 \gamma_{B\,0}^i + \frac{(\gamma_{B\,0}^i)^2}{2} \Big] \\
&\qquad + L_B^\mu \Big[2\Gamma_1^i L_B^\nu + \gamma_{B\,1}^i \Big] - \frac{1}{2} \gamma_{\nu\,1}^i(R) L_B^\nu \Bigg\} \\
&\quad + P_{ij}^{(0)}(z)\, (L_B^\mu)^2 \Big[-4\Gamma_0^i L_B^\nu - 2\beta_0 - 2\gamma_{B\,0}^i \Big] + \tilde{I}_{ij}^{(1)}(z)\, L_B^\mu \Big[2\Gamma_0^i L_B^\nu + 2\beta_0 + \gamma_{B\,0}^i \Big] \\
&\quad - 2L_B^\mu \big(\tilde{I}^{(1)} \otimes P^{(0)} \big)_{ij}(z) - 2L_B^\mu P_{ij}^{(1)}(z) + 2(L_B^\mu)^2 \big(P^{(0)} \otimes P^{(0)} \big)_{ij}(z) \\
&\quad + I_{ij}^{(2)}(R, z)\,,
\end{aligned}
\qquad \text{(E.11)}
$$

where we abbreviated

$$L_B^\mu = \ln \frac{\mu}{p_T^\text{cut}}\,, \qquad L_B^\nu = \ln \frac{\nu}{\omega}\,. \qquad \text{(E.12)}$$

We also used that the one-loop rapidity anomalous dimension vanishes, $\gamma_{\nu\,0}^i = 0$, and that the one-loop finite terms at $\mu = p_T^\text{cut}$ and $\nu = \omega$ are equal to the finite terms $\tilde{I}_{ij}(z)$ of

the b_T-dependent beam function in eq. (E.9) when using the same rapidity regulator. The two-loop finite terms in eq. (E.11), for which the relation to the b_T case no longer holds, depend on R. Expanding them as

$$I_{ij}^{(2)}(R, z) = \ln R \, I_{ij}^{(2, \ln R)}(z) + I_{ij}^{(2,c)}(z) + \mathcal{O}(R^2) \,, \tag{E.13}$$

the coefficient of $\ln R$ can be written as

$$I_{ij}^{(2, \ln R)}(z) = c_{ij}^R \Big[2 P_{ij}^{(0)}(z) - \gamma_{B\,0}^i \, \mathbf{1}_{ij}(z) \Big] \,. \tag{E.14}$$

We explicitly recomputed the coefficients c_{ij}^R, for which we found some discrepancies in the literature. [See eq. (3.25) in the main text.] Note that the terms proportional to $\delta(1-z)$ cancel in eq. (E.14) when the distributional structure of the splitting function is written purely in terms of $\delta(1-z)$, $\mathcal{L}_n(1-z)$, and regular terms in $1-z$.

E.5 Other one-loop soft and collinear-soft functions

In chapter 4 we require the one-loop $\mathcal{T}_0$ soft function [57, 300, 301],

$$S_i(k, \mu) = \delta(k) + \frac{\alpha_s(\mu)}{4\pi} \Big[-4\Gamma_0^i \, \mathcal{L}_1(k, \mu) + \frac{\pi^2}{3} C_i \, \delta(k) \Big] + \mathcal{O}(\alpha_s^2) \,. \tag{E.15}$$

and the one-loop collinear-soft function in b_T space [195],

$$\tilde{\mathcal{S}}_i(k, b_T, \mu, \nu) = \delta(k) + \frac{\alpha_s(\mu)}{4\pi} \Big\{ -\Gamma_0^i L_b \, \mathcal{L}_0(k, \mu) + \Gamma_0^i \Big[-\frac{1}{2} L_b^2 - L_b \ln \frac{\nu}{\mu} \Big] \delta(k) - \frac{\pi^2}{3} C_i \, \delta(k) \Big\}$$
$$+ \mathcal{O}(\alpha_s^2) \,. \tag{E.16}$$

For the analysis in chapter 3 we also need the one-loop jet veto soft function [67],

$$S_i(p_T^{\text{cut}}, R, \mu, \nu) = 1 + \frac{\alpha_s(\mu)}{4\pi} \Big[2\Gamma_0^i \ln \frac{\mu}{p_T^{\text{cut}}} \Big(\ln \frac{\mu}{p_T^{\text{cut}}} - 2 \ln \frac{\nu}{p_T^{\text{cut}}} \Big) - \frac{\pi^2}{3} C_i \Big] + \mathcal{O}(\alpha_s^2) \,. \tag{E.17}$$

In these expressions, we used that all the one-loop soft noncusp and rapidity anomalous dimensions vanish, and abbreviated $C_i = C_F$ for $i = q$ and $C_i = C_A$ for $i = g$.

Appendix F

Analytic NLO rapidity spectra

In this appendix we collect self-contained expressions for the Drell-Yan and $gg \to H$ partonic rapidity spectra to NLO in terms of the convenient variables (z_a, z_b), see eq. (2.64). These results, while standard, are not readily available from the literature. Since eq. (5.22) captures the full singularity structure as $z_a \to 1$ and/or $z_b \to 1$, the power corrections to it are of relative $\mathcal{O}[(1-z_a)(1-z_b)]$ and are fully integrable. Hence we can construct the exact partonic cross section in terms of (z_a, z_b) from the results in terms of (z, y) from refs. [113, 414] as

$$\hat{\sigma}_{ij}(z_a, z_b) = \text{eq. (5.22)} + \left[\frac{\mathrm{d}z\,\mathrm{d}y}{\mathrm{d}z_a\mathrm{d}z_b}\,\hat{\sigma}_{ij}\big[z(z_a, z_b), y(z_a, z_b)\big] - \text{eq. (5.22)}\right]_{z_{a,b}<1}. \qquad (F.1)$$

Here the term in square brackets is evaluated in the bulk, away from any singularities, so we can simply plug in eq. (5.69).

We find the expressions below to be in full agreement with refs. [219, 416], which in turn for Drell-Yan agree with the earliest result for the NLO rapidity spectrum in ref. [415]. In refs. [219, 416], the cross section was also parametrized in terms of $x_{a,b}$ and $z_{a,b}$, but all subtractions were written out in full at the level of the hadronic cross section.

In ref. [113], only the sum of the gq and qg coefficient functions for Higgs productions was given. The separation of the singular terms into the two channels is unique because only the gq (qg) channel can be singular as $y \to 0$ ($y \to 1$). We determined the separation of the regular terms by comparing to ref. [219]. To the best of our knowledge, this is the first time that the explicit analytic agreement between the independent NLO calculations in terms of (z_a, z_b) and (z, y) has been established.

Finally, we have also compared our numerical implementation of eqs. (F.4) through (F.11) with the rapidity spectra obtained from `Vrap 0.9` [114] for Drell-Yan and from `SusHi 1.7.0` [333, 334] for Higgs production, finding excellent agreement. Since `Vrap 0.9` implements the (z, y) parametrization, this effectively confirms the distributional identities in table 5.2 numerically with physical PDFs as test functions.

F.1 Drell-Yan production

The Born cross section for Drell-Yan production, $q\bar{q} \to Z/\gamma^* \to \ell^+\ell^-$, is given by

$$\sigma_{B,q}^{\mathrm{DY}} = \frac{4\pi\alpha_{\mathrm{em}}^2}{3N_c Q^2}\left[Q_q^2 + \frac{(v_q^2 + a_q^2)(v_\ell^2 + a_\ell^2) - 2Q_q v_q v_\ell(1 - m_Z^2/Q^2)}{(1 - m_Z^2/Q^2)^2 + m_Z^2\Gamma_Z^2/Q^4}\right], \qquad (F.2)$$

with N_c the number of colors, Q_q the quark charge in units of $|e|$, $v_{\ell,q}$ and $a_{\ell,q}$ the standard electroweak vector and axial couplings of the leptons and quarks, and m_Z and Γ_Z the mass and width of the Z boson. The complete LO cross section is given by

$$\frac{d\sigma_{\mathrm{LO}}^{\mathrm{DY}}}{dQ^2\,dY} = \frac{1}{E_{\mathrm{cm}}^2}\frac{d\sigma_{\mathrm{LO}}^{\mathrm{DY}}}{dx_a dx_b} = \frac{1}{E_{\mathrm{cm}}^2}\sum_q \sigma_{B,q}^{\mathrm{DY}}\left[f_q(x_a)\,f_{\bar{q}}(x_b) + f_{\bar{q}}(x_a)\,f_q(x_b)\right], \qquad (\mathrm{F.3})$$

where the sum runs over $q = \{u, d, c, s, b\}$. We expand the partonic cross section for Drell-Yan as

$$\hat{\sigma}_{ij}(z_a, z_b, Q, \mu) = \sum_{n=0}^{\infty}\left[\frac{\alpha_s(\mu)}{4\pi}\right]^n \sigma_{ij}^{(n)}(z_a, z_b, Q, \mu). \qquad (\mathrm{F.4})$$

The LO result corresponding to eq. (F.3) is given by $\hat{\sigma}_{q\bar{q}}^{(0)}(z_a, z_b, Q, \mu) = \sigma_{B,q}^{\mathrm{DY}}\delta(1-z_a)\,\delta(1-z_b)$. Writing $\bar{z}_a \equiv 1 - z_a$ and $\bar{z}_b \equiv 1 - z_b$ for short, the NLO coefficient for the $q\bar{q}$ channel is given by

$$\frac{1}{\sigma_{B,q}^{\mathrm{DY}}}\frac{\hat{\sigma}_{q\bar{q}}^{(1)}(z_a, z_b, Q, \mu)}{C_F}$$

$$= \delta(\bar{z}_a)\delta(\bar{z}_b)(2\pi^2 - 16) + 4\mathcal{L}_1(\bar{z}_a)\delta(\bar{z}_b) + 4\mathcal{L}_0(\bar{z}_a)\mathcal{L}_0(\bar{z}_b) + 4\delta(\bar{z}_a)\mathcal{L}_1(\bar{z}_b)$$

$$+ \left\{ -2(1+z_b)\mathcal{L}_0(\bar{z}_a) + \delta(\bar{z}_a)\left[2\bar{z}_b - 4(1+z_b)\ln\bar{z}_b - \frac{2(1+z_b^2)\ln z_b}{\bar{z}_b}\right.\right.$$

$$+ \frac{4}{\bar{z}_b}\ln\frac{2z_b}{1+z_b} + 2(1+z_b)\ln\frac{1-z_b^2}{2z_b}\right] - 4\ln\frac{\mu}{Q}\,\delta(\bar{z}_a)\left[2\mathcal{L}_0(\bar{z}_b) + \frac{3}{2}\delta(\bar{z}_b) - (1+z_b)\right]$$

$$+ \frac{2(z_a^2 + z_b^2)[(1+z_a)^2 + z_a z_b(3 + 2z_a + z_a z_b)]}{(1+z_a)(1+z_b)(z_a+z_b)^2} + (z_a \leftrightarrow z_b)\right\}, \qquad (\mathrm{F.5})$$

where $(z_a \leftrightarrow z_b)$ indicates all previous expressions in the curly brackets repeated with z_a and z_b interchanged. For the qg channel we have

$$\frac{1}{\sigma_{B,q}^{\mathrm{DY}}}\frac{\hat{\sigma}_{qg}^{(1)}(z_a, z_b, Q, \mu)}{T_F}$$

$$= 2(z_b^2 + \bar{z}_b^2)\mathcal{L}_0(\bar{z}_a) + \delta(\bar{z}_a)\left[2(z_b^2 + \bar{z}_b^2)\ln\frac{2\bar{z}_b}{1+z_b} + 4z_b\bar{z}_b\right] - 4\ln\frac{\mu}{Q}\,\delta(\bar{z}_a)(z_b^2 + \bar{z}_b^2) \qquad (\mathrm{F.6})$$

$$+ \frac{1}{(1+z_a)(z_a+z_b)^3}\left[-4z_a^5 z_b^3 - 4z_a^4 z_b^2(-1 + z_b + 2z_b^2) + 2z_a^3(1 + 4z_b^2 + 2z_b^3 - 4z_b^4 - 4z_b^5)\right.$$

$$+ 2z_a^2 z_b(1 + 4z_b + 8z_b^2 - 8z_b^3 - 4z_b^4) + 2z_a z_b^2(1 + 4z_b - 2z_b^2 - 4z_b^3) - 2z_b^3(1 - 2z_b + 2z_b^2)\right].$$

The gq channel is given by $\sigma_{gq}^{(1)}(z_a, z_b, Q, \mu) = \sigma_{qg}^{(1)}(z_b, z_a, Q, \mu)$. The results for $q \leftrightarrow \bar{q}$ are identical.

F.2 Gluon-fusion Higgs production

For gluon-fusion Higgs production, $gg \to H$, we use the effective coupling to gluons in the limit $m_H^2 \ll 4m_t^2$, see eq. (2.73) The Born cross section and LO rapidity spectrum for an

on-shell Higgs boson are given by

$$\sigma_B^{ggH} = \frac{1}{72\pi v^2 (N_c^2 - 1)}, \qquad \frac{d\sigma_{\mathrm{LO}}^{ggH}}{dY} = x_a x_b \, \sigma_B^{ggH} \, \alpha_s^2 \, f_g(x_a) \, f_g(x_b). \qquad (\mathrm{F.7})$$

We write the partonic cross section as

$$\hat{\sigma}_{ij}(z_a, z_b, m_t, m_H, \mu) \equiv \sigma_B^{ggH} \, \alpha_s^2(\mu) \, |C_t(m_t, \mu)|^2 \sum_{n=0}^{\infty} \left[\frac{\alpha_s(\mu)}{4\pi}\right]^n \hat{\eta}_{ij}^{(n)}(z_a, z_b, m_H, \mu). \quad (\mathrm{F.8})$$

The NLO coefficient function for the gg channel is given by

$$
\frac{\hat{\eta}_{gg}^{(1)}(z_a, z_b, m_H, \mu)}{C_A}
$$
$$
= 2\pi^2 \delta(\bar{z}_a)\delta(\bar{z}_b) + 4\mathcal{L}_1(\bar{z}_a)\delta(\bar{z}_b) + 4\delta(\bar{z}_a)\mathcal{L}_1(\bar{z}_b) + 4\mathcal{L}_0(\bar{z}_a)\mathcal{L}_0(\bar{z}_b) \qquad (\mathrm{F.9})
$$
$$
+ \left\{ 4\mathcal{L}_0(\bar{z}_a)\left[\frac{1}{z_b} - 2 + z_b - z_b^2\right] + 4\delta(\bar{z}_a)\frac{1}{\bar{z}_b}\left[\frac{\ln(2\bar{z}_b)}{z_b} - 3\ln\bar{z}_b + 2\ln\frac{1+z_b}{2} - \frac{\ln(1+z_b)}{z_b}\right.\right.
$$
$$
\left.- z_b(3 - 2z_b + z_b^2)\ln\frac{1+z_b}{2\bar{z}_b}\right] - 4\ln\frac{\mu}{m_H}\delta(\bar{z}_a)\left[2\mathcal{L}_0(\bar{z}_b)\frac{(1 - z_b + z_b^2)^2}{z_b}\right]
$$
$$
+ \frac{4z_b}{z_a(1+z_a)(1+z_b)(z_a+z_b)^4}\left[2z_b^2 + z_b^3 + 3z_a^6 z_b^4 + 2z_a^5 z_b^3(5 + 5z_b + 2z_b^2)\right.
$$
$$
+ z_a^4 z_b^2(16 + 17z_b + 12z_b^2 + 6z_b^3 + 2z_b^4) + z_a^3 z_b(5 + 22z_b + 12z_b^2 + 8z_b^3 + 8z_b^4 + 2z_b^5)
$$
$$
+ z_a^2(3 + 2z_b^2 + 7z_b^3 + 2z_b^4 + 4z_b^5 + 2z_b^6) + z_a z_b(4 + z_b + z_b^2 + z_b^3 + z_b^5)\Big]
$$
$$
+ (z_a \leftrightarrow z_b) \bigg\}.
$$

For the gq and qg channels we find, with $\hat{\eta}_{qg}^{(1)}(z_a, z_b, m_H, \mu) = \hat{\eta}_{gq}^{(1)}(z_b, z_a, m_H, \mu)$,

$$
\frac{\hat{\eta}_{gq}^{(1)}(z_a, z_b, m_H, \mu)}{C_F}
$$
$$
= 2\mathcal{L}_0(\bar{z}_a)\frac{2 - 2z_b + z_b^2}{z_b} + 2\delta(\bar{z}_a)\left[z_b + \frac{2 - 2z_b + z_b^2}{z_b}\left(\ln\frac{2\bar{z}_b}{1+z_b} - 2\ln\frac{\mu}{m_H}\right)\right]
$$
$$
+ \frac{2}{(1+z_a)z_b(z_a+z_b)^3}\left[z_a^3(2 - 2z_b + z_b^2) + z_a^2(4 - 2z_b - 4z_b^2 + 7z_b^3 - 2z_b^5)\right.
$$
$$
+ z_a z_b(4 - 4z_b + 4z_b^2 + z_b^3 - 2z_b^4) - z_b^2(-2 + 2z_b - 2z_b^2 + z_b^3)\Big]. \qquad (\mathrm{F.10})
$$

The $q\bar{q}$ channel is fully regular and given by

$$
\frac{\hat{\eta}_{q\bar{q}}^{(1)}(z_a, z_b, m_H, \mu)}{C_F} = \frac{N_c^2 - 1}{N_c}\frac{4(1 + z_a z_b)(z_a^4 z_b^2 + z_a^2 z_b^4 - 4z_a^2 z_b^2 + z_a^2 + z_b^2)}{(z_a + z_b)^4}. \qquad (\mathrm{F.11})
$$

The N_c-dependent prefactor accounts for the different color average compared to the Born cross section. All results for $q \leftrightarrow \bar{q}$ are again identical.

Appendix G

Additional numerical results

G.1 Differential and cumulant scale setting in $(q_T, \mathcal{T}_0)$

In this appendix we discuss the issue of differential versus cumulant scale setting as relevant for the double-differential spectra computed in chapter 4, starting with the simpler case of a cross section differential in a single observable and using 0-jettiness $\mathcal{T}_0 \equiv \mathcal{T}$ as an example. There are two equivalent quantities of interest in this case, namely the spectrum $\mathrm{d}\sigma/\mathrm{d}\mathcal{T}$ with respect to $\mathcal{T}$ and the cumulant cross section $\sigma(\mathcal{T}_{\mathrm{cut}})$ with a cut on $\mathcal{T}$. The two quantities are related by

$$\sigma(\mathcal{T}_{\mathrm{cut}}) = \int_0^{\mathcal{T}_{\mathrm{cut}}} \mathrm{d}\mathcal{T} \, \frac{\mathrm{d}\sigma}{\mathrm{d}\mathcal{T}} \,, \tag{G.1}$$

where we suppress the dependence on Q^2 and Y for the purposes of this subsection. Accordingly, in a resummation analysis one can implement the resummation scales either in terms of the differential variable $\mathcal{T}$ to directly predict the spectrum, or in terms of the cumulant variable $\mathcal{T}_{\mathrm{cut}}$ to predict the cross section integrated up to $\mathcal{T}_{\mathrm{cut}}$. The other observable then follows from eq. (G.1).

Explicitly, with differential scale setting (indicated by the subscript), the differential and cumulant cross section are given by

$$\frac{\mathrm{d}\sigma_{\mathrm{diff}}}{\mathrm{d}\mathcal{T}} = \frac{\mathrm{d}\sigma}{\mathrm{d}\mathcal{T}}\bigg|_{\mu(\mathcal{T})} ,$$

$$\sigma_{\mathrm{diff}}(\mathcal{T}_{\mathrm{cut}}) = \int^{\mathcal{T}_{\mathrm{cut}}} \mathrm{d}\mathcal{T} \left[\theta(\mathcal{T} > \mathcal{T}_{\mathrm{np}}) \frac{\mathrm{d}\sigma}{\mathrm{d}\mathcal{T}}\bigg|_{\mu(\mathcal{T})} + \theta(\mathcal{T} \leq \mathcal{T}_{\mathrm{np}}) \frac{\mathrm{d}\sigma}{\mathrm{d}\mathcal{T}}\bigg|_{\mu(\mathcal{T}_{\mathrm{np}})} \right]. \tag{G.2}$$

In the first term under the integral in the cumulant cross section, all scales μ entering the resummed and matched prediction depend on the integration variable $\mathcal{T}$. Because our setup only reliably predicts the spectrum away from the nonperturbative region, we choose to integrate the resummed spectrum with differential scale setting up from some small cutoff $\mathcal{T}_{\mathrm{np}}$, and include an "underflow" contribution given by the second term under the integral. For the underflow contribution for $\mathcal{T} \leq \mathcal{T}_{\mathrm{np}}$, the spectrum is evaluated at fixed scales corresponding to $\mathcal{T}_{\mathrm{np}}$, such that the integral can be done analytically. The underflow contribution is Sudakov suppressed and thus typically small.

Using cumulant scale setting, we instead use

$$\sigma_{\text{cumul}}(\mathcal{T}_{\text{cut}}) = \int^{\mathcal{T}_{\text{cut}}} d\mathcal{T} \left.\frac{d\sigma}{d\mathcal{T}}\right|_{\mu(\mathcal{T}_{\text{cut}})},$$

$$\frac{d\sigma_{\text{cumul}}}{d\mathcal{T}} = \left.\frac{d\sigma}{d\mathcal{T}}\right|_{\mu(\mathcal{T})} + \sum_i \left[\frac{d}{d\mu_i} \int^{\mathcal{T}} d\mathcal{T}' \frac{d\sigma}{d\mathcal{T}'}\right]_{\mu(\mathcal{T})} \frac{d\mu_i(\mathcal{T})}{d\mathcal{T}}. \tag{G.3}$$

In this case, the scales in the cumulant cross section depend on $\mathcal{T}_{\text{cut}}$, and not the integration variable $\mathcal{T}$, so the integral up to $\mathcal{T}_{\text{cut}}$ can easily be performed analytically. The expression for the differential cross section arises from taking the derivative of the cumulant cross section, where the chain rule leads to the sum of derivatives of each of the scales μ_i in μ with respect to $\mathcal{T}$.

Cumulant scale setting ensures that for $\mathcal{T}_{\text{cut}} \to Q$, the resummed and matched cumulant cross section exactly reproduces the inclusive fixed-order cross section. This follows from the generic requirement on profile scales in the fixed-order region,

$$\mu_i(\mathcal{T}_{\text{cut}}) \to \mu_{\text{FO}} \quad \text{for} \quad \mathcal{T}_{\text{cut}} \to Q. \tag{G.4}$$

Thus for cumulant scale setting, the spectrum has the correct (fixed-order) normalization. However, the additional derivatives of the scales in eq. (G.3) tend to produce artifacts in the spectrum if the profile functions $\mu_i(\mathcal{T})$ used to interpolate between the resummation region $\mathcal{T} \ll Q$ to the fixed-order region $\mathcal{T} \sim Q$ undergo a rapid transition. In particular, a smooth matching to the fixed-order prediction at the level of the differential spectrum typically requires differential scale setting. Moreover, the scale variations using cumulant scale setting tend to produce unreliable uncertainties for the spectrum.

If instead differential scale setting is used, the spectrum is free from such artifacts. However, the integral of the spectrum will not exactly recover the inclusive fixed-order cross section, and the uncertainties obtained for the cumulant by integrating the spectrum scale variations tend to accumulate and end up being much larger than they should be for the total cross section. As in the case of the spectrum with cumulant scale setting, this mismatch purely arises from residual scale dependence, and therefore is formally beyond the working order. It can however still be numerically significant.

Therefore, in general one should use the scale setting that is appropriate for the quantity of interest, i.e., one should use cumulant scale setting when making predictions for the cumulant, and differential scale setting when one is interested in the spectrum. This issue of differential versus cumulant scale setting is well appreciated in the literature for the single-differential case, see e.g. refs. [122, 203, 204, 542]. It fundamentally results from the fact that long-range correlations across the spectrum are not accounted for by the profile scales used for the differential predictions. Conversely, profile scales for the cumulant do not correctly capture the slope of the cumulant and its uncertainty. An elaborate procedure for obtaining a spectrum with differential scales that still produce the exact cross section and uncertainties was developed in ref. [542]. In the `Geneva` Monte Carlo generator, the mismatch between differential and cumulant scales is accounted for by adding explicit higher-order terms [122].

For a simultaneous measurement of q_T and $\mathcal{T}$, there are in principle four quantities of interest, namely the double-differential spectrum $\mathrm{d}\sigma/\mathrm{d}q_T\,\mathrm{d}\mathcal{T}$, the single-differential spectra $\mathrm{d}\sigma(q_T^{\mathrm{cut}})/\mathrm{d}\mathcal{T}$ and $\mathrm{d}\sigma(\mathcal{T}_{\mathrm{cut}})/\mathrm{d}q_T$ with a cut on the other variable, and the double cumulant $\sigma(q_T^{\mathrm{cut}}, \mathcal{T}_{\mathrm{cut}})$. They are all related by integration or differentiation, allowing for four different ways of setting scales in each case. For our explicit numerical results in section 4.5, we take a pragmatic approach and use the appropriate combination of differential or cumulant scale setting with respect to either q_T or $\mathcal{T}$ for each of these quantities. This is achieved by evaluating the resummed prediction at profile scales given by the setup described in sections 4.2.2 and 4.2.3 as well as section 4.4.3, but with q_T ($\mathcal{T}$) replaced by q_T^{cut} ($\mathcal{T}_{\mathrm{cut}}$) as appropriate. In this way we are guaranteed to avoid artifacts from profile functions in spectrum observables, and on the other hand ensure that cumulant observables have the correct limiting behavior; e.g., $\sigma(q_T^{\mathrm{cut}}, \mathcal{T}_{\mathrm{cut}})$ will by construction recover the inclusive fixed-order cross section when lifting both cuts, while $\mathrm{d}\sigma(q_T^{\mathrm{cut}})/\mathrm{d}\mathcal{T}$ and $\mathrm{d}\sigma(\mathcal{T}_{\mathrm{cut}})/\mathrm{d}q_T$ exactly recover the resummed and matched prediction for the respective inclusive spectrum at large values of the cut.

Nevertheless, it is interesting to ask how well the different combinations of differential and cumulant scale setting fare for observables other than the one they are designed to describe. In particular we should ask how well the $(q_T, \mathcal{T})$ scale setting we described in earlier sections performs at the level of cumulant observables and their inclusive limit. To do so, we can always promote a spectrum using differential scale setting in q_T ($\mathcal{T}$) to a prediction for the cumulant up to q_T^{cut} ($\mathcal{T}_{\mathrm{cut}}$) using the analogue of eq. (G.2). The only nontrivial new procedure is computing the double cumulant directly from $(q_T, \mathcal{T})$ scales, where we need to account for an overlap in underflow contributions as

$$
\begin{aligned}
\sigma_{\mathrm{diff,diff}}(q_T^{\mathrm{cut}}, \mathcal{T}_{\mathrm{cut}}) = \int^{q_T^{\mathrm{cut}}} \mathrm{d}q_T \int^{\mathcal{T}_{\mathrm{cut}}} \mathrm{d}\mathcal{T} \Big[&\theta(q_T > q_T^{\mathrm{np}})\,\theta(\mathcal{T} > \mathcal{T}_{\mathrm{np}}) \frac{\mathrm{d}\sigma}{\mathrm{d}q_T\,\mathrm{d}\mathcal{T}}\Big|_{\mu(q_T, \mathcal{T})} \quad \text{(G.5)} \\
+ &\theta(q_T \le q_T^{\mathrm{np}})\,\theta(\mathcal{T} > \mathcal{T}_{\mathrm{np}}) \frac{\mathrm{d}\sigma}{\mathrm{d}q_T\,\mathrm{d}\mathcal{T}}\Big|_{\mu(q_T^{\mathrm{np}}, \mathcal{T})} \\
+ &\theta(q_T > q_T^{\mathrm{np}})\,\theta(\mathcal{T} \le \mathcal{T}_{\mathrm{np}}) \frac{\mathrm{d}\sigma}{\mathrm{d}q_T\,\mathrm{d}\mathcal{T}}\Big|_{\mu(q_T, \mathcal{T}_{\mathrm{np}})} \\
- &\theta(q_T \le q_T^{\mathrm{np}})\,\theta(\mathcal{T} \le \mathcal{T}_{\mathrm{np}}) \frac{\mathrm{d}\sigma}{\mathrm{d}q_T\,\mathrm{d}\mathcal{T}}\Big|_{\mu(q_T^{\mathrm{np}}, \mathcal{T}_{\mathrm{np}})} \Big].
\end{aligned}
$$

The distinction between differential or cumulant scale setting is only relevant for q_T versus q_T^{cut} but not for the underlying resummation in b_T space, so we suppress the dependence of the hybrid scales on b_T. In practice we use $q_T^{\mathrm{np}} = \mathcal{T}_{\mathrm{np}} = 1\,\mathrm{GeV}$, and implement the integrals in eqs. (G.2) and (G.5) as sums over logarithmically spaced bins with bin size $\Delta(\log_{10} q_T) = \Delta(\log_{10} \mathcal{T}) = 0.08$, where the spectrum is evaluated at the logarithmic midpoint of the bin. Scale variations in the integrated results are performed by integrating each instance of the spectrum separately and computing maximum deviations from central in the end. The final results are interpolated for clarity.

In figures G.1 to G.3, we compare our default scale setting for various cumulant observables (solid orange) to more differential scale setting (dashed blue and dotted green), i.e.,
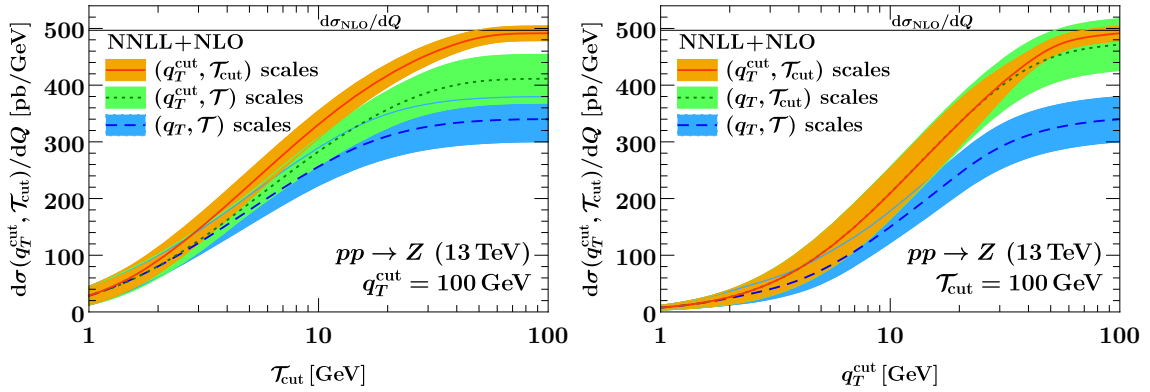
Figure G.1: The double cumulant cross section as a function of $\mathcal{T}_{\mathrm{cut}}$ for $q_T^{\mathrm{cut}} = 100\,\mathrm{GeV}$ (left) and as a function of q_T^{cut} for $\mathcal{T}_{\mathrm{cut}} = 100\,\mathrm{GeV}$ (right). The bands indicate the total perturbative uncertainty Δ_{total}, see section 4.4.4. The colors correspond to different scale setting prescriptions (default: solid orange); see the text for details.

choosing μ in terms of q_T rather than q_T^{cut} and/or $\mathcal{T}$ rather than $\mathcal{T}_{\mathrm{cut}}$. In figure G.1, we show the double cumulant cross section, for which our default is to use scales in terms of q_T^{cut} and $\mathcal{T}_{\mathrm{cut}}$. The horizontal reference line indicates the inclusive fixed-order cross section. In figure G.2 we show the $\mathcal{T}$ spectrum with a cut on q_T, for which our default scales are in terms of q_T^{cut} and $\mathcal{T}$, and the converse for figure G.3. In figures G.2 and G.3 the left panel shows the dependence on the cut at a representative point along the spectrum, with the reference line indicating the resummed prediction for the inclusive (strictly single-differential) spectrum. The right panel shows the spectrum at a representative choice of the cut.

We start by observing that in all cases, the predictions obtained using the default scale setting (solid orange) cleanly asymptote to the respective target observable (the reference line) for large values of the cut. The central double-differential prediction in the left panel of figure G.3 slightly overshoots the inclusive result beyond the phase-space boundary $\mathcal{T}_{\mathrm{cut}} \gtrsim q_T$ (where our calculation is effectively a leading-order calculation), but is monotonic within uncertainties. Furthermore, the uncertainty obtained using our default is smaller than any of the ones obtained from more differential scale setting. This is expected because differential scale setting cannot account for correlations between different bins of the spectrum, giving rise to a larger band in the cumulant cross sections.

We further note that predictions obtained using q_T or q_T^{cut} scale setting are mutually compatible, i.e., their uncertainty bands (very nearly) overlap, as long as the scale setting with respect to $\mathcal{T}$ is done the same way in both cases. This can be seen from the right panel of figure G.1 by contrasting the default $(q_T^{\mathrm{cut}}, \mathcal{T}_{\mathrm{cut}})$ scales (solid orange) and $(q_T, \mathcal{T}_{\mathrm{cut}})$ scales (dotted green). Similarly, in figure G.2 we find that the default $(q_T^{\mathrm{cut}}, \mathcal{T})$ scales (solid orange) and $(q_T, \mathcal{T})$ scale setting (dashed blue) roughly differ by their respective uncertainties. In principle these relations are expected since the unphysical scale dependence is canceled by higher-order corrections, which our scale variations are designed to probe. For the case of q_T versus q_T^{cut} scales in particular, we note that due to our specific choice of hybrid profile
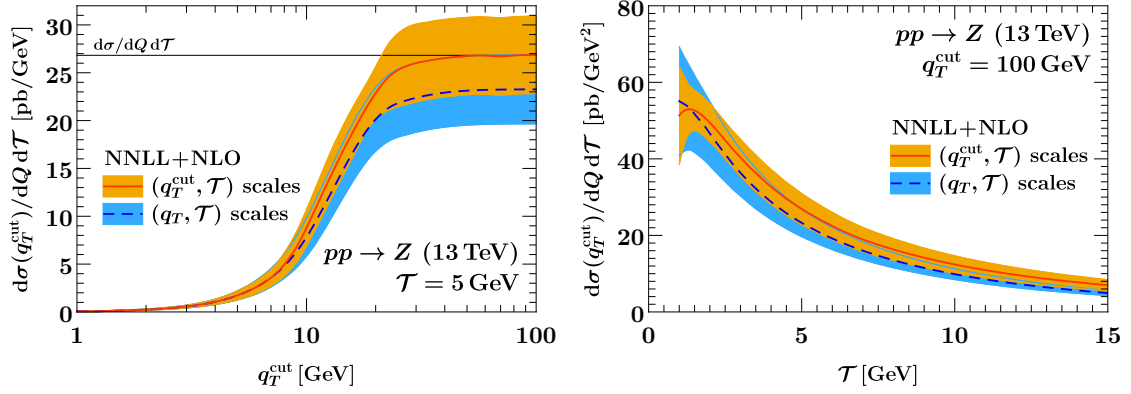
Figure G.2: The $\mathcal{T}$ spectrum with a cut on q_T as a function of q_T^{cut} at fixed $\mathcal{T} = 5\,\text{GeV}$ (left) and as a function of $\mathcal{T}$ at fixed $q_T^{\text{cut}} = 100\,\text{GeV}$ (right). The bands indicate the total perturbative uncertainty Δ_{total}, see section 4.4.4. The colors correspond to different scale setting prescriptions (default: solid orange); see the text for details.
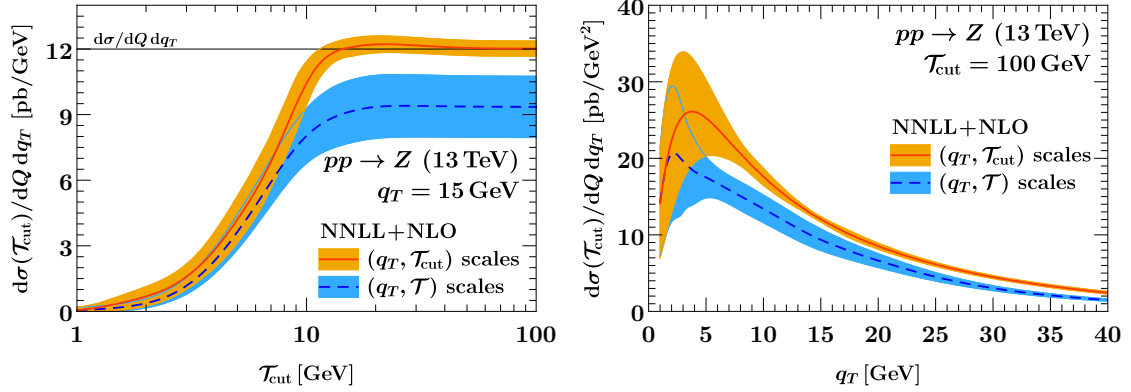

Figure G.3: The q_T spectrum with a cut on $\mathcal{T}$ as a function of $\mathcal{T}_{\text{cut}}$ for $q_T = 15\,\text{GeV}$ (left) and as a function of q_T for $\mathcal{T}_{\text{cut}} = 100\,\text{GeV}$ (right). The bands indicate the total perturbative uncertainty Δ_{total}, see section 4.4.4. The colors correspond to different scale setting prescriptions (default: solid orange); see the text for detail.

scales in eq. (4.22), differences between the two prescriptions only start to appear when turning off the resummation, such that g_{run} is nonzero. E.g. for a high $\mathcal{T}_{\text{cut}} = 100\,\text{GeV}$, which is also a good proxy for the inclusive q_T spectrum, the two prescriptions fully agree in the canonical region $q_T^{\text{cut}} \leq 20\,\text{GeV}$ (see the right panel of figure G.1). This is responsible for the good overall agreement because most of the cross section is concentrated in the canonical region.

The comparison of $\mathcal{T}$ versus $\mathcal{T}_{\text{cut}}$ scales is much less favorable, with the former failing to reproduce the latter's inclusive limit within uncertainties in all cases. This is in line with the discrepancy reported in ref. [542] for a single-differential measurement of thrust in $e^+ e^-$ collisions and at a comparable working order (NLL$'$+NLO). The mismatch is most striking between the default scales (solid orange) and $(q_T, \mathcal{T})$ scales (dashed blue) in figures G.1
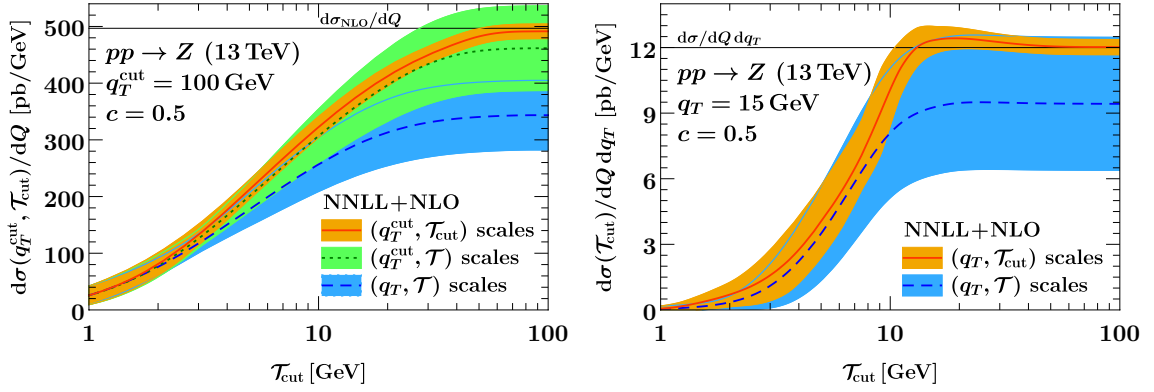
Figure G.4: Left: The double cumulant cross section as a function of $\mathcal{T}_{\mathrm{cut}}$ for $q_T^{\mathrm{cut}} = 100\,\mathrm{GeV}$ for different scale setting prescriptions, with a modified slope $c = 0.5$ of the $\mathrm{SCET_I}$ profile scales, see eq. (G.6). Right: The q_T spectrum with a cut on $\mathcal{T}$ as a function of $\mathcal{T}_{\mathrm{cut}}$ for different scale setting prescriptions, also using modified $\mathrm{SCET_I}$ profile scales with $c = 0.5$. The bands indicate the total perturbative uncertainty Δ_{total}, see section 4.4.4.

and G.3, implying that more effort is required to ensure both a correct integral and the best possible prediction for the shape of the double-differential spectrum.

From our previous discussion we conclude that the mismatch mostly reduces to the question of differential versus cumulant scale setting in $\mathcal{T}$ alone, so that the methods developed for the single-differential case in refs. [122, 542] can be brought to bear here as well if desired. However, since this is a well-known issue that is merely inherited from the single-differential case, we do not pursue this further in the main text.

Instead, we consider a modification of our profile scales to illustrate that the issue is indeed a correlated higher-order effect related to scale choices. Specifically, we can consider lowering the canonical low scale $\mu_S^{\mathrm{I}} \sim (\mu_B^{\mathrm{I}})^2/\mu_H^{\mathrm{I}} \sim \mathcal{T}$ in $\mathrm{SCET_I}$ by a factor of $c = 0.5$, which does not parametrically violate the canonical scaling. Including a smooth interpolation to the fixed-order and nonperturbative region, this can be achieved by replacing eq. (4.10) with

$$
f_{\mathrm{run}}^{\mathrm{I}}(c; x) = \begin{cases}
x_0 \left(1 + \frac{c^2 x^2}{4 x_0^2}\right) & x \leq 2 x_0/c\,, \\
c x & 2 x_0/c < x \leq x_1\,, \\
c x + \frac{(2 - c x_2 - c x_3)(x - x_1)^2}{2(x_2 - x_1)(x_3 - x_1)} & x_1 < x \leq x_2\,, \\
1 - \frac{(2 - c x_1 - c x_2)(x - x_3)^2}{2(x_3 - x_1)(x_3 - x_2)} & x_2 < x \leq x_3\,, \\
1 & x_3 < x\,,
\end{cases}
\tag{G.6}
$$

and keeping the entire remaining profile setup unchanged; setting $c = 1$ recovers eq. (4.10).

Our results using eq. (G.6) are shown in figure G.4, where we repeat the left panels of figures G.1 and G.3 using the modified setup. Note that for simplicity, we use eq. (G.6) for all results in this figure, i.e., for both differential and cumulant scale setting. We find that the simple modification eq. (G.6) already substantially improves the agreement between
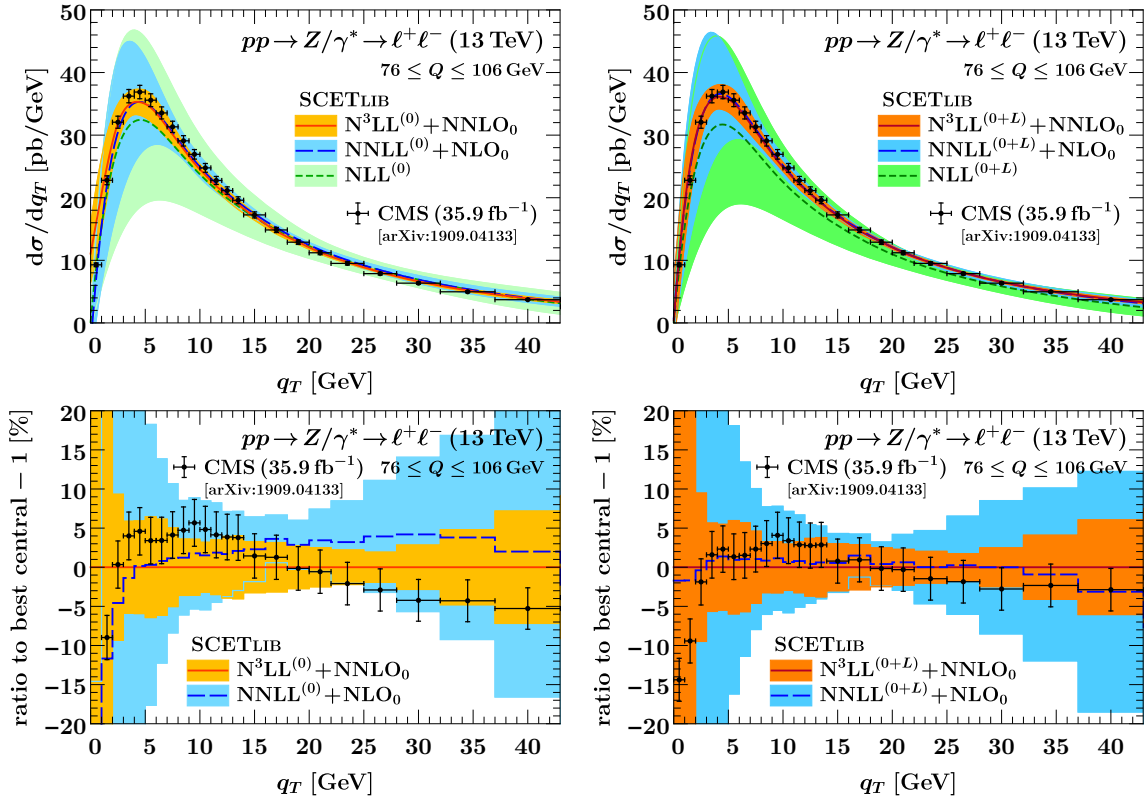
Figure G.5: Comparison to CMS 13 TeV measurements [31] analogous to figure 7.14 but for the unnormalized, absolute q_T spectrum.

differential and cumulant scale setting, with the result from $(q_T^{\mathrm{cut}}, \mathcal{T})$ scales (dotted green, left panel) covering the inclusive fixed-order cross section and the result from $(q_T, \mathcal{T})$ scales (dashed blue, right panel) covering the result from single-differential q_T resummation, at the price of much larger uncertainties.

We conclude that with additional effort, e.g. applying the methods used in refs. [122, 542], it would be possible to fully reconcile the best possible predictions for both the differential shape and the cumulant of the double-differential spectrum. However, for our purposes we can simply use the appropriate scale setting for the observable of interest. In particular, if the experimental observable of interest has cumulant-like character in either q_T or $\mathcal{T}$, e.g. if large bins in either observable are considered, the double-differential profile setup given in chapter 4, using $(q_T^{\mathrm{cut}}, \mathcal{T})$ or $(q_T, \mathcal{T}_{\mathrm{cut}})$ scales as appropriate, will be completely sufficient.

G.2 Comparison to additional experimental data

G.2.1 Unnormalized CMS 13 TeV measurements

In section 7.5, we compared our predictions to the CMS 13 TeV measurements from ref. [31] using the normalized q_T and ϕ^* spectra. For completeness, here we show the corresponding results for the unnormalized, absolute q_T spectrum in figure G.5 and ϕ^* spectrum in
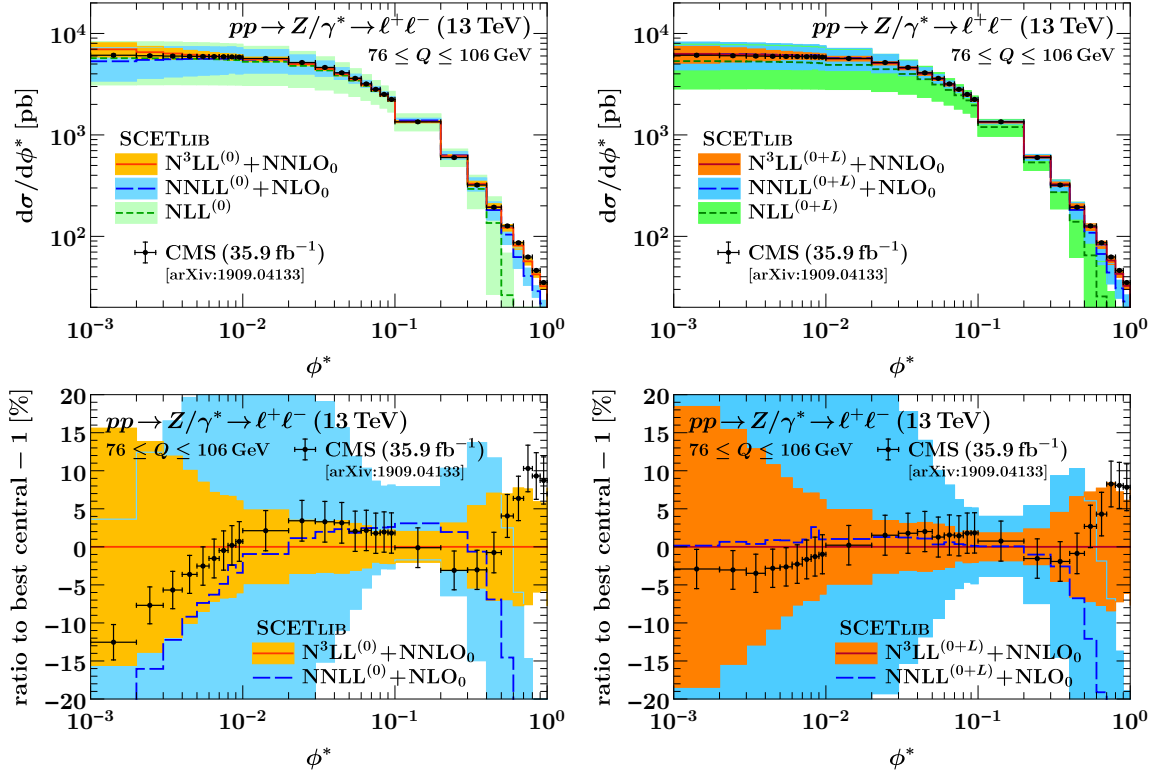
Figure G.6: Comparison to CMS 13 TeV measurements [31] analogous to figure 7.18 but for the unnormalized, absolute ϕ^* spectrum.

figure G.6. The experimental uncertainties are larger for the absolute spectra than the normalized ones but include a substantial correlated component from the overall absolute normalization of the measurement. The absolute spectra show the same systematic improvement in the predictions from resumming the fiducial power corrections.

G.2.2 Results for $\mu^+\mu^-$ channel

In section 7.5, we compared our predictions to the ATLAS 8 TeV measurements [426] in the $pp \to Z/\gamma^* \to e^+e^-$ channel. For completeness, here we provide the analogous results in the $pp \to Z/\gamma^* \to \mu^+\mu^-$ channel, which differ from the electron measurements by the lack of the lepton-rapidity exclusion region $1.37 < |\eta| < 1.52$. In figure G.7, we show the results for the q_T spectrum in the muon channel, which corresponds to figure 7.16 in the electron channel. In figure G.8, we show the results for the ϕ^* spectrum in the muon channel, which corresponds to figure 7.17 in the electron channel. The results for the muon channel are essentially identical and confirm the conclusions drawn in section 7.5.
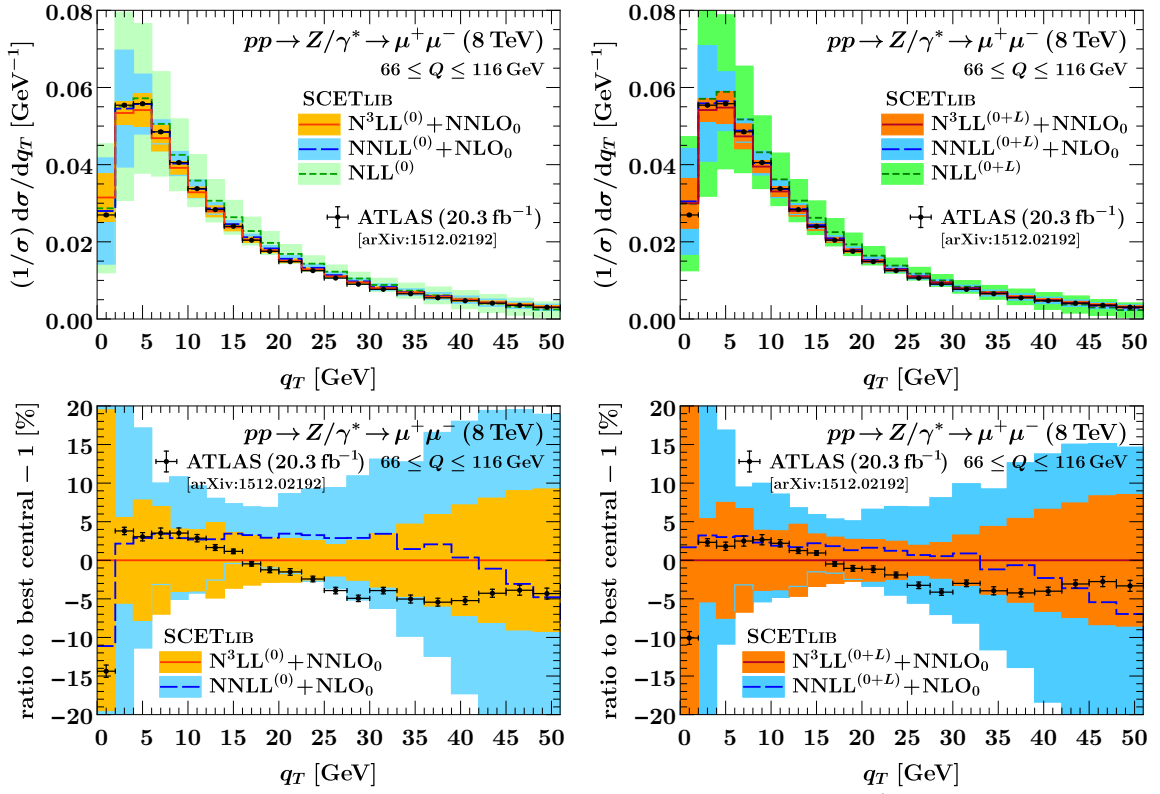
Figure G.7: Comparison to ATLAS 8 TeV q_T measurements [426] in the $\mu^+\mu^-$ channel, analogous to the e^+e^- channel in figure 7.16.
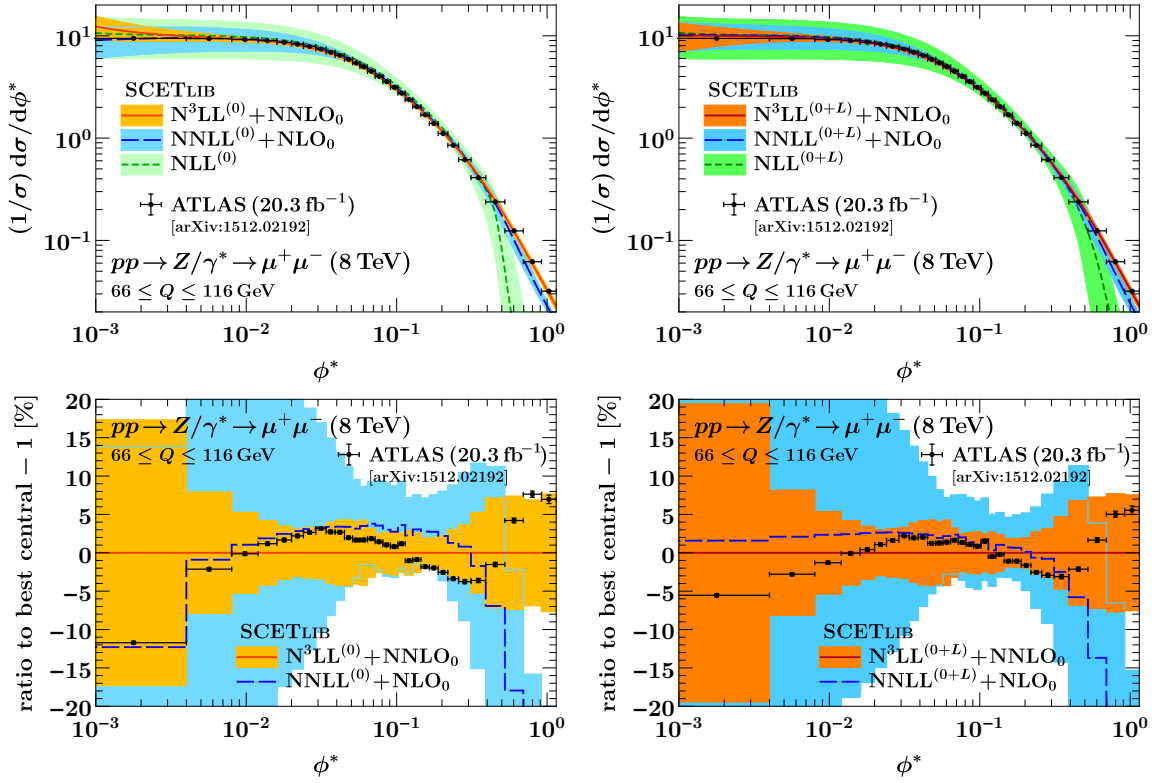

Figure G.8: Comparison to ATLAS 8 TeV ϕ^* measurements [426] in the $\mu^+\mu^-$ channel, analogous to the e^+e^- channel in figure 7.17.

References

Citing pages are listed in square brackets after each reference.

[1] M. A. Ebert, J. K. L. Michel and F. J. Tackmann, *Resummation Improved Rapidity Spectrum for Gluon Fusion Higgs Production*, *JHEP* **05** (2017) 088 [`1702.00794`]. [pp. v, 124, 307, 313, and 315]

[2] J. K. Michel, P. Pietrulewicz and F. J. Tackmann, *Jet Veto Resummation with Jet Rapidity Cuts*, *JHEP* **04** (2019) 142 [`1810.12911`]. [pp. v, 79, 80, 87, 112, 113, 121, 131, and 150]

[3] G. Lustermans, J. K. Michel, F. J. Tackmann and W. J. Waalewijn, *Joint two-dimensional resummation in q_T and 0-jettiness at NNLL*, *JHEP* **03** (2019) 124 [`1901.03331`]. [pp. v, 133, and 134]

[4] G. Lustermans, J. K. Michel and F. J. Tackmann, *Generalized Threshold Factorization with Full Collinear Dynamics*, `1908.00985`. [pp. v, 173, and 176]

[5] G. Billis, M. A. Ebert, J. K. Michel and F. J. Tackmann, *A Toolbox for q_T and 0-Jettiness Subtractions at N^3LO*, `1909.00811`. [pp. v, 72, 74, 208, 211, 212, 219, 296, and 319]

[6] M. A. Ebert, J. K. Michel, I. W. Stewart and F. J. Tackmann, *Drell-Yan q_T Resummation of Fiducial Power Corrections at N^3LL*, `2006.11382`. [pp. v, 225, 267, and 298]

[7] S. Amoroso et al., *Les Houches 2019: Physics at TeV Colliders: Standard Model Working Group Report*, in *11th Les Houches Workshop on Physics at TeV Colliders: PhysTeV Les Houches*, 3, 2020, `2003.01700`. [p. v]

[8] M. A. Ebert, J. K. L. Michel, F. J. Tackmann et al., *SCETlib: A C++ Package for Numerical Calculations in QCD and Soft-Collinear Effective Theory*, public version in development, webpage: `http://scetlib.desy.de`. [pp. v, 90, 124, 137, 165, 199, 204, 228, 266, and 302]

[9] ATLAS collaboration, *Observation of a new particle in the search for the Standard Model Higgs boson with the ATLAS detector at the LHC*, *Phys. Lett. B* **716** (2012) 1 [`1207.7214`]. [p. 1]

[10] CMS collaboration, *Observation of a New Boson at a Mass of 125 GeV with the CMS Experiment at the LHC*, *Phys. Lett. B* **716** (2012) 30 [`1207.7235`]. [p. 1]

References

[11] S. Glashow, *Partial Symmetries of Weak Interactions*, *Nucl. Phys.* **22** (1961) 579. [p. 1]

[12] S. Weinberg, *A Model of Leptons*, *Phys. Rev. Lett.* **19** (1967) 1264. [p. 1]

[13] A. Salam, *Weak and Electromagnetic Interactions*, *Conf. Proc. C* **680519** (1968) 367. [p. 1]

[14] G. 't Hooft and M. Veltman, *Regularization and Renormalization of Gauge Fields*, *Nucl. Phys. B* **44** (1972) 189. [p. 1]

[15] P. W. Higgs, *Broken Symmetries and the Masses of Gauge Bosons*, *Phys. Rev. Lett.* **13** (1964) 508. [p. 1]

[16] P. W. Higgs, *Broken symmetries, massless particles and gauge fields*, *Phys. Lett.* **12** (1964) 132. [p. 1]

[17] F. Englert and R. Brout, *Broken Symmetry and the Mass of Gauge Vector Mesons*, *Phys. Rev. Lett.* **13** (1964) 321. [p. 1]

[18] P. W. Anderson, *Plasmons, Gauge Invariance, and Mass*, *Phys. Rev.* **130** (1963) 439. [p. 1]

[19] ATLAS collaboration, *Measurements of the Higgs boson production and decay rates and coupling strengths using pp collision data at $\sqrt{s} = 7$ and 8 TeV in the ATLAS experiment*, *Eur. Phys. J. C* **76** (2016) 6 [`1507.04548`]. [p. 1]

[20] CMS collaboration, *Combined measurements of Higgs boson couplings in proton-proton collisions at $\sqrt{s} = 13$ TeV*, *Eur. Phys. J.* **C79** (2019) 421 [`1809.10733`]. [p. 1]

[21] CMS collaboration, *Inclusive search for highly boosted Higgs bosons decaying to bottom quark-antiquark pairs in proton-proton collisions at $\sqrt{s} = 13$ TeV*, `2006.13251`. [p. 1]

[22] ATLAS collaboration, *Measurement of the associated production of a Higgs boson decaying into b-quarks with a vector boson at high transverse momentum in pp collisions at $\sqrt{s} = 13$ TeV with the ATLAS detector*, `2008.02508`. [p. 1]

[23] SUPER-KAMIOKANDE collaboration, Y. Fukuda et al., *Evidence for oscillation of atmospheric neutrinos*, *Phys. Rev. Lett.* **81** (1998) 1562 [`hep-ex/9807003`]. [p. 1]

[24] SNO collaboration, Q. Ahmad et al., *Direct evidence for neutrino flavor transformation from neutral current interactions in the Sudbury Neutrino Observatory*, *Phys. Rev. Lett.* **89** (2002) 011301 [`nucl-ex/0204008`]. [p. 1]

[25] PARTICLE DATA GROUP collaboration, M. Tanabashi et al., *Review of Particle Physics*, *Phys. Rev. D* **98** (2018) 030001. [pp. 1, 17, 19, 33, and 266]

[26] CMS collaboration, *Combination of searches for heavy resonances decaying to WW, WZ, ZZ, WH, and ZH boson pairs in proton–proton collisions at $\sqrt{s} = 8$ and 13 TeV*, *Phys. Lett. B* **774** (2017) 533 [1705.09171]. [p. 2]

[27] ATLAS collaboration, *Combination of searches for heavy resonances decaying into bosonic and leptonic final states using 36 fb^{-1} of proton-proton collision data at $\sqrt{s} = 13$ TeV with the ATLAS detector*, *Phys. Rev. D* **98** (2018) 052008 [1808.02380]. [p. 2]

[28] CMS collaboration, *Combination of CMS searches for heavy resonances decaying to pairs of bosons or leptons*, *Phys. Lett. B* **798** (2019) 134952 [1906.00057]. [p. 2]

[29] ATLAS collaboration, *Dijet resonance search with weak supervision using $\sqrt{s} = 13$ TeV pp collisions in the ATLAS detector*, *Phys. Rev. Lett.* **125** (2020) 131801 [2005.02983]. [p. 2]

[30] A. Dainese, M. Mangano, A. B. Meyer, A. Nisati, G. Salam and M. A. Vesterinen, eds., *Report on the Physics at the HL-LHC,and Perspectives for the HE-LHC*, vol. 7/2019 of *CERN Yellow Reports: Monographs*. CERN, Geneva, Switzerland, 2019, 10.23731/CYRM-2019-007. [p. 2]

[31] CMS collaboration, *Measurements of differential Z boson production cross sections in proton-proton collisions at $\sqrt{s} = 13$ TeV*, *JHEP* **12** (2019) 061 [1909.04133]. [pp. 3, 225, 228, 271, 283, 285, 287, 288, 335, and 336]

[32] CMS collaboration, *Measurement of the transverse momentum spectra of weak vector bosons produced in proton-proton collisions at $\sqrt{s} = 8$ TeV*, *JHEP* **02** (2017) 096 [1606.05864]. [pp. 3 and 225]

[33] ATLAS collaboration, *Measurement of the Drell-Yan triple-differential cross section in pp collisions at $\sqrt{s} = 8$ TeV*, *JHEP* **12** (2017) 059 [1710.05167]. [pp. 3 and 225]

[34] CMS collaboration, *Measurements of differential Z boson production cross sections in pp collisions with CMS at $\sqrt{s} = 13$ TeV*, Tech. Rep. CMS-PAS-SMP-17-010, CERN, Geneva, 2019. [p. 3]

[35] ATLAS collaboration, *Measurement of the transverse momentum distribution of Drell-Yan lepton pairs in proton-proton collisions at $\sqrt{s} = 13$ TeV with the ATLAS detector*, *Eur. Phys. J. C* **80** (2020) 616 [1912.02844]. [pp. 3 and 225]

[36] ATLAS collaboration, *Measurement of the W-boson mass in pp collisions at $\sqrt{s} = 7$ TeV with the ATLAS detector*, *Eur. Phys. J.* **C78** (2018) 110 [1701.07240]. [pp. 4 and 225]

[37] F. Bishara, U. Haisch, P. F. Monni and E. Re, *Constraining Light-Quark Yukawa Couplings from Higgs Distributions*, *Phys. Rev. Lett.* **118** (2017) 121801 [1606.09253]. [p. 4]

[38] A. J. Larkoski, *An Unorthodox Introduction to QCD*, `1709.06195`. [p. 7]

[39] V. Sudakov, *Vertex parts at very high-energies in quantum electrodynamics*, *Sov. Phys. JETP* **3** (1956) 65. [p. 7]

[40] S. Höche, *Introduction to parton-shower event generators*, in *Theoretical Advanced Study Institute in Elementary Particle Physics: Journeys Through the Precision Frontier: Amplitudes for Colliders*, pp. 235–295, 2015, `1411.4085`, DOI. [p. 7]

[41] A. Gehrmann-De Ridder, T. Gehrmann and E. W. N. Glover, *Antenna subtraction at NNLO*, *JHEP* **09** (2005) 056 [`hep-ph/0505111`]. [p. 8]

[42] J. Currie, E. W. N. Glover and S. Wells, *Infrared Structure at NNLO Using Antenna Subtraction*, *JHEP* **04** (2013) 066 [`1301.4693`]. [p. 8]

[43] M. Czakon, *A novel subtraction scheme for double-real radiation at NNLO*, *Phys. Lett.* **B693** (2010) 259 [`1005.0274`]. [p. 8]

[44] M. Czakon and D. Heymes, *Four-dimensional formulation of the sector-improved residue subtraction scheme*, *Nucl. Phys.* **B890** (2014) 152 [`1408.2500`]. [p. 8]

[45] R. Boughezal, K. Melnikov and F. Petriello, *A subtraction scheme for NNLO computations*, *Phys. Rev.* **D85** (2012) 034025 [`1111.7041`]. [p. 8]

[46] S. Catani and M. Grazzini, *An NNLO subtraction formalism in hadron collisions and its application to Higgs boson production at the LHC*, *Phys. Rev. Lett.* **98** (2007) 222002 [`hep-ph/0703012`]. [pp. 8 and 296]

[47] V. Del Duca, C. Duhr, G. Somogyi, F. Tramontano and Z. Trócsányi, *Higgs boson decay into b-quarks at NNLO accuracy*, *JHEP* **04** (2015) 036 [`1501.07226`]. [p. 8]

[48] V. Del Duca, C. Duhr, A. Kardos, G. Somogyi and Z. Trócsányi, *Three-Jet Production in Electron-Positron Collisions at Next-to-Next-to-Leading Order Accuracy*, *Phys. Rev. Lett.* **117** (2016) 152004 [`1603.08927`]. [p. 8]

[49] R. Boughezal, C. Focke, X. Liu and F. Petriello, *W-boson production in association with a jet at next-to-next-to-leading order in perturbative QCD*, *Phys. Rev. Lett.* **115** (2015) 062002 [`1504.02131`]. [pp. 8, 226, and 296]

[50] J. Gaunt, M. Stahlhofen, F. J. Tackmann and J. R. Walsh, *N-jettiness Subtractions for NNLO QCD Calculations*, *JHEP* **09** (2015) 058 [`1505.04794`]. [pp. 8, 158, 293, and 296]

[51] M. Cacciari, F. A. Dreyer, A. Karlberg, G. P. Salam and G. Zanderighi, *Fully Differential Vector-Boson-Fusion Higgs Production at Next-to-Next-to-Leading Order*, *Phys. Rev. Lett.* **115** (2015) 082002 [`1506.02660`]. [pp. 8 and 294]

[52] F. Caola, K. Melnikov and R. Röntsch, *Nested soft-collinear subtractions in NNLO QCD computations*, *Eur. Phys. J.* **C77** (2017) 248 [1702.01352]. [p. 8]

[53] F. Caola, K. Melnikov and R. Röntsch, *Analytic results for color-singlet production at NNLO QCD with the nested soft-collinear subtraction scheme*, *Eur. Phys. J. C* **79** (2019) 386 [1902.02081]. [p. 8]

[54] F. Herzog, *Geometric IR subtraction for final state real radiation*, *JHEP* **08** (2018) 006 [1804.07949]. [p. 8]

[55] L. Magnea, E. Maina, G. Pelliccioli, C. Signorile-Signorile, P. Torrielli and S. Uccirati, *Local analytic sector subtraction at NNLO*, *JHEP* **12** (2018) 107 [1806.09570]. [p. 8]

[56] L. Magnea, E. Maina, G. Pelliccioli, C. Signorile-Signorile, P. Torrielli and S. Uccirati, *Factorisation and Subtraction beyond NLO*, *JHEP* **12** (2018) 062 [1809.05444]. [p. 8]

[57] I. W. Stewart, F. J. Tackmann and W. J. Waalewijn, *Factorization at the LHC: From PDFs to Initial State Jets*, *Phys. Rev.* **D81** (2010) 094035 [0910.0467]. [pp. 8, 47, 50, 66, 72, 73, 74, 79, 138, 139, 183, 184, 189, 211, 255, 305, 307, 320, and 323]

[58] I. W. Stewart, F. J. Tackmann and W. J. Waalewijn, *The Beam Thrust Cross Section for Drell-Yan at NNLL Order*, *Phys. Rev. Lett.* **106** (2011) 032001 [1005.4060]. [pp. 8 and 79]

[59] C. F. Berger, C. Marcantonini, I. W. Stewart, F. J. Tackmann and W. J. Waalewijn, *Higgs Production with a Central Jet Veto at NNLL+NNLO*, *JHEP* **04** (2011) 092 [1012.4480]. [pp. 8, 72, 73, 74, 79, 81, 110, and 313]

[60] A. Banfi, G. P. Salam and G. Zanderighi, *NLL+NNLO predictions for jet-veto efficiencies in Higgs-boson and Drell-Yan production*, *JHEP* **06** (2012) 159 [1203.5773]. [pp. 8, 79, 80, and 81]

[61] T. Becher and M. Neubert, *Factorization and NNLL Resummation for Higgs Production with a Jet Veto*, *JHEP* **07** (2012) 108 [1205.3806]. [pp. 8, 76, 79, and 80]

[62] F. J. Tackmann, J. R. Walsh and S. Zuberi, *Resummation Properties of Jet Vetoes at the LHC*, *Phys. Rev.* **D86** (2012) 053011 [1206.4312]. [pp. 8, 76, 79, 80, 81, 88, 112, 121, and 314]

[63] A. Banfi, P. F. Monni, G. P. Salam and G. Zanderighi, *Higgs and Z-boson production with a jet veto*, *Phys. Rev. Lett.* **109** (2012) 202001 [1206.4998]. [pp. 8, 79, and 80]

[64] X. Liu and F. Petriello, *Resummation of jet-veto logarithms in hadronic processes containing jets*, *Phys. Rev.* **D87** (2013) 014018 [1210.1906]. [pp. 8, 79, and 81]

[65] X. Liu and F. Petriello, *Reducing theoretical uncertainties for exclusive Higgs-boson plus one-jet production at the LHC*, Phys. Rev. **D87** (2013) 094027 [1303.4405]. [pp. 8, 79, and 81]

[66] T. Becher, M. Neubert and L. Rothen, *Factorization and N^3LL_p+NNLO predictions for the Higgs cross section with a jet veto*, JHEP **10** (2013) 125 [1307.0025]. [pp. 8, 79, 80, and 211]

[67] I. W. Stewart, F. J. Tackmann, J. R. Walsh and S. Zuberi, *Jet p_T resummation in Higgs production at NNLL'+NNLO*, Phys. Rev. **D89** (2014) 054001 [1307.1808]. [pp. 8, 56, 76, 77, 79, 80, 81, 88, 90, 124, 140, 145, 146, 211, 265, 314, and 323]

[68] A. Banfi, P. F. Monni and G. Zanderighi, *Quark masses in Higgs production with a jet veto*, JHEP **01** (2014) 097 [1308.4634]. [pp. 8 and 79]

[69] R. Boughezal, X. Liu, F. Petriello, F. J. Tackmann and J. R. Walsh, *Combining Resummed Higgs Predictions Across Jet Bins*, Phys. Rev. **D89** (2014) 074044 [1312.4535]. [pp. 8 and 79]

[70] S. Gangal, M. Stahlhofen and F. J. Tackmann, *Rapidity-Dependent Jet Vetoes*, Phys. Rev. **D91** (2015) 054023 [1412.4792]. [pp. 8, 79, 80, 100, 112, 140, and 141]

[71] A. Banfi, F. Caola, F. A. Dreyer, P. F. Monni, G. P. Salam, G. Zanderighi et al., *Jet-vetoed Higgs cross section in gluon fusion at N^3LO+NNLL with small-R resummation*, JHEP **04** (2016) 049 [1511.02886]. [pp. 8, 79, and 120]

[72] G. Zweig, *An SU_3 model for strong interaction symmetry and its breaking. Version 1*, Tech. Rep. CERN-TH-401, CERN, Geneva, 1964. [p. 13]

[73] M. Gell-Mann, *A Schematic Model of Baryons and Mesons*, Phys. Lett. **8** (1964) 214. [p. 13]

[74] G. 't Hooft, *Renormalization of Massless Yang-Mills Fields*, Nucl. Phys. B **33** (1971) 173. [pp. 13 and 17]

[75] H. Fritzsch, M. Gell-Mann and H. Leutwyler, *Advantages of the Color Octet Gluon Picture*, Phys. Lett. B **47** (1973) 365. [p. 13]

[76] H. D. Politzer, *Reliable Perturbative Results for Strong Interactions?*, Phys. Rev. Lett. **30** (1973) 1346. [pp. 13 and 19]

[77] D. J. Gross and F. Wilczek, *Ultraviolet Behavior of Nonabelian Gauge Theories*, Phys. Rev. Lett. **30** (1973) 1343. [pp. 13 and 19]

[78] C.-N. Yang and R. L. Mills, *Conservation of Isotopic Spin and Isotopic Gauge Invariance*, Phys. Rev. **96** (1954) 191. [p. 15]

[79] J. M. Pendlebury et al., *Revised experimental upper limit on the electric dipole moment of the neutron, Phys. Rev. D* **92** (2015) 092003 [1509.04411]. [p. 16]

[80] B. Graner, Y. Chen, E. Lindahl and B. Heckel, *Reduced Limit on the Permanent Electric Dipole Moment of Hg199, Phys. Rev. Lett.* **116** (2016) 161601 [1601.04339]. [p. 16]

[81] R. Peccei and H. R. Quinn, *CP Conservation in the Presence of Instantons, Phys. Rev. Lett.* **38** (1977) 1440. [p. 16]

[82] L. Faddeev and V. Popov, *Feynman Diagrams for the Yang-Mills Field, Phys. Lett. B* **25** (1967) 29. [p. 16]

[83] C. Becchi, A. Rouet and R. Stora, *Renormalization of Gauge Theories, Annals Phys.* **98** (1976) 287. [p. 17]

[84] I. Tyutin, *Gauge Invariance in Field Theory and Statistical Physics in Operator Formalism*, 0812.0580. [p. 17]

[85] J. Taylor, *Ward Identities and Charge Renormalization of the Yang-Mills Field, Nucl. Phys. B* **33** (1971) 436. [p. 17]

[86] A. Slavnov, *Ward Identities in Gauge Theories, Theor. Math. Phys.* **10** (1972) 99. [p. 17]

[87] C. Bollini and J. Giambiagi, *Dimensional Renormalization: The Number of Dimensions as a Regularizing Parameter, Nuovo Cim. B* **12** (1972) 20. [p. 17]

[88] F. Herzog, B. Ruijl, T. Ueda, J. Vermaseren and A. Vogt, *The five-loop beta function of Yang-Mills theory with fermions, JHEP* **02** (2017) 090 [1701.01404]. [p. 18]

[89] T. Luthe, A. Maier, P. Marquard and Y. Schroder, *The five-loop Beta function for a general gauge group and anomalous dimensions beyond Feynman gauge, JHEP* **10** (2017) 166 [1709.07718]. [p. 18]

[90] J. Callan, Curtis G., *Broken scale invariance in scalar field theory, Phys. Rev. D* **2** (1970) 1541. [p. 18]

[91] K. Symanzik, *Small distance behavior in field theory and power counting, Commun. Math. Phys.* **18** (1970) 227. [p. 18]

[92] K. G. Wilson, *Confinement of Quarks, Phys. Rev. D* **10** (1974) 2445. [p. 19]

[93] R. Balian, J. Drouffe and C. Itzykson, *Gauge Fields on a Lattice. 1. General Outlook, Phys. Rev. D* **10** (1974) 3376. [p. 19]

[94] M. Creutz, L. Jacobs and C. Rebbi, *Experiments with a Gauge Invariant Ising System, Phys. Rev. Lett.* **42** (1979) 1390. [p. 19]

References

[95] G. F. Sterman and S. Weinberg, *Jets from Quantum Chromodynamics, Phys. Rev. Lett.* **39** (1977) 1436. [p. 19]

[96] J. Blümlein, *The Theory of Deeply Inelastic Scattering, Prog. Part. Nucl. Phys.* **69** (2013) 28 [1208.6087]. [p. 22]

[97] M. E. Peskin and D. V. Schroeder, *An Introduction to quantum field theory.* Addison-Wesley, Reading, USA, 1995. [pp. 23 and 24]

[98] R. P. Feynman, *Very high-energy collisions of hadrons, Phys. Rev. Lett.* **23** (1969) 1415. [p. 23]

[99] J. Callan, Curtis G. and D. J. Gross, *High-energy electroproduction and the constitution of the electric current, Phys. Rev. Lett.* **22** (1969) 156. [p. 23]

[100] E. D. Bloom et al., *High-Energy Inelastic e p Scattering at 6-Degrees and 10-Degrees, Phys. Rev. Lett.* **23** (1969) 930. [p. 24]

[101] M. Breidenbach, J. I. Friedman, H. W. Kendall, E. D. Bloom, D. Coward, H. DeStaebler et al., *Observed behavior of highly inelastic electron-proton scattering, Phys. Rev. Lett.* **23** (1969) 935. [p. 24]

[102] S. Drell and T.-M. Yan, *Massive Lepton Pair Production in Hadron-Hadron Collisions at High-Energies, Phys. Rev. Lett.* **25** (1970) 316. [p. 24]

[103] A. Denner and S. Dittmaier, *Electroweak Radiative Corrections for Collider Physics, Phys. Rept.* **864** (2020) 1 [1912.06823]. [p. 25]

[104] G. T. Bodwin, *Factorization of the Drell-Yan Cross-Section in Perturbation Theory, Phys. Rev.* **D31** (1985) 2616. [pp. 27, 28, and 182]

[105] J. C. Collins, D. E. Soper and G. F. Sterman, *Factorization for Short Distance Hadron - Hadron Scattering, Nucl. Phys.* **B261** (1985) 104. [pp. 27, 28, 133, and 182]

[106] J. C. Collins, D. E. Soper and G. F. Sterman, *Soft Gluons and Factorization, Nucl. Phys.* **B308** (1988) 833. [pp. 27, 28, 133, and 182]

[107] H1, ZEUS collaboration, Z. Zhang, *HERA Inclusive Neutral and Charged Current Cross Sections and a New PDF Fit, HERAPDF 2.0, Acta Phys. Polon. Supp.* **8** (2015) 957 [1511.05402]. [p. 27]

[108] P. Jimenez-Delgado and E. Reya, *Delineating parton distributions and the strong coupling, Phys. Rev. D* **89** (2014) 074049 [1403.1852]. [p. 27]

[109] NNPDF collaboration, R. D. Ball et al., *Parton distributions for the LHC Run II, JHEP* **04** (2015) 040 [1410.8849]. [pp. 27 and 91]

[110] L. A. Harland-Lang, A. D. Martin, P. Motylinski and R. S. Thorne, *Parton distributions in the LHC era: MMHT 2014 PDFs*, *Eur. Phys. J.* **C75** (2015) 204 [1412.3989]. [pp. 27, 91, 137, 165, and 204]

[111] S. Alekhin, J. Blümlein and S. Moch, *An update of the ABM16 PDF fit*, in *26th International Workshop on Deep Inelastic Scattering and Related Subjects*, SISSA, 9, 2019, 1909.03533, DOI. [p. 27]

[112] T.-J. Hou et al., *New CTEQ global analysis of quantum chromodynamics with high-precision data from the LHC*, 1912.10053. [pp. 27 and 266]

[113] C. Anastasiou, L. J. Dixon, K. Melnikov and F. Petriello, *Dilepton rapidity distribution in the Drell-Yan process at NNLO in QCD*, *Phys. Rev. Lett.* **91** (2003) 182002 [hep-ph/0306192]. [pp. 27, 196, and 325]

[114] C. Anastasiou, L. J. Dixon, K. Melnikov and F. Petriello, *High precision QCD at hadron colliders: Electroweak gauge boson rapidity distributions at NNLO*, *Phys. Rev.* **D69** (2004) 094008 [hep-ph/0312266]. [pp. 27, 196, 199, 204, and 325]

[115] K. Melnikov and F. Petriello, *The W boson production cross section at the LHC through $O(\alpha_s^2)$*, *Phys. Rev. Lett.* **96** (2006) 231803 [hep-ph/0603182]. [p. 28]

[116] K. Melnikov and F. Petriello, *Electroweak gauge boson production at hadron colliders through $O(\alpha_s^2)$*, *Phys. Rev. D* **74** (2006) 114017 [hep-ph/0609070]. [p. 28]

[117] S. Catani, L. Cieri, G. Ferrera, D. de Florian and M. Grazzini, *Vector boson production at hadron colliders: a fully exclusive QCD calculation at NNLO*, *Phys. Rev. Lett.* **103** (2009) 082001 [0903.2120]. [p. 28]

[118] R. Gavin, Y. Li, F. Petriello and S. Quackenbush, *FEWZ 2.0: A code for hadronic Z production at next-to-next-to-leading order*, *Comput. Phys. Commun.* **182** (2011) 2388 [1011.3540]. [p. 28]

[119] R. Gavin, Y. Li, F. Petriello and S. Quackenbush, *W Physics at the LHC with FEWZ 2.1*, *Comput. Phys. Commun.* **184** (2013) 208 [1201.5896]. [p. 28]

[120] S. Höche, Y. Li and S. Prestel, *Drell-Yan lepton pair production at NNLO QCD with parton showers*, *Phys. Rev. D* **91** (2015) 074015 [1405.3607]. [p. 28]

[121] A. Karlberg, E. Re and G. Zanderighi, *NNLOPS accurate Drell-Yan production*, *JHEP* **09** (2014) 134 [1407.2940]. [p. 28]

[122] S. Alioli, C. W. Bauer, C. Berggren, F. J. Tackmann and J. R. Walsh, *Drell-Yan production at NNLL'+NNLO matched to parton showers*, *Phys. Rev.* **D92** (2015) 094020 [1508.01475]. [pp. 28, 135, 140, 293, 330, 334, and 335]

References

[123] U. Baur, S. Keller and W. K. Sakumoto, *QED radiative corrections to Z boson production and the forward backward asymmetry at hadron colliders*, Phys. Rev. **D57** (1998) 199 [`hep-ph/9707301`]. [p. 28]

[124] U. Baur, S. Keller and D. Wackeroth, *Electroweak radiative corrections to W boson production in hadronic collisions*, Phys. Rev. **D59** (1999) 013002 [`hep-ph/9807417`]. [p. 28]

[125] U. Baur, O. Brein, W. Hollik, C. Schappacher and D. Wackeroth, *Electroweak radiative corrections to neutral current Drell-Yan processes at hadron colliders*, Phys. Rev. **D65** (2002) 033007 [`hep-ph/0108274`]. [p. 28]

[126] S. Dittmaier and M. Krämer, *Electroweak radiative corrections to W boson production at hadron colliders*, Phys. Rev. **D65** (2002) 073007 [`hep-ph/0109062`]. [p. 28]

[127] U. Baur and D. Wackeroth, *Electroweak radiative corrections to $p\bar{p} \to W^{\pm} \to \ell^{\pm}\nu$ beyond the pole approximation*, Phys. Rev. **D70** (2004) 073015 [`hep-ph/0405191`]. [p. 28]

[128] V. A. Zykunov, *Weak radiative corrections to Drell-Yan process for large invariant mass of di-lepton pair*, Phys. Rev. **D75** (2007) 073019 [`hep-ph/0509315`]. [p. 28]

[129] A. Arbuzov, D. Bardin, S. Bondarenko, P. Christova, L. Kalinovskaya, G. Nanava et al., *One-loop corrections to the Drell-Yan process in SANC (I). The Charged current case*, Eur. Phys. J. **C46** (2006) 407 [`hep-ph/0506110`]. [p. 28]

[130] A. Arbuzov, D. Bardin, S. Bondarenko, P. Christova, L. Kalinovskaya, G. Nanava et al., *One-loop corrections to the Drell-Yan process in SANC (II). The Neutral current case*, Eur. Phys. J. **C54** (2008) 451 [`0711.0625`]. [p. 28]

[131] C. M. Carloni Calame, G. Montagna, O. Nicrosini and A. Vicini, *Precision electroweak calculation of the charged current Drell-Yan process*, JHEP **12** (2006) 016 [`hep-ph/0609170`]. [p. 28]

[132] C. M. Carloni Calame, G. Montagna, O. Nicrosini and A. Vicini, *Precision electroweak calculation of the production of a high transverse-momentum lepton pair at hadron colliders*, JHEP **10** (2007) 109 [`0710.1722`]. [p. 28]

[133] S. Dittmaier and M. Huber, *Radiative corrections to the neutral-current Drell-Yan process in the Standard Model and its minimal supersymmetric extension*, JHEP **01** (2010) 060 [`0911.2329`]. [p. 28]

[134] S. Dittmaier, A. Huss and C. Schwinn, *Mixed QCD-electroweak $O(\alpha_s\alpha)$ corrections to Drell-Yan processes in the resonance region: pole approximation and non-factorizable corrections*, Nucl. Phys. **B885** (2014) 318 [`1403.3216`]. [p. 28]

[135] S. Dittmaier, A. Huss and C. Schwinn, *Dominant mixed QCD-electroweak O($\alpha_s\alpha$) corrections to DrellYan processes in the resonance region*, *Nucl. Phys.* **B904** (2016) 216 [1511.08016]. [p. 28]

[136] D. de Florian, M. Der and I. Fabre, *QCD$\oplus$QED NNLO corrections to Drell Yan production*, *Phys. Rev.* **D98** (2018) 094008 [1805.12214]. [p. 28]

[137] M. Delto, M. Jaquier, K. Melnikov and R. Röntsch, *Mixed QCD$\otimes$QED corrections to on-shell Z boson production at the LHC*, *JHEP* **01** (2020) 043 [1909.08428]. [p. 28]

[138] R. Bonciani, F. Buccioni, N. Rana, I. Triscari and A. Vicini, *NNLO QCD$\times$EW corrections to Z production in the $q\bar{q}$ channel*, *Phys. Rev.* **D101** (2020) 031301 [1911.06200]. [p. 28]

[139] L. Cieri, D. de Florian, M. Der and J. Mazzitelli, *Mixed QCD$\otimes$QED corrections to exclusive Drell Yan production using the q_T-subtraction method*, 2005.01315. [p. 28]

[140] F. Buccioni, F. Caola, M. Delto, M. Jaquier, K. Melnikov and R. Röntsch, *Mixed QCD-electroweak corrections to on-shell Z production at the LHC*, 2005.10221. [p. 28]

[141] C. Duhr, F. Dulat and B. Mistlberger, *The Drell-Yan cross section to third order in the strong coupling constant*, 2001.07717. [p. 29]

[142] C. Duhr, F. Dulat and B. Mistlberger, *Charged Current Drell-Yan Production at N^3LO*, 2007.13313. [p. 29]

[143] G. Altarelli, R. Ellis and G. Martinelli, *Large Perturbative Corrections to the Drell-Yan Process in QCD*, *Nucl. Phys. B* **157** (1979) 461. [p. 29]

[144] R. Hamberg, W. van Neerven and T. Matsuura, *A complete calculation of the order α_s^2 correction to the Drell-Yan K factor*, *Nucl. Phys. B* **359** (1991) 343. [pp. 29, 231, and 307]

[145] W. van Neerven and E. Zijlstra, *The O(α_s^2) corrected Drell-Yan K factor in the DIS and MS scheme*, *Nucl. Phys. B* **382** (1992) 11. [p. 29]

[146] M. Cepeda et al., *Report from Working Group 2: Higgs Physics at the HL-LHC and HE-LHC*, 1902.00134. [pp. 30 and 31]

[147] LHC Higgs Cross Section Working Group collaboration, D. de Florian et al., *Handbook of LHC Higgs Cross Sections: 4. Deciphering the Nature of the Higgs Sector*, 1610.07922. [pp. 30 and 31]

[148] C. Duhr, F. Dulat and B. Mistlberger, *Higgs production in bottom-quark fusion to third order in the strong coupling*, *Phys. Rev. Lett.* **125** (2020) 051804 [1904.09990]. [p. 31]

[149] F. A. Dreyer and A. Karlberg, *Vector-Boson Fusion Higgs Production at Three Loops in QCD*, Phys. Rev. Lett. **117** (2016) 072001 [1606.00840]. [p. 31]

[150] T. Liu, K. Melnikov and A. A. Penin, *Nonfactorizable QCD Effects in Higgs Boson Production via Vector Boson Fusion*, Phys. Rev. Lett. **123** (2019) 122002 [1906.10899]. [p. 31]

[151] F. Wilczek, *Decays of Heavy Vector Mesons Into Higgs Particles*, Phys. Rev. Lett. **39** (1977) 1304. [pp. 31 and 307]

[152] M. A. Shifman, A. I. Vainshtein and V. I. Zakharov, *Remarks on Higgs Boson Interactions with Nucleons*, Phys. Lett. **B78** (1978) 443. [pp. 31 and 307]

[153] T. Inami, T. Kubota and Y. Okada, *Effective Gauge Theory and the Effect of Heavy Quarks in Higgs Boson Decays*, Z. Phys. **C18** (1983) 69. [pp. 31 and 307]

[154] V. P. Spiridonov and K. G. Chetyrkin, *Nonleading mass corrections and renormalization of the operators $m\bar{\psi}\psi$ and $G_{\mu\nu}^2$*, Sov. J. Nucl. Phys. **47** (1988) 522. [pp. 31 and 307]

[155] J. Michel, *Transverse Momentum Resummation at Forward Rapidities and its Applications to LHC Physics*, Master's thesis, Westfälische Wilhelms-Universität Münster, Münster, June 2017. [pp. 32, 34, 35, 39, 49, 61, and 222]

[156] CMS collaboration, *Measurements of properties of the Higgs boson decaying into the four-lepton final state in pp collisions at $\sqrt{s} = 13$ TeV*, JHEP **11** (2017) 047 [1706.09936]. [p. 32]

[157] ATLAS collaboration, *Combined measurement of differential and inclusive total cross sections in the $H \to \gamma\gamma$ and the $H \to ZZ^* \to 4\ell$ decay channels at $\sqrt{s} = 13$ TeV with the ATLAS detector*, Tech. Rep. ATLAS-CONF-2018-002, CERN, Geneva, 2018. [p. 32]

[158] ATLAS collaboration, *Measurements of Higgs boson properties in the diphoton decay channel using 80 fb^{-1} of pp collision data at $\sqrt{s} = 13$ TeV with the ATLAS detector*, Tech. Rep. ATLAS-CONF-2018-028, CERN, Geneva, 2018. [p. 32]

[159] CMS collaboration, *Measurement of inclusive and differential Higgs boson production cross sections in the diphoton decay channel in proton-proton collisions at $\sqrt{s} = 13$ TeV*, JHEP **01** (2019) 183 [1807.03825]. [p. 32]

[160] ATLAS collaboration, *Measurements and interpretations of Higgs-boson fiducial cross sections in the diphoton decay channel using 139 fb1 of pp collision data at $\sqrt{s} = 13$ TeV with the ATLAS detector*, Tech. Rep. ATLAS-CONF-2019-029, CERN, Geneva, 2019. [p. 32]

[161] CMS collaboration, *Measurements of Higgs boson properties in the diphoton decay channel at $\sqrt{s} = 13$ TeV*, Tech. Rep. CMS-PAS-HIG-19-015, CERN, Geneva, 2020. [p. 32]

[162] CMS collaboration, *Search for Higgs boson off-shell production in proton-proton collisions at 7 and 8 TeV and derivation of constraints on its total decay width*, *JHEP* **09** (2016) 051 [`1605.02329`]. [p. 33]

[163] J. S. Schwinger, *On Quantum electrodynamics and the magnetic moment of the electron*, *Phys. Rev.* **73** (1948) 416. [p. 34]

[164] C. W. Bauer, S. Fleming and M. E. Luke, *Summing Sudakov logarithms in $B \to X_s\gamma$ in effective field theory*, *Phys. Rev.* **D63** (2000) 014006 [`hep-ph/0005275`]. [pp. 34 and 35]

[165] C. W. Bauer, S. Fleming, D. Pirjol and I. W. Stewart, *An Effective field theory for collinear and soft gluons: Heavy to light decays*, *Phys. Rev.* **D63** (2001) 114020 [`hep-ph/0011336`]. [pp. 34 and 35]

[166] C. W. Bauer and I. W. Stewart, *Invariant operators in collinear effective theory*, *Phys. Lett.* **B516** (2001) 134 [`hep-ph/0107001`]. [pp. 34 and 35]

[167] C. W. Bauer, D. Pirjol and I. W. Stewart, *Soft collinear factorization in effective field theory*, *Phys. Rev.* **D65** (2002) 054022 [`hep-ph/0109045`]. [pp. 34, 35, 44, 46, 49, and 50]

[168] M. Beneke, A. P. Chapovsky, M. Diehl and T. Feldmann, *Soft collinear effective theory and heavy to light currents beyond leading power*, *Nucl. Phys.* **B643** (2002) 431 [`hep-ph/0206152`]. [pp. 34 and 35]

[169] M. Beneke and T. Feldmann, *Multipole expanded soft collinear effective theory with non-abelian gauge symmetry*, *Phys. Lett. B* **553** (2003) 267 [`hep-ph/0211358`]. [pp. 34 and 35]

[170] C. W. Bauer and I. Stewart, *The Soft-Collinear Effective Theory*, Massachusetts Institute of Technology: MIT OpenCourseWare, 2014. [pp. 34 and 41]

[171] C. W. Bauer, S. Fleming, D. Pirjol, I. Z. Rothstein and I. W. Stewart, *Hard scattering factorization from effective field theory*, *Phys. Rev.* **D66** (2002) 014017 [`hep-ph/0202088`]. [pp. 35, 42, 115, 187, and 188]

[172] T. Becher, A. Broggio and A. Ferroglia, *Introduction to Soft-Collinear Effective Theory*. Springer, Cham, 2015, 10.1007/978-3-319-14848-9, [`1410.1892`]. [p. 35]

[173] I. Z. Rothstein and I. W. Stewart, *An Effective Field Theory for Forward Scattering and Factorization Violation*, *JHEP* **08** (2016) 025 [`1601.04695`]. [pp. 38 and 75]

[174] A. V. Manohar and I. W. Stewart, *The Zero-Bin and Mode Factorization in Quantum Field Theory*, Phys. Rev. **D76** (2007) 074002 [`hep-ph/0605001`]. [p. 40]

[175] A. V. Manohar, T. Mehen, D. Pirjol and I. W. Stewart, *Reparameterization invariance for collinear operators*, Phys. Lett. **B539** (2002) 59 [`hep-ph/0204229`]. [pp. 42 and 43]

[176] C. Marcantonini and I. W. Stewart, *Reparameterization Invariant Collinear Operators*, Phys. Rev. **D79** (2009) 065028 [`0809.1093`]. [p. 42]

[177] I. Moult, I. W. Stewart, F. J. Tackmann and W. J. Waalewijn, *Employing Helicity Amplitudes for Resummation*, Phys. Rev. D **93** (2016) 094003 [`1508.02397`]. [pp. 45, 188, 255, 256, and 309]

[178] D. W. Kolodrubetz, I. Moult and I. W. Stewart, *Building Blocks for Subleading Helicity Operators*, JHEP **05** (2016) 139 [`1601.02607`]. [pp. 45 and 256]

[179] I. Moult, I. W. Stewart and G. Vita, *A subleading operator basis and matching for gg → H*, JHEP **07** (2017) 067 [`1703.03408`]. [pp. 45 and 256]

[180] I. Feige, D. W. Kolodrubetz, I. Moult and I. W. Stewart, *A Complete Basis of Helicity Operators for Subleading Factorization*, JHEP **11** (2017) 142 [`1703.03411`]. [pp. 45, 48, 256, and 257]

[181] C.-H. Chang, I. W. Stewart and G. Vita, *A Subleading Power Operator Basis for the Scalar Quark Current*, JHEP **04** (2018) 041 [`1712.04343`]. [pp. 45 and 256]

[182] L. Landau, *On the angular momentum of a system of two photons*, Dokl. Akad. Nauk SSSR **60** (1948) 207. [p. 48]

[183] C.-N. Yang, *Selection Rules for the Dematerialization of a Particle Into Two Photons*, Phys. Rev. **77** (1950) 242. [p. 48]

[184] C. W. Bauer, D. Pirjol and I. W. Stewart, *Factorization and endpoint singularities in heavy to light decays*, Phys. Rev. D **67** (2003) 071502 [`hep-ph/0211069`]. [p. 51]

[185] J. C. Collins and D. E. Soper, *Back-To-Back Jets in QCD*, Nucl. Phys. **B193** (1981) 381. [pp. 51, 66, 70, 71, 145, 226, and 263]

[186] J. C. Collins and F. V. Tkachov, *Breakdown of dimensional regularization in the Sudakov problem*, Phys. Lett. **B294** (1992) 403 [`hep-ph/9208209`]. [p. 51]

[187] J. Collins, *Rapidity divergences and valid definitions of parton densities*, PoS **LC2008** (2008) 028 [`0808.2665`]. [p. 51]

[188] T. Becher and M. Neubert, *Drell-Yan Production at Small q_T, Transverse Parton Distributions and the Collinear Anomaly*, Eur. Phys. J. **C71** (2011) 1665 [`1007.4005`]. [pp. 51, 66, and 226]

[189] M. G. Echevarria, A. Idilbi and I. Scimemi, *Factorization Theorem For Drell-Yan At Low q_T And Transverse Momentum Distributions On-The-Light-Cone*, JHEP **07** (2012) 002 [`1111.4996`]. [pp. 51, 66, and 226]

[190] J.-y. Chiu, A. Jain, D. Neill and I. Z. Rothstein, *The Rapidity Renormalization Group*, Phys. Rev. Lett. **108** (2012) 151601 [`1104.0881`]. [pp. 51, 68, and 93]

[191] J.-y. Chiu, A. Jain, D. Neill and I. Z. Rothstein, *A Formalism for the Systematic Treatment of Rapidity Logarithms in Quantum Field Theory*, JHEP **05** (2012) 084 [`1202.0814`]. [pp. 51, 66, 68, 93, and 226]

[192] Y. Li, D. Neill and H. X. Zhu, *An Exponential Regulator for Rapidity Divergences*, `1604.00392`. [pp. 51, 52, 66, 68, 212, 216, 218, 219, 220, 221, and 226]

[193] M. A. Ebert, I. Moult, I. W. Stewart, F. J. Tackmann, G. Vita and H. X. Zhu, *Subleading power rapidity divergences and power corrections for q_T*, JHEP **04** (2019) 123 [`1812.08189`]. [pp. 51, 222, 226, 229, and 257]

[194] C. W. Bauer, F. J. Tackmann, J. R. Walsh and S. Zuberi, *Factorization and Resummation for Dijet Invariant Mass Spectra*, Phys. Rev. **D85** (2012) 074006 [`1106.6047`]. [pp. 52, 134, 135, 147, and 219]

[195] M. Procura, W. J. Waalewijn and L. Zeune, *Resummation of Double-Differential Cross Sections and Fully-Unintegrated Parton Distribution Functions*, JHEP **02** (2015) 117 [`1410.6483`]. [pp. 52, 135, 136, 137, 142, 147, 148, 150, 153, 171, 211, 219, and 323]

[196] V. Gribov and L. Lipatov, *Deep inelastic e p scattering in perturbation theory*, Sov. J. Nucl. Phys. **15** (1972) 438. [p. 54]

[197] G. Altarelli and G. Parisi, *Asymptotic Freedom in Parton Language*, Nucl. Phys. B **126** (1977) 298. [p. 54]

[198] Y. L. Dokshitzer, *Calculation of the Structure Functions for Deep Inelastic Scattering and e+ e- Annihilation by Perturbation Theory in Quantum Chromodynamics.*, Sov. Phys. JETP **46** (1977) 641. [p. 54]

[199] S. Moch, J. A. M. Vermaseren and A. Vogt, *The Three loop splitting functions in QCD: The Nonsinglet case*, Nucl. Phys. **B688** (2004) 101 [`hep-ph/0403192`]. [pp. 54, 311, and 312]

[200] A. Vogt, S. Moch and J. A. M. Vermaseren, *The Three-loop splitting functions in QCD: The Singlet case*, Nucl. Phys. **B691** (2004) 129 [`hep-ph/0404111`]. [pp. 54, 311, and 312]

[201] S. Moch, B. Ruijl, T. Ueda, J. Vermaseren and A. Vogt, *Four-Loop Non-Singlet Splitting Functions in the Planar Limit and Beyond*, JHEP **10** (2017) 041 [`1707.08315`]. [pp. 54 and 311]

References

[202] H1, ZEUS collaboration, F. Aaron et al., *Combined Measurement and QCD Analysis of the Inclusive e+- p Scattering Cross Sections at HERA*, *JHEP* **01** (2010) 109 [`0911.0884`]. [p. 55]

[203] R. Abbate, M. Fickinger, A. H. Hoang, V. Mateu and I. W. Stewart, *Thrust at N^3LL with Power Corrections and a Precision Global Fit for $\alpha_s(m_Z)$*, *Phys. Rev.* **D83** (2011) 074021 [`1006.3080`]. [pp. 59, 60, 124, and 330]

[204] L. G. Almeida, S. D. Ellis, C. Lee, G. Sterman, I. Sung and J. R. Walsh, *Comparing and counting logs in direct and effective methods of QCD resummation*, *JHEP* **04** (2014) 174 [`1401.4460`]. [pp. 59 and 330]

[205] I. Moult, I. W. Stewart, G. Vita and H. X. Zhu, *First Subleading Power Resummation for Event Shapes*, *JHEP* **08** (2018) 013 [`1804.04665`]. [p. 60]

[206] M. Beneke, A. Broggio, M. Garny, S. Jaskiewicz, R. Szafron, L. Vernazza et al., *Leading-logarithmic threshold resummation of the Drell-Yan process at next-to-leading power*, *JHEP* **03** (2019) 043 [`1809.10631`]. [pp. 60, 173, and 295]

[207] M. Beneke, M. Garny, S. Jaskiewicz, R. Szafron, L. Vernazza and J. Wang, *Leading-logarithmic threshold resummation of Higgs production in gluon fusion at next-to-leading power*, *JHEP* **01** (2020) 094 [`1910.12685`]. [pp. 60, 173, and 295]

[208] I. Moult, G. Vita and K. Yan, *Subleading Power Resummation of Rapidity Logarithms: The Energy-Energy Correlator in $\mathcal{N} = 4$ SYM*, *JHEP* **07** (2020) 005 [`1912.02188`]. [pp. 60 and 226]

[209] Z. Ligeti, I. W. Stewart and F. J. Tackmann, *Treating the b quark distribution function with reliable uncertainties*, *Phys. Rev.* **D78** (2008) 114014 [`0807.1926`]. [pp. 60, 124, 300, 315, and 316]

[210] G. F. Sterman, *Summation of Large Corrections to Short Distance Hadronic Cross-Sections*, *Nucl. Phys.* **B281** (1987) 310. [pp. 62, 63, 64, 65, and 173]

[211] S. Catani and L. Trentadue, *Resummation of the QCD Perturbative Series for Hard Processes*, *Nucl. Phys.* **B327** (1989) 323. [pp. 62, 63, 64, 65, 173, and 204]

[212] A. V. Manohar, *Deep inelastic scattering as $x \to 1$ using soft collinear effective theory*, *Phys. Rev.* **D68** (2003) 114019 [`hep-ph/0309176`]. [pp. 62 and 307]

[213] T. Becher, M. Neubert and B. D. Pecjak, *Factorization and Momentum-Space Resummation in Deep-Inelastic Scattering*, *JHEP* **01** (2007) 076 [`hep-ph/0607228`]. [pp. 62 and 63]

[214] S. Fleming and O. Z. Labun, *Rapidity Divergences and Deep Inelastic Scattering in the Endpoint Region*, *Phys. Rev.* **D91** (2015) 094011 [`1210.1508`]. [pp. 62, 177, 190, 191, and 192]

[215] J. Chay and C. Kim, *Proper factorization theorems in high-energy scattering near the endpoint*, *JHEP* **09** (2013) 126 [`1303.1637`]. [p. 62]

[216] A. H. Hoang, P. Pietrulewicz and D. Samitz, *Variable Flavor Number Scheme for Final State Jets in DIS*, *Phys. Rev.* **D93** (2016) 034034 [`1508.04323`]. [pp. 62, 177, 181, 183, 190, and 191]

[217] P. Banerjee, P. K. Dhani and V. Ravindran, *Gluon jet function at three loops in QCD*, *Phys. Rev.* **D98** (2018) 094016 [`1805.02637`]. [pp. 63 and 313]

[218] R. Brüser, Z. L. Liu and M. Stahlhofen, *Three-Loop Quark Jet Function*, *Phys. Rev. Lett.* **121** (2018) 072003 [`1804.09722`]. [pp. 63 and 313]

[219] V. Ravindran, J. Smith and W. L. van Neerven, *QCD threshold corrections to di-lepton and Higgs rapidity distributions beyond N²LO*, *Nucl. Phys.* **B767** (2007) 100 [`hep-ph/0608308`]. [pp. 64, 65, 173, 196, 208, 212, 217, and 325]

[220] D. Westmark and J. F. Owens, *Enhanced threshold resummation formalism for lepton pair production and its effects in the determination of parton distribution functions*, *Phys. Rev.* **D95** (2017) 056024 [`1701.06716`]. [pp. 64, 65, 173, and 201]

[221] P. Banerjee, G. Das, P. K. Dhani and V. Ravindran, *Threshold resummation of the rapidity distribution for Higgs production at NNLO+NNLL*, *Phys. Rev.* **D97** (2018) 054024 [`1708.05706`]. [pp. 64, 65, and 173]

[222] P. Banerjee, G. Das, P. K. Dhani and V. Ravindran, *Threshold resummation of the rapidity distribution for Drell-Yan production at NNLO+NNLL*, *Phys. Rev.* **D98** (2018) 054018 [`1805.01186`]. [pp. 64, 65, 173, 201, and 293]

[223] D. Appell, G. F. Sterman and P. B. Mackenzie, *Soft Gluons and the Normalization of the Drell-Yan Cross-section*, *Nucl. Phys.* **B309** (1988) 259. [pp. 65 and 173]

[224] L. Magnea, *All Order Summation and Two Loop Results for the Drell-Yan Cross-section*, *Nucl. Phys.* **B349** (1991) 703. [pp. 65 and 173]

[225] G. P. Korchemsky and G. Marchesini, *Structure function for large x and renormalization of Wilson loop*, *Nucl. Phys.* **B406** (1993) 225 [`hep-ph/9210281`]. [pp. 65 and 173]

[226] H. Contopanagos, E. Laenen and G. F. Sterman, *Sudakov factorization and resummation*, *Nucl. Phys.* **B484** (1997) 303 [`hep-ph/9604313`]. [pp. 65 and 173]

[227] S. Catani, M. L. Mangano, P. Nason and L. Trentadue, *The Resummation of soft gluons in hadronic collisions*, *Nucl. Phys.* **B478** (1996) 273 [`hep-ph/9604351`]. [pp. 65 and 173]

[228] A. V. Belitsky, *Two loop renormalization of Wilson loop for Drell-Yan production*, *Phys. Lett.* **B442** (1998) 307 [`hep-ph/9808389`]. [pp. 65 and 173]

[229] S. Moch and A. Vogt, *Higher-order soft corrections to lepton pair and Higgs boson production*, Phys. Lett. **B631** (2005) 48 [`hep-ph/0508265`]. [pp. 65 and 173]

[230] E. Laenen and L. Magnea, *Threshold resummation for electroweak annihilation from DIS data*, Phys. Lett. **B632** (2006) 270 [`hep-ph/0508284`]. [pp. 65 and 173]

[231] A. Idilbi, X.-d. Ji and F. Yuan, *Resummation of threshold logarithms in effective field theory for DIS, Drell-Yan and Higgs production*, Nucl. Phys. **B753** (2006) 42 [`hep-ph/0605068`]. [pp. 65, 173, and 307]

[232] A. Mukherjee and W. Vogelsang, *Threshold resummation for W-boson production at RHIC*, Phys. Rev. **D73** (2006) 074005 [`hep-ph/0601162`]. [pp. 65, 173, 196, 199, 201, and 203]

[233] P. Bolzoni, *Threshold resummation of Drell-Yan rapidity distributions*, Phys. Lett. **B643** (2006) 325 [`hep-ph/0609073`]. [pp. 65, 173, 196, 199, 201, and 203]

[234] T. Becher, M. Neubert and G. Xu, *Dynamical Threshold Enhancement and Resummation in Drell-Yan Production*, JHEP **07** (2008) 030 [`0710.0680`]. [pp. 65, 173, 196, 199, 201, and 203]

[235] M. Bonvini, S. Forte and G. Ridolfi, *Soft gluon resummation of Drell-Yan rapidity distributions: Theory and phenomenology*, Nucl. Phys. **B847** (2011) 93 [`1009.5691`]. [pp. 65, 173, 196, 199, 201, and 203]

[236] M. Bonvini, S. Marzani, J. Rojo, L. Rottoli, M. Ubiali, R. D. Ball et al., *Parton distributions with threshold resummation*, JHEP **09** (2015) 191 [`1507.01006`]. [pp. 65, 173, 196, 199, and 201]

[237] B. Fuks, M. Klasen, D. R. Lamprea and M. Rothering, *Precision predictions for electroweak superpartner production at hadron colliders with Resummino*, Eur. Phys. J. **C73** (2013) 2480 [`1304.0790`]. [pp. 65 and 173]

[238] M. Bonvini and S. Marzani, *Resummed Higgs cross section at N^3LL*, JHEP **09** (2014) 007 [`1405.3654`]. [pp. 65 and 173]

[239] T. Schmidt and M. Spira, *Higgs Boson Production via Gluon Fusion: Soft-Gluon Resummation including Mass Effects*, Phys. Rev. **D93** (2016) 014022 [`1509.00195`]. [pp. 65 and 173]

[240] A. A H, A. Chakraborty, G. Das, P. Mukherjee and V. Ravindran, *Resummed prediction for Higgs boson production through $b\bar{b}$ annihilation at N^3LO+N^3LL*, JHEP **11** (2019) 006 [`1905.03771`]. [pp. 65 and 173]

[241] C. Anastasiou, C. Duhr, F. Dulat, E. Furlan, T. Gehrmann, F. Herzog et al., *Higgs boson gluon-fusion production at threshold in N^3LO QCD*, Phys. Lett. **B737** (2014) 325 [`1403.4616`]. [pp. 65, 173, 212, and 216]

[242] T. Ahmed, M. Mahakhud, N. Rana and V. Ravindran, *Drell-Yan Production at Threshold to Third Order in QCD*, Phys. Rev. Lett. **113** (2014) 112002 [1404.0366]. [pp. 65 and 173]

[243] Y. Li, A. von Manteuffel, R. M. Schabinger and H. X. Zhu, *N^3LO Higgs boson and Drell-Yan production at threshold: The one-loop two-emission contribution*, Phys. Rev. D **90** (2014) 053006 [1404.5839]. [p. 65]

[244] T. Ahmed, M. K. Mandal, N. Rana and V. Ravindran, *Rapidity Distributions in Drell-Yan and Higgs Productions at Threshold to Third Order in QCD*, Phys. Rev. Lett. **113** (2014) 212003 [1404.6504]. [pp. 65, 173, 208, 212, and 217]

[245] D. de Florian, J. Mazzitelli, S. Moch and A. Vogt, *Approximate N^3LO Higgs-boson production cross section using physical-kernel constraints*, JHEP **10** (2014) 176 [1408.6277]. [pp. 65 and 173]

[246] Y. Li, A. von Manteuffel, R. M. Schabinger and H. X. Zhu, *Soft-virtual corrections to Higgs production at N^3LO*, Phys. Rev. **D91** (2015) 036008 [1412.2771]. [pp. 65, 173, 212, and 216]

[247] S. Catani, L. Cieri, D. de Florian, G. Ferrera and M. Grazzini, *Threshold resummation at N^3LL accuracy and soft-virtual cross sections at N^3LO*, Nucl. Phys. B **888** (2014) 75 [1405.4827]. [p. 65]

[248] C. Anastasiou, C. Duhr, F. Dulat, E. Furlan, T. Gehrmann, F. Herzog et al., *High precision determination of the gluon fusion Higgs boson cross-section at the LHC*, JHEP **05** (2016) 058 [1602.00695]. [pp. 65 and 173]

[249] F. Dulat, B. Mistlberger and A. Pelloni, *Differential Higgs production at N^3LO beyond threshold*, JHEP **01** (2018) 145 [1710.03016]. [pp. 65 and 173]

[250] F. Dulat, B. Mistlberger and A. Pelloni, *Precision predictions at N^3LO for the Higgs boson rapidity distribution at the LHC*, Phys. Rev. **D99** (2019) 034004 [1810.09462]. [pp. 65, 173, 208, 212, and 294]

[251] J. C. Collins and D. E. Soper, *Back-To-Back Jets: Fourier Transform from B to K-Transverse*, Nucl. Phys. **B197** (1982) 446. [pp. 66, 70, 71, 145, 226, and 263]

[252] J. C. Collins, D. E. Soper and G. F. Sterman, *Transverse Momentum Distribution in Drell-Yan Pair and W and Z Boson Production*, Nucl. Phys. **B250** (1985) 199. [pp. 66, 71, 72, and 226]

[253] J. C. Collins and T. C. Rogers, *Equality of Two Definitions for Transverse Momentum Dependent Parton Distribution Functions*, Phys. Rev. D **87** (2013) 034018 [1210.2100]. [pp. 66 and 226]

[254] S. Catani, D. de Florian and M. Grazzini, *Universality of nonleading logarithmic contributions in transverse momentum distributions*, *Nucl. Phys.* **B596** (2001) 299 [`hep-ph/0008184`]. [p. 66]

[255] D. de Florian and M. Grazzini, *The Structure of large logarithmic corrections at small transverse momentum in hadronic collisions*, *Nucl. Phys.* **B616** (2001) 247 [`hep-ph/0108273`]. [p. 66]

[256] S. Catani and M. Grazzini, *QCD transverse-momentum resummation in gluon fusion processes*, *Nucl. Phys.* **B845** (2011) 297 [`1011.3918`]. [p. 66]

[257] J. Collins, *Foundations of perturbative QCD*, Cambridge monographs on particle physics, nuclear physics, and cosmology. Cambridge Univ. Press, New York, NY, 2011. [pp. 66 and 226]

[258] M. G. Echevarria, T. Kasemets, P. J. Mulders and C. Pisano, *QCD evolution of (un)polarized gluon TMDPDFs and the Higgs q_T-distribution*, *JHEP* **07** (2015) 158 [`1502.05354`]. [pp. 67 and 226]

[259] M. G. A. Buffing, Z.-B. Kang, K. Lee and X. Liu, *A transverse momentum dependent framework for back-to-back photon+jet production*, `1812.07549`. [pp. 67 and 211]

[260] Y.-T. Chien, D. Y. Shao and B. Wu, *Resummation of Boson-Jet Correlation at Hadron Colliders*, `1905.01335`. [pp. 67 and 211]

[261] Y.-T. Chien, R. Rahn, S. Schrijnder van Velzen, D. Y. Shao, W. J. Waalewijn and B. Wu, *Azimuthal angle for boson-jet production in the back-to-back limit*, `2005.12279`. [pp. 67 and 211]

[262] A. Gao, H. T. Li, I. Moult and H. X. Zhu, *Precision QCD Event Shapes at Hadron Colliders: The Transverse Energy-Energy Correlator in the Back-to-Back Limit*, *Phys. Rev. Lett.* **123** (2019) 062001 [`1901.04497`]. [pp. 67 and 211]

[263] M. A. Ebert and F. J. Tackmann, *Resummation of Transverse Momentum Distributions in Distribution Space*, *JHEP* **02** (2017) 110 [`1611.08610`]. [pp. 69, 71, 143, 215, 226, 301, and 302]

[264] T. Lübbert, J. Oredsson and M. Stahlhofen, *Rapidity renormalized TMD soft and beam functions at two loops*, *JHEP* **03** (2016) 168 [`1602.01829`]. [pp. 70, 72, 223, 314, 321, and 322]

[265] Y. Li and H. X. Zhu, *Bootstrapping Rapidity Anomalous Dimensions for Transverse-Momentum Resummation*, *Phys. Rev. Lett.* **118** (2017) 022004 [`1604.01404`]. [pp. 70, 72, 212, 216, 219, 221, 314, and 321]

[266] A. A. Vladimirov, *Correspondence between Soft and Rapidity Anomalous Dimensions*, *Phys. Rev. Lett.* **118** (2017) 062001 [`1610.05791`]. [pp. 70 and 314]

[267] I. Scimemi and A. Vladimirov, *Non-perturbative structure of semi-inclusive deep-inelastic and Drell-Yan scattering at small transverse momentum*, *JHEP* **06** (2020) 137 [`1912.06532`]. [pp. 71, 226, 228, 261, and 262]

[268] A. Bacchetta, V. Bertone, C. Bissolotti, G. Bozzi, F. Delcarro, F. Piacenza et al., *Transverse-momentum-dependent parton distributions up to N^3LL from Drell-Yan data*, *JHEP* **07** (2020) 117 [`1912.07550`]. [pp. 71, 226, 228, 261, and 262]

[269] M. A. Ebert, I. W. Stewart and Y. Zhao, *Determining the Nonperturbative Collins-Soper Kernel From Lattice QCD*, *Phys. Rev. D* **99** (2019) 034505 [`1811.00026`]. [p. 71]

[270] M. A. Ebert, I. W. Stewart and Y. Zhao, *Towards Quasi-Transverse Momentum Dependent PDFs Computable on the Lattice*, *JHEP* **09** (2019) 037 [`1901.03685`]. [p. 71]

[271] A. A. Vladimirov and A. Schäfer, *Transverse momentum dependent factorization for lattice observables*, *Phys. Rev.* **D101** (2020) 074517 [`2002.07527`]. [p. 71]

[272] P. Shanahan, M. Wagman and Y. Zhao, *Collins-Soper kernel for TMD evolution from lattice QCD*, *Phys. Rev. D* **102** (2020) 014511 [`2003.06063`]. [p. 71]

[273] LATTICE PARTON collaboration, Q.-A. Zhang et al., *Lattice-QCD Calculations of TMD Soft Function Through Large-Momentum Effective Theory*, `2005.14572`. [p. 71]

[274] A. A. Vladimirov, *Self-contained definition of Collins-Soper kernel*, `2003.02288`. [p. 71]

[275] S. Frixione, P. Nason and G. Ridolfi, *Problems in the resummation of soft gluon effects in the transverse momentum distributions of massive vector bosons in hadronic collisions*, *Nucl. Phys.* **B542** (1999) 311 [`hep-ph/9809367`]. [p. 71]

[276] P. F. Monni, E. Re and P. Torrielli, *Higgs Transverse-Momentum Resummation in Direct Space*, *Phys. Rev. Lett.* **116** (2016) 242001 [`1604.02191`]. [pp. 71 and 226]

[277] G. Parisi and R. Petronzio, *Small Transverse Momentum Distributions in Hard Processes*, *Nucl. Phys.* **B154** (1979) 427. [p. 71]

[278] T. Gehrmann, T. Lübbert and L. L. Yang, *Transverse parton distribution functions at next-to-next-to-leading order: the quark-to-quark case*, *Phys. Rev. Lett.* **109** (2012) 242003 [`1209.0682`]. [p. 72]

[279] T. Gehrmann, T. Lübbert and L. L. Yang, *Calculation of the transverse parton distribution functions at next-to-next-to-leading order*, *JHEP* **06** (2014) 155 [`1403.6451`]. [pp. 72 and 322]

[280] M. G. Echevarria, I. Scimemi and A. Vladimirov, *Universal transverse momentum dependent soft function at NNLO, Phys. Rev.* **D93** (2016) 054004 [1511.05590]. [p. 72]

[281] J. C. Collins and D. E. Soper, *Parton Distribution and Decay Functions, Nucl. Phys.* **B194** (1982) 445. [p. 72]

[282] S. Catani and M. Grazzini, *Higgs Boson Production at Hadron Colliders: Hard-Collinear Coefficients at the NNLO, Eur. Phys. J.* **C72** (2012) 2013 [1106.4652]. [p. 72]

[283] S. Catani, L. Cieri, D. de Florian, G. Ferrera and M. Grazzini, *Vector boson production at hadron colliders: hard-collinear coefficients at the NNLO, Eur. Phys. J.* **C72** (2012) 2195 [1209.0158]. [p. 72]

[284] M. G. Echevarria, I. Scimemi and A. Vladimirov, *Unpolarized Transverse Momentum Dependent Parton Distribution and Fragmentation Functions at next-to-next-to-leading order, JHEP* **09** (2016) 004 [1604.07869]. [pp. 72 and 223]

[285] M.-X. Luo, X. Wang, X. Xu, L. L. Yang, T.-Z. Yang and H. X. Zhu, *Transverse Parton Distribution and Fragmentation Functions at NNLO: the Quark Case,* 1908.03831. [pp. 72 and 322]

[286] M.-X. Luo, T.-Z. Yang, H. X. Zhu and Y. J. Zhu, *Transverse Parton Distribution and Fragmentation Functions at NNLO: the Gluon Case, JHEP* **01** (2020) 040 [1909.13820]. [pp. 72 and 322]

[287] M.-X. Luo, T.-Z. Yang, H. X. Zhu and Y. J. Zhu, *Quark Transverse Parton Distribution at the Next-to-Next-to-Next-to-Leading Order, Phys. Rev. Lett.* **124** (2020) 092001 [1912.05778]. [pp. 72, 212, and 296]

[288] M. A. Ebert, B. Mistlberger and G. Vita, *Transverse momentum dependent PDFs at N^3LO,* 2006.05329. [pp. 72, 212, and 296]

[289] D. Gutierrez-Reyes, S. Leal-Gomez, I. Scimemi and A. Vladimirov, *Linearly polarized gluons at next-to-next-to leading order and the Higgs transverse momentum distribution, JHEP* **11** (2019) 121 [1907.03780]. [p. 72]

[290] I. W. Stewart, F. J. Tackmann and W. J. Waalewijn, *N-Jettiness: An Inclusive Event Shape to Veto Jets, Phys. Rev. Lett.* **105** (2010) 092002 [1004.2489]. [pp. 72 and 73]

[291] T. T. Jouttenus, I. W. Stewart, F. J. Tackmann and W. J. Waalewijn, *The Soft Function for Exclusive N-Jet Production at Hadron Colliders, Phys. Rev.* **D83** (2011) 114030 [1102.4344]. [pp. 72, 73, 134, and 211]

[292] D. Kang, C. Lee and I. W. Stewart, *Using 1-Jettiness to Measure 2 Jets in DIS 3 Ways*, *Phys. Rev.* **D88** (2013) 054004 [1303.6952]. [pp. 73, 178, and 211]

[293] I. W. Stewart, F. J. Tackmann and W. J. Waalewijn, *The Quark Beam Function at NNLL*, *JHEP* **09** (2010) 005 [1002.2213]. [pp. 74, 107, 108, 110, 139, 177, 211, 312, 319, and 320]

[294] J. R. Gaunt, M. Stahlhofen and F. J. Tackmann, *The Quark Beam Function at Two Loops*, *JHEP* **04** (2014) 113 [1401.5478]. [pp. 74, 194, 212, 217, and 218]

[295] J. Gaunt, M. Stahlhofen and F. J. Tackmann, *The Gluon Beam Function at Two Loops*, *JHEP* **08** (2014) 020 [1405.1044]. [pp. 74, 194, 212, and 217]

[296] K. Melnikov, R. Rietkerk, L. Tancredi and C. Wever, *Double-real contribution to the quark beam function at N^3LO QCD*, *JHEP* **02** (2019) 159 [1809.06300]. [pp. 74 and 212]

[297] K. Melnikov, R. Rietkerk, L. Tancredi and C. Wever, *Triple-real contribution to the quark beam function in QCD at next-to-next-to-next-to-leading order*, *JHEP* **06** (2019) 033 [1904.02433]. [pp. 74 and 212]

[298] A. Behring, K. Melnikov, R. Rietkerk, L. Tancredi and C. Wever, *Quark beam function at next-to-next-to-next-to-leading order in perturbative QCD in the generalized large-N_c approximation*, *Phys. Rev. D* **100** (2019) 114034 [1910.10059]. [pp. 74, 212, and 296]

[299] M. A. Ebert, B. Mistlberger and G. Vita, *N-jettiness beam functions at N^3LO*, 2006.03056. [pp. 74, 195, 212, 294, and 296]

[300] M. D. Schwartz, *Resummation and NLO matching of event shapes with effective field theory*, *Phys. Rev.* **D77** (2008) 014026 [0709.2709]. [pp. 74 and 323]

[301] S. Fleming, A. H. Hoang, S. Mantry and I. W. Stewart, *Top Jets in the Peak Region: Factorization Analysis with NLL Resummation*, *Phys. Rev.* **D77** (2008) 114003 [0711.2079]. [pp. 74, 315, and 323]

[302] R. Kelley, M. D. Schwartz, R. M. Schabinger and H. X. Zhu, *The two-loop hemisphere soft function*, *Phys. Rev.* **D84** (2011) 045022 [1105.3676]. [p. 74]

[303] P. F. Monni, T. Gehrmann and G. Luisoni, *Two-Loop Soft Corrections and Resummation of the Thrust Distribution in the Dijet Region*, *JHEP* **08** (2011) 010 [1105.4560]. [p. 74]

[304] A. Hornig, C. Lee, I. W. Stewart, J. R. Walsh and S. Zuberi, *Non-global Structure of the $O(\alpha_s^2)$ Dijet Soft Function*, *JHEP* **08** (2011) 054 [1105.4628]. [pp. 74 and 94]

[305] D. Kang, O. Z. Labun and C. Lee, *Equality of hemisphere soft functions for e^+e^-, DIS and pp collisions at $\mathcal{O}(\alpha_s^2)$*, *Phys. Lett.* **B748** (2015) 45 [1504.04006]. [p. 74]

[306] J. R. Gaunt, *Glauber Gluons and Multiple Parton Interactions*, *JHEP* **07** (2014) 110 [`1405.2080`]. [p. 75]

[307] M. Zeng, *Drell-Yan process with jet vetoes: breaking of generalized factorization*, *JHEP* **10** (2015) 189 [`1507.01652`]. [p. 75]

[308] S. Catani, Y. L. Dokshitzer, M. Olsson, G. Turnock and B. R. Webber, *New clustering algorithm for multi - jet cross-sections in e+ e- annihilation*, *Phys. Lett.* **B269** (1991) 432. [p. 75]

[309] S. Catani, Y. L. Dokshitzer, M. H. Seymour and B. R. Webber, *Longitudinally invariant K_t clustering algorithms for hadron hadron collisions*, *Nucl. Phys.* **B406** (1993) 187. [p. 75]

[310] S. D. Ellis and D. E. Soper, *Successive combination jet algorithm for hadron collisions*, *Phys. Rev.* **D48** (1993) 3160 [`hep-ph/9305266`]. [p. 75]

[311] Y. L. Dokshitzer, G. D. Leder, S. Moretti and B. R. Webber, *Better jet clustering algorithms*, *JHEP* **08** (1997) 001 [`hep-ph/9707323`]. [p. 75]

[312] M. Cacciari, G. P. Salam and G. Soyez, *The anti-k_t jet clustering algorithm*, *JHEP* **04** (2008) 063 [`0802.1189`]. [p. 75]

[313] S. Gangal, J. R. Gaunt, M. Stahlhofen and F. J. Tackmann, *Two-Loop Beam and Soft Functions for Rapidity-Dependent Jet Vetoes*, *JHEP* **02** (2017) 026 [`1608.01999`]. [pp. 76, 80, 88, 112, 118, 119, and 211]

[314] M. A. Ebert, S. Liebler, I. Moult, I. W. Stewart, F. J. Tackmann, K. Tackmann et al., *Exploiting jet binning to identify the initial state of high-mass resonances*, *Phys. Rev.* **D94** (2016) 051901 [`1605.06114`]. [p. 79]

[315] I. W. Stewart and F. J. Tackmann, *Theory Uncertainties for Higgs and Other Searches Using Jet Bins*, *Phys. Rev.* **D85** (2012) 034011 [`1107.2117`]. [pp. 79 and 125]

[316] D. Y. Shao, C. S. Li and H. T. Li, *Resummation Prediction on Higgs and Vector Boson Associated Production with a Jet Veto at the LHC*, *JHEP* **02** (2014) 117 [`1309.5015`]. [p. 79]

[317] Y. Li and X. Liu, *High precision predictions for exclusive VH production at the LHC*, *JHEP* **06** (2014) 028 [`1401.2149`]. [pp. 79, 88, and 90]

[318] I. Moult and I. W. Stewart, *Jet Vetoes interfering with $H \rightarrow WW$*, *JHEP* **09** (2014) 129 [`1405.5534`]. [p. 79]

[319] P. Jaiswal and T. Okui, *Explanation of the WW excess at the LHC by jet-veto resummation*, *Phys. Rev.* **D90** (2014) 073009 [`1407.4537`]. [p. 79]

[320] T. Becher, R. Frederix, M. Neubert and L. Rothen, *Automated NNLL+NLO resummation for jet-veto cross sections*, *Eur. Phys. J.* **C75** (2015) 154 [`1412.8408`]. [p. 79]

[321] Y. Wang, C. S. Li and Z. L. Liu, *Resummation prediction on gauge boson pair production with a jet veto*, *Phys. Rev.* **D93** (2016) 094020 [`1504.00509`]. [p. 79]

[322] F. J. Tackmann, W. J. Waalewijn and L. Zeune, *Impact of Jet Veto Resummation on Slepton Searches*, *JHEP* **07** (2016) 119 [`1603.03052`]. [pp. 79 and 314]

[323] B. Fuks and R. Ruiz, *A comprehensive framework for studying W' and Z' bosons at hadron colliders with automated jet veto resummation*, *JHEP* **05** (2017) 032 [`1701.05263`]. [p. 79]

[324] ATLAS collaboration, *Performance of pile-up mitigation techniques for jets in pp collisions at $\sqrt{s} = 8$ TeV using the ATLAS detector*, *Eur. Phys. J.* **C76** (2016) 581 [`1510.03823`]. [p. 80]

[325] ATLAS collaboration, *Measurements of Higgs boson properties in the diphoton decay channel with 36 fb^{-1} of pp collision data at $\sqrt{s} = 13$ TeV with the ATLAS detector*, *Phys. Rev.* **D98** (2018) 052005 [`1802.04146`]. [p. 80]

[326] A. Hornig, Y. Makris and T. Mehen, *Jet Shapes in Dijet Events at the LHC in SCET*, *JHEP* **04** (2016) 097 [`1601.01319`]. [pp. 81, 93, and 96]

[327] A. Hornig, D. Kang, Y. Makris and T. Mehen, *Transverse Vetoes with Rapidity Cutoff in SCET*, *JHEP* **12** (2017) 043 [`1708.08467`]. [pp. 81, 93, 96, 97, 106, and 114]

[328] D. Kang, Y. Makris and T. Mehen, *From Underlying Event Sensitive To Insensitive: Factorization and Resummation*, *JHEP* **09** (2018) 055 [`1803.04413`]. [pp. 81 and 97]

[329] D. J. Scott and W. J. Waalewijn, *The leading jet transverse momentum in inclusive jet production and with a loose jet veto*, *JHEP* **03** (2020) 159 [`1912.06673`]. [pp. 87, 118, 119, 120, and 121]

[330] J. M. Campbell and R. K. Ellis, *An Update on vector boson pair production at hadron colliders*, *Phys. Rev.* **D60** (1999) 113006 [`hep-ph/9905386`]. [pp. 90, 124, 137, 165, and 267]

[331] J. M. Campbell, R. K. Ellis and C. Williams, *Vector boson pair production at the LHC*, *JHEP* **07** (2011) 018 [`1105.0020`]. [pp. 90, 124, 137, and 165]

[332] J. M. Campbell, R. K. Ellis and W. T. Giele, *A Multi-Threaded Version of MCFM*, *Eur. Phys. J.* **C75** (2015) 246 [`1503.06182`]. [pp. 90, 124, 137, 165, and 267]

[333] R. V. Harlander, S. Liebler and H. Mantler, *SusHi: A program for the calculation of Higgs production in gluon fusion and bottom-quark annihilation in the Standard Model and the MSSM*, Comput. Phys. Commun. **184** (2013) 1605 [`1212.3249`]. [pp. 91 and 325]

[334] R. V. Harlander, S. Liebler and H. Mantler, *SusHi Bento: Beyond NNLO and the heavy-top limit*, Comput. Phys. Commun. **212** (2017) 239 [`1605.03190`]. [pp. 91 and 325]

[335] R. V. Harlander and W. B. Kilgore, *Next-to-next-to-leading order Higgs production at hadron colliders*, Phys. Rev. Lett. **88** (2002) 201801 [`hep-ph/0201206`]. [p. 91]

[336] R. Harlander and P. Kant, *Higgs production and decay: Analytic results at next-to-leading order QCD*, JHEP **12** (2005) 015 [`hep-ph/0509189`]. [p. 91]

[337] J. Butterworth et al., *PDF4LHC recommendations for LHC Run II*, J. Phys. **G43** (2016) 023001 [`1510.03865`]. [p. 91]

[338] S. Dulat, T.-J. Hou, J. Gao, M. Guzzi, J. Huston, P. Nadolsky et al., *New parton distribution functions from a global analysis of quantum chromodynamics*, Phys. Rev. **D93** (2016) 033006 [`1506.07443`]. [p. 91]

[339] J. Gao and P. Nadolsky, *A meta-analysis of parton distribution functions*, JHEP **07** (2014) 035 [`1401.0013`]. [p. 91]

[340] S. Carrazza, S. Forte, Z. Kassabov, J. I. Latorre and J. Rojo, *An Unbiased Hessian Representation for Monte Carlo PDFs*, Eur. Phys. J. **C75** (2015) 369 [`1505.06736`]. [p. 91]

[341] Y. Hatta and T. Ueda, *Resummation of non-global logarithms at finite N_c*, Nucl. Phys. **B874** (2013) 808 [`1304.6930`]. [pp. 92 and 134]

[342] S. Caron-Huot, *Resummation of non-global logarithms and the BFKL equation*, JHEP **03** (2018) 036 [`1501.03754`]. [pp. 92 and 134]

[343] A. J. Larkoski, I. Moult and D. Neill, *Non-Global Logarithms, Factorization, and the Soft Substructure of Jets*, JHEP **09** (2015) 143 [`1501.04596`]. [pp. 92, 95, and 134]

[344] T. Becher, M. Neubert, L. Rothen and D. Y. Shao, *Factorization and Resummation for Jet Processes*, JHEP **11** (2016) 019 [`1605.02737`]. [p. 92]

[345] D. W. Kolodrubetz, P. Pietrulewicz, I. W. Stewart, F. J. Tackmann and W. J. Waalewijn, *Factorization for Jet Radius Logarithms in Jet Mass Spectra at the LHC*, JHEP **12** (2016) 054 [`1605.08038`]. [pp. 92 and 134]

[346] S. D. Ellis, C. K. Vermilion, J. R. Walsh, A. Hornig and C. Lee, *Jet Shapes and Jet Algorithms in SCET*, JHEP **11** (2010) 101 [`1001.0014`]. [p. 93]

[347] M. Procura and W. J. Waalewijn, *Fragmentation in Jets: Cone and Threshold Effects*, *Phys. Rev.* **D85** (2012) 114041 [1111.6605]. [pp. 93, 218, and 296]

[348] M. Balsiger, T. Becher and D. Y. Shao, *Non-global logarithms in jet and isolation cone cross sections*, *JHEP* **08** (2018) 104 [1803.07045]. [p. 98]

[349] G. Bell, R. Rahn and J. Talbert, *Generic dijet soft functions at two-loop order: correlated emissions*, *JHEP* **07** (2019) 101 [1812.08690]. [pp. 103 and 211]

[350] G. Bell, R. Rahn and J. Talbert, *Generic dijet soft functions at two-loop order: uncorrelated emissions*, *JHEP* **09** (2020) 015 [2004.08396]. [p. 103]

[351] I. Stewart, *Lecture Notes: 8.851 Effective Field Theory*, Massachusetts Institute of Technology: MIT OpenCourseWare, Spring 2013. [p. 109]

[352] S. Alioli and J. R. Walsh, *Jet Veto Clustering Logarithms Beyond Leading Order*, *JHEP* **03** (2014) 119 [1311.5234]. [pp. 120 and 122]

[353] M. Dasgupta, F. Dreyer, G. P. Salam and G. Soyez, *Small-radius jets to all orders in QCD*, *JHEP* **04** (2015) 039 [1411.5182]. [pp. 120 and 122]

[354] S. Catani and M. Grazzini, *Collinear factorization and splitting functions for next-to-next-to-leading order QCD calculations*, *Phys. Lett. B* **446** (1999) 143 [hep-ph/9810389]. [p. 120]

[355] S. Catani and M. Grazzini, *Infrared factorization of tree level QCD amplitudes at the next-to-next-to-leading order and beyond*, *Nucl. Phys. B* **570** (2000) 287 [hep-ph/9908523]. [p. 120]

[356] M. Ritzmann and W. J. Waalewijn, *Fragmentation in Jets at NNLO*, *Phys. Rev.* **D90** (2014) 054029 [1407.3272]. [p. 121]

[357] Z.-B. Kang, F. Ringer and I. Vitev, *The semi-inclusive jet function in SCET and small radius resummation for inclusive jet production*, *JHEP* **10** (2016) 125 [1606.06732]. [p. 121]

[358] G. Lustermans, *Scaling up the detail in particle collisions: Factorization and resummation for predictions of multi-differential cross sections*, Ph.D. thesis, Nikhef, Amsterdam, Amsterdam, 2019. [pp. 133 and 173]

[359] J. C. Collins, D. E. Soper and G. F. Sterman, *Factorization of Hard Processes in QCD*, *Adv. Ser. Direct. High Energy Phys.* **5** (1989) 1 [hep-ph/0409313]. [p. 133]

[360] A. Banfi, G. P. Salam and G. Zanderighi, *Semi-numerical resummation of event shapes*, *JHEP* **01** (2002) 018 [hep-ph/0112156]. [p. 133]

[361] A. Banfi, G. P. Salam and G. Zanderighi, *Principles of general final-state resummation and automated implementation*, *JHEP* **03** (2005) 073 [hep-ph/0407286]. [p. 133]

[362] A. Banfi, H. McAslan, P. F. Monni and G. Zanderighi, *A general method for the resummation of event-shape distributions in e^+e^- annihilation*, *JHEP* **05** (2015) 102 [1412.2126]. [p. 133]

[363] W. Bizoń, P. F. Monni, E. Re, L. Rottoli and P. Torrielli, *Momentum-space resummation for transverse observables and the Higgs $p_\perp$ at $N^3LL+NNLO$*, *JHEP* **02** (2018) 108 [1705.09127]. [pp. 133, 226, and 278]

[364] T. Sjöstrand, S. Mrenna and P. Z. Skands, *PYTHIA 6.4 Physics and Manual*, *JHEP* **05** (2006) 026 [hep-ph/0603175]. [p. 133]

[365] T. Sjöstrand, S. Ask, J. R. Christiansen, R. Corke, N. Desai, P. Ilten et al., *An Introduction to PYTHIA 8.2*, *Comput. Phys. Commun.* **191** (2015) 159 [1410.3012]. [p. 133]

[366] M. Bahr et al., *Herwig++ Physics and Manual*, *Eur. Phys. J.* **C58** (2008) 639 [0803.0883]. [p. 133]

[367] J. Bellm et al., *Herwig 7.0/Herwig++ 3.0 release note*, *Eur. Phys. J.* **C76** (2016) 196 [1512.01178]. [p. 133]

[368] T. Gleisberg, S. Hoeche, F. Krauss, M. Schonherr, S. Schumann, F. Siegert et al., *Event generation with SHERPA 1.1*, *JHEP* **02** (2009) 007 [0811.4622]. [p. 133]

[369] M. Dasgupta, F. A. Dreyer, K. Hamilton, P. F. Monni and G. P. Salam, *Logarithmic accuracy of parton showers: a fixed-order study*, *JHEP* **09** (2018) 033 [1805.09327]. [p. 134]

[370] Z. Nagy and D. E. Soper, *Parton showers with quantum interference*, *JHEP* **09** (2007) 114 [0706.0017]. [p. 134]

[371] Z. Nagy and D. E. Soper, *Parton shower evolution with subleading color*, *JHEP* **06** (2012) 044 [1202.4496]. [p. 134]

[372] Z. Nagy and D. E. Soper, *What is a parton shower?*, *Phys. Rev. D* **98** (2018) 014034 [1705.08093]. [p. 134]

[373] Z. Nagy and D. E. Soper, *Parton showers with more exact color evolution*, *Phys. Rev. D* **99** (2019) 054009 [1902.02105]. [p. 134]

[374] M. Dasgupta, F. A. Dreyer, K. Hamilton, P. F. Monni, G. P. Salam and G. Soyez, *Parton showers beyond leading logarithmic accuracy*, *Phys. Rev. Lett.* **125** (2020) 052002 [2002.11114]. [p. 134]

[375] H.-n. Li, *Unification of the k_T and threshold resummations*, Phys. Lett. **B454** (1999) 328 [`hep-ph/9812363`]. [pp. 134 and 218]

[376] E. Laenen, G. F. Sterman and W. Vogelsang, *Recoil and threshold corrections in short distance cross-sections*, Phys. Rev. **D63** (2001) 114018 [`hep-ph/0010080`]. [pp. 134 and 218]

[377] A. Kulesza, G. F. Sterman and W. Vogelsang, *Joint resummation in electroweak boson production*, Phys. Rev. **D66** (2002) 014011 [`hep-ph/0202251`]. [pp. 134 and 218]

[378] A. Kulesza, G. F. Sterman and W. Vogelsang, *Joint resummation for Higgs production*, Phys. Rev. **D69** (2004) 014012 [`hep-ph/0309264`]. [pp. 134 and 218]

[379] G. Lustermans, W. J. Waalewijn and L. Zeune, *Joint transverse momentum and threshold resummation beyond NLL*, Phys. Lett. **B762** (2016) 447 [`1605.02740`]. [pp. 134, 218, 219, 220, 222, and 223]

[380] S. Marzani and V. Theeuwes, *Vector boson production in joint resummation*, JHEP **02** (2017) 127 [`1612.01432`]. [p. 134]

[381] C. Muselli, S. Forte and G. Ridolfi, *Combined threshold and transverse momentum resummation for inclusive observables*, JHEP **03** (2017) 106 [`1701.01464`]. [p. 134]

[382] S. Marzani, *Combining Q_T and small-x resummations*, Phys. Rev. **D93** (2016) 054047 [`1511.06039`]. [p. 134]

[383] P. Pietrulewicz, F. J. Tackmann and W. J. Waalewijn, *Factorization and Resummation for Generic Hierarchies between Jets*, JHEP **08** (2016) 002 [`1601.05088`]. [p. 134]

[384] A. J. Larkoski, I. Moult and D. Neill, *Toward Multi-Differential Cross Sections: Measuring Two Angularities on a Single Jet*, JHEP **09** (2014) 046 [`1401.4458`]. [p. 134]

[385] M. Procura, W. J. Waalewijn and L. Zeune, *Joint resummation of two angularities at next-to-next-to-leading logarithmic order*, JHEP **10** (2018) 098 [`1806.10622`]. [p. 134]

[386] X. Liu, S.-O. Moch and F. Ringer, *Threshold and jet radius joint resummation for single-inclusive jet production*, Phys. Rev. Lett. **119** (2017) 212001 [`1708.04641`]. [p. 134]

[387] X. Liu, S.-O. Moch and F. Ringer, *Phenomenology of single-inclusive jet production with jet radius and threshold resummation*, Phys. Rev. **D97** (2018) 056026 [`1801.07284`]. [p. 134]

References

[388] S. Fleming, A. H. Hoang, S. Mantry and I. W. Stewart, *Jets from massive unstable particles: Top-mass determination*, Phys. Rev. **D77** (2008) 074010 [hep-ph/0703207]. [p. 134]

[389] D. Bertolini, D. Kolodrubetz, D. Neill, P. Pietrulewicz, I. W. Stewart, F. J. Tackmann et al., *Soft Functions for Generic Jet Algorithms and Observables at Hadron Colliders*, JHEP **07** (2017) 099 [1704.08262]. [pp. 134 and 211]

[390] M. Dasgupta and G. P. Salam, *Resummation of nonglobal QCD observables*, Phys. Lett. **B512** (2001) 323 [hep-ph/0104277]. [p. 134]

[391] A. Banfi, G. Marchesini and G. Smye, *Away from jet energy flow*, JHEP **08** (2002) 006 [hep-ph/0206076]. [p. 134]

[392] T. Becher, M. Neubert, L. Rothen and D. Y. Shao, *Effective Field Theory for Jet Processes*, Phys. Rev. Lett. **116** (2016) 192001 [1508.06645]. [p. 134]

[393] P. F. Monni, L. Rottoli and P. Torrielli, *Higgs transverse momentum with a jet veto: a double-differential resummation*, Phys. Rev. Lett. **124** (2020) 252001 [1909.04704]. [p. 134]

[394] S. Kallweit, E. Re, L. Rottoli and M. Wiesemann, *Accurate single- and double-differential resummation of colour-singlet processes with MATRIX+RadISH: W^+W^- production at the LHC*, 2004.07720. [pp. 134, 226, and 262]

[395] ATLAS collaboration, *Measurement of event-shape observables in $Z \to \ell^+\ell^-$ events in pp collisions at $\sqrt{s} = 7$ TeV with the ATLAS detector at the LHC*, Eur. Phys. J. **C76** (2016) 375 [1602.08980]. [pp. 135 and 292]

[396] S. Alioli, C. W. Bauer, C. J. Berggren, A. Hornig, F. J. Tackmann, C. K. Vermilion et al., *Combining Higher-Order Resummation with Multiple NLO Calculations and Parton Showers in GENEVA*, JHEP **09** (2013) 120 [1211.7049]. [pp. 135 and 293]

[397] J. R. Gaunt and M. Stahlhofen, *The Fully-Differential Quark Beam Function at NNLO*, JHEP **12** (2014) 146 [1409.8281]. [pp. 136, 176, 192, and 211]

[398] A. Jain, M. Procura and W. J. Waalewijn, *Fully-Unintegrated Parton Distribution and Fragmentation Functions at Perturbative k_T*, JHEP **04** (2012) 132 [1110.0839]. [pp. 138, 139, 151, 176, 192, and 211]

[399] D. Neill, I. Z. Rothstein and V. Vaidya, *The Higgs Transverse Momentum Distribution at NNLL and its Theoretical Errors*, JHEP **12** (2015) 097 [1503.00005]. [pp. 144 and 226]

[400] U. D'Alesio, M. G. Echevarria, S. Melis and I. Scimemi, *Non-perturbative QCD effects in q_T spectra of Drell-Yan and Z-boson production*, JHEP **11** (2014) 098 [1407.3311]. [p. 145]

[401] P. V. Landshoff and J. C. Polkinghorne, *Calorimeter Triggers for Hard Collisions*, *Phys. Rev.* **D18** (1978) 3344. [p. 150]

[402] C. Goebel, F. Halzen and D. M. Scott, *Double Drell-Yan Annihilations in Hadron Collisions: Novel Tests of the Constituent Picture*, *Phys. Rev.* **D22** (1980) 2789. [p. 150]

[403] F. Takagi, *Multiple Production of Quark Jets Off Nuclei*, *Phys. Rev. Lett.* **43** (1979) 1296. [p. 150]

[404] H. D. Politzer, *Power Corrections at Short Distances*, *Nucl. Phys.* **B172** (1980) 349. [p. 150]

[405] S. Mantry and F. Petriello, *Transverse Momentum Distributions from Effective Field Theory with Numerical Results*, *Phys. Rev.* **D83** (2011) 053007 [`1007.3773`]. [p. 151]

[406] D. Bonocore, E. Laenen, L. Magnea, L. Vernazza and C. D. White, *Non-abelian factorisation for next-to-leading-power threshold logarithms*, *JHEP* **12** (2016) 121 [`1610.06842`]. [p. 173]

[407] V. Del Duca, E. Laenen, L. Magnea, L. Vernazza and C. D. White, *Universality of next-to-leading power threshold effects for colourless final states in hadronic collisions*, *JHEP* **11** (2017) 057 [`1706.04018`]. [p. 173]

[408] M. Beneke, A. Broggio, S. Jaskiewicz and L. Vernazza, *Threshold factorization of the Drell-Yan process at next-to-leading power*, *JHEP* **07** (2020) 078 [`1912.01585`]. [pp. 173 and 295]

[409] A. Ajjath, P. Mukherjee and V. Ravindran, *On next to soft corrections to Drell-Yan and Higgs Boson productions*, `2006.06726`. [p. 173]

[410] M. Beneke, M. Garny, S. Jaskiewicz, R. Szafron, L. Vernazza and J. Wang, *Large-x resummation of off-diagonal deep-inelastic parton scattering from d-dimensional refactorization*, `2008.04943`. [p. 173]

[411] J. R. Gaunt and M. Stahlhofen, *The fully-differential gluon beam function at NNLO*, *JHEP* **07** (2020) 234 [`2004.11915`]. [pp. 176 and 294]

[412] M. Fickinger, S. Fleming, C. Kim and E. Mereghetti, *Effective field theory approach to heavy quark fragmentation*, *JHEP* **11** (2016) 095 [`1606.07737`]. [pp. 191 and 296]

[413] C. Duhr and F. Dulat, *PolyLogTools – polylogs for the masses*, *JHEP* **08** (2019) 135 [`1904.07279`]. [p. 195]

[414] C. Anastasiou, L. J. Dixon and K. Melnikov, *NLO Higgs boson rapidity distributions at hadron colliders*, *Nucl. Phys. Proc. Suppl.* **116** (2003) 193 [`hep-ph/0211141`]. [pp. 196 and 325]

[415] J. Kubar, M. Le Bellac, J. L. Meunier and G. Plaut, *QCD Corrections to the Drell-Yan Mechanism and the Pion Structure Function*, Nucl. Phys. **B175** (1980) 251. [pp. 196 and 325]

[416] P. Mathews, V. Ravindran, K. Sridhar and W. L. van Neerven, *Next-to-leading order QCD corrections to the Drell-Yan cross section in models of TeV-scale gravity*, Nucl. Phys. **B713** (2005) 333 [`hep-ph/0411018`]. [pp. 196 and 325]

[417] E. Laenen and G. F. Sterman, *Resummation for Drell-Yan differential distributions*, in *The Fermilab Meeting DPF 92. Proceedings, 7th Meeting of the American Physical Society, Division of Particles and Fields*, pp. 987–989, 11, 1992, http://lss.fnal.gov/cgi-bin/find_paper.pl?conf-92-359. [p. 201]

[418] D. Gutierrez-Reyes, I. Scimemi, W. J. Waalewijn and L. Zoppi, *Transverse momentum dependent distributions in e^+e^- and semi-inclusive deep-inelastic scattering using jets*, JHEP **10** (2019) 031 [`1904.04259`]. [p. 211]

[419] T. Kasemets, W. J. Waalewijn and L. Zeune, *Calculating Soft Radiation at One Loop*, JHEP **03** (2016) 153 [`1512.00857`]. [p. 211]

[420] P. Pietrulewicz, D. Samitz, A. Spiering and F. J. Tackmann, *Factorization and Resummation for Massive Quark Effects in Exclusive Drell-Yan*, JHEP **08** (2017) 114 [`1703.09702`]. [pp. 211, 226, and 263]

[421] Y. Li, S. Mantry and F. Petriello, *An Exclusive Soft Function for Drell-Yan at Next-to-Next-to-Leading Order*, Phys. Rev. **D84** (2011) 094014 [`1105.5171`]. [pp. 216 and 219]

[422] T. Becher and G. Bell, *Analytic Regularization in Soft-Collinear Effective Theory*, Phys. Lett. **B713** (2012) 41 [`1112.3907`]. [p. 222]

[423] ATLAS collaboration, *Measurement of angular correlations in Drell-Yan lepton pairs to probe Z/gamma* boson transverse momentum at sqrt(s)=7 TeV with the ATLAS detector*, Phys. Lett. B **720** (2013) 32 [`1211.6899`]. [p. 225]

[424] ATLAS collaboration, *Measurement of the Z/γ^* boson transverse momentum distribution in pp collisions at $\sqrt{s} = 7$ TeV with the ATLAS detector*, JHEP **09** (2014) 145 [`1406.3660`]. [p. 225]

[425] ATLAS collaboration, *Measurement of the forward-backward asymmetry of electron and muon pair-production in pp collisions at $\sqrt{s} = 7$ TeV with the ATLAS detector*, JHEP **09** (2015) 049 [`1503.03709`]. [pp. 225 and 239]

[426] ATLAS collaboration, *Measurement of the transverse momentum and ϕ_η^* distributions of Drell-Yan lepton pairs in proton-proton collisions at $\sqrt{s} = 8$ TeV with the ATLAS detector*, Eur. Phys. J. **C76** (2016) 291 [`1512.02192`]. [pp. 225, 228, 283, 284, 286, 287, 336, and 337]

[427] ATLAS collaboration, *Measurement of the angular coefficients in Z-boson events using electron and muon pairs from data taken at $\sqrt{s} = 8$ TeV with the ATLAS detector*, *JHEP* **08** (2016) 159 [`1606.00689`]. [pp. 225, 239, 242, and 246]

[428] CMS collaboration, *Measurement of the Rapidity and Transverse Momentum Distributions of Z Bosons in pp Collisions at $\sqrt{s} = 7$ TeV*, *Phys. Rev. D* **85** (2012) 032002 [`1110.4973`]. [p. 225]

[429] CMS collaboration, *Measurement of the Z boson differential cross section in transverse momentum and rapidity in proton–proton collisions at 8 TeV*, *Phys. Lett. B* **749** (2015) 187 [`1504.03511`]. [p. 225]

[430] CMS collaboration, *Angular coefficients of Z bosons produced in pp collisions at $\sqrt{s}$ = 8 TeV and decaying to $\mu^+\mu^-$ as a function of transverse momentum and rapidity*, *Phys. Lett. B* **750** (2015) 154 [`1504.03512`]. [pp. 225, 239, 242, and 246]

[431] CMS collaboration, *Measurement of differential cross sections in the kinematic angular variable ϕ^* for inclusive Z boson production in pp collisions at $\sqrt{s} = 8$ TeV*, *JHEP* **03** (2018) 172 [`1710.07955`]. [p. 225]

[432] CMS collaboration, *Measurement of the weak mixing angle using the forward-backward asymmetry of Drell-Yan events in pp collisions at 8 TeV*, *Eur. Phys. J.* **C78** (2018) 701 [`1806.00863`]. [pp. 225 and 239]

[433] C. Balazs, J.-w. Qiu and C. Yuan, *Effects of QCD resummation on distributions of leptons from the decay of electroweak vector bosons*, *Phys. Lett. B* **355** (1995) 548 [`hep-ph/9505203`]. [pp. 226, 228, and 261]

[434] C. Balazs and C. Yuan, *Soft gluon effects on lepton pairs at hadron colliders*, *Phys. Rev. D* **56** (1997) 5558 [`hep-ph/9704258`]. [pp. 226, 228, and 261]

[435] R. Ellis, D. Ross and S. Veseli, *Vector boson production in hadronic collisions*, *Nucl. Phys. B* **503** (1997) 309 [`hep-ph/9704239`]. [pp. 226, 228, and 261]

[436] G. Bozzi, S. Catani, D. de Florian and M. Grazzini, *Transverse-momentum resummation and the spectrum of the Higgs boson at the LHC*, *Nucl. Phys.* **B737** (2006) 73 [`hep-ph/0508068`]. [p. 226]

[437] G. Bozzi, S. Catani, G. Ferrera, D. de Florian and M. Grazzini, *Production of Drell-Yan lepton pairs in hadron collisions: Transverse-momentum resummation at next-to-next-to-leading logarithmic accuracy*, *Phys. Lett. B* **696** (2011) 207 [`1007.2351`]. [p. 226]

[438] A. Banfi, M. Dasgupta, S. Marzani and L. Tomlinson, *Predictions for Drell-Yan ϕ^* and Q_T observables at the LHC*, *Phys. Lett.* **B715** (2012) 152 [`1205.4760`]. [pp. 226 and 278]

[439] S. Catani, D. de Florian, G. Ferrera and M. Grazzini, *Vector boson production at hadron colliders: transverse-momentum resummation and leptonic decay*, JHEP **12** (2015) 047 [1507.06937]. [pp. 226, 228, 261, 262, and 278]

[440] S. Camarda et al., *DYTurbo: Fast predictions for Drell-Yan processes*, Eur. Phys. J. C **80** (2020) 251 [1910.07049]. [pp. 226, 228, 261, and 262]

[441] J. Collins, L. Gamberg, A. Prokudin, T. Rogers, N. Sato and B. Wang, *Relating Transverse Momentum Dependent and Collinear Factorization Theorems in a Generalized Formalism*, Phys. Rev. D **94** (2016) 034014 [1605.00671]. [p. 226]

[442] D. Kang, C. Lee and V. Vaidya, *A fast and accurate method for perturbative resummation of transverse momentum-dependent observables*, JHEP **04** (2018) 149 [1710.00078]. [p. 226]

[443] F. Coradeschi and T. Cridge, *reSolve — A transverse momentum resummation tool*, Comput. Phys. Commun. **238** (2019) 262 [1711.02083]. [p. 226]

[444] X. Chen, T. Gehrmann, E. W. N. Glover, A. Huss, Y. Li, D. Neill et al., *Precise QCD Description of the Higgs Boson Transverse Momentum Spectrum*, Phys. Lett. **B788** (2019) 425 [1805.00736]. [p. 226]

[445] W. Bizoń, X. Chen, A. Gehrmann-De Ridder, T. Gehrmann, N. Glover, A. Huss et al., *Fiducial distributions in Higgs and Drell-Yan production at $N^3LL+NNLO$*, JHEP **12** (2018) 132 [1805.05916]. [pp. 226, 262, and 278]

[446] T. Becher and M. Hager, *Event-Based Transverse Momentum Resummation*, Eur. Phys. J. C **79** (2019) 665 [1904.08325]. [pp. 226 and 278]

[447] W. Bizoń, A. Gehrmann-De Ridder, T. Gehrmann, N. Glover, A. Huss, P. F. Monni et al., *The transverse momentum spectrum of weak gauge bosons at $N^3LL+NNLO$*, Eur. Phys. J. C **79** (2019) 868 [1905.05171]. [p. 226]

[448] L. Cieri, G. Ferrera and G. F. Sborlini, *Combining QED and QCD transverse-momentum resummation for Z boson production at hadron colliders*, JHEP **08** (2018) 165 [1805.11948]. [p. 226]

[449] A. Bacchetta and M. G. Echevarria, *$QCD \times QED$ evolution of TMDs*, Phys. Lett. B **788** (2019) 280 [1810.02297]. [p. 226]

[450] G. Billis, F. J. Tackmann and J. Talbert, *Higher-Order Sudakov Resummation in Coupled Gauge Theories*, JHEP **03** (2020) 182 [1907.02971]. [pp. 226, 316, and 317]

[451] R. Boughezal, F. Caola, K. Melnikov, F. Petriello and M. Schulze, *Higgs boson production in association with a jet at next-to-next-to-leading order*, Phys. Rev. Lett. **115** (2015) 082003 [1504.07922]. [p. 226]

[452] A. Gehrmann-De Ridder, T. Gehrmann, E. Glover, A. Huss and T. Morgan, *Precise QCD predictions for the production of a Z boson in association with a hadronic jet*, *Phys. Rev. Lett.* **117** (2016) 022001 [`1507.02850`]. [p. 226]

[453] F. Caola, K. Melnikov and M. Schulze, *Fiducial cross sections for Higgs boson production in association with a jet at next-to-next-to-leading order in QCD*, *Phys. Rev. D* **92** (2015) 074032 [`1508.02684`]. [p. 226]

[454] R. Boughezal, J. M. Campbell, R. Ellis, C. Focke, W. T. Giele, X. Liu et al., *Z-boson production in association with a jet at next-to-next-to-leading order in perturbative QCD*, *Phys. Rev. Lett.* **116** (2016) 152001 [`1512.01291`]. [p. 226]

[455] A. Gehrmann-De Ridder, T. Gehrmann, E. W. N. Glover, A. Huss and T. A. Morgan, *NNLO QCD corrections for Drell-Yan p_T^Z and ϕ^* observables at the LHC*, *JHEP* **11** (2016) 094 [`1610.01843`]. [p. 226]

[456] R. Gauld, A. Gehrmann-De Ridder, T. Gehrmann, E. W. N. Glover and A. Huss, *Precise predictions for the angular coefficients in Z-boson production at the LHC*, *JHEP* **11** (2017) 003 [`1708.00008`]. [pp. 226, 227, and 237]

[457] A. Gehrmann-De Ridder, T. Gehrmann, E. Glover, A. Huss and D. Walker, *Next-to-Next-to-Leading-Order QCD Corrections to the Transverse Momentum Distribution of Weak Gauge Bosons*, *Phys. Rev. Lett.* **120** (2018) 122001 [`1712.07543`]. [p. 226]

[458] M. Grazzini, S. Kallweit, S. Pozzorini, D. Rathlev and M. Wiesemann, W^+W^- *production at the LHC: fiducial cross sections and distributions in NNLO QCD*, *JHEP* **08** (2016) 140 [`1605.02716`]. [p. 226]

[459] M. A. Ebert and F. J. Tackmann, *Impact of isolation and fiducial cuts on q_T and N-jettiness subtractions*, *JHEP* **03** (2020) 158 [`1911.08486`]. [pp. 226 and 268]

[460] C. S. Lam and W.-K. Tung, *A Systematic Approach to Inclusive Lepton Pair Production in Hadronic Collisions*, *Phys. Rev.* **D18** (1978) 2447. [pp. 227 and 237]

[461] E. Mirkes, *Angular decay distribution of leptons from W bosons at NLO in hadronic collisions*, *Nucl. Phys.* **B387** (1992) 3. [pp. 227 and 236]

[462] D. Boer and W. Vogelsang, *Drell-Yan lepton angular distribution at small transverse momentum*, *Phys. Rev.* **D74** (2006) 014004 [`hep-ph/0604177`]. [pp. 227, 237, 253, 256, 260, and 261]

[463] S. Arnold, A. Metz and M. Schlegel, *Dilepton production from polarized hadron hadron collisions*, *Phys. Rev. D* **79** (2009) 034005 [`0809.2262`]. [pp. 227, 235, and 237]

[464] S. L. Adler, *Axial vector vertex in spinor electrodynamics*, *Phys. Rev.* **177** (1969) 2426. [p. 230]

[465] J. S. Bell and R. Jackiw, *A PCAC puzzle: $\pi^0 \to \gamma\gamma$ in the σ model*, *Nuovo Cim.* **A60** (1969) 47. [p. 230]

[466] S. L. Adler and W. A. Bardeen, *Absence of higher order corrections in the anomalous axial vector divergence equation*, *Phys. Rev.* **182** (1969) 1517. [p. 230]

[467] S. Larin, *The Renormalization of the axial anomaly in dimensional regularization*, *Phys. Lett. B* **303** (1993) 113 [`hep-ph/9302240`]. [p. 230]

[468] W. Bernreuther, R. Bonciani, T. Gehrmann, R. Heinesch, T. Leineweber and E. Remiddi, *Two-loop QCD corrections to the heavy quark form-factors: Anomaly contributions*, *Nucl. Phys.* **B723** (2005) 91 [`hep-ph/0504190`]. [p. 230]

[469] D. A. Dicus and S. S. Willenbrock, *Radiative Corrections to the Ratio of Z and W Boson Production*, *Phys. Rev. D* **34** (1986) 148. [pp. 231 and 307]

[470] J. C. Collins and D. E. Soper, *Angular Distribution of Dileptons in High-Energy Hadron Collisions*, *Phys. Rev.* **D16** (1977) 2219. [pp. 233 and 235]

[471] L. Buonocore, M. Grazzini and F. Tramontano, *The q_T subtraction method: electroweak corrections and power suppressed contributions*, *Eur. Phys. J. C* **80** (2020) 254 [`1911.10166`]. [p. 247]

[472] K. Hagiwara, K.-i. Hikasa and N. Kai, *Parity Odd Asymmetries in W-Jet Events at Hadron Colliders*, *Phys. Rev. Lett.* **52** (1984) 1076. [p. 248]

[473] D. Boer, *Investigating the origins of transverse spin asymmetries at RHIC*, *Phys. Rev.* **D60** (1999) 014012 [`hep-ph/9902255`]. [p. 253]

[474] D. Boer, S. J. Brodsky and D. S. Hwang, *Initial state interactions in the unpolarized Drell-Yan process*, *Phys. Rev. D* **67** (2003) 054003 [`hep-ph/0211110`]. [p. 253]

[475] X. Wang, W. Mao and Z. Lu, *Boer-Mulders effect in the unpolarized pion induced DrellYan process at COMPASS within TMD factorization*, *Eur. Phys. J.* **C78** (2018) 643 [`1805.03017`]. [p. 253]

[476] D. Boer and P. J. Mulders, *Time reversal odd distribution functions in leptoproduction*, *Phys. Rev.* **D57** (1998) 5780 [`hep-ph/9711485`]. [p. 253]

[477] A. Bacchetta, D. Boer, M. Diehl and P. J. Mulders, *Matches and mismatches in the descriptions of semi-inclusive processes at low and high transverse momentum*, *JHEP* **08** (2008) 023 [`0803.0227`]. [p. 253]

[478] I. Scimemi and A. Vladimirov, *Matching of transverse momentum dependent distributions at twist-3*, *Eur. Phys. J.* **C78** (2018) 802 [`1804.08148`]. [p. 253]

[479] A. Bacchetta, G. Bozzi, M. G. Echevarria, C. Pisano, A. Prokudin and M. Radici, *Azimuthal asymmetries in unpolarized SIDIS and Drell-Yan processes: a case study towards TMD factorization at subleading twist*, Phys. Lett. B **797** (2019) 134850 [`1906.07037`]. [p. 256]

[480] K. S. Lee and I. W. Stewart, *Factorization for power corrections to $B \to X_s \gamma$ and $B \to X_u \ell \bar{\nu}$*, Nucl. Phys. B **721** (2005) 325 [`hep-ph/0409045`]. [p. 256]

[481] M. Beneke and T. Feldmann, *Factorization of heavy to light form-factors in soft collinear effective theory*, Nucl. Phys. **B685** (2004) 249 [`hep-ph/0311335`]. [p. 256]

[482] S. M. Freedman, *Subleading Corrections To Thrust Using Effective Field Theory*, `1303.1558`. [p. 256]

[483] I. Moult, I. W. Stewart and G. Vita, *Subleading Power Factorization with Radiative Functions*, JHEP **11** (2019) 153 [`1905.07411`]. [pp. 256 and 257]

[484] I. Moult, M. P. Solon, I. W. Stewart and G. Vita, *Fermionic Glauber Operators and Quark Reggeization*, JHEP **02** (2018) 134 [`1709.09174`]. [p. 257]

[485] C.-H. Chang, I. W. Stewart and G. Vita, *Operator approach to q_T distributions and the Regge limit beyond leading power*, to appear (MIT-CTP 5024), 2020. [p. 257]

[486] M. A. Ebert, I. Moult, I. W. Stewart, F. J. Tackmann, G. Vita and H. X. Zhu, *Power Corrections for N-Jettiness Subtractions at $\mathcal{O}(\alpha_s)$*, JHEP **12** (2018) 084 [`1807.10764`]. [pp. 257 and 261]

[487] I. Moult, L. Rothen, I. W. Stewart, F. J. Tackmann and H. X. Zhu, *Subleading Power Corrections for N-Jettiness Subtractions*, Phys. Rev. **D95** (2017) 074023 [`1612.00450`]. [p. 261]

[488] I. Moult, L. Rothen, I. W. Stewart, F. J. Tackmann and H. X. Zhu, *N-jettiness subtractions for $gg \to H$ at subleading power*, Phys. Rev. **D97** (2018) 014013 [`1710.03227`]. [p. 261]

[489] I. Scimemi and A. Vladimirov, *Analysis of vector boson production within TMD factorization*, Eur. Phys. J. C **78** (2018) 89 [`1706.01473`]. [p. 261]

[490] T. Hahn, *CUBA: A Library for multidimensional numerical integration*, Comput. Phys. Commun. **168** (2005) 78 [`hep-ph/0404043`]. [p. 267]

[491] T. Hahn, *Concurrent Cuba*, J. Phys. Conf. Ser. **608** (2015) 012066 [`1408.6373`]. [p. 267]

[492] H. Takahasi and M. Mori, *Double exponential formulas for numerical integration*, Pub. RIMS **9** (1974) 721. [p. 267]

[493] T. Ooura, *A continuous euler transformation and its application to the fourier transform of a slowly decaying function, J. Comput. Appl. Math.* **130** (2001) 259270. [p. 267]

[494] T. Ooura, *Study on numerical integration of Fourier type integrals*, Ph.D. thesis, University of Tokyo, 1997. [p. 267]

[495] R. Boughezal, J. M. Campbell, R. K. Ellis, C. Focke, W. Giele, X. Liu et al., *Color singlet production at NNLO in MCFM, Eur. Phys. J.* **C77** (2017) 7 [1605.08011]. [p. 267]

[496] A. Glazov, *Defiducialization: Providing Experimental Measurements for Accurate Fixed-Order Predictions*, 2001.02933. [p. 273]

[497] A. Banfi, S. Redford, M. Vesterinen, P. Waller and T. R. Wyatt, *Optimisation of variables for studying dilepton transverse momentum distributions at hadron colliders, Eur. Phys. J.* **C71** (2011) 1600 [1009.1580]. [pp. 277 and 278]

[498] OPAL collaboration, K. Ackerstaff et al., *Search for anomalous production of dilepton events with missing transverse momentum in e^+e^- collisions at $\sqrt{s} = 161$ GeV and 172 GeV, Eur. Phys. J.* **C4** (1998) 47 [hep-ex/9710010]. [p. 277]

[499] M. Vesterinen and T. R. Wyatt, *A Novel Technique for Studying the Z Boson Transverse Momentum Distribution at Hadron Colliders, Nucl. Instrum. Meth.* **A602** (2009) 432 [0807.4956]. [p. 277]

[500] A. Banfi, M. Dasgupta and R. M. Duran Delgado, *The a_T distribution of the Z boson at hadron colliders, JHEP* **12** (2009) 022 [0909.5327]. [pp. 278 and 280]

[501] A. Banfi, M. Dasgupta and S. Marzani, *QCD predictions for new variables to study dilepton transverse momenta at hadron colliders, Phys. Lett.* **B701** (2011) 75 [1102.3594]. [pp. 278 and 280]

[502] A. Banfi, M. Dasgupta, S. Marzani and L. Tomlinson, *Probing the low transverse momentum domain of Z production with novel variables, JHEP* **01** (2012) 044 [1110.4009]. [p. 278]

[503] M. Guzzi, P. M. Nadolsky and B. Wang, *Nonperturbative contributions to a resummed leptonic angular distribution in inclusive neutral vector boson production, Phys. Rev.* **D90** (2014) 014030 [1309.1393]. [p. 278]

[504] S. Pascoli, R. Ruiz and C. Weiland, *Heavy neutrinos with dynamic jet vetoes: multilepton searches at $\sqrt{s} = 14$, 27, and 100 TeV, JHEP* **06** (2019) 049 [1812.08750]. [p. 292]

[505] B. Fuks, K. Nordström, R. Ruiz and S. L. Williamson, *Sleptons without Hadrons*, *Phys. Rev. D* **100** (2019) 074010 [`1901.09937`]. [p. 292]

[506] L. Arpino, A. Banfi, S. Jäger and N. Kauer, *BSM WW production with a jet veto*, *JHEP* **08** (2019) 076 [`1905.06646`]. [p. 292]

[507] B. Fuks, M. Nemevšek and R. Ruiz, *Doubly Charged Higgs Boson Production at Hadron Colliders*, *Phys. Rev. D* **101** (2020) 075022 [`1912.08975`]. [p. 292]

[508] M. A. Ebert, B. Mistlberger and G. Vita, *Collinear expansion for color singlet cross sections*, `2006.03055`. [p. 294]

[509] F. Herzog, S. Moch, B. Ruijl, T. Ueda, J. Vermaseren and A. Vogt, *Five-loop contributions to low-N non-singlet anomalous dimensions in QCD*, *Phys. Lett. B* **790** (2019) 436 [`1812.11818`]. [p. 294]

[510] G. Das, S.-O. Moch and A. Vogt, *Soft corrections to inclusive deep-inelastic scattering at four loops and beyond*, *JHEP* **03** (2020) 116 [`1912.12920`]. [p. 294]

[511] A. von Manteuffel, E. Panzer and R. M. Schabinger, *Analytic four-loop anomalous dimensions in massless QCD from form factors*, *Phys. Rev. Lett.* **124** (2020) 162001 [`2002.04617`]. [pp. 294 and 311]

[512] K. Becker et al., *Precise predictions for boosted Higgs production*, `2005.07762`. [p. 296]

[513] D. P. Anderle, F. Ringer and W. Vogelsang, *QCD resummation for semi-inclusive hadron production processes*, *Phys. Rev. D* **87** (2013) 034014 [`1212.2099`]. [p. 296]

[514] A. Accardi et al., *Electron Ion Collider: The Next QCD Frontier: Understanding the glue that binds us all*, *Eur. Phys. J. A* **52** (2016) 268 [`1212.1701`]. [p. 296]

[515] T. Becher and T. Neumann, *Fiducial q_T resummation of color-singlet processes at $N^3LL+NNLO$*, `2009.11437`. [p. 297]

[516] M. Lambertsen and W. Vogelsang, *Drell-Yan lepton angular distributions in perturbative QCD*, *Phys. Rev. D* **93** (2016) 114013 [`1605.02625`]. [p. 298]

[517] S. Frixione and G. Ridolfi, *Jet photoproduction at HERA*, *Nucl. Phys.* **B507** (1997) 315 [`hep-ph/9707345`]. [p. 298]

[518] M. Grazzini, S. Kallweit and M. Wiesemann, *Fully differential NNLO computations with MATRIX*, *Eur. Phys. J.* **C78** (2018) 537 [`1711.06631`]. [p. 298]

[519] M. Höschele, J. Hoff, A. Pak, M. Steinhauser and T. Ueda, *MT: A Mathematica package to compute convolutions*, *Comput. Phys. Commun.* **185** (2014) 528 [`1307.6925`]. [p. 302]

[520] C. W. Bauer, C. Lee, A. V. Manohar and M. B. Wise, *Enhanced nonperturbative effects in Z decays to hadrons*, *Phys. Rev.* **D70** (2004) 034014 [`hep-ph/0309278`]. [p. 307]

[521] G. Kramer and B. Lampe, *Two Jet Cross-Section in e^+e^- Annihilation*, *Z. Phys.* **C34** (1987) 497. [pp. 307 and 313]

[522] T. Matsuura and W. L. van Neerven, *Second Order Logarithmic Corrections to the Drell-Yan Cross-section*, *Z. Phys.* **C38** (1988) 623. [pp. 307 and 313]

[523] T. Matsuura, S. C. van der Marck and W. L. van Neerven, *The Calculation of the Second Order Soft and Virtual Contributions to the Drell-Yan Cross-Section*, *Nucl. Phys.* **B319** (1989) 570. [pp. 307 and 313]

[524] T. Gehrmann, T. Huber and D. Maitre, *Two-loop quark and gluon form-factors in dimensional regularisation*, *Phys. Lett.* **B622** (2005) 295 [`hep-ph/0507061`]. [pp. 307 and 313]

[525] A. Idilbi, X.-d. Ji, J.-P. Ma and F. Yuan, *Threshold resummation for Higgs production in effective field theory*, *Phys. Rev.* **D73** (2006) 077501 [`hep-ph/0509294`]. [p. 307]

[526] O. V. Tarasov, A. A. Vladimirov and A. Yu. Zharkov, *The Gell-Mann-Low Function of QCD in the Three Loop Approximation*, *Phys. Lett.* **B93** (1980) 429. [p. 311]

[527] S. A. Larin and J. A. M. Vermaseren, *The Three loop QCD Beta function and anomalous dimensions*, *Phys. Lett.* **B303** (1993) 334 [`hep-ph/9302208`]. [p. 311]

[528] T. van Ritbergen, J. A. M. Vermaseren and S. A. Larin, *The Four loop beta function in quantum chromodynamics*, *Phys. Lett.* **B400** (1997) 379 [`hep-ph/9701390`]. [p. 311]

[529] M. Czakon, *The Four-loop QCD beta-function and anomalous dimensions*, *Nucl. Phys.* **B710** (2005) 485 [`hep-ph/0411261`]. [p. 311]

[530] G. P. Korchemsky and A. V. Radyushkin, *Renormalization of the Wilson Loops Beyond the Leading Order*, *Nucl. Phys.* **B283** (1987) 342. [p. 311]

[531] J. Henn, A. V. Smirnov, V. A. Smirnov, M. Steinhauser and R. N. Lee, *Four-loop photon quark form factor and cusp anomalous dimension in the large-N_c limit of QCD*, *JHEP* **03** (2017) 139 [`1612.04389`]. [p. 311]

[532] R. N. Lee, A. V. Smirnov, V. A. Smirnov and M. Steinhauser, *Four-loop quark form factor with quartic fundamental colour factor*, *JHEP* **02** (2019) 172 [`1901.02898`]. [p. 311]

[533] J. Henn, T. Peraro, M. Stahlhofen and P. Wasser, *Matter dependence of the four-loop cusp anomalous dimension*, *Phys. Rev. Lett.* **122** (2019) 201602 [`1901.03693`]. [p. 311]

[534] R. Brüser, A. Grozin, J. M. Henn and M. Stahlhofen, *Matter dependence of the four-loop QCD cusp anomalous dimension: from small angles to all angles*, *JHEP* **05** (2019) 186 [`1902.05076`]. [p. 311]

[535] J. M. Henn, G. P. Korchemsky and B. Mistlberger, *The full four-loop cusp anomalous dimension in $\mathcal{N} = 4$ super Yang-Mills and QCD*, *JHEP* **04** (2020) 018 [`1911.10174`]. [p. 311]

[536] G. Curci, W. Furmanski and R. Petronzio, *Evolution of Parton Densities Beyond Leading Order: The Nonsinglet Case*, *Nucl. Phys.* **B175** (1980) 27. [p. 312]

[537] W. Furmanski and R. Petronzio, *Singlet Parton Densities Beyond Leading Order*, *Phys. Lett.* **97B** (1980) 437. [p. 312]

[538] R. K. Ellis and W. Vogelsang, *The Evolution of parton distributions beyond leading order: The Singlet case*, `hep-ph/9602356`. [p. 312]

[539] R. V. Harlander, *Virtual corrections to $gg \rightarrow H$ to two loops in the heavy top limit*, *Phys. Lett.* **B492** (2000) 74 [`hep-ph/0007289`]. [p. 313]

[540] S. Moch, J. A. M. Vermaseren and A. Vogt, *The Quark form-factor at higher orders*, *JHEP* **08** (2005) 049 [`hep-ph/0507039`]. [p. 313]

[541] S. Moch, J. A. M. Vermaseren and A. Vogt, *Three-loop results for quark and gluon form-factors*, *Phys. Lett.* **B625** (2005) 245 [`hep-ph/0508055`]. [p. 313]

[542] D. Bertolini, M. P. Solon and J. R. Walsh, *Integrated and Differential Accuracy in Resummed Cross Sections*, *Phys. Rev.* **D95** (2017) 054024 [`1701.07919`]. [pp. 330, 333, 334, and 335]

Eidesstattliche Versicherung

Hiermit versichere ich an Eides statt, die vorliegende Dissertationsschrift selbst verfasst und keine anderen als die angegebenen Hilfsmittel und Quellen benutzt zu haben.

Die eingereichte schriftliche Fassung entspricht der auf dem elektronischen Speichermedium.

Die Dissertation wurde in der vorgelegten oder einer ähnlichen Form nicht schon einmal in einem früheren Promotionsverfahren angenommen oder als ungenügend beurteilt.

Hamburg, den 30. 9. 2020

Johannes Michel